Lecture Notes in Physics

Springer
Berlin
Heidelberg
New York
Hong Kong
London
Milan
Paris
Tokyo

Physics and Astronomy ONLINE LIBRARY

http://www.springer.de/phys/

The Editorial Policy for Edited Volumes

The series *Lecture Notes in Physics* (LNP), founded in 1969, reports new developments in physics research and teaching - quickly, informally but with a high degree of quality. Manuscripts to be considered for publication are topical volumes consisting of a limited number of contributions, carefully edited and closely related to each other. Each contribution should contain at least partly original and previously unpublished material, be written in a clear, pedagogical style and aimed at a broader readership, especially graduate students and nonspecialist researchers wishing to familiarize themselves with the topic concerned. For this reason, traditional proceedings cannot be considered for this series though volumes to appear in this series are often based on material presented at conferences, workshops and schools.

Acceptance

A project can only be accepted tentatively for publication, by both the editorial board and the publisher, following thorough examination of the material submitted. The book proposal sent to the publisher should consist at least of a preliminary table of contents outlining the structure of the book together with abstracts of all contributions to be included. Final acceptance is issued by the series editor in charge, in consultation with the publisher, only after receiving the complete manuscript. Final acceptance, possibly requiring minor corrections, usually follows the tentative acceptance unless the final manuscript differs significantly from expectations (project outline). In particular, the series editors are entitled to reject individual contributions if they do not meet the high quality standards of this series. The final manuscript must be ready to print, and should include both an informative introduction and a sufficiently detailed subject index.

Contractual Aspects

Publication in LNP is free of charge. There is no formal contract, no royalties are paid, and no bulk orders are required, although special discounts are offered in this case. The volume editors receive jointly 30 free copies for their personal use and are entitled, as are the contributing authors, to purchase Springer books at a reduced rate. The publisher secures the copyright for each volume. As a rule, no reprints of individual contributions can be supplied.

Manuscript Submission

The manuscript in its final and approved version must be submitted in ready to print form. The corresponding electronic source files are also required for the production process, in particular the online version. Technical assistance in compiling the final manuscript can be provided by the publisher‘s production editor(s), especially with regard to the publisher's own LaTeX macro package which has been specially designed for this series.

LNP Homepage (springerlink.com)

On the LNP homepage you will find:

—The LNP online archive. It contains the full texts (PDF) of all volumes published since 2000. Abstracts, table of contents and prefaces are accessible free of charge to everyone. Information about the availability of printed volumes can be obtained.

—The subscription information. The online archive is free of charge to all subscribers of the printed volumes.

—The editorial contacts, with respect to both scientific and technical matters.

—The author's / editor's instructions.

D. Alloin W. Gieren (Eds.)

Stellar Candles for the Extragalactic Distance Scale

Springer

Editors

Danielle Alloin
European Southern Observatory
Casilla 19001
Santiago, Chile

Wolfgang Gieren
Universidad de Concepción
Dept. de Física
Casilla 160-C
Concepción, Chile

Cataloging-in-Publication Data applied for

A catalog record for this book is available from the Library of Congress.

Bibliographic information published by Die Deutsche Bibliothek
Die Deutsche Bibliothek lists this publication in the Deutsche Nationalbibliografie; detailed bibliographic data is available in the Internet at http://dnb.ddb.de

ISSN 0075-8450
ISBN 3-540-20128-9 Springer-Verlag Berlin Heidelberg New York

Springer-Verlag Berlin Heidelberg New York
a member of BertelsmannSpringer Science+Business Media GmbH

springer.de

Printed in Germany

Typesetting: Camera-ready by the authors/editor
Cover design: *design & production*, Heidelberg

Printed on acid-free paper
54/3141/du - 5 4 3 2 1 0

Lecture Notes in Physics

For information about Vols. 1–590
please contact your bookseller or Springer-Verlag
LNP Online archive: springerlink.com

Vol.591: M. Beyer (Ed.), CP Violation in Particle, Nuclear and Astrophysics.

Vol.592: S. Cotsakis, L. Papantonopoulos (Eds.), Cosmological Crossroads. An Advanced Course in Mathematical, Physical and String Cosmology.

Vol.593: D. Shi, B. Aktaş, L. Pust, F. Mikhailov (Eds.), Nanostructured Magnetic Materials and Their Applications.

Vol.594: S. Odenbach (Ed.),Ferrofluids. Magnetical Controllable Fluids and Their Applications.

Vol.595: C. Berthier, L. P. Lévy, G. Martinez (Eds.), High Magnetic Fields. Applications in Condensed Matter Physics and Spectroscopy.

Vol.596: F. Scheck, H. Upmeier, W. Werner (Eds.), Noncommutative Geometry and the Standard Model of Elememtary Particle Physics.

Vol.597: P. Garbaczewski, R. Olkiewicz (Eds.), Dynamics of Dissipation.

Vol.598: K. Weiler (Ed.), Supernovae and Gamma-Ray Bursters.

Vol.599: J.P. Rozelot (Ed.), The Sun's Surface and Subsurface. Investigating Shape and Irradiance.

Vol.600: K. Mecke, D. Stoyan (Eds.), Morphology of Condensed Matter. Physcis and Geometry of Spatial Complex Systems.

Vol.601: F. Mezei, C. Pappas, T. Gutberlet (Eds.), Neutron Spin Echo Spectroscopy. Basics, Trends and Applications.

Vol.602: T. Dauxois, S. Ruffo, E. Arimondo (Eds.), Dynamics and Thermodynamics of Systems with Long Range Interactions.

Vol.603: C. Noce, A. Vecchione, M. Cuoco, A. Romano (Eds.), Ruthenate and Rutheno-Cuprate Materials. Superconductivity, Magnetism and Quantum Phase.

Vol.604: J. Frauendiener, H. Friedrich (Eds.), The Conformal Structure of Space-Time: Geometry, Analysis, Numerics.

Vol.605: G. Ciccotti, M. Mareschal, P. Nielaba (Eds.), Bridging Time Scales: Molecular Simulations for the Next Decade.

Vol.606: J.-U. Sommer, G. Reiter (Eds.), Polymer Crystallization. Obervations, Concepts and Interpretations.

Vol.607: R. Guzzi (Ed.), Exploring the Atmosphere by Remote Sensing Techniques.

Vol.608: F. Courbin, D. Minniti (Eds.), Gravitational Lensing:An Astrophysical Tool.

Vol.609: T. Henning (Ed.), Astromineralogy.

Vol.610: M. Ristig, K. Gernoth (Eds.), Particle Scattering, X-Ray Diffraction, and Microstructure of Solids and Liquids.

Vol.611: A. Buchleitner, K. Hornberger (Eds.), Coherent Evolution in Noisy Environments.

Vol.612: L. Klein, (Ed.), Energy Conversion and Particle Acceleration in the Solar Corona.

Vol.613: K. Porsezian, V.C. Kuriakose, (Eds.), Optical Solitons. Theoretical and Experimental Challenges.

Vol.614: E. Falgarone, T. Passot (Eds.), Turbulence and Magnetic Fields in Astrophysics.

Vol.615: J. Büchner, C.T. Dum, M. Scholer (Eds.), Space Plasma Simulation.

Vol.616: J. Trampetic, J. Wess (Eds.), Particle Physics in the New Millenium.

Vol.617: L. Fernández-Jambrina, L. M. González-Romero (Eds.), Current Trends in Relativistic Astrophysics, Theoretical, Numerical, Observational

Vol.618: M.D. Esposti, S. Graffi (Eds.), The Mathematical Aspects of Quantum Maps

Vol.619: H.M. Antia, A. Bhatnagar, P. Ulmschneider (Eds.), Lectures on Solar Physics

Vol.620: C. Fiolhais, F. Nogueira, M. Marques (Eds.), A Primer in Density Functional Theory

Vol.621: G. Rangarajan, M. Ding (Eds.), Processes with Long-Range Correlations

Vol.622: F. Benatti, R. Floreanini (Eds.), Irreversible Quantum Dynamics

Vol.623: M. Falcke, D. Malchow (Eds.), Understanding Calcium Dynamics, Experiments and Theory

Vol.624: T. Pöschel (Ed.), Granular Gas Dynamics

Vol.625: R. Pastor-Satorras, M. Rubi, A. Diaz-Guilera (Eds.), Statistical Mechanics of Complex Networks

Vol.626: G. Contopoulos, N. Voglis (Eds.), Galaxies and Chaos

Vol.627: S.G. Karshenboim, V.B. Smirnov (Eds.), Precision Physics of Simple Atomic Systems

Vol.628: R. Narayanan, D. Schwabe (Eds.), Interfacial Fluid Dynamics and Transport Processes

Vol.629: F. Sylos Labini, A. Gabrielli, L. Pietronero, Statistical Physics for Cosmic Structures

Vol.630: T. Brandes, S. Kettemann (Eds.), Anderson Localization and Its Ramifications

Vol.631: D. J. W. Giulini, C. Kiefer, C. Lämmerzahl (Eds.), Quantum Gravity, From Theory to Experimental Search

Vol.632: A. M. Greco (Ed.), Direct and Inverse Methods in Nonlinear Evolution Equations

Vol.633: H.-T. Elze (Ed.), Decoherence and Entropy in Complex Systems, Based on Selected Lectures from DICE 2002

Vol.634: R. Haberlandt, D. Michel, R. Stannarius (Eds.), Direct and Inverse Methods in Nonlinear Evolution Equations

Vol.635: D. Alloin, W. Gieren (Eds.), Stellar Candles for the Extragalactic Distance Scale

Preface

One of the most fundamental problems in modern astronomy concerns the ability of astronomers to measure accurately the distances to galaxies, and set up the extragalactic distance scale with the accuracy required for a precise determination of cosmological parameters, particularly the Hubble constant. Also, given the opportunities opened up by the new generation of 8-10 m telescopes to study in detail stellar populations and physical processes in nearby galaxies, it is mandatory to achieve a significant improvement in the determination of the distances of these stellar systems in order to take full advantage of such studies. The last decade has seen dramatic progress in the field of distance determination – the HST Key Project on the Extragalactic Distance Scale has been executed, SNe Ia have been improved as standard candles and have been used to determine distances out to the region of unperturbed Hubble flow, leading to the unexpected discovery of an accelerating Universe, and it has just recently become possible to use Michelson interferometry to measure the angular diameters of Cepheid variables, our most important primary standard candles. Yet, we are faced with the fact that most, if not all, methods, and in particular stellar methods used to measure the distances to nearby galaxies, are plagued with very significant systematic uncertainties at the present time, which are likely to be due to the fact that we do not properly understand how the different standard candles are affected by the environmental properties of their host galaxies. This situation is perhaps best reflected by the large and amazing current dispersion among the distance values which have been determined for the Large Magellanic Cloud from different techniques, as discussed in several reviews in this volume. In the determination of the Hubble constant as performed by the HST Key Project team, the uncertain distance to the LMC is the largest single systematic uncertainty. It is therefore both timely and urgent to investigate the causes for such discrepancies in the distance results for nearby galaxies, and to devise strategies to improve the situation in the near future.

In order to contribute to this goal, we organized the International Workshop "Stellar Candles for the Extragalactic Distance Scale" at the Universidad de Concepción, Chile between December 9-11, 2002. The meeting was sponsored by the Conicyt/FONDAP Center for Astrophysics, the European Southern Observatory, Fundación Andes, and the Universidad de Concepción. The scientific programme consisted in a number of invited review talks highlighting the usefulness of, and particularly the current problems associated with, the most important stellar standard candles, complemented by a number of contributed talks, and by posters. All invited review talks were presented by leading international experts in these fields, and have been prepared to be included in this book. Four reviews deal with Cepheid variables, including reviews of the two groups who have used HST to derive Cepheid distances to galaxies and determine the Hubble constant from such measurements, in an attempt to better understand why these groups arrive at a 20 percent discrepancy between their derived "best values" for the Hubble constant. This is supplemented by the reviews of Fouqué, Storm and Gieren who combine Galactic and Magellanic Cloud Cepheid results in the best possible way to determine an improved Galactic Cepheid period-luminosity relation which has advantages over a Magellanic Cloud relation in extragalactic applications, minimizing the dependence of such distance results on metallicity, and by Feast who focusses on current problems with Cepheid variables. Two reviews concentrate on RR Lyrae variables; Bono focusses mainly on recent theoretical progress in the correct prediction of the luminosities of these variables, and on the confrontation of these results with empirical evidence, while Cacciari and Clementini focus on the determination of globular cluster distances from RR Lyrae stars. The following reviews by Kudritzki and Przybilla, and by Bresolin, scrutinize the usefulness of blue supergiant stars as distance indicators, both from a theoretical and an empirical point of view, highlighting the great potential of these objects to have their distances derived from information which can be extracted from even low-resolution spectra. Three reviews are dedicated to describing the current situation of using supernovae as standard candles: Phillips concentrates on both Type Ia and Type II supernovae, mainly from an empirical point of view; Suntzeff focusses on the physics and phenomenology of SN Ia light curves, and on the cosmological implications of the SN Ia distance results; and Höflich and collaborators discuss SN Ia explosion models and theoretical insights about the formation and evolution of SN Ia light curves and spectra. Gilmozzi and Della Valle investigate the current usefulness and problems of novae as standard candles, followed by the review of Ciardullo on the current state of the art in using planetary nebulae, with their special advantage of being found in all kinds of environments, as promising secondary distance indicators. The book closes with the reviews by Walker on the current state of distance determinations to galaxies in the Local Group, and by Richtler on the strengths and problems of using globular clusters for distance determination, via the Globular Cluster Luminosity Function.

The more than 70 workshop participants, a significant number of astronomy students at the principal Chilean universities among them, witnessed a very intense and exciting meeting, presenting an ideal atmosphere for discussion and personal interaction. At the end of the workshop, a joint discussion took place which allowed some issues which had surfaced during the conference to be examined in greater depth, and a number of initial conclusions to be drawn regarding both new progress and new problems in the field of extragalactic distance determination. For instance, one of the immediate conclusions at this meeting was that evidence is increasing that Cepheid variables might be more complicated as a tool for distance determination than previously thought, through a dependence of the slope of the period-luminosity relation on metallicity. On the other hand evidence is mounting that red giant clump stars, observed in the near-infrared K band, are excellent standard candles. A similar conclusion is reached in the case of blue supergiant stars when the brand-new Flux-weighted Gravity-Luminosity Relationship is applied to them. Finally, we would like to share with the reader a few of the (many) remarkable statements which were made by our speakers during the workshop days, and which characterize the different attitudes and points of view of scientists in the field: “An astrophysicist is someone who sees something working in practice and wonders whether it works in principle”; “Despite the fact we don’t understand them, they are excellent standard candles” (referring to supernovae); and “The red model here is the truth. The blue lines are the observations” (again referring to the supernovae).

We very gratefully acknowledge the valuable help of Ms Pamela Bristow at ESO/Garching in the editing work. Her expertise and dedication to this project was crucial to achieve the timely publication of this book.

Santiago, Concepción
June 2003

Danielle Alloin
Wolfgang Gieren

Contents

List of Contributors

Giuseppe Bono
INAF - Osservatorio Astronomico di Roma
Via Frascati 33
I-00040 Monte Porzio Catone, Italy
bono@coma.mporzio.astro.it

Fabio Bresolin
Institute for Astronomy
University of Hawaii
Honolulu, HI 96822, USA
bresolin@ifa.hawaii.edu

Carla Cacciari
INAF - Osservatorio Astronomico
I-40127 Bologna, Italy
cacciari@astbo3.bo.astro.it

Robin Ciardullo
Pennsylvania State University
Department of Astronomy and Astrophysics
525 Davey Lab
University Park, PA 16803, USA
rbc@astro.psu.edu

Gisella Clementini
INAF - Osservatorio Astronomico
I-40127 Bologna, Italy
gisella@astbo3.bo.astro.it

Massimo Della Valle
Osservatorio Astrofisico di Arcetri
I-50125 Firenze, Italy
massimo@arcetri.astro.it

Michael Feast
Astronomy Department
University of Cape Town
Rondebosch, 7701, South Africa
mwf@artemisia.ast.uct.ac.za

Pascal Fouqué
Observatoire de Paris, LESIA
5, place Jules Janssen
F-92195 Meudon Cedex, France
pfouque@eso.org

Wendy L. Freedman
Observatories of the Carnegie Institution of Washington
813 Santa Barbara Street
Pasadena, CA 91101, USA
wendy@ociw.edu

Chris Gerardy
Department of Astronomy
University of Texas
Austin, TX 78681, USA
gerardy@eris.as.utexas.edu

Wolfgang P. Gieren
Astronomy Group,
Departamento de Física
Universidad de Concepción
Casilla 160-C, Concepción, Chile
wgieren@coma.cfm.udec.cl

Roberto Gilmozzi
European Southern Observatory
Paranal Observatory
Casilla 19001, Santiago, Chile
rgilmozz@eso.org

Peter Höflich
Department of Astronomy
University of Texas
Austin, TX 78681, USA
pah@hej1.as.utexas.edu

Rolf-Peter Kudritzki
Institute for Astronomy
University of Hawaii
Honolulu, HI 96822, USA
kud@ifa.hawaii.edu

Eric Linder
Lawrence Berkeley Laboratory
Berkeley, CA 94720, USA
evlinder@lbl.gov

Barry F. Madore
Observatories of the Carnegie Institution of Washington
813 Santa Barbara Street
Pasadena, CA 91101, USA
barry@ipac.caltech.edu

Howie Marion
Department of Astronomy
University of Texas
Austin, TX 78681, USA
hman@astro.as.utexas.edu

Mark M. Phillips
Las Campanas Observatory
Carnegie Observatories
Casilla 601, La Serena, Chile
mmp@lco.cl

Norbert Przybilla
Institute for Astronomy
University of Hawaii
Honolulu, HI 96822, USA
norbert@ifa.hawaii.edu

Tom Richtler
Astronomy Group,
Departamento de Física
Universidad de Concepción
Casilla 160-C, Concepción, Chile
tom@coma.cfm.udec.cl

Abhijit Saha
National Optical Astronomy Observatories
950 N. Cherry Avenue
Tucson, AZ 85719, USA
saha@noao.edu

Jesper Storm
Astrophysikalisches Institut Potsdam
An der Sternwarte 16
D-14482 Potsdam, Germany
jstorm@aip.de

Nicholas B. Suntzeff
Cerro Tololo
Inter-American Observatory
National Optical Astronomy Observatories
Casilla 603, La Serena, Chile
nick@ctiow5.ctio.noao.edu

Alistair R. Walker
Cerro Tololo
Inter-American Observatory
National Optical Astronomy Observatories
Casilla 603, La Serena, Chile
awalker@ctio.noao.edu

1 The HST Key Project on the Extragalactic Distance Scale: A Search for Three Numbers

Barry F. Madore and Wendy L. Freedman

Observatories of the Carnegie Institution of Washington
813 Santa Barbara Street, Pasadena, CA 91101, USA

Abstract. We present a review of the main results of the Hubble Space Telescope Key Project on the Extragalactic Distance Scale with emphasis on the new techniques that were developed in order to undertake the observations, and the methods that were adopted in both reporting the results and quantifying especially the associated statistical and systematic errors. The three numbers (the cosmological expansion rate H_o, its statistical error and the systematic uncertainty, respectively) are $H_o = 72 \pm(3) \pm[7]$ km/sec/Mpc.

1.1 Introduction

The Hubble Space Telescope (HST) was designed and built to measure the expansion rate of the Universe. And it succeeded. For decades before HST a debate was raging over a factor-of-two disagreement in the value of the Hubble constant. After 8 years of observing and data reduction the final results of the HST Key Project on the Extragalactic Distance Scale were published in Freedman *et al.* (2001) [5]. Preceding that over thirty papers were published detailing the results on the discovery and measurement of Cepheids in individual galaxies constituting the Key Project sample. And with those publications the debate over the Hubble constant has been reduced to and focused upon an interesting discussion of dominant systematics and residual random errors, but now at the 10% level.

The overall goal of the Key Project was to measure the expansion rate of the Universe, using Cepheids to calibrate a variety of independent, secondary distance indicators so as to then reach beyond the locally perturbed flow out into the cosmologically dominated expansion. Given the history of having systematic errors dominating the accuracy of distance measurements, the approach adopted by the Key Project was to explicitly assess systematics in any one approach by examining and using several different methods en route to a global measurement. These secondary methods included surface brightness fluctuations, Type II supernovae, the Tully-Fisher relation for spiral galaxies, the fundamental plane for elliptical galaxies, and finally Type Ia supernovae at the very farthest extreme in distance. Each of the secondary distance indicators had their own strengths and their own weaknesses; many overlapped in distance; some could be applied to the same galaxies; all had their own systematics, both a cluster environment and the field were being sampled. If systematic differences were to be found this experiment was designed to highlight and to quantify them.

B.F. Madore and W.L. Freedman, The HST Key Project on the Extragalactic Distance Scale: A Search for Three Numbers, Lect. Notes Phys. **635**, 1–20 (2003)
http://www.springerlink.com/

Fig. 1.1. Averaging over Systematics – An example of how averaging can reduce the noise in the statistical determination of a standard metric. In this case the measurement being undertaken is the length of a "standard rod" as defined by twenty randomly selected "feet"

And so as the Cepheid observations were made and distances began to be compiled the first order of business was to establish rigorous standards of documenting, propagating and reporting the statistical errors associated with sample sizes. This was paralleled by the enumeration and assessment of the various systematic errors associated with each decision and every step taken along the way to evaluating distances and velocities contributing to a final value of the Hubble constant.

This review will not so much dwell on the value of the Hubble constant that was finally reported, but rather the emphasis will be on the errors associated with that determination.

1.2 "Statistics, Damned Statistics, and . . . "

Benjamin Disraeli is reported to have said that there are three kinds of lies: "Lies, Damned Lies, and Statistics". Curiously, it is now regarded that Disraeli never uttered these words and that Mark Twain, who in his autobiography attributed this now famous phrase to the then Prime Minister of England was himself apparently indulging in a lie of the first kind. Whether there was a bit of hidden irony there one will never know, but what is clearly meant by the original statement, whoever really said it, it is that at least in some contexts statistics fall at the very bottom of the credibility heap. But that unfortunately, is where any new study of the expansion rate of the Universe had to start. But in the end, it was the careful application of statistics and error analysis that brought the results of this study into sharp and final focus.

There may be three types of lies, but for our purposes there are only two types of errors: statistical errors and systematic errors. Statistical (or random) errors usually are amenable to reduction by increasing the sample size, N. They obey a random-walk convergence around their mean, slowly decreasing as $1\sqrt{N}$. Various statistical errors can be combined in quadrature (if they are statistically (sic) independent), and in such a case a finally reported, single, combined error makes both mathematical and physical sense. Statistical errors measure *precision.*

Systematic errors are of an entirely different breed. They measure *accuracy.* No matter how many times an experiment may be repeated, and no matter how many samples may be taken, if the methodology is unchanged any inherent systematic errors will remain the same. Systematic errors are offsets and displacements of the answer from the truth that no increase in sample size can reveal or reduce. As such systematic errors are hard to evaluate even when they are identified, and it is even harder to know when and whether they have even been identified at all. After the noise of small numbers has been beaten down by "statistically significant" sample sizes, one is always left "dominated by the systematics". The Hubble constant long suffered from both large, but unknown, systematics, and from small, but over-worked, samples.

The *Hubble Space Telescope* took care of the sample size, as shown by Table 3 in Freedman *et al.* (2001) [5] which lists the revised Cepheid distances to thirty-one galaxies after the Key Project was completed. This is to be compared to the handful of distances available in 1990, say, after more than half a century of observing from the ground (see Madore & Freedman 1991 [7] for a compilation of Cepheid distances relevant to that pre-HST period in time).

Dealing with systematic errors required a sober enumeration of time-honored methods and an explicit evaluation of a host of implicit assumptions.

But HST did not just guarantee time to do the project as one would have done it from the ground. It demanded that the whole project be optimized. We had to know just how many observations of how many Cepheids in how many galaxies would get sufficiently reduce the statistical errors. And then we had to select those galaxies to cover and include as many tests for systematics as we could conceive of. And do this before the shutter ever opened on the first target. Below we outline how we optimized the scheduling of HST to monitor a large number of galaxies to find significant samples of Cepheids, and how the numbers of observations in the two filters were chosen so as to allow us to discover variables, select out the Cepheids, measure their periods, amplitudes, mean magnitudes and time-averaged colors, and accomplish all of this within a narrow window of time often not even as long as the periods of the longest-period Cepheids themselves.

1.3 Optimal Search Strategies

From the ground, after time is assigned on a given telescope, there is little control one can exercise over the rising and setting of the Moon, or the motion of weather patterns across the surface of the Earth. Even in sunny California one can observe only when it is dark, and even then only when it is clear. The situation from Earth-orbit is, of course, not the same; in many different ways. Every ninety minutes there is an opportunity to open the shutter and begin observing. Within those orbital constraints one can in principle schedule the telescope to point at anything that is not occulted by the Earth, Moon or Sun. HST could be scheduled in just that way. The challenge was to capitalize on this feature and optimize the use of the telescope in monitoring a fair sample of objects.

The historical precedent was not good. From the ground, Hubble, Baade, Sandage and others spent decades semi-systematically (but still more or less randomly) observing some of the most nearby galaxies (M31, IC 1613, NGC 6822, etc.) in search of variable stars. And with time and with great patience results did flow in. Nevertheless the lunar cycle still imposed aliases on the observations (Fig. 1.2), as extensive as they were, leaving gaps and clumps in the phase-folded lightcurves of some of the variables. The situation was clearly not optimal. In fact, it was not even possible to consider optimizing the situation, so little attention was paid to producing an observing strategy matched to the problem; that is, not until HST came along.

With HST it was not only possible but it quickly became mandatory that the telescope be scheduled in a highly optimized way. Time was extremely valuable and competition was fierce. Furthermore it was not just one or two additional galaxies that needed Cepheid distances determined it was an order of magnitude more than had already been done from the ground that was required in order to calibrate a variety of secondary distance indicators. So the challenge was: Observe about a dozen different galaxies. Reduce the numbers of observations from more than 100 per target down to order 10 epochs. Do this in two colors (to measure reddenings). Detect the variables. Measure their periods. Extract time-averaged luminosities, amplitudes and colors. And complete each set of discovery/detection/measurement observations in a single window, generally not exceeding 60 days.

Exposures had to be long enough to get good photon statistics on the individual measurements of the stars, so as to unequivocally discriminate variables from constant stars. Those same individual phase points had to be sufficiently high in signal-to-noise to allow a delineation of the light curve so that phasing of the data and a period determination could be made that was in itself sufficiently precise that a robust period-luminosity relation could be constructed and false non-Cepheids discriminated against either by the shape of their light curve or

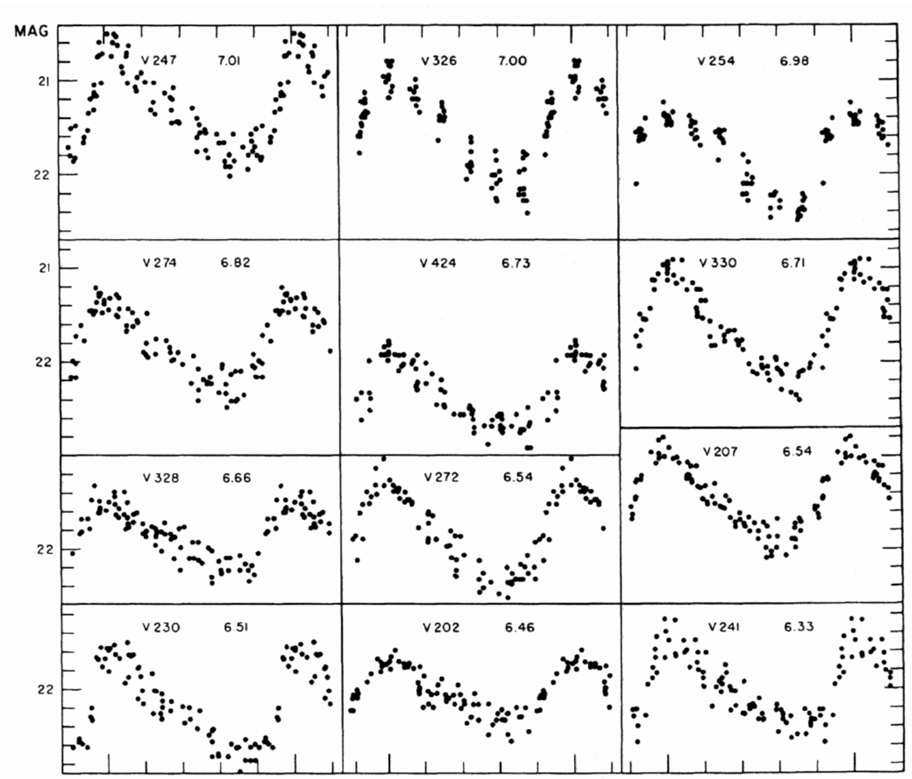

Fig. 1.2. A Sample of Light Curves of Cepheids in M31 as published by Baade & Swope (1965) [1]. Note that even with over 70 observations, taken over a period of six years there are still strong resonances in the data, especially for variables V326 and V254 whose periods are very close to an integral number of days, and in fact very close to being exactly a week

by their colors, magnitudes and/or corresponding periods. Color observations had to be woven into the observing schedule so that two independent apparent moduli could be derived and reddening corrections extracted and applied to the determination of a final true distance modulus.

Random sampling of any source (intrinsically variable or not) will only drive down the error on the mean as $1\sqrt{N}$; but for a variable with an intrinsic amplitude larger than the observing errors the empirical demands are considerably worse. In our case (for Cepheids with amplitudes expected to be anywhere up to 1.5 magnitudes in the visual) the dominant error on the mean magnitude and color is driven by the phase sampling of the light curve itself. Obviously an abundance of observations randomly clumped at maximum light would bias the mean to too bright a magnitude. Too many observations wasted at minimum light would bias the mean too low. The equivalent sigma of an intrinsic variable with a 1.0 mag amplitude is $1.0\sqrt{12}$ mag or approximately ± 0.30 mag. To drive this error on the mean down to 0.03 mag would then require on the order of 100 observations! This was unthinkable for a *Hubble Space Telescope* project intent on observing more than a dozen galaxies.

Before describing our finally adopted sampling strategy, and reasoning for it, we note that in a more general context the detection and characterization of time-dependent signals has a long and well studied history, especially in electrical engineering and its allied sciences. It will not be repeated here. However, we note that much of the theory and many of the practical applications involve equal-spaced sampling at high signal to noise, obtained over long run times, and usually covering many cycles of the searched-for, but unknown, signal. After detection, the characterization or parameterization usually involves the determination of a period, an amplitude and phase, and then finally the quantification of some shape parameters of the signal. With regard to the latter point, we note that periodic signals certainly are not always sinusoidal in form, but often they can reasonably be decomposed into the superposition of a few low-order Fourier components. Here we discuss an extreme corner of parameter space in signal detection not much explored by others: a region defined by very small numbers of observations (a mere handful), all of which are non-uniformly placed in time, covering at most a few cycles of highly asymmetric, but still periodic, signals.

1.4 A Figure of Merit

As with any parameter extraction it is useful to have a quantitative measure for the goodness of the solution. We begin by stating that the ideal distribution of points over the phase-folded waveform is that where the observations fall equally spaced over the light curve, where none are redundant (i.e., no coincident observations). With this in mind we have devised the following figure of merit: For a given number of observations (N) we first calculate a variance in phase space

$$\mathit{\Delta}_N^2 = \sum_{i=1}^{N} (\phi_{i+1} - \phi_i)^2$$

which for the case of the ideal sampling (*i.e.,* that of uniform and non-redundant placement around the light curve) reduces to

$$\mathit{\Delta}_{N,uniform}^2 = \sum_{i=1}^{N} (1/N)^2 = 1/N$$

(where $\phi_{N+1} = \phi_1 + 1.0$, and $\sum_{i=1}^{N} (\phi_{i+1} - \phi_i) = 1.0$). For the actual resultant sampling (phase-folded to a given period) the equivalent (realized) statistic $\mathit{\Delta}_N^2$ is analogously derived from the sum of the squares of intervals separating the order pairs of observations over the unit interval. The final figure of merit is then the difference between the realized $\mathit{\Delta}_N^2$ statistic and the ideal phasing statistic

$\Delta^2_{N,uniform}$, normalized by the ideal case, giving

$$U^2 = [\Delta^2_N - \Delta^2_{N,uniform}]/[(N-1)\Delta^2_{N,uniform}]$$

or

$$U^2 = [N\sum_{i=1}^{N}(\phi_{i+1} - \phi_i)^2 - 1]/(N-1)$$

Interpreted as a normalized variance, the U^2 statistic has a value of zero when the distribution of points is non-redundantly uniform over the light curve, and a value of unity when all points are coincident in phase space. The added division by (N-1) is introduced to force the variance to unity independent of sample size, when all points cluster at a single phase (*e.g.,* total redundancy). In the following however, we chose to plot the Uniformity Index (UI) which is based on U^2 but simply inverts and maps it onto the interval [0-100] by the following simple transformation: $UI = 100[1 - U^2]$. In this way a score of 100 indicates perfectly uniform sampling over the light curve, and 0 indicates total failure, resulting from complete redundancy in the phase placement of the observations where the data points, folded over the period of the variable, all end up at precisely the same phase point.

1.5 Sampling Strategies

While it is intuitively obvious that optimal sampling of a signal with known frequency should be undertaken in such a way that no two observations overlap in phase as seen by the signal, what is perhaps not so obvious is that such a uniform sampling strategy has very important consequences for that rate of convergence of such things as the measured amplitude and the error on the calculated mean (both of which are intimately related). Unlike random sampling which is a random-walk $1/\sqrt{N}$ process, uniform sampling has both of its errors on amplitude and on the calculated mean drop much more rapidly; in fact, those errors fall directly as 1/N. This is a considerable savings when additional observations come at a high premium. A factor of 3 in observing time is always easier to come by than is a factor of 10. Optimization of the type discussed here buys that difference.

In the following series of plots and diagrams (Figs.1.3–1.9) we first explore the systematics of the random sampling of highly asymmetric light curves using extremely few observations. Indeed we begin with 2, 3 and 4 observations only and then jump to 12 observations, which is the adopted number of observations typically used in the small observing window imposed by orbital constraints upon the Key project. The important details of the simulations are given in extensive captions to the figures. The simulations bear out the expectation that random sampling is highly inefficient in its error convergence properties where the clearly Gaussian distribution of errors quantities of interest (such as the mean magnitude) only go down like $1/\sqrt{N}$, and where the first-order measure of the light curve shape, the measured amplitude has a distribution that can be

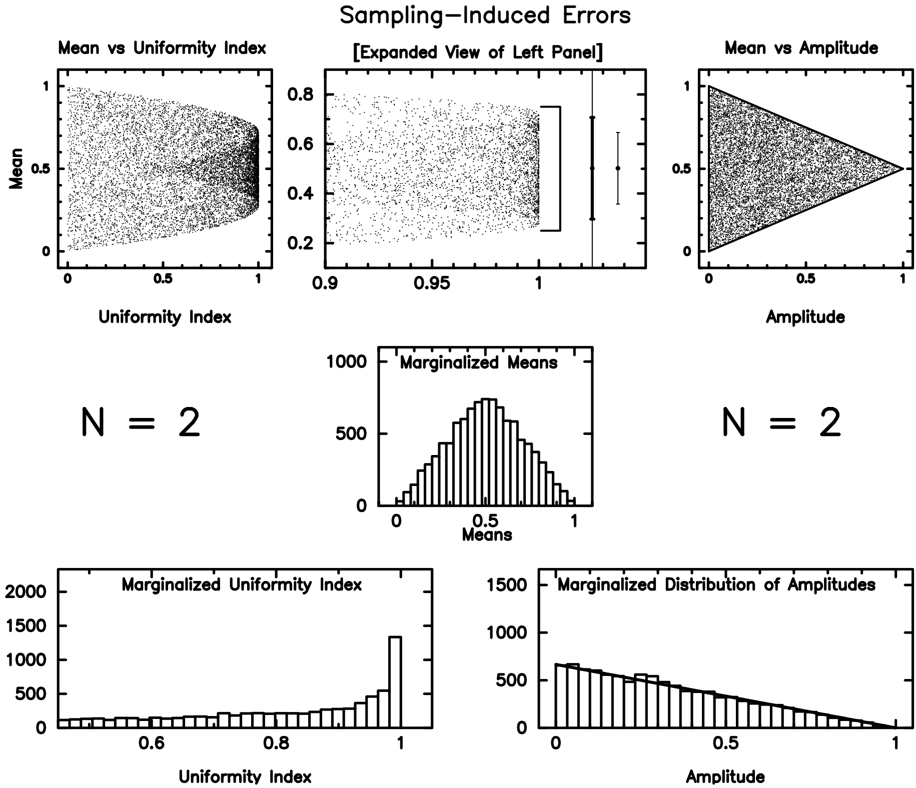

Fig. 1.3. Monte Carlo Simulations of the mean magnitude, the uniformity index and the derived amplitude for a synthetic light curve approximating that of a variable star. This panel shows the distributions and marginalized values for random samples of two observations (N = 2) only. In the upper middle panel is shown an expanded view of the correlation of the mean magnitude versus the uniformity index. The right-handed square bracket near UI = 1 shows the total range of mean magnitudes predicted for the equivalent number of observations uniformly sampling the light curve (but with random phase with respect to the periodic function). The next error bar to the right uses the simulated data and shows the data-derived standard deviation (thick line) and two-sigma (thin extension). The final error bar to the far right is the one-sigma error bar for the uniform sampling. It can be shown that the distribution function for the marginalized means (central panel) for N = 2 is a symmetrical triangular function centered on a mean of 0.5. The marginalized distribution of observed amplitudes is a ramp function with the modal value of the amplitude being zero

proven using order statistics to have exactly the form of the Beta function which only slowly converges on the true amplitude and has a long tail toward small (derived) amplitudes.

Knowing that random sampling is too inefficient and that uniform sampling over the light curve is ideal the problem becomes that of finding an observing strategy (in real time) that corresponds to uniform sampling as viewed by a

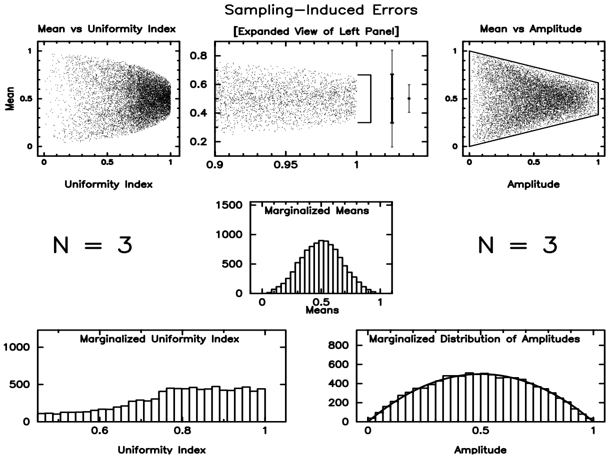

Fig. 1.4. Monte Carlo Simulations of the mean magnitude, the uniformity index and the derived amplitude for a synthetic light curve approximating that of a variable star. This panel shows the distributions and marginalized values for random samples of three observations (N = 3) only. The error bars are as discussed in Fig. 1.3; but note again how much smaller the error bar for the uniform sampling is (far right) as compared to the one-sigma error seen for random sampling (thick error bar). The distribution of marginalized means (central panel) is rapidly becoming Gaussian in appearance, while the marginalized distribution of amplitudes is very symmetric about Amplitude = 0.5

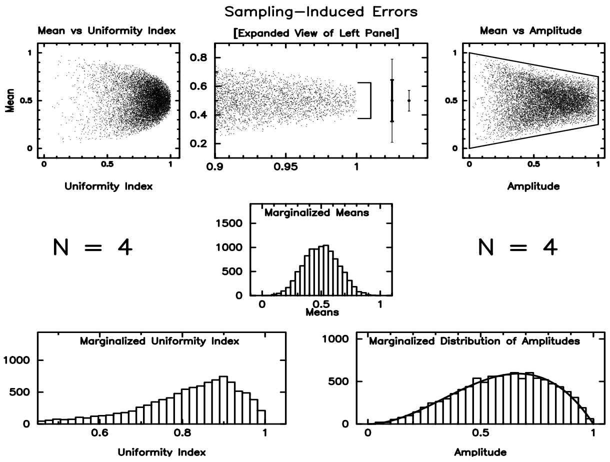

Fig. 1.5. The same as Figs. 1.3 and 1.4 except that this panel shows the results of Monte Carlo simulations of distributions and marginalized values for random sampling of a light curve using only four observations (N = 4). The marginalized means continue to become more Gaussian in their distribution, while the distribution of amplitudes and uniformity indices are both markedly asymmetric, and skewed towards larger values

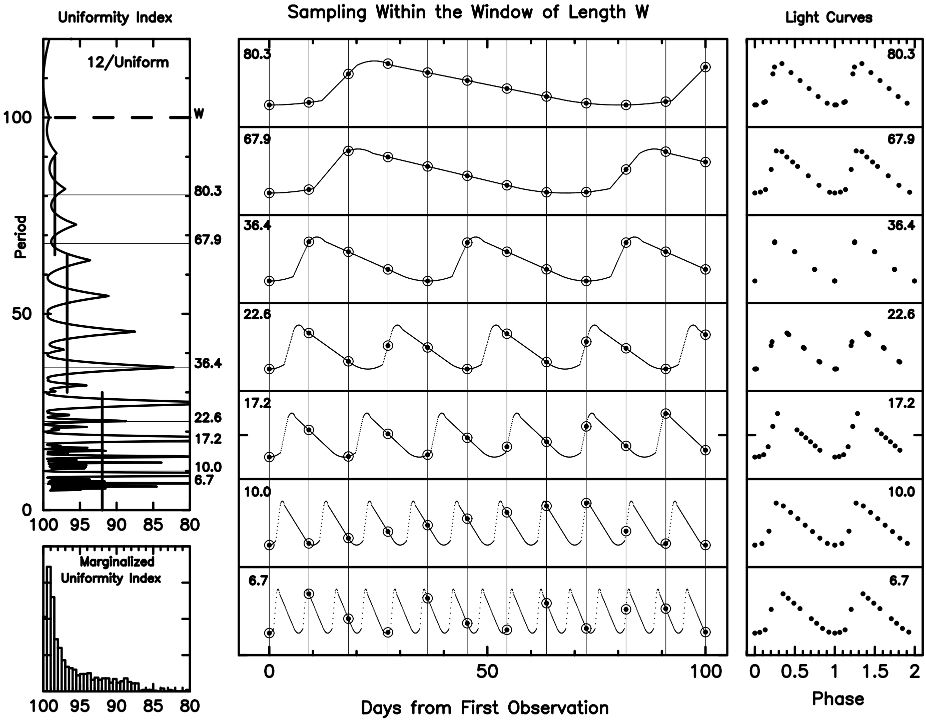

Fig. 1.6. Uniform Sampling in Time. The upper panel on the left shows the Uniformity Index (UI) as a function of period resulting from a sample of 12 observations placed equidistantly within an observing window W = 100 days. As a function of period (moving up in the panel) one can see that the mean level of the Uniformity Index (as marked by the solid vertical lines) is a decreasing function of period. Similarly, the variance in the Uniformity Index increase toward shorter periods. Excursions to low values of UI occur when data points fall redundantly at the same phase in the light curve.

The middle panel shows a selection of light curves for periods ranging from a few days up to 80 days. The actual time of the observation within the 100-day window is shown by the 12 vertical lines crossing the light curves at points marked by encircled dots. The UI for the 80-day variable (top) is very high and as can be seen in the right panel the phase-folded light curve is very uniformly sampled. The 36-day variable is also uniformly sampled but its UI is significantly lower given the fact that each plotted point represents three (overlapping) observations in the phase-folded plot. The 22-day Cepheid also shows redundant (phase-clumped) observations when folded over the known period. The 10-day variable is also very uniformly covered but a strong alias can be can be readily seen in the real-time plot of the observations in the middle panel where an equally good light curve having a period of about 100 days would produce an equally compelling fit

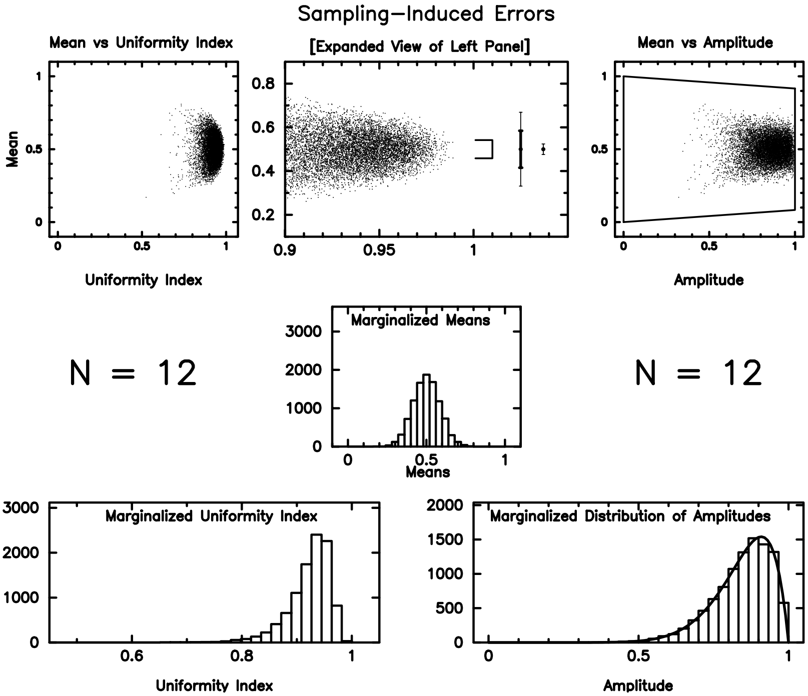

Fig. 1.7. N = 12 Random Samples. The same as Figs. 1.3 through 1.5 except that this realization has a number of observations that is more typical of the HST sampling. Notice how much smaller the uniform-sampling error bar is in the upper middle panel as compared to the random sampling error (thick error bar) which is now very highly Gaussian (middle figure). The distribution of amplitudes peaks around 0.9 but still has a long asymmetric tail stretching down to values as small as 0.5. The Uniformity Index distribution for 12 random data points peaks at a value around 0.95 but continues to have a long tail extending back at least to 0.8

multiplicity of variables, and accomplishing this for as wide a range of (*a priori* unknown) periods as possible. Armed with the Uniformity Index as our measure of success we used a plot of UI versus Period as our diagnostic tool for extensively exploring and empirically assessing a variety of sampling strategies. We discuss here only two examples: the default equally-spaced (uniform) sampling in real time (not to be confused with the desired "uniform sampling" in the phase-folded frame of the variable), and a power-law distribution of observations in real time.

Figure 1.6 shows the result of placing 12 observations equally spaced in time inside of an observing window 100 days in length. To the left we illustrate the extensively calculated Uniformity Index for each and every period between 5 and 120 days. Examples of very good sampling (UI around 100, at P = 120 for example) and extremely poor sampling, resonances and redundancies (with UI values dipping towards 0) abound.

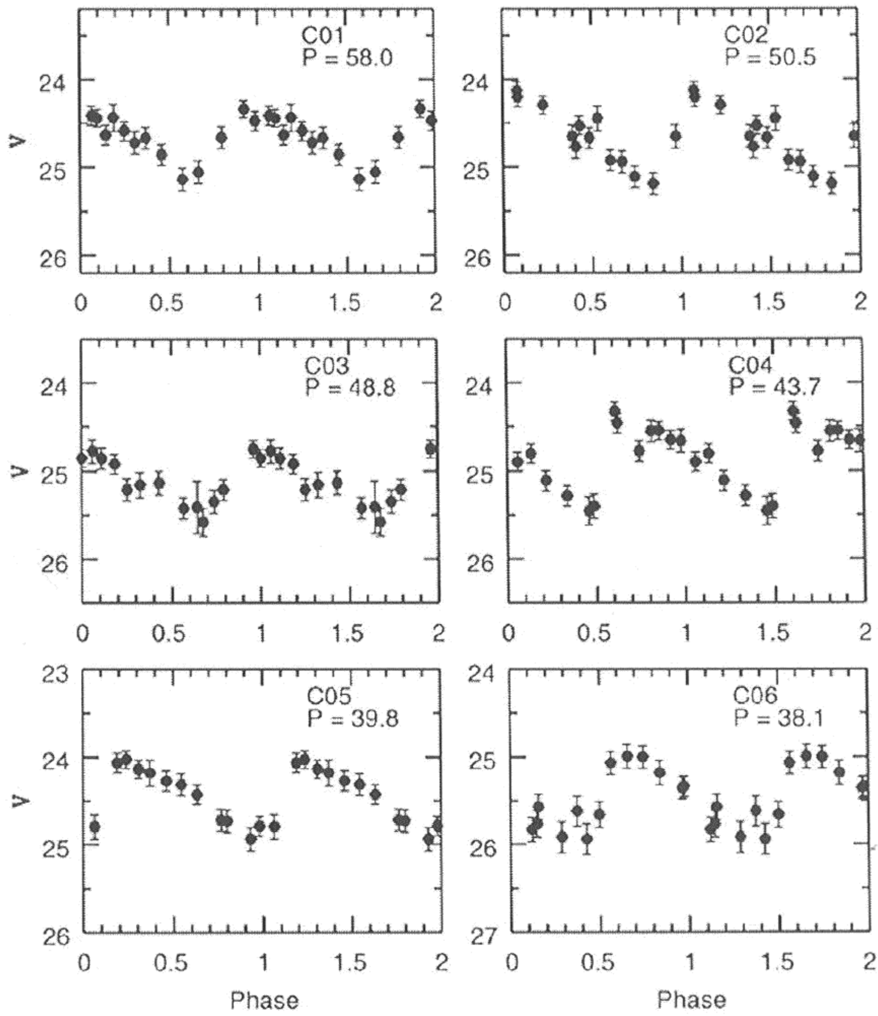

Fig. 1.8. Optimally-sampled light curves of Cepheid variables in the galaxy NGC 2090 discovered using the algorithm and sampling strategy described in this paper (data from Phelps et al. 1998) [8]

The *a priori* advantage of a power-law sampling is that power-law distributions have no preferred scale. And because we are looking to sample a variety of frequencies without any preferred periods, we are implicitly seeking a sampling sequence that has a flat (featureless) power spectrum, constrained only by its duration W. Our specific task was to choose among the infinity of possible power law distributions, using the UI vs P diagram as a diagnostic tool. The success criteria that we chose to apply are: (1) minimize the number and depth of the excursions towards low values of UI in the range of periods where Cepheids are

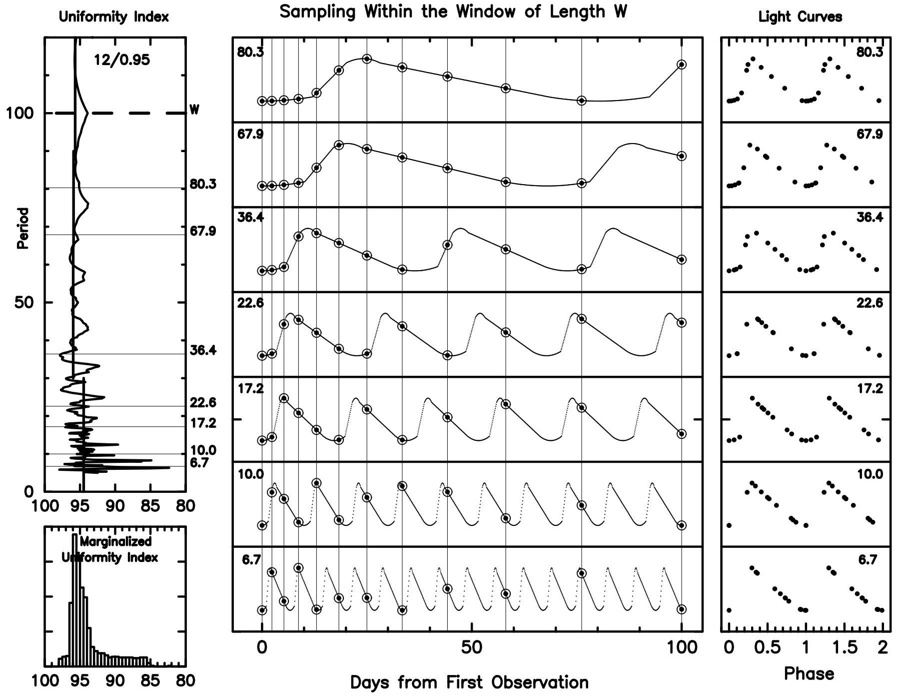

Fig. 1.9. Optimal (Power-Law) Sampling in Time. This realization uses the same 100-day window and is sampled again by 12 observations as in Fig. 1.6; however the points are non-uniformly placed in real time within the window. The adopted power-law spacing has an exponent of 0.95. As can be seen in the far left panel the uniformity index is relatively constant with period, only slightly declining in the lowest period range. And, in comparison with the uniform sampling scheme shown in Fig. 1.6 the variance in UI at all periods is significantly reduced. These two things combined mean that there is little bias in the sampling of light curves with period, and that the clumping of data points in the phase-folded light curves should be fairly indistinguishable from object to object within subranges of the considered periods. These suggestions are born out in the light curves shown for the same selected periods as in Fig. 1.6 where the redundancies and aliases due to resonances between the Nyquist sampling, the window function and the individual variables have all but disappeared. Gaps of a similar nature and distribution can be seen at all considered periods. The resonance at 10 days has complete disappeared. And the clumping of data points in the 22 and 36-day variables has been eliminated

expected to be found (in our case 10 to 60 days) and (2) maintain a constant mean level in UI over that same period range so as to minimize any period-related bias in the light-curve coverage. Hundreds of trials and simulations were run and examined individually by eye. Runs were made varying the window size, the numbers of observations and the power-law exponent. Figure 1.9 shows one of the successful combinations, consisting of 12 observations made over a period of 100 days placed down in a power-law distribution characterized by an exponent

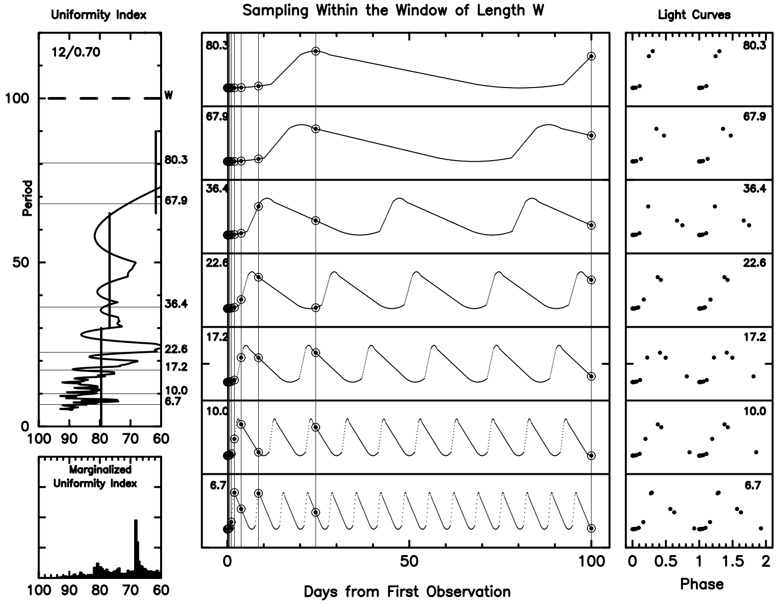

Fig. 1.10. Highly Non-Optimal (Power-Law) Sampling. This realization again uses a 100-day window and is sampled by 12 observations as in Fig. 1.6; however the points are now non-uniformly placed in real time within the window using an adopted power-law spacing that has an exponent of 0.70. This sampling strategy places an inordinate amount of power at high frequencies resulting in very poor phase coverage for the longer-period variables. The Uniformity Index over most of the period range of interest is so poor (low) that the plotted range in UI had to be increased by a factor of two over the previous two plots in order to accommodate at least a majority of the data

of 0.95. In comparison to the "equal spacing" example of Fig. 1.6 the optimization is quite self evident: reduced redundancy, good phase coverage over a wide range of periods and little bias with period over the period range of interest.

Just for comparison Fig. 1.10 shows a power-law distribution within the same window and deploying the same number of observations that fails to meet many of our criteria for success. Not all power laws are equal, but not all search strategies may require an unbiased distribution with period. Indeed if it is anticipated that only a few variables will be found at the longer periods it may be advantageous to "bias" the power-law distribution to increase the power for short-period variables, or to narrow in on a select number of frequencies or perhaps disparate ranges of frequency. The UI-Period plot gives one means of evaluating these and other possible sampling strategies.

1.6 Applications

Did this scheme work beyond the simulations? Was it in practice possible to discover Cepheids, determine accurate periods, phase-wrap the data and derive sufficiently precise magnitudes and colors, for variable stars whose periods could *a priori* fall anywhere in the range of 10 to 100 days, and do all of this with only 12 observations judiciously placed in a window no more than 60 days in total duration? Figure 1.8 shows an illustration of what was discovered for a typical galaxy in the Key Project. The light curves are convincingly Cepheid-like, and true to the promise of the optimized sampling strategy the light curves are also quite uniformly sampled. This particular galaxy, NGC 2090, was monitored over 50 days and sampled 12 times in that period (a single precursor observation was also obtained one year earlier). 34 Cepheids with periods ranging from 5 to 58 days were discovered. Independent proof that these objects are indeed Cepheids and that their periods and magnitudes are correctly estimated comes from the resulting period-luminosity relation that the ensemble of stars are seen to obey. If the stars were not Cepheids, if their periods were in error, or if their magnitudes were erroneous then the PL relation would become ill-defined and/or contain many outliers. However, the observed PL relations correspond so well (in slope, in dispersion, and in their period-color relation) it is clear that the stars are Cepheids and that the sampling strategy worked as hoped.

It may come as something of a surprise to those entering the discussion of Cepheid distances at this late date, to hear that there was a time in the not-so-distant past that corrections for reddening of Cepheids attributable to dust within the host galaxy were not even applied, and more often not even discussed, as a source of uncertainty. At most some correction for foreground Galactic extinction was added in, but through a combination of wishful thinking and perhaps an implicit hope for "a fortuitous cancelling of errors" reddening inside of the host galaxies was largely ignored. The situation began to change as Cepheids in the Magellanic Clouds were examined in more detail, but another source of systematic uncertainty, metallicity reared its ugly head at about the same time (for the same samples), and its effects were manifest most obviously on the colors as well. Alas, decoupling reddening from metallicity became problematic, especially at the shorter wavelengths where both were expected to be increasing in their influence.

It is possible to correct Cepheid observations for extinction and determine true distance moduli without ever explicitly solving for individual reddenings to individual Cepheids. The only ingredient needed is the ratio of total-to-selective absorption (for example $R_{VI} = A_V/E(V-I)$) relating the differential extinction suffered by the two bandpasses in which the Cepheids are observed. (We note in passing that by assuming this quantity to be universal, places it in the category of assumptions that can potentially propagate a systematic error throughout the entire distance scale.)

1.7 Cepheid Zero Point

The Key Project pinned the zero point of its adopted Period-Luminosity relations on the true distance modulus of the Large Magellanic Cloud which was host to the calibrating Cepheids used to define and delineate the slopes and widths of the V- and I-band PL relations. That single step is still one of the most controversial, and it alone contributes one of the largest systematic errors in the distance scale tabulated by the Key Project. Only metallicity corrections, the WFPC-2 zero-point, and the uncertain effects of bulk flows on scales larger than 10,000 km/s contribute as much to the overall *systematic* uncertainty in the distance scale.

This is good news and bad news. But it is also very old news. It is bad news because, here we are trying to measure distances out to redshifts measuring a fair fraction of the speed of light, and yet we cannot gain consensus on the distance to one of the very nearest companion galaxies to the Milky Way. But, it is also good news, because the LMC is sufficiently close that with time, space-based astrometric satellites, such as GAIA, will eventually provide a direct distance determination to this galaxy, and settle the issue with geometry rather than with rhetoric. And it is old news because the LMC has been the testbed for every distance indicator imaginable, and it only stands in sharp testimony of the many attempts, some inspired and some in vain, that astronomers have been making over the decades to bridge the gap between true parallaxes and estimated distances throughout the Universe.

At this point in time, the best that can be hoped for is that the value adopted by the Key Project is in accord with the Central Limit Theorem of applied mathematics. Although many of the individual distance estimates do not overlap to within their quoted errors, the fact that many of them are independent of each other then allows averaging over the many different systematics. In this average at least the expectation is that the resulting value will have a robust uncertainty that will stand the test of time. Although individually reported values for the true distance modulus for the LMC cover the *range* from 18.1 to 18.7 mag, corresponding to 42-55 kpc, we have adopted from the outset a true distance modulus of 18.50 $\pm$ 0.10 mag, which corresponds to a distance of 50 kpc. To illustrate the stability of this number, and the representative nature of its error, we point to survey of the literature by Gibson (2000) [6] whose data are plotted in Fig. 1.11 and gives 18.45 mag with a method-to-method dispersion of 0.15 mag, and consequently a formal uncertainty on the mean of 0.06 mag. This in turn is not sensibly different from the mean and uncertainty of 18.46 $\pm$ 0.05 mag derived by Westerlund (1997) [9] a number of years earlier. And finally, we draw attention to three very recent papers: Two [2,3] by Benedict *et al.* (2002a,b) where, in the first paper, they comprehensively update and review published distances to the LMC deriving a weighted average of 18.47 $\pm$ 0.04 mag, and in the second they obtain a direct parallax to δ Cephei and thereby deduce the true distance modulus of the LMC to be 18.58 $\pm$ 0.15 mag. And one [4] by Cacciari& Clementini (2003) delivered at this meeting which gives a weighted average of the most recent determinations of the RR Lyrae distance to the LMC which they find to be 18.48 $\pm$ 0.05 mag.

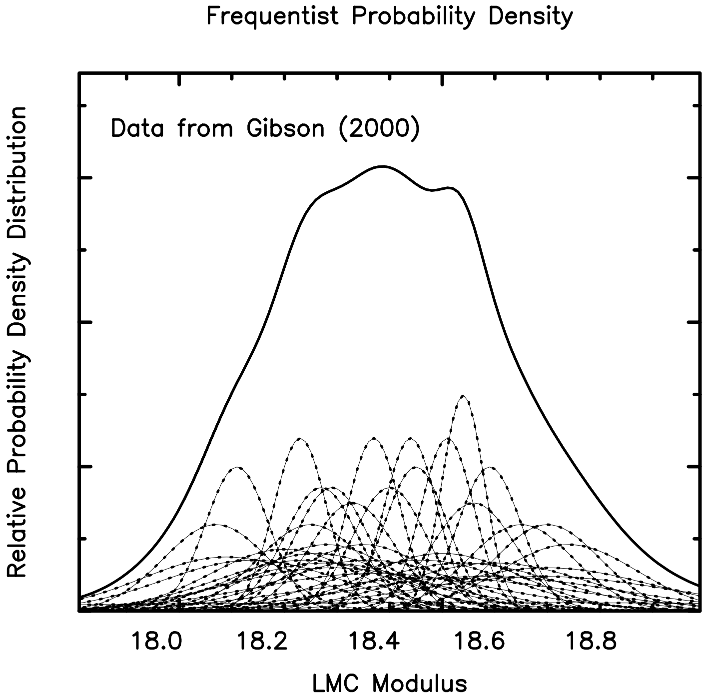

Fig. 1.11. LMC Distance Moduli. Survey data on published LMC distance moduli taken from Gibson (2000) [6] and plotted as a continuous probability density distribution for the ensemble (upper curve, and as unit-weight Gaussians (lower curves) for the individual data points

1.8 The Three Numbers

At its conclusion the Key Project delivered not just one, but three, numbers: The Cepheid-based value of the expansion rate of the Universe, $H_o = 72$ km/sec/Mpc. And two measures of the uncertainty on that number: (1) a statistical error of ± 3 km/sec/Mpc and (2) a measure of the remaining systematic uncertainty of ± 7 km/sec/Mpc. Figure 1.12 shows in graphical form how the various secondary distance determinations of the Hubble constant compare in their individual systematic and random errors, and how they individually contributed to the final determination and its associated errors. And Fig. 1.13 illustrates how the individual measurements of the expansion rate overlap and consistently flow from the nearby expansion field (mapped directly by Cepheids), to beyond the Virgo and Fornax clusters (probed by Tully-Fisher and surface brightness fluctuation methods, etc.) and out to cosmologically significant distances touched only by the Type Ia supernovae.

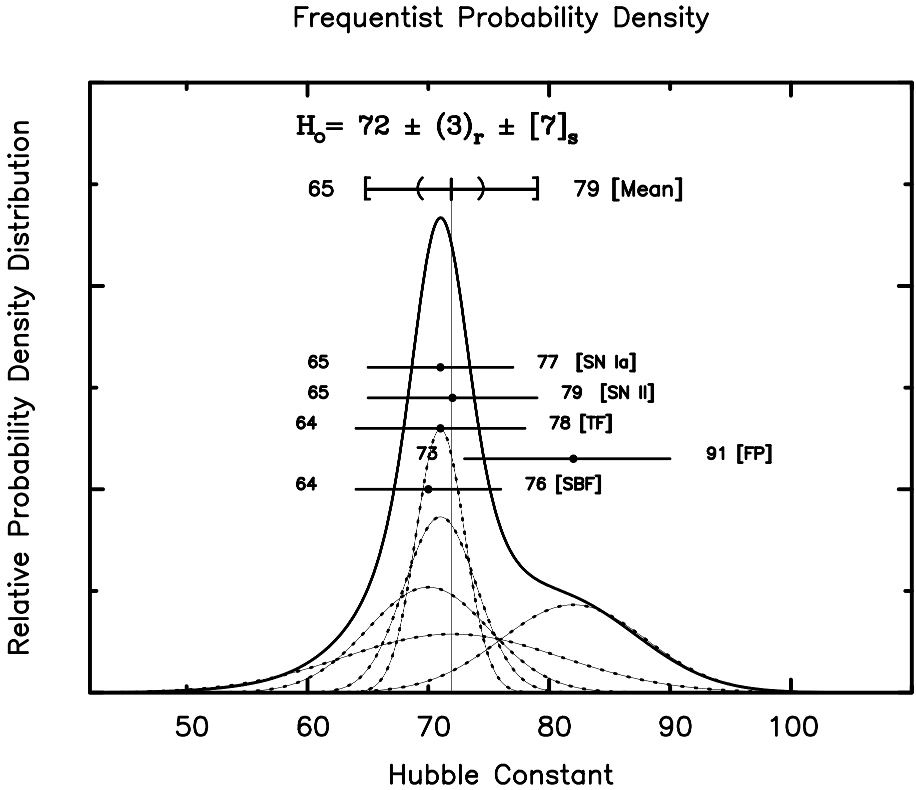

Fig. 1.12. Key Project Determinations of the Hubble Constant Values of H_0 and their uncertainties for Type Ia Supernovae, the Tully-Fisher relation, the Fundamental Plane, Surface Brightness Fluctuations, and Type II Supernovae, all calibrated by Cepheid variables. Each value is represented by a Gaussian curve (joined solid dots) with unit area and a 1-σ scatter equal to the random uncertainty. The systematic uncertainties for each method are indicated by the horizontal bars near the peak of each Gaussian. The upper curve is obtained by summing the individual Gaussians. The cumulative (frequentist) distribution has a midpoint (median) value of $H_0 = 72$ (71) $\pm 4 \pm 7$ km/sec/Mpc. The overall systematic error is obtained by adding the individual systematic errors in quadrature

Acknowledgements

The authors thank all of the Key Project Team members who contributed so energetically over the years to the success of this endeavor. Without the support of NASA, the Space Telescope Science Institute and the NSF this space-based project and its complementary ground-based support efforts would have never succeeded.

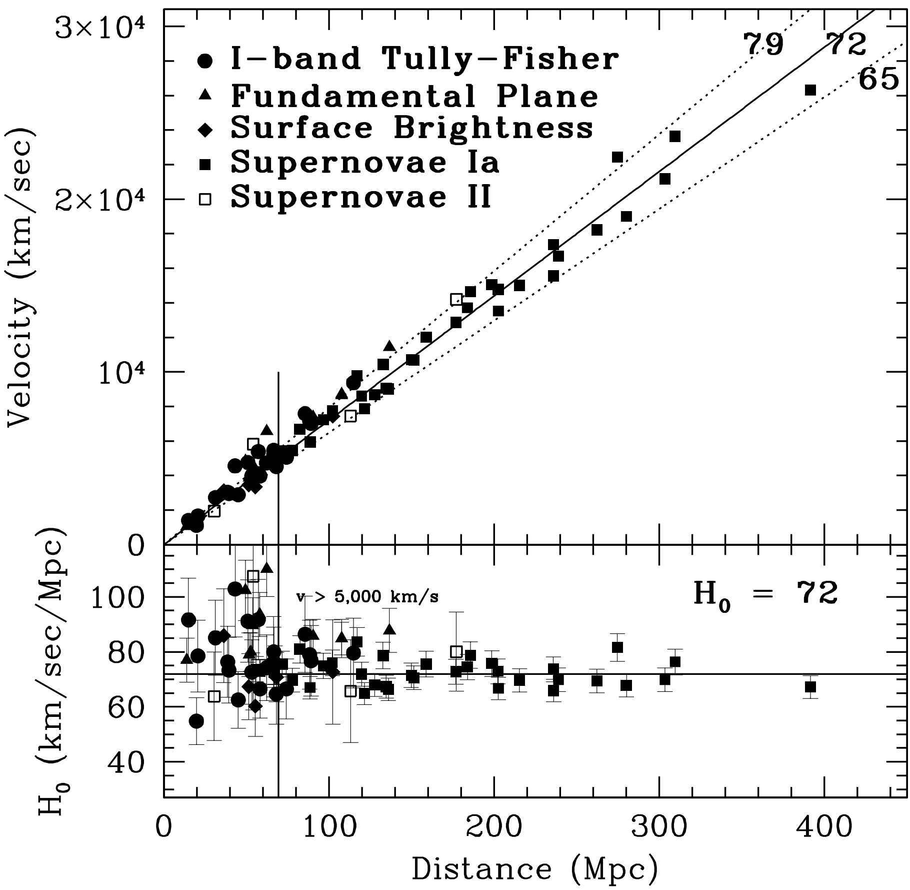

Fig. 1.13. Velocity-Distance Relationship [Top panel]: A Hubble diagram of distance versus velocity for secondary distance indicators calibrated by Cepheids. Velocities in this plot are corrected for nearby flows. The symbols are: Type Ia supernovae – squares, Tully-Fisher clusters (I–band observations) – solid circles, Fundamental Plane clusters – triangles, surface brightness fluctuation galaxies – diamonds, Type II supernovae (open squares). A best-fit expansion rate of $H_0 = 72$ is shown, flanked by ±10% lines. Beyond 5,000 km/sec (indicated by the vertical line), both numerical simulations and observations suggest that the effects of peculiar motions are small. The Type Ia supernovae extend to about 30,000 km/sec and the Tully-Fisher and Fundamental Plane clusters extend to velocities of about 9,000 and 15,000 km/sec, respectively. However, the current limit for surface brightness fluctuations is about 5,000 km/sec. [Bottom panel:] The value of H_0 as a function of distance in Mpc

References

1. W. Baade, & H.H. Swope: A.J. **70**, 212 (1965)
2. G.F. Benedict, et al.: A.J. **123**, 473 (2002a)
3. G.F. Benedict, et al.: A.J. **124**, 1695 (2002b)
4. C. Cacciari, & G. Clementini: this volume
5. W.L. Freedman, et al.: Ap.J. **553**, 47 (2001)
6. B.K. Gibson: Mem. Soc. Astron. Ital. **71**, 693 (2000) (astro-ph/9910574)
7. B.F. Madore, & W.L. Freedman: P.A.S.P. **103**, 933 (1991)
8. R. Phelps, et al.: Ap.J. **500**, 763 (1998)
9. B. Westerlund: 'The Magellanic Clouds' (Springer-Verlag, Berlin-Heidelberg-New York, 1984)

2 Calibration of the Distance Scale from Cepheids

Pascal Fouqué[1,2], Jesper Storm[3], and Wolfgang Gieren[4]

[1] Observatoire de Paris, LESIA, 5, place Jules Janssen, 92195 Meudon Cedex, France
[2] European Southern Observatory, Casilla 19001, Santiago 19, Chile
[3] Astrophysikalisches Institut Potsdam, An der Sternwarte 16, 14482 Potsdam, Germany
[4] Astronomy Group, Departamento de Física, Facultad de Ciencias Físicas y Matemáticas, Universidad de Concepción, Casilla 160-C, Concepción, Chile

Abstract. We apply the infrared surface brightness method of Fouque and Gieren to a sample of 32 Galactic Cepheids with excellent photometric and radial velocity data. The distance solutions are fully consistent with recent direct interferometric Cepheid distance measurements, and with Hipparcos parallaxes of nearby Cepheid variables, but are more accurate than these determinations. Fitting the slopes observed for large samples of LMC Cepheids to our Galactic data, we derive absolute period-luminosity (PL) relations in the VIWJHK bands which are more accurate than previous work. Comparing the Galactic and LMC PL relations, we derive the LMC distance modulus in all these bands which can be made to agree extremely well under reasonable assumptions for both, the reddening law, and the adopted reddenings of the LMC Cepheids. Our current best LMC distance modulus determination from this technique is 18.55 ± 0.06 mag. The effect of metallicity on the PL relation is discussed. Our Galactic Cepheid distance determinations yield Galactic Cepheid PL relations which are steeper than their LMC counterparts, in all photometric bands, which could be the signature of a metallicity effect. When determining Cepheid distances to solar-metallicity galaxies, it may be advantageous to use the direct Galactic calibration of the PL relation from the infrared surface brightness technique rather than a LMC PL relation, minimizing possible metallicity-related effects on the distance determination.

2.1 Introduction

Since the discovery by Ms. Leavitt almost a hundred years ago that Cepheid variables obey a tight relationship between their pulsation periods and absolute magnitudes, astronomers have made great efforts to calibrate this relationship, and use it to estimate the distances to nearby galaxies in which Cepheids were found. For a very nice review of the early history of the Cepheid period-luminosity (PL) relation, see Fernie [17]. With the course of time, the calibration of the PL relation was refined, using new methods and improving data for both Cepheids in our own Galaxy and Cepheids which were found in increasing numbers in Local Group galaxies. In particular, the Magellanic Clouds have played a fundamental role in our effort to calibrate the PL relation (and still do so today, as we will show in this review), mainly because they are just near enough to make Cepheid apparent magnitudes bright enough for accurate photometry with even

P. Fouqué, J. Storm, and W. Gieren, Calibration of the Distance Scale from Cepheids, Lect. Notes Phys. **635**, 21–44 (2003)
http://www.springerlink.com/

small telescopes, and on the other hand distant enough to have them, in a good approximation, all at the same distance. The slope of the PL relations can thus be determined directly from a sample of LMC Cepheids in contrast to a sample of Galactic Cepheids where accurate individual distances, which are fundamentally difficult to determine, are needed. In the course of the decades, it became clear that the Cepheid PL relation is a very powerful method to determine extragalactic distances, and it was (and still is) generally considered as the most accurate and reliable stellar method to calibrate the extragalactic distance scale. For that reason, the HST Key Project on the Extragalactic Distance Scale chose the strategy to detect samples of Cepheids in a number of selected late-type galaxies and use them to measure the distances to these galaxies, which then served to calibrate other, more far-reaching methods of distance measurement to determine the Hubble constant in a region of constant Hubble flow. It is clear that we have gone a very long way from the early attempts to calibrate the PL relation, to the application of this technique to Cepheids in stellar systems as distant as 20 Mpc, as successfully done by the groups who have used the Hubble Space Telescope for this purpose.

In spite of all these successes, it has also become clear over the past decade that there are still a number of problems with the calibration of the PL relation which so far have prevented truly accurate distance determinations, to 5 percent or better, as needed for the cosmological, and many other astrophysical applications. One basic problem has been the notorious difficulty to measure accurate, independent distances to Galactic Cepheids needed for a calibration of the PL relation in our own Galaxy (see next section). The alternative approach, used many times, is to calibrate the PL relation in the LMC, but this requires an independent knowledge of the LMC distance whose determination has proven to be amazingly difficult (see the review of A.R. Walker in this volume). Another problem complicating the calibration of the PL relation is that Cepheids, as young stars, tend to lie in crowded and dusty regions in their host galaxies, making absorption corrections a critical issue. In more recent years, work on the PL relation has therefore increasingly shifted to the near-infrared where the problems with reddening are strongly reduced as compared to the optical spectral region. Another potential problem with the use of the Cepheid PL relation is its possible sensitivity to chemical abundances; if such a metallicity dependence exists and is significant, it has to be taken into account when comparing Cepheid populations in different galaxies which have different metallicities. Therefore, while there has been a lot of progress on the calibration of Cepheids as distance indicators over the years, there is still room (and need) for a substantial improvement. It is the purpose of this review to contribute such progress, and our approach is to combine Galactic and LMC Cepheids in the best possible way to derive both an improved absolute calibration of the PL relation in a number of optical and near-infrared photometric bands and, in a parallel step, derive an improved distance to the Large Magellanic Cloud from its Cepheid variables. One of the reasons why a PL calibration from Galactic Cepheid variables is of advantage as compared to a calibration based on LMC Cepheids alone is the fact that in most large spiral galaxies, and in particular in those targeted by the HST Key Project, the mean metallicities are quite close to solar, implying that metallicity-related systematic effects are minimized when comparing these extragalactic PL relations to the Galactic one, rather than to the one defined by the more metal-poor population of LMC Cepheids.

In a final step, we will test what our new Cepheid PL calibration implies for other stellar candles frequently used for distance work, such as RR Lyrae stars, red giant clump stars, and the tip of the red giant branch.

2.2 The Galactic vs. the LMC Routes

2.2.1 The Infrared Surface Brightness Method

Fifteen years ago, the classical method of calibrating the PL relation for Cepheids was to use the ZAMS-fitting technique to determine the distances of a handful of open clusters which happen to contain Cepheid members (Feast & Walker [16]). However, Hipparcos revealed that the distance of the calibrating cluster, the Pleiades, had to be revised substantially downwards, at a level where the distance difference between Hyades and Pleiades can no longer be explained only by metallicity differences. Therefore, some doubts were shed on the ZAMS-fitting technique, and it became necessary to find alternative techniques of similar accuracy. It is a measure of our progress to see that two such methods have emerged in the meantime.

The main alternative method, based on the classical ideas of Baade and Wesselink, and first implemented by Barnes & Evans [2] consists in combining linear diameter measurements, as obtained from radial velocity curve integration, to angular diameter determinations coming from measurements of magnitudes and surface brightnesses to derive the mean diameter and distance of a Cepheid. The surface brightness estimates come from a relation between this parameter and a suitably chosen colour.

In a comparison of the results of both methods, Gieren & Fouqué [23] established that the Barnes-Evans zero point of the PL relation in the V band was 0.15 mag brighter than the ZAMS-fitting zero point. However, the Barnes-Evans method uses the $V-R$ colour index to estimate the surface brightness, and it was soon discovered that a much better estimate could come from infrared colours (Welch [61]; Laney & Stobie [38]).

Encouraged by the very promising near-infrared results, Fouqué & Gieren [20] calibrated the infrared surface brightness technique, using both $J-K$ and $V-K$ colours, by assuming that non-variable, stable giants and supergiants follow the same surface brightness vs. colour relation as the pulsating Cepheids. Using 23 stars with measured angular diameters, mostly from Michelson interferometry, they checked that the slope of the relation directly derived from Cepheids was consistent, within very small uncertainties, with the slope derived from stable stars. This provided confidence to also adopt the zero point from the giants and supergiants. They recalibrated the Barnes-Evans relation and showed that the accuracy of the infrared method for deriving the distances and radii of individual Cepheids was 5 to 10 times better than the results produced by an application of the optical counterpart of the technique. As in the optical surface brightness technique, a very important feature and advantage of the infrared surface brightness method is its very low, and almost negligible dependence on absorption corrections.

At that time, only one Cepheid (ζ Gem) angular diameter had been measured, with the lunar occultation technique (Ridgway et al. [50]) and the agreement with our predicted angular diameter led some support to our choice of the zero point. However, that comparison suffered from the relatively large error of the Cepheid angular diameter measurement.

More recently, Nordgren et al. [44] have confirmed our calibrating surface brightness-colour relations from an enlarged sample of 57 giants with accurate interferometric measurements of their angular diameters. Interestingly, they find a similar scatter to ours in these relations, which probably means that intrinsic dispersion has been reached. Then, they used 59 direct interferometric diameter measurements for 3 Cepheids to compute their surface brightnesses, at the corresponding pulsation phases. From these measurements, they derived surface brightness-colour relations for the first time directly from the Cepheids themselves, and confirmed that the Cepheid surface brightnesses do indeed follow the calibrating relations obtained from stable giants and supergiants in the same colour range as Cepheids, yielding a zero point fully compatible with our previous value from stable stars (3.941 ± 0.004 vs. 3.947 ± 0.003, respectively). Subsequently, Lane et al. [36] were able to go a step further and measure the angular diameter variations for 2 Cepheids, therefore allowing a measure of their distances and mean diameters independently of photometric measurements, but also confirming the adopted calibrating relations.

At the time of this review, three Cepheids have distance determinations based on interferometric measurements of their angular diameters. It is instructive to compare them to the distances derived from trigonometric parallaxes. This is done in Table 2.1. In the case of δ Cep, we have used the recent HST measurement by Benedict et al. [5], which supersedes the less accurate Hipparcos measurement. For ζ Gem, the trigonometric parallax comes from Hipparcos, while for η Aql we have used a weighted mean of Hipparcos and USNO measurements, as in Nordgren et al. [43]. The agreement is very good, especially in the case of the accurate trigonometric measurement of δ Cep. Note that the small uncertainty associated with the interferometric distance determination of δ Cep neglects the possible systematic uncertainties introduced by the use of the surface brightness vs. colour relations.

Using the Fouqué & Gieren [20] calibration, Gieren et al. [25] derived a new calibration of the PL relation in $VIJHK$ bands, based on 28 Galactic Cepheids with distances determined from the infrared surface brightness method. However, determining the slope of a linear relation from only 28 points is not very accurate, so they chose to fix the slopes to the better-determined values from LMC Cepheid samples, implicitly assuming that there is no metallicity dependence of the slopes, at least in the metallicity range bracketed by these two

Table 2.1. Comparison of Cepheid distances from interferometry and trigonometric parallaxes

Cepheid	$d_{\text{interferometry}}$	$d_{\text{trigonometry}}$
δ Cep	272 ± 6	$273\,^{+12}_{-11}$
η Aql	320 ± 32	$382\,^{+150}_{-84}$
ζ Gem	362 ± 38	$358\,^{+147}_{-81}$

Table 2.2. Slopes of various PL relations in $BVIWJHK$ bands (see explanations in the text)

Band	Galactic slopes (N)	LMC slopes		
		literature (N)	revised (N)	E(B-V)=0.10
B	-2.72 ± 0.12 (32)			
V	-3.06 ± 0.11 (32)	-2.775 ± 0.031 (651)	-2.735 ± 0.038 (644)	-2.774 ± 0.042
I	-3.24 ± 0.11 (32)	-2.977 ± 0.021 (661)	-2.962 ± 0.025 (644)	-2.986 ± 0.027
W	-3.57 ± 0.10 (32)	-3.300 ± 0.011 (668)	-3.306 ± 0.013 (644)	-3.306 ± 0.013
J	-3.53 ± 0.09 (32)	-3.144 ± 0.035 (490)	-3.112 ± 0.036 (447)	-3.127 ± 0.036
H	-3.64 ± 0.10 (32)	-3.236 ± 0.033 (493)	-3.208 ± 0.034 (447)	-3.216 ± 0.034
K	-3.67 ± 0.10 (32)	-3.246 ± 0.036 (472)	-3.209 ± 0.036 (447)	-3.215 ± 0.037

galaxies. More recently, we have revised the calibrating sample to 32 Galactic Cepheids (Storm et al. [54]), using a number of additional Cepheid variables not used in our previous studies, and also using fresh data from the literature whenever they had become available. The new Cepheid distance solutions from the infrared surface brightness technique are presented in Table 2.7. Reddenings were adopted from Fernie's database [18], column labelled FE1). In Fig. 2.1, we show one such solution for the Cepheid X Cyg which is fairly representative for our whole, updated sample of Galactic Cepheid variables. Our new Galactic Cepheid distance data confirm that the Galactic slopes of the PL relation are steeper than their LMC counterparts, in all photometric bands, as can be seen in Table 2.2. The corresponding Galactic Cepheid PL relations are shown in Fig. 2.2.

However, there are systematic differences in the way the slopes given in Table 2.2 have been determined. For instance, the reddening corrections do not follow exactly the same law in Gieren et al. [25] and in the work of the OGLE team (hereafter OGLE2), and Groenewegen [30]. Even the definition of the reddening-free parameter W varies in the literature. In order to make things fully comparable, we have derived new LMC Cepheid PL relations in the optical (VIW) from the published OGLE2 database, and in the infrared (JHK) from the sample

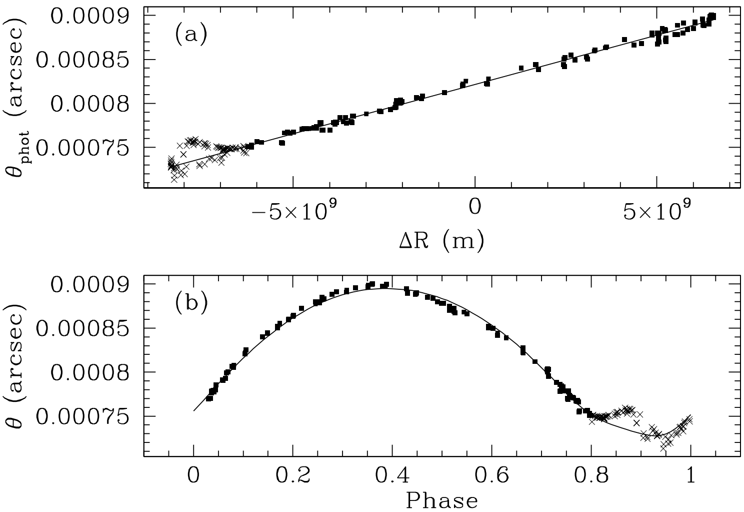

Fig. 2.1. Illustration of the ISB method in the case of X Cyg: the points represent the photometrically determined angular diameters, and the line in panel (a) shows the bisector fit to the filled points. The curve in panel (b) delineates the angular diameter obtained from integrating the radial velocity curve at the derived distance. Crosses in both panels represent points which were eliminated before the fit. This is necessary because near minimum radius the existence of shock waves in the Cepheid atmosphere, and possibly other effects, do not allow a reliable calculation of the angular diameter from the photometry

kindly provided by M. Groenewegen, adopting the same reddening law as for our Galactic calibrators. For this, we have computed the values of the various coefficients R_v, R_i, R_w, R_j, R_h, R_k for each calibrator according to the following formulae (from Laney & Stobie [37] and Caldwell & Coulson [10]):

$$R_v = \frac{A_v}{E(B-V)} = 3.07 + 0.28 \times (B-V)_\circ + 0.04 \times E(B-V) \tag{2.1}$$

$$R_i = \frac{A_i}{E(B-V)} = 1.82 + 0.205 \times (B-V)_\circ + 0.0225 \times E(B-V) \tag{2.2}$$

$$R_w = \frac{1}{1 - R_i/R_v} \tag{2.3}$$

$$R_j = \frac{A_j}{E(B-V)} = R_v/4.02 \tag{2.4}$$

$$R_h = \frac{A_h}{E(B-V)} = R_v/6.82 \tag{2.5}$$

$$R_k = \frac{A_k}{E(B-V)} = R_v/11 \tag{2.6}$$

R_w defines the Wesenheit magnitude as:

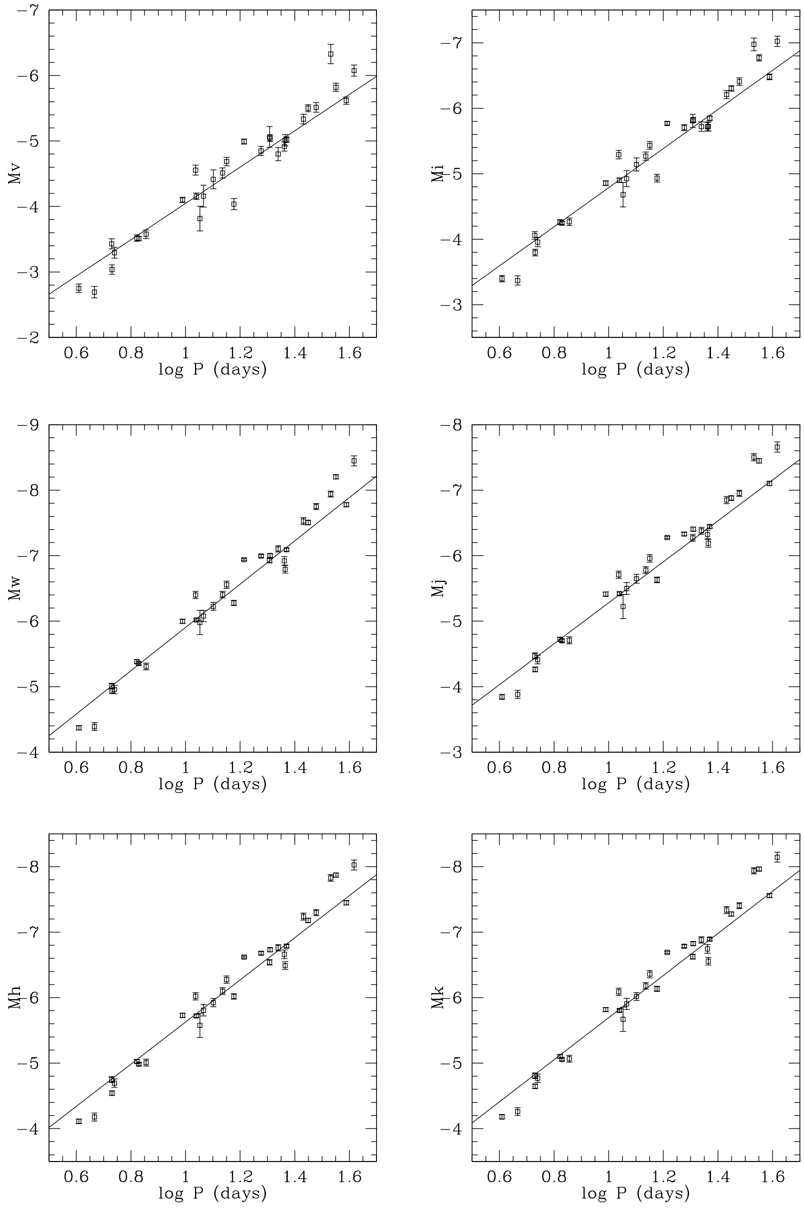

Fig. 2.2. Galactic PL relations in $VIWJHK$ bands, determined from our new infrared surface brightness distance solutions for 32 Galactic Cepheid variables. Superimposed lines correspond to the LMC PL relations from OGLE2 data, adopting $\mu(\mathrm{LMC}) = 18.50$ and a mean $E(B-V) = 0.10$

$$W = V - R_w \ (V - I) \tag{2.7}$$

Then, we have computed the mean value of these coefficients over our 32 Galactic calibrators, assumed to be representative for the entire Galactic Cepheid population. As the rms dispersions turned out to be small (from 0.003 in K to 0.036 in V), we decided to adopt the same constant values for all the Cepheids. These are:

$$R_v = 3.30 \tag{2.8}$$
$$R_i = 1.99 \tag{2.9}$$
$$R_w = 2.51 \tag{2.10}$$
$$R_j = 0.82 \tag{2.11}$$
$$R_h = 0.48 \tag{2.12}$$
$$R_k = 0.30 \tag{2.13}$$

Another possible systematic effect on PL slopes can arise from differences in the period ranges covered by the LMC and Galactic Cepheid samples. In $\log P$, it ranges from 0.1 to 1.5 for the LMC (median 0.59), versus 0.6 to 1.6 for the Milky Way (median 1.16). However, cutting the LMC sample at 0.6 removes more than half of the OGLE2 sample. We therefore adopted the cut at $\log P = 0.4$, as done by the OGLE2 team. We also removed a few stars which were rejected in our linear fits to finally adopt a common sample of 644 stars for V, I and W, and 447 stars with 2MASS random-phase magnitudes in J, H and K. The slopes of the corresponding PL relations derived from these samples are given in Table 2.2 and the LMC PL relations are shown in Fig. 2.3.

Finally, we tested for the possibility that the different PL slopes seen in the LMC and Galactic Cepheid samples could actually be an artifact of our method of distance determination. The most obvious source which could produce a significant effect on the PL slope of our Galactic sample is an error in the adopted value of the p-factor used to convert the Cepheid radial velocity into pulsational velocity. With a variation of the p-factor within any reasonable limits, however, it is clearly impossible to recover the slopes, in the different bands, seen in the LMC Cepheid sample. We also tried to eliminate the most uncertain distances in our Galactic sample, which happen when there is an apparent phase shift between the angular and linear diameter variations in our solutions. Such phase shifts are seen in about one third of our Galactic Cepheids (always smaller than 5 percent) and are most likely due to a slight phase mismatch between the radial velocity curve and the photometric curves used in the analyses, which were not obtained simultaneously (see a detailed discussion of this in Gieren et al. [24]). Eliminating those potentially "problematic" stars did not change significantly the derived Galactic slopes. Our adopted distances are based on a bisector linear least-squares fit of the angular diameters vs. linear displacements at each phase. We also tested the effect of adopting the inverse fit (all errors assumed to be carried by the angular diameters) instead of the bisector fit, as

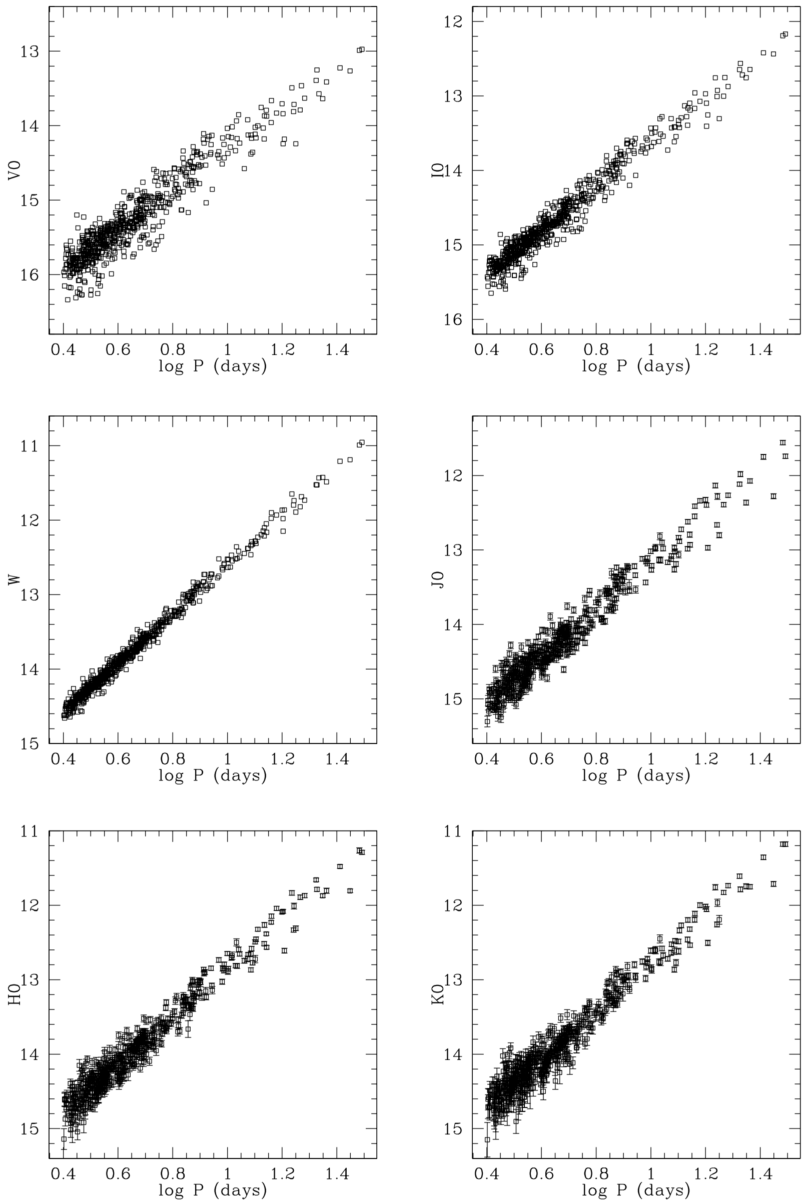

Fig. 2.3. LMC PL relations in *VIWJHK* bands. Note that the relations in the *J*, *H* and *K* bands are derived from single-phase data, which introduces an additional dispersion to the relations not present in the optical *V*, *I* and *W* relations which are based on accurate mean magnitudes from the OGLE2 database

Table 2.3. Absolute magnitudes of a 10-day period Cepheid in $VIWJHK$ bands

Band	$M_{\text{Galactic slopes}}$	$M_{\text{revised LMC slopes}}$
B	-3.320 ± 0.036	
V	-4.049 ± 0.034	-4.087 ± 0.039
I	-4.790 ± 0.034	-4.820 ± 0.038
W	-5.919 ± 0.032	-5.952 ± 0.035
J	-5.346 ± 0.029	-5.359 ± 0.038
H	-5.666 ± 0.031	-5.672 ± 0.040
K	-5.698 ± 0.031	-5.762 ± 0.040

Table 2.4. LMC distance moduli in $VIWJHK$ bands, derived by adopting the OGLE2 reddenings

Band	LMC intercept at 10 days	μ_{LMC}
V	14.318 ± 0.026	18.405 ± 0.047
I	13.631 ± 0.017	18.451 ± 0.041
W	12.597 ± 0.009	18.549 ± 0.036
J	13.185 ± 0.026	18.544 ± 0.046
H	12.853 ± 0.024	18.525 ± 0.046
K	12.793 ± 0.026	18.554 ± 0.048

recommended in Gieren et al. [24], without producing noticeable differences. As a result from these different exercises carried out on the data, we conclude that our adopted distances are very robust against these kinds of subtleties.

We therefore adopted two sets of zero points: the first one assumes our Galactic slopes and the second one assumes the revised LMC slopes. Results are given in Table 2.3.

It appears that the choice of slope only very slightly affects the adopted zero points. This justifies to force the more accurately determined LMC slopes to our 32 Galactic calibrators, and allows a determination of the LMC distance in each band. The results are given in Table 2.4.

The values in Table 2.4 show that the distance moduli increase when the reddening sensitivity of the band decreases. This is an annoying result, which we did not see in our 1998 paper (Gieren et al. [25]). The main difference is that we then used a reduced sample of about 60 LMC Cepheids (OGLE results were not available yet), among which about one half had individual reddening measurements, which yielded a mean value of $E(B-V) = 0.08$, to be compared to the OGLE2 mean value for Cepheids of 0.147.

Table 2.5. LMC distance moduli in $VIWJHK$ bands, derived by adopting a constant reddening of $E(B-V) = 0.10$

Band	LMC intercept at 10 days	$\mu_{\rm LMC}$
V	14.453 ± 0.029	18.536 ± 0.048
I	13.713 ± 0.018	18.530 ± 0.041
W	12.597 ± 0.009	18.549 ± 0.036
J	13.220 ± 0.026	18.577 ± 0.045
H	12.873 ± 0.024	18.544 ± 0.046
K	12.806 ± 0.026	18.567 ± 0.048

We therefore tested the effect of replacing the individual OGLE2 reddenings (which are constant within each of the 84 OGLE2 sub-fields, but slightly varying from field to field) by a mean value of $E(B-V) = 0.10$, as done by the HST Key Project on the Extragalactic Distance Scale (HST-KP) team. Obviously the zero points of the corresponding PL relations are modified by this change, and when combined to the Galactic zero points derived by forcing the new LMC slopes given in last column of Table 2.2 to the Galactic data, we get the LMC distance moduli shown in Table 2.5. It is clear that the agreement among the different bands is now much better and, in fact, quite satisfactory.

We note that the HST-KP for $H_\circ$ determination is not fully consistent in that sense, because they use the OGLE2 PL relations, but assume at the same time a mean LMC reddening of $E(B-V) = 0.10$. If we use our new LMC PL relations with $E(B-V) = 0.10$ (last column of Table 2.2) and assume a LMC distance modulus of 18.50 as they did, the resulting zero points are changed and appear in Table 2.6. It is seen that this introduces a significant difference in the Cepheid absolute magnitudes in the V and I bands, at a Cepheid period of 10 days.

To circumvent, or minimize the reddening problem, we prefer to exclude the V and I band results from our final determination of the distance modulus to the LMC. In fact, the W value already combines the information from V and I bands in the best possible way. We therefore take a weighted mean of the W value on one side and the infrared weighted average of J, H, K on the other side, which gives 18.541 ± 0.047 for OGLE2 reddenings and 18.563 ± 0.046 for a constant $E(B-V) = 0.10$. This gives a greater weight to W which is truly reddening free, and a lower one to the infrared values which are derived only from random-phase magnitudes. The uncertainty of the mean comes from the weighted rms dispersion of the values from all the bands.

From this procedure we find, as our best adopted value, a LMC distance modulus of 18.55 ± 0.06. The uncertainty does not include the systematic uncertainty arising if the LMC and Galactic slopes are really different. In that case, the derived offset depends on the adopted period for the zero-point. If we mea-

Table 2.6. Zero point comparison for a 10-day period Cepheid in $VIWJHK$ bands

Band	$M_{\text{Hipparcos}}$	$M_{\text{HST-KP}}$		$M_{\text{this work}}$
		literature	$E(B-V)=0.10$	
V	-4.21 ± 0.11	-4.218 ± 0.02	-4.047 ± 0.029	-4.049 ± 0.034
I	-4.93 ± 0.12	-4.904 ± 0.01	-4.787 ± 0.018	-4.790 ± 0.034
W	-5.96 ± 0.11	-5.899 ± 0.01	-5.903 ± 0.009	-5.919 ± 0.032
J		-5.32 ± 0.06	-5.280 ± 0.026	-5.346 ± 0.029
H		-5.66 ± 0.05	-5.627 ± 0.024	-5.666 ± 0.031
K	-5.76 ± 0.17	-5.73 ± 0.05	-5.694 ± 0.026	-5.698 ± 0.031

sure the offset at the median value of the LMC sample ($\log P = 0.59$) in place of $\log P = 1$, the derived W modulus becomes 18.41. We are indebted to Frédéric Pont for this remark.

2.2.2 The Hipparcos Parallaxes Method

It has been common-place in the past years to present the Galactic calibration based on Hipparcos parallaxes [33] of about 200 Cepheids as discrepant from other calibrations. This probably arose from the large distance of the LMC published in the original work of Feast & Catchpole [15], $\mu = 18.70 \pm 0.10$. However, we will see that the Hipparcos calibration is not discrepant at all, and that the problem arises in the application of the Hipparcos calibration to the determination of the LMC distance.

The outstanding idea of Feast & Catchpole [15] to combine the very uncertain, but also very numerous, parallax measurements of Cepheids by Hipparcos to derive a PL relation zero point for Cepheids has been shown to be free of biases by subsequent studies (Pont [48], Lanoix et al. [39], Groenewegen & Oudmaijer [31]). The last of these studies is probably the most accurate one, and generalizes the result to different photometric bands. We will adopt their zero points as the Hipparcos Galactic calibration, based on 236 Cepheids (median $\log P = 0.82$). For details about the method, the reader is referred to the above references.

For a 10-day period Cepheid, these zero points are given in Table 2.6 and compared to our zero points and to the adopted zero points of the HST-KP for $H_\circ$ determination (Freedman et al. [22], Macri et al. [41], based on the original OGLE2 LMC relations and on new infrared PL relations, assuming a LMC distance modulus of 18.50). Please note that the values of the slopes and the definitions of W adopted to derive these zero points vary among these works. For comparison, the original Feast & Catchpole [15] V band zero point was -4.24 ± 0.10. Table 2.6 also gives the HST-KP zero points derived adopting the new OGLE2 LMC relations based on a mean reddening of $E(B-V) = 0.10$.

We must be cautious with the conclusions to be drawn from Table 2.6: there is an apparently good agreement between the Hipparcos and the original HST-KP zero points on one hand, and between the ISB Galactic and the revised HST-KP zero points on the other hand. How is this to be interpreted?

First of all, if the Hipparcos and the original HST-KP zero points agree, why do they lead to different distance moduli for the LMC? Simply because the adopted LMC PL relations have different intercepts: Feast & Catchpole [15] adopted a LMC PL relation in V from Caldwell & Laney [11] based on 88 Cepheids with an intercept of 14.42 ± 0.02, and based on a mean adopted reddening of $E(B - V) = 0.08$ (30 have individual BVI reddenings), while Freedman et al. [22] used the originally published OGLE2 PL relations based on more than 600 Cepheids with an intercept of 14.282 ± 0.021 and a mean reddening of 0.147. The observed difference of 0.14 mag in intercepts is well explained by the difference in adopted mean reddenings ($0.067 \times 3.3 = 0.22$) and is sufficient to make the distance moduli discrepant. Please note that Feast & Catchpole [15] also added a metallicity correction of 0.04 mag, even increasing the discrepancy.

In fact, the low accuracy of the Hipparcos zero points makes the observed difference between the Hipparcos and the ISB V zero points not significant, as can be seen in Fig. 2.4 which displays, for the Cepheids with the highest weights, the value of the zero point estimate $10^{0.2\,\rho}$ vs. its uncertainty, together with the positions of the adopted Hipparcos and the ISB zero points. In the I band, the zero point difference is smaller, and clearly not significant if we consider the alternative value published by Lanoix et al. [39], which is -4.86 ± 0.09. Finally, there is a good agreement in W- and K-band zero points, but this is probably quite fortuitous for the same reasons.

Now, the excellent agreement between the revised HST-KP and the Galactic ISB Cepheid absolute magnitudes at a 10-day period is clearly more significant thanks to the high accuracy of both results. This basically demonstrates that the HST-KP adopted LMC distance modulus of 18.50 is very nearly correct.

2.2.3 The ZAMS-Fitting Calibration

Feast [14] published a revised list of 31 Galactic Cepheids belonging to open clusters or associations with distance moduli derived through the ZAMS-fitting technique. He also explained why the values may not be modified by the Pleiades distance change after the Hipparcos measurement (simultaneous change of the reference ZAMS of the same order of magnitude). In fact, his cluster distance values are very close to those published in Gieren & Fouqué [23].

Twenty-four of these cluster Cepheids lie in the period range of our Galactic calibrators of the ISB technique. We have derived PL relations from these Cepheids, which are given below, and appear to be in good agreement with those derived from the ISB distances, although they are less accurate. They support the evidence that the Galactic PL slopes are somewhat steeper than the LMC ones.

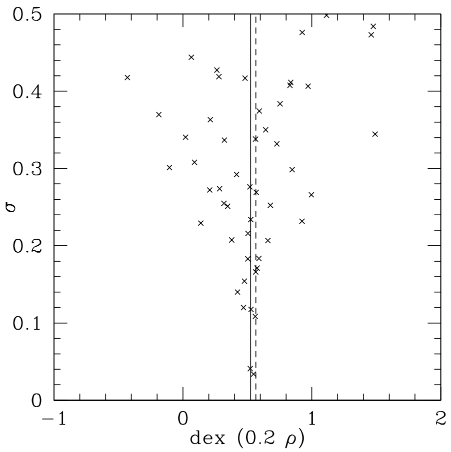

Fig. 2.4. Hipparcos V PL relation individual zero points (expressed as $10^{0.2\,\rho}$, where ρ is the zero point at $\log P = 1$) vs. their uncertainty; superimposed as vertical lines are the Hipparcos adopted mean (*solid line*) and the alternative ISB value (*dashed line*)

$$M_v = -2.767 \pm 0.173\ (\log P - 1) - 4.160 \pm 0.055\ (\sigma = 0.271\ N = 24) \quad (2.14)$$
$$M_i = -3.273 \pm 0.164\ (\log P - 1) - 4.837 \pm 0.051\ (\sigma = 0.218\ N = 18) \quad (2.15)$$
$$M_w = -3.684 \pm 0.144\ (\log P - 1) - 5.980 \pm 0.045\ (\sigma = 0.191\ N = 18) \quad (2.16)$$
$$M_k = -3.766 \pm 0.170\ (\log P - 1) - 5.694 \pm 0.051\ (\sigma = 0.217\ N = 18) \quad (2.17)$$

Very recently, Turner & Burke [56] published a revised list of 46 Cepheids belonging to clusters or associations. Fifteen of these Cepheids have ISB distances in our current sample. The weighted mean of the distance moduli differences we find is not significant and amounts to:

$$\langle \mu(\mathrm{ISB}) - \mu(\mathrm{ZAMS}) \rangle = +0.01 \pm 0.06\ \sigma = 0.24 \quad (2.18)$$

after rejection of AQ Pup (0.79 ± 0.11 difference - we note that cluster membership of this star seems to be very uncertain). Other large differences are observed for δ Cep (0.37 ± 0.11), BB Sgr (0.49 ± 0.08), and U Car (-0.45 ± 0.05). Excluding these stars, for which the case of membership in their respective clusters/associations is not strong (see original references cited in the paper of Turner & Burke), the rms dispersion is 0.10, corresponding to 3% distance precision for each set.

From this comparison, we conclude that the Cepheid distance scale based on ZAMS-fitting is consistent with the calibration from the ISB method. This may be a bit surprising given the many difficulties in the application of the ZAMS-fitting method, and the doubts shed on the method after Hipparcos.

Table 2.7. Data for the 32 Galactic calibrators, from our new infrared surface brightness analysis of these stars. R is the star mean radius in solar units, and σ_R its uncertainty

ID	$\log P$	μ_0	σ_μ	R	σ_R	M_B	M_V	M_I	M_J	M_H	M_K	M_W	$E(B-V)$
BF Oph	0.609329	9.271	0.034	32.0	0.5	−2.13	−2.75	−3.40	−3.84	−4.11	−4.18	−4.37	0.247
T Vel	0.666501	9.802	0.060	33.6	0.9	−2.05	−2.69	−3.37	−3.88	−4.18	−4.26	−4.39	0.281
δ Cep	0.729678	7.084	0.044	42.0	0.9	−2.87	−3.43	−4.06	−4.47	−4.75	−4.81	−5.01	0.092
CV Mon	0.730685	10.988	0.034	40.3	0.6	−2.46	−3.04	−3.80	−4.26	−4.54	−4.65	−4.93	0.714
V Cen	0.739882	9.175	0.063	42.0	1.2	−2.71	−3.30	−3.96	−4.41	−4.69	−4.77	−4.95	0.289
BB Sgr	0.821971	9.519	0.028	49.8	0.6	−2.82	−3.52	−4.26	−4.72	−5.02	−5.10	−5.38	0.284
U Sgr	0.828997	8.871	0.022	48.4	0.5	−2.82	−3.51	−4.25	−4.70	−4.98	−5.06	−5.35	0.403
η Aql	0.855930	6.986	0.052	48.1	1.1	−2.94	−3.58	−4.27	−4.71	−5.01	−5.07	−5.31	0.149
S Nor	0.989194	9.908	0.032	70.7	1.0	−3.34	−4.10	−4.86	−5.41	−5.73	−5.82	−6.00	0.189
Z Lac	1.036854	11.637	0.055	77.8	2.0	−3.86	−4.56	−5.29	−5.71	−6.02	−6.09	−6.40	0.404
XX Cen	1.039548	11.116	0.023	69.5	0.7	−3.43	−4.16	−4.90	−5.42	−5.72	−5.80	−6.02	0.260
V340 Nor	1.052579	11.145	0.185	67.1	5.7	−2.98	−3.82	−4.68	−5.22	−5.58	−5.67	−5.98	0.315
UU Mus	1.065819	12.589	0.084	74.0	2.9	−3.42	−4.16	−4.92	−5.50	−5.81	−5.90	−6.08	0.413
U Nor	1.101875	10.716	0.060	76.3	2.1	−3.71	−4.42	−5.14	−5.65	−5.92	−6.02	−6.23	0.892
BN Pup	1.135867	12.950	0.050	83.2	1.9	−3.76	−4.51	−5.27	−5.78	−6.10	−6.18	−6.40	0.438
LS Pup	1.150646	13.556	0.056	90.2	2.3	−3.93	−4.69	−5.43	−5.96	−6.28	−6.36	−6.56	0.478
VW Cen	1.177138	12.803	0.039	86.6	1.5	−3.15	−4.04	−4.93	−5.63	−6.02	−6.13	−6.28	0.448
X Cyg	1.214482	10.421	0.016	105.3	0.8	−4.12	−4.99	−5.77	−6.28	−6.62	−6.69	−6.94	0.288
VY Car	1.276818	11.501	0.022	112.9	1.1	−3.93	−4.85	−5.70	−6.33	−6.68	−6.78	−7.00	0.243
RY Sco	1.307927	10.516	0.034	100.0	1.5	−4.40	−5.06	−5.81	−6.27	−6.54	−6.62	−6.93	0.777
RZ Vel	1.309564	11.020	0.029	114.7	1.5	−4.25	−5.04	−5.82	−6.40	−6.73	−6.82	−7.00	0.335
WZ Sgr	1.339443	11.287	0.047	121.8	2.6	−3.87	−4.80	−5.72	−6.38	−6.76	−6.88	−7.10	0.467
WZ Car	1.361977	12.918	0.066	112.0	3.4	−4.14	−4.92	−5.72	−6.32	−6.66	−6.74	−6.92	0.384
VZ Pup	1.364945	13.083	0.057	97.1	2.5	−4.32	−5.01	−5.72	−6.19	−6.49	−6.56	−6.79	0.471
SW Vel	1.370016	11.998	0.025	117.5	1.4	−4.21	−5.02	−5.85	−6.44	−6.79	−6.89	−7.09	0.349
T Mon	1.431915	10.777	0.053	146.3	3.6	−4.36	−5.33	−6.21	−6.85	−7.24	−7.34	−7.53	0.209
RY Vel	1.449158	12.019	0.032	139.9	2.1	−4.69	−5.50	−6.30	−6.88	−7.18	−7.28	−7.51	0.562
AQ Pup	1.478624	12.522	0.045	147.9	3.1	−4.65	−5.51	−6.41	−6.95	−7.30	−7.40	−7.75	0.512
KN Cen	1.531857	13.124	0.045	185.8	3.9	−5.64	−6.33	−6.98	−7.50	−7.83	−7.94	−7.94	0.926
l Car	1.550855	8.989	0.032	201.7	3.0	−4.71	−5.82	−6.77	−7.45	−7.87	−7.96	−8.20	0.170
U Car	1.589083	10.972	0.032	161.5	2.4	−4.72	−5.62	−6.48	−7.10	−7.45	−7.56	−7.78	0.283
RS Pup	1.617420	11.622	0.076	214.7	7.5	−5.11	−6.08	−7.02	−7.66	−8.03	−8.14	−8.45	0.446

2.3 What May Still Be Wrong in the LMC Distance?

2.3.1 Reddening Effects

We have seen previously how changing the adopted reddening may change our results. By reddening we mean both the reddening values and the reddening law. There is good evidence in the literature that the LMC reddening law may differ from the Galactic one shortward of B (see, e.g., Gochermann & Schmidt-Kaler [27]). However, this is of little concern for us. What is more important is that there is some evidence that the R_v value may be lower in the LMC. For instance, Misselt et al. [42] find R_v values varying between 2.16 and 3.31, and obtain a good fit using the standard Cardelli et al. [12] reddening law for a mean value of $R_v = 2.4$. Similar, but slightly higher values (between 2.66 and 3.60) have been found in the SMC by Gordon & Clayton [28]. So, what we interpret as a smaller mean LMC reddening than the OGLE2 values may in fact be due to a lower R_v value.

Concerning the reddening values, several studies have investigated both the foreground reddening due to our Galaxy (the LMC is at $-33°$ galactic latitude), and the internal reddening. They show that the reddening is patchy, with large variations from a line of sight to another.

Concerning the foreground reddening, Schwering & Israel [53] find from $48'$ resolution maps a range of 0.06 to 0.17 in $E(B-V)$, with an average value of 0.10. By comparison, the foreground reddening in front of the SMC is found more homogeneous, only varying from 0.06 to 0.08. In the LMC, Oestreicher et al. [45] with a better resolution of $10'$ also find a large range from 0 to 0.15, with an average value of 0.06 ± 0.02.

Concerning the internal reddening, Oestreicher & Schmidt-Kaler [46] find a range of 0.06 to 0.29, with a mean $E(B-V) = 0.16$, while Harris et al. [32] find a total average extinction of 0.20, from which they conclude that the mean internal reddening amounts to $E(B-V) = 0.13$ mag.

In comparison, Udalski et al. [58] use the mean magnitude of the Red Giant Clump (RGC) to derive the total reddening variations along the 21 LMC OGLE2 fields (mainly along the bar). They divide each field into 4 sub-fields and give a mean reddening along each of the 84 lines of sight, corresponding to a resolution of $14.2'$. The zero point of their reddening scale is given by three photometric measurements from the literature. They find a range of total extinction between 0.105 and 0.201, with a mean value over the fields of 0.137, and a mean Cepheid value of $E(B-V) = 0.147$.

However, Girardi & Salaris [26] have shown that the RGC mean absolute magnitude depends on population effects (age and metallicity). This implies that the OGLE2 method is only valid as long as it can be assumed that the population characteristics do not change along the LMC bar.

In any case, Beaulieu et al. [4] have shown that the resolution of the OGLE2 maps is not sufficient to consider their reddenings as individual values for each Cepheid, since the PL residuals in V and I correlate along the reddening line in the case of LMC, as can be seen from Fig. 2.5, reproduced from their paper.

It is therefore tempting to use BVI OGLE2 measurements to derive individual reddenings, following the Dean et al. [13] precepts, adapted to the LMC metallicity as in Caldwell & Coulson [9]. Such measurements exist for 329 Cepheids, which is about one half of the calibrating sample. Unfortunately, the result is disappointing, because when we apply the derived individual reddenings to correct the mean V and I magnitudes, the dispersions of the PL relations *increase*.

Finally, some authors use period-colour (PC) relations to estimate the reddenings. This is the case for instance in the various works based on Hipparcos parallaxes. However, it is well known that the PC relations have considerable intrinsic dispersion, but as shown by Feast & Catchpole [15], these over- or under-estimated reddenings compensate in part for the intrinsic width of the PL relations. But, as the Cepheid colours vary with metallicity at a given period (see below), it is important to use a PC relation adapted to the sample under study. Only 7 Hipparcos Cepheids do not have reddening measurements

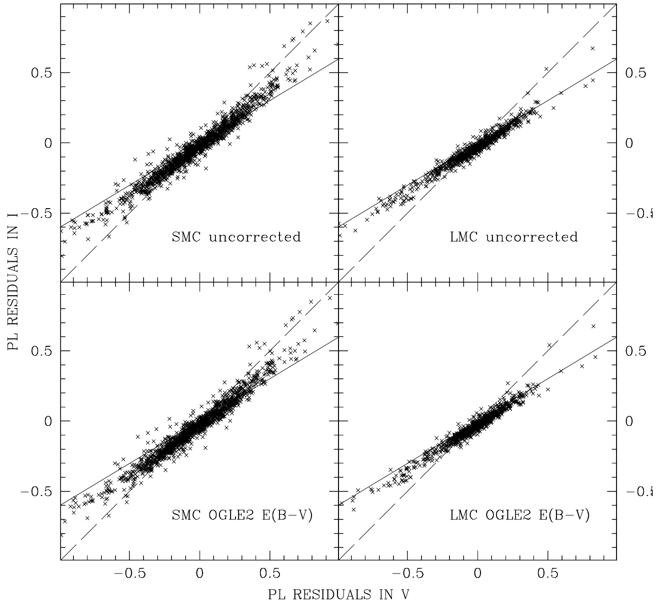

Fig. 2.5. Plot of PL relations residuals in V and I from Beaulieu et al. [4]. The data from the LMC clearly correlate along the reddening line (*solid*) even after application of the OGLE2 reddening correction

in Fernie's database [18]. We have therefore checked that using these individual reddenings in place of those derived from a PC relation indeed gives a similar result for the Galactic zero point in V.

As a summary from this discussion, it is clear that the reddening problem is still far from being overcome, but we believe that our current adopted procedures do minimize the influence of reddening on the LMC distance modulus derived in the previous section. Once more, the merits of using infrared bands or reddening insensitive parameters such as W are underlined.

2.3.2 Metallicity Effects

Theoretical Point of View. There is a long debate in the literature on the effect metallicity may have on the PL relations in different photometric bands, both on the theoretical and observational sides. From an observer's point of view, it seems that one can always find a theory which agrees with the metallicity dependence one finds by observational tests. However, not all the theories rest on the same basis. It is well known that purely radiative stellar pulsation models predict too large pulsation amplitudes for Cepheids. Some convective transport must be added, for instance by means of the Mixing Length Theory (MLT). However, time-independent MLT cannot predict the position of the red edge of the instability strip, which needs the additional introduction of a time-dependent dissipation introduced by the eddy viscosity. But time-dependent MLT models are not successful if they are too local in space. We therefore need at least a non-local time-dependent hydrodynamic pulsation code to correctly describe the coupling of pulsation and convection.

There are not so many codes available. Some linearize the equations (Yecko et al. [62]) while others solve the full non-linear equations (Bono & Stellingwerf [6], Feuchtinger [19]). It seems that their results concerning metallicity dependences basically agree. The fact that they disagree with predictions of models based on purely radiative pulsation codes which neglect the coupling of pulsation with convection (Saio & Gautschy [51], Alibert et al. [1]) seems to us an effect of these simplifications. We will therefore basically follow the predictions of the full-amplitude (non-linear) models including a non-local and time-dependent treatment of stellar convection from Bono et al. [7]. But we are aware that these models depend on a number of not well constrained parameters, the adopted values of which may change the predictions to a significant level (see Figs. 12 and 13 in Yecko et al. [62]).

These models first predict that at a given metallicity (Y and Z fixed), the width of the instability strip changes from low- to high-mass Cepheids, therefore invalidating older model predictions, which assumed that the red edge was parallel to the blue edge. Now, for a given Cepheid mass (and therefore luminosity), an increase in Z (and Y) shifts the instability strip towards cooler effective temperatures, due to a decrease in the pulsation destabilization caused by the hydrogen ionization region; therefore, at a fixed period and *assuming* a uniformly populated instability strip, metal-poor pulsators are *more* luminous than metal-rich ones.

However, this prediction for bolometric magnitudes does not necessarily apply to all photometric bands, and differences in the adopted atmosphere models may generate differences in the magnitude of the effect for a given band. Bono et al. [8] find that the dependence on metallicity is increased in the V band, due to the dependence of the bolometric correction on effective temperature, while it is smaller in the K band. But the effect is still that metal-poor pulsators are more luminous than metal-rich ones, when absolute magnitudes are derived from a PL relation. However, metallicity also affects colours, and an increase in Z at fixed period gives redder $B-V$ and $V-K$ colours. When using a PLC relation to derive the absolute magnitudes, both effects must be taken into account, and at fixed period *and* colour, metal-poor pulsators are still slightly *more* luminous in K but *less* luminous in V than metal-rich ones.

This theoretical model also predicts that the slopes of the PL relation vary with metallicity, in the sense that an increase in Z produces shallower slopes in the V and K bands, the effect being smaller in K. We observe the opposite effect. Also, the slopes of the PC relations ($B-V$ and $V-K$) are predicted to steepen when Z increases.

Observational Point of View. On the observational side, let us start with differential studies. By this, we mean studies in different regions of a given galaxy showing a spatial variation in metallicity, to assess magnitude differences, at a given period, due to the variation of metallicity. The pioneering work of Freedman & Madore [21] compared Cepheids in three fields of M 31 at different galactocentric distances; it led to inconclusive results, varying from no significant metallicity effect according to the original authors to large effects according to Gould's re-analysis [29]. A more accurate study was conducted in M 101 by Kennicutt et al. [34] who compared the derived distance moduli for 2 fields, located at different radial distances from the center of the galaxy having a difference of 0.7 dex in nebular [O/H]. They found some effect in the sense that distances to metal-rich galaxies are underestimated when derived by using the LMC Cepheid PL relation, but the share of effect between V and I bands is not specified.

In the same spirit, we have observed the Sculptor Group spiral NGC 300 in B, V and I and discovered about 120 Cepheids, well distributed all over the galaxy (Pietrzyński et al. [47]). By measuring the stellar metallicity in different regions from B and A supergiants spectra, we plan to measure any differential effect due to metallicity. This work is in progress, and we believe that this will provide the as yet most stringent observational test on the metallicity sensitivity of the Cepheid PL relation. We have also observed outer disc Cepheids of our own galaxy (Pont et al. [49]), with the hope that the metallicity difference to the solar region would mimic the metallicity difference to the LMC. It appears, however, that the metallicity range only reaches the typical LMC metallicity ([Fe/H] ~ -0.3) at about 14 kpc, where very few Cepheids are known (Luck et al. [40]). This makes evidencing metallicity effects in our own galaxy a difficult task. The task could seem easier when comparing Galactic to SMC Cepheids, as recently shown by Storm et al. [54], but here again disentangling metallicity effects from uncertain reddenings for SMC stars, depth and ridge line effects for such a small sample (5 stars) is quite a challenge.

Another approach was pioneered by Beaulieu et al. [3] and Sasselov et al. [52] in the Magellanic Clouds for V and I bands, and generalized by Kochanek [35] to 17 galaxies in $UBVRIJHK$ bands. From an analysis of 481 Cepheids detected by the EROS microlensing experiment in the LMC and SMC, and assuming that the slopes of the PL relations do not depend on metallicity, Beaulieu and Sasselov found that an SMC Cepheid is *less* luminous than a LMC Cepheid of same period by 0.06 mag in the blue EROS band (intermediate between Johnson B and V) but *more* luminous by 0.01 mag in the red EROS band (intermediate between Cousins R and I). The net effect is to overestimate the SMC distance modulus by 0.14 mag. Kochanek finds that metal-poor pulsators are *more* luminous than metal-rich ones in U and B, but *less* luminous in $VIJHK$, with the difference increasing with the wavelength. These studies then translate the metallicity dependence into a distance modulus variation per dex of [Fe/H], but nothing proves so far that such a dependence is linear.

Finally, Udalski et al. [59] presented recently an analysis of PL relations in IC 1613, a galaxy of even lower metallicity than the SMC ([Fe/H] ~ -1.0), and showed that the slopes of the V and I relations were not significantly different from those found in the LMC, giving a strong observational hint that the slopes do not depend on metallicity, at least in the range -1.0 to -0.3 in [Fe/H]. They also argue that the zero points do not depend on metallicity, but this relies on comparison with other distance indicators which themselves depend upon metallicity, so this result currently lies on less stable grounds.

From all these theoretical and observational results on the metallicity effect on Cepheid absolute magnitudes currently available, it is our impression that if a metallicity dependence of the PL relations exists, it should be small, its sign is currently not well defined and may depend on the photometric band, and it may not be a linear function of [Fe/H].

2.4 Consequence for Other Distance Indicators

At the time of this writing, no distance indicator can claim to be so accurate that other distance indicators become unnecessary. All distance indicators suffer, to some extent, from systematic uncertainties and the best way to constrain the Extragalactic Distance Scale seems to compare the results of various distance indicators for which previous work has shown that they provide relatively accurate measures of distances.

It is not the purpose of this review to compare in detail the calibrations of all the most promising distance indicators. Other review papers in this book deal with them. We just want to find out what our preferred Cepheid PL relation derived in this paper predicts for several other of the most common distance indicators.

For this purpose, we only need to know the difference in magnitude between a Cepheid of 10-day pulsation period and the following other distance indicators: Tip of the Red Giant Branch magnitude (TRGB), Red Giant Clump mean magnitude (RGC), and RR Lyrae magnitude. We adopt the following values of differences from Udalski [57], based on several nearby galaxies and his adopted corrections for different metallicities:

$$V_\circ \text{ (RR Lyrae at [Fe/H]} = -1.6) - V_\circ \text{ (Cepheid at 10 days)} = 4.60 \tag{2.19}$$
$$(V - I)_\circ \text{ (Cepheid at 10 days)} = 0.70 \tag{2.20}$$
$$I_\circ \text{ (TRGB)} - I_\circ \text{ (Cepheid at 10 days)} = 0.70 \tag{2.21}$$
$$I_\circ \text{ (RGC at [Fe/H]} = -0.5) - I_\circ \text{ (TRGB)} = 3.60 \tag{2.22}$$

From these differences and the Galactic ISB zero points from Table 2.3, it is easy to predict expected values for other distance indicators. Our current Cepheid calibration corresponds to:

$$M_v \text{ (RR Lyrae at [Fe/H]} = -1.6) = +0.55 \tag{2.23}$$
$$M_i \text{ (TRGB)} = -4.09 \tag{2.24}$$
$$M_i \text{ (RGC at [Fe/H]} = -0.5) = -0.49 \tag{2.25}$$

We leave to others the discussion of the importance of population effects on these differences to determine which precise value should be applied in any case, and the comparison of our predicted values to the range of published values in the literature. We just want to note the very good agreement with the RR Lyrae mean V magnitude presented at this conference by C. Cacciari and G. Clementini, namely $M_v = +0.59 \pm 0.03$ at [Fe/H] $= -1.5$, which corresponds to $+0.57$ at [Fe/H] $= -1.6$.

2.5 Conclusions

We have used the infrared surface brightness technique to obtain a new absolute calibration of the Cepheid PL relation in optical and near-infrared bands from improved data on Galactic stars. The infrared surface brightness distances to the Galactic variables are consistent with direct interferometric Cepheid distance measurements, and with the PL calibration coming from Hipparcos parallaxes of nearby Cepheids, but are more accurate than these determinations. We find that in all bands, the Galactic Cepheid PL relation appears to be slightly, but significantly steeper than the corresponding relation defined by the LMC Cepheids. This systematic difference has recently been confirmed by Tammann et al. [55] and could be a signature of a metallicity effect on the slope of the PL relation. Since the slope of our LMC Cepheid sample is clearly better defined than the one of the much smaller Galactic sample, we fit the LMC slopes to our Galactic calibrating Cepheid sample (which introduces only a small uncertainty) to obtain our final, adopted and improved absolute calibrations of the Cepheid PL relations in the $VIWJHK$ bands. Comparing the absolute magnitudes of 10-day period Cepheids in both galaxies which are only slightly affected by the different Galactic and LMC slopes of the PL relation, we derive values for the LMC distance modulus in all these bands which can be made to agree extremely well under reasonable assumptions for both, the reddening law, and the adopted reddenings of the LMC Cepheids. However, reddening remains an important and not satisfactorily resolved issue, and in order to obtain a LMC distance determination as independent of reddening as possible, we adopt as our final result a weighted mean of the values coming from the reddening-insensitive Wesenheit magnitude, and those derived from the near-infrared bands. This yields, as our current best estimate from Cepheid variables, a LMC distance modulus of 18.55 ± 0.06.

A discussion of the effect of metallicity on Cepheid absolute magnitudes as provided by both, existing empirical and theoretical evidence makes us conclude that at the present time, it seems likely that there is some metallicity dependence of the PL relation, of small size, whose sign is not clear, and whose size may depend on the photometric band. It may also be a non-linear function of metallicity, with some indication that the metallicity effect on the Cepheid PL relation does not change basically between very low and LMC metallicities, but that the slope of the metallicity dependence may steepen when going from LMC to solar abundances. Clearly, more work from both theory and, particularly, from the observational side has to be done to improve the constraints on the metallicity effect. Until this is achieved, it may be the best choice to use our current, Galactic calibration in applications to the distance measurement of Cepheids in solar metallicity galaxies. Thanks to its accuracy provided by the infrared surface brightness technique, the Galactic calibration is now a true alternative to using the LMC calibration, with the added benefit of minimizing metallicity-related effects when studying Cepheid samples in metal-rich spiral galaxies.

Acknowledgements

The authors are indebted to Jean-Philippe Beaulieu for comments on the validity of theoretical predictions concerning the metallicity effects on the PL relations and for authorizing us to reproduce Fig. 2.5. Giuseppe Bono also helped us to better understand the current differences among theories.

Some calculations would not have been possible without Martin Groenewegen's kindness, who sent his list of JHK magnitudes for OGLE2 Cepheids and basic data for Hipparcos-observed Cepheids.

Comments and corrections from Frédéric Pont and Daniel Cordier are very gratefully acknowledged, as well as valuable inputs from Sergei Andrievsky, David Bersier, Pierre Kervella, Francesco Kienzle, Lucas Macri, Barbara Mochejska, Georges Paturel, Eric Persson, and Grzegorz Pietrzyński.

WG gratefully acknowledges financial support for this work from the Chilean Center for Astrophysics FONDAP 15010003.

References

1. Y. Alibert, I. Baraffe, P. Hauschildt, F. Allard: A&A **344**, 551 (1999)
2. T.G. Barnes, D.S. Evans: MNRAS **174**, 489 (1976)
3. J.-P. Beaulieu, D.D. Sasselov, C. Renault, P. Grison, R. Ferlet, A. Vidal-Madjar, E. Maurice, L. Prévot, E. Aubourg, P. Bareyre, S. Brehin, C. Coutures, N. Delabrouille, J. de Kat, M. Gros, B. Laurent, M. Lachièze-Rey, E. Lesquoy, C. Magneville, A. Milsztajn, L. Moscoso, F. Queinnec, J. Rich, M. Spiro, L. Vigroux, S. Zylberajch, R. Ansari, F. Cavalier, M. Moniez, C. Gry, J. Guibert, O. Moreau, F. Tajhmady: A&A **318**, L47 (1997)
4. J.-P. Beaulieu, J.R. Buchler, Z. Kolláth: A&A **373**, 164 (2001)
5. G.F. Benedict, B.E. McArthur, L.W. Fredrick, T.E. Harrison, C.L. Slesnick, J. Rhee, R.J. Patterson, M.F. Skrutskie, O.G. Franz, L.H. Wasserman, W.H. Jefferys, E. Nelan, W. van Altena, P.J. Shelus, P.D. Hemenway, R.L. Duncombe, D. Story, A.L. Whipple, A.J. Bradley: AJ **124**, 1695
6. G. Bono, R.F. Stellingwerf: ApJS **93**, 233 (1994)
7. G. Bono, M. Marconi, R.F. Stellingwerf: ApJS **122**, 167 (1999)
8. G. Bono, F. Caputo, V. Castellani, M. Marconi: ApJ **512**, 711 (1999)
9. J.A.R. Caldwell, I.M. Coulson: MNRAS **212**, 879 (1985) and erratum in MNRAS **214**, 639 (1985)
10. J.A.R. Caldwell, I.M. Coulson: AJ **93**, 1090 (1987)
11. J.A.R. Caldwell, C.D. Laney: 'The Magellanic Clouds'. In: *IAU Symp. 148*, ed. by R. Haynes, D. Milne (Kluwer, Dordrecht 1991) p. 249

12. J.A. Cardelli, G.C. Clayton, J.S. Mathis: ApJ **345**, 245 (1989)
13. J.F. Dean, P.R. Warren, A.W.J. Cousins: MNRAS **183**, 569 (1978)
14. M.W. Feast: PASP **111**, 775 (1999)
15. M.W. Feast, R.M. Catchpole: MNRAS **286**, L1 (1997)
16. M.W. Feast, A.R. Walker: ARA&A **25**, 345 (1987)
17. J.D. Fernie: PASP **81**, 707 (1969)
18. J.D. Fernie, B. Beattie, N.R. Evans, S. Seager: IBVS No. 4148 (1995)
19. M.U. Feuchtinger: A&AS **136**, 217 (1999)
20. P. Fouqué, W.P. Gieren: A&A **320**, 799 (1997)
21. W.L. Freedman, B.F. Madore: ApJ **365**, 186 (1990)
22. W.L. Freedman, B.F. Madore, B.K. Gibson, L. Ferrarese, D.D. Kelson, S. Sakai, J.R. Mould, R.C. Kennicutt, Jr., H.C. Ford, J.A. Graham, J.P. Huchra, S.M.G. Hughes, G.D. Illingworth, L.M. Macri, P.B. Stetson: ApJ **553**, 47 (2001)
23. W.P. Gieren, P. Fouqué: AJ **106**, 734 (1993)
24. W.P. Gieren, P. Fouqué, M. Gómez: ApJ **488**, 74 (1997)
25. W.P. Gieren, P. Fouqué, M. Gómez: ApJ **496**, 17 (1998)
26. L. Girardi, M. Salaris: MNRAS **323**, 109 (2001)
27. T. Gochermann, T. Schmidt-Kaler: A&A **391**, 187 (2002)
28. K.D. Gordon, G.C. Clayton: ApJ **500**, 816 (1998)
29. A. Gould: ApJ **426**, 542 (1994)
30. M.A.T. Groenewegen: A&A **363**, 901 (2000)
31. M.A.T. Groenewegen, R.D. Oudmaijer: A&A **356**, 849 (2000)
32. J. Harris, D. Zaritsky, I. Thompson: AJ **114**, 1933 (1997)
33. The Hipparcos and Tycho Catalogues, European Space Agency, SP-1200, Noordwijk (1997)
34. R.C. Kennicutt, Jr., P.B. Stetson, A. Saha, D. Kelson, D.M. Rawson, S. Sakai, B.F. Madore, J.R. Mould, W.L. Freedman, F. Bresolin, L. Ferrarese, H. Ford, B.K. Gibson, J.A. Graham, M. Han, P. Harding, J.G. Hoessel, J.P. Huchra, S.M.G. Hughes, G.D. Illingworth, L.M. Macri, R.L. Phelps, N.A. Silbermann, A.M. Turner, P.R. Wood: ApJ **498**, 181 (1998)
35. C.S. Kochanek: ApJ **491**, 13 (1997)
36. B.F. Lane, M.J. Creech-Eakman, T.E. Nordgren: ApJ **573**, 330 (2002)
37. C.D. Laney, R.S. Stobie: MNRAS **263**, 921 (1993)
38. C.D. Laney, R.S. Stobie: MNRAS **274**, 337 (1995)
39. P. Lanoix, G. Paturel, R. Garnier: MNRAS **308**, 969 (1999)
40. R.E. Luck, W.P. Gieren, S.M. Andrievsky, V.V. Kovtyukh, P. Fouqué, F. Pont, F. Kienzle: A&A in press (2003)
41. L.M. Macri, D. Calzetti, W.L. Freedman, B.K. Gibson, J.A. Graham, J.P. Huchra, S.M.G. Hughes, B.F. Madore, J.R. Mould, S.E. Persson, P.B. Stetson: ApJ **549**, 721 (2001)
42. K.A. Misselt, G.C. Clayton, K.D. Gordon: ApJ **515**, 128 (1999)
43. T.E. Nordgren, J.T. Armstrong, M.E. Germain, R.B. Hindsley, A.R. Hajian, J.J. Sudol, C.A. Hummel: ApJ **543**, 972 (2000)
44. T.E. Nordgren, B.F. Lane, R.B. Hindsley, P. Kervella: AJ **123**, 3380 (2002)
45. M.O. Oestreicher, J. Gochermann, T. Schmidt-Kaler: A&AS **112**, 495 (1995)
46. M.O. Oestreicher, T. Schmidt-Kaler: A&AS **117**, 303 (1996)
47. G. Pietrzyński, W. Gieren, P. Fouqué, F. Pont: AJ **123**, 789 (2002)
48. F. Pont: 'Harmonizing the Cosmic Distance Scale in the post-Hipparcos Era'. In: *ASP Conf. Ser. vol. 167*, ed. by D. Egret, A. Heck (ASP, San Francisco 1999) p. 113

49. F. Pont, F. Kienzle, W. Gieren, P. Fouqué: A&A **376**, 892 (2001)
50. S.T. Ridgway, G.H. Jacoby, R.R. Joyce, M.J. Siegel, D.C. Wells: AJ **87**, 680 (1982)
51. H. Saio, A. Gautschy: ApJ **498**, 360 (1998)
52. D. Sasselov, J.-P. Beaulieu, C. Renault, P. Grison, R. Ferlet, A. Vidal-Madjar, E. Maurice, L. Prévot, E. Aubourg, P. Bareyre, S. Brehin, C. Coutures, N. Delabrouille, J. de Kat, M. Gros, B. Laurent, M. Lachièze-Rey, E. Lesquoy, C. Magneville, A. Milsztajn, L. Moscoso, F. Queinnec, J. Rich, M. Spiro, L. Vigroux, S. Zylberajch, R. Ansari, F. Cavalier, M. Moniez, C. Gry, J. Guibert, O. Moreau, F. Tajhmady: A&A **324**, 471 (1997)
53. P.B.W. Schwering, F.P. Israel: A&A **246**, 231 (1991)
54. J. Storm, B.W. Carney, W.P. Gieren, A.M. Fry, P. Fouqué: A&A in preparation (2002)
55. G.A. Tammann, A. Sandage, B. Reindl: A&A in press (2003)
56. D.G. Turner, J.F. Burke: AJ **124**, 2931 (2002)
57. A. Udalski: Acta Astron. **50**, 279 (2000)
58. A. Udalski, M. Szymański, M. Kubiak, G. Pietrzyński, I. Soszyński, P. Woźniak, K. Zebruń: Acta Astron. **49**, 201 (1999)
59. A. Udalski, L. Wyrzykowski, G. Pietrzyński, O. Szewczyk, M. Szymański, M. Kubiak, I. Soszyński, K. Zebruń: Acta Astron. **51**, 221 (2001)
60. ftp://sirius.astrouw.edu.pl/ogle/ogle2/var_stars/lmc/cep/catalog/README.PL
61. D.L. Welch: AJ **108**, 1421 (1994)
62. P.A. Yecko, Z. Kolláth, J.R. Buchler: A&A **336**, 553 (1998)

3 Current Uncertainties in the Use of Cepheids as Distance Indicators

Michael Feast

Astronomy Department, University of Cape Town, Rondebosch, 7701, South Africa.
mwf@artemisia.ast.uct.ac.za

Abstract. The methods of calibrating the luminosities of galactic Cepheids and determining Cepheid reddenings are considered in some detail. Together with work on NGC4258 this suggests that the calibration presented is valid to about 0.1 mag (s.e.) at least for Cepheids with near solar abundances. Metallicity effects are considered, partly through the use of non-Cepheid moduli of the LMC. To reduce the uncertainty substantially below ~ 0.1 mag will require extensive work on metallicity effects. Non-linearities in period-luminosity and period-colour relations will also need to be considered as will the need to distinguish unambiguously between fundamental and overtone pulsators.

3.1 Introduction

The assigned title of this paper might suggest that Cepheids are poor or untrustworthy distance indicators. In fact they are currently the best fundamental distance indicators that we have. For (classical) Cepheids within our own Galaxy, the zero-point of the period-luminosity relation in the V-band (PL(V)) is known to ~ 0.1 mag. However, if we wish to confirm this level of accuracy and improve on it, we need to consider a number of possible constraints and complexities.

I begin by considering the calibration of the zero-point of the PL(V) relation within our own Galaxy and later discuss possible complications with this relation, particularly those related to the chemical abundance of Cepheids. In this connection the indirect calibration of Cepheid luminosities through independent estimates of distances to other galaxies, particularly the LMC, will be considered.

In our own Galaxy there are basically four methods that can be used to calibrate a PL relation; trigonometrical parallaxes of Cepheids; statistical parallaxes of Cepheids; Cepheids in clusters or binary systems, and; Pulsation parallaxes (Baade-Wesselink type analyses).

3.2 Basic Relationships

In any determination of absolute magnitudes, the interstellar extinction to the objects used must be taken into account. Reddenings of individual Cepheids can be obtained from multicolour photometry (e.g. BVI photometry [1,2]). Relative reddenings of good individual accuracy can be obtained in this way for Cepheids of a given metallicity, despite the method having been questioned on

M. Feast, Current Uncertainties in the Use of Cepheids as Distance Indicators, Lect. Notes Phys. **635**, 45–70 (2003)
http://www.springerlink.com/

non-quantitative grounds [120]. This is clear from a discussion of LMC and SMC data [2]. The spread (standard deviation) in the derived individual reddenings, $E(B-V)$, after allowance for small photometric uncertainties is only 0.03 mag (LMC) and 0.02 mag (SMC). These are therefore upper limits to the intrinsic scatter in the method. In addition the derived reddenings show no dependence on period [2] [1]. Laney and Stobie [4] quote results showing good agreement between individual BVI reddenings of galactic Cepheids and those determined in other ways, although full details have not yet been published. The zero-point of the BVI reddening system in our Galaxy is determined from Cepheids in open clusters of known reddening. However as noted below a knowledge of this zero-point is not necessary in some important distance-scale applications.

Using BVI-based reddenings, or reddenings consistent with these, period-colour relations (PC) can be constructed (e.g. [3,4]). For the present discussion the following PC and PL relations have been adopted.

$$< B >_o - < V >_o = 0.416 \log P + 0.314, \tag{3.1}$$

$$< M_V > = -2.81 \log P + \rho \tag{3.2}$$

The PC relation is for galactic Cepheids [4]. The slope of the PL relation is that for the LMC [5]. These are the basic relations used by Feast and Catchpole [6] in their work on the Cepheid calibration using trigonometrical parallaxes. Later we shall require a PC relation in $(V - I)$ and adopt [7,8] for galactic Cepheids,

$$< V >_o - < I >_o = 0.297 \log P + 0.427. \tag{3.3}$$

Which is based on the same BVI reddening system as (3.1).

There is evidence in the literature of some misunderstanding regarding the use of a PC relation. Both the PC and PL relations are approximations to a period-luminosity-colour (PLC) relation and both have significant scatter. In view of the scatter, using a PC relation does not produce the best possible estimates of the reddenings of individual Cepheids. These can best be obtained from multicolour photometry. However because of the relation between the PC and the PL relations, through the PLC relation, deviations of PC-based reddenings from true reddenings compensate for deviations of luminosities from the mean PL relation. Thus the use of the two relations (3.1) and (3.2) together effectively reduces the scatter in the PL relation. This reduction in scatter, i.e. in width of the PL relation, is by a factor $((R/\beta) - 1)$, where R is the ratio of total to selective absorption $(A_V/E(B-V))$ and β is the colour coefficient in the PLC relation in V and $(B-V)$. Since for the Cepheids, R is ~ 3.3 and $\beta \sim 2.5$, the PL width is, in this way, reduced by a factor of more than 3. This is important, not only in reducing the scatter of estimates of the PL zero-point from individual stars, and hence reducing the uncertainty in the mean value, but also in reducing the effects of bias which are discussed below.

[1] But note that the angle between the intrinsic and reddening lines becomes less favourable with decreasing intrinsic colour (i.e. decreasing period). So the precision is a function of period.

The reddening derived from a PC relation is a combination of the true reddening with a measure of the deviation of the Cepheid from the mean PC and PL relations. This being the case, negative PC reddenings can be expected and must be used, as must, of course, negative reddenings which are simply due to statistical scatter. These negative reddenings are sometimes dismissed in the literature as being "unphysical", but this is due to a misunderstanding of the PC/PL method.

The zero-point of the PC relation is not of importance in distance determination provided it is used consistently for both calibrating and programme Cepheids (but note the exceptions discussed in Sects. 3.5 and 3.6).

3.3 Trigonometrical Parallaxes

It is sometimes claimed or implied that since the trigonometrical parallaxes which are currently available for many Cepheids have large percentage errors, they cannot be used to derive a trustworthy PL zero-point. This is not the case provided there is a significant sample of stars and that good estimates have been made of the standard errors of the individual parallaxes. The massive and homogeneous astrometric survey carried out by the Hipparcos mission [9] produced data which appear to satisfy these requirements. Nevertheless, the method of combining the data has to be carefully chosen.

Consider a group of objects all of the same absolute and apparent magnitude and so at the same (true) distance. The uncertainties in the absolute magnitudes derived from their measured parallaxes (π) are proportional to σ_π/π, where σ_π is the standard error of π. Suppose σ_π is the same for all the objects. Whilst the (weighted) mean parallax of the sample will be unbiased, the absolute magnitudes from underestimated parallaxes would have larger computed standard errors than those from overestimated parallaxes and a weighted mean absolute magnitude will be biased. This type of argument can be generalized as was done by Lutz & Kelker [10] and others (e.g. [11,12]; see also [13]). The correction to the derived mean absolute magnitude depends on the space distribution of the objects concerned as well as on σ_π/π. In the case of the Hipparcos parallaxes for Cepheids the necessary corrections would be large for most of the stars. Since corrections of this type, unless very small, have considerable uncertainties, they are best avoided. This can be done by working in parallax space as will now be discussed.

If objects are selected by apparent brightness (which will be so in the cases of interest here) there will be a selection bias if there is a spread in absolute magnitude about the mean, or about a relation such as the Cepheid PL relation. Bias of this kind was discussed quantitatively by Eddington [14], Malmquist [15] and others. The treatment in this section is from [16].

Consider first a group of objects with a mean absolute magnitude per unit volume of M_o and an intrinsic dispersion of σ_{M_o}. It is assumed there has been no selection of the sample to be analysed according to π or σ_π/π. The method of reduced parallaxes scales the measured parallaxes to the values they would have at the same apparent magnitude. This can be written;

$$\overline{10^{0.2M}} = \sum 0.01\pi 10^{0.2m_o} p / \sum p \tag{3.4}$$

where the parallaxes are in milliarcsec, m_o is the absorption free absolute magnitude and p is the weight given by;

$$(0.01\sigma_T 10^{0.2m_o})^2 = 1/p \tag{3.5}$$

and

$$\sigma_T^2 = \sigma_\pi^2 + b^2\pi_{M_o}^2(\sigma_{m_o}^2 + \sigma_{M_o}^2) \tag{3.6}$$

In (3.6), σ_T is derived from the uncertainty in the parallax (σ_π), the intrinsic scatter in the absolute magnitude (σ_{M_o}) and the uncertainty in the reddening corrected apparent magnitude (σ_{m_o}); also,
$b = 0.2\log_e 10 = 0.4605$.
π_{M_o} is the photometric parallax derived using the PL relation [12]. Put $x = (m_o - M_o)$. Due to observational errors in m_o and intrinsic scatter in M_o, x will differ from the true distance modulus by ϵ (say). It is then evident that (3.4) yields an estimate of;

$$\overline{10^{0.2M}} = \overline{10^{0.2(M_o+\epsilon)}} = \overline{e^{bM_o}}.\overline{e^{b\epsilon}} \tag{3.7}$$

Consider objects all of the same m_o (and x). Then [15,17];

$$\overline{e^{b\epsilon}} = e^{0.5b^2\sigma_t^2} v(x - b\sigma_t^2)/v(x), \tag{3.8}$$

where,

$$\sigma_t^2 = \sigma_{m_o}^2 + \sigma_{M_o}^2 \tag{3.9}$$

and $v(x)$ is the frequency distribution of x which would have been observed if a complete survey had been made. It is important to note that this is the case, whether or not the objects under consideration actually form a complete survey. That is, the fraction of objects of a given apparent magnitude, m_o, actually observed may be a function of m_o but this does not affect the quantity $\overline{e^{b\epsilon}}$.

Evidently at a given m_o an unbiased estimate of $10^{0.2M_o}$ is obtained by combining (3.4), (3.7) and (3.8). In general equation (3.8) is a function of x (that is m_o). Furthermore if we apply the method to large volumes of space (as is likely to be possible with GAIA parallaxes), the function $v(x)$ may not be the same in all heliocentric directions. If however we assume a constant underlying density distribution, the r.h.s of (3.8) is independent of x and becomes $10^{-2.5b^2\sigma_t^2}$ (see e.g. [17] eq. (9)). In this approximation, the best unbiased estimate of M_o is obtained by combining (3.4) above, with;

$$M_o = 5\log(\overline{10^{0.2M}}) + 1.151\sigma_t^2 - 0.23\sigma_1^2 \tag{3.10}$$

where σ_1 is the standard error of the derived value of M_o, and the final term in (3.10) accounts for the conversion between natural and logarithmic quantities.

The above discussion refers to a set of objects assumed to have a mean absolute magnitude M_o with a gaussian scatter. If this is not the case but instead the relative absolute magnitudes of the objects are a function of some measured quantity (e.g. in the case of Cepheids, the period) then two cases need to be considered. If the measuring errors of this auxiliary quantity introduce errors in M_o which are small compared to σ_{M_o}, the formulation just given can, with obvious modification, be used to find the absolute magnitude zero-point. If this is not the case a different formulation is required [16,17]. In the case of the Cepheids the periods are usually known with good accuracy and their uncertainty has a negligible effect on the predicted relative values of the absolute magnitudes, so the formulation just given can be used.

Feast and Catchpole [6] analysed the Hipparcos parallaxes of Cepheids by the method of reduced parallaxes. Similar results have been obtained by [18,19]. Because they, [6], used the PC/PL approach discussed above to reduce the effective width of the PL relation, the bias term given in (3.10) is very small (0.010 mag). This would change their derived PL zero-point (ρ) from -1.43 to -1.42. If, in an analysis of the Cepheid data, the reddenings were derived in some other way then it would be necessary to take into account the full (true) width of the PL(V) relation. There is some evidence (e.g. [3]) that Cepheids are distributed rather uniformly through a strip in the PL plane. If the half-width of this strip in magnitudes is Δ, then for a constant space density distribution, (3.8) becomes;

$$\overline{e^{b\epsilon}} = 3sinh(2b\Delta)/2sinh(3b\Delta) \tag{3.11}$$

At longer periods in the LMC, 2Δ is approximately 0.7mag [3]. If this width applies to the calibrating Cepheids, the bias correction terms amount to $\sim$ 0.05mag. This much larger bias shows the value of the PC/PL approach. Note that this bias remains the same however accurate or numerous the individual parallaxes are. It is perhaps worth noting that the need for a bias correction of this type is not necessarily avoided by working in magnitude space and applying a Lutz-Kelker type correction.

Whilst there are a large number ($\sim$ 220) of Cepheids with Hipparcos parallaxes, most of the weight in the reduced parallax analysis is in a relatively small number of stars. The final result adopted [6] depends on the 26 stars of highest weight. This should now be corrected by the bias term in (3.10) and results in the value shown in Table+3.1. If the overtone pulsator, α UMi, (see below) which carries about half the final weight in this solution is omitted, a negligibly different result is obtained, though of course with an increased standard error.

An important recent development has been the publication of a rather precise parallax of δ Cephei itself from HST observations [20]. The main uncertainty in this result probably comes from the need to convert from relative to absolute parallax. Since this star was presumably chosen for measurement and analysis because of its bright apparent magnitude and not (retrospectively) because of its parallax, a determination of its absolute magnitude does not require a correction for Lutz-Kelker bias [16]. It will however be subject to magnitude selection bias. A zero-point for the PL relation from this one star is best derived using the

Table 3.1. Cepheid trigonometrical parallax zero-points (bias corrected)

Method	ρ
25 high weight	-1.43 ± 0.13
α UMi fundamental	-2.05 ± 0.14
α UMi 1st overtone	-1.41 ± 0.14
α UMi 2nd overtone	-0.97 ± 0.14
26 high weight	-1.42 ± 0.10
δ Cep (HST)	-1.32 ± 0.10
26 high weight revised	-1.36 ± 0.08

PL/PC method and (3.10). One then obtains the result shown in Table 3.1. The "26" star solution [6] can now be improved by replacing the Hipparcos parallax of δ Cep by a weighted mean of this value with that from the HST result. This leads to the value also shown in the Table 3.1. Incorporating the result of Benedict et al. leads to a distinct lowering of the uncertainty in the zero-point. The standard errors quoted are those derived directly from the analyses. These, of course, have their own uncertainties and Monte Carlo simulations by Pont [21] suggest that in the case of the "26" star solution of [6], a more realistic estimate of the standard error is 0.12 rather than 0.10 [8]. In view of this one might feel that the uncertainty in the final value of Table 3.1 (0.08) should be somewhat increased though it would seem unlikely to be greater than 0.10.

Not all Cepheids pulsate in the fundamental mode and overtone pulsators are most frequent amongst stars with short (fundamental) periods. Double mode pulsators [22] provide the period ratio of the fundamental (P_0) to the first overtone (P_1) for galactic Cepheids, e.g.

$$P_1/P_0 = 0.720 - 0.027 \log P_0, \tag{3.12}$$

and this can be used to derive the fundamental periods of known overtone pulsators. These overtone Cepheids may be identified using the Fourier components of their light curves (e.g. [23]). They can also be identified in an (observed) period - radius diagram using Baade-Wesselink type radii. Early Baade-Wesselink work did not generally give radii of individual stars of sufficient accuracy to do this. However more recent work (e.g. using infrared photometry [24,25]) seems to be sufficiently consistent for this purpose. It would therefore be important to obtain radii of high accuracy for all the parallax stars of high weight. Only a few of them seem to have the necessary data (e.g. β Dor, l Car, Y Oph and U Sgr are confirmed as fundamental pulsators in this way, and SZ Tau as an overtone [24–26]). However the speculation [26] that the misidentification of overtone Cepheids for fundamental pulsators amongst the high weight parallax stars could have led to a significant overestimation of Cepheid luminosities seems rather unlikely to be correct.

Polaris (α UMi) is treated in the analysis as a first overtone pulsator on the basis of its derived absolute magnitude. If it were either a fundamental or second overtone pulsator it would yield a PL zero-point discrepant with the other high weight stars [6]. Evans et al. [27] have discussed other evidence that Polaris pulsates in the first overtone, including the diameter of the star derived using the interferometric angular diameter [28]. It is known from the LMC [29] that overtone Cepheids obey the normal PLC relation (at their fundamental periods). However they are in the mean brighter than the standard PL relation and intrinsically bluer than a standard PC relation. Because of the PL/PC method of analysis this means that the zero-point derived from overtone Cepheids will be slightly too faint. In the present sample the effect of this is expected to be negligible.

It has to be stressed that α UMi gives a PL zero-point in accord with that of the other high weight stars. The apparent discrepancy discussed by Di Benedetto [30] arises entirely because of the PL zero-point he adopts (-1.27 ± 0.17). However, this value is derived from a non-optimal selection of Cepheids (i.e. it does not contain all the high weight Cepheids). Note, however, that due to its larger error it is is not significantly different from the values in Table 3.1.

In later sections there will be a discussion of possible chemical abundance effects on Cepheid luminosities. This is an area of some uncertainty. The parallax Cepheids are all in the general solar neighbourhood where the variation of chemical abundance amongst young stars such as Cepheids is expected to be small. However, abundance determinations for all the high weight Cepheids would be desirable.

3.4 Statistical Parallaxes

The method of statistical parallaxes combines proper motions and radial velocities to obtain a PL or PLC zero-point. In common with the method of reduced parallaxes discussed above, this method assumes that the relative distances of the stars are known and only a scale value is to be derived. In order to carry out an analysis of this type we require a kinematic model. Both the proper motions [31] and the radial velocities [32] show clearly and independently, the dominant effect of differential galactic rotation on Cepheid motions in the Galaxy. Thus the required model must be based on differential galactic rotation. This is even more apparent when one considers that to a first approximation the amplitude of the differential rotation effect in the proper motions is independent of distance whereas for the radial velocities it is proportional to distance. Adjusting the analyses for equality of the Oort constant (A) in proper motions and radial velocities provides the best statistical parallax result for Cepheids. This is particularly the case since in this method the weight is spread over a large volume of the Galaxy and so avoids problems due to local deviations from an idealized model which almost certainly occur. In this way zero-points were found [31,33] for a PLC and for a PL relation. The zero-point of the latter, corrected for a

Table 3.2. Galactic and NGC4258 Cepheid zero-points (bias corrected)

No.	Method	ρ
1	Trigonometrical Parallax	-1.36 ± 0.08
2	Statistical Parallax	-1.46 ± 0.13
3	Clusters	-1.45 ± 0.05 (int)
4	Baade-Wesselink	-1.31 ± 0.04 (int)
	Unweighted Mean (1,2,3,4)	-1.40
5	NGC4258	-1.17 ± 0.13
	Unweighted Mean (1,2,3,4,5)	$-1.35 \pm (0.05)$

possible magnitude bias of ~ 0.01 mag (as discussed in Sect. 3.3) is given in Table 3.2.

In view of some discussions in the literature it is important to stress that in deriving a PL zero-point from statistical parallaxes, there is a great advantage, as has just been mentioned, in treating the proper motions and the radial velocities separately [31,32].

One can also attempt a solution using the solar motion obtained from a combined discussion of solar motion and differential galactic rotation using proper motions and radial velocities. In this way the solar motion has a value which is averaged out over the whole large region of the Galaxy covered by the proper motion (Hipparcos) and radial velocity Cepheids and is not confined to a small region round the Sun where local deviations from the idealized model may lead to false results. The resulting scale [34] is only 0.04 ± 0.26 mag larger than that just given. However the standard error of this result is too large for the method to have any significant weight.

The above discussion refers to the use of the systematic motions of the Cepheids. In principle one can obtain a Cepheid scale from a comparison of the dispersions about an adopted solution in radial velocities and proper motions. However the velocity dispersion of Cepheids is small. Thus any such solution will be sensitive to the treatment of observational scatter in radial velocities and proper motions. It will probably also be sensitive to the effects of group motions. For these reasons no attempt along these lines has been made here. A further discussion of statistical parallax solutions is given in [8].

The Cepheids used in the statistical parallax solutions cover a significant fraction of the galactic plane. Most of the stars lie in the range, $(R_o - 3)$ kpc to $(R_o + 4)$ kpc, where R_o is the distance of the Sun from the galactic centre. If there is a galacto-centric gradient in chemical abundances of Cepheids over this range it might affect the PL and PC relations, particularly the latter. Evidently the work now in progress on chemical abundances of Cepheids (e.g. [35] etc.) should eventually allow us to take these effects into account. However since the sample of Cepheids used in the statistical parallax work is (roughly) centred on the Sun it may well be that any effect in the final mean result will be small.

3.5 Cepheids in Open Clusters

The (re)discovery of Cepheids in open clusters by Irwin [36] was a major step in the Cepheid calibration problem. Whilst the use of this method is of considerable importance, there are a number of special problems associated with it. These are; (1) Uncertainty of cluster membership; (2) Effects of reddening and photometric uncertainties; (3) Effects of metallicity; (4) Absolute calibration of the cluster distance scale.

(1). There are 30 open clusters or associations in our Galaxy which have been listed as containing Cepheids [8]. Since that list was drawn up SZ Tau has been shown [37] from proper motions to be a non-member of the cluster to which it was formerly assigned. In addition TW Nor is not used here because its cluster membership appears doubtful [109]. Definite confirmation of membership of several others would be very valuable. It seems desirable that membership should be based on position in the cluster, radial velocity and proper motion. In the past a decision on membership has sometimes been made on the basis of whether or not the derived Cepheid luminosity fitted with preconceived ideas. This seems dangerously like an application of Merrill's [38] principle which states that when the discordant observations are rejected the remainder are found to agree very well.

(2). The relative distances of the various clusters are obtained by a main-sequence fitting procedure. Because of the steepness of the main sequence this fitting procedure is very vulnerable to errors in the photometry or in the adopted reddenings. For instance an error in $(B-V)_o$ of $\Delta(B-V)_o$ leads to an error in the derived distance modulus of $\sim 6\Delta(B-V)_o$ if the fitting is done in the $V,(B-V)$ plane. For some clusters, distance moduli with standard errors as small as 0.02 mag have been claimed. However, even the adopted $(B-V)$ colours of photometric standard stars can vary by 0.02 mag or more between standard star observers [39]. Thus estimates of the uncertainties of cluster moduli of ~ 0.15 mag as in Walker and Laney [40] seem more realistic, and the errors could be greater in some cases. If the cluster fitting is done in the $V,(V-I)$ plane an error of $\Delta(V-I)_o$ produces an error of $\sim 5\Delta(V-I)_o$ in the derived modulus.

In the case of the analysis of trigonometrical parallaxes and statistical parallaxes of Cepheids it was pointed out that the zero-point of the reddening system was not important so long as it was used consistently for both the calibrating and programme stars. This is not the case when calibrating Cepheids using clusters. Thus a change in the reddening zero-point by ΔE changes the distance modulus derived from $V,(B-V)$ by $\sim 6\Delta E$ and only $\sim 3\Delta E$ of this is recovered when dereddening the Cepheid itself.

(3). The position of the main sequence is sensitive to metallicity effects. A change in [Fe/H] of 0.1 dex leads to a change in absolute magnitude at a given $(B-V)_o$ of $\sim$ 0.1 mag, e.g. [46]. It is generally assumed that all the clusters containing Cepheids are of solar metallicity or at least of solar metallicity in the mean. The latter at least seems likely but it has not been proved and further work on the metallicities of the clusters and their Cepheids would be desirable.

(4). In the past the absolute calibration of the cluster distance scale was based on an adopted distance modulus for the Pleiades. The value which has generally been used, 5.57 mag, is the value derived by van Leeuwen [41] by fitting nearby field main-sequence stars with known parallaxes to the Pleiades main sequence though this figure has been revised by others from time to time [42,43]. It came as something of a surprise when the Hipparcos parallaxes of Pleiades stars themselves gave a smaller distance modulus, 5.37 ± 0.07 mag [44,45]. One reason for this surprise was that the van Leeuwen distance fitted rather well with theoretical results for solar-metallicity main-sequences [46]. It has been suggested that the Hipparcos distance can be reconciled with main-sequence theory if the Pleiades are metal poor ([Fe/H] $=\sim -0.15$) [47]. There appears to be some evidence in Geneva-system photometry for such a suggestion [48] ([Fe/H] $= -0.12 \pm 0.03$) but neither the Stromgren photometry [49] ([Fe/H] $= +0.02 \pm 0.03$) nor spectroscopic abundances [50] ([Fe/H] $= -0.03 \pm 0.02$) show evidence for significant metal poorness. These abundances are derived assuming that the Hyades cluster members have [Fe/H] $= +0.13$. Alternatively the Hipparcos mean parallax of the Pleiades may have a greater uncertainty than given by its formal error or there is some problem with observations (see [8]) or theory. No final agreement on this point seems to have yet been reached. However a rereduction of the Hipparcos data for the Pleiades stars suggests a possible way out of this problem [121].

In view of this uncertainty it seems best at the present to base the cluster scale on the Hyades for which there is an excellent Hipparcos-based parallax. The problem with this is that it is generally agreed that the Hyades stars are slightly metal-rich, so a correction for this has to be made, if we make the common assumption that the clusters with Cepheids are of solar metallicity in the mean. The Hipparcos based distance modulus for the Hyades is $(m-M)_o = 3.33 \pm 0.01$ [51], and the metallicity adopted by e.g. Pinsonneault et al. [46] is [Fe/H] $= 0.13$. The theoretical metallicity correction adopted by these latter authors then shows that the Hyades main sequence in $V, (B-V)$ corresponds to that expected for a solar metallicity cluster at $(m-M)_o = 3.17$ mag, or 3.12 mag if the metallicity corrections of Robichon et al. [45] are used. I adopt a mean value 3.14 mag. Since most work on clusters containing Cepheids is referred to Turner's Pleiades main sequence [52], we need to see how this is affected by the Hyades result. The Pleiades - Hyades magnitude difference in a $V, (B-V)$ diagram, corrected for reddening but not metallicity, is 2.52 mag [53]. Thus the Turner main sequence is that expected for a solar metallicity cluster at

$$(m-M)_o = 3.14 + 2.52 = 5.66.$$

Adopting this value and assuming the clusters containing Cepheids which are listed in [8] are in the mean of solar metallicity we obtain a PL zero-point of

$$\rho_1 = -1.45 \pm 0.05 \text{ (internal) mag.}$$

Here SZ Tau and TW Nor have been omitted for the reasons given above. If the Hyades metallicity suggested by Taylor [54] ([Fe/H] = +0.11) were adopted we would obtain a brighter PL zero-point (–1.47). The error of this result is internal. The true error may well be larger, partly due to uncertainties in the metallicity correction. The standard deviation of the result is 0.26 mag. Some of this is due to the width of the PL strip ($\sigma_{PL} = 0.21$ [5]) which comes in with full force here (unlike the case discussed in Sect. 3.3). Subtracting this quadratically gives 0.15 mag as the standard deviation of the cluster moduli. This agrees with a recent comparison of Baade-Wesselink and cluster moduli by Turner and Burke [122] (their table 3) from which one finds a standard deviation of 0.14 mag, presumably mainly due to the scatter in the cluster moduli since the Baade-Wesselink results are believed to have very high internal accuracy.

Whilst the adopted zero-point from clusters avoids the use of the Pleiades modulus, the cluster method cannot be considered entirely trustworthy until the problem of the Pleiades distance is fully understood.

Of the same nature as the cluster method is the use of physical companions to Cepheids whose luminosity can be independently estimated. This method has been used, notably by Evans and collaborators [55,56]. At the present time the accuracy obtained is not as good as that from other methods (see [8]).

3.6 Pulsation Parallaxes

An estimate of the luminosities of Cepheids can be made using pulsation parallaxes (Baade-Wesselink method). This method is dealt with extensively elsewhere in this volume. The procedure normally used gives results of high internal accuracy especially when implemented using infrared photometry [24,25] The method is currently being strengthened by interferometric measurements of the angular diameters of Cepheids and their variation with phase [57–60]. It remains difficult to estimate in a realistic way the true uncertainty in the results from pulsation parallaxes which depend on possible systematic errors in the derived radii and in the surface brightness estimates. For the present discussion I have adopted a PL(V) zero-point derived from the results of Laney [61] (see [8]).

3.7 Summary of the Galactic Calibration

The results discussed above are summarized in Table 3.2. The cluster and pulsation parallax methods both have small internal errors but their real (external) uncertainty is difficult to quantify. The results of Monte Carlo simulations by Pont [21] suggest that in the case of the “26” high weight parallax-solution Cepheids [6] the error might have been slightly underestimated. That may still be the case here but it is unlikely to be significantly greater than ~ 0.1 mag. Both the trigonometrical and statistical parallax methods seem rather robust. In the present paper an unweighted mean has been adopted as best galactic zero-point and this is shown in Table 3.2.

3.8 A Cepheid Zero-Point from NGC4258

A distance to the galaxy NGC4258 has been derived from the motions of H_2O masers in the central region combined with a model [62]. In this way a distance modulus of 29.29 ± 0.09 was obtained. Newman et al. [63] have obtained V,I data for Cepheids in this galaxy using the HST. Reducing their data with the PC relation in $(V - I)$ given above and a PL(V) relation of slope -2.81 leads to a PL zero-point of -1.17 ± 0.13. Here the error in the maser distance has been combined with the internal uncertainty in the Cepheid result. In obtaining this value of the zero-point a small correction for metallicity has been applied. HII region measurements [64] suggest that [O/H] is –0.05. A correction of 0.20 mag $[\mathrm{O/H}]^{-1}$ was adopted (see Sects. 3.9 and 3.10). Unless the adopted metallicity of the galaxy is grossly in error or the metallicity effect much greater than assumed, the metallicity correction is very small.

Including this zero-point (-1.17 ± 0.13) with the galactic values (Table 3.2) yields an unweighted mean of -1.35 ± 0.05, which is possibly the best current estimate of the zero-point for metal-normal Cepheids. However it has been suggested recently [111] that model uncertainties lead to possible uncertainties in the mass of the central black hole in NGC4258 of at least 25 percent and it remains to explore what effect this has on the deduced distance.

3.9 Metallicity Effects

A remaining source of uncertainty in deriving distances of Cepheids is the effect of metallicity variations on the PLC, PL and PC relations, and on multi-band intrinsic colours. In any distance derivation, the interstellar reddening and absorption must be derived as well as a prediction of the absolute magnitude of the star. The effect of metallicity change on PL relations will vary with wavelength. The effect on the derived interstellar absorption will depend on the method used for its derivation. For instance there is good evidence from a comparison of the LMC and SMC that Cepheids become bluer in $(B - V)$ at a given period with decreasing metallicity [43]. Thus a standard PC relation in $(B - V)$ will give too small a reddening for a metal-poor Cepheid. However if the reddening of a metal-poor Cepheid is derived from a standard two-colour, BVI, plot, the reddening will be too high (see e.g. [2]). If we knew precisely the dependence on metallicity of all the quantities involved and had sufficient data we could solve in any given case for the reddening and metallicity of a Cepheid and also for its luminosity and distance. An indication of how this could be done in practise using BVI photometry was given in [65].

So far as the use of a PL relation to derive luminosities together with either multi-colour data or a PC relation to derive reddenings is concerned, the metallicity problem may be broken down into three parts.

1. A possible change in bolometric luminosity at a given period.
2. A possible change in colour at a given temperature.
3. A possible change of temperature at a given period.

Laney and Stobie [66] showed that at a given period the metal-poor Cepheids in the Magellanic Clouds were slightly hotter than those in our Galaxy. Laney [67] then showed that the radii of Magellanic Cepheids as determined from Baade-Wesselink type analyses fitted the galactic period-radius relation. These observations seem to show that at a given period the bolometric luminosity of a Cepheid increases with decreasing metallicity. However the effect is small and within the uncertainties of the observations. Further work along these lines would be valuable. An effect on the bolometric luminosity obviously affects the results at all wavelengths in the same way.

The effects of items 2 and 3 above, on reddening and luminosity depend on the wavelengths and methods used. Here we consider the effects when using V, I photometry as in the HST work on extragalactic Cepheids. Other cases have also been considered, e.g. [8].

The HST work essential uses a PC relation in $(V - I)$ and a PL(V) relation to determine reddening and distance. There is some confusion in the literature regarding metallicity effects using V and I. This arises because the effects of metallicity on (3.2) and (3.3) are such that the changes affect the derived distance modulus in opposite directions. It is thus important to consider these two equations together. A direct test of this was made by Kennicutt et al. [68]. They observed Cepheids in the galaxy M101 at different distances from the centre of the galaxy where abundances had been estimated for HII regions. The abundance is above solar in the inner field and below solar in the outer field. Their results lead to a metallicity effect on a distance modulus derived using (3.2) and (3.3) of $0.24 \pm 0.16\text{mag}\,[\mathrm{O/H}]^{-1}$. This is in the sense that without the correction the distance of a metal-poor Cepheid would be overestimated. This result suggests there is a small metallicity effect in the V, I method. However the uncertainty in the result is large. It should also be borne in mind that although there seems little doubt that there is a strong metallicity gradient in M101, the absolute values of the metallicities in the fields studied by Kennicutt et al. [68] remain somewhat uncertain (see their Fig. 2 and the accompanying discussion).

Laney [67,69] (see Feast [8]) discussed Baade-Wesselink radii and colours of Cepheids in the Galaxy, the LMC and the SMC and these lead [8] to an effect in the moduli of $\sim 0.09\pm \sim 0.04(\mathrm{int})\,\mathrm{mag}\,[\mathrm{O/H}]^{-1}$ in the same sense as the Kennicutt et al. correction. Much of the weight of the Laney result depends on the SMC.

3.10 Non-Cepheid Distances to the LMC

The LMC is of great importance for the Cepheid problem. It provides the slope of the PL(V) relation currently in use. Also the LMC showed clearly that when Cepheids are dereddened using three colour photometry, the PL relation has a significant width which is reduced to within the observational errors when a PLC relation is used [70]. The zero-point of the LMC PL relation can be established if the LMC distance can be independently determined. However it is known that the LMC Cepheids are metal-deficient compared with those in the solar neighbourhood, e.g. [71]. Thus a comparison of the Cepheid luminosities in our Galaxy and in the LMC can be an important test of metallicity effects on Cepheids. This is obviously a major source of concern in the use of Cepheids as general distance indicators. It is particularly important to note that a non-Cepheid distance to the LMC does not give a PL zero-point for normal metallicity Cepheids independent of some knowledge of the metallicity effect.

The distance to the LMC is discussed elsewhere in this volume but it is necessary to give here the basis for the present discussion on the luminosities of LMC Cepheids. In the following subsections some non-Cepheid methods of determining the LMC distance will be considered. Whilst many of these methods appear promising it should be remembered that none of them have yet been subjected to the intense scrutiny that has been applied to the Cepheids themselves. In each case, some of the issues that need resolving before that particular distance indicator can be fully relied on, are mentioned. Only methods which are, or have been claimed to be, largely independent of theory are considered. For instance the magnitude of the Red-Giant-Branch tip seems to be a good indicator of relative distances but requires an absolute calibration either from stellar evolution models or through some other indicator (such as Cepheids).

3.10.1 The RR Lyrae Variables

RR Lyrae variables have long been regarded as valuable distance indicators. However the dependence of their absolute magnitudes on metallicity has been a matter for debate. Furthermore if globular clusters are taken as a guide [72] there is a significant spread in M_V at a given metallicity. Other papers in this volume discuss the RR Lyraes in detail and a full discussion is not given here. The most important recent development has been the publication by Benedict et al. [73] of a trigonometrical parallax of RR Lyrae itself. This can be used together with (3.4) above, to obtain an estimate of the mean absolute magnitude of RR Lyrae stars of this metallicity (Fe/H] = –1.39). Account needs to be taken of the fact that at this metallicity globular cluster results suggest that RR Lyraes fill a strip of width ~ 0.4 mag. One obtains [16], $+0.64 \pm 0.11$ correcting for the resulting bias using (3.11) above. Then, adopting the relation;

$$M_V = 0.18[Fe/H] + \gamma \tag{3.13}$$

from Carretta et al. [74] and a mean reddening-corrected apparent magnitude of $V_o = 19.11$ at a metallicity of [Fe/H] = –1.5 for the LMC field RR Lyraes, one obtains an LMC modulus of 18.49 ± 0.11. Note however that this standard error should probably be increased, possibly to ~ 0.16 due to the uncertainty in the bias correction as applied to the one calibrating star. Other RR Lyrae-based estimates of the LMC modulus are listed in [75] where a mean of 18.54 was adopted. The uncertainty in this latter value is probably somewhat over 0.10 mag. Whilst the determination of an accurate trigonometrical parallax for RR Lyrae is a great step forward, the accuracy of the LMC modulus derived from it must be limited if the spread in absolute magnitudes at a given metallicity is as great as that adopted above. It may however be possible to use this parallax result together with an infrared period-luminosity relation [76] to obtain a more precise result if this latter relation has a small scatter.

3.10.2 The Mira Variables

Multi-epoch infrared photometry of Mira variables in the LMC shows that both carbon-rich (C-type) and oxygen-rich (O-type) variables have a well-defined PL relation in the K band (2.2μm) [77]. For the O-Miras the relation can be written,

$$M_K = -3.47 \log P + \gamma. \tag{3.14}$$

The scatter about this relation is only 0.13 mag. Miras in the SMC, in globular clusters, as well as those with spectroscopic parallaxes from companions, all fit a PL(K) relation with the same slope [78–80]. The zero-point may be calibrated using Hipparcos parallaxes of Miras. This yields, $\gamma = +0.86 \pm 0.14$ mag [81] when small bias effects (see (3.10), above) [16] are taken into account. A zero-point can also be obtained from Miras in globular clusters. This method gives, $\gamma = 0.93 \pm 0.14$ mag [80]. To this may now be added a result from the parallaxes of OH-maser spots in Miras obtained using VLBI [113]. The four Miras with distances from this method, together with infrared photometry [114] yield, $\gamma = +1.04$ mag. The internal standard error of this result is small (0.13 mag) but the uncertainties in the individual determinations suggest that this is an underestimate and that the standard error of the mean is probably about 0.23 mag. In view of this, the last method is given half weight in combining the three estimates. One then obtains $\gamma = +0.92$ and an LMC modulus of 18.56. If full weight had been given to the third method the zero-point would only have been increased by 0.02 mag. The standard error of the adopted result is less than 0.10 mag.

In globular clusters the periods of Mira variables are a function of metallicity e.g. [82]. It is not clear whether, at a given period, the metallicity of Miras differs from system to system. However there is some evidence that the infrared colours of O-Miras at a given period are systematically different in the LMC from those of Miras in the galactic bulge. This is likely to be due to weaker H_2O bands in the LMC stars [82,83]. This could be due either to a deficiency of oxygen (an α element) or to a higher C/O ratio resulting from an overabundance of carbon. The effect of this on the PL(K) relation is not known empirically. However theoretical work [110] suggests that, if anything, a general metal deficiency, if not taken into account, will lead to an underestimation of the distance modulus.

It is perhaps worth pointing out that whilst Miras seem reliable distance indicators in the case of the Magellanic Clouds, caution is required if only a few such variables are identified in a system. In the LMC, whilst the bolometric PL relation found at short periods is continued out to periods of ~ 1000 days by dust-enshrouded Miras [84,85], there are a number of stars with periods over 420 days which lie above this relation [77] and some similar objects at shorter period. Whitelock [84,85] has pointed out that, of these, those studied by Smith et al. [86] show evidence for surface lithium and can be interpreted as hot bottom burning stars which would not be expected to obey the PL relation. Note that the Mira-like variable in IC1613 which is clearly too bright for the PL relation [87] has an unusually early spectral type for its period (641 days) and is a likely candidate for a hot bottom burning object [85].

3.10.3 Eclipsing Binaries

Deriving distances from eclipsing binaries has much in common with the determination of pulsation parallaxes by a Baade-Wesselink type analysis. In both cases a stellar radius is combined with an estimate of the surface brightness to obtain a luminosity. The method has been applied to three LMC eclipsing variables [88–90] and rediscussion of some of these results have been published [91,92]. In view of the spread in distance moduli derived, Fitzpatrick et al. [90] suggest only that they lead to an LMC modulus of ~ 18.40. Uncertainties and assumptions in the method used have been discussed [91,75].

3.10.4 SN 1987A

Panagia [93] deduced a distance to the LMC centroid from the ring round SN1987A (18.58 ± 0.05). The distance depends, amongst other things, on the assumed ellipticity of the ring. A spectral-fitting expanding-atmosphere model gives a similar result though with considerable uncertainty (18.5 ± 0.2) [94].

3.10.5 The Red Giant Clump

The use of the red giant clump as a distance indicator has been much discussed in recent years. As applied to the LMC this has led to conflicting results. Girardi and Salaris [95] investigated theoretically the dependence of the clump absolute magnitude on age and metallicity. Coupling their results with a population synthesis model of the LMC they obtained an LMC modulus of 18.55. More recently Alves et al. [96] have applied the method in the K-band and find 18.49 ± 0.04. However the need to assume theoretical age and metallicity corrections and to adopt an LMC model, reduces the usefulness of the clump as a distance indicator [95].

3.10.6 Open Clusters

It has long been realized that main-sequence fitting to young clusters in the LMC provides a method to estimate its distance. Since this is the same procedure as that used to derive distances to Cepheids in open clusters in our Galaxy (Sect. 3.5, above), the qualifications discussed there apply also in the case of LMC clusters. A particularly interesting result is that derived from extensive work on the LMC cluster NGC1866 by Walker et al. [97]. These authors deduce a reddening-corrected distance modulus of 18.35 ± 0.05 for the cluster and point out that if it lies in the plane of the LMC the mean modulus of this galaxy is 18.33.

The NGC1866 modulus is derived differentially with respect to the Hyades, adopting the Hipparcos distance for this cluster and applying a correction for the metallicity effect. The comparison between the two main sequences is made in the $V, (V-I)$ plane and a value of $A_V/E_{(V-I)}$ of 2.08 was adopted. Walker et al. obtain reddening corrected moduli of 18.37 and 18.33 for assumed values of [Fe/H] of -0.30 and -0.50. Since these metallicities span the range of metallicities measured in various ways for the cluster, they adopt an NGC1866 modulus of 18.35. It is interesting to note (as can be deduced from the diagrams in their paper) that the distance modulus of NGC1866 corrected for reddening but not for the metallicity difference between it and the Hyades ([Fe/H] $= +0.13$) is ~ 18.9. A comparison of this with the results for the two different assumptions as to the metallicity of NGC1866 shows that the applied metallicity corrections are highly nonlinear. These results may be compared with those which are obtained using the (linear) metallicity corrections of Pinsonneault et al. [46]. These are moduli of $\sim$ 18.5 and $\sim$ 18.3 for [Fe/H] of –0.30 and –0.50. Clearly the metallicity model is crucial.

One might be concerned that the relative abundances of the heavy elements might be different in the Magellanic Clouds from the Sun. Hill et al. [98] found no significant enhancement or depletion in the ratio of α-elements to iron for stars in NGC1866 ([$[\alpha/Fe] = 0.1 \pm 0.1$). However the situation is not entirely clear since depletion of the α-element oxygen seems rather general in the LMC [98,99,112].

Finally it is worth noting that the uncertainty assigned by Walker et al. to their favoured modulus for NGC1866 (0.05 mag) should probably be regarded as an internal error only. The external error is likely to be larger due to the effects of magnitude transformations and other causes. For instance they find from a comparison of their HST data with overlapping ground based data that there is a mean difference in colour of $\Delta(V-I) = -0.07 \pm 0.06$(s.d) in the sense, ground based minus HST data. They do not apply this as a correction to their HST data in view of the fact that it is much reduced if outliers are omitted. However had they applied this correction their distance modulus would have been ~ 0.35 mag greater for the same adopted reddening.This follows since a comparison with the ground based data [100] shows that the HST results are the relevant data set for the main sequence fitting. This of course does not necessarily prove that the cluster distance modulus is $18.35 + 0.35 = 18.70$. However it does indicate the uncertainties encountered in this type of work.

3.10.7 LMC Summary

Mean distance moduli from various types of objects are listed in Table 3.3. These can be combined in a variety of ways. This generally leads to mean moduli near 18.5. In view of the various points discussed above one should probably consider this to have a realistic standard error of about 0.1 despite internal accuracies better than this being claimed for some determinations. In the present connection we are not concerned with the LMC modulus per se. We require a distance which can be compared with that derived from Cepheids so as to estimate the effects of metallicity on the Cepheid scale. In doing this a remaining uncertainty is whether or not the reddenings adopted in deriving the moduli listed in Table 3.3 are consistent with those used for the Cepheids.

Table 3.3. Non-Cepheid LMC distance moduli

Object	Method	Modulus	Mean Modulus
RR Lyraes	Trig. Par.	18.49 ± 0.11	
	Hor. Branch	18.50 ± 0.12	
	Glob. Cl.	18.64 ± 0.12	
	δ Sct	18.62 ± 0.10	
	Stat. Par.	18.32 ± 0.13	
		unweighted mean	18.51
Miras		$18.56 \pm < 0.10$	18.56
Eclipsers		~ 10.40	18.40
Red Clump	V-band	18.55	
	K-band	$18.49 \pm (0.04)$	
		unweighted mean	18.52
SN1987A		18.58 ± 0.05	18.58
NGC1866		$18.33 \pm (0.05)$	18.33
All		Unweighted Mean	$18.48 \pm (0.04)$

3.11 Tests of Metallicity Effects

Table 3.4 shows the adopted non-Cepheid LMC modulus. Also shown is the Cepheid distance modulus of the LMC based on (3.2) and (3.3) and with the zero-point of the PL(V) relation from Table 3.2 (-1.35) without any metallicity correction, with the corrections used by the HST key project group [107], 0.20mag $[O/H]^{-1}$, and that derived from the work of Laney.

It is clear that the various estimates are in better agreement than we might reasonably have expected.

Some caution has to be used with these results. For instance there is evidence (see Sect. 3.10.6) that young objects in the LMC may be deficient in oxygen (an α element) relative to iron and this could affect the luminosities of some calibrators. There remains also the problem of the depth of the LMC. It is generally assumed to be small, at least for young objects. But more evidence bearing on this is required, especially for the old objects such as RR Lyrae stars which are used as LMC distance indicators. It is worth recalling that the SMC Cepheids show evidence of a considerable depth of this galaxy in the line-of-sight [3] and this tends to preclude the use of the SMC for stringent tests of the Cepheid scale and its metallicity dependence.

A similar comparison of Cepheid and non-Cepheid moduli to that described above for the LMC can be made for other galaxies. Dolphin et al. [101] and Udalski et al. [102] have published such discussions for IC1613 in which the Cepheids are believed to have a low metallicity ($[Fe/H] \sim -1.0$). These discussions suggest a relatively small metallicity effect using V, I for Cepheids of metallicity lower than that of the LMC. Dolphin et al. [101] found -0.07 ± 0.16mag $[O/H]^{-1}$ and Udalski et al. [101] suggest there is no significant metallicity effect. In the case of IC1613 there is some uncertainty, due amongst other things to the lack of good estimates of the metallicities of the Cepheids and other objects used to derive distances.

The above discussion suggests that in V, I there is a small but probably significant metallicity effect, at least for Cepheids more metal rich than the LMC. It is evident that further progress requires amongst other things improved abundances for Cepheids in both our Galaxy and nearby galaxies.

Table 3.4. LMC moduli: Cepheid–non-Cepheid comparison

Object	Method	Modulus
Non-Cepheid		$18.48 \pm (0.04)$
Cepheid	V.I Uncorrected	18.60
	V,I Laney Correction	18.56
	V,I HST Adopted Correction	18.52 (Range 18.57 - 18.47)

In view of the uncertainty in the metallicity correction it is advisable to avoid the need for using it if possible. This is the case for the galaxies in the HST key project [107]. The mean metallicity of these galaxies, weighted by their contribution to the finally adopted value of H_o is close to solar ([O/H] = –0.08). It has been hypothesised by some workers that the metallicity effect at V, I could be as high as 0.6mag $[O/H]^{-1}$. Whilst it seems unlikely that it could be as high as this, even such a large value will only have a small effect on a value of the HST key project H_o if this is based on the galactic (or NGC4258) calibration.

3.12 Cepheids – General Problems

There is evidence of a metallicity gradient for Cepheids in our own Galaxy, e.g. [35], and this will need to be taken into account in future analyses of Cepheid data (see e.g. Sects. 3.3 and 3.4 above). Abundance determinations are also important since they can help distinguish first- and later-crossing Cepheids. Most Cepheids are expected to be second-crossing stars and abundance analyses (see [103] and papers referenced there) which show that they have undergone first dredge-up, are consistent with this. The Cepheid SV Vul does not seem to have undergone first dredge-up [104] and is therefore likely to be a first-crossing Cepheid. Evidently chemical analyses together with accurate parallaxes will be a powerful way of investigating the multiple crossings and their effect on the use of Cepheids as distance indicators.

In most discussions of Cepheid luminosities it is assumed that the slope of the PL(V) relation can be taken from the LMC. In using this in our own and other galaxies, this assumes that the slope is independent of metallicity. The empirical evidence on this point is not strong. Caldwell and Laney [5] found a slope of -2.63 ± 0.08 for the SMC Cepheids. The value (adopted in the present paper) for the LMC is -2.81 ± 0.06 [5]. Udalski et al. [105] found $-2.76 \pm (0.03)$ for the LMC. The standard error is placed in brackets since much of the weight of this determination is in short-period Cepheids. Gieren et al. [106] obtained -3.04 ± 0.14 for Cepheids in the general solar vicinity using pulsation parallax results. There is a slight hint of a trend SMC, LMC, Galaxy i.e. a metallicity effect. The evidence for such a trend is evidently marginal and requires confirmation. The slope is of importance since, for instance, the weighted mean log-period of the Cepheids used in the Hipparcos parallax solution is smaller than the weighted mean log-period of the extragalactic Cepheids used to determine H_o, e.g. [107]. If the Gieren et al. slope had been used this would have resulted in an approximately seven percent increase in the parallax distance scale as applied to the HST key-project galaxies. Adopting the OGLE slope [105] would have had only a small effect.

In the present discussion it has been assumed that the reddenings of Cepheids are derived from a PC relation. The relations in B, V and V, I ((3.1) and (3.3) above) are both based on the system of BVI reddenings and should be compatible. However there still remains work to make certain that these form a completely self-consistent set. Some estimates of the PC slope in $(V - I)$ are

Table 3.5. Slope of the PC($V-I$) relation

Method	Slope
Galaxy (Caldwell, Coulson) [7]	0.297 ± 0.014
LMC (Udalski et al.) [105]	0.202 ± 0.037
Difference	0.095 ± 0.040
LMC (Caldwell, Coulson) [3]	0.318 ± 0.054
SMC (Caldwell, Coulson) [3]	0.227 ± 0.038
Difference	0.091 ± 0.066

shown in Table 3.5. The value for the LMC derived from Udalski et al. [105] is based primarily on short period Cepheids and is uncomfortably different from the galactic value. It suggests the possibility of a change in slope at about 10 days [108]. This is currently a cause for concern. The LMC slope of Caldwell and Coulson [3] which is weighted to longer periods than that of Udalski et al. differs from the latter and the LMC and SMC slopes also seem to differ. However none of these differences are vastly larger than their standard errors. The question of changes of slope with metallicity and at a period of about 10 days thus remains to be finally settled.

I have chosen to adopt here the galactic PC slope in $(V-I)$ for two reasons. Firstly, as just mentioned, the determination of Udalski et al. [105] is heavily weighted by short-period Cepheids. Such stars have little weight in the zero-point calibrations discussed earlier or in the current applications of Cepheids in galactic astronomy and in the determination of H_o. Secondly, it happens that the mean metallicity of the galaxies studied in the HST key project is close to solar when weighted according to their contributions to the final value of H_o. It is thus of some interest to compare the present calibration for metal-normal Cepheids with that adopted by the HST key project group [107]. Some years ago [115] there was a difference of about 8 percent (0.17 mag) between the Cepheid scale derived from Hipparcos parallaxes [6] and that adopted by the key project group. This difference has been essentially eliminated by two factors. Firstly, the Cepheid zero-point for metal-normal Cepheids adopted from the various estimates in Table 3.2 is 0.08 mag fainter than that derived from Hipparcos parallaxes alone by Feast and Catchpole [6]. Secondly, though the key project group still adopt an LMC modulus of 18.50, they apply a metallicity correction which implies that their scale for metal-normal Cepheids has been increased by 0.08 mag. The true value of H_o, however, still remains somewhat contentious e.g. [108].

3.13 Very Short Period Cepheids

The discussions above have left out of consideration the very short period Cepheids (periods less than $\sim$ 2 days). For instance the analysis of Udalski et al. [105], although heavily weighted to shorter period stars, omits Cepheids with periods less than 2.5 days. However, very short period Cepheids are known to be numerous in the SMC and other young metal-poor systems and although they are relatively faint, they are potentially important as distance indicators for systems such as the metal-poor dwarf galaxies [116].

In the SMC there is a steepening of the PL relations for periods shorter than 2 days, as was originally pointed out by Bauer et al. [117]. The OGLE data for these very short period Cepheids in the SMC [118] has been used by Dolphin et al. [116] to derive slopes of –3.10 and –3.31 for the PL(V) and PL(I) relations of fundamental mode pulsators and –3.30 and –3.41 for the first overtone pulsators (which constitute about half the OGLE sample).

Dolphin et al. [116] have also discussed the relative distances of the SMC and the dwarf galaxies, IC1613, Leo A and Sex A. The Cepheids in these systems are expected to be metal poor since the values of $12+\log(O/H)$ from HII regions are; SMC, 8.0; IC1613, 7.9; Leo A, 7.3; Sex A, 7.6 [119]. From a comparison of the relative distances derived from the very short period Cepheids in these systems with relative distances from other indicators (RR Lyrae variables, RGB tip, red clump) Dolphin et al. conclude that there is no significant effect of metallicity on the luminosities of these very short period metal-poor Cepheids.

3.14 Conclusions

The present discussion suggests that the luminosities of metal-normal Cepheids are now known within a standard error of 0.1 mag or possibly less. However it has to be recognized that deviations from the true value considerably in excess of one standard error are entirely possible statistically. It is therefore very desirable to further strengthen the empirical determinations. Some remaining issues that need to be resolved are as follows.

1. Do the slopes of PL (and PC) relations at different wavelengths vary with metallicity?
2. Are there non-linearities in the PL and PC relations? Particularly is there a significant slope difference between short and long period ($>\sim$ 10 days) Cepheids that would seriously affect the calibration and use of PL and PC relations?
3. Are reddening effects being correctly and consistently treated in the calibration and use of Cepheids?
4. Is the reddening law being used really applicable to all Cepheids in our own and other galaxies?
5. Can better empirical estimates be obtained of the effects of metallicity variations on Cepheid luminosities and colours?
6. Do the relative abundances of heavy elements (e.g. the ratio of α elements, such as oxygen, to iron) affect Cepheid PL and PC relations?

7. Are a significant number of calibrating or programme Cepheids undiscovered overtone pulsators?
8. Can we distinguish (probably by spectroscopic analysis) first-crossing Cepheids from others? Are the luminosities of such stars significantly different from others of the same period? If so, are these stars sufficiently numerous to create a problem for the use of Cepheids as distance indicators?

References

1. J.F. Dean, P.R. Warren, A.W.J. Cousins: MNRAS, **183**, 569 (1978)
2. J.A.R. Caldwell, I.M. Coulson: MNRAS, **212**, 879 (1985) (erratum **214**, 639)
3. J.A.R. Caldwell, I.M. Coulson: MNRAS **218**, 223 (1986)
4. C.D. Laney, R.S. Stobie: MNRAS,**266**, 441 (1994)
5. J.A.R. Caldwell, C.D. Laney: In: The Magellanic Clouds, ed. by R. Haynes, D. Milne (Kluwer, Dordrecht 1991) p.249
6. M.W. Feast, R.M. Catchpole: MNRAS,**286**, L1 (1997)
7. J.A.R. Caldwell, I. M. Coulson: AJ, **93**, 1090 (1987)
8. M.W. Feast: PASP, **111**, 775 (1999)
9. M.A.C. Perryman et al.: The Hipparcos and Tycho Catalogues, ESA SP-1200 (1999)
10. T.E. Lutz, D.H. Kelker: PASP, **85**, 573 (1973)
11. R.B. Hanson: MNRAS,**186**, 875 (1979)
12. C. Koen, C.D. Laney: MNRAS, **301**, 582 (1998)
13. A. Sandage, A. Saha: AJ, **123**, 2047 (2002)
14. A.S. Eddington: MNRAS, **73**, 359 (1913)
15. K.G. Malmquist: Lund Medd. Ser. II, no 22 (1920)
16. M.W. Feast: MNRAS, **337**, 1035 (2002)
17. M.W. Feast: Vistas in Astronomy, **13**, 207 (1972)
18. M.A.T. Groenewegen, R.D. Oudmaijer: A&A,**356**, 849 (2000)
19. P. Lanoix, G. Paturel, R. Garnier: MNRAS, **308**, 969 (1999)
20. G.F. Benedict et al.: astro-ph/0206214 (2002)
21. F. Pont: In, ASP Conf. Ser. **167**, Harmonizing the Cosmic Distance Scale in the Post-Hipparcos Era, ed. by D Egret, A. Heck (San Francisco) p.113 (1999)
22. C. Alcock et al.: AJ, **109**, 1653 (1995)
23. E. Poretti: A&A, **285**, 524 (1994)
24. C.D. Laney, R.S. Stobie: MNRAS, **274**, 337 (1995)
25. W.P. Gieren, P. Fouqué, M. Gómez: ApJ, **496**, 17 (1998)
26. M.E. Sachkov: Astron. Lett. **28**, 589 (2002)
27. N.R. Evans, D.D. Sasselov, C. I. Short: ApJ, **567**, 1121 (2002)
28. T.E. Nordgren et al.: AJ, **118**, 3032 (1999)
29. J.P. Beaulieu et al.: A&A, **303**, 137 (1995)
30. G.P. Di Benedetto: AJ, **124**, 1213 (2002)
31. M.W. Feast, P.A. Whitelock: MNRAS, **291**, 693 (1997)
32. F. Pont, M. Mayor, G. Burki: A&A, **285**, 415 (1994)
33. M.W. Feast, F. Pont, P. A. Whitelock: MNRAS, **298**, L43 (1998)
34. M.W. Feast: MNRAS, **313**, 596 (2000)
35. S.M. Andrievsky et al.: astro-ph/0208056 (2002)
36. J.B. Irwin: Mon. Not. Ast. Soc Sth. Afr., **14**, 38 (1955)
37. H. Baumgardt, C. Dettbarn, R. Wielen: A&A Sup., **146**, 251 (2000)

38. P.W. Merrill: The Spectra of Long-Period Variable Stars (Chicago University Press) p. 63 (1940)
39. J.W. Menzies et al.: MNRAS,**248**, 642 (1991)
40. A.R. Walker, C.D. Laney: MNRAS, **224**, 61, (1987)
41. F. van Leeuwen: Ph.D. Thesis. Leiden University (1983)
42. A.R. Sandage, C. Cacciari: ApJ, **350**, 645 (1990)
43. M.W. Feast: In, Observational Tests of Cosmological Inflation, ed T. Shanks et al. (Kluwer, Dordrecht) p. 147 (1991)
44. F. van Leeuwen: A&A, **341**, L71 (1999) and in, ASP. Conf. Ser., **198**, Stellar Clusters and Associations, ed. by R. Pallavicini et al. (San Francisco, ASP), p.85 (2000)
45. N. Robichon et al.: In, ASP Conf. Ser., **198**, Stellar Clusters and Associations, ed. by R. Pallavicini et al. (San Francisco, ASP) p141 (2000)
46. M.H. Pinsonneault et al.: ApJ, **504**, 170 (1998)
47. V. Castellani et al.: MNRAS, **334**, 193 (2002)
48. M. Grenon:In, ASP Conf. Ser., **223**, Proc. 11th Cambridge Workshop on Cool Stars, ed. by R. J. Garcia Lopez et al., (San Francisco, ASP) p. 359 (1999)
49. D. Stello, P.E. Nissen: A&A, **374**, 105 (2001)
50. E. Friel, A.M. Boesgaard: ApJ, **387**, 480 (1990)
51. M.A.C. Perryman et al.: A&A, **331**, 81 (1998)
52. D.G. Turner: PASP. **91**, 642 (1979)
53. J-W. Pel: In, Cepheids: Theory and Observations, ed. by B. Madore (Cambridge, CUP) p. 1 (1985)
54. B.J. Taylor: A&A, **362**, 563 (2000)
55. N. Evans: ApJ, **372**, 597 (1991)
56. N. Evans: ApJ, **389**, 657 (1992)
57. P. Kervella et al.: A&A, **367**, 876 (2001)
58. T.E. Nordgren et al.: ApJ, **543**, 972 (2000)
59. J.T. Armstrong et al.: AJ, **121**, 476 (2001)
60. B.F. Lane et al.: ApJ, **573**, 330 (2002)
61. C.D. Laney: In, ASP Conf. Ser., **135**, A Half-Century of Stellar Pulsation Interpretations, ed. by P.A. Bradley, J.A. Guzik (San Francisco, ASP), p180 (1998)
62. J.R. Herrnstein et al.: Nature, **400**, 539 (1999)
63. J.A. Newman et al.: ApJ, **553**, 562 (2001)
64. D. Zaritsky, R.C. Kennicutt, J.P. Huchra: ApJ, **420**, 87 (1994)
65. M.W. Feast: In, ASP Conf. Ser. **4**, The Extragalactic Distance Scale, ed. by S. van den Bergh (San Francisco, ASP), p. 9 (1988)
66. C.D. Laney, R.S. Stobie: MNRAS, **222**, 449 (1986)
67. C.D. Laney: In IAU Symp. **192**, The Stellar Content of Local Group Galaxies, ed. by P.A. Whitelock, R. Cannon (San Francisco, ASP) p. 459 (1999)
68. R.C. Kennicutt et al.: ApJ, **498**, 181 (1998)
69. C.D. Laney: In, ASP Conf. Ser. **203**, The Impact of Large-Scale Surveys on Pulsating Star Research, ed. by L. Szabados, D.W. Kurtz (San Francisco, ASP), p. 199 (2000)
70. W.L. Martin, P.R. Warren, M.W. Feast: MNRAS, **188**, 139 (1979)
71. R.E. Luck et al.: AJ, **115**, 605 (1998)
72. A.R. Sandage: ApJ, **350**, 603 (1990)
73. G.F. Benedict et al.: AJ, **123**, 473 (2002)
74. E. Carretta et al.: ApJ, **533**, 215 (2000)
75. M.W. Feast: In IAU Symp. **201**, New Cosmological Data and the Values of the Fundamental Parameters in press

76. A.J. Longmore et al.: MNRAS, **247**, 684 (1990)
77. M.W. Feast et al.: MNRAS **241**, 375 (1989)
78. P.R. Wood: In, ASP Conf. Ser. 83, Astrophysical Applications of Stellar Pulsations, ed. by R.S. Stobie, P.A. Whitelock (San Francisco, ASP) p. 127 (1995)
79. P.W. Whitelock et al.: MNRAS, **267**, 711 (1994)
80. M.W. Feast, P.A. Whitelock, J.W. Menzies: MNRAS, **329**, L7 (2002)
81. P.A. Whitelock, M.W. Feast: MNRAS, **319**, 759 (2000)
82. M.W. Feast, P.A. Whitelock: In, The Evolution of the Milky Way, ed. by F. Matteucci, F. Giovannelli (Kluwer, Dordrecht) p. 229 (2000)
83. M.W. Feast: MNRAS, **278**, 11 (1996)
84. P.A. Whitelock, M.W. Feast: Mem. Soc. Ast. It. **71**, 601, (2000)
85. P.A. Whitelock: In, Mass-losing Pulsating Stars and their Circumstellar Matter, ed. by Y. Nakada, M. Honma (Kluwer, Dordrecht) in press
86. V.V. Smith et al.: ApJ, **441**, 735 (1995)
87. R. Kurtev et al.: A&A, **378**, 449 (2001)
88. E.F. Guinan et al.: ApJ, **509**, L21 (1998)
89. E.L Fitzpatrick et al: ApJ, **564**, 260 (2002)
90. I. Ribas et al.: ApJ, **574**, 771 (2002)
91. C.A. Nelson et al.: AJ, **119**, 1205 (2000)
92. M.A.T. Groenewegen, M. Salaris: A&A, **366**, 752 (2001)
93. N. Panagia: Mem. Soc. Ast. It. **69**, 225 (1998)
94. R.C. Mitchell et al.: ApJ, **574**, 293 (2002)
95. L. Girardi, M. Salaris: MNRAS, **323**, 109 (2001)
96. D.R. Alves et al.: ApJ, **573**, L51 (2002)
97. A.R. Walker et al.: ApJ, **560**, L139 (2001)
98. V. Hill et al.: A&A, **364**, L19 (2000)
99. G. Gilmore, R.F.G. Wyse: ApJ, **367**, L55 (1991)
100. A.R. Walker: AJ, **110**, 638 (1995)
101. A.E. Dolphin et al.: ApJ, **550**, 554 (2001)
102. A. Udalski et al.: Act. Ast., **51**, 221 (2001)
103. I.S. Usenko, V.V. Kovtyukh, V.G. Klochkova: A&A, **377**, 156 (2001)
104. R.E. Luck, V.V. Kovtyukh, S.M. Andrievsky: A&A, **373**, 589 (2001)
105. A. Udalski et al.: Act. Ast., **49**, 201 (1999)
106. W.P. Gieren et al.: ApJ, **496**, 17 (1998)
107. W.L. Freedman et al.: ApJ, **553**, 47 (2001)
108. G.A. Tammann et al.: In, ASP Conf. Ser. —, A New Era in Cosmology, ed. by T Shanks, N. Metcalfe (San Francisco, ASP) in press, Basel preprint 129
109. A.M. Orsatti, E.I. Vega, H.G. Marraco: A&A, **380**, 130 (2001)
110. P.R. Wood: In, From Miras to Planetary Nebulae, ed. by M.O, Mennessier, A. Omont (Editions Frontières, Gif-sur-Yvette), p. 67 (1990)
111. J.-M. Huré: In, ASP Conf. Ser. —, Active Galactic Nuclei, ed. by S. Collin, F. Combes, I. Shlosman (San Francisco, ASP) in press, Astro-ph 0210421
112. V.V. Smith et al.: astro-ph 0208417
113. W. Vlemmings: Circumstellar Maser Properties through VLBI Observations. Ph.D. Thesis, Leiden University, Leiden (2002)
114. P.A. Whitelock, F. Marang, M.W. Feast: MNRAS, **319**, 728 (2000)
115. M.W. Feast: MNRAS, **293**, L27 (1998)
116. A.E. Dolphin et al.: astro-ph 0211486
117. F. Bauer et al.: A&A, **348**, 175 (1999)
118. A. Udalski et al.: Act. Ast. **49**, 437 (1999)

119. S. van den Bergh: *The Galaxies of the Local Group* (Cambridge University Press, 2000)
120. B.F. Madore, W.L. Freedman: PASP, **103**, 933 (1991)
121. V.V. Makarov: AJ, **125**, 3299 (2002)
122. D.G. Turner, J.F. Burke: AJ, **124**, 2931, (2002)

4 The Cepheid Calibration of Type Ia Supernovae as Standard Candles

Abhijit Saha

National Optical Astronomy Observatory, 950 N. Cherry Ave, Tucson AZ, USA

Abstract. The experiment to establish the peak brightness of nearby supernovae of type Ia (SNe Ia) as standard candles is summarized. We show that while the entire set of SNe Ia can differ in peak brightness by over 1.5 mag, it is possible to define a subset based on color at maximum light, which has well behaved properties. By using second parameter corrections on this subset (aka the Parodi sample), the scatter in peak brightness in V is reduced to 0.13 mag rms, which makes these excellent standard candles. The results for the absolute calibration of the peak brightness of the Parodi sample via Cepheid distances to nearby SNe Ia host galaxies are presented. Procedural details that we have used to minimize the errors (on a case by case basis) in determining the peak brightness of these SNe Ia are described. We highlight the sources of the difference between our derived value of the Hubble constant $H_0 = 60$ kms^{-1} Mpc^{-1} and the 20% higher value obtained by the HST 'key project' group, and demonstrate the differences lie not in photometry, but in the details of the methodology, in how the problem of reddening in the host galaxy is handled and in external issues such as the calibration of the Cepheids themselves.

4.1 Introduction

The peak brightness of supernovae of Type Ia (SNe Ia) have been shown empirically to be the most precise photometric standard candle that probes distances where Hubble expansion velocities dominate over local peculiar motions. They are now being used as cosmological probes not only to measure the Hubble constant, but also at high redshifts (up to $z = 1.7$). The high-z results, which apparently indicate an acceleration in the expansion rate of the Universe, are challenging our understanding not only of the cosmos, but also of the fundamental nature of matter and energy.

There are two distinct aspects to using SNe Ia as photometric standard candles. The first is how well they behave as a class, and how well the *relative* brightness of a particular SN Ia can be predicted versus another. The second is the absolute calibration which assigns a true brightness to these objects. Each of these aspects has its own points of interest, and are discussed here separately.

The details of the experiments, and the process by which we have arrived at our current level of understanding this problem is well documented in the literature. This article is not a review. The purpose here is to summarize the current state of knowledge, to highlight the areas where our own approach to this problem differs from that of others, and to explain why we have done things the way we have. In particular, we critically examine the basis for the 20%

A. Saha, The Cepheid Calibration of Type Ia Supernovae as Standard Candles, Lect. Notes Phys. **635**, 71–83 (2003)
http://www.springerlink.com/

difference in H_0 between our analysis, and the re-analysis of the same data by another group.

4.2 The Relative Scatter of Peak Brightness among Individual SNe Ia

Since SNe Ia are very bright, they are easily seen and measured at distances well into the smooth Hubble flow, i.e. at distances where the peculiar velocities of galaxies relative to the cosmic microwave background (CMB) co-moving frame is much smaller than the recession velocity due to the Hubble expansion field. Thus for recession velocities larger than say 1200 kms^{-1}, and out to redshifts of $z = 0.1$ (beyond which second order terms in the time derivative of the cosmological scale factor can contribute), the recession velocity of the host galaxy is a measure of *relative* distance. The relative intrinsic luminosity at peak brightness of SNe Ia may thus be gleaned from the observed apparent brightness, after interstellar reddening and extinction effects (including in the host galaxy) are accounted for. In other words, for an *assumed* value of H_0, we can predict the absolute magnitude of any SN Ia observed in the above redshift range, provided we can make extinction corrections. This has proved very useful, since it has allowed investigators to look for systematic dependence of the absolute peak brightness on intrinsic properties of individual SNe Ia. This bears on understanding the photometric properties of SNe Ia as a class, and of devising *a priori* criteria for defining a sample of 'good' SNe Ia (those whose properties we are confident of being able to predict) as well as accounting for second parameter effects within such a sample.

4.2.1 Variations in Light Curve Shape, Spectra, and Color among SNe Ia

There are differences in how different groups of investigators have approached the problem of second parameter corrections. Phillips [1] showed that the light curve decline rate (usually measured as $\Delta m_{15}(B)$, which is the amount in magnitudes by which the brightness in B diminishes in the first 15 days after peak B brightness) correlates with the intrinsic peak brightness. Other ways of characterizing light curve shapes and how they affect brightness exist in the literature, but the idea is the same. Branch et al. [2] did a spectroscopic comparison of about a hundred SNe Ia and showed that while an overwhelming majority of these objects have spectra that are virtually carbon copies of one another (at maximum light, as well as how they evolve in time as the brightness declines), there are some that are different: most notably those that have Ti absorption features at maximum light. These SNe Ia can be significantly underluminous (as much as 1.5 mag) compared with those that have so called 'Branch normal' spectra. The Branch normal SNe Ia themselves exhibit a much smaller scatter ($\sigma(M_V) \approx 0.3$ mag). Also, with one exception (SN1991T: which is peculiar in a way that is different from all the others), all of Branch et al.'s spectroscopically peculiar SNe Ia were redder at maximum light than $(B_{max} - V_{max})$ of 0.2.

4.2.2 Identifying a Well Behaved Sample of SNe Ia Using Simple *a priori* Criteria: The Parodi Sample

These differences in intrinsic properties presumably arise from variables in the physics of the explosion. While understanding the explosion mechanism is of tremendous importance, our particular interest lies in being able to identify a robust *empirical* sample of SNe Ia based on *a priori* observational criteria for which there is minimal scatter in intrinsic brightness with or without a second parameter correction. Preferably it should be based only on parameters that can in fact be observed even for the faint SNe Ia seen at high redshifts. This has been approached in several ways by different investigators, and a full discussion is beyond the scope here. The method preferred by us is the one by Parodi et al. [3].

The Parodi et al. sample selects SNe Ia with well determined V_{max} and B_{max}, where, after applying an extinction correction for foreground Galactic extinction only, $B_{max} - V_{max} \leq 0.20$. When applied to SNe Ia after 1985 with indisputably good quality light curves, this produces a sample that has mean $B_{max} - V_{max} = 0.02$, and standard deviation 0.05. Spectroscopically peculiar objects like SN1986G and SN1991bg which are redder than the selection limit (as mentioned in §2.1), as well as spectroscopically normal SNe Ia with large reddening, are both excluded from this sample. In Fig. 4.1, the Parodi sample SNe Ia *with recession velocities greater than 1200* kms^{-1} are shown as crosses: inferred absolute magnitudes are shown against log of the recession velocity for 3 different assumed values of H_0 (the figure will illustrate other issues to be discussed later). Only foreground extinction corrections have been applied. The standard deviation in M_V is about 0.3 mag, which is already quite good.

4.2.3 Second Parameter Variations within the Parodi Sample

Parodi et al. found a smaller dependence of peak brightness on decline rate for their sample than is found if redder SNe Ia are included. This reflects the fact that a single relationship between M_V and $\Delta m_{15}(B)$ is not adequate to describe all SNe Ia. Thus the slope of the relation for $\Delta m_{15}(B)$ that is suitable for the Parodi sample is in general different from the slope that one gets by attempting to fit any other subset of SNe Ia. In addition, there is another second parameter identified by Parodi et al.: they found that peak brightness depends on the color at peak brightness (after Galactic foreground reddening is removed). This dependence is found to be orthogonal to that from $\Delta m_{15}(B)$. Some component of it could be a result of residual reddening (from the host galaxies), but the dependence in different passbands shows that it is not consistent with being from reddening alone. There is intrinsic dependence on color at peak brightness. The slope of this relation as given by Parodi et al. (their equations (9)–(11)), which is mild, gives valid corrections for a sample of SNe Ia identified by their criteria.

Figure 4.2 is the same as Fig. 4.1, except that the correction for the two second parameters has been made. Note how the scatter in M_V has shrunk now to a standard deviation of only 0.13 mag. This demonstrates just how good

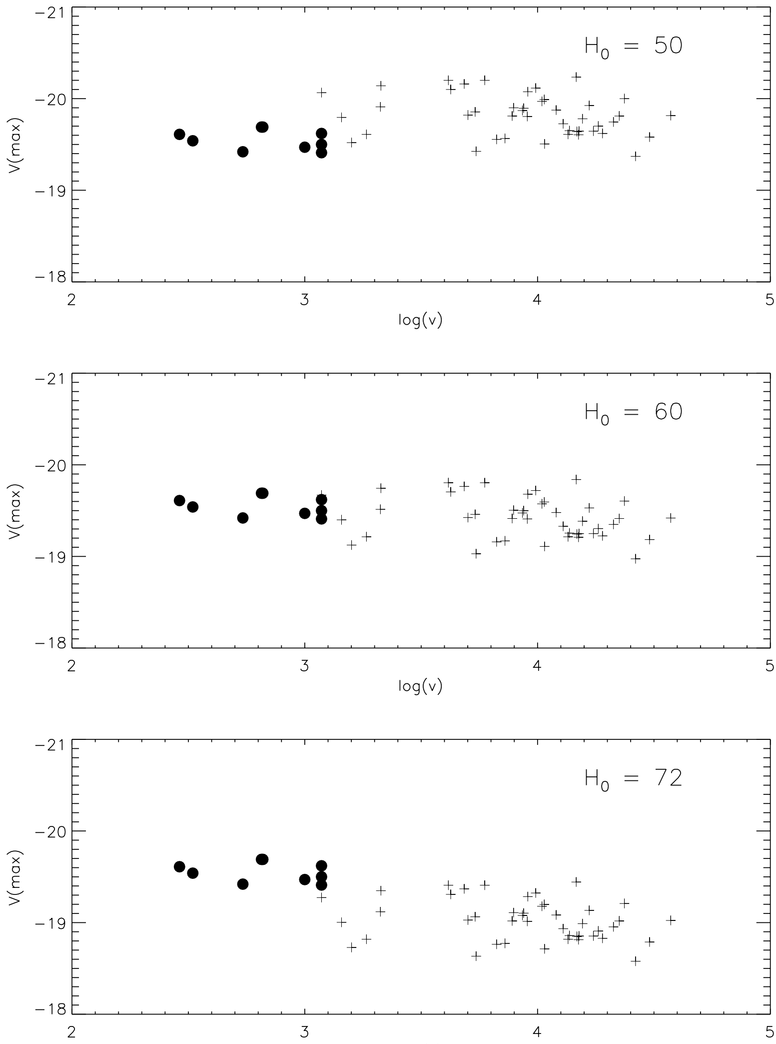

Fig. 4.1. This figure is a projection of the Hubble diagram for 3 assumed values of H_0. The crosses are SNe Ia with $B_{max} - V_{max} \leq 0.20$ (after correction for foreground Galactic extinction alone) with recession velocities that place them in the linear regime of the smooth Hubble expansion flow. Using their observed V_{max} (foreground extinction corrected) and an assumed value of H_0, the implied *absolute* magnitude in V is shown in the ordinate. As the assumed value of H_0 is increased, the points marked in crosses become fainter in intrinsic brightness. Note that the scatter in brightness of the SNe Ia sample (the Parodi sample) based on color alone is already as small as 0.3 mag, before any corrections for light curve shape or color are applied. The filled circles mark the *measured* absolute brightness of the nearby Cepheid calibrated SNe Ia. Their brightness is held fixed in the different panels, because they do not change in ordinate with assumed H_0. The correct value of H_0 is that for which the filled circles and the crosses are aligned in the ordinate

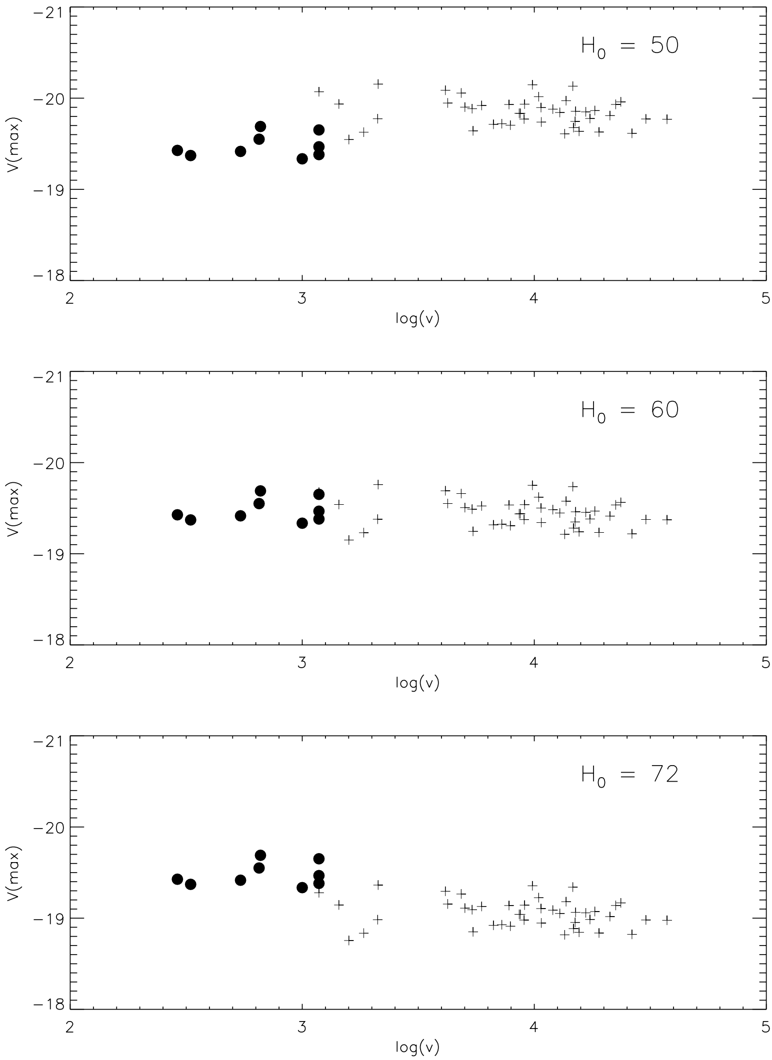

Fig. 4.2. Same as Fig. 4.1, but with corrections applied to both sets of points for light curve shape and color as appropriate for the Parodi sample. The scatter in absolute brightness of the crosses is now only 0.13 mag rms. The robustness of our derived value of $H_0 = 60$ is demonstrated graphically. Note that for an assumed $H_0 = 72$, none of the SNe Ia marking the Hubble flow is implied to be brighter than the faintest of the Cepheid calibrated SNe Ia. A systematic change that makes the Cepheid calibrated SNe Ia fainter by 0.4 mag is required to obtain $H_0 = 72$

SNe Ia are as standard candles. What remains is to discuss how the absolute magnitudes are assigned to them.

4.3 Cepheid Distances to Host Galaxies

4.3.1 The Results of the Experiment

A few SNe Ia have historically been observed in galaxies that are close enough for the detection and calibration of Cepheids. By finding distances to these host galaxies, the absolute peak brightness for these few SNe Ia can be found. Of course, we must restrict ourselves to a sample chosen by the same rules as the Parodi sample, and we must apply the same correction for second parameter effects as we do for the Parodi sample. This experiment was conceived by Allan Sandage and Gustav Tammann, who led a team to do this using the Hubble Space Telescope. Their results thus far appear in a series of papers, culminating in [4]. Primarily as a result of this effort, and supplemented by a few additional cases, there are today 9 SNe Ia with Cepheid distances to their host galaxies, and resulting absolute magnitudes for the SNe Ia at peak brightness. The results are summarized in Table 4.1.

The Cepheid derived values of M_V are shown in bold symbols in Fig. 4.1. The second parameter corrected values M_V^{corr} are shown in bold symbols in Fig. 4.2. Note that in these figures the bold symbols do not move in ordinate with assumed value of H_0. Rather, the correct value of H_0 is the one where the bold symbols and the crosses are aligned in ordinate. In the following discussion, we shall return repeatedly to Fig. 4.2, which is a graphic demonstration of how well the internal scatter is constrained.

4.3.2 Some Procedural Details

This concerns how distances to host galaxies and absolute brightness of the SNe Ia hosted by it were derived, once the Cepheids were identified and their light curves determined. The observations consisted of 12 or more epochs in V, spaced optimally over about 60 days, so that phase coverage is even throughout the period range from 10 to 60 days. This also minimizes aliasing problems. The periods and light curves were thus determined only from the V observations. To economize on observing time with HST, only a few epochs in I were obtained (at most 5 epochs). With light curves and ephemerides known from the V observations, these few I observations were used to deduce the mean value over the pulsation cycle $\langle I \rangle$ using the procedure in [5]. Armed with $\langle V \rangle$ and $\langle I \rangle$, the multi-band calibration for M_V and M_I by Madore & Freedman [6] were used to derive the apparent moduli in V and I. Their relations, which are based on an *assumed* distance modulus to the LMC of 18.50 are:

$$M_V = -2.76 \log P - 1.40 \tag{4.1}$$

and

$$M_I = -3.06 \log P - 1.81 \tag{4.2}$$

Table 4.1. Mean absolute B, V, and I magnitudes of nine SNe Ia without and with corrections for decline rate and color

SN (1)	Galaxy (2)	$(m-M)^0$ (3)	M_B^0 (4)	M_V^0 (5)	M_I^0 (6)
1937C	IC 4182	28.36 (12)	-19.56 (15)	-19.54 (17)	...
1960F	NGC 4496A	31.03 (10)	-19.56 (18)	-19.62 (22)	...
1972E	NGC 5253	28.00 (07)	-19.64 (16)	-19.61 (17)	-19.27 (20)
1974G	NGC 4414	31.46 (17)	-19.67 (34)	-19.69 (27)	...
1981B	NGC 4536	31.10 (12)	-19.50 (18)	-19.50 (16)	...
1989B	NGC 3627	30.22 (12)	-19.47 (18)	-19.42 (16)	-19.21 (14)
1990N	NGC 4639	32.03 (22)	-19.39 (26)	-19.41 (24)	-19.14 (23)
1998bu	NGC 3368	30.37 (16)	-19.76 (31)	-19.69 (26)	-19.43 (21)
1998aq	NGC 3982	31.72 (14)	-19.56 (21)	-19.48 (20)	...
		straight mean:	-19.57 (04)	-19.55 (04)	-19.26 (06)
		weighted mean:	-19.56 (07)	-19.53 (06)	-19.25 (09)

SN (1)	Δm_{15} (7)	$(B-V)^0$ (8)	$M_B^{\rm corr}$ (9)	$M_V^{\rm corr}$ (10)	$M_I^{\rm corr}$ (11)
1937C	0.87 (10)	-0.02	-19.39 (18)	-19.37 (17)	...
1960F	1.06 (12)	0.06	-19.67 (18)	-19.65 (22)	...
1972E	0.87 (10)	-0.03	-19.44 (16)	-19.42 (17)	-19.12 (20)
1974G	1.11 (06)	0.02	-19.70 (34)	-19.69 (27)	...
1981B	1.10 (07)	0.00	-19.48 (18)	-19.46 (16)	...
1989B	1.31 (07)	-0.05	-19.42 (18)	-19.41 (16)	-19.20 (14)
1990N	1.05 (05)	0.02	-19.39 (26)	-19.38 (24)	-19.02 (23)
1998bu	1.08 (05)	-0.07	-19.56 (31)	-19.55 (36)	-19.31 (21)
1998aq	1.12 (03)	-0.08	-19.35 (24)	-19.34 (23)	...
			-19.49 (04)	-19.47 (04)	-19.16 (06)
			-19.47 (07)	-19.46 (06)	-19.19 (09)

The apparent modulus derivation can be done for the ensemble of Cepheids (where we denote the ensemble moduli by μ_V and μ_I), and also on an *object by object* basis (when they are denoted by U_V and U_I), since differential extinction in the host galaxy can cause them to be extincted independently. Note that individual reddening is then simply:

$$E(V-I) = U_V - U_I. \tag{4.3}$$

The true modulus for an individual Cepheid is then:

$$U_0 = 2.45U_I - 1.45U_V \tag{4.4}$$

where a reddening law with $A_V/A_I = 1.7$ has been used. This is the standard procedure for de-reddening, but it requires some caution, since errors of measurement, particularly in I propagate strongly into the de-reddened or true modulus.

In cases where a large scatter in the observed period color relation is seen, the cause can be either large differential reddening, or large scatter due to measuring errors, or both. If it is due to a measuring error where the errors are not symmetrically distributed, then interpreting all color scatter as due to differential reddening can produce skewed results. While currently available photometry programs can estimate very realistic errors from fitting residuals, errors from confusion noise is harder. Artificial star experiments to model confusion errors do not work quite as well as we would wish for HST/WFPC2 data, since the PSFs are acutely undersampled.

Fortunately there is a way to learn if there are large measurement errors as opposed to differential extinction alone. The slope of the reddening line is nearly degenerate with the lines of equal period that cut across the instability strip (i.e. change of color with brightness, given a period). Hence in the plane of U_V versus $U_V - U_I$ (the latter is a color excess), true Cepheids can occupy only a small strip along the reddening vector. Excess scatter must be measurement errors. This idea is developed fully in [7]. In particular, see their Fig. 11.

We have encountered a variety of cases, ranging from high S/N data and little if any differential reddening, to cases where *both* severe differential reddening, as well as confusion noise from crowding are present. Each case has been treated according to its own merits, keeping in mind that the primary objective is to get the peak absolute brightness of the SNe Ia, and that the true modulus to the host galaxy is but an intermediary. This is best exemplified in the case of NGC 5253, as detailed in [8]. In this case, the Cepheids, which were all outside the central region of this amorphous galaxy, showed remarkable consistency in the apparent V modulus U_V, but with wide scatter in U_I. Clearly, this indicates that the culprit is measurement error in I, presumably because of the very few epochs used, as also the fact that background confusion is higher in the near infra-red (the color of the unresolved or quasi-resolved fainter stars) than in V. Differential reddening would have produced larger scatter in U_V than in U_I. Given this situation, if we go through a formal de-reddening procedure, the error on the true distance modulus derived for this galaxy would be nearly ± 0.30. Instead, the constancy of U_V with position in the field provides a *differential* measurement of the V modulus to SN1972E, which is similarly placed in distance from the center of the galaxy. This assertion of equal reddening to both Cepheids and SN is preferred in this particular case. This approach is suited for this case, but not for others. Adopting a "consistent" method for all cases is not necessarily the best approach as this example illustrates.

4.3.3 Are Some Calibrating SNe Ia Better Than Others?

There are several subtle issues that come up in the context of this experiment. Essentially all of them arise as a result of the fact that SNe Ia are not frequent events, and their occurrence in the nearby Universe in galaxies where Cepheids can be found is small, about one every 3 years. Until recent surveys began, even nearby SNe Ia were not always detected before they reached maximum light, and light curve information is sometimes incomplete. In other instances, like for SN1937C, debates have raged over the photometric quality from photographic plates that also involve the difficulty of transforming colors from plate material. In Table 4.1 we propagate reasonable estimates of these uncertainties. Some authors in the literature have discarded some of the older supernovae in Table 4.1 citing these uncertainties. However the net error in calibration depends not only on the quality of the supernova light curve, but also in how well the distance to the host galaxy can be determined. Several of the host galaxies are difficult cases which one would not normally choose as candidates for Cepheid searches. NGC 5253, for instance, is an amorphous galaxy with serious crowding and confusion issues. NGC 4536 and NGC 3627 are highly inclined, so we see through lots of stars and dust in the disk which complicates photometry and interpretation. Also, the average SNe Ia calibrating galaxy is farther away from the average galaxy studied by the 'key project' to investigate other secondary distance indicators. We cannot afford to be choosy about which galaxies to study, since there are so few of them. It is perhaps a coincidence that the galaxies with the best determined Cepheid distances are the ones with the SNe Ia with the most contentious photometry, and vice versa. As a result, the errors in calibrating the peak absolute magnitudes (in B, V and I), which are shown parenthetically in columns (4) to (6) in Table 4.1 are not very different from one SN to the next (particularly the error in M_V, where the range is a factor of 1.5) even though the estimated errors in $(m - M)$ range over a factor of 3 from one galaxy to another. One must also ask if all the SNe Ia in Table 4.1 satisfy the criteria of the Parodi sample. Strictly speaking, SN1989B does not - since it is highly reddened in the host galaxy, and its observed color is too red. However, since its reddening is known to good accuracy, and since its intrinsic color satisfies the Parodi criteria, we have included it due to the sheer shortage in the number of calibrating SNe Ia. All of these caveats aside, it is clear from looking at Figs. 4.1 and 4.2 that discarding any two or three SNe Ia from among the calibrating set does not alter the mean significantly.

4.4 The Value of the Hubble Constant from SNe Ia

Let us return to Figs 4.1 and 4.2. The filled circles, which are the calibrating Cepheids from Table 4.1 are consistent with the Hubble flow field SNe Ia near $H_0 = 60$. The formal answer, after second parameter corrections are applied (Fig. 4.2), is

$$H_0 = 60.3 \pm 1.8 \mathrm{kms}^{-1}\mathrm{Mpc}^{-1} \tag{4.5}$$

where it is to be emphasized that the error estimate is the statistical error that reflects the scatter in Fig. 4.2, but not possible systematic errors.

There is not much room to maneuver in Fig. 4.2. At an assumed H_0 of 72, the faintest calibrating SN Ia is as bright or brighter than *all* of the Hubble flow tracing SNe Ia. Yet this is the value derived by Freedman et al. [9], using the same data from HST as used by the Sandage/Tammann group. The only real way to that value is to move *all* the calibrating Cepheids in Fig. 4.2 fainter by almost 0.4 mag. It is therefore necessary to examine the differences in detail between our analysis and theirs.

4.5 Comparison with the Freedman et al. Result

4.5.1 Differences in Cepheid Discovery, Photometry, and Analysis Methodology

The re-analysis of the HST data was done by Gibson et al. [10], and the photometric results were reprocessed in [9]. The net result of the Gibson re-analysis is to claim that on average the SNe Ia calibrating galaxies are 0.17 mag closer in modulus compared to our work. It is an often mistaken notion that the differences are due to systematic differences in photometry. They are not: as mentioned even by Gibson et al., for the 118 Cepheids in *common* found in (all) the 7 galaxies compared, the net difference is that the Gibson et al. are brighter in both V and I by 0.04 mag. The differences arise not from the photometry, but from the samples of Cepheids used. The discrepancy of 0.17 mag is not seen if only the Cepheids in common are used. The analysis of the Cepheids in the galaxies native to the 'key project', compared results from the ALLFRAME based reductions and Cepheid identification/photometry with parallel results from a DoPHOT based approach (the latter procedure is exactly the same as the one used by us). In those galaxies, only those Cepheids deemed usable by *both* approaches were used in the final analysis. To be at par with the 'key project' results, only the Cepheids found in common by us and by Gibson et al. should be used.

Let us take NGC 5253 as an example, because it has the largest alleged discrepancy. In [8] we refrained from quoting a true modulus to the galaxy, for the reasons mentioned above, i.e. that the uncertainty is huge (0.3 mag), and that a more useful answer for the brightness of SN1972E can be obtained differentially from the Cepheids. Gibson et al. quote us as saying $\mu_0 = 28.08 \pm 0.2$: the value is what is implied by our numbers, but the uncertainty implied by what we said is ±0.3, not ±0.2. From their own analysis, Gibson et al. find $\mu_0 = 27.61 \pm 0.11 \pm 0.16$. The large difference is not significant given the errors estimated. The 5 individual putative Cepheids that are in common have photometry in excellent agreement between the two analyses, but only 2 were deemed suitable by both sets of investigators. If we use only these 2 Cepheids, the modulus is 27.95, with an uncertainty of 0.25 mag. This illustrates how it is the samples of Cepheids chosen that drive the difference. And in this case where the discrepancy is apparently the largest, the problem is in trying to use the true modulus of the galaxy. This intermediate step is the S/N bottleneck. If the Gibson et al. V photometry alone is used, even given the differences in chosen samples, the brightness of SN1972E obtained by using the differential approach described above would be only ≈ 0.1 mag fainter than ours, instead of a half magnitude difference.

We believe that the approach taken by us to go in the path of the highest signal to noise which is different for each case encountered is the correct one, and stand by our results.

4.5.2 Is the Cepheid P-L Relation Universal?

In [9], Freedman et al. revise Cepheid distances from [10] (as well as for other galaxies studied by the 'key project'). The basis of this change is the adoption of new P-L relations in V and I that have resulted from the OGLE data on LMC Cepheids by Udalski et al. [11]. The new P-L relation has a significantly shallower slope in the I band than the Madore & Freedman relations. As a result, when the colors are used to de-redden in the usual way, the effect is to change the modulus from a Cepheid with period P by:

$$\Delta U_0 = -0.24 \log P + 0.24. \tag{4.6}$$

The majority of the SNe Ia host galaxies with Cepheids are relatively far away, and in many of them only Cepheids with periods longer than 20 days have adequate brightness to be used in distance determination. Therefore, this revision results in a reduced distances to these galaxies, and makes the SNe Ia fainter (on average) by 0.15 mag.

At this meeting G.A. Tammann has shown that the situation with the P-L relation difference is far more complex. For one thing, the Udalski et al. data show that there is a break in the slope of the LMC P-L relations near 10 days. Another is that the slope of the P-L relation in the Galaxy is much steeper than in the Clouds. Tammann, Sandage, & Reindl [12] used hundreds of fundamental-mode Galactic Cepheids based on excellent photometry by Berdnikov, Voziakova, & Ibragimov [13] and reddening values by Fernie et al. [14] to determine their period-color (P-C) relation. They have shown that Galactic Cepheids are redder than those in LMC. They have also used distances of 25 Cepheids in open clusters and associations [15] and of 28 Cepheids with Baade-Becker-Wesselink (BBW) distances [16] to calibrate a highly consistent and linear, but surprisingly steep Galactic P-L$_{B,V,I}$ relation.

Comparing with the OGLE data for LMC and SMC Cepheids, it is shown that LMC Cepheids are measured to be brighter by 0.5 mag for $\log P = 0.4$ (somewhat dependent on the adopted LMC distance) than their Galactic counterparts, but they are fainter than the latter when $\log P \geq 1.4$. It can be shown that the change of slope is a necessary effect of the metal-dependent blanketing effect, but in addition a temperature variation is required in the sense that low-metallicity Cepheids must be hotter at fixed luminosity. The presence of a break in the P-L slope at $P = 10^d$ in the LMC and SMC, but its absence in the Galaxy, is not foreseen in any existing models.

The more distant SNe Ia host galaxies resemble the Galaxy more than they do the Clouds. The use of the Galactic P-L relation is thus more appropriate. For Cepheids with periods near 30 days, the Galactic and LMC P-L relations yield no significant differences in modulus. Clearly the last word on this subject has not been spoken, but there is ample justification to not use the Udalski et al. LMC relations universally. Particularly, they are more likely to misrepresent the Cepheids in the more distant SNe Ia host galaxies.

4.5.3 Other Differences

Taken together, the re-reduction by Gibson et al., and the new P-L relation adopted by Freedman et al. as discussed above, explains 0.32 mag of the 0.37 mag difference needed to explain the discrepancy between $H_0 = 60$ and $H_0 = 71$. There are a host of other smaller differences.

A mild metallicity dependence in the Cepheids is used in [9], which makes the Freedman et al. calibration *brighter* by 0.06 mag. We think now, in light of the Tammann et al. results, that the metallicity dependence is likely to be more complex than a simple zero-point shift. As discussed above, this is still an open issue.

Freedman et al. use only 6 of the calibrating SNe Ia in Table 4.1 (one of ours, 1998aq came later than their work). The actual effect of this is complex – since it depends on the weighting used. It is further complicated by the fact they use a steeper slope for the light curve shape correction than we do. The calibrating SNe Ia should behave like the Parodi sample, which has about half the dependence on $\Delta m_{15}(B)$ than the one used in [9]. Taken together the result is an additional reduction of effective distance modulus by 0.10 mag for the calibrating SNe Ia.

We have thus identified the net difference of 0.36 mag (if we add all the differences identified in this section) in the calibration of the absolute magnitudes of the SNe Ia between our own work, and that of Freedman et al. This is the difference required to explain the discrepancy of their value of $H_0 = 71$ versus ours of $H_0 = 60$. We have argued why our own approach is the more appropriate one.

Acknowledgements

I would like to express my heartfelt thanks to the organizers of this meeting. One of the most interesting issues arising in this and several other presentations at this meeting concerns the question of the universality of the Cepheid P-L relation. It is particularly appropriate that this issue should surface so prominently at this meeting organized by Alloin and Gieren, since Gieren and his collaborators were among the first to see the steeper slope of the Galactic P-L relation.

References

1. M.M. Phillips: ApJL **413**, L105 (1993)
2. D. Branch, A. Fisher, P. Nugent: AJ **106**, 2383 (1993)
3. B.R. Parodi, A. Saha, A. Sandage, G. A. Tammann: ApJ **540**, 634 (2000)
4. A. Saha, A. Sandage, G.A. Tammann, A.E. Dolphin, J. Christensen, N. Panagia, F.D. Macchetto: ApJ **550**, 554 (2001)
5. L. Labhardt, A. Sandage, G.A. Tammann: A&A **322**, 751L (1997)
6. B.F. Madore, W.L. Freedman: PASP **103**, 933 (1991)
7. A. Saha, A. Sandage, L. Labhardt, G.A. Tammann, N. Panagia, F.D. Macchetto: ApJ **466**, 55 (1996)
8. A. Saha, A. Sandage, L. Labhardt, H. Schwengeler, G.A. Tammann, N. Panagia, F.D. Macchetto: ApJ **438**, 8 (1995)
9. W.L. Freedman et al.: ApJ **553**, 47 (2001)
10. B.K. Gibson et al.: ApJ **529**, 723 (2000)
11. A. Udalski et al.: Acta Astron. **49**, 201 (1999)
12. G.A. Tammann, A. Sandage, B. Reindl: A&A in press (2003)
13. L.N. Berdnikov, O.V. Oziakova, M.A. Ibragimov: IBVS **4141**, 1 (2000)
14. J.D. Fernie, B. Beattie, N.R. Evans, S. Seager: IBVS **4148** (1995)
15. M.W. Feast: PASP **111**, 775 (1999)
16. W.P. Gieren, P. Fouqué, M. Gomez: ApJ **496**, 17 (1998)

5 RR Lyrae Distance Scale: Theory and Observations

Giuseppe Bono

INAF – Rome Astronomical Observatory, Via Frascati 33, 00040 Monte Porzio Catone, Italy

Abstract. The RR Lyrae distance scale is reviewed. In particular, we discuss theoretical and empirical methods currently adopted in the literature. Moreover, we also outline pros and cons of optical and near-infrared mean magnitudes to overcome some of the problems currently affecting RR Lyrae distances. The importance of the K-band Period-Luminosity-Metallicity (PLZ_K) relation for RR Lyrae is also discussed, together with the absolute calibration of the zero-point. We also mention some preliminary results based on NIR (J,K) time series data of the LMC cluster Reticulum. This cluster hosts a sizable sample of RR Lyrae and its distance is found to be 18.45 ± 0.04 mag using the predicted PLZ_K relation and 18.51 ± 0.06 using the PLZ_J relation. We briefly discuss the evolutionary status of Anomalous Cepheids and their possible use as distance indicators. Finally, we point out some possibilities to improve the intrinsic accuracy of theory and observations.

5.1 Introduction

During the last half a century RR Lyrae stars have been the crossroad of paramount theoretical and observational efforts. The reasons are manifold. From a theoretical point of view RR Lyrae play a crucial role because they are a fundamental laboratory not only to test the accuracy of evolutionary (Cassisi et al. [34] Brown et al. [21]; VandenBerg & Bell [91]) and pulsation (Bono & Stellingwerf [19]; Bono et al. [10]; Feuchtinger [52]) models but also to constrain fundamental physics problems such as the neutrino magnetic moment (Castellani & Degl'Innocenti [41]).

From an observational point of view RR Lyrae are even more important since they are the most popular primary distance indicators for old, low-mass stars (see e.g. Smith [84]; Caputo [24]; Walker [95,93]; Carretta et al. [32]; Walker, this volume; Cacciari & Clementini, this volume). Dating back to Baade [2,3], RR Lyrae stars have been also adopted to trace the old stellar component in the Galaxy (Suntzeff et al. [88]; Layden [62]) and in nearby galaxies (Mateo [68]; Monelli et al. [72]). The use of RR Lyrae as stellar tracers received during the last few years a new spin. On the basis of time-series data, recent photometric surveys identified a local overdensity of RR Lyrae stars in the Galactic halo (Vivas et al. [92]). Current empirical (Yanny et al. [96]; Ibata et al. [58]; Martinez-Delgado et al. [66]) and theoretical (Helmi [56], and references therein) evidence suggests that such a clump is the northern tidal stream left over by the Sagittarius dwarf spheroidal (dSph).

G. Bono, RR Lyrae Distance Scale: Theory and Observationss, Lect. Notes Phys. **635**, 85–104 (2003)
http://www.springerlink.com/

This notwithstanding, several empirical phenomena connected with the evolutionary and pulsation properties of RR Lyrae stars have not been settled yet. We still do not know the physical mechanisms that govern the occurrence of the *Blazhko effect* (Kolenberg et al. [59]; Smith et al. [85]) as well as of the mixed-mode behavior (Bono et al. [9]; Feuchtinger [51]). The same outcome applies for the formation and propagation of the shock front along the pulsation cycle (Bono et al. [15]; Chadid et al. [42]).

However, the lack of a detailed knowledge of the physical phenomena that take place in the interior, in the envelope, and in the atmosphere of RR Lyrae stars only partially hampers the use of these objects as standard candles. In the following we discuss pros and cons in using different theoretical and empirical relations to derive RR Lyrae distances. In particular, we will focus our attention on optical and near-infrared (NIR) data for field and cluster RR Lyrae. Finally, we briefly outline the current status of RR Lyrae and classical Cepheid distance scales.

5.2 Theoretical and Empirical Circumstantial Evidence

At present, the most popular approach to estimate the RR Lyrae distances is the M_V-[Fe/H] relation. This relation is widely adopted because it only requires two observables, namely the apparent visual magnitude and the metallicity. From a theoretical point of view it is also well-defined, because the RR Lyrae instability strip is located in a region of the Horizontal Branch (HB) that is quite flat. In spite of these straightforward positive features the absolute calibration of the M_V-[Fe/H] relation is still an open problem. Current theoretical and empirical calibrations provide difference in absolute distances that range from 0.1 to 0.25 mag (Bono et al. [12]). Oddly enough, the internal errors are quite often of the order of a few hundredths of magnitude. This indicates that current methods might be affected by deceptive systematic errors. The main problems affecting the M_V-[Fe/H] relation are the following:

i) Evolutionary Effects. The use of the M_V-[Fe/H] relation relies on the assumption that RR Lyrae stars are on the Zero-Age-Horizontal-Branch (ZAHB). This is on average a plausible but thorny assumption, since field and cluster RR Lyrae do show a spread in luminosity. Moreover, theoretical (Bono et al. [16]; Cassisi & Salaris [35]) and empirical (Carney, Storm, & Jones [29]; Sandage [82]) evidence suggest that the intrinsic width in luminosity of the ZAHB becomes larger when moving from metal-poor to metal-rich Galactic Globular Clusters (GGCs). As a consequence, RR Lyrae samples at different metal contents are differentially affected by off-ZAHB evolution as well as by the HB morphology (Caputo [24], and references therein). Moreover, a spread in luminosity of the order of ± 0.1 dex causes a spread in the visual magnitude of the order of ± 0.25 mag (see Fig. 1 in Bono et al. [12]). To investigate in more detail this effect we estimated, using the atmosphere models provided by Castelli, Gratton, & Ku-

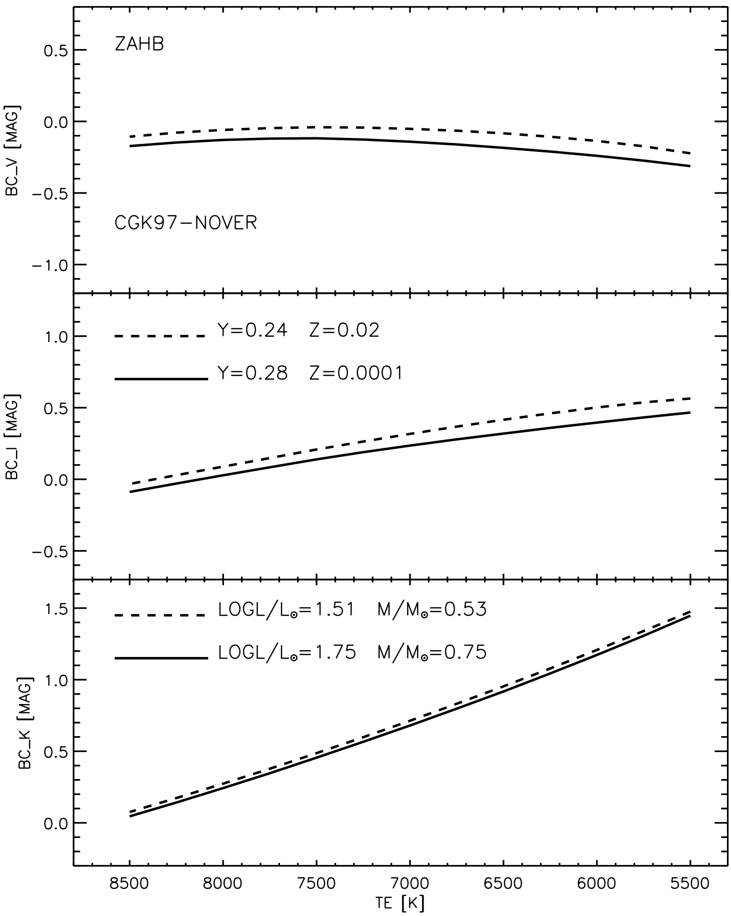

Fig. 5.1. *Top:* predicted bolometric correction in the visual band as a function of the effective temperature. The *solid line* shows the change of BC_V along the ZAHB for very metal-poor RR Lyrae stars (Z=0.0001), while the *dashed line* is for metal-rich ones (Z=0.02). The BC_V values were estimated using the atmosphere models with no overshooting (NOVER) provided by CGK97. *Middle:* same as top, but the bolometric corrections refer to the I-band. *Bottom:* same as top, but the bolometric corrections refer to the K-band

rucz [38,39][1], the bolometric correction in the V-band for two different ZAHBs that cover the metallicity range typical of Galactic RR Lyrae. According to current evolutionary predictions we adopted $\log L/L_\odot = 1.75$, $M/M_\odot = 0.75$ for Z=0.0001 and $\log L/L_\odot = 1.51$, $M/M_\odot = 0.55$ for Z=0.02. Data plotted in the top panel of Fig. 5.1 show that spread in luminosity is mainly due to the change

[1] The models labeled *NOVER* were constructed by adopting a canonical treatment for the mixing-length, i.e. the convective overshooting into the convective stable regions is neglected.

in the bolometric correction. When moving from the hot (blue) to the cool (red) edge of the instability strip BC_V undergoes a changes of the order of 0.1 mag[2]. Therefore, RR Lyrae stars with exactly the same stellar mass and luminosity but different effective temperatures (pulsation periods) present an intrinsic spread in the visual magnitude of approximately a tenth of a magnitude. Data plotted in the top panel are also suggesting that the ZAHB luminosity, at fixed bolometric magnitude, tilts when moving toward hotter effective temperatures (Brocato et al. [20]).

This trend presents a substantial change when moving toward longer wavelengths, and indeed the bolometric correction in the I-band provides for the same ZAHBs a change of the order of 0.3-0.4 mag. This means that GGCs characterized by well-populated instability strips start to display a slope when moving from hotter to cooler objects. Therefore, cluster RR Lyrae stars with the same stellar mass and luminosity become systematically brighter when moving from shorter to longer periods. It turns out that RR Lyrae in the I-band start to obey a Period-Luminosity (PL) relation. This effect become more and more evident once we move from the I to the K-band, and indeed the bolometric correction increases by more than one magnitude when moving from the blue to the red edge of the instability strip. Therefore, RR Lyrae stars should show a well-defined PL relation in the K-band. This result strongly supports the seminal empirical finding brought forward by Longmore et al. [65] concerning the occurrence of the K-band PL relation among cluster RR Lyrae. Moreover, the PL_K should also be marginally affected by the intrinsic spread in luminosity, since a mild decrease in the effective temperature (increase in the period) causes a strict increase in brightness, and in turn a decrease in M_K. It is worth mentioning that in performing this test we adopted the same evolutionary predictions (bolometric magnitudes and effective temperatures) and that the change from the V to the K-band is mainly due to the bolometric corrections and the color-temperature relations predicted by atmosphere models. Finally we note that RR Lyrae M_K magnitudes, in contrast with M_V magnitudes, are also marginally affected by a spread in stellar mass inside the instability strip (see Fig. 2 in Bono et al. [12]).

ii) Linearity. Recent theoretical and empirical evidence indicates that the M_V-[Fe/H] relation is not linear when moving from metal-poor to metal-rich RR Lyrae (Castellani, Chieffi, Pulone [40]; Caputo et al. [25]; Layden [63]). In particular, the slope appears to be quite shallow in the metal-poor regime (0.18 for $[Fe/H] \leq -1.6$) while it is quite steep in the metal-rich regime (0.35 for $[Fe/H] > -1.6$). However, recent photometric and spectroscopic measurements of RR Lyrae stars in the Large Magellanic Cloud (LMC) do not show evidence of a change in the slope at $[Fe/H] \approx -1.5$ (Clementini et al. [44]). The change in the slope, if confirmed by new and independent estimates, means that metal abundance might also introduce a systematic uncertainty when moving from metal-poor to metal-rich RR Lyrae. In fact, an uncertainty of ± 0.2 dex in metallicity implies an uncertainty in visual magnitude that ranges from 0.04 to 0.07

[2] Note that we assumed a range in temperature of more than 3,000 K to account for the temperature variation along the pulsation cycle.

mag. Note that such an uncertainty would affect not only the slope but also the zero-point of the M_V-[Fe/H] relation. On the other hand, data plotted in the bottom panel of Fig. 5.1 and in Fig. 3 by Bono et al. [12], together with K-band observational data (Longmore et al. [65]) suggest that the PL_K presents a linear dependence on the metal content.

iii) Reddening. It is well-known that an uncertainty in the reddening, E(B-V), of 0.01 mag implies an uncertainty of the order of 0.03 mag in the visual magnitude. The same error in the reddening causes an uncertainty that is a factor of two smaller in the I-band, and negligible in the K-band (Cardelli et al. [27]). Moreover, new empirical optical (B-V, V-I) relations based on cluster (Kovacs & Walker [60]) and field (Piersimoni, Bono, & Ripepi [75]) fundamental mode RR Lyrae stars might supply accurate individual reddening estimates. Interestingly enough, these relations rely on reddening free parameters, such as period, luminosity amplitude, and metallicity and present a small intrinsic dispersion.

iv) Mean Magnitudes. The mean magnitude of RR Lyrae stars is estimated as time average either in magnitude or in intensity along the pulsation cycle. However, current theoretical (Bono, Caputo, & Stellingwerf [14]; Marconi et al. [67]) and empirical (Corwin & Carney [45]) evidence suggest that the two mean magnitudes present a systematic difference with the mean "static" magnitude of equivalent nonpulsating stars. The discrepancy for fundamental RR Lyrae stars (*RRab*) increases from a few hundredths of a magnitude close to the red edge to ≈ 0.1 mag close to the blue edge. This discrepancy becomes marginal in the K-band, since the luminosity amplitude becomes a factor of ≈ 3 smaller than in the V-band.

v) Metallicity. Recent spectroscopic investigations based on high-resolution spectra collected with 8m-class telescopes disclosed that hot HB stars present a quite complicate pattern of both helium and heavy element abundances (Behr et al. [4]; Moehler et al. [70]). These peculiarities have also been identified as jumps along the ZAHB in the near ultraviolet bands (Grundhal et al. [54]; Momanhy et al. [71]). According to current beliefs these peculiar abundances are the balance between two competing effects, namely gravitational settling and radiative levitation (Michaud, Vauclair, & Vauclair [69]). Up to now high resolution spectra are available only for a few field RR Lyrae (Clementini et al. [43]), and therefore we do not know whether cluster RR Lyrae present the same chemical peculiarities. Moreover, the metallicity of cluster RR Lyrae is generally estimated using the ΔS method or the *hk* index (Anthony-Twarog et al. [1]; Rey et al. [79]) but both of them are based on the Ca abundance, that is an $\alpha - element$. The empirical scenario was further jazzed up by the evidence that the stellar rotation shows a bimodal distribution in the hot region of the HB (Recio-Blanco et al. [77]). On the other hand, current empirical evidence indicates that RR Lyrae stars do not rotate rapidly enough for the rotation to be detected (Peterson, Carney, & Latham [74]).

Together with this, there is the indisputable fact that we are still facing the problem of the metallicity scale. In fact, the Zinn & West [97] and the Carretta

& Gratton [31] scales show in the intermediate metallicity range a difference of the order of 0.2 dex (Rutledge, Hesser, & Stetson [80]; Kraft & Ivans [61]). Note that the zero-point of the M_V-[Fe/H] relation is generally estimated at [Fe/H]=-1.5, and therefore current uncertainties on the metallicity scale might introduce an error of the order of 0.04 mag(!). Finally, we mention that we still lack a detailed knowledge of $\alpha - element$ abundances among cluster RR Lyrae stars. This parameter is crucial to estimate the global metallicity, i.e. the metallicity currently adopted in constructing both evolutionary and pulsation models (Salaris, Chieffi, & Straniero [81]; Zoccali et al. [98]). According to current empirical evidence the overabundance of $\alpha - elements$ should decrease when moving from metal-poor to metal-rich stars (Carney [28]), but current spectroscopic data for RR Lyrae stars are scanty.

Obviously the abundance of $\alpha - elements$ also affects atmosphere models, and in turn the BCs and the color-temperature (CT) relations. We performed a test using the $\alpha - enhanced$ atmosphere models recently constructed by Castelli et al. (2003[3]) assuming an α over iron enhancement of $[\alpha/Fe] \approx 0.4$. We found that at fixed iron abundance $(-2.0 \leq [Fe/H] \leq -1)$ the difference in BCs and in CTs, for surface gravities ($\log g = 2.5 - 3.0$) and effective temperatures ($5300 \leq T_e \leq 8300$ K) typical of RR Lyrae stars, between solar-scaled and $\alpha - enhanced$ models is small and of the order of a few hundredths of magnitude.

vi) Microturbulent Velocity. Theoretical and empirical evidence suggests that the microturbulent velocity (ξ) in the atmosphere of RR Lyrae stars ranges from a few km/s to more than 10 km/s along the pulsation cycle and peaks close to the phases of maximum compression (Benz & Stellingwerf [6]; Cacciari et al. [22]; Fokin, Gillet, & Chadid [53]). The sample of RR Lyrae for which this information is available is quite limited; however, current data seem to indicate that the microturbulent velocity is larger than 5 km/s for a substantial fraction of the pulsation period.

On the other hand, current atmosphere models are constructed by adopting a microturbulent velocity of 2 km/s, since this is a typical value for static stars. As a consequence, evolutionary and pulsation predictions when transformed into the observational plane might be affected by a systematic uncertainty. Therefore we decided to investigate the dependence of both BCs and CTs on this fundamental parameter. Figure 5.2 shows the variation of BCs, at fixed surface gravity ($\log g = 2.5$), for two sets of $\alpha - enhanced$ atmosphere models constructed by adopting different iron abundances and microturbulent velocities (see labeled values)[4]. Data plotted in the top panel show quite clearly that BC_V values of metal-poor models are marginally affected by this parameter inside the instability strip, while the metal-rich ones present a difference of the order of a few hundredths of magnitude. The same outcome applies for the BC_Is. Once again the BC in the

[3] These models as well as the Castelli et al. [38] models are available at the following web site `http://kurucz.harvard.edu`

[4] Current models are also available in the Kurucz web site. Note that for [Fe/H]=-2.0 we adopted $\xi = 1$ and 4 km/s, because $\alpha - enhanced$ atmosphere models for $\xi = 0$ are not available yet.

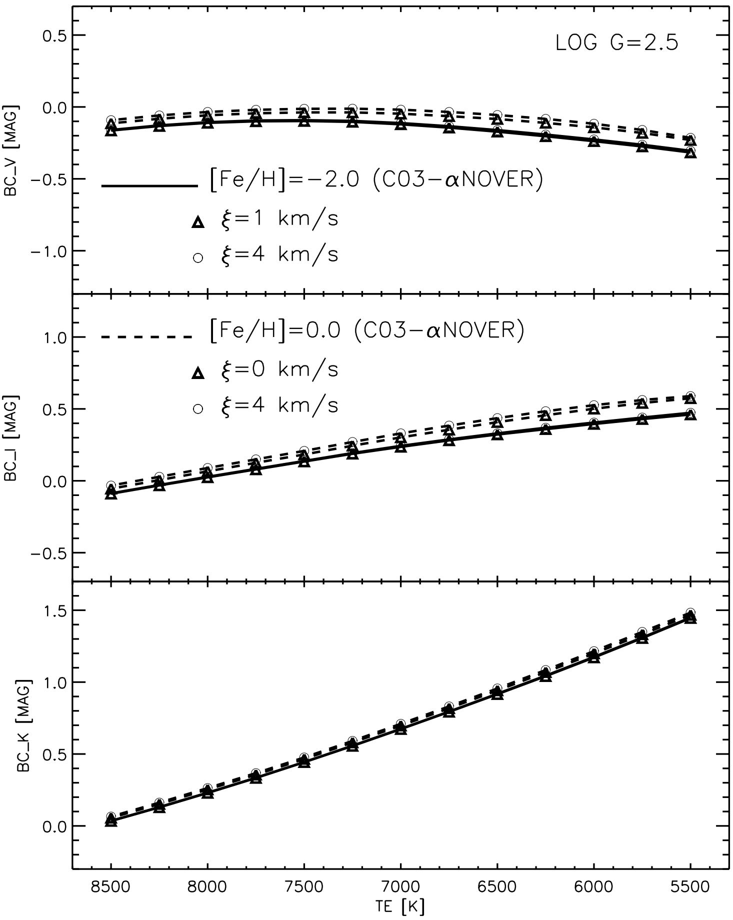

Fig. 5.2. *Top:* predicted bolometric correction in the visual band as a function of the effective temperature. The *solid* and the *dashed lines* display the change of BC_V at fixed gravity ($\log g = 2.5$) for metal-poor ([Fe/H]=-2.0) and metal-rich ([Fe/H]=0.0) RR Lyrae stars. The atmosphere models (C03) adopted to estimate the BC_V values were constructed by adopting an overabundance of α-elements of $[\alpha/Fe] = 0.4$ and different assumptions for the microturbulent velocity (see labeled values). *Middle:* same as the top, but the bolometric corrections refer to the I-band. *Bottom:* same as the top, but the bolometric corrections refer to the K-band

K band shows marginal changes both in the metal-poor and in the metal-rich regime.

Let us now investigate the dependence of the CT relations on the microturbulent velocity. The top panel of Fig. 5.3 shows the B-V color as a function of the effective temperature for the same grid of atmosphere models adopted in Fig. 5.2. Metal-poor B-V colors present a marginal dependence on ξ inside the instability strip. On the other hand, the models at solar chemical composi-

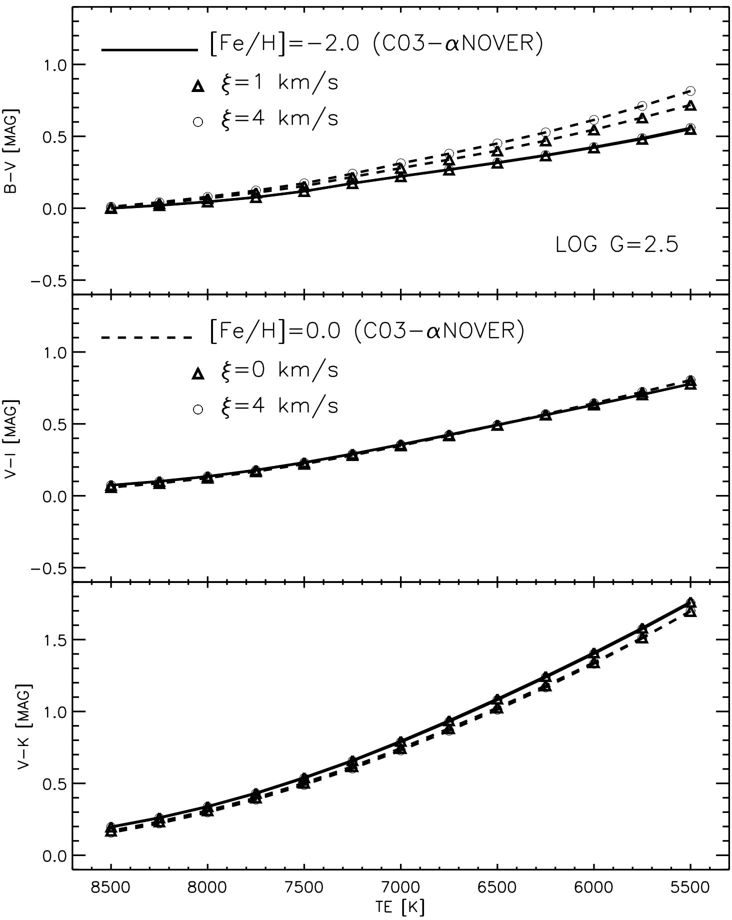

Fig. 5.3. *Top:* same as Fig. 1, but for the B-V color. *Middle:* same as the top, but for the V-I color. *Bottom:* same as the top, but for the V-K color

tion show that the difference between the models with $\xi = 0$ and $\xi = 4$ km/s strictly increases when moving from hotter to cooler effective temperatures. The difference, close to the red edge of the instability strip, becomes of the order of a tenth of magnitude (!). Interestingly enough, the V-I colors (middle panel) do not show any dependence at all on the metal abundance as well as on the microturbulent velocity, thus suggesting that in the V and the I-band the two effects cancel out. Finally, the V-K colors (bottom panel) show a mild *reversed* (Bono et al. [12]) dependence on metal abundance and a marginal dependence on the microturbulent velocity. In this context it is worth mentioning that Cacciari et al. [23] have recently revised the zero-point of the Baade-Wesselink (BW) method using a new set of atmosphere models that partially overlaps with the atmosphere models currently adopted. Using the entire set of photometric and spectroscopic data available in the literature for two field RR Lyrae they found that the absolute magnitude of RR Cet ([Fe/H]=−1.45) is ≈ 0.12 mag brighter than previously estimated. However, they did not find any significant change between old and new estimates for SW And ([Fe/H]=−0.24).

In this section we discussed some possible uncertainties affecting the RR Lyrae distance scale. It is worth mentioning that several of them might affect both theory and observations, therefore it is quite difficult to estimate the global error budget on a quantitative basis. However, it turns out that sets of atmosphere models, constructed by adopting different physical assumptions, predict BCs that might differ by a few hundredths of magnitude. The impact on the B-V colors is larger and of the order of 0.1 mag.

5.3 New Theoretical Approach

The circumstantial evidence discussed in the previous section suggested that the K-band PL relation of RR Lyrae should present several advantages when compared with the other methods currently adopted in the literature. Moreover, and even more importantly, Longmore et al. [65] demonstrated, on the basis of K-band photometry for a good sample of GGCs, that cluster RR Lyrae do obey a well-defined PL relation. Therefore, we decided to investigate whether nonlinear, time-dependent convective models of RR Lyrae (Bono & Stellingwerf [19]) support this empirical scenario. To cover the metal abundances typical of Galactic RR Lyrae we computed several sequences of models ranging from Y=0.24, Z=0.0001 to Y=0.28, Z=0.02. For each given chemical composition we adopted a single mass-value and 2-3 different luminosity levels to account for off-ZAHB evolution and for possible uncertainties on the ZAHB luminosity predicted by current evolutionary models. The main advantage in adopting this approach is that the edges of the instability region can be consistently estimated. Even though current predictions depend on the adopted mixing-length parameter, they do not rely on *ad hoc* assumptions concerning the position of the red edge (Bono et al. [18]).

We found that RR Lyrae models do obey to a well-defined PLZ_K relation:

$$M_K = 0.139 - 2.071(\log P + 0.30) + 0.167 \log Z \tag{5.1}$$

with an intrinsic dispersion of 0.037 mag. The symbols have their usual meaning. On the basis of this relation and of K-band data for RR Lyrae stars in M3 collected by Longmore et al. [65] we found for this cluster a true distance modulus of 15.07 ± 0.07 mag. This estimate is in very good agreement with the distance provided by Longmore et al., i.e. $DM = 15.00 \pm 0.04 \pm 0.15$ mag, where the former error refers to uncertainties in the zero-point, while the latter in the slope of the PL relation. It is noteworthy that the quoted distances are also in good agreement with the M3 distance based on the First Overtone Blue Edge (FOBE) method developed by Caputo et al. [25]. This method is based on the comparison between the predicted first overtone blue edge and the location of *RRc* variables in the $\log P$ vs M_V plane. The accuracy of this method depends on the number of *RRc* variables present in a given stellar system and seems to provide accurate distances for GCs characterized by well-populated instability strips. In the case of M3 they found $DM = 15.00 \pm 0.07$ mag.

Although the PLZ_K relation for RR Lyrae presents several indisputable advantages, when compared with other methods available in the literature, we still lack accurate measurements of mean K-band magnitude for cluster RR Lyrae. Therefore, the comparison with empirical PL relations did not allow us to constrain the intrinsic accuracy of our predictions. Fortunately enough, Benedict et al. [5] provided an accurate estimate of the trigonometric parallax of RR Lyr itself using FGS3, the interferometer on board of the Hubble Space Telescope (HST). Note that the new estimate, $\pi_{abs} = 3.82 \pm = 0.20$ mas, is approximately a factor of three more accurate than the previous evaluation provided by *Hipparcos*, i.e. $\pi_{abs} = 4.38 \pm = 0.59$ mas. Therefore, we investigated whether the theoretical framework we developed accounts for this accurate absolute distance. By adopting for RR Lyr a mean interstellar extinction of $< A_V >= 0.12 \pm 0.1$ (Benedict et al. [5]), an iron abundance of [Fe/H]=-1.39 ($Z \approx 0.0008$, Fernley et al. [49]; Clementini et al. [43]), a mean K magnitude $K = 6.54 \pm 0.04$ mag (Fernley, Skillen, & Burki [50]), and a period of $\log P = -0.2466$ (Hardie [55]) we found a pulsation parallax of $\pi_{abs} = 3.858 \pm = 0.131$ mas. The absolute distance we obtained agrees quite well with the new parallax for RR Lyr provided by HST. This result, once confirmed by new and accurate geometrical distances, emphasizes the potential of the PLZ_K in view of a new NIR RR Lyrae distance scale.

5.4 New Observational Approach

We already mentioned that accurate mean K-band magnitudes are only available for a limited sample of cluster RR Lyrae (Liu & Janes [64]; Longmore et al. [65]; Storm et al. [86,87]). These data are not very accurate, since NIR photometry with small format detectors was partially hampered by crowding. A few K-band measurements have also been collected by Carney et al. [30] for RR Lyrae stars in the Galactic bulge. However, field RR Lyrae whose distances were estimated using the BW method (26 *RRab* plus 3 RR Lyrae pulsating in the first overtones, *RRc*) have mean K-magnitudes with an accuracy of the order of a few hundredths of magnitude. A preliminary comparison between distances based on the BW method and on the PLZ_K relation discloses a systematic difference that decreases when moving from metal-poor to metal-rich objects (Bono et al. [11]). It is worth mentioning that this discrepancy between the two different methods is substantially reduced once we adopt the new calibration of the BW method provided by Cacciari et al. [23].

It goes without saying that new and accurate mean K-band magnitudes for cluster RR Lyrae are mandatory to improve current theoretical and empirical scenarios. Therefore, we decided to start a new observational project aimed at collecting J and K band data in a dozen Galactic and Magellanic Cloud clusters. Figures 5.4 and 5.5 show the K,V-K and the J,V-J Color-Magnitude Diagram of the LMC cluster Reticulum. We selected this cluster because it contains a sizable

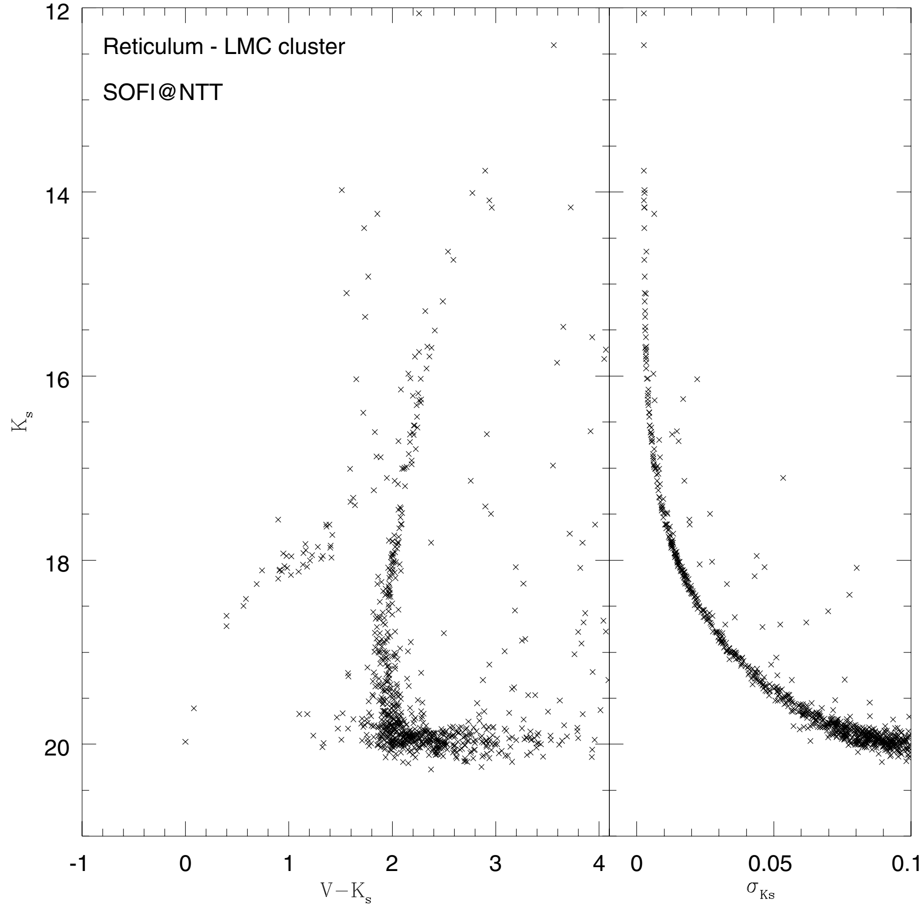

Fig. 5.4. *Left:* Color magnitude diagram of the LMC cluster Reticulum in K,V-K. Data were collected over three different observing runs with SOFI@NTT and reduced using DAOPHOT/ALLFRAME. A glance at the data shows that RR Lyrae stars in this cluster present a well-defined slope. *Right:* intrinsic photometric error. The strategy adopted to perform the photometry allowed us to reach a K-band limiting magnitude of 19.5 with an accuracy better than 0.05 mag

sample of RR Lyrae (32) and it is characterized by a very low central density. Moreover, accurate periods for the entire sample are available in the literature (Walker [94]).

Optical (UBVI) data were collected using SUSI2 at ESO/NTT, the NIR ones with SOFI at ESO/NTT and cover a time interval of three years. In summary, we collected approximately 170 phase points in the K-band and roughly 50 phase points in the J-band. The individual exposure times range from 1 to 2 minutes in the K-band and from 20 s to 1 minute in the J-band. To improve the accuracy of individual measurements we adopted a new reduction strategy, i.e. we performed

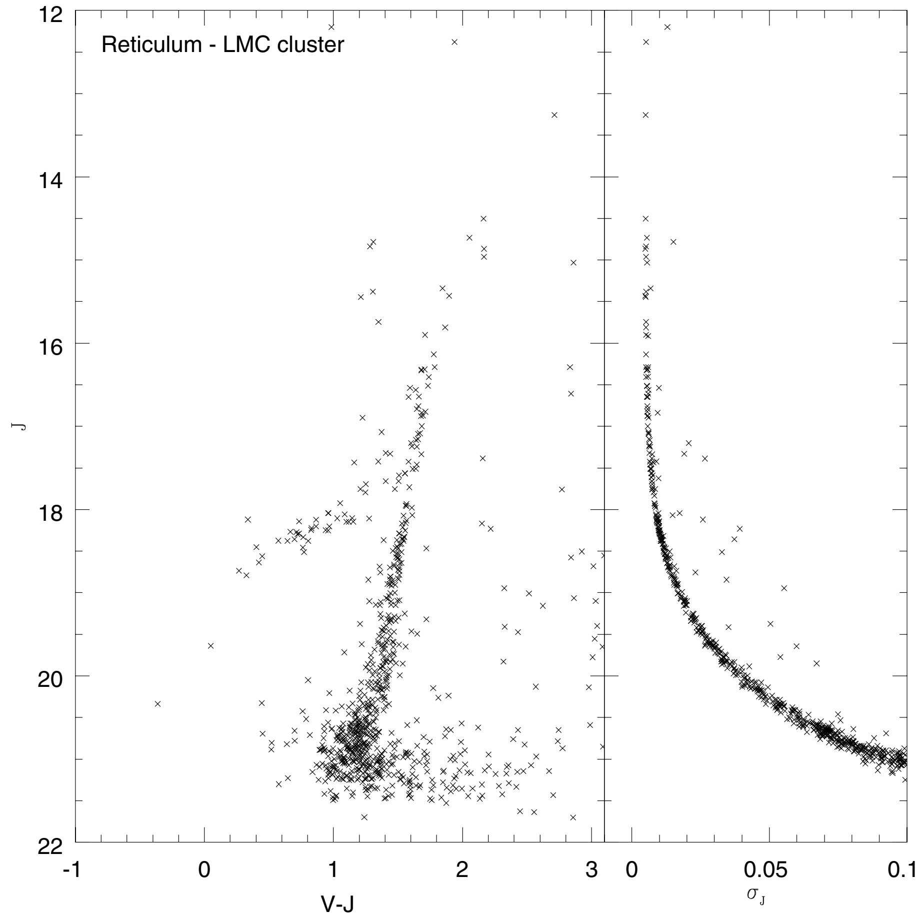

Fig. 5.5. *Left:* same as Fig. 5.4, but the CMD is J,V-J. *Right:* intrinsic photometric error. Note that RR Lyrae stars also show a slope in the J-band but flatter than in the K-band. The strategy adopted to perform the photometry allowed us to reach a J-band limiting magnitude of 20.5 with an accuracy better than 0.05 mag

with DAOPHOT/ALLFRAME the photometry over the entire set of J and K individual exposures.

A glance at the data plotted in Figs. 5.4 and 5.5, and in particular the small color dispersion along the HB and the Red Giant Branch (RGB) show that photometry is very accurate down to limiting magnitudes of $K \approx 19.5$ and $J \approx 20.5$. Moreover and even more importantly RR Lyrae stars show a well-defined slope both in the J and in the K-band.

Using the mean K magnitudes provided by ALLFRAME, a mean metallicity of [Fe/H]=-1.71 based on spectroscopic data (Suntzeff et al. [89]), a mean reddening of E(B-V)=0.02 (Walker [94]), the Cardelli et al. [27] relation, and the PLZ_K relation discussed in Sect. 5.3, we found a true distance modulus of

18.45 ± 0.04 mag, where the uncertainty only accounts for internal photometric errors. Interestingly enough, by adopting the mean J-band magnitude, the same assumptions concerning metallicity and reddening, and a new PLZ_J relation, we found a distance modulus of 18.51 ± 0.06 mag, where the uncertainty only accounts for internal photometric errors.

5.5 Anomalous Cepheids

Anomalous Cepheids are an interesting group of variable stars, since they are brighter than RR Lyrae stars and have periods that range from 0.5 days to a few days. They have been identified booth in GGCs and in LG dwarf galaxies (Nemec, Nemec, & Lutz [73]). Dating back to Demarque & Hirshfeld [47] and to Hirshfeld [57] the common belief concerning the evolutionary status of these objects is that they are metal-poor, intermediate-mass stars with an age of the order of 1 Gyr. This hypothesis was confirmed by more recent evolutionary (Castellani & Degl'Innocenti [37]; Caputo & Degl'Innocenti [26]) and pulsational (Bono et al. [13]) investigations. However, the region of the HR diagram roughly located at $\log L/L_\odot = 2$ presents several intrinsic features worth being discussed in some detail. The top panel of Fig. 5.6 shows the HR diagram for metal-poor, intermediate-mass stars ranging from 2.2 to 3.5 $M/M_\odot$. It is worth mentioning that the minimum mass that performs the blue loop for this composition is $2.2 M/M_\odot$. This mass value is smaller than the corresponding minimum mass for the chemical compositions typical of the Small ($3.25 M/M_\odot$, Z=0.004) and of the Large ($4.25 M/M_\odot$, Z=0.01) Magellanic Cloud (Bono et al. [8]). This means that metal-poor stellar systems such as IC1613 should produce a substantial fraction of short-period classical Cepheids. This suggestion is supported by current empirical evidence (Udalski et al. [90]). Moreover and even more importantly evolutionary tracks plotted in this panel show that the blue loop takes place at hotter effective temperatures when moving from 2.2 to 3.5 $M/M_\odot$. The occurrence of this behavior was explained by Cassisi & Castellani [33] as the consequence of the fact that metal-poor intermediate-mass models do not reach the Hayashi track before central helium ignition. Therefore, these models do not undergo the canonical dredge-up phase. We also note that for evolutionary models more massive than $3.5 M/M_\odot$ the amount of time spent inside the instability strip is substantially shorter (Pietrinferni et al. 2003, in preparation) when compared to more metal-rich models.

Data plotted in the bottom panel of Fig. 5.6 show quite clearly that the structures less massive than 2.2 $M/M_\odot$ show a substantially different behavior, and indeed they start to burn helium in the center at effective temperatures of the order of $\log T_e = 3.9 - 4.0$. The temperature range moves to lower effective temperatures and crosses the instability strip for structures with mass values of the order of 1.4-1.8 $M/M_\odot$. These structures spend a substantial amount of He-burning phases inside the instability strip and should produce Anomalous Cepheids. The central He-burning phases of less-massive structures performs a "hook", i.e. they move at first toward lower effective temperatures (1.0-1.2

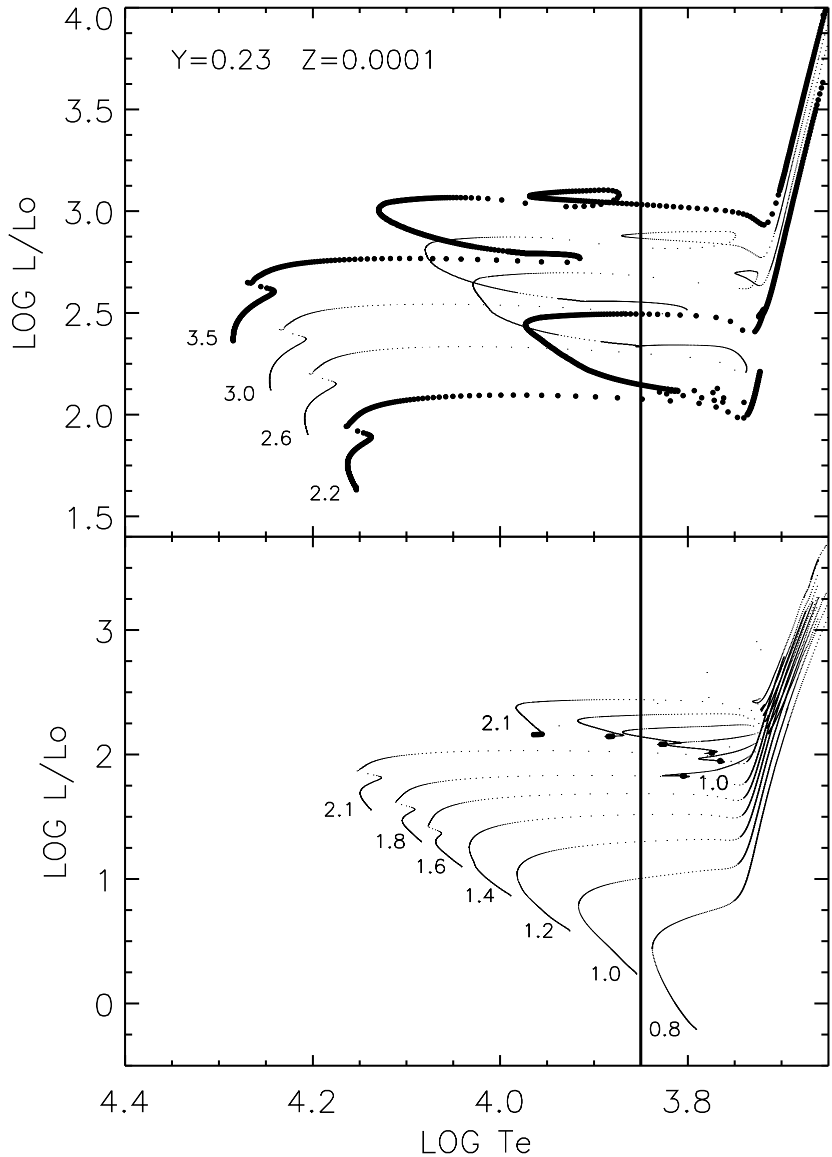

Fig. 5.6. *Top:* HR diagram for intermediate-mass stars at fixed chemical composition (Y=0.23, Z=0.0001). Note that the blue loop when moving from 2.2 $M_{\odot}$ evolutionary models to 3.5 $M_{\odot}$ takes place at hotter effective temperatures. The *vertical line* marks the center of the Cepheid instability strip. The width in temperature of the instability strip is typically ±0.05 dex. *Bottom:* same as the top panel but for low and intermediate-mass stars. *Filled circles* mark the beginning of central He-burning phases for models ranging from 1.0 $M_{\odot}$ to 2.1 $M_{\odot}$. Data plotted in this figure illustrate that central He-burning phases take place inside the instability strip for evolutionary models more massive than 1.4 $M_{\odot}$ and less massive than 1.0 $M_{\odot}$

$M/M_\odot$) and then toward higher effective temperatures (0.9-1.0 $M/M_\odot$). Structures with mass values smaller than the latter limit produce RR Lyrae stars. This is a very qualitative scenario and a more detailed analysis can be found in Castellani & Degl'Innocenti [37]. A few *caveats* concerning the previous observational scenario: *i)* The evolutionary tracks plotted in Fig. 5.6 have been computed by adopting a Reimers mass-loss rate with $\eta = 0.4$. This means that mass values that cross the instability strip slightly depend on this assumption. *ii)* Stellar structures producing Anomalous Cepheids and classical Cepheids show a substantial difference in the age range covered by main sequence stars. In fact, evolutionary models with stellar mass $\approx 1.6 M/M_\odot$ spend on the main sequence a lifetime of roughly 0.7 Gyr, while models of 3.0 $M/M_\odot$ leave the main sequence after approximately 0.2 Gyr. This means that stellar systems producing classical Cepheids should also show a well-populated blue main sequence region when compared with stellar systems producing Anomalous Cepheids. *iii)* Current evolutionary scenarios for Anomalous Cepheids rely on the assumption that they are the aftermath of single star evolution. However, the occurrence of a few Anomalous Cepheids in GGCs suggest that a fraction of them might be the progeny of binary collisions or of binary mergings (Renzini [78]; Nemec et al. [73]; Bono et al. [13]).

The observational scenario concerning Anomalous Cepheids has been substantially improved during the last few years (Siegel & Majewski [83]; Bersier & Wood [7]; Dolphin et al. [48]; Pritzl et al. [76]). Figure 5.7 shows the distribution of both RR Lyrae and Anomalous Cepheids detected by Dall'Ora et al. [46] in the Carina dwarf galaxy. The comparison between theory and observations supports the evolutionary scenario we discussed in this section. In fact, Dall'Ora et al. [46] and Monelli et al. [72] found, on the basis of pulsational and evolutionary arguments that these objects are approximately a factor of two more massive than RR Lyrae stars present in the same galaxy. Note that the metal abundance adopted for this stellar system is Z=0.0004. Interestingly enough, evolutionary predictions also suggest that more metal-rich structures should not produce Anomalous Cepheids, since the so-called "hook" of intermediate-mass helium burning structures do not cross the instability strip.

Theory and observations suggest that Anomalous Cepheids pulsate both in the fundamental and in the first overtone (Nemec, et al. [73]; Bono et al. [13]). However, more data are required to constrain on a quantitative basis the accuracy of distance determinations based on these objects (Pritzl et al. [76]). Obviously LG dwarf galaxies are crucial systems to investigate this problem, since several of them host both RR Lyrae, Anomalous Cepheids, and large samples of red clump stars.

5.6 Conclusions

The results concerning the RR Lyrae distance scale can be summarized along two different paths:

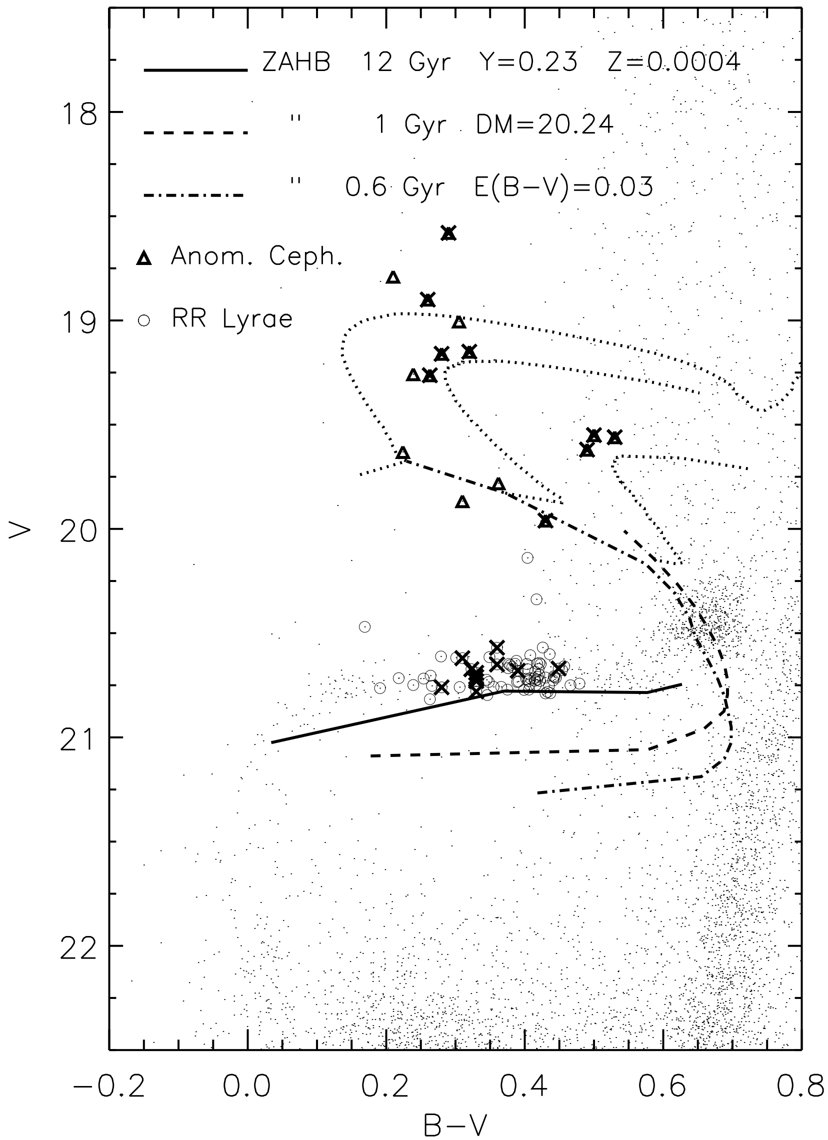

Fig. 5.7. Comparison between predicted He-burning structures at fixed chemical composition (Z = 0.0004, Y = 0.23) and bright stars in the Carina dwarf galaxy (Dall'Ora et al. [46]; Monelli et al. [72]). Data plotted in this figure show static (*small dots*) and variable stars: *circles* RR Lyrae stars, *triangles*, ACs. *Crosses* mark variables that present poor-phase coverage. *Solid, dashed*, and *dotted-dashed lines* display predicted Zero Age He-burning structures for different progenitor ages ranging from 12 ($M = 0.8M_{\odot}$) to 0.6 ($M = 2.2M_{\odot}$) Gyr. The dotted lines show the He-burning evolution for three intermediate-age structures of 1.8 (redder), 2.0, and 2.2 (bluer) $M/M_{\odot}$

Theoretical Path. a) Theoretical predictions based on pulsation models, namely the PLZ_K relation and the FOBE method supply, within current uncertainties, similar absolute distances. The distance to M3 provided by the former method is in very good agreement with the empirical calibration provided by Longmore et al. [65]. Moreover, the pulsation parallax obtained for RR Lyr itself is in remarkable agreement with the trigonometric parallax recently obtained by Benedict et al. [5]. These findings, once confirmed by independent investigations, together with plain physical arguments concerning the dependence of the bolometric correction and of the color-temperature relation on input physics indicate that the PLZ_K might be less affected by deceptive uncertainties affecting the other methods. This approach can be further improved. Up to now theoretical and empirical PLZ_K relations were derived by simultaneously accounting for *RRab* and *RRc* variables. First overtones (FOs) are "fundamentalized" by adding 0.13 to the logarithm of the period. However, preliminary theoretical results suggest that FOs also obey a well-defined PLZ_K relation. The main advantage in using FOs is that the instability region of these objects is narrower when compared with fundamental mode RR Lyrae. Therefore the FO PLZ_K relation presents a smaller intrinsic dispersion.

b) Theoretical predictions based on evolutionary models have been widely discussed in the literature (Bono, Castellani, & Marconi [17]; Cassisi et al. [34]; Caputo et al. [25]). The main outcome of these investigations is that current HB models seem to predict HB luminosities that are ≈ 0.1 mag brighter than estimated using the pulsational approach. However, different sets of HB models constructed by adopting different assumptions on input physics present a spread in HB luminosities of the order of 0.15 mag. This means that in the near future new observational constraints based either on geometrical distances or on robust distance indicators might supply the unique opportunity to nail down the intrinsic accuracy of the ingredients currently adopted in evolutionary and pulsation models.

c) In Sect. 5.2, we mentioned that we still lack homogeneous sets of atmosphere models that cover a broad range of microturbulent velocities. New models are strongly required to check on a quantitative basis the impact that such a parameter has on the transformation of theoretical predictions into the observational plane. The new models might also play a crucial role in understanding the plausibility of the physical assumptions currently adopted by the BW method.

Observational Path. a) Theoretical and empirical evidence suggests that the PLZ_K relation for RR Lyrae presents several advantages when compared with other methods available in the literature. This notwithstanding we still lack accurate K-band measurements for both field and cluster RR Lyrae. The use of current generation NIR detectors at 4m class telescopes and careful reduction strategies seem to suggest that accurate mean K-band magnitudes can be obtained down to $K \approx 18.5 - 19.0$. This means that we should be able to supply an accurate distance scale for Galactic and Large Magellanic cloud clusters. In the near future the use of NIR detectors at 8m class telescopes should allow us to detect and measure RR Lyrae stars in several Local Group galaxies. This is a fundamental step to improve the global accuracy of cosmic distances, because LG galaxies display complex star formation histories, and often host not only RR Lyrae but also intermediate-mass distance indicators, such as Red Clump stars, Anomalous Cepheids, and classical Cepheids.

b) We focused our attention on the mean K-band magnitude of RR Lyrae stars. However, theory and observations suggest that RR Lyrae do obey a PL relation also in the J and the H-bands. Once again the amount of data available in the literature for these bands is quite limited.

Acknowledgements

It is a pleasure to the thank several collaborators with whom I share this intriguing ongoing effort aimed at understanding evolutionary and pulsational properties of radial variables across the HR diagram. Special thanks to S. Cassisi and S. Degl'Innocenti for sending me evolutionary tracks for low and intermediate-mass stars in advance of publication. I am very grateful to V. Castellani, F. Caputo, H.+Smith, and A. Walker for a detailed reading of an early draft of this paper and for many enlightening discussions and suggestions. This work was partially supported by MIUR/Cofin 2001 under the project: "Origin and Evolution of Stellar Populations in the Galactic Spheroid" and by MIUR/Cofin 2002 under the project: "Stellar Population in Local Group Galaxies".

References

1. B.J. Anthony-Twarog, J.N. Laird, D. Payne, B.A. Twarog: AJ, **101**, 1902 (1991)
2. W. Baade: ApJ, **100**, 147 (1944)
3. W. Baade: in Stellar Populations, ed. D.J.K. O'Connell, (Amsterdam: North Holland), 303 (1958)
4. B.B. Behr, J.G. Cohen, J.K. McCarthy, S.G. Djorgovski: ApJ, **5i7**, L135
5. G.F. Benedict, et al.: AJ, **123**, 473
6. W. Benz, R.F. Stellingwerf: ApJ, **297**, 686 (1985)
7. D. Bersier, P.R. Wood: AJ, **123**, 840 (2002)
8. G. Bono, F. Caputo, S. Cassisi, M. Marconi, L. Piersanti, A. Tornambè: ApJ, **543**, 955 (2000)
9. G. Bono, F. Caputo, V. Castellani, M. Marconi: ApJ, **471**, L33 (1996)
10. G. Bono, F. Caputo, V. Castellani, M. Marconi: A&A, **121**, 327 (1997)
11. G. Bono, F. Caputo, V. Castellani, M. Marconi, S. Degl'Innocenti, J. Storm: MNRAS, submitted (2003)
12. G. Bono, F. Caputo, V. Castellani, M. Marconi, J. Storm: MNRAS, **326**, 1183 (2001)
13. G. Bono, F. Caputo, P. Santolamazza, S. Cassisi, A. Piersimoni: 1997, AJ, **113**, 2209
14. G. Bono, F. Caputo, R.F. Stellingwerf: ApJ, **423**, 294 (1994)
15. G. Bono, F. Caputo, R.F. Stellingwerf: ApJ, **432**, L51 (1994)
16. G. Bono, V. Castellani, S. Degl'Innocenti, L. Pulone: A&A, **297**, 115 (1995)
17. G. Bono, V. Castellani, M. Marconi: ApJ, **532**, L129 (2000)
18. G. Bono, M. Marconi, R.F. Stellingwerf: ApJS, **122**, 167 (1999)

19. G. Bono, R.F. Stellingwerf: ApJS, **93**, 233 (1994)
20. E. Brocato, V. Castellani, G. Raimondo, A.R. Walker: ApJ, **527**, 230 (1999)
21. T.M. Brown, A.V. Sweigart, T. Lanz, W.B. Landsman, I. Hubeny: ApJ, **562**, 368 (2001)
22. C. Cacciari, G. Clementini, L. Prevot, R. Buser: A&A, **209**, 141 (1989)
23. C. Cacciari, G. Clementini, F. Castelli, F. Melandri: in IAU Colloq. 185, Radial and Nonradial Pulsations as Probes of Stellar Physics, ed. C. Aerts, T. Bedding, J. Christensen-Dalsgaard (San Francisco: ASP), 176 (2000)
24. F. Caputo: A&AR, **9**, 33 (1998)
25. F. Caputo, V. Castellani, M. Marconi, V. Ripepi: MNRAS, **316**, 819 (2000)
26. F. Caputo, S. Degl'Innocenti: A&A, **298**, 833
27. J.A. Cardelli, G.C. Clayton, J.S. Mathis, ApJ, **345**, 245 (1989)
28. B.W. Carney: PASP, **108**, 900 (1996)
29. B.W. Carney, J. Storm, R.V. Jones: ApJ, **386**, 663 (1992)
30. B.W. Carney, J.P. Fulbright, D.M. Terndrup, N.B. Suntzeff, A.R. Walker: AJ, **110**, 1674 (1995)
31. E. Carretta, R.G. Gratton: A&AS, **121**, 95 (1997)
32. E. Carretta, R.G. Gratton, G. Clementini, F. Fusi Pecci, ApJ, **533**, 215 (2000)
33. S. Cassisi, V. Castellani: ApJS, **88**, 509 (1993)
34. S. Cassisi, V. Castellani, S. Degl'Innocenti, M. Salaris, A. Weiss: A&AS, **134**, 103 (1999)
35. S. Cassisi, M. Salaris: MNRAS, **285**, 593 (1997)
36. V. Castellani: 'Post-Hipparcos cosmic candles', ed. A. Heck, F. Caputo (Kluwer, Dordrecht 1999), 269
37. V. Castellani, S. Degl'Innocenti: A&A, **298**, 827 (1995)
38. F. Castelli, R.G. Gratton, R.L. Kurucz: A&A, **318**, 841
39. F. Castelli, R.G. Gratton, R.L. Kurucz: A&A, **324**, 432
40. V. Castellani, A. Chieffi, L. Pulone: ApJS, **76**, 911 (1991)
41. V. Castellani, S. Degl'Innocenti: ApJ, **402**, 574 (1993)
42. M. Chadid, D. Gillet, A.B. Fokin: A&A, **363**, 568 (2000)
43. G. Clementini, E. Carretta, R.G. Gratton, R. Merighi, J.R. Mould, J.K. McCarthy: AJ, **110**, 2319 (1995)
44. G. Clementini, R. Gratton, A. Bragaglia, E. Carretta, L. Di Fabrizio, M. Maio: AJ, 125, 1309 (2003)
45. T.M. Corwin, B.W. Carney: AJ, **122**, 3183 (2001)
46. M. Dall'Ora, et al.: AJ, accepted, astro-ph/0302418
47. P. Demarque, A.W. Hirshfeld: ApJ, **202**, 346 (1975)
48. A.E. Dolphin, et al.: AJ., **123**, 3154 (2002)
49. J. Fernley, T.G. Barnes, I. Skillen, S.L. Hawley, C.J. Hanley, D.W. Evans, E. Solano, R. Garrido: A&A, **330**, 515 (1998)
50. J. Fernley, I. Skillen, G. Burki: A&AS, **97**, 815 (1993)
51. M.U. Feuchtinger: A&A, **337**, L29 (1998)
52. M.U. Feuchtinger: A&A, **351**, 103 (1999)
53. A.B. Fokin, D. Gillet, M. Chadid: A&A, **344**, 930 (1999)
54. F. Grundahl, M. Catelan, W.B. Landsman, P.B. Stetson, M.I. Andersen: ApJ, **524**, 242 (1999)
55. R.H. Hardie: ApJ, **122**, 256 (1955)
56. A. Helmi: Ap&SS, **281**, 351 (2002)
57. A.W. Hirshfeld: ApJ, **241**, 111 (1980)
58. R. Ibata, M. Irwin, G.F. Lewis, A. Stolte: ApJ, **547**, L133 (2001)

59. K. Kolenberg, C. Aerts, A. Fokin, W. Dziembowski, M. Chadid, D. Gillet: in Interplay of Periodic, Cyclic and Stochastic Variability in Selected Areas of the H-R Diagram, ed. C. Sterken (San Francisco: ASP), 171
60. G. Kovacs, A.R. Walker: A&A, **374**, 264 (2001)
61. R.P. Kraft, I.I. Ivans: PASP, **115**, 143 (2003)
62. A.C. Layden: AJ, **110**, 2288 (1995)
63. A.C. Layden: in IAU Colloq. 185, Radial and Nonradial Pulsations as Probes of Stellar Physics, ed. C. Aerts, T. Bedding, J. Christensen-Dalsgaard (San Francisco: ASP), 118 (2000)
64. T. Liu, K.A. Janes: ApJ, **360**, 561 (1990)
65. A.J. Longmore, R. Dixon, I. Skillen, R.F. Jameson, J.A. Fernley: MNRAS, **247**, 684
66. D. Martinez-Delgado, A. Aparicio, M.A. Gomez-Flechoso, R. Carrera: ApJ, **549**, L199 (2001)
67. M. Marconi, M. Di Criscienzo, F. Caputo: in preparation (2003)
68. M. Mateo: ARA&A, **36**, 435 (1998)
69. G. Michaud, G. Vauclair, S. Vauclair: ApJ, **267**, 256 (1983)
70. S. Moehler, A.V. Sweigart, W.B. Landsman, S. Dreizler: A&A, **395**, 37 (2002)
71. Y. Momany, G. Piotto, A. Recio-Blanco, L.R. Bedin, S. Cassisi, G. Bono: ApJ, **576**, L65 (2002)
72. M. Monelli, et al.: AJ, accepted, astro-ph/0303493
73. J.M. Nemec, A.F. Linnell-Nemec, T.E. Lutz: AJ, **108**, 222 (1994)
74. R.C. Peterson, B.W. Carney, D.W. Latham: ApJ, **465**, L47, (1996)
75. A.M. Piersimoni, G. Bono, V. Ripepi: AJ, **124**, 1528 (2002)
76. B.J. Pritzl, T.E. Armandroff, G.H. Jacoby, G.S. Da Costa: AJ, 124, 1464 (2002)
77. A. Recio-Blanco, G. Piotto, A. Aparicio, A. Renzini: ApJ, 572, L71 (2002)
78. A. Renzini: MemSait, **51**, 749 (1980)
79. S.-C. Rey, Y.-W. Lee, J.-M. Joo, A.R. Walker, S. Baird: AJ, **119**, 1824 (2000)
80. G.A. Rutledge, J.E. Hesser, P.B. Stetson: PASP, **109**, 907 (1997)
81. M. Salaris, A. Chieffi, O. Straniero: ApJ, **414**, 580 (1993)
82. A. Sandage: AJ, **106**, 687 (1993)
83. M.H. Siegel, S.R. Majewski: AJ, 120, 284 (2000)
84. H.A. Smith: 'RR Lyrae Stars', (Cambridge: Cambridge Univ. Press) (1995)
85. H.A. Smith, et al.: PASP, **115**, 43 (2003)
86. J. Storm, B.W. Carney, D.W. Latham, A&A, **290**, 443 (1994)
87. J. Storm, B. Nordström, B.W. Carney, J. Andersen, A&A, 291, 121 (1994)
88. N.B. Suntzeff, T.D. Kinman, R.P. Kraft: ApJ, **367**, 528 (1991)
89. N.B. Suntzeff, R.A. Schommer, E.W. Olszewski, A.R. Walker: AJ, **104**, 1743 (1992)
90. A. Udalski, et al.: AcA, **51**, 221 (2001)
91. D.A. VandenBerg, R.A. Bell: NewAR, **45**, 577 (2001)
92. A.K. Vivas, et al.: ApJ, **554**, L33 (2001)
93. A.R. Walker: in IAU Colloq. 176, The Impact of Large-Scale Surveys on Pulsating Star Research, ed. L. Szabados & D. Kurtz. (San Francisco: ASP), 165 (2000)
94. A.R. Walker: AJ, **103**, 1166 (1992)
95. A.R. Walker: 'Post-Hipparcos cosmic candles', ed. A. Heck, F. Caputo (Kluwer, Dordrecht), 125 (1999)
96. B. Yanny, et al.: ApJ, **540**, 825 (2000)
97. R. Zinn, M.J. West, ApJS, **55**, 45 (1984)
98. M. Zoccali, S. Cassisi, G. Bono, G. Piotto, R.M. Rich, S.G. Djorgovski: ApJ, **538**, 289 (2000)

6 Globular Cluster Distances from RR Lyrae Stars

Carla Cacciari and Gisella Clementini

INAF – Osservatorio Astronomico, 40127 Bologna, Italy

Abstract. The most common methods to derive the distance to globular clusters using RR Lyrae variables are reviewed, with a special attention to those that have experienced significant improvement in the past few years. From the weighted average of these most recent determinations the absolute magnitude of the RR Lyrae stars at $[Fe/H] = -1.5$ is $M_V = 0.59 \pm 0.03$, corresponding to a distance modulus for the LMC $(m - M)_0 = 18.48 \pm 0.05$.

6.1 Introduction

Globular clusters (GC) have traditionally been considered as good tracers of the process that led to the formation of their host galaxy, whether this was a "monolithic" relatively rapid collapse of the primeval gas cloud, as described by [37], or a "hierarchical" capture of smaller fragments on a longer time baseline, as described by [74]. We refer the reader to [44] for a recent review on this issue.

Therefore, knowing the distance to GCs with high accuracy is important in several respects:

- Cluster distances, along with information on the dynamical, kinematic and chemical properties of the clusters, are essential to provide a complete description of the galaxy formation, early evolution and chemical enrichment history.
- Accurate distances are needed in order to derive the age of GCs from the stellar evolution theory, i.e. by comparing the absolute magnitude of the Main-Sequence Turn-off (MS-TO) region in the Color-Magnitude diagram with the corresponding luminosity of theoretical isochrones. The precise knowledge of absolute ages has important cosmological implications (e.g. the age of the Universe), whereas relative ages provide detailed information on the formation process of the host galaxy.
- The Luminosity Function (LF) of a GC system is one of the most powerful candles for extragalactic distance determinations, as it peaks at a rather bright luminosity ($M_V \sim -7.5$), and GCs are numerous in both spiral and elliptical galaxies. An accurate calibration is essential both for testing the assumption of universality of the LF and for deriving its absolute value, hence again the importance of disposing of accurate distances to local GC calibrators.

Distances to GCs can be obtained by several methods that use either the cluster as a whole (direct astrometry) or some "candle" stellar population belonging

C. Cacciari and G. Clementini, Globular Cluster Distances from RR Lyrae Stars, Lect. Notes Phys. **635**, 105–122 (2003)
http://www.springerlink.com/

to the cluster, e.g. Horizontal Branch (HB) and RR Lyrae stars, Main Sequence stars, White Dwarfs, Eclipsing Binaries, the tip of the Red Giant Branch (RGB), the clump along the RGB. In the latter case the distance stems from the determination of the absolute magnitude of the selected "candle", which in turn may depend on a purely theoretical or a (semi)-empirical calibration.

Here we review the distance determinations to GCs using only RR Lyrae (and HB) stars. Distance determinations to GCs using also the other possible methods have been reviewed by [11].

6.2 RR Lyrae Stars as Standard Candles

RR Lyrae stars have been traditionally the most widely used objects for the purpose of distance determination (see [78] for a general review), because they are i) easy to identify thanks to their light variation; ii) luminous giant stars (although less bright than the Cepheids) hence detectable to relatively large distances; iii) typical of old stellar systems that do not contain Population I distance indicators (such as the classical Cepheids), and iv) much more numerous than the Population II Cepheids. But of course the property that qualifies them as *standard candles* is their mean brightness, which has been known to be "nearly constant" in any given globular cluster (within a narrow range of variation) since Bailey's work in early 1900.

However, accurate studies have shown a few decades later that the mean intrinsic brightness of the RR Lyrae stars is not strictly constant: first, it is a (approximately linear) function of metallicity, i.e. $M_V(RR) = \alpha[Fe/H] + \beta$ [70,71] with a variation of $\sim$0.25 mag over 1 dex variation in metallicity; second, even within the same cluster, i.e. at fixed metallicity, there is an intrinsic spread in the HB luminosity due to evolutionary effects, whose extent can vary from $\sim$0.1 to $\sim$0.5 mag as a function of metallicity ([72]); finally, it has recently been shown that the luminosity-metallicity relation is not strictly linear, because it depends also on the HB morphology and stellar population [19,34].

Notwithstanding these aspects that introduce a significant intrinsic variation in the absolute magnitude of the RR Lyrae variables, these stars remain excellent distance indicators once these effects are properly known and taken into account.

As a first approximation, and for the purpose of taking into account small corrections due to metallicity differences, when needed in comparing different results, we assume that the $M_V(RR)$-[Fe/H] relation is linear, with the parameters estimated by [28] as the average of several methods, i.e.

$$M_V(RR) = (0.23 \pm 0.04)[Fe/H] + (0.93 \pm 0.12) \tag{6.1}$$

[11] found the same slope and 0.92 for the zero-point.

We shall now consider the main methods of absolute magnitude determination for RR Lyrae stars, with special attention to those that have experienced a substantial improvement recently. The aim is to estimate the most accurate and reliable value for the β parameter in (6.1), which can then be used to derive the distance to globular clusters and other old stellar systems of known metallicity.

For this purpose also studies dealing with field RR Lyrae stars will be reviewed, on the verified assumption that globular cluster and field RR Lyrae stars share the same characteristics [27,22].

6.2.1 Statistical Parallaxes

This method works by balancing two measurements of the velocity ellipsoid of a given stellar sample, obtained from the stellar radial velocities and from the proper motions plus distances, via a simultaneous solution for a distance scale parameter. The underlying assumption is that the stellar sample can be adequately described by a model of stellar motions in the Galaxy.

[61] provided the most recent review of this method, and summarized the results previously obtained by various groups on field RR Lyraes using slightly different algorithms and assumptions but basically the same sample of stars and very similar input data. From the work of [45] on 147 RR Lyrae stars, which contains a very careful analysis and corrections for all relevant biases, the average magnitude is $M_V(RR) = 0.77 \pm 0.13$ at [Fe/H]=–1.6. A very interesting result is the analytic expression for the relative error in the distance scale parameter reported by [66] (and references therein). They show that for a group of stars with a given velocity dispersion and bulk motion, and with observational errors smaller than the velocity dispersion, the relative error in the distance scale parameter is proportional to $N^{-1/2}$ where N is the number of stars in the sample. For a halo stellar population such as the RR Lyraes, where observational errors in the radial and tangential velocities are typically 20-30 km/s and velocity dispersions are $\sim$ 100 km/s, a more effective way of improving the results is by increasing the number of stars in the sample rather than improving further the quality of the velocity determinations. [45] tried this way by defining the radial velocity ellipsoid using 716 metal-poor non-variable and 149 RR Lyrae stars, and matching it with the distance-dependent ellipsoid derived from the proper motions of the RR Lyraes alone. The result is $M_V(RR) = 0.80 \pm 0.11$ at [Fe/H]=–1.71. The accuracy of this hybrid solution, however, is hardly any better given the bigger chance of thick disk contaminants even at low metallicity. We remind that [4] find that the local fraction of metal-poor stars that might be associated with the Metal Weak Thick Disk (MWTD) is on the order of 30%-40% at abundances below [Fe/H]=–1.0, and a significant fraction of these may extend to metallicities below [Fe/H]=–1.6.

[33] applied this method to a sample of 262 local RR Lyrae variables. They separated “halo” from “thick disk” objects by metallicity ($[Fe/H] < -1.0$) and kinematic criteria, and assumed an initial distance scale $< M_V > (RR) = 1.01 + 0.15[Fe/H]$ (i.e. $M_V = 0.79$ at [Fe/H]=–1.5) to transform proper motions into space velocity components. They then determined $M_V(RR) = 0.76 \pm 0.12$ for the “halo” population at [Fe/H]=–1.6. This result is in agreement with the previous ones from this method. However, the possibility of kinematic inhomogeneities within the “halo” sample is strongly reassessed by [10], who identify two different populations among the metal-poor subset in this sample of stars. These two spherical subsystems would have different dynamical characteristics and origins,

the slowly rotating subsystem being associated to the Galactic thick disk, and the fast rotating (possibly with retrograde motion) subsystem belonging to the accreted outer halo.

It is not quite clear if and to what extent the kinematic selection criteria adopted to separate "halo" and "thick disk" populations introduce a bias in the subsequent kinematic analysis of this method, and the effects on the final result of the adopted distance scale and possible contamination from the MWTD stellar component. It is not impossible that the application of the Statistical Parallax method to the local RR Lyrae stars might need a more detailed and accurate modelling of the stellar motions in the Galaxy, as well as a much larger sample of stars to work on, in order to provide reliable and robust results.

For the purpose of the present review we can summarize the results of the Statistical Parallax method as $< M_V(RR) >= 0.78 \pm 0.12$ mag at [Fe/H]=–1.5.

6.2.2 Trigonometric Parallax for RR Lyr

Trigonometric parallaxes are the most straightforward method of distance determination, being based on geometrical quantities independent of reddening. Only with *Hipparcos* trigonometric parallaxes for a good number of HB and RR Lyrae stars have become available. However, they are not accurate enough for a reliable individual distance determination, except for the nearest star, RR Lyr, for which a relatively high precision estimate of π (4.38±0.59 mas) was derived by *Hipparcos* [65]. A previous ground-based estimate (i.e. 3.0±1.9 mas) was reported in the Yale Parallax Catalog [3].

The new and very important result in this field is the determination of a more accurate parallax for RR Lyr using HST-FGS3 data ($\pi = 3.82 \pm 0.20$ mas) by [5]. This leads to a true distance modulus $\mu_0 = 7.09 \pm 0.11$ mag, or 7.06 ± 0.11 mag if one adopts instead the weighted average of all three parallax determinations $< \pi >= 3.87 \pm 0.19$ mas.

RR Lyr has $< V >= 7.76$ mag and [Fe/H]=–1.39 [29,39]. Depending on whether one assumes $< A_V >= 0.07 \pm 0.03$ mag as the average absorption value from the reference stars surrounding RR Lyr, or $< A_V >= 0.11 \pm 0.10$ mag as the linearly interpolated local value from the same reference stars, one obtains $M_V = 0.61 \pm 0.11$ mag or $M_V = 0.57 \pm 0.15$ mag, respectively.

Following [5] we adopt $M_V = 0.61 \pm 0.11$ mag, which leads to $M_V(RR) = 0.58 \pm 0.13$ at [Fe/H]=–1.5. This final error takes into account also the cosmic scatter in luminosity due to the finite width of the instability strip, by adding in quadrature an adopted value for the cosmic dispersion of 0.07 mag. This effect, which is negligible when many stars are involved, should be taken into account when dealing with individual stars.

6.2.3 Trigonometric Parallaxes for HB Stars

Since, as we discuss in Sect. 6.2.5, RR Lyraes are HB stars, [46] adopted the approach of considering all field metal-poor HB stars with *Hipparcos* values of π in a magnitude limited sample, $V_0 < 9$. This selection criterion led to a sample of 22 stars, of which 10 were HB stars on the blue side of the instability strip, 3 were RR Lyrae stars, and 9 were red HB stars. Using the globular cluster M5 as a template to reproduce the shape of the HB, [46] estimated the correction in M_V to apply to each star in order to report it to the middle of the instability strip, and derived $< M_V >= 0.69 \pm 0.10$ mag at [Fe/H]=–1.41, or $< M_V >= 0.60 \pm 0.12$ mag at [Fe/H]=–1.51 excluding one red HB star suspected of belonging to the red giant population.

A reanalysis of this sample was performed by [66], who eliminated all red HB stars from the sample as a prudent way to ensure that no contamination from the Red Giant Branch (RGB) was present, applied a different weighting procedure by the observational errors, and considered the effect of intrinsic scatter in M_V in the estimate of the Malmquist bias. Their result was $< M_V >= 0.69 \pm 0.15$ at [Fe/H]=–1.62 (but [23] point out that this result may be questionable since the metallicity scale for blue HB stars is not well determined). Finally, [54] using all stars of this sample and taking into account the intrinsic scatter in the HB magnitudes when correcting for the Lutz-Kelker effect, derived $M_V = 0.62$ mag at [Fe/H]=–1.5.

A final reanalysis of this problem was performed by [23] who provided a revised value $< M_V >= 0.62 \pm 0.11$ at [Fe/H]=–1.5.

6.2.4 Baade-Wesselink (B-W)

This method derives the distance of a pulsating star by comparing the linear radius variation, that can be estimated from the radial velocity curve, with the angular radius variation, that can be estimated from the light curve.

It is common belief that the B-W results are “faint”, based on the large amount of work done on field RR Lyrae stars during the past decade by several independent groups, and revised and summarized by [40]:

$$M_V(RR) = (0.20 \pm 0.04)[Fe/H] + (0.98 \pm 0.05) \tag{6.2}$$

hence $M_V(RR) = 0.68$ at [Fe/H]=–1.5.

This method was reapplied by [14] to RR Cet ([Fe/H]=–1.43, average value from [29] and [39]) with the following improvements with respect to the previous analyses:

- Use of various sets of model atmospheres, with and without overshooting treatment of convection, [α/Fe]=+0.4; some experimental models with no convection, that mimic the effects of a different treatment of convection e.g. the [16] approximation, were also tried.
- Use of the detailed variation of gravity with phase, rather than the mean value; the values of log$g$ at each phase step were calculated from the radius percentage variation (assuming $\Delta R / < R > \sim 15\%$) plus the acceleration component derived from the radial velocity curve.
- Use of new semi-empirical calibrations for bolometric corrections, based on the temperature scale for Population II giants defined from RGB and HB stars in several globular clusters using infrared colors [64].

- Use of various assumptions on the γ-velocity, and turbulent velocity = 2km/s and 4km/s over all or part of the pulsation cycle.
- Use of BVRIK photometric data.
- The matching of the linear and angular radius variations was performed on the phase interval $0.25 \leq \phi \leq 0.70$ to avoid shock-perturbed phases.

It was found that i) the use of K magnitudes and V–K colors provided the most reliable and stable results, and ii) all other options produced similar results within 0.03 mag, except the test case that used an unrealistically large amplitude of the γ-velocity curve.

The resulting mean magnitude for RR Cet is $M_V = 0.57 \pm 0.10$ mag, i.e. 0.55 ± 0.12 mag when reported to [Fe/H]=–1.5, and taking into account the cosmic dispersion (see Sect. 6.2.2).

6.2.5 Evolutionary Models of Horizontal Branch Stars

From the evolutionary point of view, RR Lyrae stars are low-mass stars in the stage of core helium burning located in a well defined part of the HB, i.e. the temperature range approximately 5900-7400 K, known as the "instability strip". Therefore theoretical models of HB stars within this temperature interval should in first approximation be able to describe the average properties of RR Lyrae variables, were they not be pulsating.

Theoretical models (hence the HB morphology and luminosity level) depend significantly on assumed input parameters. The strongest dependence besides [Fe/H] is on the helium abundance, but other parameters may have an effect, such as [CNO/Fe], peculiar surface abundances due to mixing during the RGB phase, diffusion or sedimentation, rotation, magnetic field strength, some other yet unknown factor that affects mass loss efficiency, or a combination of any of these, as well as theoretical assumptions such as the equation of state, the treatment of plasma neutrino energy loss, the correct treatment of conductive opacities in RGB stars, the 3-alpha reaction rate, etc. briefly on anything that can affect the ratio total mass vs core mass of the star.

For these reasons several research groups have been actively working on the construction of new HB models trying to include as much improved input physics as possible. Without entering into the details of the individual choices and assumptions, for which we refer the reader to the original papers, we report the results found by six independent groups, namely [35], [15], [25], [41] (based on the work by [79]), [34] (from outer halo globular clusters only), and [82].

We show in Fig. 6.1 how $M_V(HB)$ varies with [Fe/H], where $M_V(HB)$ is the mean absolute V magnitude of an HB star at logT_{eff}=3.85, that is taken to represent the equilibrium characteristics of an RR Lyrae star near the middle of the instability strip.

The original theoretical data usually refer to the Zero Age Horizontal Branch (ZAHB) rather than the average HB (or RR Lyrae) magnitude level. The two quantities $M_V(ZAHB)$ and $M_V(HB)$ are not identical. The stars in this evolutionary phase evolve rapidly away from the ZAHB: less than $\sim 10\%$ of their

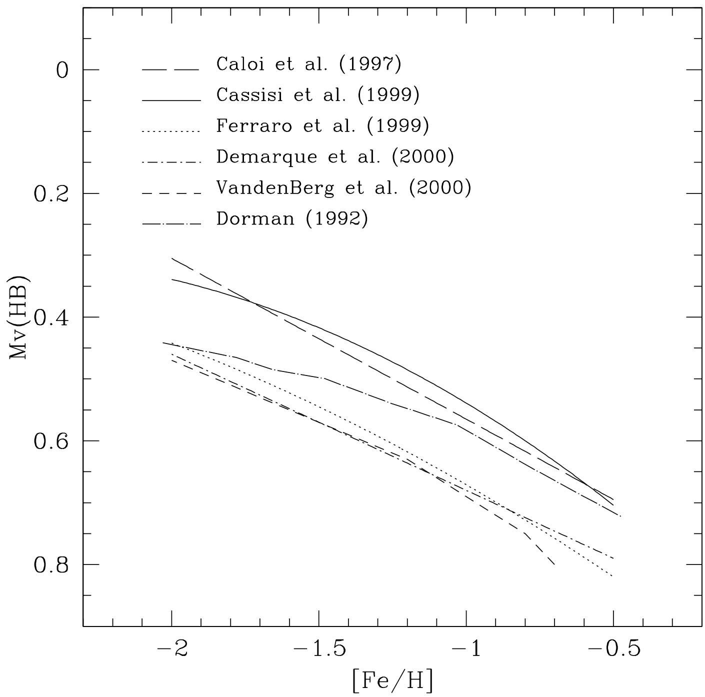

Fig. 6.1. M_V(HB) vs [Fe/H] from various sets of evolutionary models

total HB lifetime is spent on the ZAHB itself, and the remaining time is spent at 0.1-0.2 mag brighter luminosities [41]. This aspect of stellar evolution has been discussed in several papers (see e.g. [17,21,24]).

Therefore the real ZAHB is intrinsically poorly populated, and when a comparison is made with the lower envelope of the observed HBs, which would represent the ZAHB, this is of difficult definition because of the uncertainties due to small sample statistics and photometric errors. So the comparison between HB theoretical models and observed HBs (including RR Lyrae stars) is made at the (brighter) magnitude level where the stars spend most of their HB lifetime. This is usually taken into account by correcting the theoretical $M_V(ZAHB)-[Fe/H]$ relation by a fixed offset (of the order of 0.08-0.10 mag), or by applying an empirical correction that is itself a function of [Fe/H], such as the one derived by [73]:

$$\Delta V(ZAHB - HB) = 0.05[Fe/H] + 0.16 \tag{6.3}$$

For the sake of simplicity we apply a fixed evolutionary correction of –0.08 mag to $M_V(ZAHB)$, which is very close to Sandage's correction near the middle of the metallicity range at [Fe/H]=–1.5.

We can derive a few conclusions from this comparison (see Fig. 6.1):

i) all models agree that the slope of the $M_V(HB) - [Fe/H]$ relation is not unique, i.e. this relation is *not universal* and is *not strictly linear*, as originally suggested by [26]. As a first approximation, however, all models can be roughly described by a linear relation with average slope ~ 0.23, excluding the oldest set of models [35] that are flatter.

ii) As far as the zero-point is concerned, there are two families of results differing by ~ 0.13 mag, i.e. [25] and [15] with $< M_V(HB) >$ =0.43 ± 0.12 at [Fe/H]=–1.5, and [41] ([79]), [34] and [82] with $< M_V(HB) >$ =0.56 ± 0.12. Again, [35] models differ as they fall exactly in between these two estimates.

6.2.6 Pulsation Models for RR Lyrae Stars

Visual Range. New pulsation models have been calculated recently by [19], based on non-linear convective hydrodynamical models with updated opacities and the classical MLT treatment of convection [6]. In combination with HB evolutionary models it is then possible to derive the Period-Luminosity-Metallicity relation for first overtone pulsators (RRc stars) at the blue edge of the instability strip, which in turn allows to estimate the luminosity $< M_V(RR) >$ of the RR Lyrae stars at the reference temperature logT_{eff}=3.85.

The behaviour of $M_V(RR)$ vs. [Fe/H] has been found to vary with the HB morphology and metallicity range, and could possibly be approximated by a quadratic relation. However, for the sake of simplicity this relation can be described by two linear relations that, for [α/Fe]=+0.3, are:

$$M_V(RR) = (0.17 \pm 0.04)[Fe/H] + (0.80 \pm 0.10) \ at \ [Fe/H] \ < \ -1.5 \qquad (6.4)$$

and

$$M_V(RR) = (0.27 \pm 0.06)[Fe/H] + (1.01 \pm 0.12) \ at \ [Fe/H] \ > \ -1.5. \qquad (6.5)$$

At the junction point [Fe/H]=–1.5 there is a discontinuity of 0.06 mag, the average value being $M_V(RR)$ =0.58±0.12.

The relations expressed in (6.4) and (6.5), and comparison data points for a number of galactic globular clusters, are shown in Fig. 6.2. Compared with the theoretical HB models shown in Fig. 6.1, these pulsation models are consistent with the family of results that produce the fainter magnitudes.

Infrared Range. Infrared (K-band) observations of RR Lyrae stars had shown already several years ago that there exist a relatively tight relation between period P and mean K absolute magnitude $< M_K >$, with no (or little) dependence on metallicity [63,62,49]). These empirical relations, however, had to be calibrated on some independent method of absolute magnitude determination, which was usually the Baade-Wesselink method in its various versions, hence different zero-points. Also the dependence on metallicity, admittedly small, was not assessed unambiguously. The values of M_K so derived could vary on a range of $\sim$ 0.15 mag.

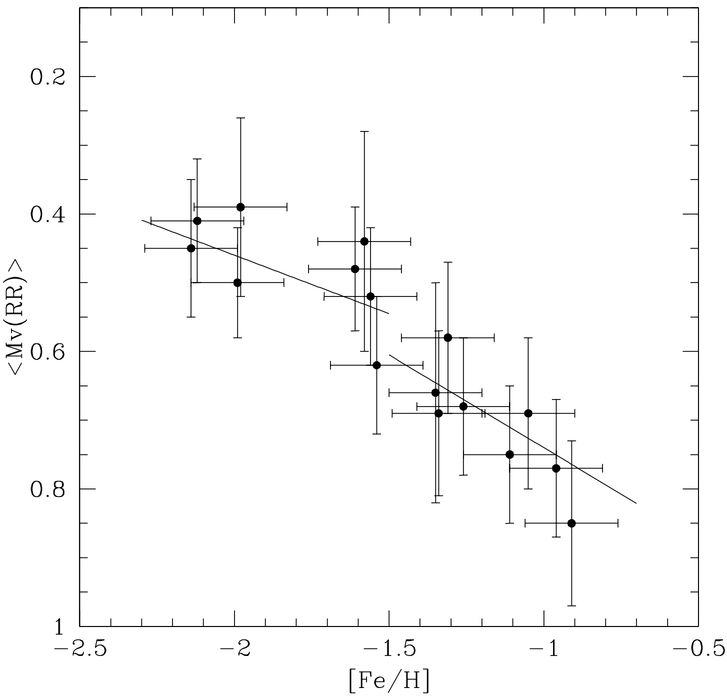

Fig. 6.2. $< M_V(RR) >$ vs [Fe/H] from the pulsation models by [19]. The dots represent galactic globular clusters, for comparison

Based on the same set of updated non-linear convective pulsation models described above, [7] have defined a theoretical Period-Luminosity-Metallicity relation in the infrared K band ($PL_K Z$), which is much less sensitive to reddening and metallicity than the visual equivalent relation, and therefore is supposedly more accurate (total intrinsic dispersion σ_{Mk}=0.037 mag):

$$M_K = -2.071 logP + 0.167[Fe/H] - 0.766 \qquad (6.6)$$

Note that this relation has been derived for models with solar scaled metallicities; models with [α/Fe]=+0.3, that are well mimicked by models with $[M/H] = [Fe/H] + 0.21$ according to the recipe by [69], would produce fainter M_K by $\sim$ 0.035 mag.

In principle, the non-linearity of the $logL(HB) - [Fe/H]$ relation and the change of slope at [Fe/H]∼–1.5 could be taken into account by defining two separate linear relations for models with [Fe/H]<–1.5 and [Fe/H]>–1.5, respectively. In practice, the effect of non-linearity and the change of slope are negligibly small and the linear relation defined over the entire metallicity range that is relevant for RR Lyrae stars and globular clusters provides the same M_K values within the errors.

Very recently [9] have revised the above analysis and derived improved Period-(V–K)Color-Luminosity-Metallicity (PCL_KZ) relations for fundamental and first-overtone pulsators separately (see Bono, this volume, for more details). These new relations, also based on solar-scaled metallicity models, seem to give systematically brighter magnitudes by a few hundredths of a magnitude with respect to the PL_KZ relation expressed in (6.6).

We now apply the PL_KZ relation in (6.6) to a few test cases for which accurate data are available, i.e. the RR Lyrae stars in the globular clusters M3 and ω Cen, the 7 field RR Lyrae stars with $[Fe/H] = -1.5 \pm 0.15$ for which the Baade-Wesselink method was applied, and the field variable RR Lyr itself.

- **M3.**
  Seventeen non-Blazhko RRab variables and nine RRc variables in M3 have K photometry [63]. Assuming [Fe/H]=–1.47 ([60]), and correcting the periods of the type-c variables to fundamental mode by the addition of a constant (0.127) to their $logP$ values, we obtain a K distance modulus $(m - M)_K = 15.03 \pm 0.05$, that can be considered as intrinsic modulus since the reddening of M3 is at most E(B–V)=0.01 mag [36], assuming $A_V = 3.1E(B - V)$ and $A_K = 0.11A_V$ [20]. For these same stars $< V >= 15.64 \pm 0.05$ [32], hence $< M_V(RR) >= 0.58 \pm 0.08$.
- **ω Cen.**
  In addition to the K photometric data obtained by [63] on 30 RR Lyrae variables, new K photometry of 45 RR Lyrae variables has been recently obtained by [42]. There are no stars in common between these two sets of data, therefore the consistency of the photometric calibrations cannot be checked but *a posteriori*, by comparing the distance moduli derived from the two sets separately. Metal abundances for a number of RR Lyrae variables in ω Cen have been recently derived by [67], and have been used to derive M_K via (6.6). We obtain $(m-M)_K = 13.69 \pm 0.09$ and 13.65 ± 0.13 from [63] and [42] data sets, respectively. The difference, well within the errors, could be ascribed to photometric calibration. Since [42] data are more recent and for a larger number of stars, we adopt their result that leads to $(m - M)_0 = 13.60 \pm 0.13$ assuming E(B–V)=0.13 and $A_K = 0.36E(B - V)$ [20]. This result compares very well with the value of 13.65 ± 0.11 obtained by [80] using the eclipsing binary OGLE17 to derive the distance to ω Cen.
  If we now consider only the variables with [Fe/H] $= -1.5 \pm 0.10$, they have $< V_0(RR) > \; = 14.14 \pm 0.11$ [67], hence $M_V(RR) = 0.54 \pm 0.17$ at [Fe/H] $= -1.5$.
- **Field RR Lyrae Stars**
  Approximately 30 field RR Lyrae stars have been analyzed with the Baade-Wesselink method and therefore have very accurate V and K light curves (see [40] for a review). From this sample we have selected 7 stars with $[Fe/H] = -1.5 \pm 0.15$, that are listed in Table 6.1. The V and K data are from [62] for all stars except UU Cet (data from [12]) and WY Ant (data from [77]). Using this average value of metallicity we have then derived the corresponding M_K values from (6.6), the distance moduli and M_V values. Assuming a realistic

Table 6.1. Field RR Lyrae stars with average [Fe/H]=–1.5±0.15 and good V and K data

Name	[Fe/H] (1)	[Fe/H] (2)	$< V_0 >$	$< K_0 >$	M_K	$(m-M)_0$	M_V
WY Ant	–1.48	–1.32	10.710	9.621	–0.518	10.139	0.571
RR Cet	–1.48	–1.38	9.625	8.524	–0.485	9.009	0.616
UU Cet	–1.28	–1.38	12.005	10.841	–0.565	11.406	0.599
RX Eri	–1.33	–1.63	9.529	8.358	–0.538	8.896	0.633
RR Leo	–1.60	–1.37	10.576	9.660	-0.302	9.962	0.614
TT Lyn	–1.56	–1.64	9.833	8.630	–0.553	9.183	0.650
TU UMa	–1.51	–1.38	9.764	8.656	–0.493	9.149	0.615

(1) From [39]
(2) From [29]

error of ~ 0.1 mag on each individual estimate, the weighted average of these estimates is $< M_V >= 0.61 \pm 0.04$ mag. For comparison, the average Baade-Wesselink result on these same stars, as reported by [40], is 0.68 ± 0.15, whereas the application of the revised PCL_KZ relation leads [9] to estimate an average value of 0.54±0.03 mag.

- **RR Lyr**
  Equation (6.6) can be applied to RR Lyr, for which $[Fe/H] = -1.39 \pm 0.10$ [29,39], logP=–0.2466 [52], $< K >= 6.54 \pm 0.04$ mag [38], and $< V >= 7.76$ mag [39].
  The result is $M_K = -0.487$, hence a distance modulus $(m-M)_0$=7.02 or 7.01 depending on the assumed absorption, i.e. $A_V = 0.07 \pm 0.03$ or 0.11 ± 0.10 (see Sect. 6.2.2). This in turn leads to $< M_V >= 0.67 \pm 0.11$ or 0.64 ± 0.11, respectively. By comparison, the results obtained by [5] using a highly accurate estimate of the trigonometric parallax are $\sim$ 0.06 mag brighter (as described in more detail in Sect. 6.2.2).
  This same analysis, performed by [8] in search of the "pulsation parallax" of RR Lyr, leads to $M_K = -0.541 \pm 0.062$ mag, whereas the application of the PCL_KZ relation leads to $M_K = -0.536 \pm 0.04$ mag ([9] and this volume).
  If we follow [5] choice of reddening ($A_V = 0.07$), then the value of M_V reported to [Fe/H]=–1.5 is 0.64±0.11 mag (or 0.59 from the PCL_KZ relation).

The weighted average of these 4 examples is $< M_V >= 0.61 \pm 0.03$ taking the results from the PL_KZ relation in (6.6). We have seen that the revised and possibly improved PCL_KZ relation produces absolute magnitudes ~0.06 mag brighter; on the other hand all these values would be fainter by ~0.04 mag had non-solar-scaled metallicities (i.e. $[\alpha/Fe] = +0.3$) be taken into account.

Therefore we assume as average result of this section $< M_V >= 0.59 \pm 0.10$ at [Fe/H]=−1.5, where the error tries to account realistically for all the uncertainties still affecting this method.

Double-Mode Pulsators. Another new result of pulsation models refers to double-mode RR Lyrae variables (RRd). From the pioneering work of [1] on stellar pulsation we know that the period of a fundamental (or first overtone) pulsator is related with its mass, luminosity and temperature via well known formulae, of which we report a recent redetermination by [18] that includes also some dependence on metallicity:

$$logP_0 = 11.242 + 0.841logL - 0.679logM - 3.410logT_e + 0.007logZ \qquad (6.7)$$

and

$$logP_1 = 10.845 + 0.809logL - 0.598logM - 3.323logT_e + 0.005logZ \qquad (6.8)$$

The double-mode pulsators, that pulsate simultaneously in the fundamental mode with period P_0 and in the first overtone with period P_1, allow to define a relation between stellar luminosity, temperature, periods and metallicity, where the dependence on mass is eliminated. Since periods and metallicities are observed quantities and temperatures can be derived from colors and adequate (empirical or theoretical) color-temperature calibrations, luminosities (hence distances) can be obtained.

Based on linear nonadiabatic pulsation models and various assumptions on opacities and detailed element abundances, [58] applied this method to the RRd stars in the Galactic globular clusters M15, M68 and IC4499. They did not provide direct values of M_V but only a comparison with the results of the Fourier-decomposition method, and estimated the distance modulus to the LMC as 18.45-18.55. The same data were later reanalyzed by [55] along with $\sim$ 180 RRd variables in the LMC from the MACHO database [2]. No M_V values are given, but only distance moduli reported to the LMC. The weighted average of the four distance determinations to the LMC turns out to be $< (m - M)_o > (LMC) = 18.50 \pm 0.05$. In this method the main source of error is due to ambiguity in the zero-point T_0 of the color-temperature transformation.

To derive the absolute V magnitude of RR Lyraes from the above results we need accurate observed V magnitudes of such stars in the LMC, with a good knowledge of their reddenings. The problem of the absolute and differential reddening across the LMC is a thorny problem that we cannot analyse here (see [31] and Feast in this volume for a detailed discussion); here we have assumed the values derived by the individual authors.

A few data sets can meet these requirements, in particular:

- [31] report the results of observations in two fields of the LMC bar, where 108 RR Lyrae stars were measured. The data in these two fields were corrected by their respective reddenings, i.e. 0.086 and 0.116. The mean magnitude of these RR Lyrae stars at average [Fe/H]=–1.5 is $< V_0 >= 19.06 \pm 0.06$. Spectroscopic metal abundances were also derived, and the slope of the luminosity-metallicity relation was found to be 0.214 ± 0.047, well consistent with the value of 0.23 used here.

- [83] presented and discussed the data for 160 RR Lyraes in 6 globular clusters (excluding NGC 1841 that may be significantly closer to us) at average [Fe/H]=–1.9. The data were corrected by the respective reddening for each individual cluster (ranging from 0.03 to 0.13 mag with average 0.07 mag). The mean magnitude of these 160 RR Lyrae stars is $< V_0 >= 18.98 \pm 0.06$.
- Other data for field RR Lyrae variables in the LMC are provided by the MACHO experiment [2]: 680 stars, $< V_0 >= 19.14 \pm 0.10$ at [Fe/H]=–1.7, assumed reddening E(B–V)=0.10.
- The OGLE experiment [81]: 6000 RR Lyrae stars, $< V_0 >= 18.91 \pm 0.10$ at [Fe/H]=–1.6, assumed reddening E(B–V)$\sim$0.143.

The error we associate to the MACHO and OGLE estimates is larger than the values quoted by the respective authors, but we believe it better represents the uncertainties due to photometric calibrations and reddening estimates still affecting these data sets. The large difference between these two results can only in part be accounted for by different values of the assumed reddening. Because of these uncertainties, we prefer not to use these results in the following considerations in spite of the very large number of involved stars.

A weighted average of the first two results only, after reporting them to [Fe/H]=–1.5, is $< V_0 >= 19.07 \pm 0.04$. Incidentally, we note that the average value of the last two results from the MACHO and OGLE data, that we have not considered because less accurate, is $< V_0 >= 19.06 \pm 0.07$ at [Fe/H]=–1.5, although the close agreement may be fortuitous.

If we then use the value estimated by [55] from RRd pulsators for the distance to the LMC, namely $< (m - M)_o > (LMC) = 18.50 \pm 0.05$ (see also A. Walker, this volume), then the average magnitude of the RR Lyrae stars is $< M_V >= 0.57 \pm 0.06$.

6.2.7 Fourier Parameters of Light Curves

During the past decade a series of studies were conducted, aimed at deriving *empirical* relations between the Fourier parameters of the light curves of RR Lyrae variables and their physical parameters. In particular, *RRc* variables were studied by [75] and [76], and *RRab* variables were studied by Kovács and collaborators in several papers (e.g. [50,56,57,59]).

This method is based on the assumption that period and shape of the light curves are correlated with the intrinsic physical parameters of the star. There is no known theoretical justification for this assumption, however well defined empirical correlations do indeed seem to exist, and the quoted studies have tried to define the combinations of Fourier parameters that best correlate with e.g. metallicity, intrinsic colors and absolute magnitude. The advantages of this method are potentially relevant, since its application only requires the use of accurate V light curves, that are now becoming available for large numbers of variables thanks to the many photometric surveys carried out in the past few years for different purposes. In particular we consider the relation

$$M_V(RR) = -1.876 logP - 1.158A_1 + 0.821A_3 + K \tag{6.9}$$

derived by [59] from 383 RRab variables in globular clusters. This formula fits the data with $\sigma = 0.04$ mag. The zero-point K, however, must be determined by some calibrator. The most recent and accurate estimate of K has been obtained by [53] using RR Lyr. This star is affected by the Blazhko effect (a 41-d modulation of its amplitude whose amplitude in turn varies over a 4-year period). The Fourier parameters of this star correspond approximately to those of a normal RRab star only near maximum amplitude of the primary Blazhko cycle and minimum amplitude of the secondary cycle [51]. By analysing data taken during one such epoch [53] finds that the Fourier coefficients A_1 and A_3 are respectively 0.31539 and 0.09768. Using M_V=0.61 for RR Lyr (see Sect. 6.2.2) he then finds K=0.43.

Based on this calibration, we apply the relation in (6.9) to 55 normal RRab stars in M3 whose Fourier parameters have been recently determined from very accurate light curves [13]. We find an average value $M_V = 0.615 \pm 0.003$, with an *rms* deviation for a single star of 0.02 mag. This very small *formal* error is purely statistical, and is due to the large number of stars involved in this estimate combined with a “tightening” effect by a factor ~ 2 of these M_V estimates with respect to the observed V values, whose intrinsic distribution has instead a $\sigma \sim 0.05$ mag [13].

A further test can be done using the field variable RR Cet for which excellent light curves are available. For this star the Fourier coefficients A_1 and A_3 are respectively 0.31924 and 0.10760, and logP=–0.257, hence M_V=0.63 mag to which we can associate an *rms* error of 0.05 mag.

Both M3 and RR Cet have very similar metallicity, $[Fe/H] = -1.47$ and -1.43 respectively, and if we report the average of these two determinations to $[Fe/H] = -1.5$ we obtain $M_V = 0.61 \pm 0.05$ mag.

6.3 Summary and Conclusions

We have reviewed the methods of absolute magnitude determination for RR Lyrae variables, that can be used for distance determinations to globular clusters and all other stellar systems containing this type of stars.

We have adopted $M_V(RR)$ at [Fe/H]=–1.5 as the most convenient reference parameter (i.e. zero-point magnitude) for distance determination, assuming in first approximation that the dependence of $M_V(RR)$ on metallicity [Fe/H] is linear with a slope ~ 0.23.

We collect in the following Table 6.2 all the determinations of $M_V(RR)$ described in the previous sections. If we take the weighted average of these results, we obtain **<M_V(RR)> = 0.59±0.03** mag (r.m.s. error of the mean) at **[Fe/H]=–1.5**.

Table 6.2. Summary of $M_V(RR)$ determinations at [Fe/H]=–1.5 from the methods described in the text.

Method	$M_V(RR)$ at [Fe/H]=–1.5	Reference
Statistical parallaxes	0.78±0.12	Sect. 6.2.1
Trigonometric parallaxes (RR Lyr)	0.58±0.13	Sect. 6.2.2
Trigonometric parallaxes (HB stars)	0.62±0.11	Sect. 6.2.3
Baade-Wesselink (RR Cet)	0.55±0.12	Sect. 6.2.4
HB stars: evolutionary models - bright	0.43±0.12	Sect. 6.2.5
HB stars: evolutionary models - faint	0.56±0.12	Sect. 6.2.5
Pulsation models (visual)	0.58±0.12	Sect. 6.2.6
Pulsation models (PL_KZ)	0.59±0.10	Sect. 6.2.6
Pulsation models (RRd)	0.57±0.06	Sect. 6.2.6
Fourier parameters	0.61±0.05	Sect. 6.2.7
Weighted average value	0.59±0.03	

The last two values of the list, from the double-mode pulsators and Fourier parameters, have smaller errors than the other results mainly because of the large number of stars considered by these two methods. If we do not wish to attach to them more weight than they probably deserve for intrinsic merits, and consider instead a typical error of ±0.10 mag for each of them, the previous average result and related error remain unchanged. Similarly, we may want to consider the results from the HB evolutionary models separately for the bright and faint groups: this would make a difference of at most 0.01 mag on the weighted average.

We note that the average value derived above is virtually identical to the value obtained by [28], only the error is now significantly smaller. Also [11] obtained a very similar average result (0.57 ± 0.04) by including the values from other distance determination methods, e.g. Eclipsing Binaries and Main-Sequence fitting to local Sub-Dwarfs. We might be tempted to conclude that we are approaching a robust result on this issue.

Using the value of $< V_0 >= 19.07 \pm 0.04$ at [Fe/H]=–1.5 estimated in Sect. 6.2.6 for the RR Lyrae variables in the LMC, this translates into a distance modulus to the LMC $(m-M)_0 = 18.48{\pm}0.05$. We refer to A. Walker and M. Feast (this volume) for a summary on distance determinations to the LMC.

It may be interesting to compare the present result with two other $M_V(RR)$ or $M_V(HB)$ determinations that are important for different reasons:

i) The method of globular cluster Main-Sequence fitting to local Sub-Dwarfs (SD) is considered probably the most accurate and reliable method presently available, provided adequate precautions are taken in analyzing the data. The most recent results are given by [47], who have reanalyzed three clusters (47 Tuc, NGC6397 and NGC6752) using the most accurate data and assumptions, in particular high resolution (VLT-UVES) abundances and accurate photometry and reddening for MS and SD stars, all in the same scale and with the same treatment. The result obtained by [47] is $M_V(RR) = 0.61 \pm 0.07$ mag at [Fe/H]=–1.5.

ii) Color-Magnitude diagrams have been derived for several globular clusters in M31 using *HST* data [68]. From these an estimate of the mean HB magnitudes at the middle of the instability strip could be derived. These estimates are of course affected by significantly larger errors than any of those discussed in this review, however they are important because they allow to compare the same type of results in the Milky Way and in M31, in the framework of the similarities and differences between these two galaxies.

A preliminary analysis of 17 clusters shows that a slope ~0.23 is adequate to describe the $V_0(HB) - [Fe/H]$ relation, and $< V_0(HB) >= 25.06 \pm 0.15$ at [Fe/H]=–1.5. The corresponding value of $M_V(HB)$ depends on the assumed distance to M31: if we assume the widely used value $(m - M)_0 = 24.43 \pm 0.06$ by [43], based on the Cepheid distance scale, then $M_V(HB) = 0.63 \pm 0.16$ mag. An independent distance determination to the centroid of the M31 globular cluster system by [48], by fitting theoretical isochrones to the observed red giant branches of 14 globular clusters in M31, yields $(m - M)_0 = 24.47 \pm 0.07$, hence $M_V(HB) = 0.59 \pm 0.17$ at [Fe/H]=–1.5.

It is reassuring to see that these results, in spite of the different intrinsic accuracy and statistical weight, agree with the average value estimated from the data listed in Table 6.2 within 1σ.

Acknowledgements

We are very grateful to T. Kinman for providing his calibration based on RR Lyr in advance of publication. We thank A. Gould for reminding us of cosmic scatter when dealing with individual stars.

References

1. van Albada, T.S., Baker, N. 1971, ApJ, 169, 311
2. Alcock, C. et al. 2000, ApJ, 542, 257
3. van Altena, W.F., Lee, J.T. & Hoffleit, E.D. 1995, Yale Parallax Catalog (4th ed.: New Haven: Yale Univ. Obs.) (YPC95)
4. Beers, T.C., Drilling, J.S., Rossi, S. et al. 2002, AJ, 124, 931
5. Benedict, G.F., McArthur, B.E., Fredrick, L.W. et al. 2002, AJ, 123, 473
6. Bono, G., Caputo, F., Cassisi, S., Incerpi, R. & Marconi, M. 1997, ApJ, 483, 811

7. Bono G., Caputo, F., Castellani, V., Marconi, M. & Storm, J. 2001, MNRAS, 326, 1183
8. Bono, G., Caputo, F., Castellani, V., Marconi, M. & Storm, J. 2002, MNRAS, 332, L78
9. Bono, G., Caputo, F., Castellani, V., Marconi, M., Storm, J. & Degl'Innocenti, S. 2003, in preparation
10. Borkova, T.V, Marsakov, V.A. 2002, A&A, in press (astro-ph/0211263)
11. Cacciari, C. 2002, in *New Horizons in Globular Cluster Astronomy*, eds G. Piotto & G. Meylan, ASP Conf. Ser. in press
12. Cacciari, C., Clementini, G., Fernley, J.A. 1992, ApJ, 396, 219
13. Cacciari, C., Corwin, T.M., Carney, B.W. 2003, in preparation
14. Cacciari, C., Clementini, G., Castelli, F. & Melandri, F. 2000, in *The Impact of Large-Scale Surveys on Pulsating Star Research*, Eds. L. Szabados & D.W. Kurtz, ASP Conf. Ser. Vol. 203, p. 176
15. Caloi, V., D'Antona, F. & Mazzitelli, I. 1997, A&A, 320, 823
16. Canuto, V.M. & Mazzitelli, I. 1991, ApJ, 370, 295
17. Caputo, F., Martinez Roger, C. & Paez, E. 1987, A&A, 183, 228
18. Caputo, F., Marconi, M., Santolamazza, P. 1998, MNRAS, 293, 364
19. Caputo, F., Castellani, V., Marconi, M. & Ripepi, V. 2000, MNRAS, 316, 819
20. Cardelli, J.A., Clayton, G.C. & Mathis, J.S. 1989, ApJ, 345, 245
21. Carney, B.W., Storm, J. & Jones, R.V. 1992, ApJ, 386, 663
22. Carretta, E., Gratton, R.G. & Clementini, G. 2000, MNRAS, 316, 721
23. Carretta, E., Gratton, R.G., Clementini, G. & Fusi Pecci, F. 2000, ApJ, 533, 215
24. Cassisi, S. & Salaris, M. 1997, MNRAS, 285, 593
25. Cassisi, S., Castellani, V., Degl'Innocenti, S., Salaris, M. & Weiss, A. 1999, A&AS, 134, 103
26. Castellani, V., Chieffi, A., Pulone, L. 1991, ApJS, 76, 911
27. Catelan, M. 1998, ApJ, 495, L81
28. Chaboyer, B. 1999, in *Post-Hipparcos Cosmic Candles*, Eds. A. Heck & F. Caputo, Kluwer Ac. Pub., p. 111
29. Clementini, G., Carretta, E., Gratton, R.G., Merighi, R., Mould, J.R. & McCarthy, J.K. 1995, AJ, 110, 2319
30. Clementini, G., Federici, L., Corsi, C.E., Cacciari, C., Bellazzini, M. & Smith, H.A. 2001, ApJ, 559, L109
31. Clementini, G., Gratton, R.G., Bragaglia, A., Carretta, E., Di Fabrizio, L. & Maio, M. 2003, AJ, in press (astro-ph/0007471 revised V.2)
32. Corwin, T.M & Carney, B.W. 2001, AJ, 122, 3183
33. Dambis, A.K. & Rastorguev, A.S. 2001, Astron. Lett. Vol. 27, 108
34. Demarque, P., Zinn, R., Lee, Y-W. & Yi, S. 2000, AJ, 119, 1398
35. Dorman, B. 1992, ApJS81, 221
36. Dutra, C.M & Bica, E. 2000, A&A, 359, 347
37. Eggen, O.J., Lynden-Bell, D. & Sandage, A. 1962, ApJ, 136, 748
38. Fernley, J.A., Skillen, I. & Burki, G. 1993, A&AS, 97, 815
39. Fernley, J.A, Barnes, T.G., Skillen, I., Hawley, S.L., Hanley, C.J., Evans, D.W., Solano, E. & Garrido, R. 1998a, A&A, 330, 515
40. Fernley, J., Carney, B.W., Skillen, I., Cacciari, C. & Janes, K. 1998b, MNRAS, 293, L61
41. Ferraro, F.R., Messineo, M., Fusi Pecci, F., De Palo, M.A., Straniero, O., Chieffi, A. & Limongi, M. 1999, AJ, 118, 1738
42. Ferraro, F.R. et al. 2003, in preparation

43. Freedman, W.L. & Madore, B.F. 1990, ApJ, 365, 186
44. Freeman, K. & Bland-Hawthorn, J. 2002, ARA&A, 40, 487
45. Gould, A. & Popowski, P. 1998, ApJ, 508, 844
46. Gratton, R.G. 1998, MNRAS, 296, 739
47. Gratton, R.G., Carretta, E., Bragaglia, A., Clementini, G. & Grundahl, F. 2002, in *New Horizons in Globular Cluster Astronomy*, eds G. Piotto & G. Meylan, ASP Conf. Ser. in press
48. Holland, S. 1998, AJ, 115, 1916
49. Jones, R.V., Carney, B.W., Storm, J., Latham, D.W. 1992, ApJ, 386, 646
50. Jurcsik, J. & Kovács, G. 1996, A&A, 312, 111
51. Jurcsik, J., Benkö, J.M. & Szeidl, B. 2002, A&A, 390, 133
52. Kazarovets, E.V., Samus, N.N & Durlevich, O.V. 2001, IBVS, 5135, 1
53. Kinman, T.D. 2002, IBVS 5354
54. Koen, C. & Laney, D. 1998, MNRAS, 301, 582
55. Kovács, G. 2000, A&A, 363, L1
56. Kovács, G. & Jurcsik, J. 1996, ApJ, 466, L17
57. Kovács, G. & Jurcsik, J. 1997, A&A, 322, 218
58. Kovács, G., Walker, A.R. 1999, ApJ, 512, 271
59. Kovács, G., Walker, A.R. 2001, A&A, 371, 579
60. Kraft, R.P., Sneden, C., Langer, G.E. & Prosser, C.F. 1992, AJ, 104, 645
61. Layden, A.C. 1999, in *Post-Hipparcos Cosmic Candles*, Eds. A. Heck & F. Caputo, Kluwer Ac. Pub., p. 37
62. Liu, T., Janes, K.A. 1990, ApJ, 354, 273
63. Longmore, A.J., Dixon, R., Skillen, I., Jameson, R.F. & Fernley, J.A. 1990, MNRAS, 247, 684
64. Montegriffo, P., Ferraro, F.R., Origlia, L. & Fusi Pecci, F. 1998, MNRAS, 297, 872
65. Perryman, M.A.C. et al. 1997, A&A, 323, L49
66. Popowski, P. & Gould, A. 1999, in *Post-Hipparcos Cosmic Candles*, Eds. A. Heck & F. Caputo, Kluwer Ac. Pub., p. 53
67. Rey, S-C., Lee, Y-W., Joo, J-M., Walker, A. & Baird, S. 2000, AJ, 119, 1824
68. Rich, R.M., Corsi, C.E., Bellazzini, M., Federici, L., Cacciari, C. & Fusi Pecci, F. 2001, in *Extragalactic Star Clusters*, ed. E.K. Grebel, D. Geisler & D. Minniti, ASP Conf Ser. Vol. 207, in press
69. Salaris, M., Chieffi, A. & Straniero, O. 1993, ApJ, 414, 580
70. Sandage, A. 1981a, ApJ, 244, L23
71. Sandage, A. 1981b, ApJ, 248, 161
72. Sandage, A. 1990, ApJ, 350, 603
73. Sandage, A. 1993, AJ, 106, 719
74. Searle, L. & Zinn, R. 1978, ApJ, 225, 357
75. Simon, N.R. & Clement, C.M. 1993a, in *New Perspectives on Stellar Pulsation and Pulsating Variable Stars*, ed. J.M. Nemec & J.M. Matthews (Cambridge: Cambridge Univ. Press), p. 315
76. Simon, N.R. & Clement, C.M. 1993b, ApJ, 410, 526
77. Skillen, I., Fernley, J.A., Stobie, R.S. & Jameson, R.F. 1993, MNRAS, 265, 301
78. Smith, H.A. 1995, in *RR Lyrae Stars*, Cambridge Univ. Press
79. Straniero, O., Chieffi, A. & Limongi, M. 1997, ApJ, 490, 425
80. Thompson, I.B., Kaluzny, J., Pych, W. et al. 2001, AJ, 121, 3089
81. Udalski, A. 2000, Acta Astron., 50, 279
82. VandenBerg, D.A., Swenson, F.J., Rogers, F.J., Iglesias, C.A. & Alexander, D.R. 2000, ApJ, 532, 430
83. Walker,A.R. 1992, ApJ, 390, L81

7 Blue Supergiants as a Tool for Extragalactic Distances – Theoretical Concepts

Rolf-Peter Kudritzki and Norbert Przybilla

Institute for Astronomy, University of Hawaii, Honolulu, HI 96822, USA

Abstract. Because of their enormous intrinsic brightness blue supergiants are ideal stellar objects to be studied spectroscopically as individuals in galaxies far beyond the Local Group. Quantitative spectroscopy by means of efficient multi-object spectrographs attached to 8m-class telescopes and modern NLTE model atmosphere techniques allow us to determine not only intrinsic stellar parameters such as effective temperature, surface gravity, chemical composition and absolute magnitude but also very accurately interstellar reddening and extinction. This is a significant advantage compared to classical distance indicators like Cepheids and RR Lyrae. We describe the spectroscopic diagnostics of blue supergiants and introduce two concepts to determine absolute magnitudes. The first one (Wind Momentum – Luminosity Relationship) uses the correlation between observed stellar wind momentum and luminosity, whereas the second one (Flux-weighted Gravity–Luminosity Relationship) relies only on the determination of effective temperature and surface gravity to yield an accurate estimate of absolute magnitude. We discuss the potential of these two methods.

7.1 Introduction

The best established stellar distance indicators, Cepheids and RR Lyrae, suffer from two major problems, extinction and metallicity dependence, both of which are difficult to determine for these objects with sufficient precision. Thus, in order to improve distance determinations in the local universe and to assess the influence of systematic errors there is definitely a need for alternative distance indicators, which are at least as accurate but are not affected by uncertainties arising from extinction or metallicity. It is our conviction that blue supergiants are ideal objects for this purpose. The big advantage is the enormous intrinsic brightness in visual light, which makes them available for accurate quantitative spectroscopic studies even far beyond the Local Group using the new generation of 8m-class telescopes and the extremely efficient multi-object spectrographs attached to them [2]. Quantitative spectroscopy allows us to determine the stellar parameters and thus the intrinsic energy distribution, which can then be used to measure reddening and the extinction law. In addition, metallicity can be derived from the spectra. We emphasize that a reliable *spectroscopic* distance indicator will always be superior, since an enormous amount of additional information comes for free, as soon as one is able to obtain a reasonable spectrum.

In this review we concentrate on blue supergiants of spectral types late B to early A. These are the the brightest "normal" stars at visual light with absolute

R.-P. Kudritzki and N. Przybillai, Blue Supergiants as a Tool for Extragalactic Distances – Theoretical Concepts, Lect. Notes Phys. **635**, 123–148 (2003)
http://www.springerlink.com/

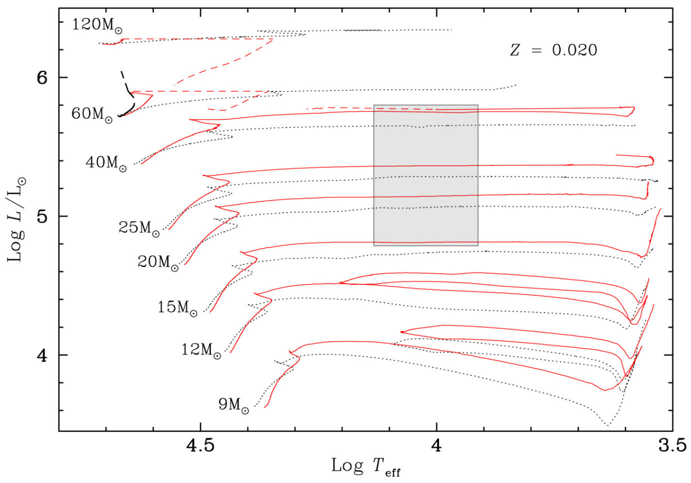

Fig. 7.1. Evolutionary tracks of massive stars in the Hertzsprung-Russell diagram and the location of blue supergiants of late B and early A spectral types (*shaded box*). The tracks are from [18]. *Solid tracks* include the effects of stellar rotation, whereas *dotted tracks* are for non-rotating stars. Solar metallicity has been adopted for the calculations. The tracks are labelled by the initial masses (in solar units) at the zero-age main sequence (ZAMS). Note that effects of mass-loss due to stellar winds are included in the calculations so that actual masses are smaller than ZAMS-masses in later stages of the evolution

magnitudes $-7.0 \geq M_V \geq -9.5$, see [5]. By "normal" we mean stars evolving peacefully without showing signs of eruptions or explosions, which are difficult to handle theoretically and observationally.

Figure 7.1 shows the location of these objects in a Hertzsprung-Russell diagram (HRD) with theoretical evolutionary tracks. With initial ZAMS-masses between 15 and 40 $M_\odot$ they do not belong to the most massive and the most luminous stars in galaxies. O-stars can be significantly more massive and luminous, however, because of their high atmospheric temperatures they emit most of their radiation in the extreme and far UV. Late B and early A supergiants are cooler and because of Wien's law their bolometric corrections are small so that their brightness at visual light reaches a maximum value during stellar evolution.

In the temperature range of late B and early A-supergiants there are also always a few objects brighter than $M_V = -9.5$. Generally, those are more exotic objects such as Luminous Blue Variables (LBVs) with higher initial masses and with spectra characterized by strong emission lines and sometimes in dramatic evolutionary phases with outbursts and eruptions. Although their potential as distance indicators is also very promising, we regard the physics of their evolution and atmospheres as too complicated at this point and, thus, exclude them from our discussion.

The objects of our interest evolve smoothly from the left to the right in the HRD crossing the temperature range of late B and early A-supergiants on the order of several 10^3 years [18]. During this short evolutionary phase stellar winds with mass-loss rates of the order 10^{-6} $M_\odot\,yr^{-1}$ or less [13] do not have time enough to reduce the mass of the star significantly so that the mass remains constant. In addition, as Fig. 7.1 shows, the luminosity stays constant as well. The fact that the evolution of these objects can very simply be described by constant mass, luminosity and a straightforward mass-luminosity relationship makes them a very attractive stellar distance indicator, as we will explain later in this review.

As evolved objects the blue supergiants are older than their O-star progenitors, with ages between 0.5 to 1.3×10^7 years [18]. All galaxies with ongoing star formation or bursts of this age will show such a population. Because of their age they are spatially less concentrated around their place of birth than O-stars and can frequently be found as isolated field stars. This together with their intrinsic brightness makes them less vulnerable as distance indicators against the effects of crowding even at larger distances, where less luminous objects such as Cepheids and RR Lyrae start to have problems.

With regard to the crowding problem we also note that the short evolutionary time of 10^3 years makes it generally very unlikely that an unresolved blend of two supergiants with very similar spectral types is observed. On the other hand, since we are dealing with spectroscopic distance indicators, any contribution of unresolved additional objects of different spectral type is detected immediately, as soon as it affects the total magnitude significantly.

Thus, it is very obvious that blue supergiants seem to be ideal to investigate the properties of young populations in galaxies. They can be used to study reddening laws and extinction, detailed chemical composition, i.e. not only abundance patterns but also gradients of abundance patterns as a function of galactocentric distance, the properties of stellar winds as function of chemical composition and the evolution of stars in different galactic environment. Most importantly, as we will demonstrate below, they are excellent distance indicators.

It is also very obvious that the use of blue supergiants as tools to understand the physics of galaxies and to determine their distances depends very strongly on the accuracy of the spectral diagnostic methods which are applied. The attractiveness of blue supergiants for extragalactic work, namely their outstanding intrinsic brightness, has also always posed a tremendous theoretical problem. The enormous energy and momentum density contained in their photospheric radiation field leads to significant departures from Local Thermodynamic Equilibrium and to stellar wind outflows driven by radiation. It has long been a problem to model non-LTE and radiation driven winds realistically, but significant theoretical progress was made during the past decade resulting in powerful spectroscopic diagnostic tools which allow to determine the properties of supergiant stars with high precision.

We describe the status quo of the spectroscopic diagnostics in the following chapters. We will then demonstrate how the spectroscopic information can be used to determine distances. We will introduce two completely independent theoretical concepts for distance determination methods. The first method, the Wind Momentum – Luminosity Relationship (WLR), uses the strengths of the radiation driven stellar winds as observed through the diagnostics of H_α as a measure of absolute luminosity and, therefore, distance. The second method, the Flux-weighted Gravity – Luminosity Relationship (FGLR), determines the stellar gravities from all the higher Balmer lines and uses gravity divided by the fourth power of effective temperature as a precise measure of absolute magnitude. A short discussion of the potential of these new concepts will conclude the paper.

7.2 Stellar Atmospheres and Spectral Diagnostics

The physics of the atmospheres of blue supergiant stars is complex and very different from standard stellar atmosphere models. They are dominated by the influence of the radiation field, which is characterized by energy densities larger than or of the same order as the energy density of atmospheric matter. Another important characteristic are the low gravities, which lead to extremely low densities and an extended atmospheric plasma with very low escape velocity from the star. This has two important consequences. First, severe departures from Local Thermodynamic Equilibrium (LTE) of the level populations in the entire atmosphere are induced, because radiative transitions between ionic energy levels become much more important than inelastic collisions with free electrons. Second, a supersonic hydrodynamic outflow of atmospheric matter is initiated by line absorption of photons transferring outwardly directed momentum to the atmospheric plasma. This latter mechanism is responsible for the existence of the strong stellar winds observed.

Stellar winds can affect the structure of the outer atmospheric layers substantially and change the profiles of strong optical lines such as H_α and H_β significantly. The effects of the departures from Local Thermodynamic Equilibrium ("NLTE") can also become crucial depending on the atomic properties of the ion investigated. A comprehensive and detailed discussion of the basic physics behind these effects and the advancement of model atmosphere work for blue supergiants is given in [8] and [11]. More recent work is described in [29],[19] and [28].

For late B and early A-supergiants considerable progress has been made during the last four years in the development of a very detailed and accurate modelling of the NLTE radiative transfer enabling very precise determinations of stellar parameters and chemical abundances, see [1], [20], [23], [21], [22] and [24]. Figure 7.2 gives an impression of the effort put into the atomic models and corresponding radiative transfer of individual ions.

7.2.1 Effective Temperature and Gravity

Effective temperature $T_{\rm eff}$ and gravity $\log g$ are the most fundamental atmospheric parameters. They are usually determined by fitting simultaneously two sets

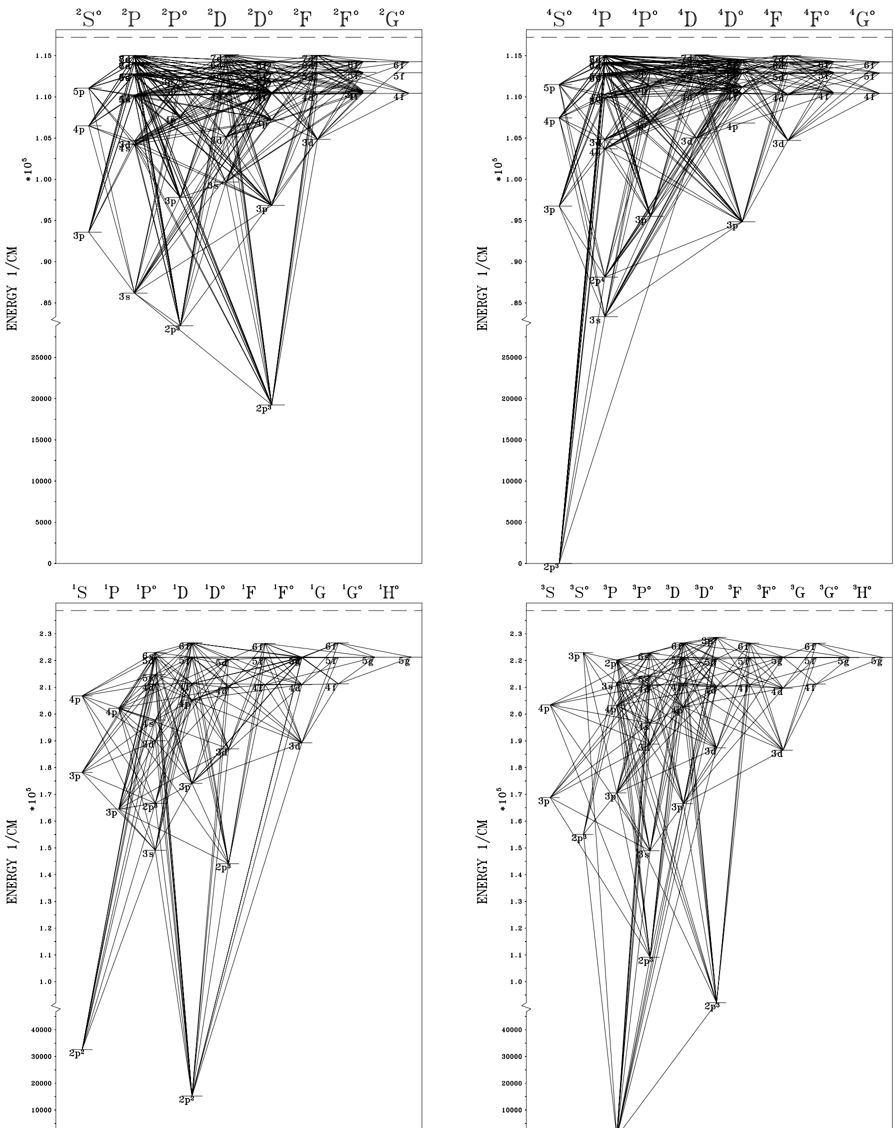

Fig. 7.2. Model atoms for N I (*top*) and N II (*bottom*) as used in the NLTE model calculations for late B and early A-supergiants; from [23]

of spectral lines, one depending mostly on $T_{\rm eff}$ and the other on $\log g$. Figure 7.3 indicates how this is done in principle. When fitting the ionization equilibria of elements spectral lines of two or more ionization stages have to be brought into simultaneous agreement with observations. At different locations in the ($\log g$,

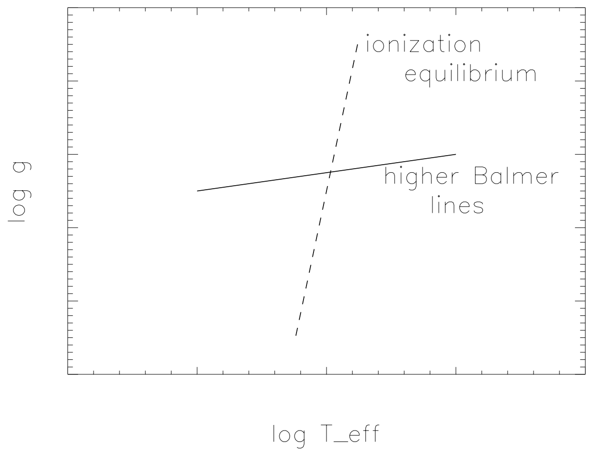

Fig. 7.3. Schematic fit diagram of temperature- and gravity-sensitive spectral lines in the ($\log g$, log $T_{\rm eff}$)-plane. Along the *dashed curve* the computed spectral lines of two different ionization stages of one element agree with the observations. Typical ionization equilibria for late B-supergiants are Si II/III, N I/II, O I/II and S II/III, and for A-supergiants one can use Mg I/II and N I/II. Along the *solid curve* the computed profiles of the higher Balmer lines agree with the observations. The intersection determines $T_{\rm eff}$ and $\log g$

log $T_{\rm eff}$)-plane this can be achieved only for different elemental abundances. Thus, along the fit curve for the ionization equilibrium in Fig. 7.3 the abundance of the corresponding element varies and the intersection with the fit curve for the Balmer lines leads to an automatic determination of the abundance of the element, for which the ionization equilibrium is investigated. (Note that the old technique of fitting ratios of equivalent widths of lines in different ionization stages and to regard those as being independent of abundance is less reliable, since the lines might be on different parts on the curve of growth).

For A-supergiants the technique has been pioneered by [32]. Most recent examples for applications are [24,33–35]. Examples are given in Figs. 7.4–7.6.

The accuracy in the determination of $T_{\rm eff}$ and $\log g$, which can be achieved when using spectra of high S/N and sufficient resolution is astonishing. $\Delta T_{\rm eff}/T_{\rm eff} \sim 0.01$ and $\Delta \log g \sim 0.05$ are realistic values.

7.2.2 Chemical Composition

The development of very detailed model atoms and using new and very accurate atomic data, [7,30], has led to an enormous improvement of the precision to which elemental abundances even in extreme blue supergiants can be determined [20,23,21,22,24,34,35]. On the average, the uncertainties are now reduced to 0.1 dex in the abundance relative to hydrogen. Figure 7.7 displays a nice example for the fit of the equivalent widths of CNO lines in blue supergiants.

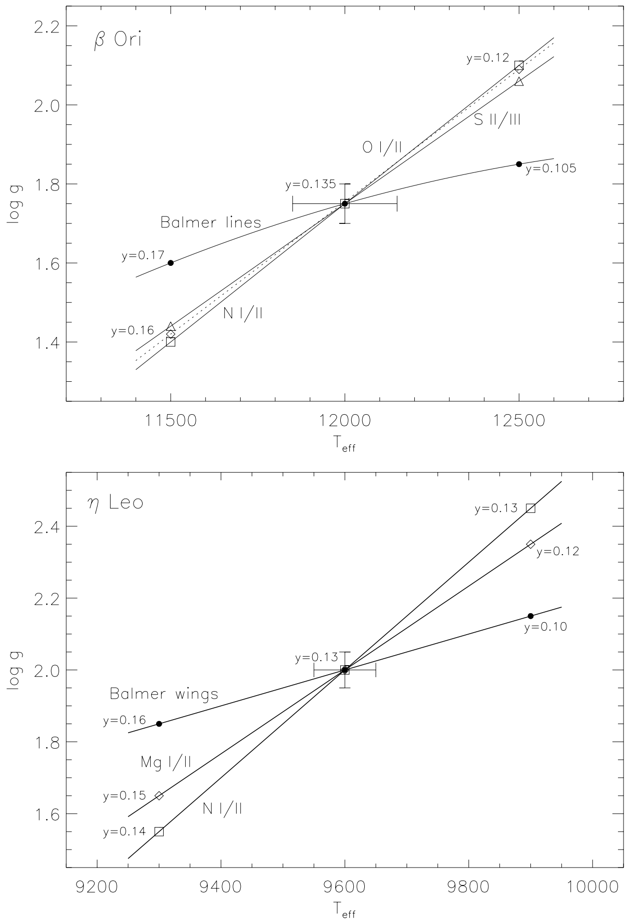

Fig. 7.4. Fit diagram for the supergiants β Ori (*top*) and η Leo (*bottom*). The curves are parameterized by surface helium abundance y (by number); from [24]

The amount of information about chemical elements is impressive. Figure 7.8 gives an overview about the chemical elements the abundances of which can be determined from the optical spectra of blue supergiants. Figure 7.8 shows characteristic abundance patterns, as they can be derived for supergiants in the Milky Way and Fig. 7.9 displays results for two M 31 supergiants.

7.2.3 Stellar Wind Properties

In principle, two types of lines are formed in a stellar wind, P-Cygni profiles with a blue absorption trough and a red emission peak and pure emission profiles. The difference is caused by the re-emission process after the photon has been absorbed within the line transition. If the photon is immediately re-emitted by

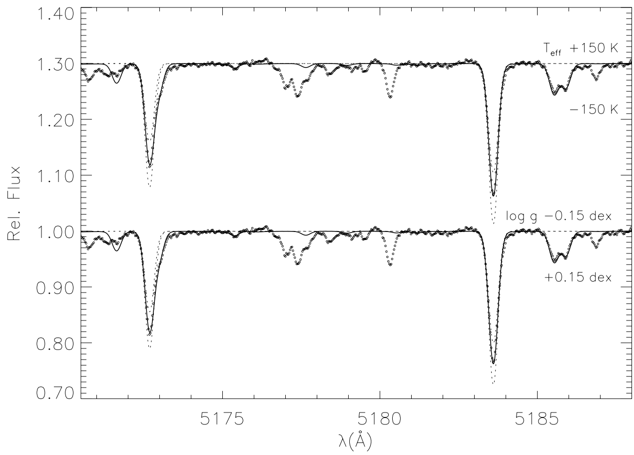

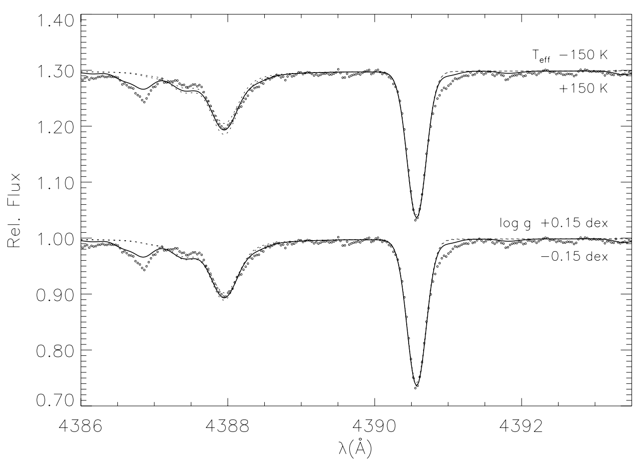

Fig. 7.5. Temperature and gravity dependence of Mg I (top) and Mg II (*bottom*) of η Leo. Results from the NLTE computations for the final stellar parameters (*full line*) are compared with synthetic spectra for modified parameters (*dotted lines*), as indicated, against observation (*dots*); from [24]

spontaneous emission, then we have the case of line scattering with a source function proportional to the geometrical dilution of the radiation field and a P-Cygni profile will result. If the re-emission occurs as a result of a different atomic process, for instance after a recombination of an electron into the upper level or after a spontaneous decay of a higher level into the upper level or after a collision, then the line source function will possibly not dilute and may roughly stay constant as a function of radius so that an emission line results. Typical examples for P-Cygni profiles are UV resonance transitions connected with the ground level, whereas excited lines of an ionization stage into which frequent

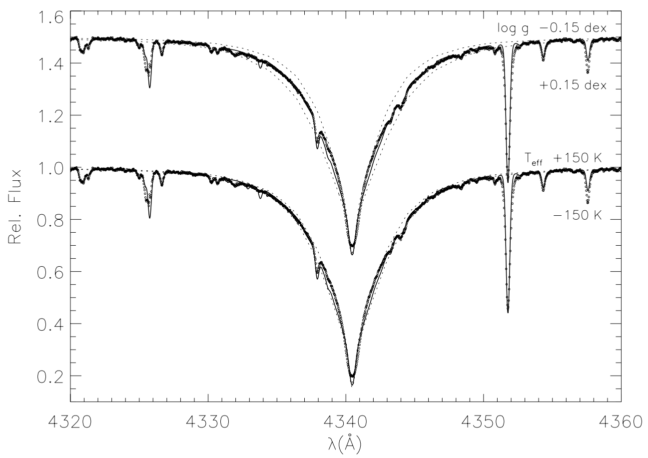

Fig. 7.6. Temperature and gravity dependence of H_γ of η Leo. See Fig. 7.5 for further annotations; from [24]

recombination from higher ionization stages occurs will produce emission lines. H_α in O-stars and early B-supergiants is a typical example for the latter case. However, for late B- and A-supergiants, when Ly_α becomes severely optically thick and the corresponding transition is in detailed balance, the first excited level of hydrogen becomes the effective groundstate and H_α starts to behave like a resonance line showing also the shape of a P-Cygni profile (for a more comprehensive discussion of the line formation process in winds see [8,11] and the most recent review [13]).

Terminal velocities can be determined very precisely from the blue edges of P-Cygni profiles and the red emission wings, normally with an accuracy of 5 to 10 percent (but see [13] for details). In addition, H_α profiles normally allow for a very accurate (20 percent) determination of mass-loss rates in all cases of O, B, and A-supergiants [27,12,16], but see [13,28] for details and problems.

Figure 7.10 gives an impression about the accuracy of the stellar wind spectral diagnostics for A-supergiants.

7.2.4 Spectral Resolution

For extragalactic applications beyond the Local Group spectral resolution becomes an issue. The important points are the following. Unlike the case of late type stars, crowding and blending of lines is not a severe problem for hot massive stars, as long as we restrict our investigation to the visual part of the spectrum. In addition, it is important to realize that massive stars have angular momentum, which leads to usually high rotational velocities. Even for A-supergiants, which have already expanded their radius considerably during their evolution and, thus, have slowed down their rotation, the observed projected rotational velocities are still on the order of $30\,\mathrm{km\,s^{-1}}$ or higher. This means that the in-

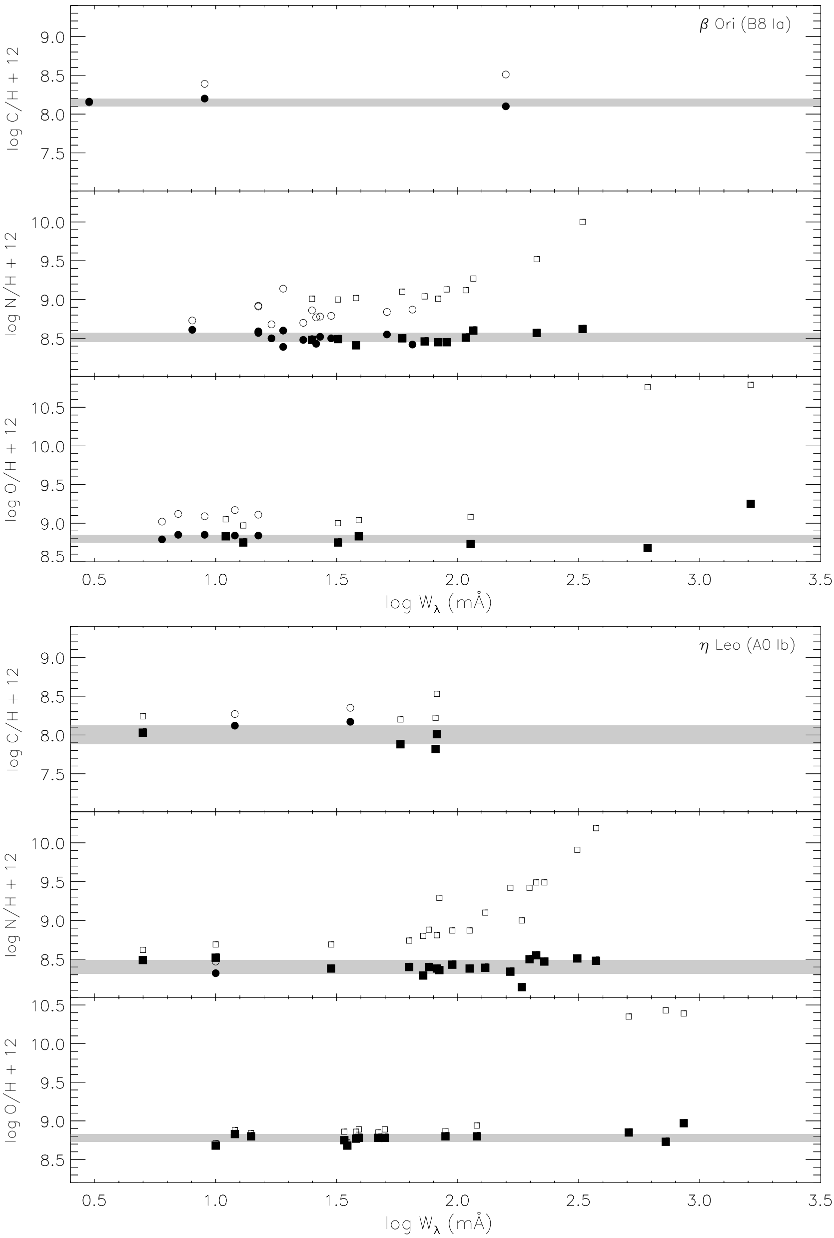

Fig. 7.7. Element abundances derived from individual spectral lines of CNO plotted as a function of equivalent width. *Top:* β Ori, *bottom:* η Leo. Open symbols refer to LTE calculations for the line formation, whereas solid symbols show the results of NLTE radiative transfer, for neutral (*boxes*) and ionized species (*circles*). It is evident that LTE fails badly, in particular, for stronger lines. The NLTE results are remarkably consistent; from [25]

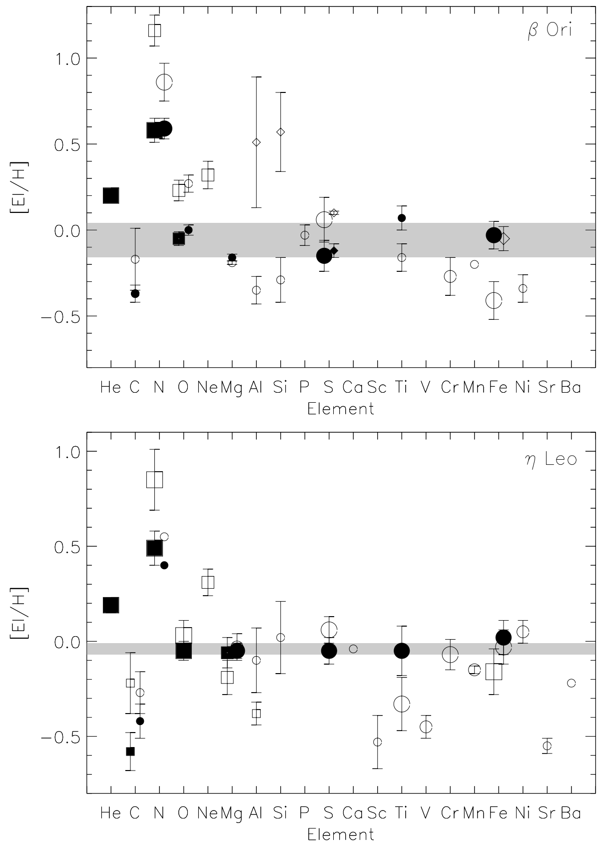

Fig. 7.8. Abundance pattern determined for the two Milky Way supergiants β Ori and η Leo, relative to the solar standard [6] on a logarithmic scale. NLTE (*filled symbols*) and LTE abundances (*open symbols*) for neutral (*boxes*), single-ionized (*circles*) and double-ionized (*diamonds*) species. The symbol size codes the number of spectral lines analyzed. Error bars represent 1σ-uncertainties from the line-to-line scatter. The grey shaded area marks the deduced stellar metallicity within 1σ-errors. The NLTE computations reveal a striking similarity to the solar abundance distribution, except for the light elements which have been affected by mixing with nuclear-processed matter; from [24]

trinsic full half-widths of metal lines are on the order of 1 Å. In consequence, for the detailed studies of supergiants in the Local Group a resolution of 25,000 sampling a line with five data points is ideal. This is indeed the resolution, which has been applied in most of the work referred to in the previous sections.

However, as we have found out empirically [24], degrading the resolution to 5,000 (FWHM = 1 Å) has only a small effect on the accuracy of the diagnostics, as long as the S/N remains high (i.e. 50 or better). Even for a resolution of 2,500

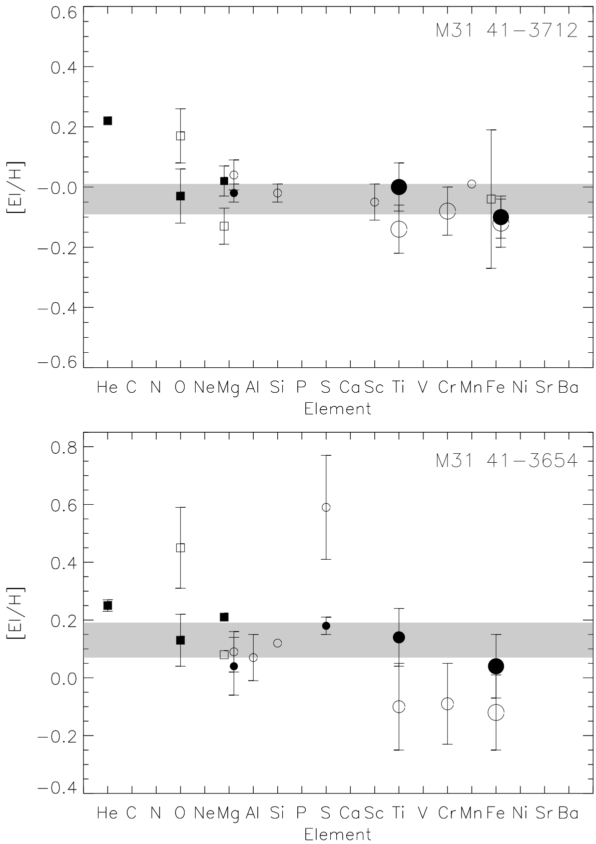

Fig. 7.9. Abundance pattern of the two M 31 A-supergiants 41-3712 and 41-3654. See Fig. 7.8 for further annotations; from [24]

(FWHM = 2 Å) it is still possible to determine T_{eff} to an accuracy of 2 percent, $\log g$ to 0.05 dex and individual element abundances to 0.1 or 0.2 dex.

References [2], [3], [4], [5] and [15] have used FORS at the VLT with a resolution of 1,000 (FWHM = 5 Å) to study blue supergiants far beyond the Local Group. The accuracy in the determination of stellar properties at this rather low resolution is still remarkable. The effective temperature is accurate to roughly 4 percent and the determination of gravity remains unaffected and is still good to 0.05 dex (an explanation will be given in Sect. 7.4). However, at this resolution it becomes difficult to determine abundance patterns of individual elements (except for emission line stars, see [4]) and, thus, one is restricted to the determination of the overall metallicity which is still accurate to 0.2 dex.

We can conclude that an optimum for extragalactic work is a resolution of 2,500 (FWHM = 2 Å). Blue supergiants are bright enough even far beyond the Local Group to allow the achievement of high S/N with reasonable exposure

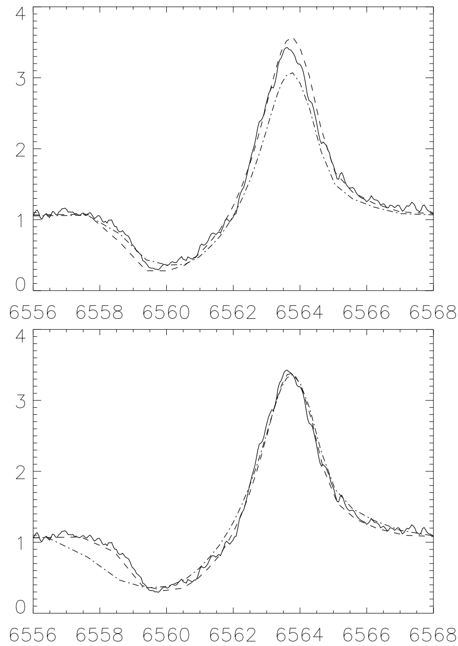

Fig. 7.10. *Top:* The influence of the mass-loss rate $\dot{M}$ on the H_α profile of the M 31 A-supergiant 41-3654. Two models with $\dot{M} = 1.65$ and $2.15 \times 10^{-6}\,M_\odot\,yr^{-1}$ (*dashed-dotted*, *dashed*) and otherwise identical parameters are shown superimposed on the observed profile. Bottom: The determination of v_∞. Two models with $v_\infty = 200$ and $250\,km\,s^{-1}$ (*dashed*, *dashed-dotted*) and $\dot{M}$ adopted to fit the height of the emission peak are shown superimposed to the observed profile. All other parameters are identical; from [16]

times at 8m-class telescopes with efficient multi-object spectrographs at this resolution, which then makes it possible to determine stellar parameters and chemical composition with sufficient precision. This resolution is also good enough to determine stellar wind parameters from the observed H_α profiles, since the stellar wind velocities (and therefore the corresponding line widths) are larger than $150\,km\,s^{-1}$.

7.3 The Wind Momentum–Luminosity Relationship

The concept of the Wind Momentum–Luminosity Relationship (WLR) has been introduced by [10] and [27]. It starts from a very simple idea. The winds of blue supergiants are initiated and maintained by the absorption of photospheric radiation and the photon momentum connected to it. Thus, the mechanical momentum flow of a stellar wind $\dot{M}v_\infty$ should be a function of the photon momentum rate L/c provided by the stellar photosphere and interior

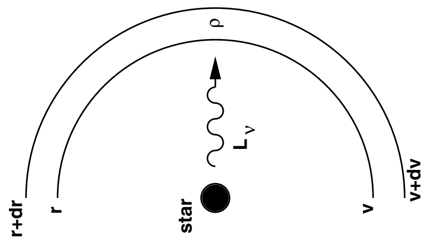

Fig. 7.11. Sketch of a blue supergiant irradiating its own stellar wind envelope. L_ν is the spectral luminosity at frequency ν. v is the wind outflow velocity at radius r and ϱ is the mass density

$$\dot{M} v_\infty = f(L/c) \ . \tag{7.1}$$

If this is true and if we are able to find this function f, this would enable us to determine directly stellar luminosities from the stellar wind by using the inverse relation

$$L = f^{-1}(\dot{M} v_\infty) \ . \tag{7.2}$$

In other words, by measuring the rate of mass-loss and the terminal velocity directly from the spectrum we would be able to determine the luminosity of a blue supergiant. This is an exciting perspective, because it would give us a completely new, purely spectroscopic tool to determine stellar distances. Quantitative spectroscopy would yield $T_{\rm eff}$, gravity, abundances, intrinsic colours, reddening, extinction, $\dot{M}$ and v_∞. With the luminosity from the above relation one could then compare with the dereddened apparent magnitude to derive a distance.

In the previous section, we already demonstrated how $\dot{M}$ and v_∞ can be determined from the spectrum with high precision. Thus, deriving the theoretical relationship and confirming and calibrating it observationally will enable us to introduce a new distance determination method. An accurate analytical solution of the hydrodynamic equations of line driven winds has been provided by [9]. These solutions were then used by [10] and [27] to exactly derive the relationship. Here, we apply a simplified approach, see also [11], which is not exact but gives insight in the underlying physics.

We assume that the wind is stationary and spherical symmetric and obeys the equation of continuity

$$\dot{M} = 4\pi r^2 \varrho(r) v(r) \ . \tag{7.3}$$

Then we consider the star as a point source of photons irradiating and accelerating its own stellar wind (see Fig. 7.11) and calculate the amount of photon momentum absorbed by one spectral line

$$\frac{L}{c} \frac{L_{\nu_i}(1 - e^{-\tau_i}) \mathrm{d}\nu^{\rm width}}{L} = \frac{L}{c^2} \frac{\nu_i L_{\nu_i}}{L} (1 - e^{-\tau_i}) \mathrm{d}v \ . \tag{7.4}$$

The first factor on the left side gives the total photon momentum rate provided by the star, the second describes the fraction absorbed by one spectral line in an outer shell of thickness dr. τ_i is the optical thickness of such an outer shell in the line transition i. $L_{\nu_i}\mathrm{d}\nu^{\mathrm{width}}$ is the stellar spectral luminosity at the frequency of line i multiplied by the spectral width of the line. This luminosity can in principle be absorbed by the line if it is entirely optically thick (i.e. $\tau_i \gg 1$). However, depending on the optical thickness only the fraction $(1-e^{-\tau_i})$ is really absorbed. If we are in the supersonic part of the wind, then the spectral width $\mathrm{d}\nu^{\mathrm{width}}$ is not determined by the thermal motion of the ions but rather by the increment of the velocity outflow dv via the Doppler formula

$$\mathrm{d}\nu^{\mathrm{width}} = \nu_i \frac{\mathrm{d}v}{c} \,, \tag{7.5}$$

which leads to the right hand side of (4).

After calculation of the photon momentum absorbed by a single spectral line we can consider the momentum balance in the stellar wind. The photon momentum absorbed by all lines will just be a sum over all lines i of the expression shown on the right hand side of (4). Almost all of this absorbed momentum will be transformed into gain of mechanical stellar wind flow momentum $\dot{M}\mathrm{d}v$ of the outer shell except the fraction $g(r)\mathrm{d}M_r$, which is the momentum required to act against the gravitational force ($g(r) = GM_*/r^2$ is the local gravitational acceleration and $\mathrm{d}M_r = \varrho 4\pi r^2 \mathrm{d}r$ is the mass within the spherical stellar wind shell)

$$\dot{M}\mathrm{d}v = \frac{L}{c^2}\sum_i \frac{\nu_i L_{\nu_i}}{L}(1-e^{-\tau_i})dv - G\frac{M*(1-\Gamma)}{r^2}\varrho 4\pi r^2 \mathrm{d}r \,. \tag{7.6}$$

Note that this momentum balance also includes the photon momentum transfer by Thomson scattering, which leads to the correction factor $(1-\Gamma)$ in the local gravitational acceleration.

Now, the important next step is to deal with the sum over all lines in the above momentum balance. Here, the complication arises from the term in parentheses containing the local optical depth τ_i of each line. τ_i will not only be different for each of the thousands of lines driving the wind, it will also vary through the stellar wind as a function of radius. On the other hand, one of the enormous simplifications in supersonically expanding envelopes around stars is that the optical thickness is well described by (see for instance [8])

$$\tau_i = k_i \kappa_{\mathrm{Thom}} \frac{v_{\mathrm{therm}}}{\mathrm{d}v/\mathrm{d}r} \,, \tag{7.7}$$

where v_{therm} is the thermal velocity of the ion and k_i is the (dimensionless) *line strength* defined as

$$k_i = \frac{\kappa_i}{\kappa_{\mathrm{Thom}}} \,, \tag{7.8}$$

i.e. the opacity of line i

$$\kappa_i = \frac{1}{\Delta\nu_{\mathrm{Dopp}}} \frac{\pi e^2}{m_e c} n_l f_{lu} \left(1 - \frac{n_u}{n_l}\frac{g_l}{g_u}\right) \tag{7.9}$$

in units of the continuous Thomson scattering opacity or in units of the local density

$$\kappa_{\mathrm{Thom}} = n_{\mathrm{e}}\sigma_{\mathrm{e}} = \varrho s_{\mathrm{e}} \; . \tag{7.10}$$

σ_{e} is the cross section for Thomson scattering of photons on free electrons, n_{e} the local number density of free electrons. In a hot plasma with hydrogen as the main constituent mostly ionized and with $Y_{\mathrm{He}} = n_{\mathrm{He}}/n_{\mathrm{H}}$ and I_{He} the number of electrons provided per helium nucleus we have (m_{H} is the mass of the hydrogen atom)

$$s_{\mathrm{e}} = \frac{1 + I_{\mathrm{He}}Y_{\mathrm{He}}}{1 + 4Y_{\mathrm{He}}} \frac{\sigma_{\mathrm{e}}}{m_{\mathrm{H}}} \; . \tag{7.11}$$

Thus, if the degree of ionization of helium is roughly constant as a function of radius r in the wind, s_{e} is also constant and we have

$$\tau_i = k_i s_{\mathrm{e}} \varrho(r) \frac{v_{\mathrm{therm}}}{\mathrm{d}v/\mathrm{d}r} \; , \tag{7.12}$$

with the line strength k_i proportional to oscillator strength f_{lu}, wavelength λ_i and the occupation number n_l of the lower level divided by the mass density ϱ

$$k_i \propto \frac{n_l}{\varrho} f_{lu} \lambda_i \; . \tag{7.13}$$

Thus, the line strength is roughly independent of the depth in the atmosphere and is determined by atomic physics (f_{lu}, λ_i) and atmospheric thermodynamics (n_l/ϱ). Since ϱ and $\mathrm{d}v/\mathrm{d}r$ vary strongly through the wind a line can be optically thick in deeper layers

$$\tau_i \gg 1 \Longrightarrow (1 - e^{-\tau_i})\mathrm{d}v \approx \mathrm{d}v \tag{7.14}$$

and can become optically thin further out

$$\tau_i \ll 1 \Longrightarrow (1 - e^{-\tau_i})\mathrm{d}v \approx k_i \varrho \mathrm{d}r \; . \tag{7.15}$$

For the calculation of the photon momentum transfer this means that line contributions can have an entirely different functional form depending on the optical thickness of the lines.

This problem can be solved in a very elegant way by introducing a *line strength distribution function*

$$\begin{aligned} n(k,\nu)\mathrm{d}\nu\mathrm{d}k = {} & \text{number of lines with } \nu_i \text{ from } (\nu, \nu + \mathrm{d}\nu) \\ & \text{and with } k \text{ from } (k, k + \mathrm{d}k) \; . \end{aligned}$$

Since the modern hydrodynamic model atmosphere codes (see Sect. 7.2) contain atomic data and occupation numbers for millions of lines in NLTE, we can investigate the physics of the line strength distribution function. As it turns out, [31,13,26,14], the distribution in line strengths – to a very good approximation – obeys a power law

$$n(k,\nu)\mathrm{d}\nu\mathrm{d}k = g(\nu)\mathrm{d}\nu k^{\alpha-2}\mathrm{d}k \; , 1 \le k \le \infty \tag{7.16}$$

independent (to first order) of the frequency. The exponent α depends weakly on $T_{\rm eff}$ and varies (in the temperature range of OB-stars) between

$$\alpha = 0.6 \ldots 0.7\,. \tag{7.17}$$

α is mostly determined by the atomic physics and basically reflects the distribution function of the oscillator strengths. One can, for instance, show that for the hydrogen atom the distribution of the Lyman-series oscillator strengths is a power law with exponent $\alpha = 2/3$, see [11]. It is important to realize that α is not a free parameter but, instead, is well determined from the thousands of lines taken into account in the model atmosphere calculations. Examples for the power law dependence of line strengths are given in [11] or [26].

With the line strength distribution function we can replace the sum in the momentum balance by a double integral, which is then analytically solved (see also [8]):

$$\sum_i \frac{\nu_i L_{\nu_i}}{L}(1-e^{-\tau_i}) \longrightarrow \int\limits_0^\infty\int\limits_0^\infty (1-e^{-\tau(k)})\frac{\nu L_\nu}{L} n(k,\nu)\mathrm{d}\nu\mathrm{d}k \longrightarrow N_o\left\{\frac{\mathrm{d}v/\mathrm{d}r}{\varrho}\right\}^{\alpha-1}\,. \tag{7.18}$$

This means that the momentum transfer from photons to the stellar wind plasma depends non-linearly on the gradient of the velocity field. The degree of the non-linearity is determined by the steepness of the line strength distribution function α. N_o is proportional to the number of lines in the line strength interval $1 \leq k \leq \infty$.

We can now re-formulate the momentum balance to obtain

$$\dot{M}\mathrm{d}v = \frac{L}{c^2}N_o\left\{\frac{\mathrm{d}v/\mathrm{d}r}{\varrho}\right\}^{\alpha-1}\mathrm{d}v - G\frac{M_*(1-\Gamma)}{r^2}4\pi r^2\varrho\mathrm{d}r \tag{7.19}$$

yielding a non-linear differential equation for the stellar wind velocity (note that we replaced the density through the mass conservation equation)

$$r^2 v\frac{\mathrm{d}v}{\mathrm{d}r} = \frac{L}{\dot{M}^\alpha}\frac{N_o}{c^2}(4\pi)^{\alpha-1}\left\{r^2 v\frac{\mathrm{d}v}{\mathrm{d}r}\right\}^\alpha - GM_*(1-\Gamma) \tag{7.20}$$

which looks much more complicated than it really is. The solution is easy, see [9]. We obtain $\dot{M}$ as the uniquely determined eigenvalue of the problem

$$\dot{M} \propto L^{1/\alpha}\{M_*(1-\Gamma)\}^{1-1/\alpha} \tag{7.21}$$

and a terminal velocity proportional to the escape velocity $v_{\rm esc}$

$$v_\infty \propto v_{\rm esc} \propto \{GM_*(1-\Gamma)/R_*\}^{1/2}\,. \tag{7.22}$$

Combining the two yields the stellar wind momentum

$$\dot{M}v_\infty \propto \frac{1}{R_*^{1/2}}L^{1/\alpha}\{M_*(1-\Gamma)\}^{3/2-1/\alpha}\,, \tag{7.23}$$

which – as expected – depends strongly on the luminosity but also on the photospheric radius and the expression in the parentheses, which contains the stellar mass and distance from the Eddington limit. It is this expression which can vary significantly for different blue supergiants and, therefore, causes the large scatter in the observed correlations of mass-loss rates with luminosity and terminal velocity with escape velocity as discussed previously. However, for the product of mass-loss rate and terminal velocity, the stellar wind momentum rate, the exponent of the term in brackets should be – thanks to the laws of atomic physics – very close to zero, since $\alpha \approx 2/3$. This means that to first order the wind momentum rate should be determined by

$$\dot{\mathbf{M}}\mathbf{v}_\infty \propto \frac{1}{R_*^{1/2}} \mathbf{L}^{1/\alpha} \, . \tag{7.24}$$

This is the *Wind Momentum - Luminosity Relationship.* It predicts a strong dependence of wind momentum rate on the stellar luminosity with an exponent determined by the statistics of the strengths of the tens of thousands of lines driving the wind. It also contains a weak dependence on stellar radius which comes from the fact that the stellar wind has to work against the gravitational potential when accelerated by photospheric photons.

References [27], [12] and [13] were the first to prove that the theoretically predicted WLR is really observed. O-stars, B and A-supergiants all follow this relationship. As to be expected, the relationship depends on spectral types, since lines of different ionization stages contribute to the mechanism of line driving at different spectra types. F. Bresolin, in this volume [5], gives a detailed overview about the most recent observational work on the WLR. Here, we only want to show the recent best calibration for A-supergiants using (only) four Milky Way and two M31 objects in Fig. 7.12. Although a calibration based on merely six objects is only moderately convincing, we are again encouraged by the small scatter over the remarkable range in luminosity. Future calibration work will be crucial to establish the method as an accurate distance indicator.

Also shown in Fig. 7.12 are recent theoretical stellar wind calculations for A-supergiants (R.P. Kudritzki, in prep.), which are based on the new radiation driven wind algorithm developed by [14]. The calculations provide a clear prediction about the metallicity dependence of A-supergiant wind momenta in agreement with previous work discussed in [13] and the recent work by [36] and [37]. F. Bresolin, in this volume [5], will discuss most recent extragalactic stellar wind diagnostics on blue supergiants and compare them with the model predictions.

7.4 The Flux-Weighted Gravity–Luminosity Relationship

It is an old idea that the strengths of the hydrogen Balmer lines and the absolute luminosities of massive stars must be related (see [5] in this volume for an overview). The concept behind this idea is very simple. Because of the effects of Stark broadening the Balmer lines in hot stars are very sensitive to the number

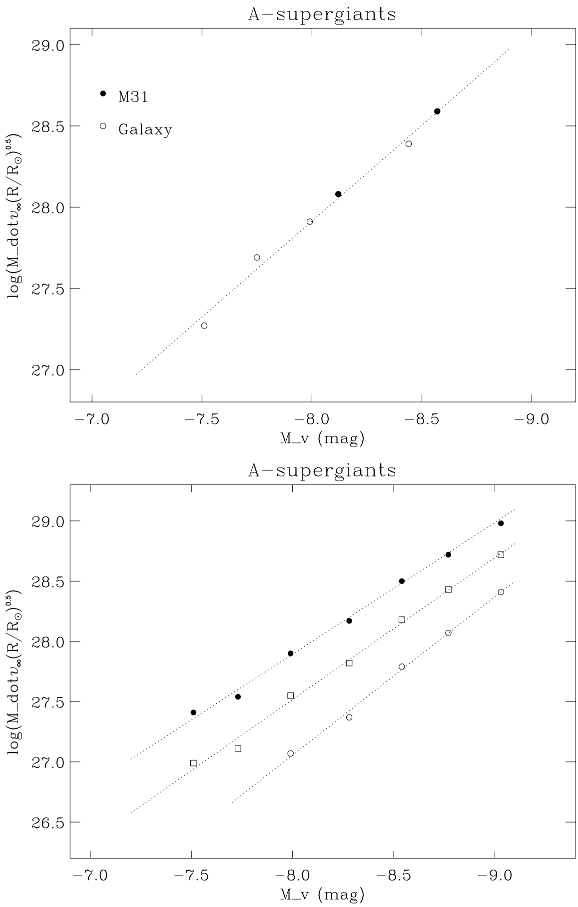

Fig. 7.12. The Wind Momentum – Luminosity Relationship of A-supergiants. Top: observed stellar wind momentum as a function of absolute magnitude for objects in the Milky Way and M 31; from [2]. Bottom: Theoretical calculations using the stellar wind code by [14], for solar metallicity (*solid circles*), 0.4 solar (*open squares*) and 0.1 solar (*open circles*)

densities of electrons and protons in those atmospheric layers, where the wings of the Balmer lines are formed. The number densities, on the other hand, depend on the photospheric gravity as the result of the hydrostatic equilibrium in stellar photospheres. Stellar gravities, however, reflect the evolution of massive stars away from the ZAMS (where all gravities are roughly the same) towards lower effective temperatures. They become smaller, as further the star evolves, and, if we compare objects with exactly the same effective temperature, more massive supergiant stars with higher luminosities are expected to have lower gravities than their counterparts with lower mass.

We illustrate the situation by using the stellar evolution models from Fig. 7.1. We select three values of $T_{\rm eff} = 12000$, 9500 and 8350 K, corresponding to spectral types B8, A0 and A4, respectively (see [5], this volume), and calculate absolute visual magnitudes and gravities for each track at each of the three $T_{\rm eff}$ values. Figure 7.13 displays the corresponding correlation of M_V with $\log g$ for each temperature. While the correlations are nicely parallel, the temperature dependence as a result of stellar evolution and bolometric correction is obvious.

We can now calculate atmospheric models for each pair of $T_{\rm eff}$ and $\log g$ and plot calculated H_γ equivalent widths EW as function of gravity and then, finally, produce a diagram of absolute magnitude versus H_γ equivalent width. This is also done in Fig. 7.13. Since the strengths of the Balmer lines do not only depend on gravity but also on temperature, the final correlation

$$M_V = f(EW(\mathrm{H}\gamma)\ , \mathbf{T_{eff}}) \tag{7.25}$$

depends very strongly on $T_{\rm eff}$. The equivalent widths are much stronger at lower $T_{\rm eff}$ and, as an additional complication, the slope of the correlation is strongly temperature dependent. While this result is, at least qualitatively, confirmed by observation [5], it is clear that simple empirical magnitude – equivalent width relations will have to suffer quite some intrinsic scatter unless it is restricted to accurate spectral sub-types. We, therefore, suggest a method, which overcomes the problem of the strong temperature dependence.

Before we do this important step, we draw attention to an important detail in Fig. 7.13. The plot equivalent width versus $\log g$ reveals that gravities can be determined with high precision for each effective temperature. An error of $\sim$10 percent in EW transforms to an error of 0.05 dex in $\log g$. Knowing that we will have many higher Balmer lines in the blue spectra of supergiants we feel confident that we can determine gravities with such accuracies, even if the spectroscopic resolution is only moderate.

We now turn to the derivation of the *Flux-Weighted Gravity – Luminosity Relationship* (FGLR), which was introduced very recently by [15]. When discussing Fig. 7.1 in Sect. 7.1 we noted that massive stars evolve through the domain of blue supergiants with constant luminosity and constant mass. This has a very simple, but very important consequence for the relationship of gravity and effective temperature along each evolutionary track. From

$$L \propto R^2 T_{\rm eff}^4 = \text{const.}; M = \text{const.} \tag{7.26}$$

follows immediately that

$$M \propto g\ R^2 \propto L\ (g/T_{\rm eff}^4) = \text{const.} \tag{7.27}$$

This means that each object of a certain initial mass on the ZAMS has its specific value of the *"flux-weighted gravity"* $g/T_{\rm eff}^4$ during the blue supergiant stage. This value is determined by the relationship between stellar mass and luminosity, which to a good approximation is a power law

$$L \propto M^x\ . \tag{7.28}$$

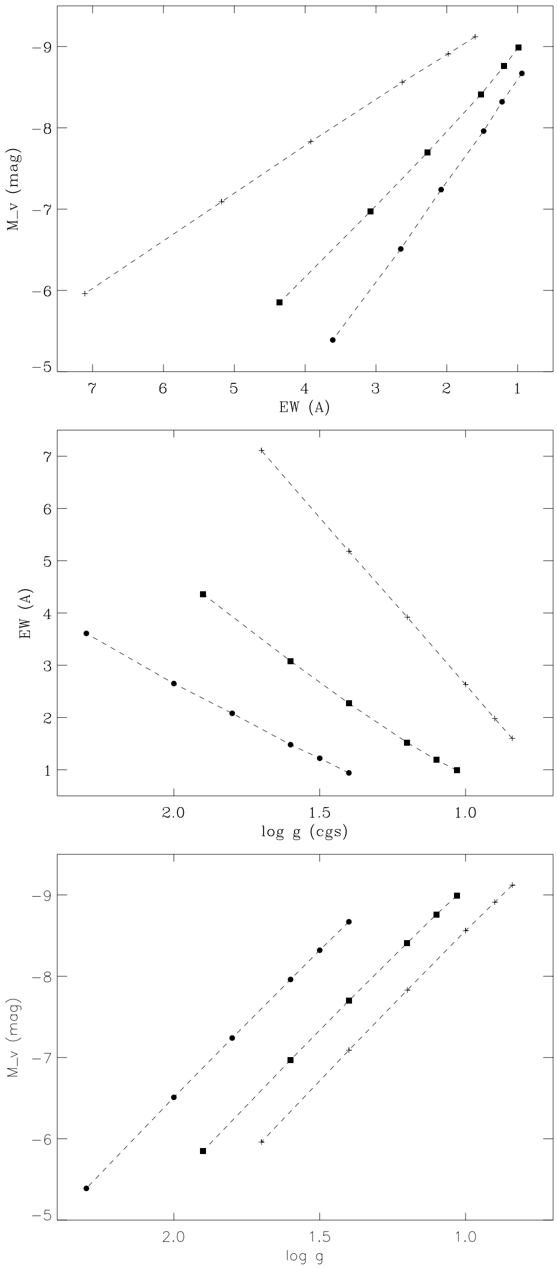

Fig. 7.13. Three steps to calculate the theoretical correlation between absolute magnitude M_V and H_γ equivalent width EW for three different values of $T_{\rm eff} = 8350\,$K (*crosses*), 9500 K (*squares*), 12000 K (*circles*). *Top:* M_V vs. EW. *Middle:* EW vs. $\log g$ as obtained from model atmospheres. *Bottom:* M_V vs. $\log g$ as obtained from stellar evolution

Inspection of evolutionary calculations with mass-loss, cf. [17] and [18], shows that $x = 3$ is a good value in the range of luminosities considered, although x changes towards higher masses. With the mass – luminosity power law we then obtain

$$L^{1-x} \propto (g/T_{\rm eff}^4)^x \ , \tag{7.29}$$

or with the definition of bolometric magnitude $M_{\rm bol} \propto -2.5 \log L$

$$-M_{\rm bol} = a \log(g/T_{\rm eff}^4) + b \ . \tag{7.30}$$

This is the FGLR of blue supergiants. Note that the proportionality constant a is given by the exponent of the mass – luminosity power law through

$$a = 2.5x/(1-x) \ . \tag{7.31}$$

and $a = -3.75$ for $x = 3$. Mass-loss will depend on metallicity and therefore affect the mass – luminosity relation. In addition, stellar rotation through enhanced turbulent mixing might be important for this relation. In order to investigate these effects we have used the models of [17] and [18] to construct the stellar evolution FGLR, which is displayed in Fig. 7.14. The result is very encouraging. All different models with or without rotation and with significantly different metallicity form a well defined very narrow FGLR.

With this nice confirmation of our basic concept we discuss the possible observational scatter arising from uncertainties in the determination of $T_{\rm eff}$ and $\log g$. As discussed in Sect. 7.2 and as also demonstrated by [15], effective temperature and gravity can be determined within 4 percent and 0.05 dex, respectively. Treating these errors as independent we derive an expected one sigma scatter $\Delta M_{\rm bol} = 0.3$ mag for the FGLR per individual object, which is again very encouraging and suggests that the method, after careful observational calibration (see [15] and [5], this volume), might become a powerful distance indicator.

Figure 7.15 demonstrates how precisely the Balmer lines can be fitted to yield a very accurate $\log g$ and Fig. 7.16 shows the first verification of the existence of a very tight FGLR for spiral galaxies beyond the Local Group. Further results are shown in [15] and [5].

7.5 Conclusions

We conclude that blue supergiants provide a great potential as excellent extragalactic distance indicators. The quantitative analysis of their spectra – even at only moderate resolution – allows the determination of stellar parameters, stellar wind properties and chemical composition with remarkable precision. In addition, since the spectral analysis yields intrinsic energy distributions over the whole spectrum from the UV to the IR, multi-colour photometry can be used to determine reddening, extinction laws and extinction. This is a great advantage over classical distance indicators, for which only limited photometric information is available, when observed outside the Local Group. Spectroscopy also allows to deal with the effects of crowding and multiplicity, as blue supergiants, due to

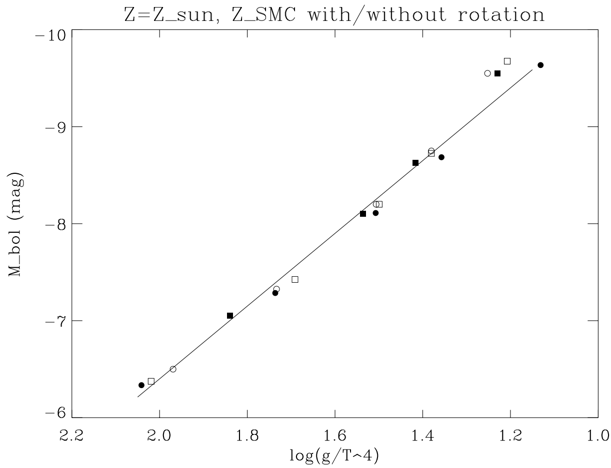

Fig. 7.14. The FGLR of stellar evolution models from [17] and [18]. *Circles* correspond to models with rotation, *squares* represent models without the effects of rotation. *Solid symbols* refer to galactic metallicity and *open symbols* represent SMC metallicity. The *solid curve* corresponds to $a = -3.75$ in the FGLR

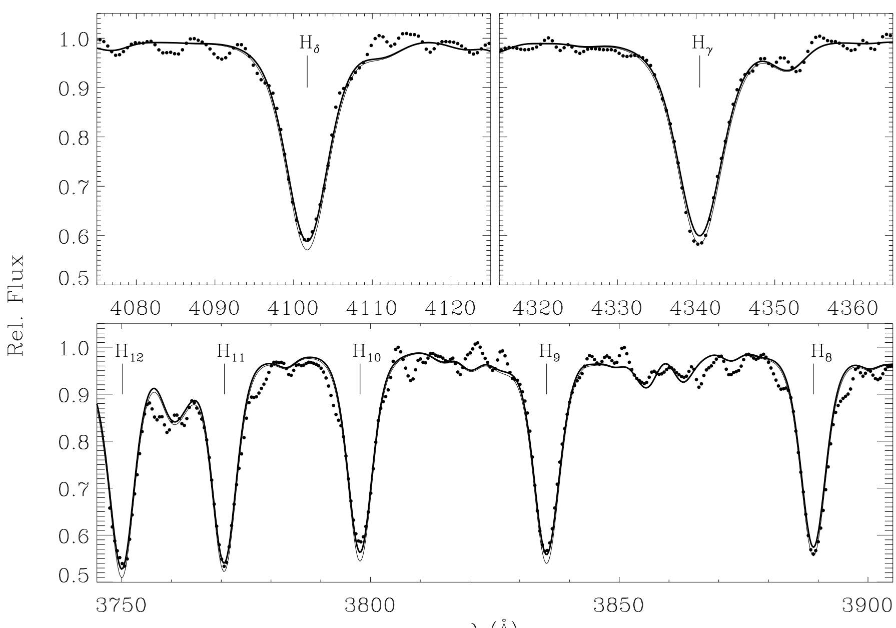

Fig. 7.15. Fit of the higher Balmer lines of an A-supergiant in the Sculptor galaxy NGC 300 using two atmospheric models with $T_{\rm eff} = 9500\,$K and $\log g = 1.60$ (*thick line*) and 1.65 (*thin line*), respectively. The data were taken with FORS at the VLT. For further discussion see [15]

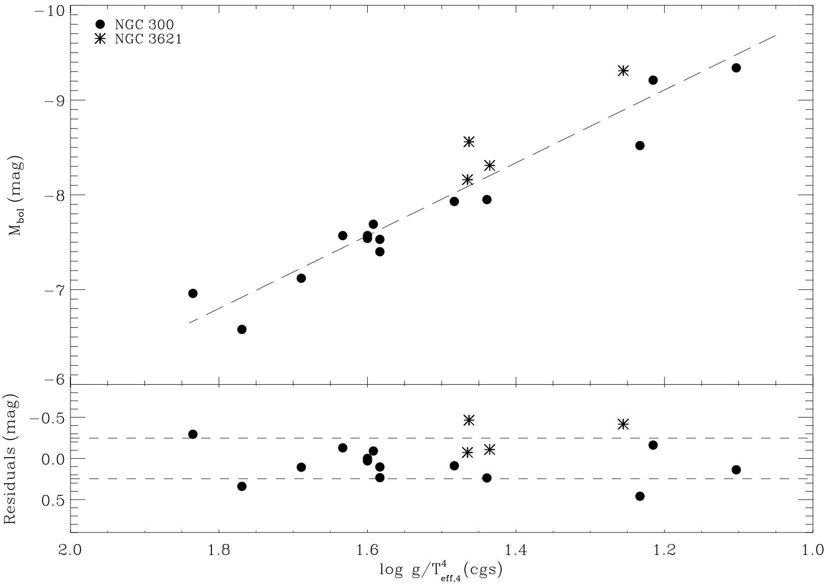

Fig. 7.16. The FGLR of B8 to A4 supergiants in NGC 300 and NGC 3621; from [15]

their enormous brightness, are less affected by such problems than for instance Cepheids, which are fainter.

Two tight relationships exist, the WLR and the FGLR, which can be used to derive accurate absolute magnitudes from the spectrum with an accuracy of 0.3 mag per individual object. Applying the methods on objects brighter than $M_V = -8$ mag and using multi-object spectrographs at 8 to 10m-class telescopes, which allow for quantitative spectroscopy down to $m_V = 22$ mag, we estimate that with 20 objects per galaxy we will be able to determine distances out to distance moduli of $m - M \sim 30$ mag with an accuracy of 0.1 mag. We note that these distances will not be affected by uncertainties in extinction and metallicity, because we will be able to derive the corresponding quantities from the spectrum.

Acknowledgements

It is a pleasure to thank the organizers of the workshop for a very stimulating meeting. We gratefully acknowledge the hospitality and support of the local team. We also wish to thank our colleagues Fabio Bresolin and Wolfgang Gieren for their significant contributions to this work.

References

1. S.R. Becker: ‘Non-LTE Line Formation for Iron-Group Elements in A Supergiants’. In: *Boulder-Munich II: Properties of Hot, Luminous Stars*, ed. by I.D. Howarth (ASP, San Francisco 1998) pp. 137–147

2. F. Bresolin, R.P. Kudritzki, R.H. Méndez, N. Przybilla: ApJ **548**, L159 (2001)
3. F. Bresolin, W. Gieren, R.P. Kudritzki, G. Pietrzynski, N. Przybilla.: ApJ **567**, 277 (2002)
4. F. Bresolin, R.P. Kudritzki, F. Najarro, W. Gieren, G. Pietrzynski: ApJ **577**, L107 (2002)
5. F. Bresolin: this volume (2003)
6. N. Grevesse, A.J. Sauval: Space Sci. Rev. **85**, 161 (1998)
7. D.G. Hummer, K.A. Berrington, W. Eissner, A.K. Pradhan, H.E. Saraph, J.A. Tully: A&A, **279**, 298 (1993)
8. R.P. Kudritzki: 'The Atmospheres of Hot Stars: Modern Theory and Observation'. In: *18th Advanced Course of the Swiss Society of Astrophysics and Astronomy (Saas-Fee Courses): Radiation in Moving Gaseous Media*, ed. by Y. Chmielewski and T. Lanz (Geneva Observatory 1988) pp. 1–192
9. R.P. Kudritzki, A.W.A. Pauldrach, J. Puls, D.C. Abbott: A&A **219**, 205 (1989)
10. R.P. Kudritzki, D.J. Lennon, J. Puls: 'Quantitative Spectroscopy of Luminous Blue Stars in Distant Galaxies'. In: *Science with the VLT*, ed. by J.R. Walsh, J. Danziger (Springer, Berlin 1995) pp. 246–255
11. R.P. Kudritzki: 'The Brightest Blue Supergiant Stars in Galaxies'. In: *Proc. VIII Canary Island Winter School of Astrophysics: Stellar Astrophysics for the Local Group*, ed. by A. Aparicio, A. Herrero, F. Sánchez (Cambridge University Press, Cambridge 1998) pp. 149 – 262
12. R.P. Kudritzki, J. Puls, D.J. Lennon, K.A. Venn, J. Reetz, F. Najarro, J.K. McCarthy, A. Herrero: A&A **350**, 970 (1999)
13. R.P. Kudritzki, J. Puls: ARA&A **38**, 613 (2000)
14. R.P. Kudritzki: ApJ **577**, 389 (2002)
15. R.P. Kudritzki, F. Bresolin, N. Przybilla: ApJ **582**, L83 (2003)
16. J.K. McCarthy, R.P. Kudritzki, D.J. Lennon, K.A. Venn, J. Puls: ApJ **482**, 757 (1997)
17. G. Meynet, A. Maeder, G. Schaller, D. Schaerer, C. Charbonnel: A&AS **103**, 97 (1994)
18. G. Meynet, A. Maeder: A&A **361**, 101 (2000)
19. A.W.A. Pauldrach, T.L. Hoffmann, M. Lennon: A&A **375**, 161 (2001)
20. N. Przybilla, K. Butler, S.R. Becker, R.P. Kudritzki, K.A. Venn: A&A **359**, 1085 (2000)
21. N. Przybilla, K. Butler, S.R. Becker, R.P. Kudritzki: A&A **369**, 1009 (2001)
22. N. Przybilla, K. Butler, R.P. Kudritzki: A&A **379**, 936 (2001)
23. N. Przybilla, K. Butler: A&A **379**, 955 (2001)
24. N. Przybilla: PhD Thesis, Ludwig-Maximilians-Universität, München (2002)
25. N. Przybilla, R.P. Kudritzki, K. Butler, S.R. Becker: 'Non-LTE line-formation for CNO'. In: *CNO in the Universe*, ed. by C. Charbonnel, D. Schaerer, G. Meynet (ASP, San Francisco 2003) in press
26. J. Puls, U. Springmann, M. Lennon: A&AS **141**, 23 (2000)
27. J. Puls, R.P. Kudritzki, A. Herrero, A.W.A. Pauldrach, S.M. Haser, D.J. Lennon, R. Gabler, S.A. Voels, J.M. Vilchez, S. Wachter, A. Feldmeier: A&A **305**, 171 (1996)
28. J. Puls, T. Repolust, T. Hoffmann, A. Jokuthy, R. Venero: 'Advances in Radiatively Driven Wind Models'. In: *A Massive Star Odyssey, from Main Sequence to Supernova, Proceedings of IAU Symposium No. 212*, ed. by K.A. van der Hucht, A. Herrero, C. Esteban (ASP, San Francisco 2003) in press
29. A.E. Santolaya-Rey, J. Puls, A. Herrero: A&A **323**, 488 (1997)

30. M.J. Seaton, Y. Yu, D. Mihalas, A.K. Pradhan: MNRAS, **266**, 805 (1994)
31. U. Springmann: PhD Thesis, Ludwig-Maximilians-Universität, München (1997)
32. K.A. Venn: ApJS **99**, 659 (1995)
33. K.A. Venn: ApJ **518**, 405 (1999)
34. K.A. Venn, J.K. McCarthy, D.J. Lennon, N. Przybilla, R.P. Kudritzki, M. Lemke: ApJ **541**, 610 (2001)
35. K.A. Venn, D.J. Lennon, A. Kaufer, J.K. McCarthy, N. Przybilla, R.P. Kudritzki, M. Lemke, E.D. Skillman, S.J. Smartt: ApJ **547**, 765 (2001)
36. J.S. Vink, A. de Koter, H.J.G.L.M. Lamers: A&A **362**, 295 (2000)
37. J.S. Vink, A. de Koter, H.J.G.L.M. Lamers: A&A **369**, 574 (2001)

8 Blue Supergiants as a Tool for Extragalactic Distances – Empirical Diagnostics

Fabio Bresolin

Institute for Astronomy, University of Hawaii, Honolulu, HI 96822, USA

Abstract. Blue supergiant stars can be exceptionally bright objects in the optical, making them prime targets for the determination of extragalactic distances. I describe how their photometric and spectroscopic properties can be calibrated to provide a measurement of their luminosity. I first review two well-known techniques, the luminosity of the brightest blue supergiants and, with the aid of recent spectroscopic data, the equivalent width of the Balmer lines. Next I discuss some recent developments concerning the luminosity dependence of the wind momentum and of the flux-weighted gravity, which can provide, if properly calibrated, powerful diagnostics for the determination of the distance to the parent galaxies.

8.1 Introduction

Massive stars can reach, during certain phases of their post-main sequence evolution, exceptional visual luminosities, approaching $M_V \sim -10$ in extreme cases. It is thus natural to try and use them as standard candles for extragalactic studies, as was realized long ago by Hubble. For this contribution I will concentrate on the blue supergiants, a rather broad but useful definition for the stars contained in the upper part of the H–R diagram and with spectral types O, B and A. This includes 'normal' supergiants (Ia) and hypergiants (Ia$^+$), as well as more exotic objects such as the Luminous Blue Variables (LBV's). Very bright stars can also be found among the yellow hypergiants, however their identification in extragalactic systems is more problematic, because their intermediate color coincides with that of numerous Galactic foreground dwarfs.

From the point of view of the extragalactic distance scale, it is not the most massive, intrinsically most *luminous* O-type stars ($M_{bol} \leq -11$) which are appealing. Because of the decrease of the bolometric correction with temperature from O to A stars down to $\sim 7000\,\mathrm{K}$, the *visually brightest* supergiants found in galaxies are mostly 25–40 $\mathcal{M}_\odot$ mid-B to early-A type stars, with M_{bol} between -8 and -9 [48]. This can be seen from Table 8.1, which is a (probably incomplete) compilation of the visually brightest blue stars in the Milky Way, LMC and SMC, excluding in general LBV's with maximum light amplitudes larger than 0.5 mag. The label LBV in the last column identifies known or suspected LBV's, from the compilation of [87]. Sources for the photometry and spectral types are given as a footnote to the table, however in a few cases the data have been updated with more recent determinations. The absolute visual magnitudes have generally been corrected for extinction by assuming the spectral type vs. $B-V$

F. Bresolin, Blue Supergiants as a Tool for Extragalactic Distances – Empirical Diagnostics, Lect. Notes Phys. **635**, 149–174 (2003)
http://www.springerlink.com/

Table 8.1. The visually brightest blue stars in the Milky Way, LMC and SMC

Star ID		$M_{V,0}$	Spectral Type
Milky Way	$M_{V,0} \leq -8.0$		
HD	other		
	Cyg OB2-12	−10.4	B5 Ie LBV
80077		−9.4	B2/3 Ia^+ LBV
92693		−8.73	A2 Ia
152236	ζ^1 Sco	−8.70	B1.5 Ia^+
	WRA977	−8.7	B1.5 Ia^+
92207		−8.55	A0 Ia
197345	α Cyg	−8.45	A2 Iae
168607		−8.4	B9 Ia^+ LBV
316285	He3-1482	−8.4	BIe LBV
169454		−8.29	B1 Ia^+
	MWC314	−8.2	<B2 LBV
92964		−8.17	B2.5 Iae
223385	6 Cas	−8.00	A3 Iae
LMC	$M_{V,0} \leq -8.5$		$m - M = 18.5$
HD	Sk		
33579	−67 44	−9.57	A4 Ia^+
269902	−69 239	−9.34	B9 Iae
32034	−67 17	−9.03	B9 Iae
270086	−69 299	−8.91	A1 Ia^+
269546	−68 82	−8.89	B3 Iab
269923	−69 247	−8.85	B6 Iab
269857	−68 131	−8.80	A9 Ia
269781	−67 201	−8.77	A0 Iae
269331	−69 93	−8.67	A5 Ia
268654	−69 7	−8.63	B9 Iae
268835	−69 46	−8.60	B8p
269128	−68 63	−8.6	B2.5 Ia^+ LBV
269661	−69 170	−8.56	B9 Ia^+
268718	−69 16	−8.52	B9 Iabe
268946	−66 58	−8.51	A0 Ia
37836	−69 201	−8.5	B pec LBV
SMC	$M_{V,0} \leq -8.0$		$m - M = 19.0$
AV	Sk		
475	152	−9.15	A0 Ia^+
136	54	−8.41	A0 Ia
	56	−8.32	B8 Ia^+
315	106	−8.30	A0 Ia
78	40	−8.30	B1.5 Ia^+
443	137	−8.21	B2.5 Ia
56	31	−8.17	B2.5 Ia
65	33	−8.15	B8 Ia^+
48	27	−8.08	B5 Ia
76	39	−8.07	B9 Ia^+

SOURCES — MILKY WAY - [34]. Distance to HD 92207, HD 92693, HD 92964 and HD223385: [23]. Cyg OB2-12: [49]. LBV data from [87]. LMC - [67]. SMC - [6], [47].

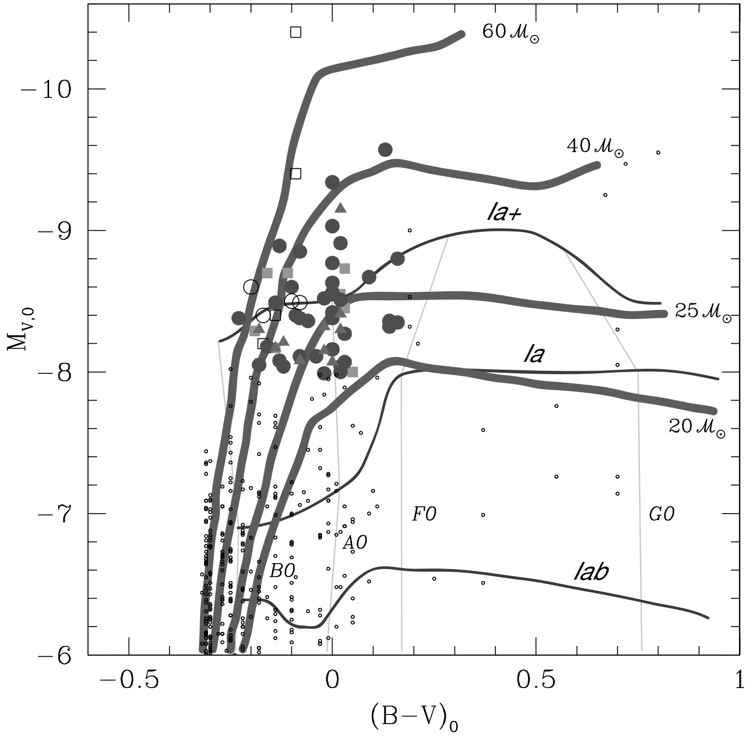

Fig. 8.1. In this color-magnitude diagram the brightest stars having $M_V < -8$ in the Milky Way (*squares*), LMC (*circles*) and SMC (*triangles*) are shown with the larger symbols. *Open symbols* refer to confirmed or candidate LBV's with magnitude variations smaller than 0.5 mag. The *small points* represent Galactic stars fainter than $M_V = -8$ and/or of spectral type F and later. Schematic evolutionary models at solar metallicity and various ZAMS masses from [52] are shown by the *thick lines.* The grid giving luminosity classes and spectral types is from [45]

color index relation in the MK system given by [45] and $A_V = 3.1 \times E_{B-V}$. Stars brighter than $M_V = -8.0$ in all three galaxies are plotted in the color-magnitude (c-m) diagram of Fig. 8.1, together with the loci of Ia$^+$, Ia and Iab stars, and stellar tracks for 60, 40, 25 and 20 $\mathcal{M}_\odot$ from [52].

Extragalactic stellar astronomy has quickly evolved from the identification, via photometry and qualitative spectroscopy, of individual bright stars mostly within galaxies of the Local Group, to the quantitative analysis of stellar spectra well beyond the boundaries of the Local Group. The observation and analysis of extragalactic supergiants has important ramifications for the study of massive stellar evolution with mass loss, supernova progenitors, stellar instabilities near the upper boundary of the stellar luminosity distribution, and chemical abundances. Here I review four different techniques concerning the use of blue supergiants in the context of measuring extragalactic distances. Two of them have quite a long history:

- *luminosity of the brightest blue supergiants*
- *equivalent width of the Balmer lines*

while the two remaining ones are based on more recent developments in the analysis of stellar winds and the atmospheres of blue supergiant stars:

- *the wind momentum–luminosity relationship*
- *the flux-weighted gravity–luminosity relationship*

8.2 The Luminosity of the Brightest Blue Supergiants as a Standard Candle

Since the pioneering work of Hubble [29] a great amount of efforts have been devoted to the calibration of the luminosity of the visually brightest blue and red supergiant stars in nearby galaxies as a distance indicator. This work culminated in a series of papers by A. Sandage, R. Humphreys and others in the 1970–80's on the bright stellar content of galaxies in the Local Group and in a handful of more distant late-type spirals (see reviews by [70], [31] and, more recently, [68]). While the brightest red supergiants were soon recognized as a more accurate secondary standard, thanks to the smaller dependence of their brightness on the parent galaxy luminosity, here I will briefly summarize the work concerning the brightest blue stars, generally of types from late B to A. Note that a photometric color selection criterion $(B - V)_0 < 0.4$ isolates supergiants of spectral type earlier than F5. Even if nowadays this method is not considered sufficiently accurate when compared with the best available extragalactic distance indicators, it has been adopted also during the past decade whenever observational material on more accurate distance indicators (Cepheids, TRGB, SN Ia, etc.) was lacking.

Some of the main difficulties in using the luminosity of the brightest stars in galaxies as a standard candle were recognized by Hubble himself, namely the unavoidable confusion between real 'isolated' stars and unresolved small stellar clusters or H II regions, and the presence of foreground objects in the Galaxy. While the latter problem is easily solved by avoiding stars of intermediate color in the c-m diagram, the former is much more subtle, eventually becoming the main criticism to the bright blue star method raised by Humphreys and collaborators [33,32], who, with stellar spectroscopy in some of the nearest galaxies, revealed the composite nature of many of those objects which were previously considered to be the brightest stars.

Hubble's original calibration of the mean absolute magnitude of the three brightest stars in a galaxy, $M_B(3)_0$, introduced as a more robust measure of the visually most luminous stars than the single brightest star, was flawed (he adopted $< M_{pg} > \simeq -6.3$, about 3 magnitudes too faint), which was partly responsible for the large value he found for the expansion rate of the universe.

The dependence of $M_B(3)_0$ on the parent galaxy luminosity $[M_B(3)_0 \propto M(\mathrm{gal})_0]$, an effect already discussed by Hubble and by Holmberg, was first investigated in detail by [71] as part of a series of papers on the brightest stars in resolved spiral and irregular galaxies, with distances calibrated via observations of Cepheids (see [69], and references therein). The existence of such a correlation hampers the use of the luminosity of the brightest blue stars as a standard candle. Moreover, the standard deviation of a single observation as measured by [71] was $\simeq 0.5$ mag, much larger than their quoted 0.1 mag for the standard deviation of the mean of the three brightest red supergiants. The latter were later also found to obey a dependence on the parent galaxy luminosity, albeit with a shallower slope.

The $M_B(3)_0$–$M(\mathrm{gal})_0$ relationship has been customarily interpreted as a statistical effect, since more luminous and larger galaxies can populate the stellar luminosity function up to brighter magnitudes than smaller galaxies. A flattening of this relation might be detected in galaxies brighter than $M(\mathrm{gal})_0 = -19$ [70], corresponding to the total luminosity of large spirals, in which the observed limit is simply imposed by the luminosity of the brightest post-main sequence B- and A-type stars in the H–R diagram. Therefore, while large, late-type spiral galaxies, such as M101, may contain stars as bright as $M_B \simeq -10$, the brightest blue stars in dwarfs like NGC 6822 or IC 1613 are found at $M_B \simeq -7$. Numerical simulations by [73] and [25] have provided support for the statistical interpretation, making variations in the stellar luminosity and mass function among galaxies unnecessary to explain the observed trend.

Among the most recent compilations of the brightest blue stars in nearby resolved galaxies is that of [24], based on updated stellar photometry of galaxies included in previous works by [59], [38] and [68]. The resulting relation between $M_B(3)_0$ and parent galaxy total luminosity is shown in Fig. 8.2, where different symbols are used for 17 *standard* galaxies and a few *test* galaxies (only those with available Cepheid distances from the list of [24] are shown, together with IC 4182 [69]). In this plot, distances for some of the galaxies have been updated from the results of the HST Key Project, as summarized by [20] (as an aside, no systematic study of the brightest stars in the whole sample analyzed by the Key Project has been published). The standard galaxies define a linear regression:

$$M_B(3)_0 = -1.76\ (\pm 0.45) + [0.40\ (\pm 0.03)]\ M_B(\mathrm{gal})_0 \tag{8.1}$$

with a standard deviation $\sigma(M_B) = 0.26$. The rather small dispersion is, at least partly, a result of the particular selection of the ‘standard’ galaxies made by [24]. In fact, $\sigma(M_B) \simeq 0.6$ is obtained from the data of [59] and [68]. Differences in the treatment of foreground and internal extinction exist between different authors. Furthermore, [70] has advocated the use of the irregular blue variables among the brightest blue stars, a view strongly opposed by [33]. We must also note that consensus still has to be reached concerning the choice of the individual brightest blue stars in the most luminous galaxies in Fig. 8.2. For example, spectroscopy of bright objects in M81 by [96] has revealed that none of the seven brightest supergiant candidates could be confirmed as a single star, imposing a fainter upper limit for $M_B(3)_0$. The points in Fig. 8.2 corresponding to the other luminous galaxies, M31 and M101, are likely to be affected by similar problems, and could therefore also be revised to lower $M_B(3)_0$ values.

Numerical simulations such as those by [73], shown by the dotted (50 % limits of the probability distribution) and long-dashed (99.5 %) curves, can explain

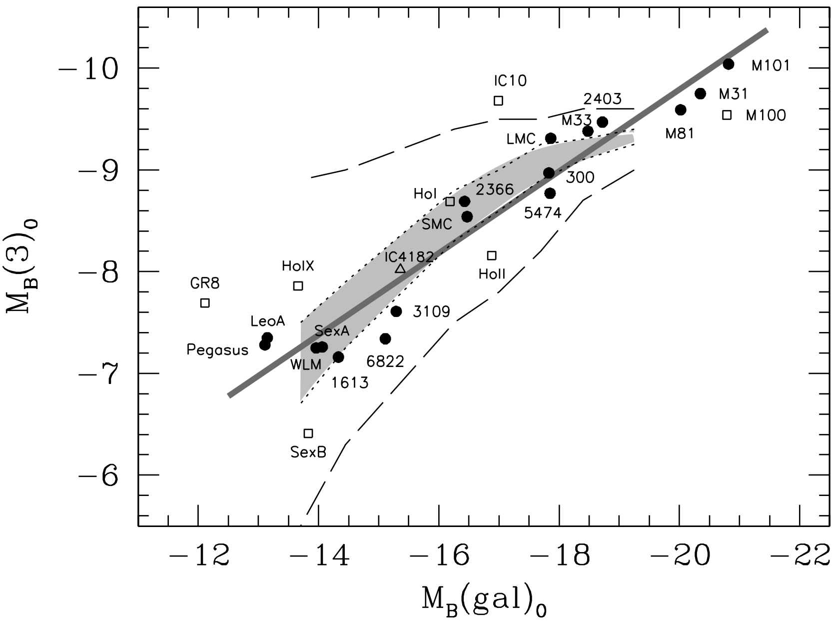

Fig. 8.2. The relationship between the average magnitude of the three brightest blue stars and the magnitude of the parent galaxy. Data from [24], with minor updates on the distances. *Full dots* refer to the calibration galaxies, while the *open symbols* are used for the additional test galaxies for which a Cepheid distance is available. The *straight line* represents the linear regression to the calibration points. The numerical simulations showing the 50 % and 99.5 % limits of the probability distribution (*dotted* and *long-dashed* lines, respectively) are from [73]

both the trend, which however is predicted not to be linear, and the dispersion in the observational data, at least up to the maximum galaxy brightness considered in the models. It appears that removing objects with Cepheid distances from the linear regression as done by [24] (those shown here by the open symbols) might not be fully justified, since a considerable dispersion at the low-luminosity end is expected from the incomplete filling of the stellar luminosity function. However, considerations on the evolutionary status of some of the dwarf galaxies might provide some justification for the removal of some of the data points.

The general conclusion we can draw from these results is that distance moduli to individual galaxies cannot be determined from the simple photometry of bright blue stars to better than at least 0.5 mag (0.9 mag according to [68]). This is larger than $\sigma(M_B)$, as a result of the strong dependence of $M_B(3)_0$ on $M(\mathrm{gal})_0$. Moreover, the necessity of spectroscopic confirmation of the brightest stars must be stressed. Outside of the Local Group, after the initial efforts at moderate resolution in M81, NGC 2403, M101 [32,96], high-quality spectroscopy of the bright stellar content of galaxies has come within reach of modern equipment on 8m-class telescopes at increasing distances. As an example, I cite the work by [8] and [9] in NGC 3621 and NGC 300, which will be discussed later in this paper.

To conclude the section on extragalactic distances based on the luminosity of the brightest blue stars, a handful of works published in the last decade can be highlighted:

– *brightest stars in galaxies with radial velocities* $< 500\,km\,s^{-1}$*:* a project aiming at the measurement of the distance of a large number of (mostly dwarf) resolved galaxies in the Local Volume ($v_{rad} < 500\,\mathrm{km\,s^{-1}}$) has been carried out since 1994 by Karachentsev and collaborators, using a $M_B(3)_0$ calibration obtained by [38] (see [75], [16] and references therein). Recently the TRGB method is being used [39].

– *brightest stars in Virgo galaxies:* brightest star candidates have been detected from ground-based images taken under excellent seeing conditions in two Virgo spirals, NGC 4523 [74] and NGC 4571 [57]. Distances of 13 (±2) and 14.9 (±1.5) Mpc were derived, respectively, from yellow and blue supergiants. The brightest stars in a third galaxy in Virgo, M100, were discussed by [21], based on HST WFPC2 images. The Cepheid distance from the HST Key Project is 14.3 (±0.5) Mpc.

– *additional galaxies in the field (D$\sim$ 7-8 Mpc):* the brightest blue and red supergiants have been used by [77], [78] and [79] to measure distances to a few spiral galaxies, including NGC 925 and NGC 628, adopting the calibration of [68].

8.3 Spectroscopic Diagnostics: Equivalent Width of the Balmer Lines

The spectroscopic approach alleviates the major difficulties of the photometric method described in the previous section. Small clusters, close companions and H II regions can be easily identified from line profiles, composite appearance of the spectrum and presence of nebular lines. In addition, the analysis of the spectral diagnostics (equivalent widths, line profiles, continuum fluxes) can provide detailed information on element abundances, spectral energy distributions, wind outflows and stellar reddening.

The discovery of a relationship between stellar optical spectral lines and luminosity dates back to the 1920's, when the character of the lines, diffuse vs. sharp, and their strength were found to correlate with the absolute magnitude of stars of type A and B [1,2,17,93]. The hydrogen Balmer lines in particular were soon recognized to play an important role in connection with the problem of measuring stellar luminosities using spectra, a fact which continues to hold true even for the most recent techniques involving the spectral analysis of blue supergiants. The luminosity effect on the width of the Balmer lines derives from their dependence on the pressure (Stark broadening), as realized by [30] and [80], with a line absorption coefficient in the wings proportional to the electron pressure (and also dependent on the temperature). As a result, narrower and weaker lines are formed with decreasing pressure and surface gravity, and consequently with increasing luminosity.

I will not discuss here additional, somewhat related methods, including: *i*) the relationship between M_V and the strength of the O I triplet at $\lambda \sim 7774$ Å, which holds for the A–G spectral types [4]; *ii*) the strength and the effective wavelength of the Balmer jump, as in the Barbier, Chalonge & Divan classification system [12], and *iii*) photometric indexes centred on selected Balmer lines, such as the β index used by [14], [15] and [95]. Another luminosity diagnostic for B9–A2 supergiants, the strength of the Si II $\lambda\lambda 6347, 6371$ lines, was proposed by [66], but [19] showed that this indicator breaks down for bright SMC stars, as a likely effect of the reduced metallicity.

Work by [56] on the equivalent width of the Hγ line, W(Hγ), led to a calibration of its relationship with absolute magnitude, lower values of W(Hγ) being found for high-luminosity stars. A spectral type dependence among the B and A stars of different luminosity classes was also detected. The cut-off at the bright end of this early calibration ($M_V > -7$) was imposed by the scarcity of supergiant stars with known distances.

Refinements to the calibration of this technique were introduced by [7] and by [37]. The latter used a W(Hγ)–M_V calibration based on Galactic stars to estimate the distance to the Magellanic Clouds, thus pioneering stellar spectroscopy as a way to determine extragalactic distances (see also [13]). More recent calibrations have been proposed by [54] (O–A dwarfs and giants), [92] and [28] (supergiants), accounting for the spectral type dependence. Among the applications, I recall the work by [5], who used W(Hγ) to determine luminosity classes for a large number of stars in the SMC.

Correlations between Balmer lines of blue supergiants and stellar luminosity are not restricted to the use of Hγ. A strong luminosity effect on the Hα line was found from narrow-band photometry of Galactic early-type stars by [3]. Later [82] turned their attention to the equivalent width of the Hα and Hβ lines in a sample of B–A supergiants in the LMC and SMC. The availability in these extragalactic systems of a large number of blue supergiants up to extreme luminosities, all at a common distance and with small reddening, is a major advantage for calibration purposes. The Hα and Hβ lines are in emission for the visually brightest blue stars in the Clouds, as recognized since the early stellar spectroscopic work in these galaxies [18], a signature of the presence of extended atmospheres and mass loss through stellar winds. The luminosity effect is particularly strong in Hα, which in late-B and early-A supergiants begins to show a clear emission nature, mostly with a characteristic P-Cygni profile, around $M_V = -7$ [65]. The filling of the line profiles by stellar wind becomes progressively smaller as one proceeds to Balmer lines of higher order, so that Hγ, Hδ, etc. are increasingly better diagnostics of stellar surface gravity. Examples of Hα, Hβ and Hγ line profiles are shown in Fig. 8.3 for stars of different visual brightness, from $M_V = -9.3$ to -6.2 in the LMC (the two brightest objects), the Milky Way (HD 92207) and NGC 300 (the three fainter objects), all plotted at the same intermediate spectral resolution. Excellent examples of higher resolution

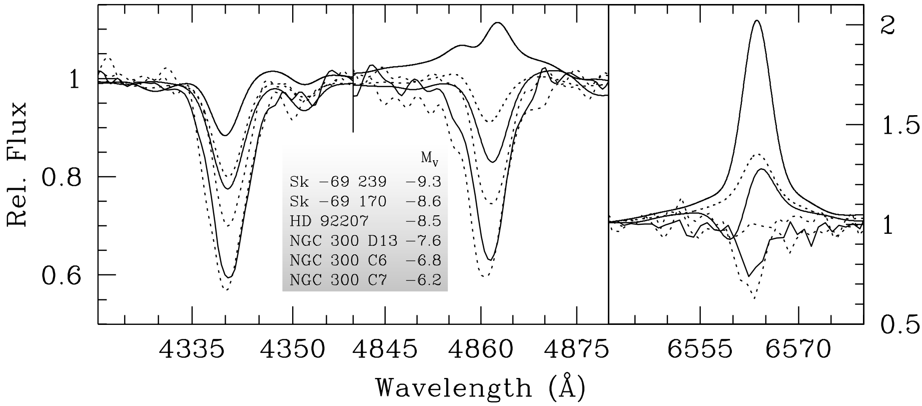

Fig. 8.3. Examples of Hγ (*left*), Hβ (*middle*) and Hα (*right*) line profiles in blue supergiants of different visual brightness (decreasing from top to bottom, as indicated in the legend) in the LMC, Milky Way and NGC 300. The LMC and Galactic spectra (courtesy N. Przybilla and R. Kudritzki) have been degraded to the 5 Å resolution of the NGC 300 data

profiles of Balmer lines of B–A supergiants can be found in the papers by [65], [40] and [89].

For extragalactic distance studies it is essential that the scatter in the relationships between observables be small. In the case of the equivalent width of Hα and Hβ vs. magnitude, the rms scatter found by [82] for about 40 B5–A0 supergiants in the LMC was 0.3–0.4 mag. However, the scatter doubles for similar stars in the SMC, an effect attributed to a metallicity dependence of the mass loss rate. When Hγ and Hδ are considered [83] a ~ 0.5 mag dispersion is found in the LMC. On the other hand, [92] and [28], using their W(Hγ)–M_V calibration, claim a probable error $\simeq 0.2$ mag (standard deviation $\simeq 0.3$ mag), for a single observation. However, we note that in the latter two works stars brighter than $M_V = -8$ are excluded from the calibration, somewhat reducing its usefulness for extragalactic work.

Since the mid-1980's not much work has been published about new applications of the W(Hγ)–M_V relationship, possibly because of the somewhat uncertain results obtained in the Clouds and, most of all, because of the lack of high-quality spectra for blue supergiants in galaxies beyond the Magellanic Clouds. With the availability of 8–10m telescopes in recent times the spectroscopy of a large number of stars well beyond the Local Group boundaries has become feasible, and new calibrations and tests of spectroscopic luminosity diagnostics are likely to appear in future years. Several projects are underway within our group and others to use the current generation of multi-object spectrographs (FLAMES, FORS and VIMOS at the VLT, DEIMOS at Keck, GMOS at Gemini) to observe a large fraction of the bright stellar content in galaxies of the Local Group and beyond.

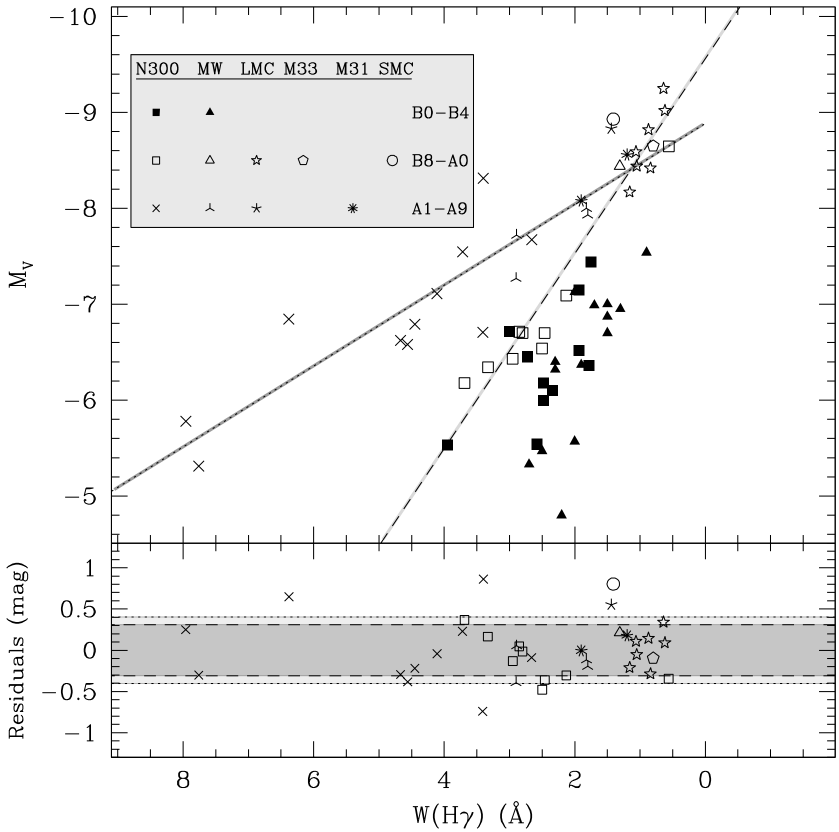

Fig. 8.4. (*Top*) The W(Hγ)–M_V relationship for B–A supergiants in NGC 300, Milky Way, Magellanic Clouds, M31 and M33. The sample has been divided into three classes: B0–B4 (*full symbols*), B8–A0 (*open*) and A1–A9 (*crosses*). The regression lines for the latter two are shown. (*Bottom*) Residual plot from the regressions for B8–A0 (*open symbols*) and A1–A9 supergiants (*crossed*). The standard deviation is shown by *dashed* and *dotted lines*, respectively

A first, modern version of the W(Hγ)–M_V relation for B and A supergiants, based on CCD spectra collected within our group, is reproduced in Fig. 8.4. The sample shown contains objects from the following galaxies: NGC 300 [9], Milky Way [40], LMC and SMC [60], M33 and M31 [50,51]. It has been subdivided, somewhat arbitrarily, into three separate classes according to the stellar spectral type range: early B (B0–B4, full symbols), B8–A0 (open symbols) and A1–A9 (crosses).

The slope of the empirical relationship in Fig. 8.4 becomes shallower for the later spectral types, as indicated by the regressions corresponding to the B8–A0 (dashed line) and A1–A9 (dotted line) classes. This trend with spectral type is well-known from previous work, with a maximum W(Hγ) at a given M_V around type F0 for supergiants [37]. Contrary to the calibration by [28], the new diagram is populated up to very bright magnitudes, $M_V \simeq -9$. The relationship defined by the B8–A0 subgroup is rather tight, with a standard deviation of about 0.3 mag (bottom panel of Fig. 8.4), and is given by

$$M_V = -9.56\ (\pm 0.15) + [1.01\ (\pm 0.07)]\ W(\mathrm{H}\gamma)\ . \tag{8.2}$$

The scatter for the later A-type supergiants is 50 % larger. A further subdivision of this broad class might reveal tighter correlations, but currently this is prevented by the small number of objects available. We note the rather large discrepancy of the only A0 Ia supergiant plotted for the SMC (AV 475) from the regression line, with an Hγ line too strong for its magnitude. A metallicity effect cannot be excluded at this stage to explain this discrepancy. The measurements of W(Hγ) in SMC supergiants by [5], combined with M_V's obtained from magnitudes and spectral types in the catalog by [6], are in general agreement with those shown in Fig. 8.4, although they show a larger scatter. This might be, at least partly, related to the necessity of redefining the spectral type classification at low metallicity, as shown by [47].

To conclude, by restricting the analysis to a narrow range in spectral types (B8 to A0) the scatter about the mean W(Hγ)–M_V relation is on the order of 0.3 mag, which makes this spectroscopic technique rather appealing for its simplicity and accuracy, at least for metallicities comparable to that of the LMC and larger, whenever moderate resolution spectra of a sufficient number of B8–A0 supergiants in a given galaxy are available. Additional tests at lower metallicity (for example in the SMC) should be carried out to verify the dependence on chemical abundance.

8.4 The Wind Momentum–Luminosity Relationship

The discovery and empirical verification of a relationship between the intensity of the stellar wind momentum and the luminosity of massive stars is certainly one of the foremost successes of the theory of line driven winds, which is presented in R. Kudritzki's contribution in this volume (see also [42] for a review). The predicted Wind Momentum–Luminosity Relationship (WLR) can be written as:

$$\log D_{mom} = \log D_0 + x \log \frac{L}{L_\odot} \tag{8.3}$$

where the linear regression coefficients D_0 and x are derived empirically from observations of O, B and A stars at known distances. The modified wind momentum $D_{mom} = \dot{M} v_\infty (R/R_\odot)^{0.5}$, i.e. the product of the mass-loss rate, wind terminal velocity and square root of stellar radius, is determined spectroscopically, once the magnitude of the star is measured. A spectral type dependence is found, as shown in Fig. 8.5, as a result of the different ionic species driving the wind at different stellar temperatures. In fact the slope x corresponds to the reciprocal of the exponent α' of the power-law describing the line-strength distribution function. The predicted value lies around $\alpha' = 1/x = 0.6$. The effects

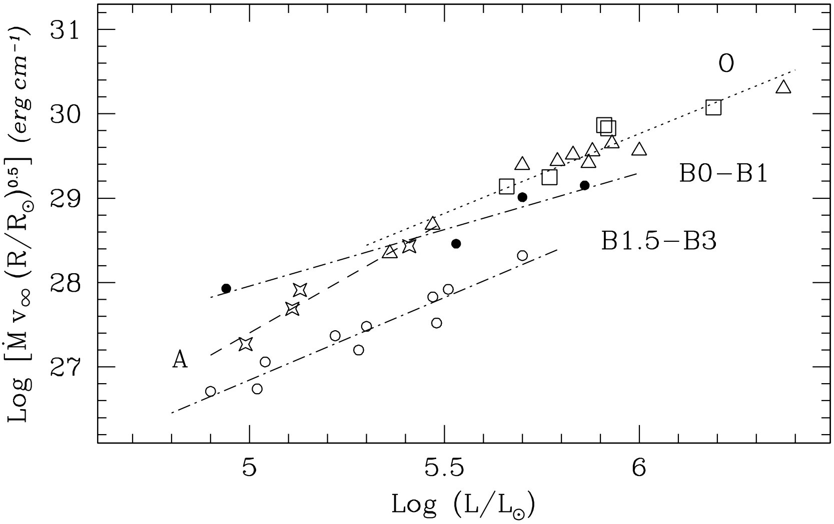

Fig. 8.5. Spectral type dependence of the WLR for Galactic supergiant stars. Different symbols are used for the different spectral type ranges, and regression lines are drawn. Adapted from [40], with data from the same paper. For O stars the blanketed model results of [64] and [27] have been used

of metallicity Z are also to be empirically verified, while the predictions for the dependence of both $\dot{M}$ and v_∞ indicate that approximately $D_{mom} \propto Z^{0.8}$ [91].

Since all massive and luminous blue stars show signs of mass loss, it is interesting to take advantage of this through the WLR as a way to measure extragalactic distances. In practice, one needs to obtain the mass-loss rate from the Hα line fitting, and the photospheric parameters (temperature, gravity and chemical composition) from optical absorption lines in the blue optical spectral region (4000–5000 Å). An empirically calibrated WLR as a function of metallicity would then allow the determination of distances, once the apparent magnitude, reddening and extinction are known. The latter quantities can be derived from the observed spectral energy distribution and theoretical models calculated with the appropriate photospheric parameters. The method is backed by a strong theoretical framework, especially for the hot O stars, which allows us to deal quantitatively with the spectral diagnostics of blue supergiants. However, its observational application requires careful spectroscopic analysis and modeling, which can make it intimidating at first. On the other hand, the same analysis provides us with a large amount of information on the physics of massive stars. Here I will briefly summarize the results obtained so far concerning the calibration of the WLR, by discussing the O stars separately from the B–A supergiants, referring the reader to the papers cited above for the theoretical aspects and for details on how the stellar and wind parameters are extracted from the observational data.

8.4.1 O Stars

For O stars the reference work remains the paper by Puls et al. [63], in which theoretical results from unified model atmosphere calculations were used to measure mass-loss rates from Hα line profiles. Their method overcomes the inaccuracies related to the use of the equivalent width of the Hα line from the wind emission, corrected for photospheric contribution, as done by [46] and [44]. For a sample of Galactic and Magellanic Clouds stars the relevant parameters were measured from spectra in the UV (v_∞, based on the P-Cygni profiles of strong resonance lines) and in the optical (T_{eff}, $\log g$), and from the analysis of the Hα line profile ($\dot{M}$, wind velocity law). Separate relations were found by Puls and collaborators for different luminosity classes, the supergiants having larger wind momenta than giants and dwarfs at a given luminosity. Moreover, reduced wind momenta were measured in the Magellanic Clouds when compared with the Milky Way stars, as a manifestation of a metallicity effect on the strength of the wind. More recently, [27] have determined the WLR for O stars in a single Galactic association, Cyg OB2, thus reducing the uncertainty in stellar distances as a source of scatter in the calibration. Recent improvements in the stellar models allowed these authors to account for the effects of line blocking and blanketing from metals. As explained by [64] the consequent cooler temperature scale for O stars, when compared with T_{eff} calibrations based on unblanketed atmospheres, modifies the WLR significantly, leading in particular to an indication that the luminosity class dependence might be no longer present, in agreement with the theoretical predictions by [90], but instead that wind clumping might mimic higher mass-loss rates in the more extreme cases, affecting preferentially stars with an Hα profile in emission. Figure 8.6 illustrates these results, where the Galactic sample of [64] and the Cyg OB2 stars of [27] have been divided according to the nature of the Hα line profile, i.e. in emission (open symbols) or in absorption partly filled by wind emission (full symbols). The resulting tight relations are clearly displaced from one another by about 0.3 dex, with the less extreme objects (Hα in absorption, optically thin winds) lying very close to the theoretical relationship defined by [90]. The hypothesis of clumping to explain the apparently higher mass-loss rates in stars with Hα in emission is very appealing, but requires further observational confirmation, with the UV-to-IR spectral analysis of a large number of O stars.

8.4.2 B and A Supergiants

Even if the WLR calibration for the O stars is probably the best available to date, and the one upon which most observational and theoretical work has been concentrated, it is the late-B and the A supergiants which offer the largest potential as extragalactic distance indicators. In fact, these stars are in general much less affected by crowding and confusion problems, which afflict O stars, normally found in OB associations and/or within H II region complexes. Besides, they attain brighter magnitudes in the optical ($M_V \simeq -9$ for A hypergiants, vs. $M_V \simeq -7$ for the brightest O Ia stars), as the result of a combination of stellar evolution

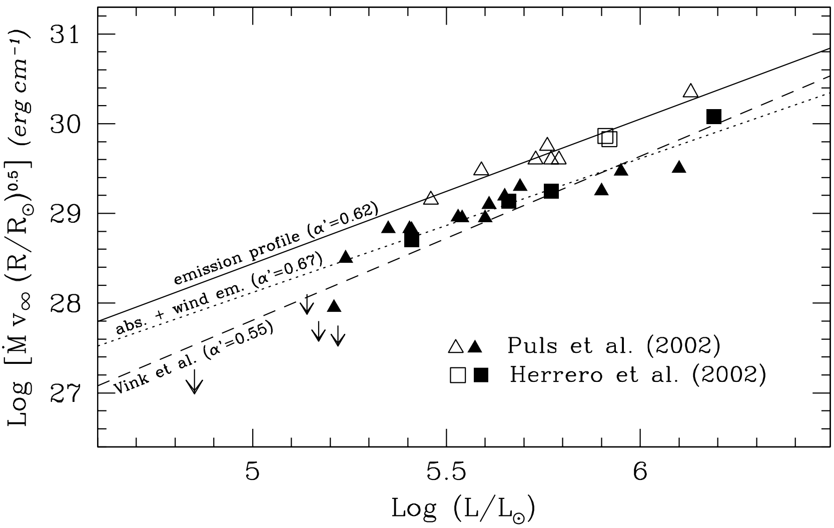

Fig. 8.6. The WLR for Galactic O stars, with data from [64] and [27]. The O star sample has been subdivided according to the character of the Hα profile, either in emission (*open symbols*) or in absorption partly filled by wind emission (*full symbols*). The linear fits to the two sub-samples are shown, together with the theoretical models by [90]. The slope of the line strength distribution function $\alpha' = 1/x$ is indicated for each regression

across the upper H–R diagram at roughly constant luminosity and smaller bolometric corrections in the covered temperature range ($T_{eff} \simeq 13000 - 7500\,\mathrm{K}$). Their extreme luminosities make their analysis less affected by the presence of fainter companions, which can be, if bright enough to be of importance, detected by their spectral signatures. As a downside, a large fraction of the brightest supergiants are photometrically variable at the 0.1–0.2 mag level [86,26], and this should be taken into account when trying to use them as distance indicators.

With the modern spectroscopic capabilities at 8m-class telescopes, A-type supergiants should be within reach of a quantitative analysis out to distance moduli $(m - M) \simeq 30$–31, i.e. out to the distance of the Virgo Cluster. A great amount of work, however, still needs to be done regarding the identification of suitable targets on one hand, and the calibration of the WLR on the other.

Selecting the Candidates. For those resolved galaxies where extensive stellar classification work has not already been carried out, which in practice, with a few exceptions, means all galaxies outside of the Local Group, as well as a considerable fraction of Local Group members, spectral types of blue supergiant candidates must be found from scratch, overall a rather lengthy process. This is accomplished by first obtaining stellar photometry in two or more bands, typically B and V, from CCD images, and subsequently concentrating the spectroscopic follow-up on those isolated objects in the color and magnitude range expected for blue supergiants. We have found it very helpful, if not necessary, to obtain also narrow-band Hα images, to limit as much as possible the contamination on the final stellar spectra from nebular lines. This is particularly true in the late-type, star-forming galaxies which are the natural targets for the application of the WLR. The availability of large-format CCD mosaics at several 2–4 meter telescopes around the globe, covering as much as half a degree or more on the sky in a single exposure, is making the photometric surveys required for target selection time-efficient even when considering a large number of nearby galaxies.

The photometric selection is always affected at some level by the presence of 'intruders' in the c-m diagram (unresolved stellar groups, unidentified small H II regions, stars with greatly different extinction, and more exotic objects), and can be verified only *a posteriori*, once the spectroscopy has been carried out. This is becoming less of a problem, with the availability of multiobject spectrographs, like FLAMES at the VLT, which allow the simultaneous observation of hundreds of spectra.

As an example of some recent results, Fig. 8.7 shows the c-m diagram of the Sculptor Group galaxy NGC 300, obtained from 2.2m/WFI CCD images at La Silla by W. Gieren, where the objects we have studied spectroscopically with FORS1 at the VLT have been indicated [9]. With our original selection criterion ($-0.3 < B - V < 0.3$, $V < 21.5$) we intended to isolate late-B and early-A supergiants. The confirmed stellar types, from B0 to F2, correspond rather well with the expected location in the c-m diagram. The few pre-selected H II regions have rather blue $B - V$ colors, while some objects characterized by a composite spectrum are found at faint magnitudes. More interesting interlopers are a foreground Galactic white dwarf and a WN11 emission line star, the latter analyzed by [10]. The high success rate in the case of NGC 300 has been made possible by the careful analysis of the broad-band and Hα images, in combination with the modest distance (2 Mpc), and likely by the small foreground+internal reddening, even though a number of bright supergiants were found to be contaminated by nebular emission in subsequent Hα spectra used for the mass-loss determination. Work similar to the one described for NGC 300 has been carried out at the VLT by our group in two additional galaxies, NGC 3621 [8] and a second galaxy in Sculptor, NGC 7793 (work in preparation). We are also securing wide-field images of about a dozen nearby ($D < 7$ Mpc) galaxies from La Silla and Mauna Kea, as well as obtaining HST/ACS imaging of selected fields in NGC 300, NGC 3621 and M101 for accurate stellar photometry of confirmed and candidate blue supergiants.

Calibration of the WLR. The current calibration of the WLR for Galactic A-type supergiants, given by [40], rests on only four stars, because of the difficulty to measure reliable distances and reddening corrections for this type of objects when located in the Milky Way. In their paper, 14 early B supergiants were also studied, but I will not include them in the following discussion because of their somewhat lower appeal (being fainter) for extragalactic distances work.

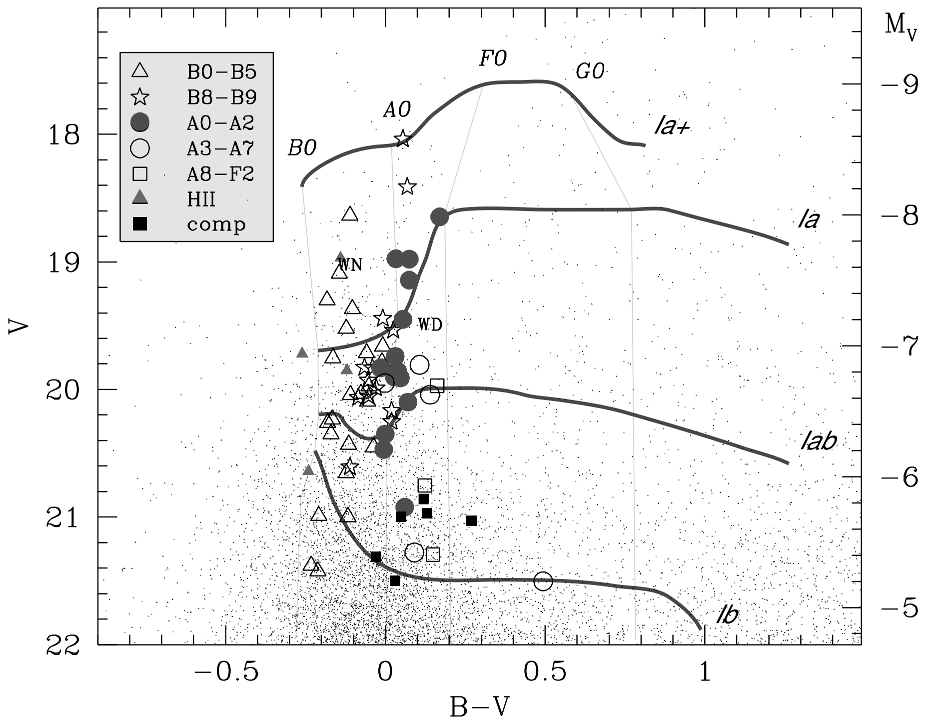

Fig. 8.7. Color-magnitude diagram of NGC 300. The supergiants studied spectroscopically by [9] have been divided into separate ranges of spectral type, according to the legend in the upper left. Observed H II regions and objects with composite spectra are also indicated, together with the locations of a foreground white dwarf (WD) and a WN11 star (WN). The magnitude-color calibration for Ia^+, Ia, Iab and Ib stars is the same as in Fig. 8.1

Apparently they also do not conform to the same relationship as the A supergiants, as seen in Fig. 8.5. A subset of these stars (those in the B1.5–B3 spectral type range) were found to have low wind momenta when compared to the O and early B stars, an anomaly which is not currently understood within the theoretical framework. I simply mention here that several observing programs are underway on the early B supergiants in Local Group galaxies, utilizing optical spectroscopy to derive photospheric parameters and abundances [76], [81] and UV spectroscopy to measure wind velocities [84], [11], in order to obtain a better understanding of their wind properties.

From the paucity of Galactic calibrators it is clear that the sample must be enlarged by observing additional bright B–A supergiants in nearby galaxies, before any attempt to measure independent distances with the WLR is made. The first high resolution spectra of A supergiants in M33 and M31, two in each galaxy, have been obtained with the Keck telescope by [50] and [51], respectively, demonstrating that, at least at distances smaller than 1 Mpc, all stellar wind parameters ($\dot{M}$, v_∞ and the exponent β of the wind velocity law) can be satisfactorily obtained from fitting the Hα line profile. The paper on the M31 stars, in particular, shows several examples of how varying the wind parameters influences the calculated profiles. The wind analysis from the Hα line must still be carried out in a larger number of supergiants in these two galaxies, however. The M33 spiral, in particular, appears to be an ideal target, because of its moderate distance and its favorable inclination on the plane of the sky. The radial chemical abundance gradient in this galaxy is such that it will allow the investigation of the metallicity effect on the WLR. We are currently planning to secure spectra at the required resolution (about 1–2 Å) with Keck equipped with the new multiobject spectrograph DEIMOS.

In 1999 we have started to use the FORS spectrograph at the VLT in order to increase the sample of extragalactic A-type supergiants having a spectroscopic coverage. Two are the principle goals: to determine stellar abundances, which are important for galactic and stellar evolution investigations, and to measure wind momenta, for an experimental verification and calibration of the WLR. The very first targets, a handful of blue supergiants in NGC 6822, were observed during the commissioning phase of FORS1, confirming that even at relatively low resolution (5 Å) quantitative spectroscopy can be successfully carried out, with regard to both stellar metallicities and mass-loss rates [55]. An important step was taken with the subsequent analysis of stellar spectra in NGC 3621 [8], so far the most distant galaxy, at $D \simeq 6.7\,\mathrm{Mpc}$, for which spectroscopy of individual supergiants has been published. Unfortunately, red spectra covering Hα are still unavailable for this galaxy, so that the mass-loss rate of the blue supergiants discovered could not be determined, except for a highly luminous A1 Ia star ($M_V = -9.0$), for which the wind-affected Hβ has been used.

After having verified the potential of the available instrumentation, we have turned to more nearby galaxies, NGC 300 and NGC 7793 in the Sculptor Group, combining our project with an investigation of their Cepheid content [58]. While the FORS2 data for NGC 7793 have just recently come in, the analysis of the blue supergiants in NGC 300 has already provided important results concerning the classification and the first A-type supergiant abundance estimates [9], the A-supergiant WLR (in preparation) and the metallicity of the B-type stars [85].

The wind analysis has been carried out so far for six A-type supergiants (B8 to A2) from red spectra obtained at the VLT/FORS1 in September 2001. The unblanketed version of the non-LTE line formation code FASTWIND [72] has been used to fit the observed Hα line profiles. The major drawback when using spectroscopic data at moderate resolution is that the terminal velocity cannot be determined from the line fits, forcing us to adopt a reasonable estimate for it, $v_\infty = 150\,\mathrm{km\,s^{-1}}$. Although such a velocity is typical for well studied Galactic A supergiants, this assumption is currently the major source of uncertainty in the calculation of the wind momentum in the NGC 300 sample. Figure 8.8 illustrates profile fits to Hγ (mostly sensitive to gravity) and Hα (mass-loss rate) for three bright A-type supergiants in NGC 300. As can be seen, in some cases we cannot reproduce the observed extended electron scattering wings of Hα, however these features arise in the photosphere, and do not affect the mass-loss rate determina-

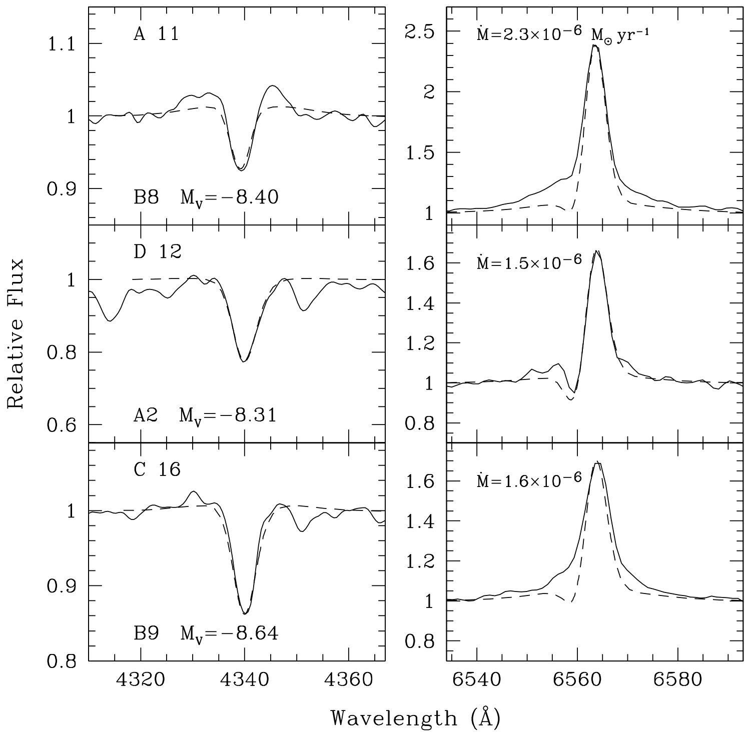

Fig. 8.8. Hγ (*left*) and Hα (*right*) line profile fits (*dashed lines*) to the spectra of three bright supergiants in NGC 300, obtained with FASTWIND [72]. The identification number from [9] is given in the upper left of each plot. Spectral types and absolute magnitudes are indicated in the lower part of the Hγ panels, and mass-loss rates in $M_\odot\,yr^{-1}$ in the Hα panels

tion, which is carried out from the peak of the emission. We can also neglect the discrepancies in the blue absorption part of the P-Cygni profiles. This feature is often affected by variability in high luminosity objects, but the corresponding wind momentum variations are contained within the scatter of the WLR [41].

The WLR determined for the NGC 300 stars analyzed so far, expressed as a relation between modified wind momentum and both M_V and M_{bol}, is shown in Fig. 8.9. The diagrams also include the four Galactic A supergiants studied by [40], the two stars in M31 from [51] and the only star in NGC 3621 for which we were able to determine the mass-loss rate from the Hβ line (again, assuming here $v_\infty = 150\,\mathrm{km\,s^{-1}}$).

The metallicity for the NGC 300 stars, which lie all at a similar galactocentric distance, is estimated, from the known H II region oxygen abundance gradient [94] and from the appearance of the stellar spectra, to be around $0.4 \pm 0.1\,Z_\odot$. The NGC 3621 star has a comparable metallicity. If we adopt an empirical ‘calibration’ of the WLR at solar metallicity as provided by a fit to the Milky

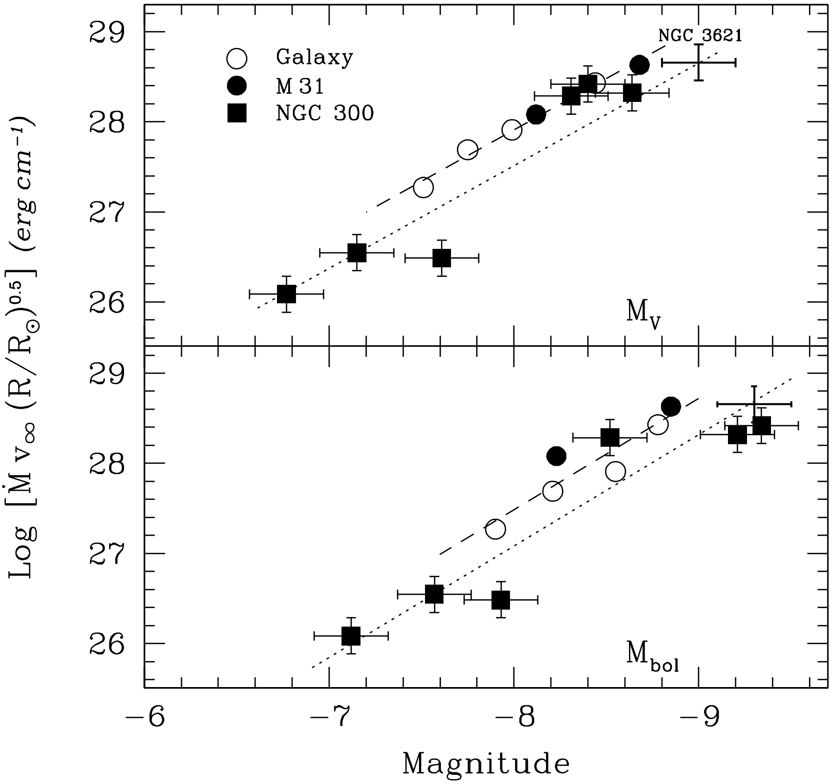

Fig. 8.9. The WLR for A-type supergiants, represented in terms of M_V (*top*) and M_{bol} (*bottom*). The stellar objects are drawn from samples of blue supergiants in the Milky Way, M31, NGC 300 and NGC 3621. The linear fits to the Galactic and M31 supergiants are given by the *dashed lines*. A theoretical scaling factor is applied to provide the expected relations at $0.4\,Z_\odot$ (*dotted lines*)

Way and M31 points, given by the dashed lines, we can then scale to the lower metallicity using a $Z^{0.8}$ dependence. This is shown by the dotted lines in Fig. 8.9.

Let us concentrate on the $D_{mom} - M_{bol}$ relation, since the sample of objects considered varies in spectral type from B8 to A3, implying different bolometric corrections by up to 0.7 mag. The corresponding plot in Fig. 8.9 shows a rather well defined WLR for the Galactic and M31 stars, with a scatter of about 0.2 dex in the modified wind momentum. All the points corresponding to NGC 3621 and NGC 300, except one, agree with the expected approximate location for $Z = 0.4\,Z_\odot$. We have yet to carry out the chemical abundance analysis of the discrepant point, and we have currently no obvious explanation for its location in the diagram. Despite this, it appears that even with the moderate resolution spectra at our disposal we can well define the WLR in a galaxy at a distance of 2 Mpc. Of course this result is only preliminary, in the sense that we are still lacking a real calibration of the WLR which we could use to determine extragalactic distances. Analyzing a larger sample of objects, with a range in metallicity from $Z_\odot$ down to $0.1\,Z_\odot$, still remains among our top priorities. The obvious candidates for such work are stars in the Magellanic Clouds, and in a number of nearby spirals and irregulars rich in blue supergiants, such as M33, M31 and NGC 6822. Moreover, an improved spectral analysis which takes into account the blanketing and blocking effects of metals in the stellar atmosphere must be carried out.

8.5 A New Spectroscopic Method: The Flux-Weighted Gravity–Luminosity Relationship

A very promising luminosity diagnostic for blue supergiants has been very recently proposed by [43], based on the realization that the fundamental stellar parameters, surface gravity and effective temperature, are predicted to be tightly coupled with the stellar luminosity during the post-main sequence evolution of massive stars. While quickly crossing the upper H–R diagram from the main sequence to the red supergiant phase both the mass and the luminosity of late-B to early-A supergiants remain roughly constant, so that by postulating an approximate mass-luminosity relationship ($L \sim \mathcal{M}^3$) we derive:

$$M_{bol} = a \log(g/T_{\mathit{eff}}^4) + b \tag{8.4}$$

with $a \simeq -3.75$. This equation defines a *Flux-weighted Gravity–Luminosity Relationship* (FGLR), since the quantity g/T_{eff}^4 can be interpreted as the flux-weighted gravity. Even for the most massive stars in the range of interest, 30–40 $\mathcal{M}_\odot$, the mass-loss rate is still small enough that during the typical timescale of this evolutionary phase its effects on the FGLR are negligible, thus justifying our assumption of mass constancy. This is also true, to first order, for the effects of differing metallicities and rotational velocities, as confirmed by the results of evolutionary models [53].

The FGLR is conceptually very simple, and its empirical verification only requires, besides the visual magnitude, the measurement of $\log g$ and T_{eff} from the stellar spectrum. A complication arises from the difficulty of measuring these parameters with sufficient accuracy in extremely bright supergiants and hypergiants. Recently, however, sophisticated non-LTE modeling of A supergiants can provide us with tools to determine the stellar parameters with high reliability [88,61,62].

As a first test, we have analyzed the spectra of blue supergiants from a number of Local Group galaxies, observed as part of our investigation of the WLR, together with our FORS data on NGC 300 and NGC 3621, as described in Sect. 8.4. Effective temperatures were estimated from the observed spectral types, according to the correspondence shown in Table 8.2, except for the lower metallicity objects in SMC, M33 and NGC 6822, for which T_{eff} was derived from the non-LTE ionization equilibrium of Mg I/II and N I/II. Surface gravities were measured from a simultaneous fit to the higher Balmer lines (Hγ, Hδ, ...), therefore minimizing the wind emission contamination on the lower-order hydrogen

Table 8.2. Adopted temperature scale for supergiants

Spectral Type	T_{eff}
B8	12000
B9	10500
A0	9500
A1	9250
A2	9000
A3	8500
A4	8350

lines. Despite the moderate spectral resolution of the FORS data, which prevents us to fit the wings of the spectral lines, we are able to achieve a similar *internal* accuracy as for the higher resolution spectra by fitting the line cores, about 0.05 dex in $\log g$. In practice at low resolution we are fitting the Balmer line equivalent widths to measure stellar gravities, and the FGLR technique is therefore reminiscent of the Hγ–M_V relation discussed in Sect. 8.3. However, we are now considering a larger number of Balmer lines, and including a correction for the temperature dependence through the T_{eff}^4 term. The bolometric correction and the intrinsic color, which allow us to account for reddening and extinction, are also determined from the spectral analysis.

The results are displayed in Fig. 8.10, where the dashed line is the linear regression:

$$M_{bol} = 3.71\ (\pm 0.22)\ \log(g/T_{eff,4}^4) - 13.49\ (\pm 0.31) \tag{8.5}$$

with a standard deviation $\sigma = 0.28$ (note that T_{eff} is expressed in units of 10^4 K). This is a very encouraging result for extragalactic work. As can be seen from Fig. 8.10, the points corresponding to the blue supergiants in NGC 300 define a tight relationship ($\sigma = 0.20$), despite the intermediate resolution of the spectra available. For NGC 3621 the FGLR with just four stars would suggest a distance slightly larger than the assumed Cepheid distance, however the upcoming photometry from HST/ACS is required before we can draw any firm conclusion.

The slope of the empirical FGLR reproduces very well the theoretical expectations from the evolutionary models of [53], while the offset can be interpreted, for example, as a systematic effect on the determination of the stellar parameters, which would not be important in a strictly differential analysis. The apparent increase of the dispersion at high luminosities might be a consequence of the larger role played by stellar rotation and/or metallicity on the flux-weighted gravity. Still, with a standard deviation of 0.3–0.35 mag and with the analysis of about ten blue supergiants in a given galaxy we could be able to determine a mean relationship, and therefore the distance modulus, with an accuracy of ~ 0.1 magnitudes. Our aim is to apply the FGLR method to distances of up to $m - M = 30.5$, where stars brighter than $M_V = -8$ can be observed with the high-efficiency spectrographs currently available at 8–10m telescopes.

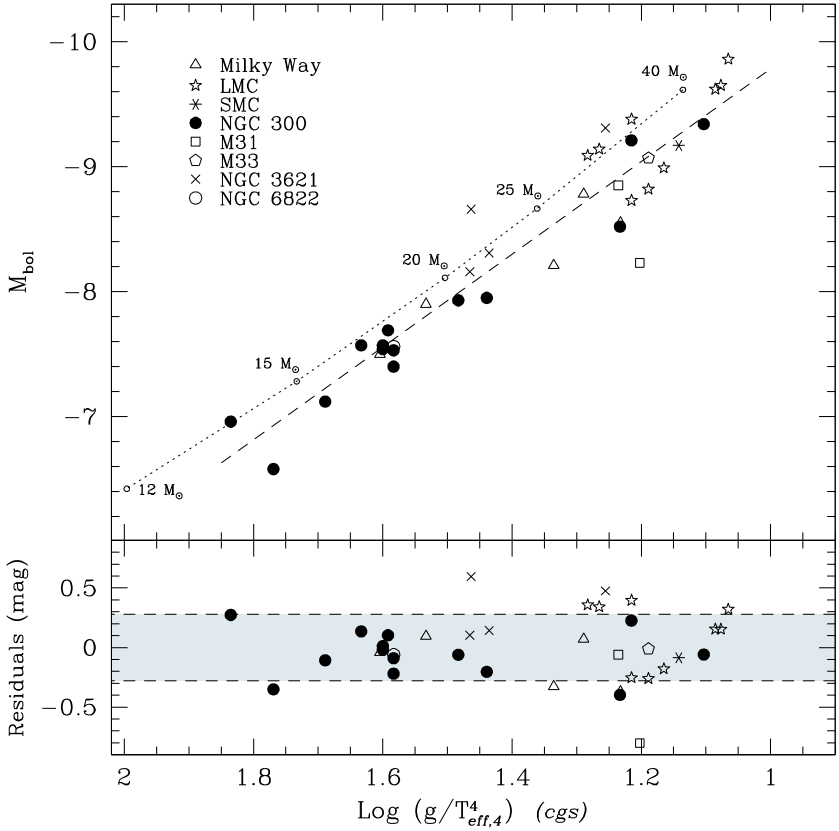

Fig. 8.10. (*Top*) The relationship between the flux-weighted gravity g/T_{eff}^4 (T_{eff} in units of 10^4 K) and M_{bol} for B8–A4 supergiants in Local Group galaxies, NGC 300 and NGC 3621. The *dashed line* represents the linear regression to all the data points. The models at $T_{\mathit{eff}} = 10^4$ K from the evolutionary calculations accounting for rotation (v_{in} = 300 km s^{-1}) and at solar metallicity of [53] are connected by the *dotted line*, labeled with the corresponding ZAMS masses. (*Bottom*) Residuals from the regression shown in the top panel, with the standard deviation indicated by the *dashed line*

Is the FGLR going to replace the WLR as a more promising distance indicator for blue supergiants? The advantages of the FGLR are multiple. Medium resolution spectra seem to be sufficient, and no red spectrum covering Hα is required, thus reducing the amount of time at the telescope. All the stellar classification work, the chemical abundance analysis and the fit to the higher Balmer lines can be carried out in the blue spectral region, which is also less contaminated by night sky lines. Work on the WLR, however, should continue, especially for early-B stars, for which the assumptions upon which the FGLR rests could fail.

The results shown here are just the starting point in the study of the FGLR. A detailed and extensive calibration work must be carried out in Local Group galaxies, where with instrument like FLAMES (VLT) or DEIMOS (Keck) we can obtain hundreds of blue supergiant spectra. Such observations, besides providing us with an accurate calibration of the FGLR, will also improve our understanding of the effects on stellar evolution of those parameters, like metallicity, mass-loss and angular momentum, which are relevant for a theoretical explanation of the relationship.

As a concluding remark, one may ask the question why we should insist in using spectroscopic methods for blue supergiants, such as the WLR or the FGLR, as extragalactic distance indicators, when other well-tested photometric techniques (e.g. Cepheids and Tip of the Red Giant Branch) promise to obtain perhaps higher accuracy and to reach more distant objects with arguably less observational efforts. The answer is of course that a greater physical insight is gained from the analysis of the stellar spectra, allowing us to determine *for each individual stellar target* the crucial parameters of metallicity and reddening. The discrimination against unresolved companions or small clusters is also possible through the appearance of the spectra. Because of the importance of each of these factors in the application of the main distance indicators used nowadays, possibly leading to some systematic errors in the distance scale if uncorrected for, it is important to continue our efforts to measure a number of 'spectroscopic' distances to galaxies of the nearby universe.

Acknowledgements

I wish to thank the Organizing Committee, W. Gieren and D. Alloin in particular, for inviting me to this workshop and for the hospitality, and R.P. Kudritzki and W. Gieren for their help and encouragement. I am also grateful to N. Przybilla for making his spectra of Magellanic Cloud supergiants available. This research has made use of the SIMBAD database, operated at CDS, Strasbourg, France.

References

1. W.S. Adams, A.H. Joy: ApJ **56**, 242 (1922)
2. W.S. Adams, A.H. Joy: ApJ **57**, 294 (1923)
3. P.J. Andrews: MRAS **72**, 35 (1968)
4. A. Arellano Ferro, S. Giridhar, E. Rojo Arellano: Rev. Mex. de Astron. y Astrof., in press (astro-ph/0210695) (2002)
5. M. Azzopardi: A&AS **69**, 421 (1987)
6. M. Azzopardi, J. Vigneau: A&AS **149**, 213 (1982)
7. L. Balona, D. Crampton: MNRAS **166**, 203 (1974)
8. F. Bresolin, R.P. Kudritzki, R. Mendez, N. Przybilla: ApJ **547**, 123 (2001)
9. F. Bresolin, W. Gieren, R.P. Kudritzki, G. Pietrzynski, N. Przybilla.: ApJ **567**, 277 (2002)
10. F. Bresolin, R.P. Kudritzki, F. Najarro, W. Gieren, G. Pietrzynski: ApJ **577**, L107 (2002)
11. F. Bresolin, R.P. Kudritzki, D.J. Lennon, S.J. Smartt, A. Herrero, M. Urbaneja, J. Puls: ApJ, **580**, 213 (2002)

12. D. Chalonge, L. Divan: A&A **23**, 69 (1973)
13. D. Crampton: ApJ **230**, 717 (1979)
14. D.L. Crawford: AJ **83**, 48 (1978)
15. D.L. Crawford: AJ **84**, 1858 (1979)
16. I.O. Drozdovsky, I.D. Karachentsev: A&AS **142**, 425 (2000)
17. D.L. Edwards: MNRAS **87**, 365 (1927)
18. M.W. Feast, A.D. Thackeray, A.J. Wesselink: MNRAS **121**, 25 (1960)
19. M.W. Feast: MNRAS **174**, 9 (1976)
20. W.L. Freedman et al.: ApJ, **553**, 47 (2001)
21. W.L. Freedman et al.: ApJ, **435**, L31 (1994)
22. C.D. Garmany, P.S. Conti, P. Massey: AJ, **93**, 1070 (1990)
23. C.D. Garmany, R.E. Stencel: A&AS **94**, 211 (1992)
24. T.B. Georgiev, B.I. Bilkina, N.M. Dencheva: Astronomy Letters **23**, 644 (1997)
25. L. Greggio: A&A **160**, 111 (1986)
26. G.R. Grieve, B.F. Madore: ApJS **62**, 451 (1986)
27. A. Herrero, J. Puls, F. Najarro: A&A **396**, 949 (2002)
28. G.M. Hill, G.A.H. Walker, S. Yang: PASP **98**, 1186 (1986)
29. E. Hubble: ApJ **84**, 158 (1936)
30. E.O. Hulburt: ApJ **59**, 204 (1924)
31. R.M. Humphreys: 'The Brightest Stars as Distance Indicators'. In: *The Extragalactic Distance Scale*, ed. by S. van den Bergh, C.J. Pritchet (BYU Press, Provo 1988) pp. 103–112
32. R.M. Humphreys, M. Aaronson: AJ **94**, 1156 (1987)
33. R.M. Humphreys, M. Aaronson: ApJ **318**, L69 (1987)
34. R.M. Humphreys, C. Blaha, D.B. McElroy: 'Catalog of Luminous Stars in Associations and Clusters'. (Univ. of Minnesota, 1984) unpublished
35. R.M. Humphreys: ApJS **39**, 389 (1979)
36. R.M. Humphreys: ApJS **38**, 309 (1978)
37. J.B. Hutchings: MNRAS **132**, 433 (1966)
38. I.D. Karachentsev, N.A. Tikhonov: A&A **286**, 718 (1994)
39. I.D. Karachentsev et al.: A&A **389**, 812 (2002)
40. R.P. Kudritzki et al.: A&A **350**, 970 (1999)
41. R.P. Kudritzki: 'The Wind Momentum – Luminosity Relationship of Blue Supergiants'. In: *Variable and Non-spherical Stellar Winds in Luminous Hot Stars, Proceedings of the IAU Colloquium No. 169*, ed. by B. Wolf, O. Stahl, A.W. Fullerton (Springer, Berlin, 1999) pp. 405–415
42. R.P. Kudritzki, J. Puls: ARAA **38**, 613 (2000)
43. R.P. Kudritzki, F. Bresolin, N. Przybilla: ApJ **582**, L83 (2003)
44. H.J.G.L.M. Lamers, C. Leitherer: ApJ **412**, 771 (1993)
45. K.R. Lang: *Astrophysical Data* (Springer, New York 1992)
46. C. Leitherer: ApJ **326**, 356 (1988)
47. D.J. Lennon: A&A **317**, 871 (1997)
48. P. Massey: 'Observations of the Most Luminous Stars in Local Group Galaxies'. In: *Stellar Astrophysics for the Local Group: VIII Canary Islands Winter School of Astrophysics*, ed. by A. Aparicio, A. Herrero, F. Sanchez (Cambridge University Press, Cambridge, 1998) pp. 95–147
49. P. Massey, A.B. Thompson: AJ **101**, 1408 (1991)
50. J.K. McCarthy, D.J. Lennon, K.A. Venn, R.P. Kudritzki, J. Puls, F. Najarro: ApJ **455**, L135 (1995)
51. J.K. McCarthy, R.P. Kudritzki, D.J. Lennon, K.A. Venn, J. Puls: ApJ **482**, 757 (1997)

52. G. Meynet, A. Maeder, G. Schaller, D. Schaerer, C. Charbonnel: A&AS **103**, 97 (1994)
53. G. Meynet, A. Maeder: A&A **361**, 101 (2000)
54. C.G. Millward, G.A.H. Walker: ApJS **57**, 63 (1985)
55. B. Muschielok et al.: A&A **352**, L40 (1999)
56. R.M. Petrie: Publications of the Dominion Astrophysical Observatory **12**, no. 9, 317 (1965)
57. M. Pierce, R.D. McClure, R. Racine: ApJ **393**, 523 (1992)
58. G. Pietrzynski, W. Gieren, P. Fouqué, F. Pont: AJ **123**, 789 (2002)
59. G. Piotto, M. Capaccioli, F. Bresolin: Memorie della Società Astronomica Italiana **63**, 465 (1992)
60. N. Przybilla (private communication)
61. N. Przybilla, K. Butler, S.R. Becker, R.P. Kudritzki: A&A **369**, 1009 (2001)
62. N. Przybilla, K. Butler: A&A **369**, 955 (2001)
63. J. Puls et al.: A&A **305**, 171 (1996)
64. J. Puls, T. Repolust, T. Hoffmann, A. Jokuthy, R. Venero: 'Advances in Radiatively Driven Wind Models'. In: *A Massive Star Odyssey, from Main Sequence to Supernova, Proceedings of IAU Symposium No. 212*, ed. by K.A. van der Hucht, A. Herrero, C. Esteban (ASP, San Francisco, 2003) in press
65. J.D. Rosendhal: ApJ **186**, 909 (1973)
66. J.D. Rosendhal: ApJ **187**, 261 (1974)
67. J. Rousseau, N. Martin, L. Prevot, E. Rebeirot, A. Robin, J.P. Brunet: A&AS **31**, 243 (1978)
68. R. Rozanski, M. Rowan-Robinson: MNRAS **271**, 530 (1994)
69. A. Sandage, G. Carlson, J. Kristian, A. Saha, L. Labhardt: AJ **111**, 1872 (1996)
70. A. Sandage: 'Brightest Stars in Galaxies as Distance Indicators'. In *Luminous Stars and Associations in Galaxies, Proceedings of IAU Symposium No. 116*, ed. by C.W.H. De Loore et al. (Reidel, Dordrecht, 1986) pp. 31–41
71. A. Sandage, G.A. Tammann: ApJ **191**, 603 (1974)
72. A.E. Santolaya-Rey, J. Puls, A. Herrero: A&A **323**, 488 (1997)
73. H. Schild, A. Maeder: A&A **127**, 238 (1983)
74. T. Shanks, N.R. Tanvir, J.V. Major, A.P. Doel, C.N. Dunlop, R.M. Myers: MNRAS **256**, 29 (1992)
75. M.E. Sharina, I.D. Karachentsev, N.A. Tikhonov: Astronomy Letters **25**, 322 (1999)
76. S.J. Smartt, P.A. Crowther, P.L. Dufton, D.J. Lennon, R.P. Kudritzki, A. Herrero, J.K. McCarthy, F. Bresolin: MNRAS **325**, 257 (2001)
77. Y.-J. Sohn, T.J. Davidge: AJ **115**, 130 (1998)
78. Y.-J. Sohn, T.J. Davidge: AJ **112**, 2559 (1996)
79. Y.-J. Sohn, T.J. Davidge: AJ **111**, 2280 (1996)
80. O. Struve: ApJ **69**, 173 (1929)
81. C. Trundle, P.L. Dufton, D.J. Lennon, S.J. Smartt, M.A. Urbaneja: A&A **395**, 519 (2002)
82. R.B. Tully, S.C. Wolff: ApJ **281**, 67 (1984)
83. R.B. Tully, J.M. Nakashima: 'Distances Using A Supergiant Stars'. In *Galaxy Distances and Deviations from Universal Expansion*, ed. by B.F. Madore, R.B. Tully (Reidel, Dordrecht, 1986) pp. 25–28
84. M.A. Urbaneja, A. Herrero, R.P. Kudritzki, F. Bresolin, L.J. Corral, J. Puls: A&A **386**, 1019 (2002)
85. M.A. Urbaneja, A. Herrero, F. Bresolin, R.P. Kudritzki, W. Gieren, J. Puls: ApJ, submitted (2003)

86. A.M. van Genderen: A&A **208**, 135 (1989)
87. A.M. van Genderen: A&A **366**, 508 (2001)
88. K.A. Venn, J.K. McCarthy, D.J. Lennon, N. Przybilla, R.P. Kudritzki, M. Lemke: ApJ **541**, 610 (2001)
89. E. Verdugo, A. Talavera, A.I. Gomez de Castro: A&AS **137**, 351 (1999)
90. J.S. Vink, A. de Koter, H.J.G.L.M. Lamers: A&A **362**, 295 (2000)
91. J.S. Vink, A. de Koter, H.J.G.L.M. Lamers: A&A **369**, 574 (2001)
92. G.A.H. Walker, C.G. Millward: ApJ **289**, 669 (1985)
93. E.T.R Williams: 'A Spectrophotometric Study of Class A Stars. In: *Proceedings of the National Academy of Sciences of the United States of America* **15**, no. 11, 832 (1929)
94. D. Zaritsky, R.C. Kennicutt, J.P. Huchra: ApJ **420**, 87 (1994)
95. E. Zhang: AJ **88**, 825 (1983)
96. F.-J. Zickgraf, T. Szeifert, R.M. Humphreys: A&A **312**, 419 (1996)

9 Supernovae as Cosmological Standard Candles

Mark M. Phillips

Las Campanas Observatory, Carnegie Observatories, Casilla 601, La Serena, Chile

Abstract. The use of supernovae as Cosmological Standard Candles has matured in the last ten years to the point that these objects are now the distance indicator of choice for measuring the Hubble constant, the deceleration parameter, and the geometry of the universe. In this paper, we review the methods that have been developed for deriving distances from both type Ia and type II supernovae, and present the most recent results on the value of the Hubble constant based on these techniques.

9.1 Classification of Supernovae

Since the pioneering work of Minkowski [1], supernovae have been classified based on their *spectroscopic* characteristics. The defining parameter is the presence or absence of lines due to hydrogen: type I events show no evidence for hydrogen in their spectra whereas type II supernovae do. Type I supernovae are observed to occur in galaxies of all types, whereas type II events are nearly always associated with star-forming regions in spiral and irregular galaxies implying an origin in the core collapse of massive stars.

This simple classification scheme worked well for more than 40 years until the appearance of SN1983N in NGC 5236 which, while lacking hydrogen in its spectrum, differed in significant ways – spectroscopically, photometrically, and in its radio emission properties – from the classical type I supernovae [2,3]. Several more such events were soon identified, and the realization was made that these supernovae – the so-called type Ib/Ic events – also had their origin in the core collapse of massive stars [4]. By default, the classical type I supernovae, which are now universally believed to arise from the thermonuclear disruption of a white dwarf in a binary system, came to be labeled as type Ia events [5]. Modern day supernova classification includes even more subtypes (e.g., the type II supernovae are often divided into IIP "Plateau", IIL "Linear", and IIn "Narrow" subtypes depending on the shape of the light curve or the presence of narrow hydrogen emission lines in the spectrum) and, in the case of the type Ib/c and type II events, the distinction between categories is sometimes blurred.

At one time or another, attempts have been made to derive distances from essentially all the types of supernovae. However, the most successful work has been carried out with the type Ia and type II events. In the remainder of this paper, I shall concentrate on reviewing results based on these two major supernova types.

M.M. Phillips, Supernovae as Cosmological Standard Candles, Lect. Notes Phys. **635**, 175–185 (2003)
http://www.springerlink.com/

9.2 Type Ia Supernovae

Type Ia supernovae (SNe Ia) are the most luminous of all supernovae, and have been observed to redshifts as large as $z \sim 1.7$ with the Hubble Space Telescope [6,7]. In a SN Ia explosion, all of the energy liberated by thermonuclear burning goes toward overcoming the gravitational binding of the white dwarf progenitor, accelerating the material of the ejecta to high velocities. The single most important property for determining the luminosity is the mass of the radioactive isotopes synthesized in the explosion. We know from spectroscopic evidence that a significant fraction ($\sim$ half) of the material in the white dwarf is burned to the iron group, with ^{56}Ni the most abundant radioactive product. The ^{56}Ni decays with a half-life of $\sim$6 days to ^{56}Co, and the energy released is responsible for much of the luminosity at the peak of the light curve. The ^{56}Co then decays to ^{56}Fe with a half-life of $\sim$77 days, powering the light curve for at least the next few years. The energetic radiation and particles emitted by radioactive decay either escape the ejecta altogether, or are absorbed and thermalized.

Since the 1960s, the light curves of SNe Ia have been known to be remarkably homogeneous. Kowal [8] published a Hubble diagram for 22 SN I (most of which were SNe Ia) with a dispersion of 0.6 mag, demonstrating the potential utility of these events as cosmological standard candles. Hubble diagrams published by Sandage & Tammann [9,10] and Tammann & Leibundgut [11] showed dispersions within the observational errors (0.3-0.5 mag), suggesting that SNe Ia might have identical light curves and peak luminosities. Nevertheless, more precise photometric and spectroscopic observations carried out in the 1980s and 1990s have definitively shown that type Ia supernovae are not all identical [12–17].

The light curves of SNe Ia are characterized principally by differing decline rates. A frequently-used parameter for measuring the decline rate is $\Delta\mathrm{m}_{15}(B)$, which is the amount in magnitudes which the B light curve declines during the first 15 days after maximum [18]. Nugent et al. [19] showed that certain spectral features of SNe Ia at maximum light correlate with $\Delta\mathrm{m}_{15}(B)$, and that the decline rate sequence translates to a temperature sequence, with the slowest-declining SNe Ia corresponding to higher effective temperatures, and the faster-declining events being characterized by lower effective temperatures. This temperature sequence almost certainly reflects the fact that SNe Ia are produced with a range of radioactive ^{56}Ni masses.

Hamuy et al. [20,21] found that SNe Ia in E/S0 galaxies are characterized, on average, by faster decline rates than those events that occur in spiral or irregular galaxies. Moreover, blue galaxies do not produce fast-declining SNe Ia [21–23]. This implies that younger environments preferentially produce the slowest-declining SNe Ia. On the other hand, Hamuy et al. [21] have shown that the slowest-declining SNe Ia tend to be hosted by lower luminosity galaxies. Moreover, the average maximum brightness of SNe Ia appears to decrease with host galaxy radius [24,25]. These observations suggest that metal-poor environments may harbor the slowest-declining SNe Ia. Obviously more observations of SNe Ia in differing galaxy environments are needed to sort out these possible dependencies.

There is by now irrefutable evidence that SNe Ia do not all reach the same luminosity at maximum light. The range in peak brightness of events considered to be "normal" is > 1 mag in the B band [20]. This luminosity range almost certainly reflects differing ^{56}Ni masses – most likely in the range 0.4-1.1 $M_\odot$ [26,27] – consistent with the evidence that the decline rate sequence is a temperature sequence. Fortunately, a tight correlation exists between the decline rate of the light curve and the maximum luminosity [18,20,28]. This relationship can be used to correct the peak luminosity of any SN Ia to a standard value, allowing them to be used to measure precise distances. A caveat is that the physics behind the luminosity vs. decline rate relation is not yet fully understood, although significant progress has been made in recent years [29].

The correct relationship between luminosity and $\Delta m_{15}(B)$ cannot be ascertained without first correcting for absorption due to dust in the host galaxy. This is complicated by the fact that the color evolution of SNe Ia is a function of $\Delta m_{15}(B)$. Fortunately, the $B - V$ evolution from 30-90 days after maximum is very similar for SNe Ia, independent of the decline rate [30]. This fact can be used to calibrate $B_{max} - V_{max}$ and $V_{max} - I_{max}$ as a function of $\Delta m_{15}(B)$. Figure 9.1 shows these color relations as derived by Phillips et al. [28], along with the more recent calibration of Jha [31] which is in fairly close agreement.

Given the shape of the luminosity vs. decline rate relation and these color relations for correcting for the host galaxy reddening, it is a reasonably straightforward matter to derive relative distances to galaxies which have hosted well-observed SNe Ia. Three different techniques – "$\Delta m_{15}(B)$" [32], "MLCS" [33], and "Stretch" [34] – have been developed to date for this purpose. Each uses the optical photometry to characterize the light curve decline rate, which is then used to derive a luminosity correction to a standard decline rate. A dispersion < 0.2 mag in the Hubble diagram is typically obtained after making the decline rate and host reddening corrections. As opposed to other distance indicators of comparable precision, SNe Ia are readily observed to large distances where the peculiar velocities of the host galaxies are small compared to the Hubble flow velocity. *SNe Ia are thus the distance indicator of choice for determining the Hubble constant.* However, to derive the Hubble constant, the absolute magnitude corresponding to the standard decline rate must be determined.

Presently, the calibration of SNe Ia absolute magnitudes is based on a handful of well-observed events which occurred in galaxies for which Cepheid distances have been measured using the Hubble Space Telescope (HST). The number of calibrators can be increased by including SNe Ia whose host galaxy distances have been measured via the Surface Brightness Fluctuations (SBF), Planetary Nebula Luminosity Function (PNLF), and Tip of the Red Giant Branch (TRGB) methods since these techniques have now also been calibrated via HST Cepheid observations. Until recently, attempts to combine the Cepheid, SBF, PNLF, and TRGB methods to calibrate the SNe Ia Hubble diagram did not always lead to consistent results [20]. As illustrated in Fig. 9.2, these discrepancies have now essentially disappeared with the HST Key Project [35] results. In the figure are plotted the absolute magnitudes in B, V, I, and H as a function of $\Delta m_{15}(B)$

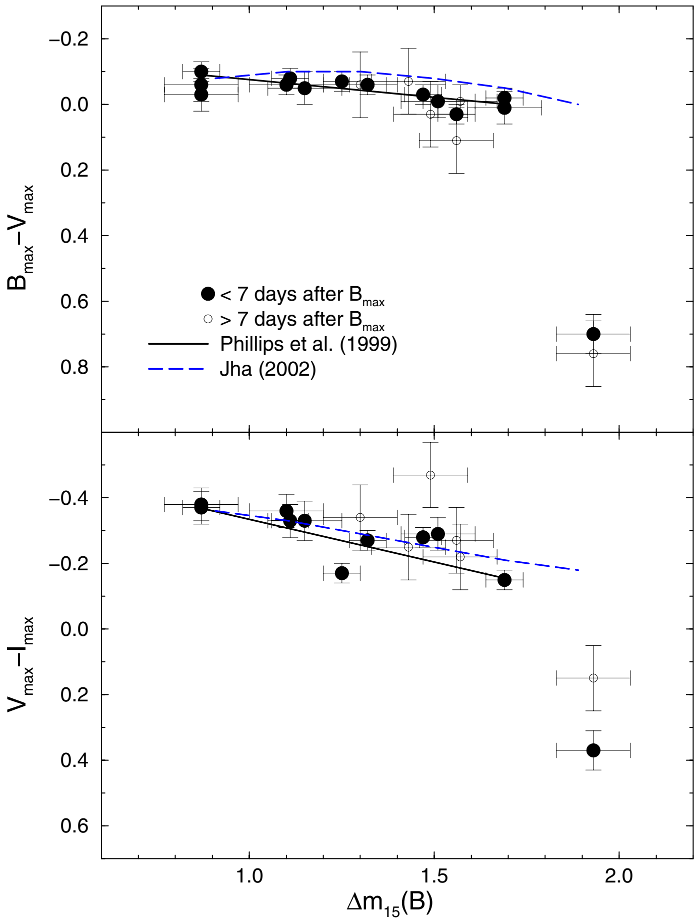

Fig. 9.1. The pseudo-colors $B_{max} - V_{max}$ and $V_{max} - I_{max}$ are plotted versus the decline rate parameter $\Delta m_{15}(B)$ for a sample of 20 SNe Ia which are believed to have suffered little or no host galaxy reddening

for 15 SNe Ia with distances obtained via Cepheids, SBF, PNLF, or TRGB. The luminosities of these events are in excellent agreement with those of a larger sample of SNe Ia in the Hubble flow ($0.01 \lesssim z \lesssim 0.1$) for a value of the Hubble constant of $H_o = 74$ km s^{-1} Mpc^{-1}.

It should be emphasized that, in spite of the impressive consistency seen in Fig. 9.2, universal agreement on the actual value of the Hubble constant implied by the SNe Ia data has not yet been achieved. In Table 9.1 are listed the values of the Hubble constant which I obtain using the Cepheid distances from three recent papers. *These distances are based on the very same HST data, and the same assumption of an LMC distance modulus of 18.5.* The discrepancies are traced to the use of different Cepheid samples and P-L relationships, and different assumptions concerning metallicity corrections. It seems clear from this

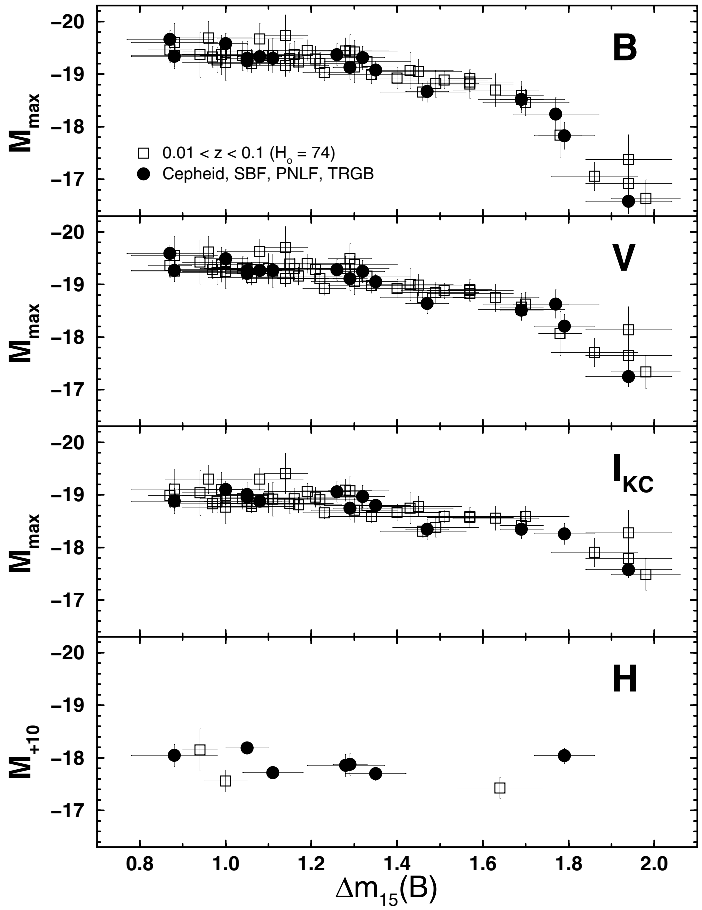

Fig. 9.2. Absolute magnitudes in $BVIH$ versus $\Delta m_{15}(B)$ for 66 well-observed SNe Ia

table that the Hubble constant is not yet known with confidence to a precision of 10%.

As detailed by Suntzeff in this volume, distances measured for high-redshift ($0.3 \lesssim z \lesssim 1.7$) SNe Ia have led to startling conclusions on the geometry of the universe and the existence of a dark energy component. Fortunately, these results are not dependent on the outcome of the debate as to the actual value of the Hubble constant since they are based only on a relative comparison of distant and nearby SNe Ia. However, there are legitimate concerns that the results obtained at high redshifts may be affected by progenitor age and metallicity, or unusual dust properties. For this reason it is imperative that we continue to intensively observe local SNe Ia to better ascertain the magnitude of such effects since the range of ages and metallicities observed in the local sample of galaxies is comparable to that expected when looking back to redshifts of $z \sim 0.5$ or more. In addition, as a check on the results obtained from optical photometry, it is

Table 9.1. Hubble Constant Values

Cepheid Calibration	H_o	Notes
Saha et al. [36]	62.7 ± 0.8	Compare with 60-61 (Saha, this volume)
Gibson et al. [37]	68.2 ± 0.9	Re-analysis of HST Cepheid data
Freedman et al. [35]	73.9 ± 1.0	Gibson et al. [37] distances;
		Udalski et al. [38] P-L relation;
		metallicity correction to P-L relation

important to characterize the near-IR light curves of SNe Ia where the effects of reddening can essentially be ignored, and where the slope of the luminosity vs. decline rate relation may be nearly flat (see Fig. 9.2). Finally, we need to understand the more peculiar members of the type Ia class, and learn to identify them reliably in the high-redshift samples.

9.3 Type II Supernovae

9.3.1 Expanding Photosphere Method

Type II supernovae (SNe II) result from the core collapse of massive (> 8 $M_\odot$) stars and constitute the most common class of SNe. Compared to SNe Ia, SNe II have been known for some time to comprise a relatively heterogeneous class of objects. Based on the work of Barbon et al. [39], the optical light curves of SNe II have historically been divided into two main types: the SNe IIP ("plateau") which decline very slowly ($\lesssim 3.5$ mag) for the first 100 days following maximum, and the SNe IIL ("linear") which display a rapid, exponential decline phase, dimming by $\gtrsim 3.5$ mag over the same period [40]. There is considerable evidence that SNe IIL interact significantly with a pre-existing circumstellar medium, whereas the progenitors of SNe IIP do not appear to suffer much mass loss before exploding. The majority of SNe II observed to date have absolute magnitudes in the range -16.0 $\lesssim M_B \lesssim$ -17.5, although a few examples have reached luminosities approaching those of SNe Ia. No obvious segregation in peak luminosity between the IIP and IIL classes is evident.

The first attempt to use SNe II to measure distances was made by Kirshner & Kwan [41] who, acting on a suggestion by Leonard Searle, applied the Baade-Wesselink method to SN1969L and SN1970G. This technique, which today is commonly referred to as the Expanding Photosphere Method (EPM), involves measuring a photometric angular radius

$$\theta = R/D \tag{9.1}$$

and a spectroscopic physical radius

$$R = R_o + v(t - t_o) \tag{9.2}$$

from the measured expansion velocity, v, of a selected absorption line at a time, t, after the time of explosion, t_o. The initial radius of the progenitor, R_o, can be ignored, leading to the following relation for the distance

$$D = v(t - t_o)/\theta \tag{9.3}$$

Assuming that the continuum radiation of the supernova arises from a spherically-symmetric photosphere, a photometric measurement of its color and magnitude determines its angular radius. However, since SNe II are not perfect blackbodies, a "flux dilution" correction factor (denoted by ζ) must be applied to derive the angular radius. Using detailed NLTE atmosphere models for Plateau SNe II, Eastman et al. [42] found that the most important variable determining ζ was the effective temperature. For a given temperature, ζ changed by only 5-10% over a very large variation in the other model parameters. If correct, this result leads to a great simplification because it implies that EPM has the potential to measure accurate distances without the need for a specially-crafted model for each SN.

The supreme advantage of EPM distances is that they are independent of the "cosmic distance ladder". Photometric and spectroscopic observations at two epochs and a physical model for the SN atmosphere lead directly to a distance. Moreover, additional observations of the same SN are essentially independent distance measurements as the properties of the photosphere change over time. This provides a valuable internal consistency check: all EPM-derived distances (at different epochs) must give *identical* distances to the same SN.

EPM was first applied to a significant sample of SNe II by Schmidt et al. [43,44] who analyzed data from 16 events. Their Hubble diagram yielded a value of H_0=73 km s^{-1} Mpc^{-1} and a scatter that implied an average uncertainty of 10% in the EPM distances. From a sample of 12 SNe with better photometric and spectroscopic sampling than the Schmidt et al. dataset, Hamuy [45] rederived the Hubble diagram obtaining $H_0 = 67 \pm 7$ and an uncertainty in an individual EPM distance of 20%, i.e., two times larger than previously claimed (see Fig. 9.3). These conclusions were somewhat hampered, however, because 1) the lack of simultaneous photometric and spectroscopic observations produced 12% interpolation errors, and 2) half of the sample was not sufficiently far out in the Hubble flow ($cz < 2000$ km s^{-1}).

It is possible that EPM can deliver distances with precisions better than 20%, but this will require a new sample of SNe II with $cz > 2000$ km s^{-1} and virtually simultaneous photometric and spectroscopic observations (no more than 2 days separation). Even with such a data set, however, it is not clear that the Eastman et al. [42] models predict consistent values of ζ for supernovae for which both optical and near-infrared photometry is available. This is illustrated by the well-observed SN IIP 1999em, for which Hamuy et al. [46] found a systematic difference of 20% between EPM distances derived independently from BV and

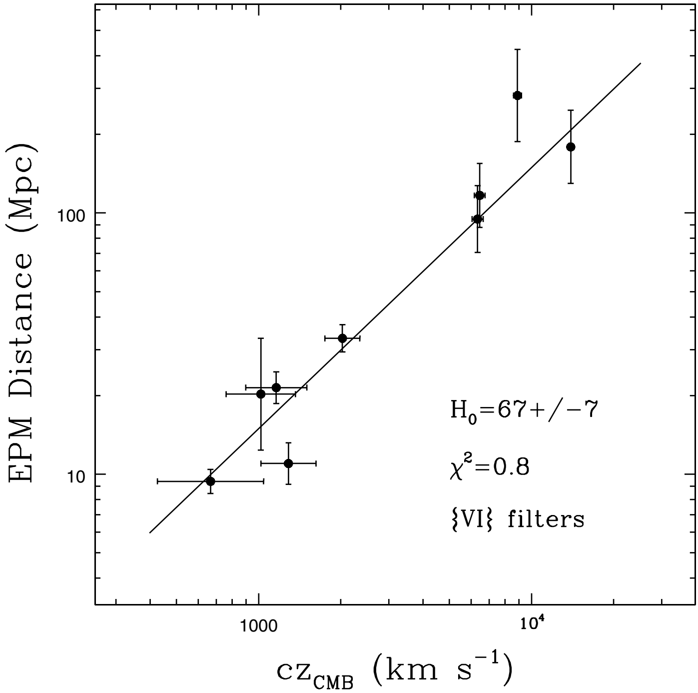

Fig. 9.3. EPM distance versus velocity in the Cosmic Microwave Background (CMB) rest frame. Figure taken from [45]

VK photometry. It would seem that EPM will require more work on the theoretical side before we can have more confidence in the Hubble constant results based on this technique. Yet a further complication is the increasing evidence that essentially all core-collapse supernovae are generally asymmetric at levels around 10-30% [47]. Such asymmetries may well affect the distances obtained to individual SNe II, although with large enough samples these errors should average out and not seriously affect the value of the Hubble constant derived.

9.3.2 Standard Candle Method

SNe IIP display such a wide range in their luminosities that their direct use as actual standard candles would appear to be ruled out. However, Hamuy & Pinto [48] recently found using a sample of 17 SNe II that the plateau luminosity appears to be well-correlated with the expansion velocity of the ejecta, which reflects that while the explosion energy increases so do the internal and kinetic energies (Fig. 9.4). This correlation implies that the luminosities of SNe II can be standardized from a spectroscopic measurement of the SN ejecta velocity. This "standard candle method" (SCM) yields Hubble diagrams with a scatter of 0.39 mag and 0.29 mag in the V and I bands, respectively. Hamuy & Pinto further showed that when their supernova sample was restricted to the eight

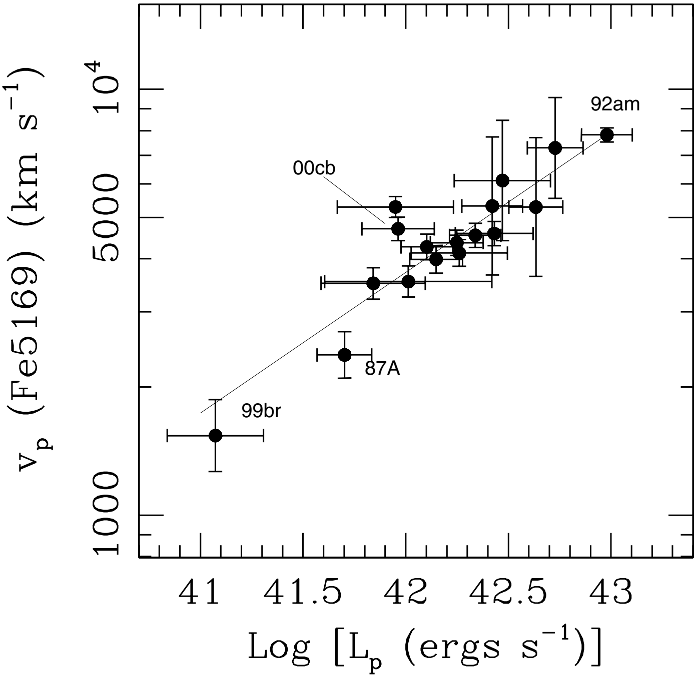

Fig. 9.4. Expansion velocities measured from the minimum of the Fe II λ5169 absorption vs. bolometric luminosity. Both quantities were measured in the middle of the plateau (day 50). Figure from [48]

objects with $cz > 2000$ km s^{-1}, the dispersion decreased to only 0.20 mag in both bands, suggesting that SCM can produce distances with a precision of 9%, comparable to the 7% precision yielded by SNe Ia.

In order to derive the Hubble constant from SCM, we need to have independent distances for at least one of the objects in the sample. HST Cepheid distances have been measured to the hosts of four well-observed SNe IIP (SN1968L, SN1970G, SN1973R, and SN1999em), but only two of these (SN1970G and SN1973R) have been published to date. Using the distances to these two supernovae as calibrated by the HST Key Project [35], Hamuy [49] finds Ho = 81±10 km s^{-1} Mpc^{-1}, which is consistent with the value of 74 yielded by SNe Ia using the same calibration.

SCM is an empirical method which affords a new opportunity to derive independent and potentially precise extragalactic distances. Nevertheless, before we can fully trust SCM, it is necessary to populate the Hubble diagram with a larger sample of SNe II with $cz > 2000$ km s^{-1}. A group at the Carnegie Observatories led by M. Hamuy is currently carrying out a program at the Las Campanas Observatory to obtain optical/IR photometry and optical spectroscopy of just such a sample. These data should also prove extremely useful for exploring techniques to improve the host galaxy dust reddening estimates for SNe IIP which are not yet optimal [49].

9.4 Conclusions

Techniques for using SNe Ia as cosmological standard candles have now reached a level of precision, at least in a relative sense, comparable to that of the best stellar distance indicators. Although distances derived from SNe II have not quite yet reached this level of confidence, the fact that EPM distances are completely independent of the standard cosmic distance ladder should provide the incentive for a new push to improve the models upon which this technique rests. SCM is also valuable as an independent check on the EPM distances, but this will require that more Cepheid distances be obtained for the host galaxies of well-observed SNe IIP in the coming years. An eventual goal of this work should be to obtain distances out to $z \sim 0.3 - 0.5$ using SNe II, thus providing completely independent verification of the cosmological results already obtained at these redshifts with SNe Ia. This should prove to be a difficult but exciting challenge in the coming years.

Acknowledgements

Special thanks to Mario Hamuy for providing much of the material in the section on SNe II. I also wish to thank my collaborators at Cerro Tololo and Carnegie for having helped to make the last ten years of my research career so exciting and gratifying. This review is dedicated to the memory of my dear friend and colleague Bob Schommer.

References

1. R. Minkowski: PASP **53**, 224 (1941)
2. R.A. Sramek, N. Panagia, K.W. Weiler: ApJ **285**, L59 (1984)
3. A. Uomoto, R. P. Kirshner: A&A **149**, L7 (1985)
4. J.C. Wheeler, R. Levreault: ApJ **294**, L17 (1985)
5. J.H. Elias, K. Matthews, G. Neugebauer, S.E. Persson: ApJ **296**, 379 (1985)
6. R.L. Gilliland, P.E. Nugent, M.M. Phillips: ApJ **521**, 30 (1999)
7. A.G. Riess, et al.: ApJ **560**, 49 (2001)
8. C.T. Kowal: AJ **73**, 1021 (1968)
9. A. Sandage, G.A. Tammann: 'Current Problems of Determining Distances to Galaxies'. In: *Supernovae as Distance Indicators*, ed. by N. Bartel (Springer-Verlag, Berlin, Heidelberg, New York 1985) pp. 1–13
10. A. Sandage, G.A. Tammann: ApJ **415**, 1 (1993)
11. G.A. Tammann, B. Leibundgut: A&A **236**, 9 (1990)
12. D. Branch: ApJ **316**, L81 (1987)
13. M.M. Phillips, et al.: PASP **99**, 592 (1987)
14. A.V. Filippenko, et al.: ApJ **384**, L15 (1992)
15. M.M. Phillips, et al.: AJ **103**, 1632 (1992)

16. A.V. Filippenko, et al.: AJ **104**, 1543 (1992)
17. B. Leibundgut, et al.: AJ **105**, 301 (1993)
18. M.M. Phillips: ApJ **413**, L105 (1993)
19. P. Nugent, M.M. Phillips, E. Baron, D. Branch, P. Hauschildt: ApJ **455**, L147 (1995)
20. M. Hamuy, M.M. Phillips, N.B. Suntzeff, R.A. Schommer, J. Maza, R. Aviles: AJ **112**, 2391 (1996)
21. M. Hamuy, S.C. Trager, P.A. Pinto, M.M. Phillips, R.A. Schommer, V. Ivanov, N.B. Suntzeff: AJ **120**, 1479 (2000)
22. M. Hamuy, M.M. Phillips, J. Maza, N.B. Suntzeff, R.A. Schommer, R. Aviles: AJ **109**, 1 (1995)
23. D. Branch, W. Romanishin, E. Baron: ApJ **465**, 73 (1996)
24. L. Wang, P. Hoeflich, J.C. Wheeler: ApJ **483**, L29 (1997)
25. A.G. Riess, et al.: AJ **117**, 707 (1999)
26. P.A. Mazzali, E. Cappellaro, I.J. Danziger, M. Turatto, S. Benetti: ApJ **499**, L49 (1998)
27. G. Contardo, B. Leibundgut, W.D. Vacca: A&A **359**, 876 (2000)
28. M.M. Phillips, et al.: AJ **118**, 1766 (1999)
29. P.A. Pinto, R.G. Eastman: NewA **6**, 307 (2001)
30. P. Lira: Masters thesis, University of Chile, Santiago (1995)
31. S. Jha: Ph.D. thesis, Harvard University, Cambridge (2002)
32. M. Hamuy, M.M. Phillips, N.B. Suntzeff, R.A. Schommer, J. Maza, R. Aviles: AJ **112**, 2398 (1996)
33. A.G. Riess, W.H. Press, R.P. Kirshner: ApJ **473**, 88 (1996)
34. S. Perlmutter, et al.: ApJ **517**, 565 (1999)
35. W.L. Freedman, et al.: Astrophys. J. **553**, 47 (2001)
36. A. Saha, A. Sandage, G.A. Tammann, A.E. Dolphin, J. Christensen, N. Panagia, F.D. Macchetto: ApJ **562**, 314 (2001)
37. B.K. Gibson, et al.: ApJ **529**, 723 (2000)
38. A. Udalski, M. Szymanski, M. Kubiak, G. Pietrzynski, I. Soszynski, P. Wozniak, K. Zebrun: AcA **49**, 201 (1999)
39. R. Barbon, F. Ciatti, L. Rosino: A&A **72**, 287 (1979)
40. F. Patat, R. Barbon, E. Cappellaro, M. Turatto: A&A **282**, 731 (1994)
41. R.P. Kirshner, J. Kwan: ApJ **193**, 27 (1974)
42. R.G. Eastman, B.P. Schmidt, R. Kirshner: ApJ **466**, 911 (1996)
43. B.P. Schmidt, R.P. Kirshner, R.G. Eastman: ApJ **395**, 366 (1992)
44. B.P. Schmidt, R.P. Kirshner, R.G. Eastman, M.M. Phillips, N.B. Suntzeff, M. Hamuy, J. Maza, R. Aviles: ApJ **432**, 42 (1994)
45. M. Hamuy: Ph.D. thesis, University of Arizona, Tucson (2001)
46. M. Hamuy, et al.: ApJ **558**, 615 (2001)
47. L. Wang: American Astronomical Society Meeting 200, abstract No. 32.05 (2002)
48. M. Hamuy, P.A. Pinto: ApJ **566**, L63 (2002)
49. M. Hamuy: 'The Latest Version of the Standardized Candle Method for Type II Supernovae'. In: *Carnegie Observatories Astrophysics Series, Vol. 2: Measuring and Modeling the Universe*, ed. by W. L. Freedman (Pasadena, Carnegie Observatories)
`http://www.ociw.edu/ociw/symposia/series/symposium2/proceedings.html`

10 Type Ia Supernovae and Cosmology

Nicholas B. Suntzeff

Cerro Tololo Inter-American Observatory, National Optical Astronomy Observatories, Casilla 603, La Serena, Chile

Abstract. The direct evidence for the acceleration of the local Universe away from a matter-dominated frame rests on a simple observational result: the Type Ia supernovae at $z \sim 0.5$ are about 0.25 magnitude too faint relative to a matter dominated universe with $(\Omega_M, \Omega_\Lambda) = (0.3, 0.0)$. We choose to interpret our observations in a simple fashion: the faintness of the supernovae is due to increased luminosity distances to the supernovae. In turn, the increased size of the local Universe can be interpreted as the effect of the cumulative repulsion from a dark energy associated with the cosmological constant of Einstein. In this short summary, I will explore the technique for the measurement of luminosities distances using SNe Ia, and some of the underlying assumptions we have made.

10.1 Introduction

There was general agreement about the Standard Model of the Universe around 1995 – or perhaps an agreement to disagree – which divided reasonably cleanly between theoreticians and observers. The theoretical choice was clear – the Universe must be flat because inflation is so compelling. Universal inflation at faster-than-light "velocities" would smooth out all local spatial curvatures, implying a flat geometry at the end of inflation and a natural explanation for the isotropy of galaxies in a present universe where the distant horizons only extend a few tens of degrees. It was further argued that given that theory demands $\Omega_T = \Omega_\Lambda + \Omega_M = 1$, there was no physical explanation why $\Omega_\Lambda \sim \Omega_M$ should be the order of unity. Therefore $\Omega_\Lambda = 0$ exactly and $\Omega_M = 1$ exactly. The annoying consequence of this line of reasoning was that $H_0 < 50$ km s^{-1} Mpc^{-1} and that the Universe was very young. This contradicted the age of the stars from isochrone work on globular clusters, as well as the ages from radioactive thorium decay in old stars, white dwarf ages, and the best value of the Hubble constant. The theoreticians pointed out correctly that these measurements of the age of the Universe were uncertain, and historically have changed in much larger jumps than expected from the observational error.

While some observers agreed with this reasoning, most observers did not. The evidence from galaxy structure and from partially virialized velocities of galaxies in clusters seemed to show that $\Omega_M < 1$. The matter making up Ω_M was mostly dark matter, which was another mystery.

A third model was possible in 1995: $\Omega_M \sim 0.2$ and $\Omega_\Lambda \sim 0.8$ but because of the strong objections to the coincidence that $\Omega_\Lambda \sim \Omega_M$, there were very few proponents of this model.

N.B. Suntzeff, Type Ia Supernovae and Cosmology, Lect. Notes Phys. **635**, 187–202 (2003)
http://www.springerlink.com/

The theoretical problem for a non-zero cosmological constant was well stated by [1]. As they write: “Unfortunately, the modern physical interpretation of the cosmological constant… gives little support to the idea that a cosmological constant contributes a significant fraction of the critical mass density today. On the contrary, the simplest arguments suggest a value that is many, many orders of magnitudes larger than is acceptable, leading to what is referred to as the cosmological constant problem. … it is difficult to understand how it would give the very tiny value required rather than zero. Although one can solve the age problem by introducing a cosmological constant, it is far from being an attractive solution”.

At the time of the writing of this article in 2003, the WMAP project has just announced its exciting results, where they find $\Omega_T = 1.02 \pm 0.02$ improving by a factor of two the error bars on Ω_T from the ground-based CMB measurements. The Universe is clearly flat (or very close), and a large number of experiments since 1995 have consistently shown that Ω_M is much less than critical. By trivial arithmetic, this implies the existence of a positive Ω_Λ, but does not directly detect its effect on the cosmology. The direct detection of the effects of a cosmological constant (or similar dark energy) has been provided by the measurements of the luminosity distances to Type Ia supernovae.

In this summary, I will explore some of the issues of using Type Ia supernovae to measure luminosity distances, stressing unsolved problems associated with estimating intrinsic luminosities of Type Ia events. What is not solved, however, is the cosmological problem mentioned above. The coincidences that $\Omega_\Lambda \sim \Omega_M$ at our epoch and that Ω_Λ is so close to zero but not precisely zero are no longer arguments against the standard (at least, this year's standard) cosmology of $(\Omega_M, \Omega_\Lambda) = (0.3, 0.7)$. It is now accepted as a deeper problem in physics. As with dark matter, in the near term we may quickly become used to having dark energy without understanding the physics it represents. The quest for understanding the physics of this dark energy was listed as one of the “Eleven Science Questions for the New Century” in the Turner Report for the Board on Physics and Astronomy of the NAS [2].

10.2 The Quest for q_0 with Type Ia SNe

The modern effort to measure the geometry of the Universe begins with the Sandage paper [3] where he laid out the various strategies for measuring the geometry of the Universe with data from the Palomar 200″ telescope. He parameterized the geometry using the deceleration parameter $q_0 \equiv -\dot{R}R/\ddot{R}^2$ which can be rewritten using the Friedmann equation as $q_0 = \Omega_M/2 - \Omega_\Lambda$ in a radiationless universe. He pointed out that as q_0 goes from $+1 \Rightarrow -1$ at $z = 0.5$, that is, from a over-critical mass-dominated universe to a steady-state universe, objects will dim by $\delta m \sim 0.9$. His best estimate was $q_0 = 1 \pm 0.5$, a value which stood for two decades.

The next important paper was [4] where it was shown that supernovae could be used to measure q_0 provided that accurate photometry at $m \approx 23$ could be achieved. His technique, however, rested on the use of the Baade-Wesselink analysis [5] of the photometry and radial velocities of spectral absorption lines in its modern implementation [6,7]. Interestingly, Wagoner anticipated the need for accurate galaxy subtraction to use the photometry for distance measurements.

The search for high redshift supernovae was pioneered by the Danish group [8,9] who found a Type II supernova at redshift of $z = 0.28$ and a Type Ia supernovae SN1988U at $z = 0.31$. They used hour long exposures in V of Abell clusters with the facility CCD at the 1.5m Danish telescope, and found SNe by differencing and blinking monthly exposures. In the latter supernova they also verified the prediction from general relativity of time dilation (see [10] for a more modern discussion of this effect).

Their techniques were extended by Perlmutter and Pennypacker resulting in seven new high redshift supernovae announced in 1994-5 (with the first SN discovered in 1992) [12–14] at redshifts out to $z = 0.46$ using the Isaac Newton Telescope. In a parallel effort started in 1994, the High-z Supernova Team co-founded by Brian Schmidt and me, found its first high-redshift supernova SN1995K at $z = 0.49$ [11]. Both the Perlmutter group (now called the Supernova Cosmology Project) and the High-z Supernova Team began to use the CTIO 4m telescope in 1995 for the supernova searches, which allowed them to extend the search to $z \sim 0.9$ over the next few years. The excellent image quality, large format detectors, and clear weather during the summer observing season allowed both groups to guarantee finding SNe, which in turn did not put the followup telescopes at Keck, CFHT, APO, and *HST* at risk with no objects to observe.

While the switch to a wide-field telescope at a good site was critical for the discovery of high-z supernovae, equally critical was the precise calibration of the intrinsic luminosities and colors of Type Ia supernovae, based on nearby events.

10.3 Intrinsic Properties of Nearby Type Ia Supernovae

10.3.1 The Physics of the Light Curve

The exact progenitor of a Type Ia supernova has not been determined: it is clear however that a Type Ia supernova is a thermonuclear deflagration or detonation of a white dwarf (probably a CO white dwarf near the Chandrasekhar mass or a merged double generate white dwarf). All supernovae after explosion are powered by the radioactive decay chain of ^{56}Ni $\rightarrow$ ^{56}Co $\rightarrow$ ^{56}Fe. The early parts of the light curves in $UBVR$ have "humps" which represent the release of stored energy, both radioactive and kinetic converted to thermal energy, which is diffusing through the photosphere as it recedes in mass. Type II and Type Ib/c core collapse supernovae also have an initial period of sudden adiabatic cooling which lasts a few days. A similar adiabatic phase in Type Ia supernovae is not visible because the explosion starts in a very small object, a white dwarf.

At maximum light, the instantaneous energy input from the radioactive nuclides is balanced by energy release measured from the observed bolometric light curve: Arnett's law [17].

For the redder colors $RIzYJHK$, there is a secondary maximum in Type Ia supernovae. The physics of the secondary maximum is understood, but is not easy to explain in words. Pinto & Eastman [18,19] note that the rise to a secondary maximum is due to a rapid change in the flux mean opacity. After maximum light, the thermalized energy input to the light curve from the radioactive nuclides is less than the observed luminosity, implying qualitatively that the post-maximum luminosity is powered by a reservoir of previously trapped radiation. If the post-maximum opacity decreases due to a drop in the effective temperature, the diffusion times drop and the trapped energy escapes more rapidly leading to a pause in the rapid luminosity decline. This bolometric flux excess appears in the redder colors because the opacities are very low and there are ample emission sources such as FeII and CaII. A similar explanation has been given by Höflich and the Texas group [20,21].

By day 50 or so, the energy deposition in a typical Type Ia supernova due to the thermalization of γ rays occurs in regions which are optically thin in the optical and near-infrared [18]. Thus, the luminosity at this epoch responds rapidly to the input energy source, which at this time is ^{56}Co. The light curve declines very linearly (in magnitude units) for large parts of this phase, but with one large difference between the decline rates between Type Ia and Type II supernovae: the Type II supernovae decline at the rate given by the e-folding time (77d) of the radioactive decay of ^{56}Co whereas the Type Ia supernovae decline more quickly.

This points to an important distinction between Type Ia and Type II supernovae: Type II supernovae thermalize the energy input from the radioactive energy input throughout their bright optical phase, whereas Type Ia supernovae leak the γ ray radiation (and perhaps positrons at late time). As shown by Leibundgut and Pinto [22,23], a significant fraction of the γ rays leak out of the supernova debris going from 10% at B_{max} to over 50% 40 days after maximum. The more rapid decline in the exponential phase for Type Ia supernovae is due to the rapidly declining optical depth to the trapping of the γ rays and positrons.

It is fortunate that only the order of 10% of the radioactive energy input is escaping at maximum light in Type Ia supernovae – this is a key feature which allows us to use these events as standardizable candles. This small escape fraction is much less than the estimated range in ^{56}Ni masses produced in the explosion. Leibundgut and collaborators [24,25] have estimated uvoir bolometric light curves by integrating optical broad-band magnitudes. Applying Arnett's law to the peak bolometric luminosities, they found a range of more than a factor in 10 in the ^{56}Ni masses for a group of nearby Type Ia SNe. In [26], a V magnitude with a bolometric correction was used to study the γ-ray trapping in the late-time light curves, which also showed a significant range in ^{56}Ni masses. It is the range in synthesized ^{56}Ni which is presumably the physical factor leading to the range in intrinsic peak luminosities in Type Ia SNe.

The rapidly falling optical depth to γ rays after maximum light should give us concern though. This means that the energy deposition from γ rays may not be local – that is, a γ ray may traverse a large part of the nickel nebula before

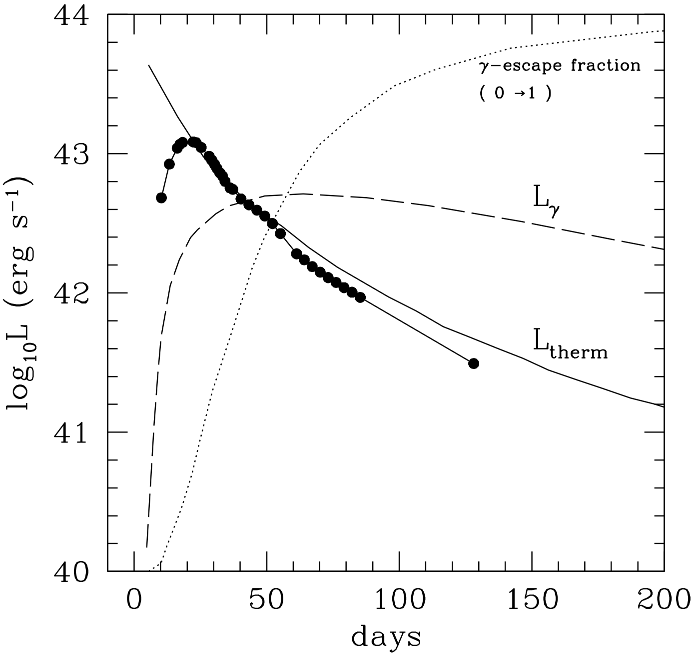

Fig. 10.1. Bolometric light curve of SN2001el [16] compared to simple model predictions for the luminosity of a Type Ia supernova [22]. The observed bolometric light curve represents the "uvoir" integration of *UBVRIJHK*. The observed curve has been shifted by 21 days. The *upper solid curve* is the theoretical prediction for the instantaneous thermalized luminosity (L_{therm}). The *upper dashed curve* represents the expected γ-ray luminosity due to γ-ray leakage (L_γ). The *dotted curv*e is the escape fraction for the γ-rays, running from 0 at the bottom (no escape) to 1.0 at the top (full escape). Note that even near maximum light, a significant amount ($\sim$ 10%) of γ-rays can be escaping from the Type Ia nebula. The theoretical curves are taken from [22]

thermalizing, if it thermalizes at all. The subsequent light curve shape and color, then could be a function not only of the amount of ^{56}Co present, but also how it is distributed in the debris.

Pinto & Eastman [27] show that four fundamental physical parameters affect the light curve: the opacity, the distribution of ^{56}Ni, the mass of ^{56}Ni, and the explosion energy. In their paper [19], they find that the peak luminosity is governed by the mass of ^{56}Ni and is relatively insensitive to most other parameters in Chandrasekhar-mass explosions. They conclude that the cosmological results are unlikely to suffer from systematic effects stemming from evolution in the explosions' progenitors. But until we understand the nature of the progenitor, we cannot be certain of the real source of the small variations in the maximum brightness of Type Ia supernovae. In Fig. 10.1, we show the bolometric light curve of SN2001el, compared to simple model predictions for the luminosity of Type Ia supernovae [22].

10.3.2 Light Curve Observations

In Fig. 10.2 I show a typical light curve for the well observed nearby Type Ia supernova SN2001el [16] in the bands $UBVRIJHK$. The bluer colors ($UBVR$) show a rise to maximum light ($\sim$ 20 days: see [28,29]), a fall from maximum which is reasonably symmetric with the rise time, and a final exponential decline starting around 40 days after maximum light. The redder colors, including the new data in $YJHK$ in the near-infrared, show a variable secondary maximum before the exponential decline.

The use of light curves of supernovae was pioneered by Kowal [30] who used around 20 supernovae, mostly discovered by Zwicky, to form a Hubble diagram for Type I supernovae (at this time, the distinction between Type Ia and the core collapse Type Ib/c was not known). In 1979, José Maza began a supernova search in the southern hemisphere by blinking two epochs of photographic plates [31]. Sandage and Tammann began a photographic search similar to the Maza survey

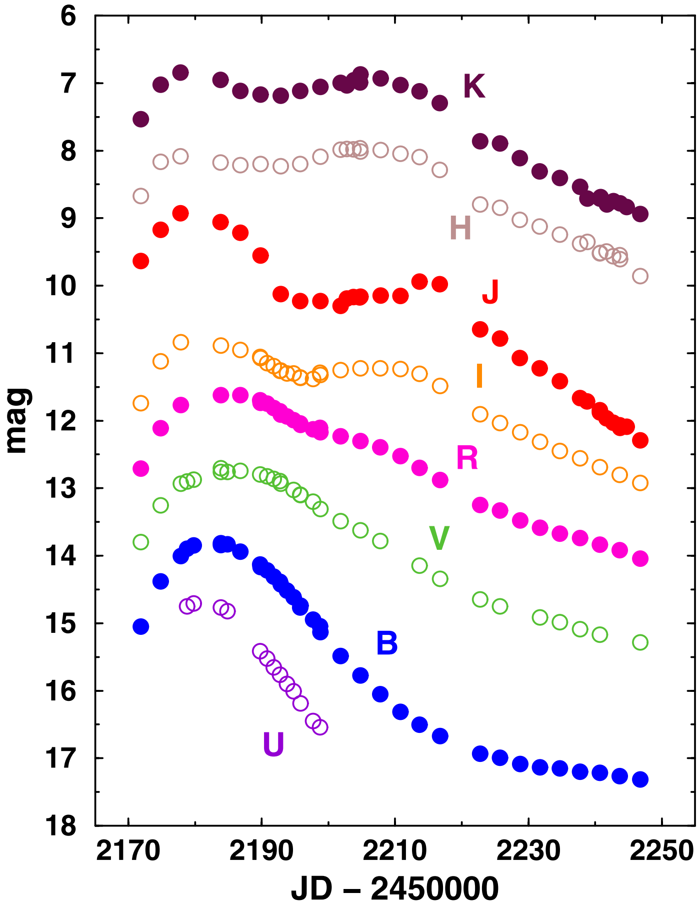

Fig. 10.2. Light curves for the nearby Type Ia supernova SN2001el in NGC 1448 [16]

at Las Campanas. Their search was severely hampered by the poor quality of photographic plates made at the time. In 1989, Sandage encouraged the Chile group (Hamuy, Maza, Phillips, and Suntzeff) to continue the search using plate blinking, and after three years of searching, over 50 supernovae were found. Roughly 30 Type Ia supernovae were found out to redshift of $z \sim 0.15$, a sample which is known as the Calán/Tololo sample. These supernovae had precise BVI light curves using facility CCD detectors. Parallel to this effort the Calán/Tololo group observed bright supernovae with the same CCD detectors.

In 1988, Leibundgut published his thesis [35] which collected all the supernova light curves, and brought order to the vast number of light curves of supernovae. He also introduced a standard template in B light for a Type Ia supernova. With the use of the template and colors of supernovae derived by Leibundgut, we were able to begin to see differences between individual events that were not merely due to dust obscuration. Events such as SN1986G in Cen A [36] clearly did not fit the Leibundgut template, and served as a warning that Type Ia supernovae were not standard candles.

With precise CCD photometry and secondary distances to the nearby galaxies hosting SNe, Phillips [33] was able to show a clear range in peak brightnesses of Type Ia supernovae. He invented a parameter called "Δm_{15}" (patterned after an earlier parameter defined by Pskovskii [34]) which measures the decline in brightness over the 15 days after maximum light. In effect, it measures the evolutionary speed of a supernova away from maximum light. He found that the fainter supernovae were more rapidly declining from maximum light.

The distances to the host galaxies used by Phillips were not very precise (the SBF and T-F distances have improved dramatically since then). A more precise way to measure a relative distance to an object is using the residuals in the Hubble flow. To do this, one must have a sample of galaxies in the "quiet" Hubble flow, away from large-scale motion and the effects of peculiar velocities. Assuming a precision of 0.15 mag in peak brightness and a typical peculiar velocity of around 300 km s^{-1}, the Hubble law, written differentially as $\delta v/v \sim 0.46\delta m$ implies that for redshifts greater than $z = 0.013$, the dispersion in the Hubble law is due to the dispersion in the supernova luminosities and not in peculiar velocities. We can then use the residual brightness calculated from the Hubble diagram for SNe at $z > 0.013$ to calibrate quantities measured from the light curve with respect to the intrinsic brightness.

The results of the calibration of intrinsic luminosities of Type Ia supernovae from the Calán/Tololo survey were published in [37–43]. In the Calán/Tololo analysis, families of templates in BVI for a number of well observed supernovae were parameterized as a function of Δm_{15}. Similar statistical techniques were invented by the CfA group [44,45] (called MLCS) and the SCP (called "stretch": see [48]) also using the Calán/Tololo sample. In the latter paper by the CfA group, they included the reddening estimate as part of the fitting procedure, which was later incorporated by the Calán/Tololo group [46]. The precision of the Hubble diagram of Type Ia supernovae can be appreciated in Fig. 10.3 taken from the recent thesis of Jha where he plots 80 supernovae. The dispersion in the

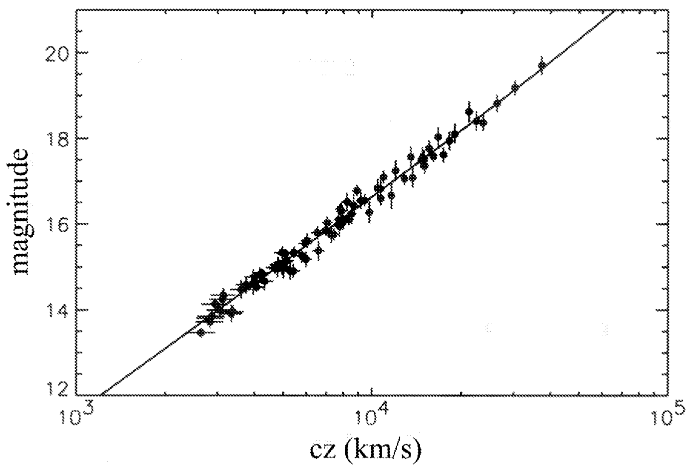

Fig. 10.3. Observed Hubble diagram for 80 Type Ia supernovae from the thesis of Jha [49]

corrected intrinsic luminosities ranges from 0.12 to 0.18 magnitudes, depending on the sample chosen.

A key to the use of Type Ia supernovae for measuring cosmological distances is understanding the evolution of the intrinsic colors and the reddening. The intrinsic colors cannot calculated from theory and we must rely on observations. An important advance in the understanding of reddening was provided by Lira in her thesis [47] who found that during certain phases of the color evolution of Type Ia SNe, the colors for unreddened events seem to be uniform. Phillips et al. [46] used this to reevaluate the intrinsic colors of Type Ia SNe where they found that the $(B_{max} - V_{max})$ colors were much more uniform than previously thought. The problem of reddening is complicated by the fact that most "unreddened" supernovae chosen to define the locus of unreddened colors come from dominantly early-type galaxies. Noting that the age of the progenitors for Type Ia's in early type galaxies are probably much older than in late-type galaxies, there is no empirical reason to believe that the colors (as a function of Δm_{15}) between young and old supernovae must be the same at the few hundredths of a magnitude level. Studies to date [50–52] have not found any systematic differences in the color – Δm_{15} relation-ship between early and late type galaxies, despite the fact that only in late-type galaxies do the very brightest SNe appear.

The most recent Δm_{15} luminosity calibration is shown in Fig. 10.4. Our group at LCO and CTIO have been adding near-infrared light curve distances to the Hubble diagram to try to provide nearly reddening-free luminosities for nearby SNe. With the few H-band magnitudes, the correction to standard luminosity is close to zero: the H-band peak magnitudes may turn out to be true standard candles. Figure 10.4 also shows that the nearby supernovae, with distances based on Cepheids, SBF, and PN work, and the distant supernovae with relative luminosities calculated from the residuals in the Hubble diagram, have

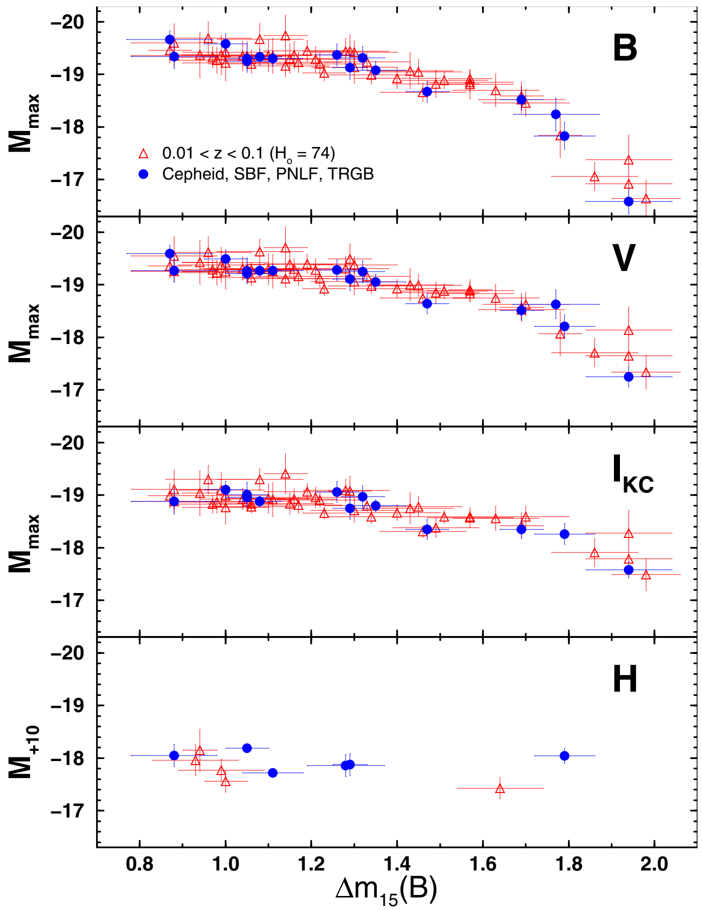

Fig. 10.4. Absolute magnitudes for Type Ia SNe in $BVIH$ as a function of Δm_{15} from [16]. The solid points represent luminosities calculated from direct distances measured to host galaxies based on Cepheid, SBF, or PN distances. The open symbols represent relative distances measured from the quiet Hubble flow

identical luminosity- Δm_{15} relationships. Except for the reddening calculation, these two samples should have no common systematic errors in the estimation of the intrinsic luminosities. The agreement between the two samples is excellent.

The Hubble diagram of the supernovae in the quiet Hubble flow can be combined with the HST distances to host galaxies which have had Type Ia supernovae to measure a Hubble constant. Results from the Calán/Tololo group [55] using the Cepheid calibration from the Saha/Sandage group yielded a Hubble constant of 63.9+/-2.2(internal)+/-3.5(external) km s^{-1} Mpc^{-1}, However, a revision of the HST photometric scale and the Cepheid reddening law by [54], has led to a new value of the Hubble constant based on Type Ia SNe: 71+/-2 (random)+/-6 (systematic) [53]. The underlying problems associated with the *HST* Cepheid calibration are explored in this volume in papers by Madore and Saha.

10.4 q_0 and the Acceleration of the Universe as Measured from Supernovae

The technique for measuring the local acceleration of the Universe is very similar to the measurement of the local Hubble flow with Type Ia supernovae. In one sense it is easier: the search is simple to do. There are roughly 2 Type Ia supernovae per sq-degree out to $z = 0.5$ that appear every month, with peak magnitudes of $R = 22.1$. Precise relative photometry (0.05 mag) at this magnitude range is within easy reach of a 4m class telescope or *HST*. Searching this area is also no problem. The transfer of photometric zero-point from the Landolt standards at 12-15th magnitude is tedious, if not hard. Wide field imagers on 4m class telescopes are now as large as 1/3 to 1 sq-degree. One can easily search 10 sq-degrees per night. To push to $z = 1$ is much more difficult, but still can be done from the ground. Peak magnitudes at $z = 1$ are $I = 23.5$ with an observed rate of about 6.5 SNe (cumulative) per sq-degree [56]. The technique for searching is also standard now: present epoch images differenced with kernel-matched template images. Thus finding the supernovae and measuring a light curve in an observed photometric system (typically RI) is not difficult.

Similarly, once the supernovae are converted to a rest frame photometric system via a K-correction or similar technique, the measurement of the distance modulus is identical to the procedures above, using the Δm_{15}, MLCS, or stretch techniques to calculate the reddening and bring the supernova to a standardized luminosity.

The two difficult steps in the process are the calculations of the K-corrections and the spectral observations. The spectra are required for the classification of the supernova and the redshift. For the cosmology, the redshifts are only needed to $\delta z \sim 0.025$ or so. For most supernovae, the redshifts are measured from the host galaxy spectra. However, for some fraction of the supernovae, the supernova is significantly brighter than the galaxy and we must use the supernova spectrum to estimate the redshift. Perhaps 25% of our supernovae appear in faint galaxies. Given that the peak luminosity of a supernova is $M_B \sim -19.5$, it remains an unexplored issue if supernovae are appearing in systematically fainter galaxies at higher redshifts. Certainly there is no selection bias here. Since the galaxies at redshifts of 0.5 or greater are only slightly above sky in RI, the subtracted images of galaxies are dominated purely by sky noise independent of the host galaxy. For the "hostless" supernovae, we rely on fitting template supernova spectra to the observed spectra to derive redshifts. Both Tonry and Riess of our group have written programs to measure SN-based redshifts [56].

For the high-z supernova spectra, both high-z supernova groups have relied on Keck spectroscopy. The difficulty with the spectra is that the important spectral features for classifying Type Ia SNe (the silicon and sulfur features near 6000Å) redshift out to near 1μm where variable airglow makes the sky subtraction difficult. Recent spectra taken with the Gemini 8m GMOS in "nod and shuffle" mode have produced much better sky subtracted spectra. In addition, the grism spectra with ACS at *HST* have also produced excellent spectra at $z = 1$ with the equivalent exposure times to Keck.

A discussion of the K-corrections for the supernova photometry is well beyond the limits of this conference paper. The K-corrections are presently the most difficult part of the supernova light curve measurement to carry out. The possible covariance between the K-corrections and the intrinsic supernova properties of reddening and luminosity correction leaves us open to systematic errors in the final luminosity distances. The SCP group has published two important papers modifying the K-correction techniques. In [57], the K-correction was modified to include cross-band (for instance R to B) corrections. In [58], the cross-band K-correction is calculated from template supernova spectra by warping the template spectrophotometry with a spline to fit the observed colors of the supernova.

Once the data have been K-corrected, the light curves (typically RI corrected to rest frame BV) are used to measure luminosity distances. The luminosity distance is defined as:

$$d_l \equiv \left(\frac{L}{4\pi F}\right)^{1/2} = d_l(z : \Omega_M, \Omega_\Lambda)$$

converted to distance modulus:

$$\mu_p = 5 \log d_l(Mpc) + 25$$

For small z:

$$d_l H_0 = z + z^2 \left(\frac{1 - q_0}{2}\right) + O(z^3)$$
$$\Delta q_0 \approx 0.9 \Delta m/z$$

Thus to measure q_0 to an error of 0.1 units at $z = 0.5$ we will need an error of 0.06 mag in the ensemble average of distance moduli. The observables are (z, μ_p) from which we must derive (Ω_M, Ω_Λ), and $\Omega_{tot} \equiv \Omega_M + \Omega_\Lambda = 1 - \Omega_k$. Finally, given a local value of the Hubble constant, we can derive the age of the Universe t_0 as $H_0 t_0 = f(\Omega_M, \Omega_\Lambda)$ where f is a simple function.

10.4.1 Recent Results

Both the SCP and the High-z Supernova Team began the search for high-z supernovae in 1995 at CTIO. Early results from the SCP favored a large deceleration which they interpreted as $\Omega_M \sim 1$ [59]. A subsequent analysis by both groups showed that the deceleration was much smaller than implied by a $\Omega_M = 1$ Universe [60,61]. With expanded samples, in 1998, both groups simultaneously announced the supernovae luminosity distances apparently showed the Universe in acceleration [62,63]. Such an acceleration would require a previously

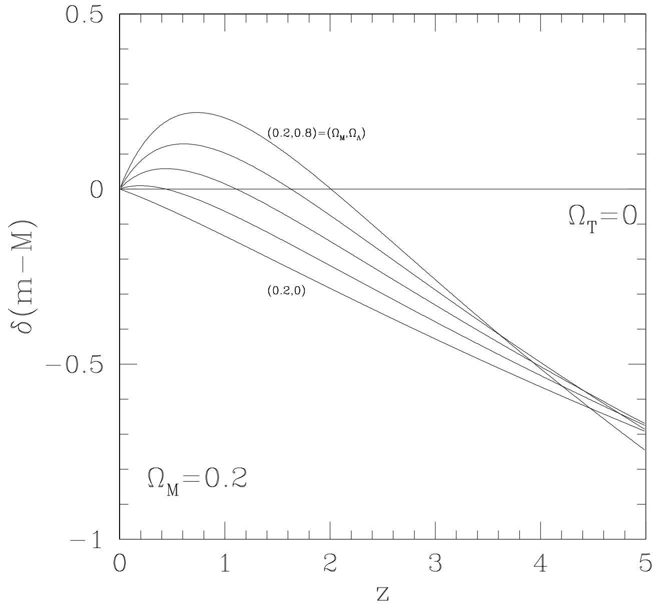

Fig. 10.5. The effects of the cosmological constant Ω_Λ on the luminosity distances (converted to distance moduli). The distance moduli are calculated relative to the distance modulus in an empty universe ($\Omega_T = 0$). This plot shows the effect of starting with an open universe with $\Omega_M = 0.2$ (lower curve) and adding dark energy in the form of a cosmological constant until the Universe is flat (upper curve). Each curve represents a step of 0.2 in Ω_Λ. The sense of the diagram is that objects appear fainter than expected as one moves up the diagram. The effect of adding Ω_Λ is to make objects *fainter* than expected. The difference between the (0.2,0) and (0.2,0.8) Universe is a maximum of 0.32 mag at $z \sim 0.8$

undetected negative pressure in the Universe which was large enough to compare with the geometrical effects of the matter density of the Universe. It apparently was a "dark energy" associated with a cosmological constant or an energy density associated with a field affecting the vacuum of the Universe. The argument against the cosmological constant – that $\Omega_M \sim \Omega_\Lambda$ – went from being a powerful argument against $\Omega_M \sim 1$ and a small value of the Hubble constant – to the realization that we may have a large gap in our understanding of the physics of gravitation and perhaps particle physics [64].

The observations have sparked a tremendous interest among theoretical physicists to find a "natural" explanation for the source of the field associated with the dark energy. To date, more than 2 dozen models for the source of the field have been suggested. The observations are simple and clear however: distant supernova at roughly $z = 0.5$ are fainter by about 0.25 mag than expected for an empty or a matter dominated universe. Figure 10.5 shows that fainter implies a cosmological constant. Put into a Newtonian model: the supernovae are fainter than expected, and therefore farther away, implying a force accelerating the local Universe against gravitation from matter.

Of course, there are other natural explanations for the faintness of distant supernovae: reddening, luminosity evolution, or selection biases. Both groups do measure the reddening to the distant supernovae and so far this does not seem to be the explanation, even assuming "grayer" inter-galactic dust proposed by [65]. See the reviews [66,67] for more discussion about the non-cosmological explanations for the dimming of the distant supernovae.

At the time of the writing of this article (March 2003), our High-z Team has submitted a paper discussing the cosmological results based on 230 Type Ia supernovae, analyzed in conjunction with the WMAP and 2dF surveys [56]. This sample includes 79 supernovae with redshifts greater than 0.3. A summary of our results is:

- For an equation of state parameter $w = -1$, $H_0 t_0 = 0.96 \pm 0.04$ and $\Omega_\Lambda - 1.4\Omega_M = 0.35 \pm 0.14$.
- If $\Omega_T = 1.0$, $\Omega_M = 0.28 \pm 0.05$ independent of any large-scale structure measurements.
- Assuming a prior based on the 2dF measurement of Ω_M, we find that the equation of state parameter for dark energy must lie in the range $-1.48 < w < -0.72$ (95% confidence) for a flat universe. If we assume that $w > -1$ we find that $w < -0.73$ (95% confidence), similar to the WMAP results. So far, the data are consistent with the dark energy being a cosmological constant.

The error contours for our analysis are shown in Fig. 10.6.

To end this summary, I would like to return to the observations. In Fig. 10.7 I show the Hubble diagram of 170 Type Ia SNe from [56], the product of over 14 years of observations of supernovae. The mean trend of the data at $z \sim 0.5$ shows that the supernovae are fainter than expected, which is the signal of acceleration. However, at the highest redshifts, the data are hinting at a turn-down, which would mean that the supernovae are becoming brighter than the empty universe model. As can be seen in Fig. 10.5, this is the expected behavior in the early universe, where the much higher mean density (which overcomes the effects of a cosmological constant) of the Universe causes deceleration. Have we detected the epoch of deceleration? These data and the partial light curve of SN1997ff in the HDF [68] are not yet convincing, but with improved ground-based data and new ACS data from *HST*, in the next few years we should be able to measure the transition from a decelerating to accelerating universe.

Acknowledgements

I would like to thank my many colleagues in the High-z Supernova Team and the Calán/Tololo Survey who have worked hard to help us understand the use of Type Ia supernovae as standard candles. Support for Proposal Number GO-07505.02A, GO-08177.6, and GO-08641.07A was provided by NASA through

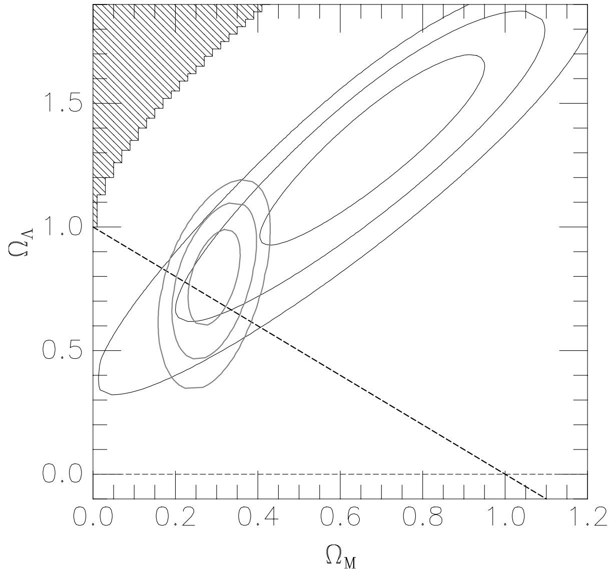

Fig. 10.6. Probability contours shown at the 1,2,3σ level under the assumption of $w = -1$ [56]. The same contour levels are shown assuming the prior of $\Omega_M h = 0.20 \pm 0.03$ from the 2dF survey. Note the SNe alone, or the SNe combined with the 2dF prior clearly show the existence of a positive Ω_Λ and a Universe which is flat. These data are independent of WMAP or other microwave measurements of the CMB

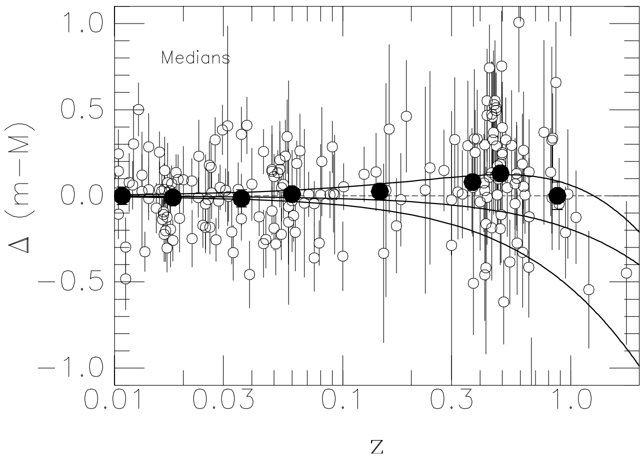

Fig. 10.7. The 170 supernova sample plotted in a residual Hubble diagram with respect to an empty universe. The highlighted points correspond to median values in eight redshift bins. From top to bottom the curves show $(\Omega_M, \Omega_\Lambda) = (0.3, 0.7)$, (0.3,0.0), and (1.0,0.0), respectively

a grant from the Space Telescope Science Institute, which is operated by the Association of Universities for Research in Astronomy, Inc., under NASA contract NAS5-26555. With this paper I mark the death of our friend and colleague Robert A. Schommer on 12 December 2001. Bob was an important member of our High-z Supernova Search Team and we valued his scientific guidance and friendship.

References

1. J.G. Bartlett, et al.: Science, **267**, 980 (1995)
2. Turner, M. et al.: *From Quarks to the Cosmos: Eleven Science Questions for the New Century* (National Academy Press, Washington DC, 2003)
3. A. Sandage: ApJ, **133**, 355 (1961)
4. R.V. Wagoner: ApJ, **214**, L5 (1977)
5. W. Baade: Astronomische Nachrichten, **228**, 359 (1926)
6. D. Branch, & B. Patchett: MNRAS, **161**, 71 (1973)
7. R.P. Kirshner, & J. Kwan: ApJ, **193**, 27 (1974)
8. L. Hansen, et al.: A&A, **211**, L9 (1989)
9. H.U.Nørgaard-Nielsen, et al.: Nature, **339**, 523 (1989)
10. B. Leibundgut et al.: ApJ, **466**, L21 (1996)
11. B.P. Schmidt, et al.: ApJ, 507, 46 (1998)
12. S. Perlmutter et al.: IAUC, **5956**, 1 (1994)
13. S. Perlmutter et al.: IAUC, **6263**, 1 (1994)
14. S. Perlmutter et al.: ApJ, **440**, L41 (1995)
15. M. Phillips et al.: IAUC, **6160**, 1 (1995)
16. K. Krisciunas et al.: AJ, **125**, 166 (2003)
17. W.D. Arnett: ApJ, **253**, 785 (1982)
18. P.A. Pinto, & R.G. Eastman: ApJ, **530**, 757 (2000)
19. P.A. Pinto & R.G. Eastman: New Astronomy, **6**, 307 (2001)
20. P. Höflich: ApJ, **443**, 89 (1995)
21. P. Höflich, A.M. Khokhlov, & J.C. Wheeler: ApJ, **444**, 831 (1995)
22. B. Leibundgut, & P.A. Pinto: ApJ, **401**, 49 (1992)
23. B. Leibundgut: A&A Rev., **10**, 179 (2000)
24. W.D. Vacca, & B. Leibundgut: ApJ, **471**, L37 (1996)
25. G. Contardo, B. Leibundgut, & W.D. Vacca,: A&A, **359**, 876 (2000)
26. E. Cappellaro, et al.: A&A, **328**, 203 (1997)
27. P.A. Pinto, & R.G. Eastman: ApJ, **530**, 745 (2000)
28. A.G. Riess, A.V. Filippenko, W. Li, & B.P. Schmidt: AJ, **118**, 2668 (1999)
29. G. Aldering, R. Knop, & P. Nugent: AJ, **119**, 2110 (2000)
30. C.T. Kowal: AJ, **73**, 1021 (1968)
31. J. Maza, et al.: PASP, **93**, 239 (1981)
32. M. Hamuy, et al.: AJ, **106**, 2392 (1993)
33. M.M. Phillips: ApJ, **413**, L105 (1993)
34. Y.P. Pskovskii: Soviet Astronomy, **28**, 658 (1984)
35. B. Leibundgut: Ph.D. Thesis, University of Basel. (1988)
36. M.M. Phillips et al.: PASP, **99**, 592 (1987)
37. J. Maza, et al.: ApJ, **424**, L107 (1994)
38. M. Hamuy, et al.: AJ, **108**, 2226 (1994)
39. M. Hamuy, et al.: AJ, **109**, 1 (1995)

40. M. Hamuy, et al.: AJ, **112**, 2391 (1996)
41. M. Hamuy, et al.: AJ, **112**, 2398 (1996)
42. M. Hamuy, et al.: AJ, **112**, 2408 (1996)
43. M. Hamuy, et al.: AJ, **112**, 2438 (1996)
44. A.G. Riess, W.H. Press, & R.P. Kirshner: ApJ, **438**, L17 (1995)
45. A.G. Riess, W.H. Press, & R.P. Kirshner: ApJ, **473**, 88 (1996)
46. M.M. Phillips, et al.: AJ, **118**, 1766 (1999)
47. P. Lira: Masters Thesis, University of Chile (1995)
48. G. Goldhaber, et al.: ApJ, **558**, 359 (2001)
49. S. Jha: Ph.D. thesis, Harvard University (2002)
50. M. Hamuy, & P.A. Pinto: AJ, **117**, 1185 (1999)
51. V.D. Ivanov, M. Hamuy, & P.A. Pinto: ApJ, **542**, 588 (2000)
52. M. Hamuy, et al.: AJ, **120**, 1479 (2000)
53. W.L. Freedman, et al.: ApJ, **553**, 47 (2001)
54. B.K. Gibson, et al.: ApJ, **529**, 723 (2000)
55. N.B. Suntzeff, et al.: AJ, **117**, 1175 (1999)
56. J. Tonry: ApJ, submitted (2003)
57. A. Kim, A. Goobar, & S. Perlmutter: PASP, **108**, 190 (1996)
58. P. Nugent, A. Kim, & S. Perlmutter: PASP, **114**, 803 (2002)
59. S. Perlmutter, et al.: ApJ, **483**, 565 (1997)
60. P.M. Garnavich, et al.: ApJ, **493**, 53 (1998)
61. S. Perlmutter, et al.: Nature, **391**, 51 (1998)
62. A.G. Riess, et al.: AJ, **116**, 1009 (1998)
63. S. Perlmutter, et al.: ApJ, **517**, 565 (1999)
64. M.S. Turner: PASP, **113**, 653 (2001)
65. A. Aguirre: ApJ, **525**, 583 (1999)
66. A.G. Riess: PASP, **112**, 1284 (2000)
67. B. Leibundgut: ARAA, **39**, 67 (2001)
68. A.G. Riess, et al.: ApJ, 560, 49 (2001)

11 Models for Type Ia Supernovae

Peter Höflich[1], Chris Gerardy[1], Eric Linder[2], and Howie Marion[1]

[1] Dept. of Astronomy, University of Texas, Austin, TX 78681, USA
[2] Lawrence Berkeley Laboratory, Berkeley, CA 94720, USA

Abstract. We give an overview of the current understanding of Type Ia supernovae relevant for their use as cosmological distance indicators. We present the physical basis to understand their homogeneity of the observed light curves and spectra and the observed correlations. This provides a robust method to determine the Hubble constant, $67 \pm 8(2\sigma) km\ Mpc^{-1}\ sec^{-1}$, independently from primary distance indicators. We discuss the uncertainties and tests which include SNe Ia based distance determinations prior to δ-Ceph measurements for the host galaxies. Based on detailed models, we study the small variations from homogeneities and their observable consequences. In combination with future data, this underlines the suitability and promises the refinements needed to determine accurate relative distances within 2 to 3% and to use SNe Ia for high precision cosmology.

11.1 Overview

Type Ia Supernovae (SNe Ia) are the result of a thermonuclear explosion of a white dwarf star. What we observe is not the explosion itself but light emitted from the material of the disrupted white dwarf (WD) for weeks to months afterward. After the first few seconds, this rapidly moving gas expands freely. As a consequence, the matter density decreases with time and the expanding material becomes increasingly transparent, allowing us to see progressively deeper layers. Thus, a detailed analysis of the observed light curves (the time series of emitted flux) and spectra reveals the density and chemical structure of the entire star.

The structure of a WD is determined by degenerate electrons and thus largely independent of details such as the temperature or chemical composition. The explosion energy is determined by the binding energy released during the nuclear burning, and the burning products can be observed. The tight relation between the explosion and the observables and their insensitivity to details are the building blocks on which our understanding of the homogeneity in the observable relations for SNe Ia is based. Indeed, both the peak fluxes and light curve shapes of SNe Ia show an impressive level of homogeneity, making them the astronomical objects closest to a standard candle distance estimator. This allows their use for precision estimation of cosmological parameters.

The thumbnail sketch of our understanding is as follows:

- Type Ia supernovae are nearly homogeneous because nuclear physics determines the structure of white dwarfs, and the explosion.

P. Höflich, C. Gerardy, E. Linder, and H. Marion, Models for Type Ia Supernovae and Cosmology, Lect. Notes Phys. **635**, 203–227 (2003)
http://www.springerlink.com/

- The total production of nuclear energy is almost constant since very little of the WD remains unburned. The final explosion energy depends on the binding energy of the WD, which is given by its structure.
- The light curves are powered by the radioactive decay of ^{56}Ni produced during the explosion, independently from details of the explosion physics and progenitors. The amount of ^{56}Ni determines the absolute brightness.
- The energy released from the nickel decay ties together the luminosity and the temperature dependent opacity, i.e. how much flux is emitted and how quickly. Explicitly, less Ni means a lower luminosity, but at the same time lower temperature in the gas and so lower opacity. Thus, energy escape is more rapid. So dimmer SN are quicker, i.e. have narrower light curves. This is variously called the brightness decline, peak magnitude - light curve width, or stretch relation.
- To be in agreement with the narrowness of the brightness decline relation [66], the mass of the progenitors and the explosion energies must be similar. This is automatically satisfied in the currently most successful model: a Chandrasekhar mass C/O-WD in which the burning starts off as a deflagration front (propagating at well below the speed of sound) and subsequently turns into a detonation (with $\approx$ the speed of sound).
- To agree with observations of intermediate mass elements at the outer layers, the WD must be pre-expanded. Most likely, an initial deflagration phase causes the pre-expansion. This depends mainly on the amount of energy release but not on the details of the deflagration front. Within this paradigm, 1) the entire WD is burned, and 2) the production of ^{56}Ni is dominated by a single parameter characterizing the transition between deflagration and detonation, determining the amount of burning during the deflagration.

  The deflagration-detonation model thus gives a natural and well motivated origin for a narrow brightness decline relation. In addition, the resulting chemical layering is shell like as observed.
- Homogeneity can be established down to a level of 0.2 magnitudes. Beyond this, secondary parameters are expected to become important, namely the progenitor mass on the main sequence, its metallicity, and stellar rotation. In particular, the pre-conditioning of the WD prior to the thermonuclear runaway may hold the key to understanding the variety of SNe Ia.

  With more detailed observations, these characteristics will help to improve the current accuracy of SNe Ia as distance indicators.

In the following sections, we address the current status of our understanding of SNe in more detail and elaborate on how future observations by ground based telescopes and dedicated space missions, in combination with detailed modeling, will help to bring us to a new level of understanding. These include new insights into the nature of SNe including the progenitors, the thermonuclear runaway that leads to the explosion, the propagation of nuclear burning fronts and their 3-dimensional nature. These studies will help to discover and understand new relations between observables to get a handle on the relation of SNe Ia with their environment, including evolutionary effects with redshift, and to improve the accuracy of SNe Ia as cosmological distance indicators.

11.2 A Simplified Explosion Model

The following scenario summarizes one possibility for the creation and characteristics of a SNe Ia. This is designed solely to give the reader a simple example to relate a variety of concepts.

Consider a white dwarf (WD) in a binary system, accreting mass from its companion (Fig. 11.1). This initial phase ends when the total mass approaches the Chandrasekhar mass (beyond which the star would collapse to a neutron star or black hole) and causes compressional heating of the core and the thermonuclear runaway. Likely, the burning front starts as a deflagration (velocity well below the sound speed). The energy release lifts the WD in its potential and causes pre-expansion of the star needed to reduce the density under which burning occurs. After a few seconds, the burning front makes a transition to a detonation (or very fast deflagration). All material in the high density regions is

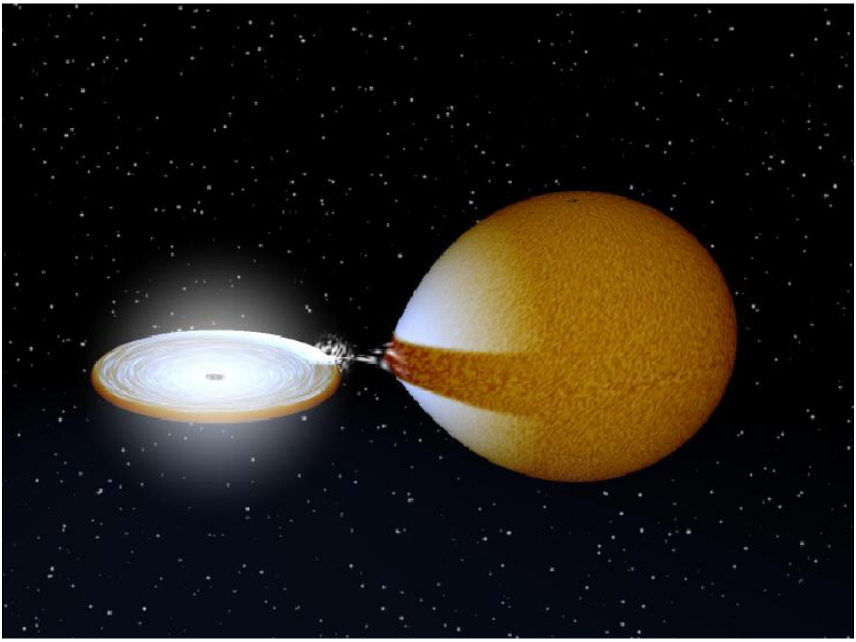

Fig. 11.1. Possible scenario for a progenitor system of a SN Ia. A white dwarf accretes material from a close companion by Roche lobe overflow. Initially, the WD has a mass between 0.6 and 1.2 $M_{\odot}$ and, by accretion, approaches the Chandrasekhar mass limit. The companion star may be a main sequence star or red giant, or a helium star or another WD. Depending on this, the accreted material may be either H, He or C/O rich. If H or He is accreted, nuclear burning on the surface converts it to a C/O mixture at an equal ratio in all cases. Despite the different evolutionary pathways, the final result will be the same: the explosion of a C/O-WD with a mass close to M_{Ch} and with very similar SN properties. Some small fraction of SNe Ia may also be the result of merging of two WDs on a dynamical time scale

burned to ^{56}Ni while outer shells of Si, S, etc. and a small fraction of the original C and O remain. The specific energy released by these reactions unbinds the material and causes a rapid acceleration of the matter. As the radioactive ^{56}Ni decays, the resulting γ-ray energy is thermalized and produces the optical luminosity, or light curve (LC), over tens of days to months. The rise time and decay time are given by the decay rate and the opacity and expansion. Spectral time series map out the SN structure as the photosphere recedes through the material.

The simplified physics picture is as follows: The rate of the free expansion is determined by the specific nuclear energy production which, for a C/O-WD, is rather insensitive to the burning process and the final burning products. The complete burning of the white dwarf in the explosion fixes the total nuclear energy release and hence kinetics; the transition density determines the nickel mass produced; the nickel decay fixes the energy input to the supernova material, determining its luminosity and opacity. The opacity and explosion energy together give the shape of the light curve, namely the brightness decline relation.

Alternate model pathways, in fact, converge to the same major points after each stage, driven by the physics and constrained by the observations. Several examples of such "stellar amnesia" indemnify the observables against details of how the final state is reached. For example what is predominantly important for the energy production is that the overwhelming majority of the star burns, not how it does because the release of energy by the fusion of C/O up to Si/S dominates over the relatively little binding energy in the last stage to iron.

On the other hand, the tight relation between the observables evinced by the homogeneity of the brightness-width relation only occurs in certain classes of models. This constrains the possibilities, as do such data as infrared spectra showing little unburned original C-O material. Together, amnesia from the physics and empirical data from observations weave a tight net around the possible ingredients that can be important in determining the absolute brightness.

11.3 Physics of the Explosion, Light Curves, and Spectra

As stated in the overview, nuclear physics determines the structure of the progenitor and is responsible for the homogeneity of SNe Ia. As the SN Ia expands, we see deeper layers with time due to the geometrical dilution. The unveiling of the layers reveals the structure of the WD. The observable data provide a rich resource for testing and refining models. E.g., the light curves provide critical information about integrated quantities such as the total energy generation and mass and energetics of the expanding material. The spectra are mostly sensitive to the composition and velocity at the photosphere (the deepest unveiled layer).

The spectra of SNe Ia are dominated by elements (C,O,Si,S,Ca,Fe/Co/Ni) that are the characteristic products of explosive nuclear burning at densities between $10^{6-9} g/cm^3$. These densities are typical only for a C/O-WD, i.e. a star stabilized by a degenerate electron gas. For such a degenerate equation of state, the initial structure of the exploding WD depends only weakly on the temperature and the C/O ratio as a function of depth. WD radii are between 1500 to 2000 km/sec, mainly depending on density at the time of the accretion which is mainly given by the accretion rate (see [25] and above). Typical binding energies are ≈ 5 to $6 \times 10^{50} erg$. If the entire WD is burned, about $2 \times 10^{51} ergs$ are released over time scales of seconds. The energy released is given by the difference between the binding energy per nucleon of unburned compared to burned matter. Because the nuclear binding energy of both the of the fuel, i.e. carbon and oxygen, and the final burning product, i.e. Si and Ni, are rather similar, variations in the specific energy release per mass of burned matter is limited to $\approx 10\%$. Neutrino losses are less than 1 to 2% and, thus, little energy is lost in contrast to core collapse SNe where more $\approx 99\%$ of the release energy is lost by neutrinos. In the explosion, a WD with a radius of about 1500 km expands with observed velocities of the order of 10,000 km/sec, consistent with the specific nuclear energy release in such an environment. Because this rapid increase in volume and the adiabatic cooling, the nuclear energy is used to overcome the binding energy and to accelerate the WD matter. Based on this evidence, there is general agreement that SNe Ia result from some process of combustion of a degenerate WD. The amount and products of the nuclear reactions – "burning" – depend mainly on the time scale of reactions compared to the hydrodynamical time scale of expansion, which is $\approx 1 sec$. The reaction rate depends sensitively on the temperature and the energy release per volume element. The specific energy release is a function of the density and, to a smaller extent, the initial chemical composition, namely the C/O ratio of the progenitor (which depends on the initial stellar mass). At densities $\geq 10^7$, $\geq 4 \times 10^6$, and $\geq 10^6 g/cm^3$, the main burning products are Fe/Co/Ni, S/Si and Mg/O, respectively. We will see, however, that the details of the burning process have little impact. These quantities we discussed – the explosion energy, mass, and the burning product – are directly linked in SNe Ia, and accessible to observations.

As just mentioned, virtually none of the initial stored energy from the WD will contribute to the luminosity of the supernova but it goes to expansion. Instead, the energy input is entirely caused by the radioactive decay of freshly synthesized ^{56}Ni that decays via $^{56}Ni \rightarrow ^{56} Co \rightarrow ^{56} Fe$ with life times of 8.8 and ≈ 111 days, respectively. This slow nuclear energy release is due to a gain of nuclear binding energy between isotopes rather than change of elements. The total energy released by radioactive decays is about 3% of the initial energy release, namely, $\approx 7 \times 10^{49} erg$ for a ^{56}Ni production of 0.5 $M_\odot$ vs. $2 \times 10^{51} erg$ released during the early explosive burning and any changes in the expansion velocities are less than 2%. The energy release in the form of luminosity is dominated by the location of the photosphere within the expanding material, a function of the expansion and the opacity. As we will see below, small differences in the expansion rate caused by the central density of the WD, chemistry and expansion rate will produce small deviations from the homogeneity in the light curves on a 10 to 20% level.

In the case of a Type Ia SN, acceleration of the material takes place during the first few seconds to minutes, followed by the phase of free expansion. In lack of further acceleration, the radius of a gas element from the center is simply proportional to the velocity $r \sim v$. This means that gas further out moves faster and hence stays further out; each shell expands without crossing another, maintaining the original structure. As in cosmology it is useful to think in comoving coordinates, moving with the expansion. In these coordinates each shell, and hence slice of the original stellar structure, is preserved. So while material expands out through a fixed radial distance from the center, the mass within a comoving radius is constant with time. Therefore we often discuss the structure in terms of mass or velocity coordinates. Due to the expansion, the material cools almost adiabatically as the volume increases rapidly: $V \sim r^3 \sim t^3$. The increase in volume causes a corresponding decrease in density and hence optical depth. So the photosphere slips deeper within the material, simultaneously allowing us to see further in. Note though that it still expands in physical radius, at least up to the time of peak magnitude.

The well determined energy source for the luminosity and the tight relation between the explosion and the observables, with their simultaneous insensitivity to details, are the building blocks on which our understanding of the homogeneity in the observable relations for SNe Ia is based.

To go beyond the homogeneity and take full advantage of the intrinsic properties of SNe Ia and to test for the influence of the metallicities, progenitors etc., we can perform detailed calculations which are consistent with respect to the progenitors, explosion, light curves and spectra. These calculations include detailed nuclear networks, γ-ray transport, non-LTE level populations, and multidimensionality for parts of the problem. The numerical methods are briefly described in the Appendix. For more details, see [19,20,27,29], and references therein. The only remaining free parameters to address are the initial structure of the WD and the description of the nuclear burning front, which we discuss in the next section.

11.4 Detailed Models, Observations, and Cosmology

In examining possible scenarios, from the progenitor state to the explosion, we will see that the most important properties are those that change the overall energetics, such as the total energy content of the fuel and the amount of matter of the WD that undergoes burning. As we have alluded to in the previous discussions of "stellar amnesia", many of the results are quite stable, i.e. model independent. In fact, we find 1) insensitivity of the WD structure to the progenitor star and system. This is caused by the electron degeneracy enforcing the mentioned weak dependence on the temperature and composition. 2) The time of the explosion (and therefore the WD density) is governed by the accretion rate shortly before the thermonuclear runaway causing the explosion. 3) Moreover, the final outcome of the explosion is rather insensitive to details of the nuclear burning. While this is beneficial for the tightness of the observed luminosity relation, it makes it difficult to investigate the pre-supernova physics, e.g. the explosion scenario.

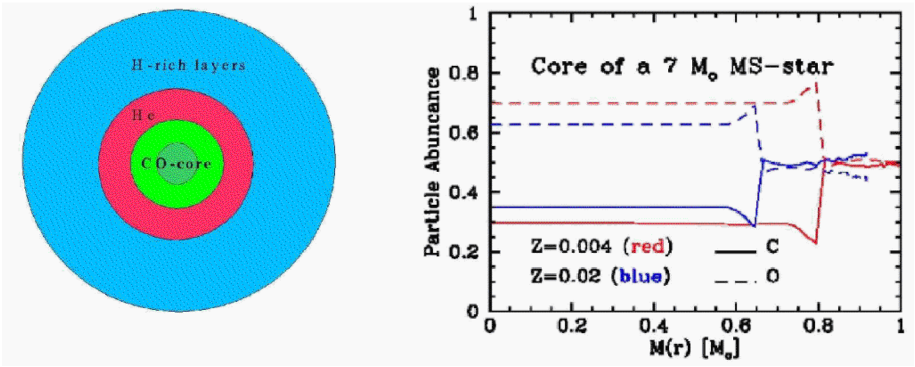

Fig. 11.2. Stellar structure at the final stage of the evolution of a 7 $M_\odot$ main sequence star. At this stage, the star loses its H and He rich material with the central C/O-core remaining. This forms the C/O white dwarf which, eventually, becomes the accreting progenitor in typical SNe Ia scenarios. On the right, we show the composition of the core as a function of mass (in $M_\odot$). The region of reduced C abundance is produced during the central helium burning which is convective (see also dark green center, left plot). Because the size of the helium burning core depends on the main sequence mass and the convection depends on the metallicity, the final structure depends on both (from [26])

However, new, high quality data and advances in supernovae simulations have opened up new opportunities to constrain the physics of supernovae and to improve the accuracy of their use as standardized candles below the 0.2^m level. For the first time, a direct relation with the progenitors seems to be within reach. In particular, there is mounting evidence that the properties of the progenitor are directly responsible for the variety in SNe Ia. These properties include the chemical structure, rotation, and central density [25,81,27].

There is general agreement that SNe Ia result from some process of combustion of a degenerate WD [31]. WDs are the final stages of stellar evolution for all stars with less than 7-8 $M_\odot$ (see Fig. 11.2). During the stellar evolution on the main sequence, stars gain their energy from central burning of hydrogen to helium until H is exhausted in the central region. Subsequently, the star burns He to C and O in the center, surrounded by a hydrogen burning shell. When He becomes more depleted, the triple-α process becomes less efficient and $^{12}C(\alpha,\gamma)^{16}O$ takes over, resulting in an inner region of low C abundance (see Fig. 11.2, right panel). The size of the He burning core depends on the mass of the star and on the metallicity/opacity because it is convective, i.e. material from different radii mixes (e.g. [9]). At these final stages, the star loses most of its mass but with the C/O core remaining: a WD is born. If the star is a member of a close binary system it may gain mass at a sufficient rate to become a SNe Ia [58]. Because about 0.2 to 0.7 $M_\odot$ are accreted from an accretion disk, the resulting WD may be strongly differential rotating [42].

The exact method of gaining mass sufficient to cause a supernova defines three classes of models: (1) An explosion of a CO-WD, with mass close to the

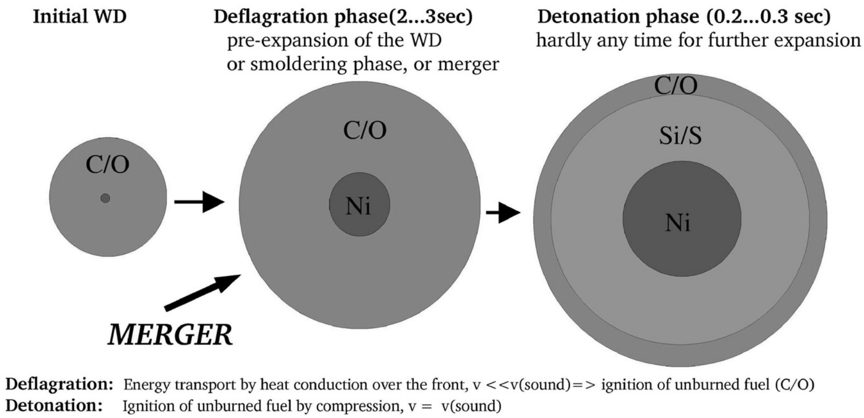

Fig. 11.3. Schematics of the explosion of a white dwarf near the Chandrasekhar mass. A thermonuclear runaway occurs near the center and a burning front propagates outwards [28]. Initially, the burning front must start as a deflagration to allow a pre-expansion because, otherwise, the entire WD would be burned to Ni. Alternatively, the pre-expansion may be achieved during the non-explosive burning phase just prior to the thermonuclear runaway [27]. Subsequent burning is either a fast deflagration or a detonation. In pure deflagration models, a significant amount of matter remains unburned at the outer layers, and the inner layers show a mixture of burned and unburned material. In contrast, the models making a transition to a detonation produce the observed layered chemical structure with little unburned matter, wiping out the history of deflagration (see text and Fig. 11.4). Note that all scenarios have a similar, pre-expanded WD as an intermediate state

Chandrasekhar mass M_{Ch}, having accreted mass through gravitational stripping of the outer layers (called Roche-lobe overflow) from an evolved companion star [85]. The explosion is mainly triggered by compressional heating near the WD center. (2) An explosion of a rotating configuration formed from the merging of two low-mass WDs, caused by the loss of angular momentum due to gravitational radiation from the binary system [83,32,62]. (3) An explosion of a low mass CO-WD triggered by the detonation of a helium layer accreted from a close companion [57,86,87]. This third class, the so-called edge-lit sub-Chandrasekhar WD model, has been ruled out on the basis of predicted light curves and spectra [24,60]. The first model, accretion to M_{Ch}, is the most successful when compared to observations.

Within the M_{Ch} scenario (see Fig. 11.1), the free model parameters are: 1) The chemical structure of the exploding WD – given by the evolution of the progenitor star and the central He-burning; 2) Its central density ρ_c at the time of the explosion – dependent mainly on the accretion rate onto the WD; 3) The description of the initial, subsonic burning front (deflagration); and 4) The amount of burning prior to the transition from deflagration to detonation (see Fig. 11.3). From these, the light curves and evolution of spectra follow directly.

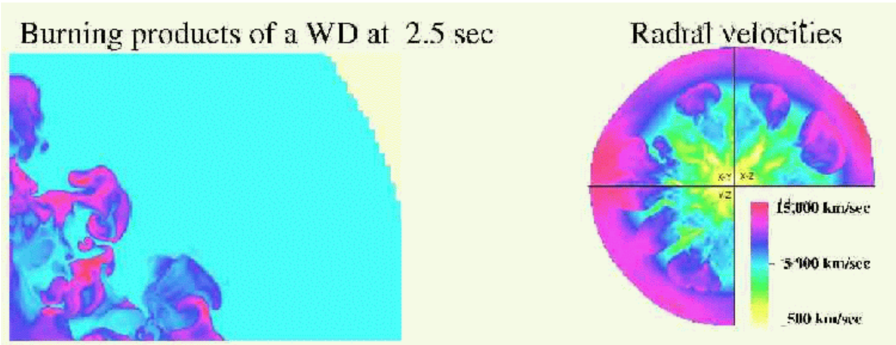

Fig. 11.4. Structure of the deflagration front in an exploding C/O-WD (left) and the velocity field (right) at about 2 seconds after runaway based on 3-D calculations by Khokhlov [38]. Light green and dark red/blue mark unburned and burned material, respectively. During this phase, the expansion of the material is already almost spherical (right), and deviations of the density from sphericity are less than 2%. In normal bright SNe Ia, the transition to the detonation should occur in delayed detonation models at about the time of these snapshots. In this case, the density in the inner region is sufficient to burn the unburned material up to Ni, eliminating the chemical contrast and leaving a layered structure. In contrast, in pure deflagration models, the density will drop further before burning can take place, thus leaving intact the chemical contrast of the inner layers. In addition, the expansion of the outer layers is already close to the speed of sound, faster than the burning front. As a consequence, all deflagration models show a massive outer layer of unburned matter

Comparison with observations allow to constrain the parameters for a particular SNe Ia, its distance and the interstellar reddening (see below and Fig. 11.8).

The first two parameters set the stage. For the merging scenario, the front will start as a detonation making parameters 3 and 4 dependent but adding the mass of the orbiting envelope as a free parameter. The M_{Ch} scenario requires parameters 3 and 4 because if the WD exploded purely from a thermonuclear runaway reaction then almost all of the material would burn to ^{56}Ni, in contradiction to observations that show only about 0.6 $M_\odot$ is produced. Instead, a pre-expansion is needed to lower the density (see Fig. 11.3). This likely occurs during an initial phase of a slow deflagration that preserves the structure but decreases the binding energy. The lift in potential energy depends mainly on the amount of burning, i.e. total energy produced, and almost not at all on the actual rate [8]. Thus, fortunately, details of nuclear burning in the non-linear regime of deflagration, about which our understanding is currently limited, will hardly affect the final LCs and spectra.

Successful models need either a rapidly increasing deflagration speed and no radial mixing (e.g. W7 [59] – see footnote [1]), or a deflagration-detonation

[1] The pure deflagration model W7 is a spherical model and, consequently, shows a layered structure which is typical for detonations. Realistic 3-D deflagration models do not show a radial layering of the abundances.

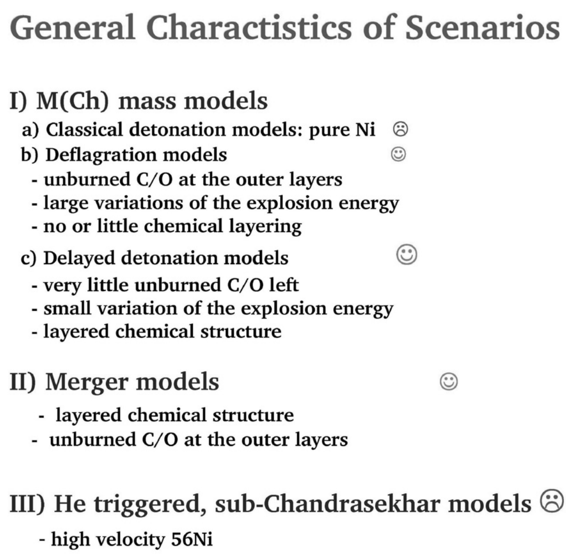

Fig. 11.5. General properties of various explosion scenarios. Delayed detonation models and, possibly, merger models are the scenarios most likely realized in SNe Ia. Merger models may contribute to the populations but their large amount of unburned C/O at the outer layers is inconsistent with the (few) IR-spectra obtained up to now and can likely constitute only a small fraction of the SNe Ia population. Currently, pure deflagration models show no layered chemical structure, in disagreement with observations. However, as of now, 3-D deflagration models consider only the regime of large scale instabilities, i.e. Rayleigh-Taylor, and start from static WDs (see text)

transition (DDT) (see Fig. 11.3). The detonation or a very rapid deflagration is required to match observations that almost the entire WD is burned (see Fig. 11.6). Current infrared observations place tight upper limits on the amount of unburned material. Depending on the specific SN Ia and the quality of the data, the constraints imposed lie between 0.01 to $0.2 M_\odot$ [84,27,50,72]. For general comparison of models, see Fig. 11.5. Delayed detonation (DD) models [34,88,89], those possessing a DDT, have been found to reproduce the optical and infrared light curves and spectra of "typical" SNe Ia reasonably well [20–22,12,60,84,45]. Here the burning starts as a well subsonic deflagration and then turns to a nearly sonic, detonative mode of burning. Due to the one-dimensional nature of the model, the speed of the subsonic deflagration and the moment of the transition to a detonation are free parameters hence numbers 3 and 4 mentioned above. The moment of deflagration-to-detonation transition is conveniently parameterized by introducing the transition density, $\rho_{\rm tr}$, at which it occurs. The amount of ^{56}Ni, M_{56Ni}, depends primarily on ρ_{tr} [20,21,79], and to a much lesser extent on the assumed value of the deflagration speed, initial central density of the WD, and initial chemical composition (ratio of C to O).

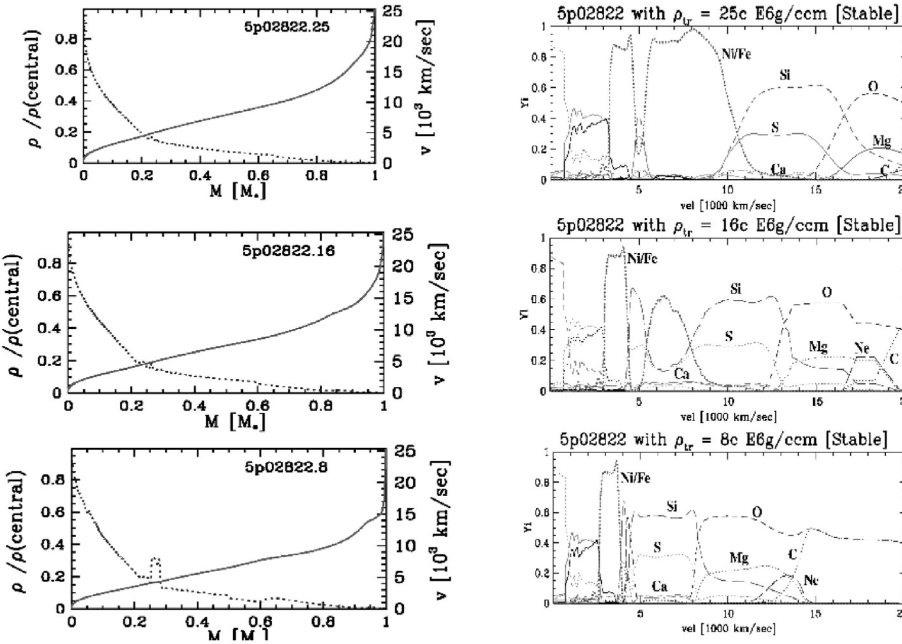

Fig. 11.6. Density (*blue, dotted*) and velocity (*red, solid*) as a function of the mass coordinate [in M_{Ch}] (*left panels*), and abundances of stable isotopes as a function of the expansion velocity (*right panels*), for delayed detonation models with $\rho_{tr} = 8$, 16 and $25 \times 10^6 g/cm^3$ (bottom to top). All models are based on the same M_{Ch} progenitor with a main sequence mass of 3 $M_\odot$, solar metallicity and a central density of $2 \times 10^9 g/cm^3$ at the time of the explosion. These models produce 0.09, 0.26 and 0.6 $M_\odot$ of ^{56}Ni, respectively. In all cases, the entire WD is burned and, thus, all models have similar explosion energies (from [27])

In essence this fixes the power source for the supernova light: models with a smaller transition density give less nickel and hence both lower peak luminosity and lower temperatures [20,21,79] (Figs. 11.6, 11.7). This is the first element in explaining the homogeneity of SNe Ia.

The second element is that, in DDs, almost the entire WD is burned, i.e. the total production of nuclear energy is almost constant, and the density and velocity structures hardly vary with the ^{56}Ni production (Fig. 11.6). Together these form the basis of why, to first approximation, the SNe Ia relation between peak magnitude and light curve width forms a one-parameter family. This can be well understood as an opacity effect [23], i.e. as a consequence of the rapidly dropping opacity at low temperatures [19,35]. Less Ni means lower temperature so the emitted flux is shifted from the UV towards longer wavelengths where there is less line blocking; as a consequence, the mean opacities are reduced. Less opacity means the photosphere retreats more rapidly to deeper layers, causing a faster release of the stored energy and, as a consequence, steeper declining LCs together with the decreasing brightness. DD models thus give a natural and

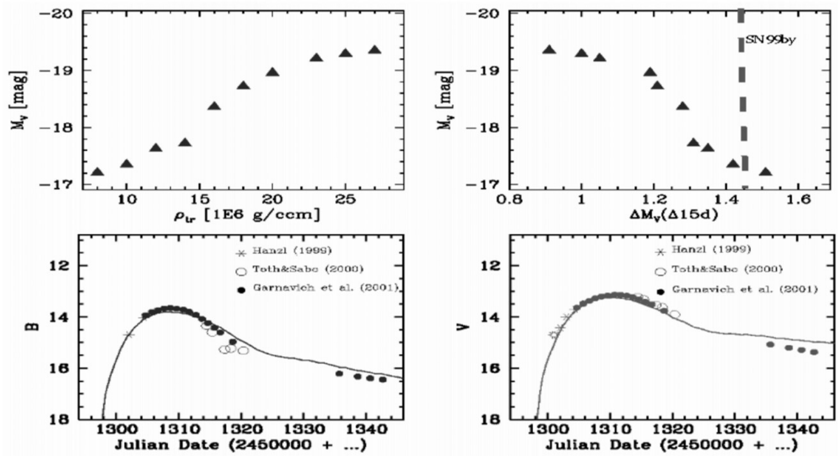

Fig. 11.7. Maximum brightness M_V as a function of ρ_{tr} (upper left) and $M_V(\Delta M_{\Delta t=15d})$ (upper right) for delayed detonation models with ρ_{tr} of 8, 10, 12, 14, 16, 18, 20, 23, 25 and 27 $\times 10^6 g/cm^3$ from left to right. The *dark red, vertical bar* (upper right) gives the brightness decline ratio as observed for SN1999by. In the lower panels, the comparison between theoretical and observed B and V LCs is given, implying a distance of 11 ± 2.5 Mpc, consistent with independent estimates [4]. By varying a single parameter, the transition density at which detonation occurs, a set of models has been constructed which spans the observed brightness variation of SNe Ia. The absolute maximum brightness depends primarily on the ^{56}Ni production, which for DD-models depends mainly on the transition density ρ_{tr} [27]. The brightness-decline relation $M_V(\Delta M_{\Delta t=15d})$ observed in normal bright SNe Ia is also reproduced in these models (from [27])

physically well-motivated origin for the magnitude-light curve width relation of SNe Ia within the paradigm of thermonuclear combustion of Chandrasekhar-mass C/O-WDs. These models are able to reproduce light curves and spectra, and to determine the Hubble constant independently from primary distance indicators (see Fig. 11.8). Furthermore, they can explain both normal bright and very subluminous SNe Ia within the same model (Figs. 11.7 and 11.9).

One of the uncertainties within SN modeling is the description of the nuclear burning fronts. While the propagation of a detonation front is well understood the description of the deflagration front and the deflagration to detonation transition pose problems. On a microscopic scale, a deflagration propagates due to heat conduction by electrons. Though the laminar flame speed in SNe Ia is well known, the front has been found to be Rayleigh-Taylor (R-T) unstable (see Fig. 11.4) increasing the effective speed of the burning front [56]. More recently, significant progress has been made toward a better understanding of the physics of flames. Starting from static WDs, hydrodynamic calculations of the deflagration fronts have been performed in 2-D [68,46] and 3-D [47,36,38]. It has been demonstrated that R-T instabilities govern the morphology of the burning front in the regime of linear instabilities, i.e. as long as perturbations remain

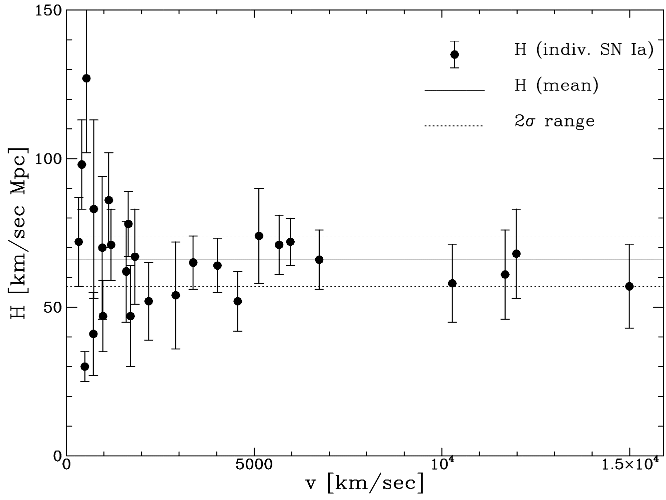

Fig. 11.8. Hubble values H are shown based on model fitting of the light curves and spectra of 27 individual SNe Ia including SN1988U at a redshift of 0.38 (not shown) [22]. We obtain $H_o = 67 \pm 8km/sec/Mpc$ within a 95% level. This determination does not depend on δ-Ceph. calibration or other primary distance indicators. It is based on basic nuclear physics and spectral constraints, and hardly depends on details of the explosion models. One of the main uncertainties is related to the bolometric correction BC which connects the bolometric luminosity, i.e. the of ^{56}Ni with the monochromatic brightness. However, the accuracy of the bolometric correction can be tested model-independent (see Fig. 11.16). The range for H_o owes its stability from spectral constraints. Namely, the observed maximum and minimum velocities of the ^{56}Ni and Si/S layers which are $\leq 10,500$ and $\geq 8000 km/sec$ for normal bright SNe Ia, respectively. The former hardens the lower value for H_o because it provides an upper limit for the ^{56}Ni mass which can be speezed within a certain expansion velocity (see Fig. 11.6). In the same way, the Si/S velocity sets the stage for the minimum ^{56}Ni mass

small. During the first second after the thermonuclear runaway, the increase of the flame surface due to R-T instability remains small and the effective burning speed is close to the laminar speed ($\approx 50\,km/s$) if the ignition occurs close to the center. Khokhlov [38] also shows that the effective burning speed is very sensitive to the energy release by the fuel, i.e. the local C/O ratio. Therefore, the actual flame propagation may depend on the detailed chemical structure of the progenitor. Moreover, all current experiments are based on static WDs and assumed off-center points of ignition. Recent simulations of the final phases before the explosion put the validity of these assumptions into question [28]. Despite advances, the mechanism is not well understood which leads to a DDT or, alternatively, to a fast deflagration in the non-linear regime of instabilities. Possible candidates for the mechanism are, among others, the Zel'dovich mechanism, i.e. mixing of burned and unburned material [37], crossing shock waves produced in the highly turbulent medium, or shear flows of rising bubbles at low densities [48,49]. An additional way is related shear instabilities present in

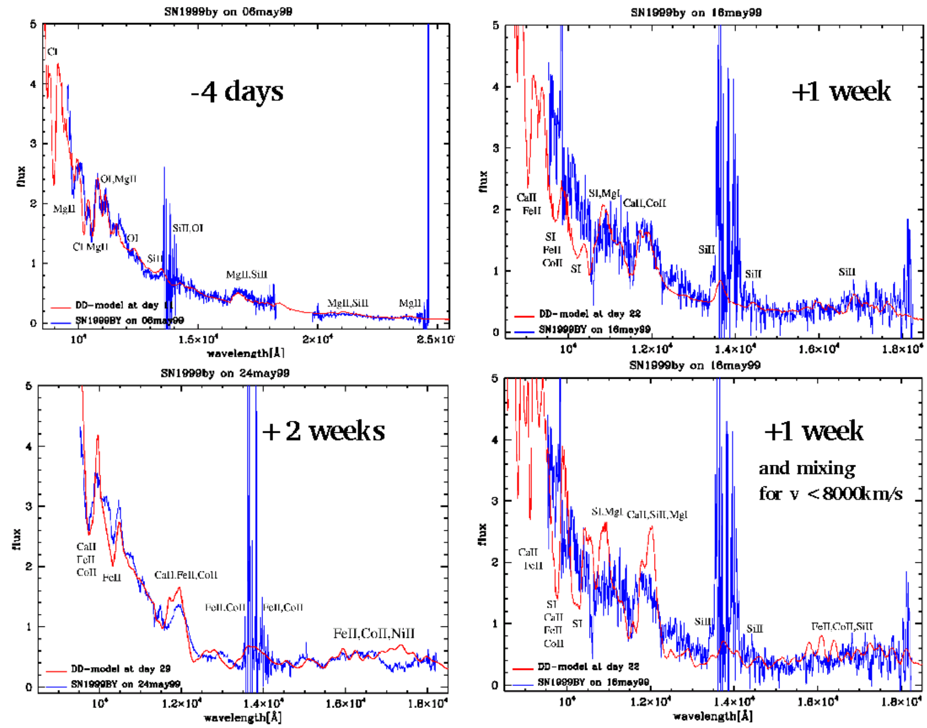

Fig. 11.9. Comparison of the observed near infrared spectra of the very subluminous SN99by on May 6 (*upper left*), May 16 (upper right), and May 24, 1999 (*lower left*). At those times, the Thomson scattering photosphere is located at v = 13,000, 7000 and 4000 km/s, respectively. For SN99by, the spectra are formed in layers of explosive C and incomplete Si burning up to about 2 weeks after maximum light. This is in strict contrast to normal bright SNe Ia where the photosphere enters the layers of complete Si burning already at about maximum light. In very subluminous SNe Ia, the transition density is low and the pre-expansion sufficiently large (see Fig. 11.6) that the layers up to 8000 km/s are not burned to ^{56}Ni but to Si only. Hence, the ^{56}Ni plumes produced during the deflagration phase should survive (see Fig. 11.4). In the lower right, we show a comparison of the observed and theoretical spectrum if we impose mixing of the inner 0.7 $M_\odot$. Obviously, strong mixing of the inner layers can be ruled out (see text and [27]). Current 3-D models for the deflagration phase starting from a static WD are insufficient. Pre-conditioning of the progenitor is a key element, e.g. turbulent motions in the progenitor or rapid rotation. This is supported by spectropolarimetry of SN99by which shows an overall asymmetry of about 10% with a well defined axis [30]

rapidly, differentially rotating WDs. Then, as soon as rising plumes enter this region of instability, they will be disrupted and strong mixed will occur. As a consequence, the burning rate will strongly increase which may cause a DDT. As discussed above, we must expect differential rotation in progenitors because a significant fraction of the progenitor mass has been accreted from a Kepler-disk. Currently, none of the proposed mechanisms have been worked out in detail and

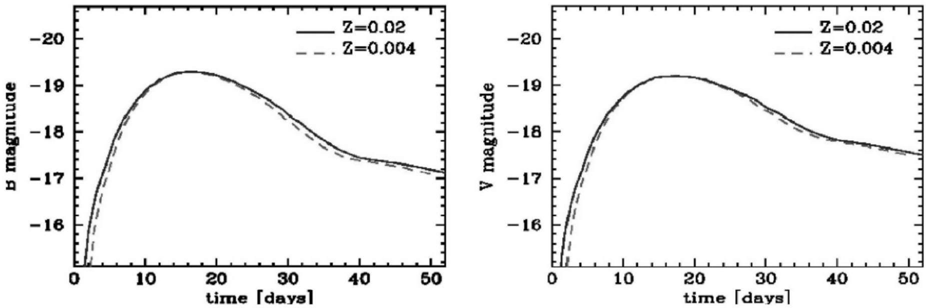

Fig. 11.10. Influence of the metallicity Z on the B and V light curves for a progenitor star of 7 $M_\odot$ on the main sequence (see Fig. 11.2). For the composition structure, see Fig. 11.2. The explosion model is based on a delayed detonation model typical for "normal" SNe Ia (from [26]). The absolute brightness at maximum light is hardly affected ($\Delta M = 0.02^m$). The rise time changes by about 1d and the decline rate over 15 days, $\Delta M_{\Delta t=15d}$, also changes. When using the standard brightness decline relation, this would produce an offset by 0.1^m. The dependencies can be well understood as a consequence of the mean C/O ratio and the temperature dependence of the opacities like the brightness decline relation (see text and [25]). In our example, the total ^{56}Ni production is similar. As usual, the luminosity at maximum light is provided by both energy due to instant radioactive decay and thermal energy stored in the optically thick regions produced by radioactive decays at earlier times. The total explosion energies declines with the mean C/O ratio. The lower expansion rate causes less energy loss of thermal energy due to adiabatic expansion At maximum light, the distance of a given mass element doubles on time scales of $\approx$ 10 to 11 days, respectively. At the same time after the explosion, more energy is available for low C/O ratios, and the corresponding model shows a slower rise similar to a model with a larger ^{56}Ni production. However, this delay also causes a larger excess of luminosity compared to the instant energy production by radioactive decays, and the photosphere is slightly cooler. The larger excess means a larger total decline past maximum to the level of instant energy production, and the cooler photosphere results a faster receding of the photosphere. Consequently, the decline rate is faster very similar to a slightly less luminous SNe Ia. Models with a lower mean C/O ratio show a slower increase and and a faster decline [25]. Because the limited dependence of the nuclear energy production on the C/O ratio, off-sets in the brightness decline relation are limited to $\approx 0.3^m$ for the entire range of potential progenitor masses and metallicities [9], and may cause a spread of a similar order around the mean brightness decline relation

shown to work in the environment of SNe Ia. However, as a common factor, all these mechanisms will depend on the physical conditions prior to the DDT. In the current state of the art we cannot predict a priori the distribution of brightness in a SNe sample because, within the most favored model, ρ_{tr} determines the brightness. Rather we take this as an input parameter and can investigate the small deviations from the brightness decline relation.

Although pure deflagration models are possible, current 3-D models show properties inconsistent with the observations (Fig. 11.5). Namely, pure defla-

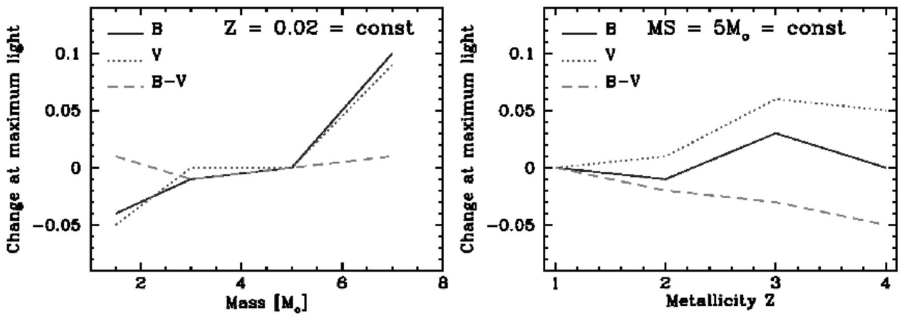

Fig. 11.11. Influence of main sequence mass (left) and initial metallicity (right) on B (—), V (····) and B-V (- - -) magnitudes at maximum light. All quantities are given relative to the reference model with a main sequence mass of $5M_\odot$ and solar metallicity. In the right panel, the numbers 1,2,3,4 on the axis refer to Z of 0.02, 0.001, 0.0001 and 10^{-10}, respectively (from [9])

gration models predict a significant fraction of the C/O WD remains unburned and a mixture of burned and unburned material at all radii/velocities (e.g. [3,11] and see Fig. 11.9). Constraints from infrared observations provide good evidence that the WD is almost fully incinerated in normal bright SNe Ia [84,72,50]. And in contrast to pure deflagration models, in DD-models the detonation front erases the chemical structure left behind by the deflagration (Fig. 11.4). Note that the "classical" deflagration model W7 [59] shows a layered structure similar to DD-models because it has been calculated in spherical geometry rather than the unlayered structure to be expected from 3-D deflagration models.

In conclusion, the transition to a detonation or (less likely) to a very fast deflagration determines the ^{56}Ni production and causes the one-parameter relation between peak magnitude and LC width. To a much lesser extent variations of the other parameters lead to some deviation from perfect homogeneity on the 0.2^m level. For example, an increase in the central density increases the electron capture close to the center, shifting the nuclear statistical equilibrium away from ^{56}Ni [23]. Empirically, the magnitude-light curve width relation has been well established with a rather small statistical error σ (0.18^m [14], 0.12^m [69], 0.16^m [75], 0.14^m [67], 0.17^m [63]). These correspond to 5-8% in distance. Note the predicted dispersion for DD models is somewhat larger than observed but significantly smaller than generic models which show a dispersion of 0.7^m [23].

This may imply a correlation between free model parameters, namely the properties of the burning front, and the main sequence mass of the progenitor M_{MS}, metallicity Z, and the central density of the WD at the time of the explosion. As we have discussed above, there is growing evidence that the final outcome of the explosion is determined by the pre-conditioning of the WD, namely the properties of the WD, its rotation and the final evolution which leads to the thermonuclear runaway [25,26,9,28]. Thus, we must expect that correlations between observables exist and can be used to further tighten the dispersion caused by second order parameters (Figs. 11.10 and 11.11; see the summary table in

Feature	Effect on LC & spectra	Size of effect
Initial metallicity Z	a) little effect on B, V, R, I, ... (B-V) becomes bluer at maximum b) strong influence on U and UV c) Strong, individual lines (e.g. 1μm FeII)	Δ(B-V)$_{[max]}$ = 0,-0.02,-0.05^m for Z = 0.02(solar), 0.001, 0. factor 3 in Z -> 0.2 to 0.5^m PopI -> strong line; PopII-> no l.
C/O ratio depends on MS mass of prog. and Z	a) Change of the rise-time/decline rel. b) Expansion velocities (Doppler shift of lines) c) Peak to tail ratio (PT)	M = 0.1 t[days] Δv(Si)[km/sec] = +20,000 ΔM PT = C ΔM with C = +1
Change of central density of the initial WD ->region with neutron capture increases	a) Similar brightness at maximum for same ^{56}Ni production but faster, earlier rise and slower decline with increasing density b) Peak to tail ratio changes c) Si velocity at maximum light and asymptotic Si velocity is higher	A change of rho(c) from 1.5E9 to 2.5E9 g/ccm changes width of LC by 2 days = 0.2 mag PT =C ΔM with C = -1 Δv(Si)[km/sec] = -20,000 ΔM
Merger/PDDs vs. classical DD	a) Slower rise and decline compared to DD b) Spectra: significant amount of C/O	change by ~2 to 4 days C/O down to 13-14,000 km/sec upper limit of Mg, etc.

Fig. 11.12. Summary of observational effects due to changes in the initial metallicity, main sequence mass, and central density for Chandrasekhar mass WD progenitors, and in the progenitor scenario [20,22,25,26,9]

Fig. 11.12). From this very argument, we must also expect a shift with redshift in the mean properties of the order of 0.2^m due to the population drift in the progenitor characteristics and environments. Nevertheless, the spread around the brightness decline relation may show little change. As one possible example, the mean metallicity and typical progenitor mass at the main sequence will decrease with redshift and cause systematic changes in the brightness decline relation (Figs. 11.10 and 11.11). These effects can be recognized and compensated for if well observed light curves and spectra are obtained. Figure 11.12 summarizes many of the relevant features, their expected size, and their effect on the observables based on advanced models. Note that detailed analyzes of observed spectra and light curves indicate that mergers and deflagration models such as W7 may contribute to the SN population [22,15]. To determine the nature of the dark energy through the use of SNe Ia as precision distance indicators, we need to reduce the residual systematic uncertainties well below the statistical dispersions [63,64,1]. This is the reason why we need comprehensive observational programs producing well characterized samples, from ground based supernovae surveys such as the Nearby SN Factory [55], the ESSENCE project [10], and the CFH Legacy Survey [6] for low redshifts, and the w-project and space-based missions such as the Supernova/Acceleration Probe [76] for high redshifts.

11.5 Conclusions

Supernovae studies have greatly progressed over the last several years due to advances in both observations and modeling. We are now able to analyze the explosion and resulting SNe properties in some detail, and can obtain answers to a number of long standing, interesting questions. While we cannot predict a priori the peak magnitude, we have seen that we can understand the origin of both the near homogeneity and those tight observable relations describing the first order deviations. Stability of the SNe Ia observables – stellar amnesia – arise because the nuclear physics determines the structure of the white dwarfs, and the explosion. Although pathways to SNe Ia span a variety, the information about the specific history is largely lost along the way to the progenitor and during the explosion. Thus, convergence due to physics leads to a generic accuracy of SNe Ia as distance indicators on the 0.2^m level. However, these details are needed for the next level of precision. In particular, pre-conditioning of the explosion seems to be a key element. These secondary parameters can be revealed through detailed models in combination with comprehensive observations which include both spectra extending to the near infrared and light curves from early times to well after maximum light (see table in Fig. 11.12). This approach is supported by current observations (e.g. [67]). Future surveys will provide the rich resource of data to constrain and refine our understanding of SN progenitors and explosion physics. Using all the empirical data the supernovae provide, together with the tight relation between the observables and models enables us to significantly deduce their absolute magnitude with confidence. Thus, SNe Ia are simple, and will be well understood, standardizable candles for cosmological distance tests.

Acknowledgements

It is a pleasure to thank A. Khokhlov for the permission to show in Fig. 11.4 some of the results of his 3-D calculations, and for many helpful discussions. This research is supported by the NASA grant NAG5-7937.

References

1. Albrecht A., Weller J. 2000, BAAS, 197, 6106
2. Arbour R., Papenkova M., Li, W.D., Filippenko A.V., Armstrong M. 1999, IAU Circular 7156
3. Barbon R., Benetti S., Cappellaro E., Rosino L., Turatto M. 1990, A&A 237, 79
4. Bonanos A., Garnavich P., Schlegel E., Jha S., Challis P., Kirshner R., Hatano K., Branch D. 1999, BAAS 195, 3806
5. Bowers E.J.C., Meikle W.P.S., Geballe T.R., Walton, N.A., Pinto, P.A., Dhillon, V.S., Howell, S.B., Harrop-Allin, M.K. 1997, MNRAS, 290, 663
6. Canada-France-Hawaii Telescope Legacy Survey, `http://www.cfht.hawaii.edu/Science/CFHLS`
7. Collela P., Woodward P.R. 1984, J. Comp. Phys., 54, 174
8. Domínguez I., Höflich P. 2000, ApJ, 528, 854
9. Domínguez I., Höflich P., Straniero O. 2001, ApJ, 557, 279
10. ESSENCE Project, `http://www.ctio.noao.edu/wproject`
11. Fisher A., Branch D., Höflich P., Khokhlov A. 1995, ApJ, 447, 73
12. Fisher A., Branch D., Höflich P., Khokhlov A. 1998, ApJ, 494, 47
13. Fisher A., Branch D., Hatano K., Baron E. 1999, MNRAS, 304, 679

14. Hamuy M. et al. 1996, AJ, 112, 2391
15. Hatano K., Branch D., Lentz E. J., Baron E., Filippenko A.V., Garnavich P. 2000, ApJ 543L, 49
16. Höflich P. 1988, PASAu 7, 434 A&A, 248, L7
17. Höflich P., Khokhlov A., Müller E. 1991, A&A, 248, L7
18. Höflich P., Khokhlov A., Müller E. 1992, A&A, 257, 641
19. Höflich P., Khokhlov A., Müller E. 1993, A&A, 270, 223
20. Höflich P. 1995, ApJ, 443, 89
21. Höflich P., Khokhlov A., Wheeler J.C. 1995, ApJ, 444, 211
22. Höflich P., Khokhlov A. 1996, ApJ, 457, 500
23. Höflich P., Khokhlov A., Wheeler J.C., Phillips M.M., Suntzeff N.B., Hamuy M. 1996a, ApJ, 472, L81
24. Höflich P., Dominik C., Khokhlov A., Müller E., Wheeler J.C. 1996b, in 17^{th} Texas Symposium on Relativistic Astrophysics, Annals of the New York Academy of Science, 759, 348
25. Höflich P., Wheeler J.C., Thielemann F.K. 1998, ApJ, 495, 617
26. Höflich P., Nomoto K., Umeda H., Wheeler J.C. 2000, ApJ, 528, 590
27. Höflich P., Gerardy C., Fesen R., Sakai S. 2002, ApJ 568, 791
28. Höflich P., Stein J. 2002, ApJ 568, 771 & astro- ph/0104226
29. Höflich P., in: Stellar Atmospheres, eds. Hubeney et al., in press & astro-ph/0207103
30. Howell A., Höflich P., Wang L., Wheeler J. C. 2001, ApJ, 556, 302
31. Hoyle P., Fowler W.A. 1960, ApJ, 132, 565
32. Iben Jr I., Tutukov A.V. 1984, ApJs, 54, 335
33. Itoh N., Mitake S., Iyetomi H., Ichimaru S. 1983, ApJ 273, 774
34. Khokhlov A. 1991, ApJ, 245, 114
35. Khokhlov A., Müller E., Höflich P. 1993, A&A, 270, 223
36. Khokhlov A. 1995, ApJ, 449, 695
37. Khokhlov A., Oran E.S., Wheeler J.C. 1997, ApJ, 478, 678
38. Khokhlov A. 2001, ApJ, submitted & astro-ph/0008463
39. Kirshner R. P., Jeffery D., Leibundgut B., Challis P., Sonneborn G., Phillips M.M., Suntzeff N., Smith R., Winkler P., Frank W., Winge C. 1993, ApJ 415, 589
40. Kurucz R.L. 1993, Atomic Data for Opacity Calculations, Cambridge/Center for Astrophysics, CD
41. Kurucz R.L. 1994, Solar Abundance Model Atmospheres for 0,1,2,4,8 km/s, Kurucz CD-Rom No. 19
42. Langer N., et al. 2002, A&A, in press
43. Leibundgut B. et al. 1993, AJ, 105, 301
44. Lentz E.J., Baron E., Branch D., Hauschildt P., Nugent,P. 2000, ApJ, 530, L9
45. Lentz E.J., Baron E., Branch D., Hausschildt P. 2001, ApJ, 557, 2001
46. Lisewski A.M., Hillebrandt W., Woosley S.E., Niemeyer J.C., Kerstein A. R. 2000, ApJ 537, 405L
47. Livne E. 1993, ApJ 406, 17L
48. Livne E. 1998, ApJ, 527, 97
49. Livne E. 1998, talk in workshop on SNe Ia, private communication with P. Höflich, Aspen 1998.
50. Marion H., Höflich P., Vacca D., Wheeler J.C. 2002, ApJ, submitted
51. Meikle W.P.S. et al. 1996, MNRAS, 281, 263
52. Mendoza C., Cunto W. 1993, AA, 275, L5
53. Mihalas D. 1978, Stellar Atmospheres, San Francisco, Freeman 124,503

54. Müller E., Höflich P. 1994, A&A 281, 51
55. Nearby Supernovae Factory, `http://snfactory.lbl.gov`
56. Nomoto K., Sugimoto S., Neo S. 1976, ApSS, 39, L37
57. Nomoto K. 1980, ApJ, 248, 798
58. Nomoto K. 1982, ApJ 253, 798
59. Nomoto K., Thielemann F. -K., Yokoi K. 1984, ApJ, 286, 644
60. Nugent P., Baron E., Hauschildt P., Branch. D. 1997, ApJ, 485, 812
61. Ostriker P., Steinhardt P.J. 2001, Scientific American, Jan. 2001, p. 47
62. Paczyński B., 1985, in: Cataclysmic Variables and Low-Mass X-Ray Binaries, eds. D.Q. Lamb, J. Patterson, Reidel, Dordrecht, p.1 IAU-C 7156
63. Perlmutter S., et al. 1999a, ApJ 517, 565
64. Perlmutter S., Turner M.S., White M. 1999, Physical Review Letters 83, 670
65. Perlmutter C. et al. 1997, ApJ 483, 565
66. Phillips M.M. et al. 1987, PASP 90, 592
67. Phillips M.M., Lira P., Sunzeff N.B., Schommer R.A., Hamuy M., Maza J. 1999, AJ 118, 1766
68. Reinecke M., Hillebrandt W., Niemeyer J., Klein R., Gröbl A. 1999, AA 347, 724
69. Riess A.G., Press W.H., Kirshner R.P. 1996, ApJ 473, 88
70. Riess A.G., et al. 1998, AJ 116, 1009
71. Riess A.G., et al. 1999, AJ 118, 2675
72. Rudy R.J., Lynch D.K., David K., Mazuk S.M., Venturini C.C., Puetter R.C., Höflich P. ApJ 565, 413
73. Saha A., Sandage A., Labhard L., Tammann G.A., Macchetto F.D., Panagia N. 1997, ApJ Suppl. 486, 1
74. Saha A., Sandage A., Thim F., Labhard L., Tammann G.A., Christensen J., Panagia N., Macchetto F.D. 2001, ApJ 551, 973
75. Schmidt, B. P., et al. 1998, ApJ 507, 46
76. SNAP Project, `http://snap.lbl.gov`
77. Straniero O. Chieffi A. and Limongi M. 1997, ApJ 90, 425
78. Thielemann F.K., Nomoto K., Hashimoto M. 1996, ApJ, 460, 408
79. Umeda H., Nomoto K., Kobayashi C., Hachisu I., Kato M. 1999, ApJ, 522, L43
80. Wang L., Wheeler J.C., Höflich P. 1997, ApJ, 476, L27
81. Wang L., Höflich P., Wheeler C.J. 1998, ApJ Let. 487, 29
82. Wang L., Howell A., Höflich P., Wheeler J.C. 2001, ApJ 550, 1030
83. Webbink R.F. 1984, ApJ, 277, 355
84. Wheeler J.C., Höflich P., Harkness R. P., Spyromilio J. 1998, ApJ, 496, 908
85. Whelan J., Iben Jr. I. 1973, ApJ, 186, 1007
86. Woosley S.E., Weaver T. A., Taam, R.E. 1980, in: Type I Supernovae, ed. J. C. Wheeler, Austin, U. Texas, p. 96
87. Woosley S.E., Weaver T.A. 1986, ARAA, 24, 205
88. Woosley S.E., Weaver T.A. 1994, ApJ, 423, 371
89. Yamaoka H., Nomoto K., Shigeyama T., Thielemann F.K. 1992, ApJ, 393, 55

Appendix A: Numerical Radiation Hydrodynamics

The computational tools summarized below were used to carry out many of the analyzes of SNIa and Core Collapse Supernovae ([16], Höflich, Müller & Khokhlov 1993, [20], [30], ...). A consistent treatment of the explosion, light curves and spectra are needed (see Fig. 11.13). Details of the numerical methods and codes, namely HYDRA, can be found in [29] and references therein. Here we give a brief outline of the basic concepts.

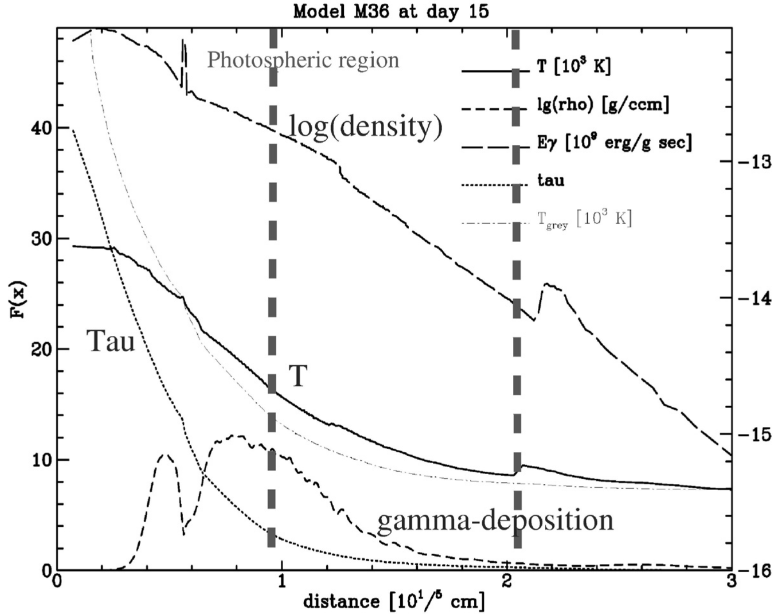

Fig. 11.13. Temperature T, energy deposition due to radioactive decay E_γ, Rosseland optical depth Tau (left scale) and density $\log(\rho)$ (right scale) are given as a function of distance (in $10^{15} cm$) for a typical SNe Ia at 15 days after the explosion. For comparison, we give the temperature T_{grey} for the grey extended atmosphere. The light curves and spectra of SNe Ia are powered by energy release due to radioactive decay of $^{56}Ni \rightarrow ^{56} Co \rightarrow ^{56} Fe$. The two dotted, vertical lines indicate the region of spectra formation. Most of the energy is deposited within the photosphere and, due to the small optical depth and densities, strong NLTE effects occur up to the very central region. At maximum light, the diffusion time scales are comparable to the expansion time scales mandating a consistent treatment of LCs and spectra (from Höflich 1995)

A.1 Hydrodynamics

The explosions are calculated using a spherical radiation-hydro code, including nuclear networks ([25] and references therein). This code solves the hydrodynamical equations explicitly by the piecewise parabolic method [7] and includes the solution of the frequency averaged radiation transport implicitly via moment equations, expansion opacities (see below), and a detailed equation of state. Nuclear burning is taken into account using a network which has been tested in many explosive environments (see [78], and references therein). The propagation of the nuclear burning front is given by the velocity of sound behind the burning front in the case of a detonation wave, and in a parameterized form during the deflagration phase, calibrated by detailed 3-D calculations (e.g. [38]). The density for the transition from deflagration to detonation is treated as a free parameter.

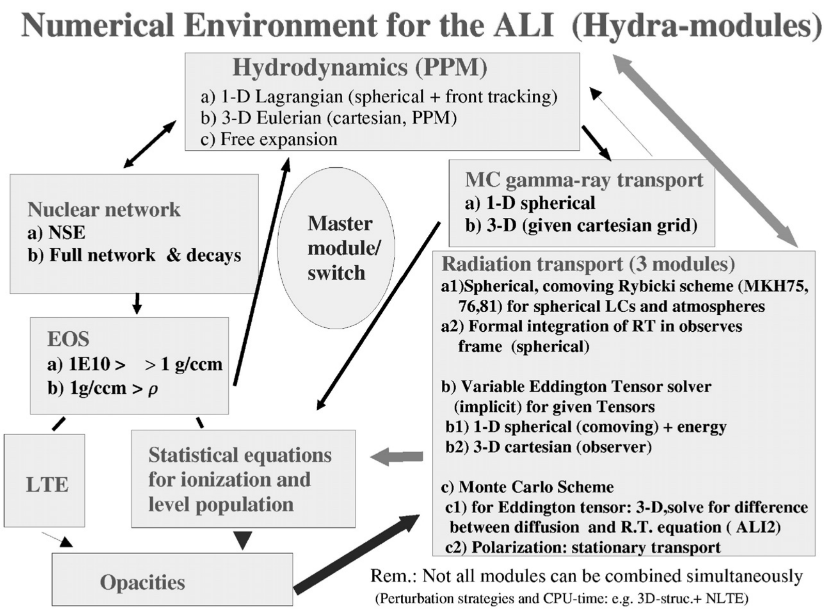

Fig. 11.14. Block diagram of our numerical scheme to solve radiation hydrodynamical problems including detailed equation of state, nuclear and atomic networks. For specific problems, a subset of the modules is employed (see text, and e.g. Figs. 11.7 and 11.9)

A.2 Light Curves

From these explosion models the subsequent expansion and bolometric and broad band light curves (LC) are calculated following the method described by [25], and references therein. The LC-code is the same as used for the explosion except that γ-ray transport is included via a Monte Carlo scheme and nuclear burning is neglected. In order to allow a more consistent treatment of the expansion, we solve the time-dependent, frequency-averaged radiation moment equations. The frequency-averaged variable Eddington factors and mean opacities are calculated from the frequency-dependent transport equations in a co-moving frame at each time step. The averaged opacities have been calculated assuming local thermodynamic equilibrium (LTE). Both the monochromatic and mean opacities are calculated in the narrow line limit. Scattering, photon redistribution, and thermalization terms, calibrated by the full non-LTE-atomic models, have been included. About one thousand frequencies (in one hundred frequency groups) and about nine hundred depth points are used.

A.3 Spectral Calculations

Our non-LTE code ([20], and references therein) solves the relativistic radiation transport equations in a co-moving frame. The spectra are computed for various epochs using the chemical, density, and luminosity structure and γ-ray deposition resulting from the light curve coder. This provides a tight coupling between the explosion model and the radiative transfer. The effects of instantaneous energy deposition by γ-rays, the stored energy (in the thermal bath and in ionization) and the energy loss due to the adiabatic expansion are taken into account. Bound-bound, bound-free and free-free opacities are included in the radiation transport, which has been discretized with about 2×10^4 frequencies and 97 radial points.

The radiation transport equations are solved consistently with the statistical equations and ionization due to γ-radiation for the most important elements and ions. Typically, between 27 and 137 bound levels are used for C, O, Mg, Si, Ca, Ti, Fe, Co, Ni with a total of about 40,000 individual NLTE-lines. The neighboring ionization stages have been approximated by simplified atomic models restricted to a few NLTE levels + LTE levels. The energy levels and cross sections of bound-bound transitions are taken from [40,41] starting at the ground state. The bound-free cross sections are taken from TOPBASE [52]. Collisional transitions are treated in the "classical" hydrogen-like approximation [53] that relates the radiative to the collisional gf-values. All form factors are set to 1. About 10^6 additional lines are included (out of a line list of 4×10^7) assuming LTE-level populations. The scattering, photon redistribution, and thermalization terms are computed with an equivalent-two-level formalism.

Appendix B: Uncertainties

In the detailed numerical models described in the last section we can identify three kinds of uncertainties: 1) uncertainties in the nuclear and atomic data such as cross-sections and opacities, 2) errors due to inconsistencies, discretization, and approximations for the numerical solution, and 3) conceptual simplifications in the supernova scenario. In Fig. 11.15 and [17,19,35], the effects of the opacities, scattering ratio, approximations for (gray) radiation transport and different frequency averaging procedures have been tested with respect to typical properties of the LCs such as the absolute brightness M_V, rise time t_V and color index B-V (Figs. 11.15, 11.16). Before these papers, theoretical models were based on the diffusion approximation and opacities that were constant with density, chemistry and time. Clearly, those assumptions were not adequate. However, within reasonable simplifications, the uncertainties in bolometric luminosity L_{bol}, absolute magnitude in V band M_V, time of peak V magnitude t_V, and color (flux ratio) B-V have been found to be less than 10%, even if the opacities have been scaled by a factor of 3 either way.

Within this narrow range the numerical solution of the radiation transport problem helps to improve the differences between L_{bol} and the energy production due to ^{56}Ni. As discussed in sections III and IV there exists a strong physical basis for this as well as tight model restrictions on the variation. Extensive tests showed variations in L_{bol}/E_γ are less than $\pm 20\%$ even if we allow for model assumptions which have since been ruled out or for use of clearly simplified approximations (e.g. one-zone model). The exact time of maximum light is go-

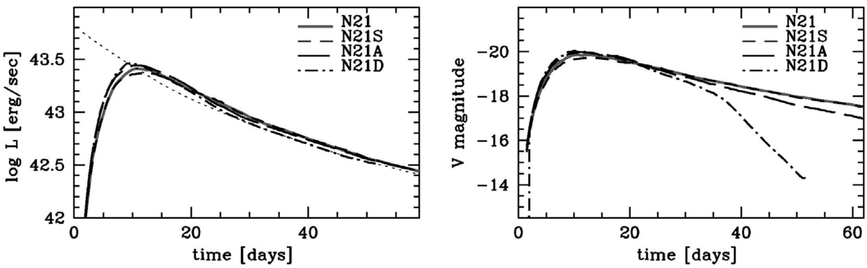

Fig. 11.15. Systematic study of the influence of physical approximations for an early ($\approx$ 1990) DD-model based on frequency averaged LC calculations [19]. N21: scattering + absorption + full RT, N21S: N21 but pure scattering lines, N21A: N21 - but pure absorption lines, N21D: diffusion approximation. Nowadays, we use multi-group, NLTE-LCs, and more realistic WDs are used (e.g. [22,25])

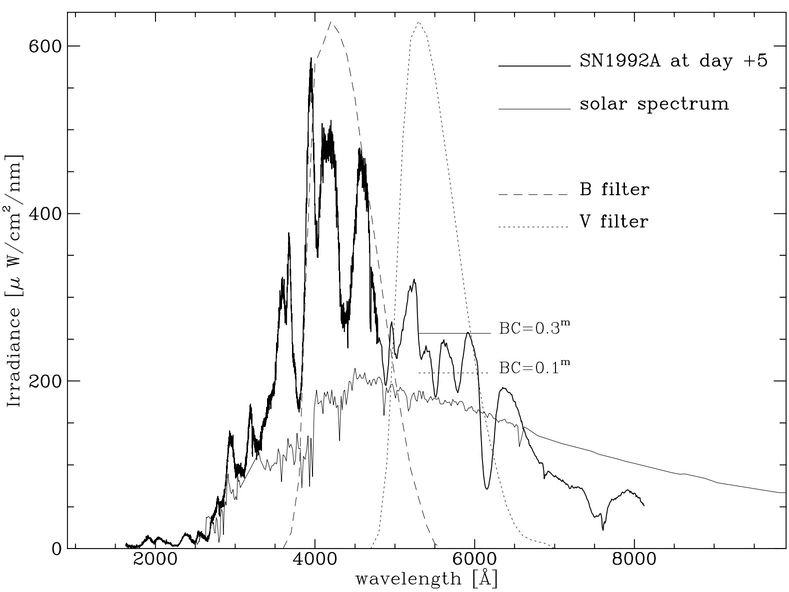

Fig. 11.16. Observational test for the bolometric correction BC. BC is defined by the difference of a spectral distribution in V compared to the solar irradiance. We give the comparison of the solar flux (thin line) and SN1992A at about 5 days past maximum light [39]. In addition, the filter functions for B and V are shown. The horizontal line at about 5500 Å (labeled BC=0.1^m) gives the level predicted by the model for SN1999A (from [22]). BC=0.7^m and -0.6^m would be required for values of H_o being 50 and 80 $km/sec/Mpc$ and, clearly, can be ruled out

verned by when the temperature drops below $\approx 10,000K$, i.e. when the mean opacity drops by several orders of magnitude [17,19,35]. Prior to maximum light, the drop in the temperature is governed by the expansion work and only to a small degree by radiation transport effects [19]. Note that V is well determined because it is in the linear tail of the emissivity. Uncertainties in B, in particular past maximum light, have been found to be up to 0.2^m because the size of line blocking and photon redistribution effects change drastically over the period considered.

We can also test the global energy conservation based purely on observations and predictions. Figure 11.16 shows the relation between luminosity and the monochromatic colors, known as the bolometric correction BC. The empirical and model based factors for BC agree to better than 0.1^m [22]. Another class of test is based on predictions of distances for individual SNe Ia [18,54] made prior to their determination based on δ-Ceph stars by HST: all but one agreed well within the 1σ-error bars (see table 1 from [22]). A notable exception was the peculiar SN1991T for which [17] predicted a distance of 14.5 ± 2 Mpc while distance measurements of a neighboring galaxy (host of 60f) suggested a distance of 19Mpc [73]. However, recently a direct measurement of the host galaxy by δ-Ceph reduced the distance to 13.5 Mpc [74].

Discretization errors have been tested by doubling the number of depth points (e.g. [35,20]). Typically, we use 456 to 912 depth points. The errors are found to be less than a few percent in the total energy and the production of elements during the explosion. For the LCs and spectra, the resulting fluxes change by less than 1% [20]. In the LC flux calculations, the main sources of errors are due to the limitations of the frequency grid, the neglect of aberration terms in the radiation transport equation, and the use of simplified atomic models for the frequency redistribution of photons. If we compare the LCs with the spectral calculations, the resulting error is $< 10\%$ in the flux and about 0.05^m and 0.2^m in B-V around maximum light and about 2 weeks after maximum, respectively [20,5,25,27].

Errors can arise because the models are simplifications of reality, e.g. adopting spherical symmetry. Deviations from this could be due to either global asymmetries in the density or the distribution of elements [80,82,30]. In general, only upper limits for normal bright SNe Ia are given; recent observations with VLT indicate a level of about 0.1%, which translates into a direction dependent luminosity of $\approx 0.1^m$ [17]. However, the subluminous SN1999by shows polarization as high as 0.7% [30], and rotational symmetry. This implies that the luminosity will vary by about 0.3^m, depending on the position of the observer.

Another possible breakdown in geometry is the description of the burning front but, currently, the size of this effect is hard to estimate. As noted above, 3-D models are currently limited to the regime of linear instabilities and a significant amount of C/O remains unburned ($\approx 0.5 - 0.8 M_\odot$). Clearly, these early 3-D attempts are in contradiction with observations.

12 Novae as Distance Indicators

Roberto Gilmozzi[1] and Massimo Della Valle[2]

[1] European Southern Observatory, Paranal Observatory, Chile
[2] Osservatorio Astrofisico di Arcetri, Firenze, Italy

Abstract. We review the status of Novae as distance indicators. We discuss the problem of the correct calibration of the *life-luminosity* relationship for Galactic novae on the basis of the properties of the M31 and LMC nova populations and show that linear regressions, normally used to interpolate the Galactic data, fit M31 and LMC only as a very rough first order of approximation. We show that the use of the VLT can improve the efficiency of nova detections in galaxies outside the Local Group by one order of magnitude with respect to previous studies, and that Novae can play a central role both in the determination of the extragalactic distance scale up to $\gtrsim 50$ Mpc and to provide a valuable alternative to Cepheids in calibrating the absolute magnitude at maximum of type Ia Supernovae.

12.1 Introduction

A classical Nova event is the third most violent explosion that occurs in galaxies, exceeded only by γ-ray bursts and supernovae. It occurs onto the surface of the white dwarf (WD) component of a cataclysmic variable binary system, in which a less evolved companion has filled in its Roche lobe and is losing hydrogen-rich material through the inner Lagrangian point onto the primary. Theoretical studies show that the accreted layer grows until a temperature of $\gtrsim 10^7$K and a pressure $\gtrsim 10^{19}$ dyne cm^{-2} are reached at its base, and thermonuclear runaways can ignite and start the ejection of the accreted envelope. These giant explosions cause the star to increase its brightness by hundreds thousand times in a few days or hours and to produce about 10^{45} ergs of energy within a few weeks, thus making these objects among the brightest transient sources in the sky. The brightest novae achieve, at maximum light, an absolute magnitude of $M_V \lesssim -9$, which makes them easily recognizable inside the Milky Way and in external systems. Therefore they are perfectly suitable to measure the cosmic distances inside the Local Group of galaxies [4,5] and beyond [38,11].

With respect to Cepheids, the mostly used distance indicators up to $\lesssim$ 30 Mpc, Novae have the advantage to be, on average, brighter than the Cepheids of the longest periods, by $\sim$ 2 magnitudes. Moreover they can be found in all types of galaxies, both spirals and ellipticals, while Cepheids are found only in spirals. The main reason which has prevented for a long time the systematic use of Novae for distance measurements is the unpredictable nature of these events, which implies expensive (telescope) time consuming campaigns. This explains why, in the past, nova surveys in external galaxies have not been so popular among astronomers, although remarkable exceptions do exist [24,1,42,51]. The

R. Gilmozzi and M. Della Valle, Novae as Distance Indicators, Lect. Notes Phys. **635**, 229–241 (2003)
http://www.springerlink.com/

use of new CCD detectors, new observational strategies [47] and 8-10m class telescope [11] seem to have inverted this trend.

12.2 Historical Background

The first systematic studies of Galactic novae, aimed at measuring their distances and absolute magnitude at maximum, date back to 1922. Lundmark [29] derived an average absolute magnitude at maximum of $M_V = -6.2$, characterized by a very large dispersion, typified by Nova Lac 1910, $M_V = -1.1$, and T Sco 1860, $M_V = -9.1$. In a subsequent paper [30] he revised the previous value of the absolute magnitude at maximum of novae by averaging the distances obtained with four different methods and obtained $M_V = -7.2$. On the basis of this result, Lundmark was able to establish the existence of a relationship between magnitude at maximum and amplitude (his Fig. 3) of the nova outburst, later on confirmed by modern nova studies (Fig. 5.4 in [59]). This fact proves that Galactic nova observations in the early 20's coupled with the first detections of novae in M31, obtained a few years before by Shapley [48] and Richtley [40,41], at magnitude $m_{pg} \sim 17/18$, had the potential for setting the distance scale debate of that era. Unfortunately, this opportunity was missed because of the confusion between novae and supernovae [55]. For example Zwicky [61] perceived the existence of a "life-luminosity" relationship for novae of the form $M_{max} = -5 \times \log\tau_{\Delta m}$+const (with $\tau_{\Delta m}$ the time necessary to decrease Δm magnitudes), but unfortunately used two Galactic novae (Nova Aql 1918 and Nova Per 1901) and three supernovae, SN 1936A (SN in NGC 4273), SN 1926A (SN in NGC 4303) and SN 1885A (S And) to calibrate it (see Fig. 12.1). Although qualitatively correct, the Zwicky's relationship led to misleading results because of the wrong calibrators.

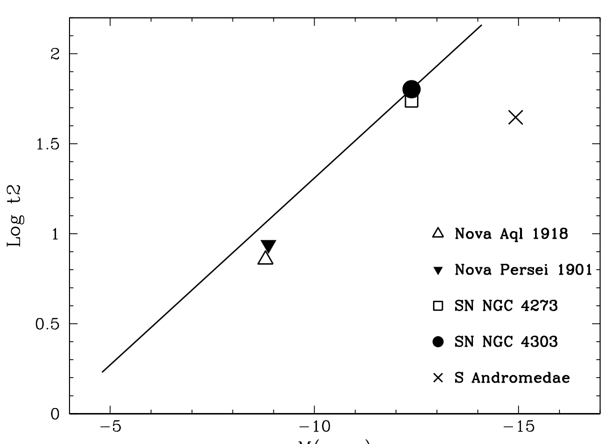

Fig. 12.1. The Zwicky relationship for "Novae"

This "life-luminosity" relationship, nowadays labeled Maximum Magnitude *vs.* Rate of Decline relationship (hereafter MMRD), is the basic tool to use novae as distance indicators [56]. Its potential is extraordinary: it enables us to derive the absolute magnitude of novae at maximum light, and in turn their distance, from a mere inspection of their light curve.

12.3 The Calibration of the MMRD Relationship

The first calibration of the MMRD relation entirely based on novae was carried out in the early 40's by McLaughlin [32–34]. It was based on the 13 Galactic novae whose distance and absolute magnitudes at maximum were determined by 3 different methods, i.e. nebular parallaxes, intensities of interstellar lines, and residual velocities from interstellar lines interpreted as due to galactic rotation, complemented by M31 novae coming from the Hubble survey [24] and 3 novae in the Large Magellanic Cloud. Although not quoted explicitly by the author, the relationship shown by his graph (his Fig. 1) has both zero point and shape rather different from modern values, due to the adopted distance moduli for M31 and LMC, (m–M)=22.4 and 17.1 (cfr. $(\mathrm{m{-}M})_{M31} = 24.3$ [4] and $(\mathrm{m{-}M})_{LMC} = 18.55$ [35] respectively).

After McLaughlin's paper a number of calibrations, based on different samples of calibrators and assumptions on the galactic absorption (from 0.8 mag/kpc [34] up to 3.5 mag/kpc [26]), have been provided by different authors:

$\mathrm{M}_\circ = 2.0 \times \log t_3 - 10.1$ (Vorontsov-Velyaminov 1947) [58]
$\mathrm{M}_\circ = 3.7 \times \log t_3 - 13.8$ (Kopylov 1952) [26]
$\mathrm{M}_{pg} = 2.5 \times \log t_{3,pg} - 11.8$ (Schmidt 1957) [46]
$\mathrm{M}_{pg} = 2.5 \times \log t_{3,V} - 11.5$ (Schmidt 1957) [46]
$\mathrm{M}_V = 2.5 \times \log t_{3,V} - 11.75$ (Schmidt 1957) [46]
$\mathrm{M}_B = 1.8 \times \log t_{2,B} - 11.5$ (Pfau 1976) [37]
$\mathrm{M}_{pg} = 2.4 \times \log t_3 - 11.3$ (de Vaucouleurs 1978) [15]

In the early 80's a study to recover old nova shells around historical post-novae [6,7] reported the size for 19 nova shells. These, together with the observed velocities, the assumption that the velocity of ejection was equal in all directions, and individual estimates of the galactic absorption toward each nova, provided nova distances and a new calibration of the MMRD relationship, with the advantage over previous works to be based on a set of data homogeneously acquired and treated. The new fit yielded:

$\mathrm{M}_V = 2.41 \pm 0.23 \times \log t_2 - 10.70 \pm 0.30$ [7].

More recently [16] have increased this sample to 28 objects and improved the quality of some "old" measurements of nova shells around other 9 post-novae with ground-based and *HST* data (see Fig. 12.3). The linear fit gives:

$\mathrm{M}_V = 2.54 \pm 0.35 \times \log t_3 - 11.99 \pm 0.56$
or
$\mathrm{M}_V = 2.55 \pm 0.32 \times \log t_2 - 11.32 \pm 0.44$ [16].

12.4 The True Shape of the MMRD Relationship from Novae in M31 and LMC

Local effects and the difficulty of determining nova distances accurately suggest looking in other galaxies to determine the "true" shape of the MMRD relationship. Following Hubble's [24] pioneering survey in M31, other searches aimed at detecting novae at maximum light have been carried out by Arp [1], Rosino [42–44] and Sharov & Alksnis [52]. Data for LMC novae are mainly derived from the Graham [20–22] survey, supplemented by more fragmentary observations reported in the IAU Circulars, all of this summarized in [5]. Figure 12.2 shows the data for 105 M31 novae corrected for the (modern) distance modulus (see above) and for foreground extinction. A simple inspection of Fig. 12.2 shows that the trend of the relationship between $v_d = 2/t_2$ and the absolute magnitude at maximum is linear only over the range $0.04 \lesssim v_d \lesssim 0.2$ ($10 \lesssim t_2 \lesssim 50$ or $17 \lesssim t_3 \lesssim 90$ days), whereas for the entire range of v_d (or t_2, t_3) the analytic representation is a reverse S-shaped function:

$$\mathrm{M}_V = -7.92 - 0.81 \times \arctan(1.32 - \log t_2)/0.23 \text{ [13].}$$

The linear fits to Galactic novae are superimposed on Fig. 12.2. They are inadequate to describe the data distribution for M31 and LMC novae. Linear best fits are the result of a limited statistics (less than 30 objects) combined with the large dispersion affecting the Galactic data points, mainly caused by the problem of estimating correctly the amount of the interstellar absorption along the line of sight to each single nova. These effects can be largely minimized by studying the nova populations in external galaxies.

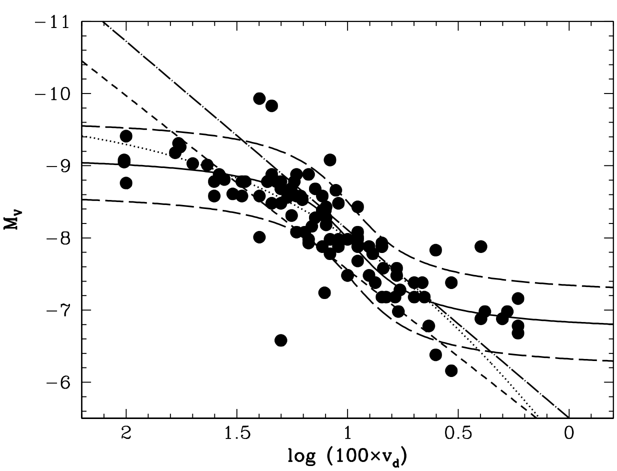

Fig. 12.2. The MMRD relationship for Novae in M31 and LMC. The Arp, Rosino, and Capaccioli et al data are corrected for distance and foreground absorption. "Fit" lines are explained in the text

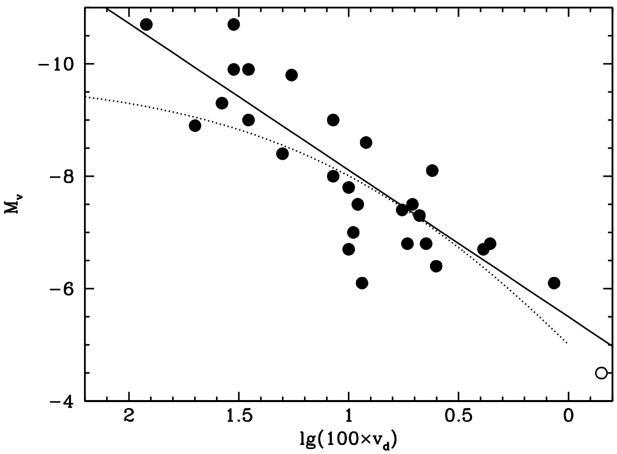

Fig. 12.3. Galactic Novae MMRD relationship (adapted from [16]), with the addition of DO Aql (open circle [12]). The data do not contradict a continuous decreasing trend (see text; dotted curve: model by [27])

Theoretical attempts to explain the MMRD relation also provide evidence that linear regressions fit the nova data only as a very rough first order approximation. After Hartwick & Hutchings [23] and Shara [49], Livio [27] was able to derive a simple relationship between the absolute magnitude at maximum and the mass of the underlying WD, which is the most important parameter influencing the strength and the evolution of a nova outburst (having the accretion rate, the temperature of the WD and the strength of the WD magnetic field, more modest effects):

$$\mathrm{M}_B^{max} \approx -8.3 - 10 \times \log M_{WD}/M_{\odot}$$

and in turn a theoretical MMRD relation of the form:

$$\mathrm{t3}{=}1.3 \times 10^{0.1\times(M_B+9.76)} \times [10^{(M_B+9.76)/15} - 10^{(-M_B-9.76)/15}]^{1.5}\mathrm{days.}$$

The dotted line in Fig. 12.2 shows the theoretical relation, superimposed on the M31 and LMC data. The flattening of the observed distribution at high luminosities is real and can be interpreted as indicating that the mass of the WD, in systems which result in super-*Eddington* novae, is approaching the Chandrasekhar limit. The flattening at faint level of luminosity, characterized by $\mathrm{m}_{pg} \sim 19$, was very near the photographic detection limit of the M31 Rosino survey, and may well represent the bright wing of *Eddington* novae which are populating the bottom of the MMRD relation: thus the observed flattening may be the result of a trivial observational bias (see [59]). Some evidence in this direction comes from Galactic novae, for which the distances have been computed via nebular parallaxes. Fig. 12.3 shows that the galactic data extend to $\mathrm{M}_V \sim -6$ (which is about 1 mag fainter than M31 data) and do not contradict a continuous decreasing trend. However we note that the nature of the outburst for very low mass WD ($< 0.6/0.7 M_{\odot}$) has not been explored in detail, and therefore it is still possible that the flattening at low levels of brightness is a consequence of the physics of the outburst [28].

The conclusion from all this is that unless the Galactic nova population follows a very different MMRD relation from those of M31 and LMC, unique linear fits to Galactic novae are inadequate to describe the observed distribution.

12.4.1 Other Distance Indicators Using Novae

A number of other methods for using novae as distance indicators have been suggested by different authors.

The Absolute Magnitude 15 Days Past Maximum. Buscombe and De Vaucouleurs [3] first pointed out that all novae, irrespective of their rate of decline have the same absolute magnitude, $\langle M_{15} \rangle$ at 15 days past maximum. This is a simple consequence of the MMRD relationship for which the more luminous is a nova at maximum, the faster is the rate of decline of its brightness. This has been theoretically explained by [50]. Recent calibration of this relationship give $\mathrm{M}_{15}^{V} = -5.24 \pm 0.15$ [57], $\mathrm{M}_{15}^{V} = -5.60 \pm 0.43$ [7], $\mathrm{M}_{15}^{V} = -5.69 \pm 0.42$ [4]. The existence of a small class of super-bright novae [9] imposes some degree of caution when applying this method to small samples of extragalactic novae.

The Luminosity Function of Novae. Nova studies in the Milky Way and in M31 have shown that the luminosity function of novae is bimodal [4,10] and characterized by a stable "dip" at $\mathrm{M}_V = -8.2 \pm 0.15$ (Fig. 12.4). It is worth noting that this indicator self-controls the Malmquist bias. Indeed, if both peaks

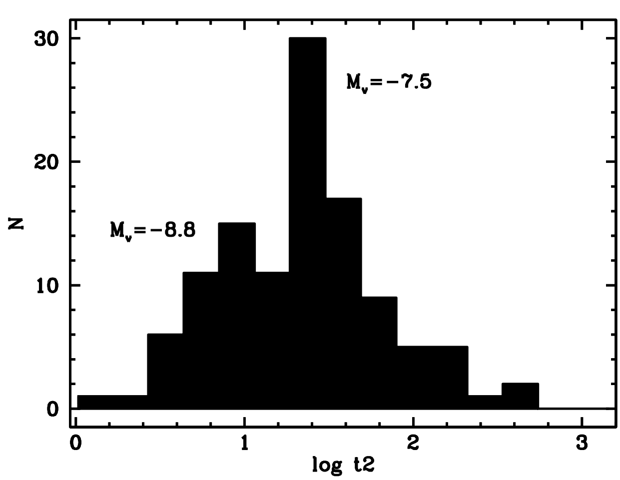

Fig. 12.4. Frequency distribution for the rates of decline in galactic novae. The same trend is visible in the LMC and M31 data (in fact, this was first detected in M31)

of the luminosity function of a nova population in an extragalactic system are seen, this means the minimum has been detected. On the other hand, if the observed luminosity function shows just one peak, this will point out that the nova sample is biased.

The Period of Visibility. This method has been discussed by [56]. These authors have shown the existence of a tight correlation between the mean period of visibility of the novae, in an extragalactic system, down to some limiting magnitude, and the corresponding absolute magnitude. The method has been calibrated to the nova population of M31, as $\log\langle t\rangle = 0.67 \times m_{lim} - 11.0$ and it has been used to determine the distance to M33 [8] and Virgo [38]. The method assumes that the distribution of the rate of decline of the calibrator nova population (M31) is similar to that of the nova population for which we are measuring the distance. This imposes some degree of caution when comparing nova population of bulge dominated systems, like M31, with disk dominated system such as LMC.

12.5 Novae as Distance Indicators: Are They Really Good?

The reasons for which novae are, at least in principle, excellent distance indicators, can be summarized as follows:

- Novae are bright, they can reach $M_B \lesssim -9$, about 2 magnitudes more luminous than Cepheids of larger periods.
- Unlike Cepheids that can be detected only in spirals, novae can be "easily" recognized also in ellipticals.
- The calibration of the MMRD relationship can be carried out inside the galaxies of the Local Group [13].
- The cosmic scatter of the MMRD relationship is small. The observed one (i.e. including the uncertainty on the magnitudes at maximum) is $1\sigma = 0.17$ mag. Therefore, the intrinsic scatter is likely smaller than 0.1 mag and should be due to other effects than the mass of the WD, affecting the properties of nova outburst, such as the strength of the magnetic field, the temperature of the WD, the accretion rate.
- Intrinsic differences in the outburst properties, existing between novae associated with the bulge/thick disk or spiral arm stellar populations [10] do not affect the zero point of the MMRD relationship, but only change the relative percentage of fast and bright novae.
- There exists a good theoretical understanding of the tool to be used, i.e. the MMRD relation.

The usefulness and reliability of novae as distance indicators is not only *potential* but also demonstrable through *observations*. Since it is commonly accepted that Cepheids are the best distance indicators for spiral galaxies, we compare

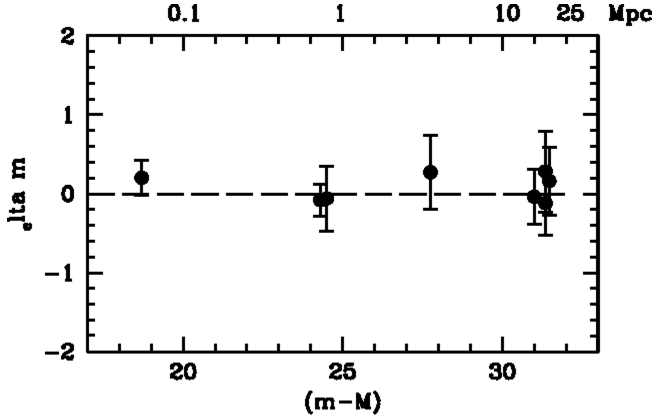

Fig. 12.5. Cepheids vs. Novae distance scale difference as a function of distance

Table 12.1. Nova Distances vs. Cepheids

Galaxy	$(m\text{–}M)_{novae}$	Number of Novae	$(m\text{–}M)_{Cep}$	Δm	Ref_{novae}	Ref_{Cep}
LMC	18.7±0.2	15	18.50 ± 0.10	$+0.20 \pm 0.22$	[5]	[19]
M31	24.3±0.2	84	24.38 ± 0.05	-0.08 ± 0.20	[4]	[19]
M33	24.5±0.4	5	24.56 ± 0.10	-0.06 ± 0.41	[8]	[19]
M81	27.75±0.4	1	27.48 ± 0.24	$+0.27 \pm 0.47$	[51]	[19]
M100	31.0±0.3	1	31.04 ± 0.17	-0.04 ± 0.40	[17]	[18]
Virgo	31.35±0.35	6	31.47±0.21 31.07±0.38	−0.12±0.41 +0.28±0.52	[38,13]	[54,19]
Fornax*	31.47±0.34	4	31.32 ± 0.20	$+0.15 \pm 0.40$	[11]	[31,53]

(*) Cepheids distance derived from the spiral NGC 1365

(in Table 12.1) the distances obtained via novae (col. 2) and via Cepheids (col. 4), for all available spirals. In col. 5 we report the magnitude difference between the two methods which are also displayed in Fig. 12.5 as a function of the distance.

An inspection of Table 12.1 and Fig. 12.5 shows that 1) the differences between the central values of the two methods translate to 13% difference in the two distance scales (at most) and 2) there is no evidence for systematic deviation from the linearity at least up to $\lesssim 25$ Mpc. The large error-bars associated to nova measurements (with the exception of LMC and M31) are due to the small number of novae (col. 3) which have been used to measure the distances of the galaxies. This simple exercise suggests that *novae can be distance indicators as good as Cepheids*, with the advantage that they can be observed in all Hubble type galaxies.

This result is of particular interest if one considers the problem of measuring the distances to early type galaxies. Indeed, the situation for ellipticals and lenticulars is not clear at all. Classical distance indicators for these systems, like the turn-over magnitude of the luminosity function of globular cluster (see [60] for a review) or the cut-off magnitude of the luminosity function of planetary nebulae (see [25] for a review) seem to suffer from some problems. For instance [14] have shown (their Tables 5 and 7) that the absolute magnitude at maximum of normal type Ia SNe calibrated via GCs (5 objects) and PNe (6 objects) is fainter by 0.6–0.9 mag than the average absolute magnitude at maximum of 7 type Ia SNe located in spirals and calibrated via Cepheids [45]. Even assuming the existence of a systematic difference between the peak luminosities of type Ia in Spirals and in lenticulars/ellipticals, this difference should not be larger than 0.3 mag [2]. Given typical uncertainties of $\lesssim 0.2$ mag in the absolute magnitude at maximum of SNe, the residual differences are probably just reflecting the uncertainties in the tuning of the "zero" points of the distance indicators used.

The excellent match existing between the "zero" points of the Cepheid and nova distance scales would indicate that novae are potentially able to provide reliable distances for early type galaxies.

12.6 Pilot Program on NGC 1316 (Fornax A)

The selected target for our pilot program was NGC 1316, the parent galaxy of the type Ia Supernovae 1980N and 1981D. These SNe are believed to suffer from little absorption and their maxima have been measured with relatively good accuracy (± 0.2 mag). Therefore, although their magnitudes are "old" photographic measurements, they are perfectly suitable to confirm or to refute the existence of an 0.6-0.9 mag difference between the absolute magnitude at maximum of type Ia SNe occuring in early and late type galaxies (as would be inferred from distances derived with PNe or GCs).

The observations were performed during nine nights distributed over a period of time from 25 Dec 1999 to 19 January 2000. They were carried out in service mode at the 8.2m VLT/ANTU telescope equipped with the FORS-1 and a 2048×2048 CCD camera having a projected pixel size of $0.2''$ and a field of view of 6.8×6.8 arcmin^2. Each exposure lasted twice 10 min and was carried out in three optical filters (B,V, and I) under similar seeing conditions $\sim 0.9''$. The background light due to the galaxy was removed by subtracting a median filtered version of each image from the original frame. This procedure generates images containing only stars and faint galaxies.

The novae were discovered by blinking each "background-subtracted" B frame with the one obtained on 25 Dec. Photometric measurements have been performed with Sextractor and aperture photometry properly corrected to account for seeing variations. We have found 4 transient objects (see Fig. 12.6) which were characterized by blue colors, (B-V) ~ 0, quite typical for novae observed around maximum. In addition we note that the time scale of the variability (Fig. 12.7), the apparent brightness and the colors are inconsistent with other types of variable stars, such as Mira, Cepheids, Hubble-Sandage variables or foreground objects like RR Lyr and flare stars.

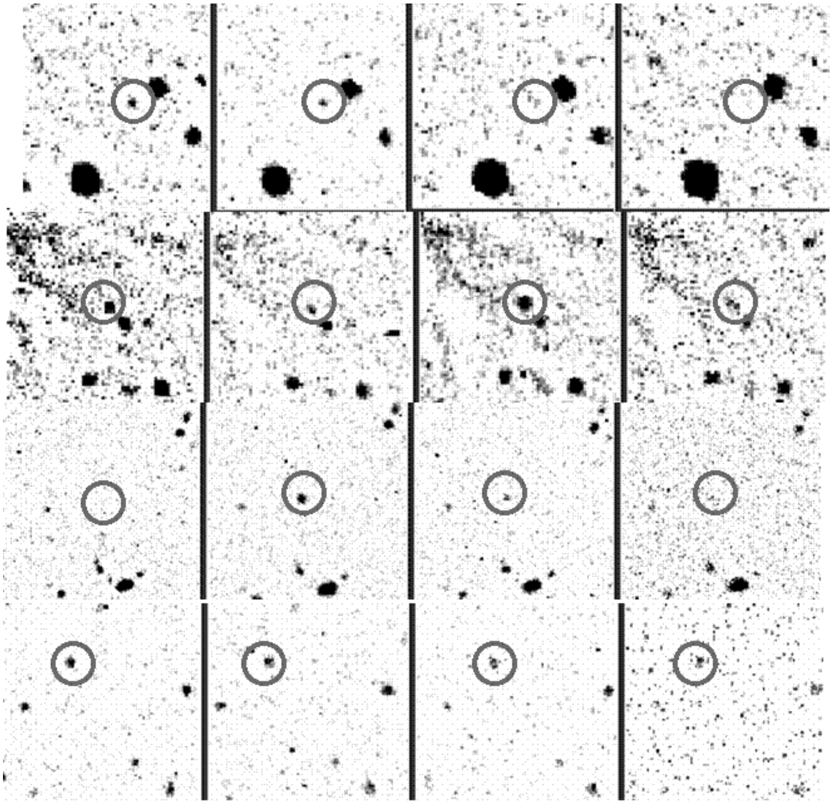

Fig. 12.6. Novae in NGC 1316

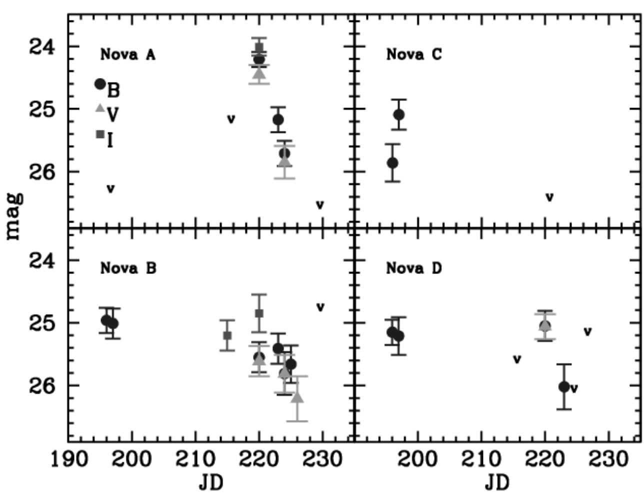

Fig. 12.7. Light curves of novae in NGC 1316

12.6.1 Results

We have discovered 4 novae in NGC 1316. This is the first time that novae are detected and studied beyond the Virgo Cluster. Although their maxima have been missed, the sampling of the light curves is adequate to estimate the distance to the galaxy through the "Buscombe-de Vaucouleurs" law (see above). Since the last data points of the lightcurves have been obtained not more than 20 days past maximum, the corresponding apparent magnitudes allow us to set an upper limit to the distance modulus of the galaxy of $(m-M) \leq 31.50\pm0.25$ (1σ). Nova n.1 has been caught during the early decline, therefore the last data point can be used only to set a lower limit to the distance, i.e. $(m-M) \geq 31.30 \pm 0.25$. The above reported distances imply an absolute magnitude at maximum of $M_B = -19.20\pm0.35$ and $M_B = -19.10\pm0.35$ for SN 1980N and SN 1981D, respectively. This result is consistent (though of course not conclusively) with the existence of an 0.3 mag deficiency in the luminosity at maximum of type Ia Supernovae occuring in early type galaxies, with respect to the ones found in spirals as was argued in the past [2].

Simulated VLT observations of novae in Fornax, performed during the feasibility study of this project, have shown that our nova sample could suffer from some incompleteness, up to 20%. With this in mind and by applying the control time technique [62], we estimate for NGC 1316 a nova rate of about 90 to 180 novae per year. After normalizing this rate to the total luminosity of the parent galaxy, we find that NGC 1316 tends to produce novae less prolifically than some other types of spirals. Recent studies report extraordinary cosmological scenarios on the basis of 0.25 mag deficiency observed in the luminosity at maximum of high-z SNe Ia [36,39]. This fact itself clearly points out the need to perform the calibration of the absolute magnitude at maximum of "local" SNe Ia to better than 0.25 mag. One possibility involves the use of Cepheids. We propose, as an alternative, to study the Zwicky relationship (MMRD) in parent galaxies of well observed type Ia Supernovae. The requested accuracy can be obtained by studying about a dozen novae, caught close to maximum light. The VLT observations presented here demonstrate that this goal can be nowadays achieved with 8-10m class telescopes within a modest amount of telescope time.

12.7 Future Studies

The main drawback in using novae to measure cosmic distances, especially beyond the Local Group of galaxies, is the unpredictable nature of these events which makes their detection and study exceedingly (telescope-)time consuming. For example, already in the "CCD era", Pritchet and van den Bergh [38] discovered with the CFH telescope 9 novae in the Virgo Cluster in 15 half nights, corresponding to about 56 hours of observations with a 4m class telescope. This implies a *yield* per night, in terms of telescope time per nova, of about 6.2 hours per nova. The recent coming into operation of 8-10m telescopes, equipped with larger and more efficient detectors, can dramatically change this. Indeed, our VLT pilot program in NGC 1316, yielded 4 novae in only 3 hours of observing time, i.e. about 0.8 hour per nova, distributed over 9 nights. This experiment has pointed out that large telescopes and new detectors have the potential to measure the distances to galaxies up to ~ 50 Mpc with an uncertainty of the order of 10-15% with about 20 novae (keeping in mind that the scatter of the relation is no larger than ~ 0.17 mag at 1σ), within a modest amount of telescope time, of the order of only $15-30$ hours, quite typical for a medium sized observational programs. In other words, modern capabilities are able to improve the efficiency of nova searches in extragalactic systems by a factor of ~ 10, as compared to previous searches. Thus novae can play a pivotal role both in the quest for the local extragalactic distance scale and in providing a valuable alternative to the Cepheids calibration of the absolute magnitude of type Ia Supernovae.

References

1. Arp, H.C. 1956, AJ, 61, 15
2. Branch, D., Romanishin, W., Baron, E. 1996, ApJ, 467, 473
3. Buscombe, W., de Vaucouleurs, G. 1955, Obs., 75, 170
4. Capaccioli, M., Della Valle, M., D'Onofrio, M., Rosino, L. 1989, AJ, 97, 1622
5. Capaccioli, M., Della Valle, M., D'Onofrio, M., Rosino, L. 1990, ApJ, 360, 63
6. Cohen, J.G., Rosenthal, A.J. 1983, ApJ, 268, 689
7. Cohen, J.G. 1985, ApJ, 292, 90
8. Della Valle, M. 1989, in "The Extragalactic Distance Scale", ASP Conference Series, n. 4, p. 73, eds. S. van den Bergh & C.J. Pritchet
9. Della Valle, M. 1991, A&A, 252, L9
10. Della Valle, M. 2002, in Classical Nova Explosions, Sitges, Spain 2002, Eds. M. Hernanz & J. José
11. Della Valle, M., Gilmozzi, R. 2002, Science, 296, 1275
12. Della Valle, M., Gilmozzi, R., 2003, in preparation
13. Della Valle, M., Livio, M. 1995, ApJ, 452, 704
14. Della Valle, M., Kissler-Patig, M., Danziger, J., Storm, J. 1998, MNRAS, 299, 267
15. de Vaucouleurs, G. 1978, ApJ, 223, 751
16. Downes, R.A., Duerbeck, H. 2000, AJ, 120, 2007
17. Ferrarese, L. et al. 1996a, ApJ, 464, 568
18. Ferrarese, L. et al. 1996b, ApJ, 468, L95
19. Freedman, W.L. et al. 2001, ApJ, 553, 47
20. Graham, J.A., Araya, G. 1971, AJ, 76, 768
21. Graham, J.A. 1975, PASP, 87, 641
22. Graham, J.A. 1979, PASP, 91, 79
23. Hartwick, F.D., Hutchings, J.B. 1978, ApJ, 226, 203
24. Hubble, E.P. 1929, ApJ, 69, 103
25. Jacoby, G.H. 1997, in the Extragalactic Distance Scale, ed. M. Donahue, M. Livio, N. Panagia (STScI, Baltimore), p.197
26. Kopylov, I.M. 1952, Comm. Crimean Ap. Obs. 9, 116
27. Livio, M. 1992, ApJ, 393, 516
28. Livio, M. 1997, in the Extragalactic Distance Scale, ed. M.Donahue, M.Livio, Panagia, N. (STScI, Baltimore), p.186
29. Lundmark, K. 1922, PASP, 34, 207
30. Lundmark, K. 1923, PASP, 35, 95

31. Madore et al. 1996, AAS, 189, 108.04
32. McLaughlin, D.B. 1942, Pop. Astron., 50, 233
33. McLaughlin, D.B. 1945a, PASP, 57, 69
34. McLaughlin, D.B. 1945b, AJ, 51, 136
35. Panagia, N.; Gilmozzi, R.; Macchetto, F.; Adorf, H.-M.; Kirshner, R.P. 1991, ApJ, 380, L23
36. Perlmutter et al. 1998, Nature 391, 51
37. Pfau, W. 1976, A&A, 50, 113
38. Pritchet, C.J., van den Bergh, S. 1987, 318, 507
39. Riess et al. 1998, AJ 116, 1009
40. Ritchey, G.W. 1917a, PASP, 29, 210
41. Ritchey, G.W. 1917b, PASP, 29, 253
42. Rosino, L. 1964, Ann. Astrophys., 27, 498
43. Rosino, L. 1973, A&AS, 9, 347
44. Rosino, L., Capaccioli, M., D'Onofrio, M., Della Valle, M. 1989, AJ, 97, 83
45. Saha, A., Sandage, A., Tammann, G. A.; Dolphin, A. E.; Christensen, J.; Panagia, N.; Macchetto, F. D. 2001, ApJ, 562, 314
46. Schmidt, T. 1957, Zs.f.Ap., 41, 182
47. Shafter, A.W., Ciardullo, R., Pritchet, C.J. 2000, ApJ, 530, 193
48. Shapley, H. 1917, PASP, 29, 213
49. Shara, M.M. 1981a, 243, 926
50. Shara, M.M. 1981b, 243, 268
51. Shara, M.M., Sandage, A., Zurek, D. 1999, PASP, 111, 1367
52. Sharov, A.S., Alksnis, A. 1992, Ap&SS, 190, 119
53. Silbermann, N.A. et al. 1999, ApJ, 515, 1
54. Tammann, G., Federspiel, M. 1997, in The Extragalactic Distance Scale, ed. M.Donahue, M.Livio, Panagia, N. (STScI, Baltimore), p.137
55. van den Bergh, S. 1988, Comm. Astrophys., 12, 131
56. van den Bergh, S., Pritchet, C.J. 1986, PASP, 98, 110
57. van den Bergh, S., Younger P.F. 1987, A&AS, 70, 125
58. Vorontsov-Velyaminov, B.A. 1947, AJ, USSR, 24, 83
59. Warner, B. 1995, in Cataclysmic Variable Stars, Cambridge Astrophys. Ser. 28, Cambridge University Press
60. Whitmore, B. 1997, in the Extragalactic Distance Scale, ed. M.Donahue, M.Livio, Panagia, N. (STScI, Baltimore), p.254
61. Zwicky, F. 1936, PASP, 48, 191
62. Zwicky, F. 1942, ApJ, 96, 28

13 Extragalactic Distances from Planetary Nebulae

Robin Ciardullo

The Pennsylvania State University, Department of Astronomy and Astrophysics, 525 Davey Lab, University Park, PA 16803, USA

Abstract. The [O III] $\lambda 5007$ planetary nebula luminosity function (PNLF) occupies an important place on the extragalactic distance ladder. Since it is the only method that is applicable to all the large galaxies of the Local Supercluster, it is uniquely useful for cross-checking results and linking the Population I and Population II distance scales. We review the physics underlying the method, demonstrate its precision, and illustrate its value by comparing its distances to distances obtained from Cepheids and the Surface Brightness Fluctuation (SBF) method. We use the Cepheid and PNLF distances to 13 galaxies to show that the metallicity dependence of the PNLF cutoff is in excellent agreement with that predicted from theory, and that no additional systematic corrections are needed for either method. However, when we compare the Cepheid-calibrated PNLF distance scale with the Cepheid-calibrated SBF distance scale, we find a significant offset: although the relative distances of both methods are in excellent agreement, the PNLF method produces results that are systematically shorter by $\sim$ 15%. We trace this discrepancy back to the calibration galaxies and show how a small amount of internal reddening can lead to a very large systematic error. Finally, we demonstrate how the PNLF and Cepheid distances to NGC 4258 argue for a short distance to the Large Magellanic Cloud, and a Hubble Constant that is $\sim$ 8% larger than that derived by the *HST* Key Project.

13.1 Introduction

The brightest stars have been used as extragalactic distance indicators ever since the days of Edwin Hubble [1]. However, it was not until the early 1960's that it was appreciated that young planetary nebulae (PNe) also fall into the "brightest stars" category. In their early stages of evolution, planetary nebulae are just as luminous as their asymptotic giant branch (AGB) progenitors; the fact that most of their continuum emission emerges in the far ultraviolet, instead of the optical or near infrared, in no way affects their detectability. On the contrary, because most of the central star's flux comes out at energies shortward of 13.6 eV, the physics of photoionization guarantees that this energy is reprocessed into a series of optical, IR, and near-UV emission lines. In fact, $\sim$ 10% of the flux emitted by a young, planetary nebula comes out in a single emission line of doubly-ionized oxygen at 5007 Å. Thus, for cosmological purposes, a PN can be thought of as a cosmic apparatus which transforms continuum emission into monochromatic flux.

Although the idea of using PNe as standard candles was first presented in the early 1960's [2,3], it was not until the late 1970's that pioneering efforts in the

R. Ciardullo, Extragalactic Distances from Planetary Nebulae, Lect. Notes Phys. **635**, 243–263 (2003)
http://www.springerlink.com/

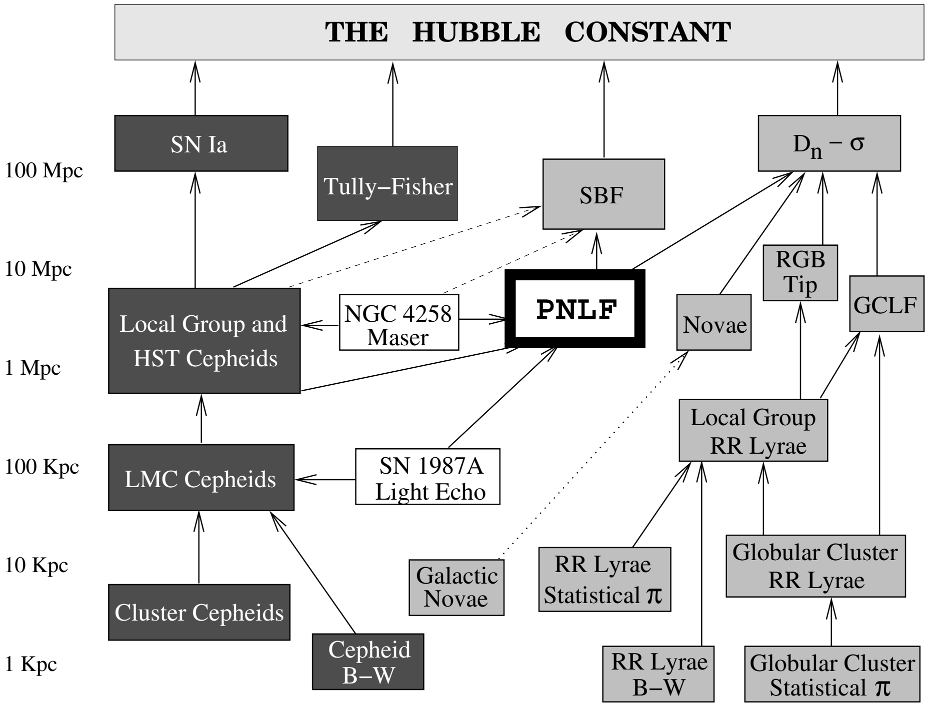

Fig. 13.1. The extragalactic distance ladder. The dark boxes show techniques useful in star-forming galaxies, the lightly-filled boxes give methods that work in Pop II systems, and the open boxes represent geometric distance determinations. Uncertain calibrations are noted as dashed lines. The PNLF is the only method that is equally effective in all the populations of the Local Supercluster

field were made. Ford and Jenner [4] had noticed that the visual magnitudes of the brightest planetary nebulae in M31, M32, NGC 185, and NGC 205 were the same to within ~ 0.5 mag. This suggested that bright planetary nebulae could be used as standard candles. Based on this premise, crude PN-based distances were obtained to M81 [4], NGC 300 [5], and even several Local Group dwarfs [6]. These distance estimates were not very persuasive, since at the time nothing was known about the systematics of bright planetary nebulae or their luminosity function. Moreover, it had long been known that Galactic PNe are definitely *not* standard candles [7–9]. (It is an irony of the subject that in the Milky Way, factor of two distance errors are the norm [10–14].) Thus, it was not until 1989 when the [O III] λ5007 PN luminosity function (PNLF) was modeled [15], and compared to the observed PNLFs of M31 [16], M81 [17], and the Leo I Group [18], that PNe became generally accepted as a distance indicator. Today, the [O III] λ5007 PNLF is one of the most important standard candles in extragalactic astronomy, and the only method that can be applied to all the large galaxies of the Local Supercluster, regardless of environment or Hubble type (see Fig. 13.1).

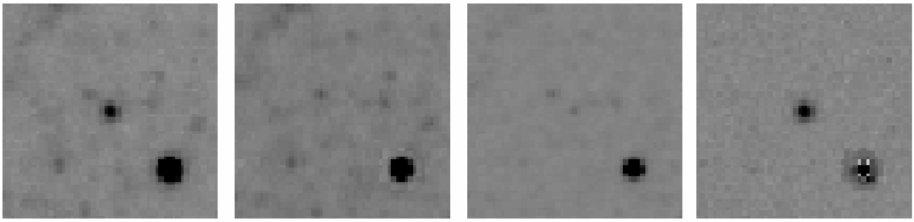

Fig. 13.2. The first three panels show images of a PN in NGC 2403 in [O III] λ5007, continuum λ5300, and Hα. The last column displays the [O III] on-band minus off-band difference image. The PN candidate is in the middle of the frame. All PNe in the top $\sim$ 1 mag of the PNLF are stellar, invisible in the continuum, and much brighter in [O III] λ5007 than Hα

13.2 Planetary Nebula Identifications

PNLF observations begin with the selection of a narrow-band filter. Ideally, this filter should be centered at 5007 Å at the redshift of the target galaxy and be 25 Å to 50 Å wide. Narrower filters may miss objects that are redshifted out of the filter's bandpass by the galaxy's internal velocity dispersion, while broader filters admit too much continuum light and invite contamination by [O III] λ4959. One subtlety of the process is that the characteristics of the filter at the telescope will not be the same as those in the laboratory. The central wavelength of an interference filter typically shifts $\sim$ 0.2 Å to the blue for every 1° C drop in temperature. In addition, fast telescope optics will lower the filter's peak transmission, shift its central wavelength to the blue, and drastically broaden its bandpass [19]. The observer must consider these factors when planning an observation, since without an accurate knowledge of the filter transmission curve, precise PN photometry is not possible.

PN observations in early-type galaxies are extremely simple. One images the galaxy through the narrow on-band filter, and then takes a similar image through a broader, off-band filter. The two frames are then compared, either by "blinking" the on-band image against the off-band image, or by creating an on-band minus off-band "difference" frame. Point sources which appear on the on-band frame, but are completely invisible on the offband frame, are planetary nebula candidates (see Fig. 13.2). In this era of wide-field mosaic CCD cameras, V filters are often used in place of true off-band filters. This works for most extragalactic programs, but is not ideal. Since the V-band includes the 5007 Å emission line, its use as an "off-band" may cause bright PNe to appear (faintly) in the continuum. Photometric techniques which use the difference image will therefore be compromised.

Since virtually every [O III] λ5007 source in an elliptical or lenticular galaxy is a planetary nebula, PNLF measurements in these systems are straightforward. However, in spiral and irregular galaxies, this is not the case. H II regions and supernova remnants are also strong [O III] λ5007 emitters, and in late-type systems, these objects can numerically overwhelm the planetaries. Fortunately,

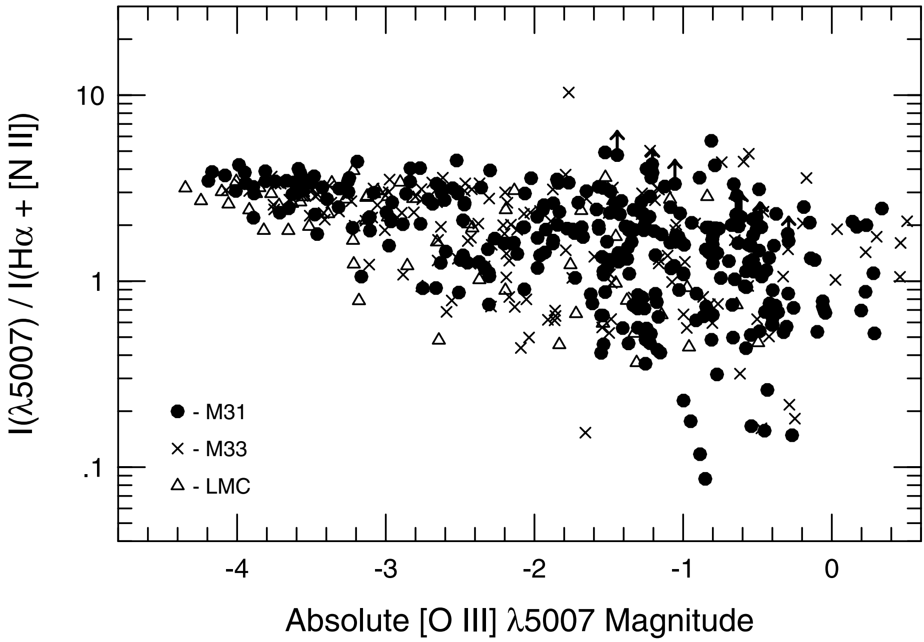

Fig. 13.3. The [O III] λ5007 to Hα+[N II] line ratio for PNe in the bulge of M31 [16], the disk of M33 [22], and the Large Magellanic Cloud [23–26]. This line ratio is useful for discriminating bright PNe from compact H II regions

most H II regions are resolvable (at least in galaxies closer than $\sim$ 10 Mpc), whereas extragalactic PNe, which are always less than 1 pc in radius [20], are stellar. Thus, any object that is not a point source can immediately be eliminated from the sample. To remove the remaining contaminants, one can use Hα as a discriminant. Planetary nebulae inhabit a distinctive region of [O III] λ5007-Hα emission-line space. As illustrated in Fig. 13.3, objects in the top magnitude of the PNLF all have λ5007 to Hα+[N II] line ratios greater than $\sim$ 2. This is in contrast to H II regions, which typically have ratios less than one [21]. This difference in excitation is an effective diagnostic for removing whatever compact H II regions remain in the sample.

There are two other sources of contamination which may occur in deep planetary nebula surveys. The first is background galaxies. At z = 3.12, Lyα is redshifted in the bandpass of the [O III] λ5007 filter, and at fluxes below $\sim 10^{-16}$ ergs cm^{-2} s^{-1}, unresolved and marginally resolved galaxies with extremely strong Lyα emission (equivalent widths $\gtrsim$ 300 Å in the observers frame) do exist [27–29]. Fortunately, the density of these extraordinary objects is relatively low, $\sim$ 1 arcmin^{-2} per unit redshift interval brighter than 5×10^{-17} ergs cm^{-2} s^{-1} [30]. Thus while an occasional high-redshift interloper may be found within the body of a galaxy [31], these objects are unlikely to distort the shape of the luminosity function.

The second source of confusion is specific to the Virgo Cluster. Between 10% and 20% of the stellar mass of rich clusters lies outside of any galaxy in intergalactic space [32–34]. PN surveys within these systems will therefore be contaminated by intracluster objects. In clusters such as Fornax, where the line-of-sight thickness is small [35,36], the effect of intracluster planetaries on the target galaxy's PNLF is minimal. However, the Virgo Cluster's depth is substantial [37–40], so surveys in this direction will contain a significant number of foreground sources. These intracluster objects can distort the galactic PNLF and possibly produce a biased distance estimate. The best way to minimize the effect is to limit PN surveys to the inner regions of galaxies (where the ratio of galactic to intracluster light is high), or statistically subtract the contribution of intracluster objects [41].

13.3 Deriving Distances

Once the PNe are found, the next step is to measure their brightnesses and define a statistically complete sample. The first step is easy. A significant advantage of the PNLF method is that it does not require complex crowded-field photometric algorithms. Raw instrumental magnitudes can be derived using simple aperture photometry or point-spread-function fitting procedures, and then turned into monochromatic [O III] λ5007 fluxes using the techniques described in [42]. These fluxes are usually quoted in terms of magnitudes via

$$m_{5007} = -2.5 \log F_{5007} - 13.74 \tag{13.1}$$

The zero point of this system is not completely arbitrary. In this "standard" system, a PN's λ5007 magnitude is roughly equal to the magnitude it would have if viewed through the broadband V filter [15]. Bright PNe in M31 have $m_{5007} \sim 20$, while the brightest planetaries in Virgo have $m_{5007} \sim 26.5$.

The determination of statistically complete samples can be more time consuming. Although the onset of incompleteness can be found via the "traditional" method of adding artificial stars to frames and measuring the recovery fraction, there is a short cut. Experiments have shown that PN counts are not affected by incompleteness until the recorded signal-to-noise drops below a threshold value of ~ 10 [43,44]. Since extragalactic PNe are faint, this means that the probability of PN detection is a function of two parameters: the instrumental magnitude of the planetary, and the brightness of the underlying background. In early-type systems, where the galactic background is smooth and well-behaved, the creation of a statistical sample is therefore straightforward. One chooses an isophote and uses the signal-to-noise threshold to calculate the completeness limit (see [17,18]). In spiral and irregular galaxies, where the underlying background is irregular and complex, the process is more empirical: one selects the brightest (most uncertain) background in the sample, and uses the signal-to-noise each PN would have if it were projected on that background [45]. In either case, the limiting magnitude for completeness need not be precise. The PNLF method depends far more on the brightest objects in the sample than the dimmest; small errors at the faint end of the luminosity function have little effect on the final derived distance.

Once a statistical sample of planetaries has been defined, PNLF distances are obtained by fitting the observed luminosity function to an empirical law. For simplicity, Ciardullo *et al.* [16] have fit the bright-end cutoff with the function

$$N(M) \propto e^{0.307M}\{1 - e^{3(M^* - M)}\} \tag{13.2}$$

though other forms of the relation are possible [46]. In the above equation, the key parameter is M^*, the absolute magnitude of the brightest possible planetary nebula. Despite some efforts at Galactic calibrations [47,46], the PNLF remains a secondary standard candle. The original value for the zero point, $M^* = -4.48$, was based on an M31 infrared Cepheid distance of 710 kpc [48] and a foreground extinction of $E(B-V) = 0.11$ [49]. Since then, M31's distance has increased [50], its reddening has decreased [51], and, most importantly, the Cepheid distances to 12 additional galaxies have been included in the calibration [52]. Somewhat fortuitously, the current value of M^* is only 0.01 mag fainter than the original value, $M^* = -4.47$ [52].

Before proceeding further, it is important to note that equation (13.2) only seeks to model the top ~ 1 mag of the PN luminosity function. At fainter magnitudes, large population-dependent differences exist. For example, in M31's bulge the PNLF monotonically increases according to the exponent in the empirical law [16,53]. However the luminosity functions of the Small Magellanic Cloud and M33 are not so well-behaved: compared to M31, these galaxies are a factor of ~ 2 deficient in PNe in the magnitude range $-2 < M_{5007} < +2$ [54,22]. Fortunately, this behavior (which depends on the system's star-formation history and is easily explained in terms of stellar evolution and photoionization theory) does not affect the bright end of the PNLF. It is therefore irrelevant for PNLF distance determinations.

Finally, before any distance can be derived, one must consider the effect of extinction on the distance indicator. For PNLF observations, the ratio of total to differential extinction is non-negligible ($A_{5007} = 3.5E(B-V)$ [55]), so this issue has some importance. There are two sources to consider: foreground extinction from the Milky Way, and internal extinction from the program galaxy. The former quantity is readily obtainable from reddening maps derived from H I measurements and galaxy counts [56] and/or from the DIRBE and IRAS satellite experiments [51]. However, the latter contribution to the total extinction is more problematic. In the Galaxy, the scale height of PNe is significantly larger than that of the dust [57]. If the same is true in other galaxies, then we would expect the bright end of the PNLF to always be dominated by objects in front of the dust layer. This conclusion seems to be supported by observational data [45,52] and numerical models [45], both of which suggest that the internal extinction which affects a galaxy's PN population is $\lesssim 0.05$ mag. We will, however, revisit this issue in Sect. 13.5.

13.4 Why the PNLF Works

The effectiveness of the PNLF technique has surprised many people. After all, a PN's [O III] $\lambda 5007$ flux is directly proportional to the luminosity of its central star, and this luminosity, in turn, is extremely sensitive to the central star's mass. Since the distribution of PN central star masses depends on stellar population via the initial mass-final mass relation [58], one would think that the PNLF cutoff would be population dependent.

Fortunately, this does not appear to be the case, and, in retrospect, the invariance is not difficult to explain. First, consider the question of metallicity. The [O III] $\lambda 5007$ flux of a bright planetary is proportional to its oxygen abundance, but since $\gtrsim 10\%$ of the central star's flux comes out in this one line, the ion is also the nebula's primary coolant. Consequently, if the abundance of oxygen is decreased, the nebula's electron temperature will increase, the number of collisional excitations per ion will increase, and the amount of emission per ion will increase. The result is that the flux in [O III] $\lambda 5007$ depends only on the square root of the nebula's oxygen abundance [15].

Meanwhile, the PN's core reacts to metallicity in the opposite manner. According to models of AGB and post-AGB evolution [59,60] if the metal abundance of a star is decreased, then the bound-free opacity within the star will decrease, and the emergent UV flux will increase. This will cause additional energy to be deposited into the nebula, and increase the amount of [O III] $\lambda 5007$ emission. Since this effect is small, and works in the opposite direction as the nebular dependence, the overall result is that the bright-end cutoff of the PNLF should be almost independent of metallicity.

A more sophisticated analysis by Dopita, Jacoby, & Vassiliadis [61] confirms this behavior. According to their models, the dependence of M^* on metallicity is weak and non-monotonic; a quadratic fit to the relation yields

$$\Delta M^* = 0.928[\mathrm{O/H}]^2 + 0.225[\mathrm{O/H}] + 0.014 \qquad (13.3)$$

where [O/H] is the system's logarithmic oxygen abundance referenced to the solar value of $12 + \log(\mathrm{O/H}) = 8.87$ [62]. Inspection of equation (13.3) reveals that M^* is brightest when the population's metallicity is near solar. In super-metal rich systems M^* fades, but since all metal-rich galaxies contain substantial populations of metal-poor stars, this part of the metallicity dependence should not be observed. Moreover, although M^* also fades in metal-poor systems, the change is gradual, so as long as the oxygen abundance of the host galaxy is $12 + \log(\mathrm{O/H}) \gtrsim 8.3$ (*i.e.,* greater than two-thirds that of the LMC), the effect on distance determinations should be less than 10%. This weak dependence on metallicity is one reason why PNLF distances are so robust.

The reaction of the PNLF cutoff to population age is slightly less obvious, but no more complicated. Post-AGB evolutionary models [63,64] predict that the maximum luminosity and temperature achieved by a PN's central star is highly dependent on its core mass, with (very roughly) $L \propto M^3$ and $T_{\max} \propto M^{2.5}$ for intermediate-mass hydrogen burning models. Consequently, high-mass central

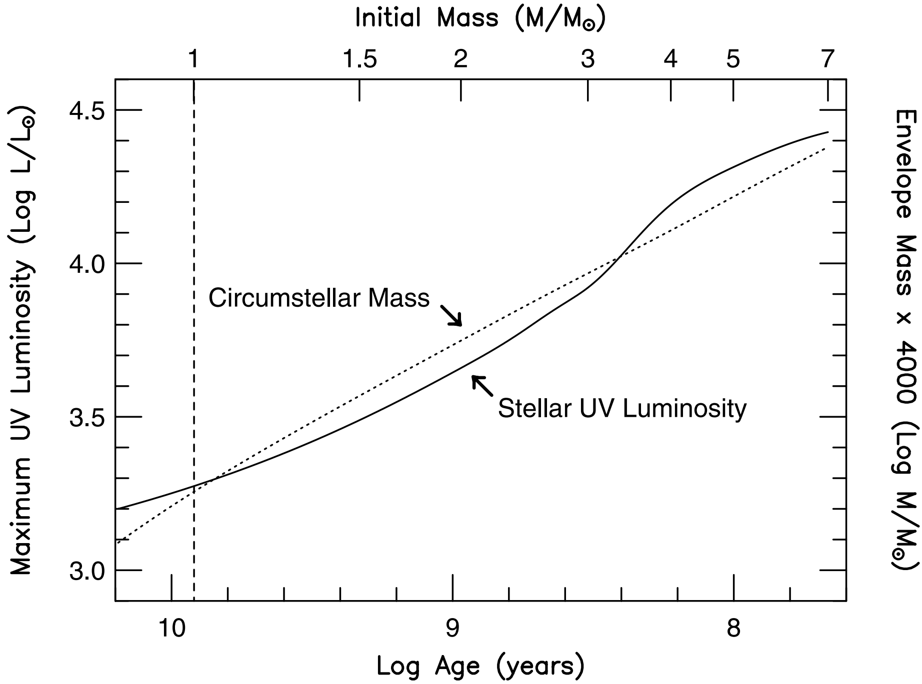

Fig. 13.4. A comparison of the maximum amount of ionizing radiation emitted by PN central stars against the mass of the stars' envelopes. The curves assume that the central stars are hydrogen burners [64] and use the Wiedemann initial-mass final-mass relation [58] with minimal RGB mass loss. The approximate lower-mass limit for PN progenitors is noted by a dotted line [66]; the conversion between initial mass and age comes from Iben and Laughlin [67]. The similarity of the relations implies that extinction will act to suppress the [O III] $\lambda5007$ emission from high core-mass planetaries

stars should be extremely bright in the UV and their nebulae should be exceptionally luminous in [O III] $\lambda5007$. Since the mass of a central star is proportional to the mass of its progenitor (through the initial-mass final-mass relation [58]), this line of reasoning seems to imply the existence of some extremely luminous Population I planetaries. In fact, these over-luminous objects do exist. In the Magellanic Clouds, 9 out of the 74 planetaries with well-calibrated spectrophotometry [23,24,26] have intrinsic [O III] $\lambda5007$ magnitudes brighter than M^*. Conversely, in the central regions of M31, where the bulge population dominates, only one out of 12 spectrophotometrically observed PNe is superluminous in [O III] [65]. However, *in every case,* these over-luminous objects are heavily extincted by circumstellar material, so that no PN has an observed [O III] $\lambda5007$ flux brighter than M^*.

In order to understand this phenomenon, one needs to consider the ratio of a nebula's input energy to its own circumstellar extinction. The former quantity is

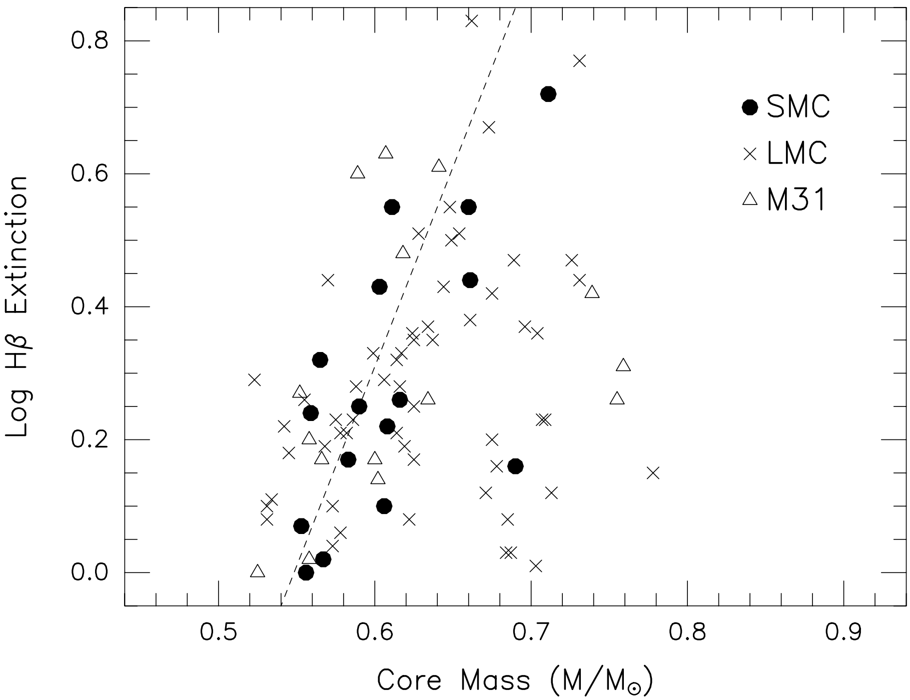

Fig. 13.5. The correlation between circumstellar extinction and central star mass for planetary nebulae in the Magellanic Clouds and M31. The extinction values are based on the Balmer decrement; the core masses have been derived via comparisons with hydrogen-burning evolutionary tracks. The slope of the relation is 5.7 ± 0.7 for the SMC, 6.3 ± 1.3 for the LMC, and 8.5 ± 1.6 for M31

dictated by the central star's flux shortward of 912 Å, which via the initial-mass final-mass relation, depends sensitively on the mass of the star's progenitor. The latter value is proportional to the amount of mass lost during the star's AGB phase, which is also set by the progenitor mass. Figure 13.4 compares these two values at the time when the central star's UV flux is greatest. Remarkably, the two functions are extremely similar throughout the entire range of progenitor masses. If the efficiency of circumstellar extinction is the same for all planetaries, then the figure implies that M^* will be independent of population age to within ~ 0.2 mag. Since self-extinction is probably more efficient around high-mass cores (since their faster evolutionary timescales give the material less time to disperse), this simple analysis suggests that high-mass PNe which are intrinsically more luminous than M^* will always be extincted below the empirical PNLF cutoff.

Observational support for this scenario is shown in Fig. 13.5, which plots the relation between PN core mass and circumstellar extinction for [O III]-bright planetaries in the LMC, the SMC, and M31 [68]. The core masses of Fig. 13.5 have been derived by placing the central stars on the HR diagram (via photoionization modeling of the PNe's emission lines), and comparing their positions to the evolutionary tracks of hydrogen-burning post-AGB stars [64]; the plotted extinction estimates have been inferred from the PNe's Balmer line ratios. Since the derived temperatures and luminosities of central stars have some uncertainty, and a fraction of PNe will be burning helium instead hydrogen, a good amount of scatter in the diagram is expected. Nevertheless, there is a statistically significant correlation between core mass and circumstellar extinction for the PN populations of all three galaxies. The best-fitting slope of ~ 6 mag/$M_{\odot}$ more than compensates for the increased UV luminosity associated with the high-mass cores. In fact, when combined with the initial-mass final-mass relation [58], the steep slope of Fig. 13.5 predicts that M^* should vary by less than ~ 0.1 mag in all populations older than 0.4 Gyr [68]. In younger populations, M^* may fade, but since all galaxies contain at least some stars older than ~ 0.4 Gyr, this behavior should not be observable. The value of M^* in a star-forming galaxy should therefore be the same as that of an old stellar population.

13.5 Tests of the Technique

In the past decade, the PNLF has been subjected to a number of rigorous tests. In general, these tests fall into four categories.

13.5.1 Internal Tests within Galaxies

The first and perhaps simplest test applied to the PNLF involves taking advantage of population differences within galaxies. Spiral galaxies have significant metallicity gradients [69], and the stellar population of a spiral's bulge is certainly different from that of its disk and halo. Population differences exist in elliptical galaxies as well, as their radial color gradients attest [70]. If one can measure the distance to a sample of planetaries projected close to a galaxy's nucleus, and then do the same for PN samples projected at intermediate and large galactocentric radii, one can determine just how sensitive the PNLF is to changes in stellar population.

Four galaxies now have large enough PN samples for this test: two Sb spirals (M31 [53] and M81 [71]), one large elliptical (NGC 4494 [72]), and one blue, interacting elliptical (NGC 5128 [44]). The data for M31 are shown in Fig. 13.6. No significant change in the PNLF cutoff has been observed in any of these objects. Given the diversity of stellar populations sampled, this result, in itself, is impressive proof of the robustness of the method.

13.5.2 Internal Tests within Clusters

A second internal test of the PNLF uses multiple galaxies within a common cluster. Galaxy groups are typically ~ 1 Mpc in diameter. PNLF distances to individual cluster members should therefore be consistent to within this value. Moreover, if the technique really is free of systematic errors, the measured

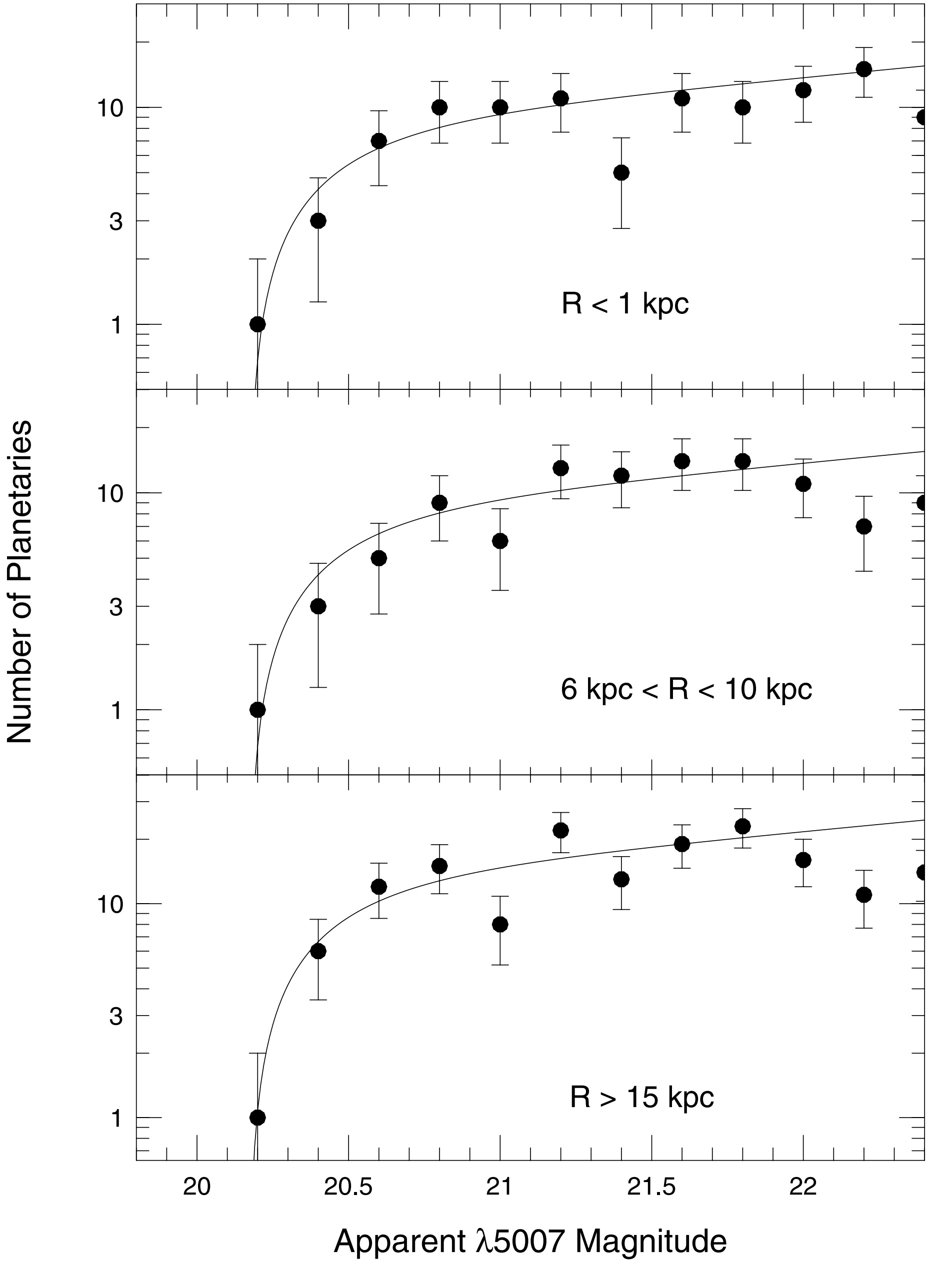

Fig. 13.6. The observed planetary nebula luminosity functions for samples of M31 PNe projected at three different galactocentric radii. The curves show the best-fitting empirical law. The derived PNLF distances are consisted to within ~ 0.05 mag. The turnover in the luminosity function past $m_{5007} \gtrsim 22$ in the intermediate and large-radii samples is real, and indicates the presence of relatively massive PN central stars

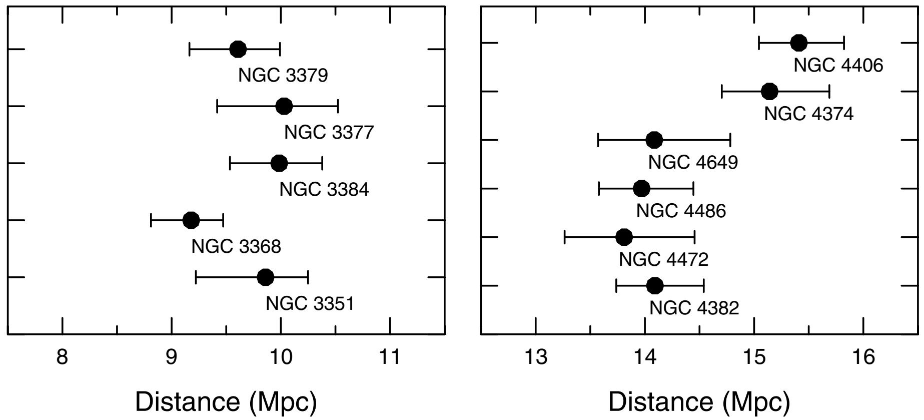

Fig. 13.7. PNLF distance measurements to the Leo I Group (*left*) and the Virgo Cluster (*right*). The Leo I galaxies possess a range of Hubble types from SBb to E0; the Virgo galaxies are all ellipticals or lenticulars, but range in color from $1.28 < (U-V) < 1.64$. The PNLF measurements in Leo I place all the galaxies within ~ 1 Mpc of each other, while in Virgo, the method easily resolves the background galaxies NGC 4374 and 4406 from the main body of the cluster

distances should be uncorrelated with any galactic property, such as color, luminosity, metallicity, or Hubble type.

To date six galaxy clusters have multiple PNLF measurements: the M81 Group (M81 and NGC 2403 [17,45]), the NGC 1023 Group (NGC 891 and 1023 [73]), the NGC 5128 Group (NGC 5102, 5128, and 5253 [74,44,75]), the Fornax Cluster (NGC 1316, 1399, and 1404 [35]), the Leo I Group (NGC 3351, 3368, 3377, 3379, and 3384 [52,45,18]), and the Virgo Cluster (NGC 4374, 4382, 4406, 4472, 4486, and 4649 [37]). In each system, the observed galaxies have a range of color, absolute magnitude, and Hubble type. In none of the clusters is there any hint of a systematic trend. Indeed, as Fig. 13.7 indicates, PNLF measurements in Virgo easily resolve the M84/M86 Group, which is falling into the main body of Virgo from behind [76].

13.5.3 Comparisons with Cepheid Distances

Perhaps the most interesting test one can perform for any distance indicator is to compare its results to those of other methods. Such tests are crucial to the scientific method. While consistency checks, such as those described above, provide important information on the systematic behavior of a standard candle, external comparisons are the only way to assess the total uncertainty associated with a given rung of the distance ladder.

Figure 13.8 compares the PNLF distances of 13 galaxies (derived using the foreground extinction estimates from DIRBE/IRAS [51]) with the final Cepheid distances produced by the *HST Key Project* [50]. Neither set of numbers has been corrected for the effects of metallicity. Since the absolute magnitude of the

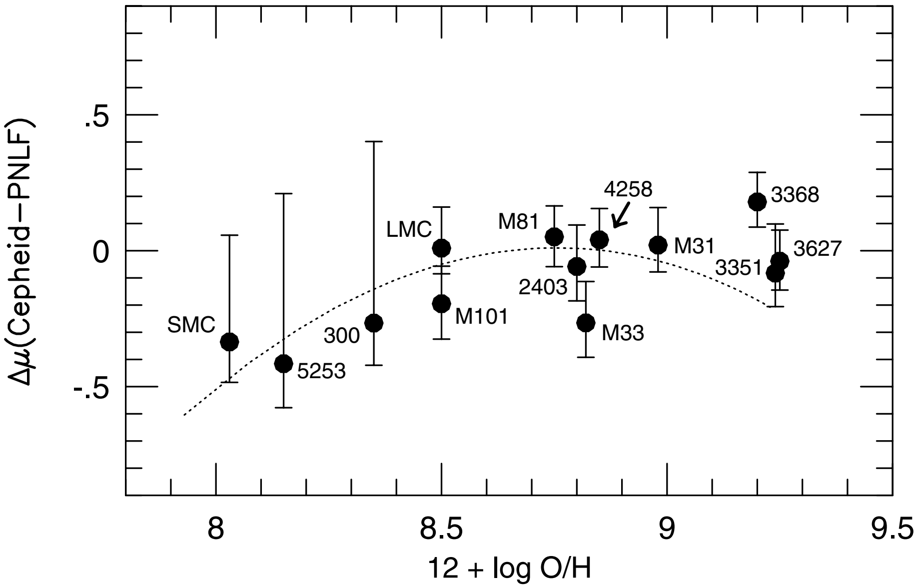

Fig. 13.8. A comparison of the PNLF and Cepheid distance moduli as function of galactic oxygen abundance, as estimated from the systems' H II regions [77]. No metallicity correction has been applied to either distance indicator. The error bars represent the formal uncertainties of the methods added in quadrature; small galaxies with few PNe have generally larger errors. The curve shows the expected reaction of the PNLF to metallicity [61]. Note that metal-rich galaxies should not follow this relation, since these objects always contain enough low metallicity stars to populate the PNLF's bright-end cutoff. The agreement between the two distance estimators is excellent, and the scatter is consistent with the internal errors of the methods

PNLF cutoff, M^*, is based on these Cepheid distances, the weighted mean of the distribution must, by definition, be zero. However, the residuals about this mean, and the systematic trends in the data, are valid indicators of the accuracy of the measurements.

As Fig. 13.8 illustrates, the scatter between the Cepheid distances and the PNLF distances is impressively small. Except for the most metal-poor systems, the residuals are perfectly consistent with the internal uncertainties of the methods. Moreover, the systematic shift seen at low-metallicity is exactly that predicted by PNLF theory [61]. If M^* were to be corrected using equation (13.3), the systematic error would completely disappear. This excellent agreement strongly suggests that neither the PNLF nor the Cepheid measurements need further metallicity corrections.

13.5.4 Comparisons with Surface Brightness Fluctuations

Another instructive comparison involves distances derived from the measurement of Surface Brightness Fluctuations (SBF) [36]. SBF distances have a precision

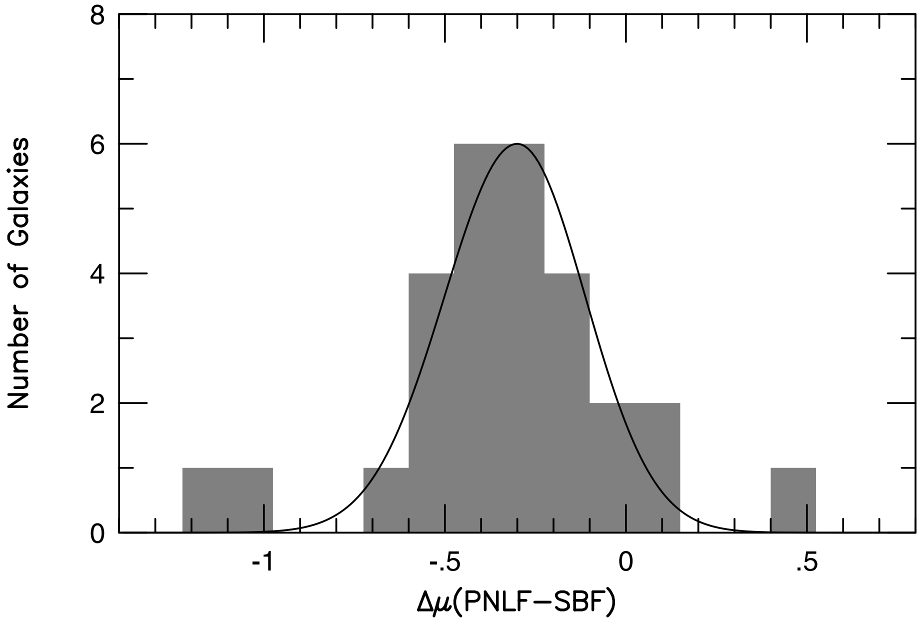

Fig. 13.9. A histogram of the difference between the PNLF and SBF distance moduli for 28 galaxies measured by both methods. The two worst outliers are the edge-on galaxies NGC 4565 ($\Delta\mu = -0.80$) and NGC 891 ($\Delta\mu = +0.71$). NGC 4278 is also an outlier ($\Delta\mu = -0.70$). The curve represents the expected dispersion of the data. The figure demonstrates that the absolute scales of the two techniques are discrepant, but the internal and external errors of the methods agree

comparable to that of the PNLF, but the technique can only be applied to smooth stellar populations, such as those found in elliptical and lenticular galaxies. Like the PNLF, SBF distances rely on Cepheid measurements for their calibration; consequently, a comparison of the two indicators gives a true measure of the external error associated with climbing a rung of the distance ladder.

To date, 28 galaxies have been measured with both the PNLF and SBF methods. A histogram of the distance residuals is shown in Fig. 13.9. There are three important features to note.

The first interesting property displayed in the figure is the presence of three obvious outliers. The two worst offenders are NGC 4565 (-0.8 mag from the mean) and NGC 891 ($+0.7$ mag from the mean). Both are edge-on spirals – the only two edge-on spirals in the sample. Clearly one (or both) methods have trouble measuring the distances to such objects. Given the sensitivity of SBF measurements to color gradients, it is likely that the problem with these galaxies lies there, but an error in the PNLF technique cannot be ruled out.

The second important feature of Fig. 13.9 involves the scatter between the PNLF and SBF distance estimates. The curve plotted in the figure is not a fit to the data: it is instead the *expected* scatter in the measurements, as determined

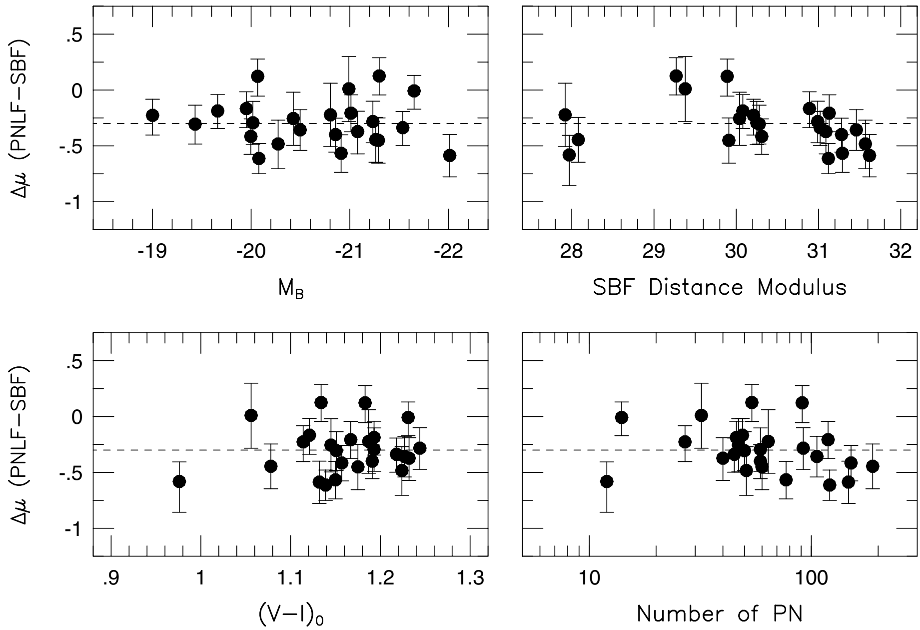

Fig. 13.10. The difference between SBF and PNLF distance moduli plotted against galactic absolute magnitude, distance, color, and number of PNe in the statistical sample. The three discrepant galaxies, NGC 891, 4565, and 4278, have not been plotted. The correlation with SBF distance modulus is marginally significant ($P \sim 0.1$), due to the low values of the five most distant objects; if these galaxies are removed from the sample, the significance of the correlation disappears. No other correlations exist in any of the panels

by propagating the uncertainties associated with the PNLF distances, the SBF distances, and Galactic reddening. It is obvious that the derived curve is in excellent agreement with the data. This proves that the quoted uncertainties in the methods are reasonable. It also leaves little room for additional random errors associated with measurements.

The latter conclusion is confirmed in Fig. 13.10. If either method were significantly affected by population age or metallicity, or if the PNLF fitting-technique were incorrect, then the PNLF-SBF distance residuals would correlate with galactic absolute magnitude, color, or PN population. No such trend exists. In fact, the only possible correlation present in the figure is with distance: if one *only* considers galaxies with $(m - M)_{\rm SBF} > 30.6$, then the residuals do correlate with distance at the 95% confidence level. Such behavior might be expected if the PN samples found in distant galaxies were contaminated by background emission-line galaxies (or in the case of rich clusters, foreground intracluster stars). However, if the five most distant objects are deleted from the sample, the correlation goes away, proving that, in terms of relative distances, the PNLF and SBF techniques are in excellent agreement.

Interestingly, the same cannot be said for the methods' absolute distances. The PNLF zero point comes from planetary nebula observations in the 13 Cepheid galaxies displayed in Fig. 13.8; the formal uncertainty in M^* is ~ 0.05 mag. Similarly, the SBF zero point is based on fluctuation measurements in the bulges of six Cepheid spirals; its estimated uncertainty is ~ 0.04 mag. If both calibrations were accurate, then the mean of the PNLF-SBF distance residuals would be 0.0 ± 0.07. It is not: as Figs. 13.9 and 13.10 indicate, SBF distances are, on average 0.30 ± 0.05 mag larger than PNLF distances. Even if the five most distant galaxies are excluded, the remaining ~ 0.26 mag offset is more than $3\,\sigma$ larger than expected. Clearly, there is an important source of error that is not being considered by one (or both) techniques.

The most likely explanation for the discrepancy involves internal extinction in the Cepheid calibration galaxies. To calibrate an extragalactic standard candle with Cepheids, one needs to measure the apparent brightness of the candle, m, and assume some value for the intervening extinction. Hence

$$M = m - \mu_{Cep} - R_\lambda\, E(B-V) \tag{13.4}$$

where M is the derived absolute magnitude of the object and R_λ is the ratio of total to differential reddening at the wavelength of interest. For most methods (including the PNLF), if the reddening to a galaxy is underestimated, then the brightness of the standard candle is underestimated, and the distance scale implied by the observations is underestimated. However, in the case of the I-band SBF technique, the standard candle, $\bar{M}_I$ has a strong color dependence, with $\bar{M}_I = C + 4.5(V-I)_0$ [36]. Consequently, the zero-point of the system, C, is defined through

$$C = \bar{m}_I - \mu_{Cep} - 4.5(V-I)_{\rm obs} + (4.5\,R_V - 5.5\,R_I)\,E(B-V) \tag{13.5}$$

Because $R_V > R_I$, an underestimate of reddening results in an overestimate of the brightness of the standard candle, and a distance scale that is too large. Since the PNLF and SBF methods react in opposite directions to reddening, even a small amount of internal extinction in the bulges of the calibrating spirals can lead to a large discrepancy between the systems in the exact sense that is seen. Specifically, if only the SBF measurements are affected, then the technique's distance scale will be too large by $4.2\,\sigma_{E(B-V)}$ [55]. Moreover, if both techniques are affected, then $\sigma_{\Delta\mu} = 7.7\,\sigma_{E(B-V)}$. With such a large coefficient, it would take only a small amount of internal reddening, $E(B-V) \sim 0.04$ mag to explain the discrepancy seen in the figures.

If internal extinction really is responsible for the offset displayed in Fig. 13.9, then the zero points of both systems must be adjusted. These corrections will propagate all the way up the distance ladder. For example, according to the *HST Key Project,* the SBF-based Hubble Constant is 69 ± 4 (random) ± 6 (systematic) km s^{-1} Mpc^{-1} [50]. However, if we assume that the calibration galaxies are internally reddened by $E(B-V) \sim 0.04$, then the zero point of the SBF system fades by 0.17 mag, and the SBF Hubble Constant increases to 75 km s^{-1} Mpc^{-1}. This one correction is as large as the technique's entire systematic error budget.

Such an error could not have been found without the cross-check provided by PNLF measurements.

13.5.5 Comparisons with Measurements outside the Distance Ladder

No technique is perfectly calibrated, so distance measurements based on secondary standard candles, such as the PNLF, cannot avoid a component of systematic uncertainty. However, there are two galaxies in the local universe with distance estimates that do not rely on the distance ladder. The first is NGC 4258, which has a resolved disk of cold gas orbiting its central black hole. The proper motions and radial accelerations of water masers associated with this gas have been detected and measured: the result is an unambiguous geometric distance to the galaxy of 7.2 ± 0.3 Mpc [78]. The second benchmark comes from the light echo of SN 1987A in the Large Magellanic Cloud. Although the geometry of the light echo is still somewhat controversial, the most detailed and complete analysis of the object to date gives a distance of $D < 47.2 \pm 0.1$ kpc [79]. In Table 13.1 we compare these values with the distances determined from the PNLF [52] and from the measurements of Cepheids [50].

According to the table, the Cepheid and PNLF methods both overestimate the distance to NGC 4258 by ~ 0.14 mag, *i.e.,* by $\sim 1.3\,\sigma$ and $1.0\,\sigma$, respectively. In the absence of some systematic error affecting both methods, the probability of this happening is $\lesssim 5\%$. On the other hand, there is no disagreement concerning NGC 4258's distance *relative to that of the LMC:* the Cepheids, PNLF, and geometric techniques all agree to within $\pm 2\%$! Such a small error is probably fortuitous, but it does suggest the presence of a systematic error in the entire extragalactic distance scale.

In fact, the *HST Key Project* distances are all based on an LMC distance modulus of $(m - M)_0 = 18.50$ [50], and, via the data of Fig. 13.8, the PNLF scale is tied to that of the Cepheids. If the zero point of the Cepheid scale were shifted to $(m - M)_0 = 18.37$, then all the measurements would be in agreement. This consistency supports a shorter distance to the LMC, and argues for a 7% increase in the *HST* Key Project Hubble Constant to 77 km s^{-1} Mpc^{-1}.

Table 13.1. Benchmark Galaxy Distances

Method	LMC	NGC 4258	$\Delta\mu$ (mag)
Geometry	$< 18.37 \pm 0.04$	29.29 ± 0.09	10.92 ± 0.10
Cepheids	18.50	29.44 ± 0.07	10.94 ± 0.07
PNLF	18.47 ± 0.11	29.43 ± 0.09	10.96 ± 0.14

13.6 Future Directions

The planetary nebula luminosity function is an excellent standard candle for measuring extragalactic distances within $\sim$ 20 Mpc. PNLF measurements are precise, and, in terms of telescope time, much more efficient than variable star monitoring or OB star spectroscopy. However, the technique cannot be extended much farther. Extragalactic PNe are point sources and their photometry is sky noise limited. Hence to maintain a constant signal-to-noise ratio, exposure times must grow as the fourth power of distance. Since PNLF measurements in Virgo already require $\sim$ 4 hr of 4-m class telescope time in $\sim 1''$ seeing, observations at distances larger than $\sim$ 25 Mpc are prohibitively expensive. Improvements in seeing, telescope aperture, and instrumentation will help slightly, but the PNLF will never be competitive with techniques such as Surface Brightness Fluctuations or the Tully-Fisher relation.

On the other hand, PNLF observations are unlikely to disappear. There will always be some objects, such as NGC 4258, for which an additional, high-precision distance measurement is useful. However, most future PNLF studies are likely to be performed as by-products of other investigations. Planetary nebulae are powerful tools for the study of astrophysics and cosmology. In addition to being excellent standard candles, PNe are useful probes of stellar population, unique tracers of chemical evolution, and excellent test particles for stellar kinematics and dark matter studies. Moreover, photometry and spectroscopy of planetary nebulae is the best and perhaps only way to study the line-of-sight distribution and kinematics of intracluster stars. Our study of the evolutionary state of nearby galaxy clusters has always been hampered by the limited number of test particles available for study [80]. However, these systems have plenty of planetary nebulae – in the core of Virgo alone, $\gtrsim 15,000$ intracluster planetaries are within reach of today's telescopes. Thus wide-field [O III] λ5007 imaging and follow-up spectroscopy in clusters such as Virgo and Fornax will be common in the coming decade.

All these programs, from the study of chemical evolution to the analysis of cluster kinematics, begin with the identification and photometric measurement of planetary nebulae. PNLF distances will therefore continue to be measured in the local universe.

Acknowledgements

I would like to thank G. Jacoby, J. Feldmeier, and P. Durrell for their comments during the preparation of this paper. This work made use of the NASA Extragalactic Database and was supported in part by NSF grant AST 00-71238.

References

1. E. Hubble: Ap. J. **84**, 270 (1936)
2. K.G. Henize, B.E. Westerlund: Ap. J. **137**, 747 (1963)

3. P.W. Hodge: *Galaxies and Cosmology.* (McGraw-Hill, New York 1966)
4. H.C. Ford, D.C. Jenner: Bull. A.A.S. **10**, 665 (1978)
5. D.G. Lawrie, J.A. Graham: Bull. A.A.S. **15**, 907 (1983)
6. G.H. Jacoby, M.P. Lesser: A. J. **86**, 185 (1981)
7. L. Berman: Lick Obs. Bull. **18,** 57 (1937)
8. R. Minkowski: Pub. Obs. Univ. Mich. **10,** 25 (1951)
9. I.S. Shkolvski: Astron. Zh. **33,** 222 (1956)
10. J.H. Cahn, J.B. Kaler, L. Stanghellini: Astr. Ap. Suppl. **94**, 399 (1992)
11. G.C. Van de Steene, A.A. Zijlstra: Astr. Ap. **293**, 541 (1995)
12. C.Y. Zhang: Ap. J. Suppl. **98**, 659 (1995)
13. T. Bensby, I. Lundström: Astr. Ap. **374**, 599 (2001)
14. J.P. Phillips: Ap. J. Suppl. **139**, 199 (2002)
15. G.H. Jacoby: Ap. J. **339**, 39 (1989)
16. R. Ciardullo, G.H. Jacoby, H.C. Ford, J.D. Neill: Ap. J. **339**, 53 (1989)
17. G.H. Jacoby, R. Ciardullo, H.C. Ford, J. Booth: Ap. J. **344**, 704 (1989)
18. R. Ciardullo, G.H. Jacoby, H.C. Ford: Ap. J. **344**, 715 (1989)
19. R.H. Eather, D.L. Reasoner: Appl. Optics **8**, 227 (1969)
20. A. Acker, F. Ochsenbein, B. Stenholm, R. Tylenda, J. Marcout, C. Schohn: *Strasbourg-ESO Catalogue of Galactic Planetary Nebulae.* (European Southern Observatory, Munich, 1992)
21. P.A. Shaver, R.X. McGee, L.M. Newton, A.C. Danks, S.R. Pottasch: M.N.R.A.S. **204**, 53 (1983)
22. P.R. Durrell, R. Ciardullo, M.B. Laychak, G.H. Jacoby, J.J. Feldmeier: Bull. A.A.S. in press (2003)
23. S.J. Meatheringham, M.A. Dopita: Ap. J. Suppl. **75**, 407 (1991)
24. S.J. Meatheringham, M.A. Dopita: Ap. J. Suppl. **76**, 1085 (1991)
25. E. Vassiliadis, M.A. Dopita, D.H. Morgan, J.F. Bell: Ap. J. Suppl. **83**, 87 (1992)
26. G.H. Jacoby, A.R. Walker, R. Ciardullo: Ap. J. **365**, 471 (1990)
27. E.M. Hu, L.L. Cowie, R.G. McMahon: Ap. J. **504**, 622 (1998)
28. R.-P. Kudritzki, R.H. Méndez, J.J. Feldmeier, R. Ciardullo, G.H. Jacoby, K.C. Freeman, M. Arnaboldi, M. Capaccioli, O. Gerhard, H.C. Ford: Ap. J. **536**, 19 (2000)
29. K.C. Freeman, M. Arnaboldi, M. Capaccioli, R. Ciardullo, J. Feldmeier, H. Ford, O. Gerhard, R. Kudritzki, G. Jacoby, R.H. Méndez, R. Sharples: 'Intracluster Planetary Nebulae in the Virgo Cluster'. In: *Dynamics of Galaxies: From the Early Universe to the Present, ASP Conference 197*, ed. by F. Combes, G.A Mamom, V. Charmandaris (Astronomical Society of the Pacific, San Francisco 2000) pp. 389-392
30. R. Ciardullo, J.J. Feldmeier, K. Krelove, G.H. Jacoby, C. Gronwall: Ap. J. **566**, 784 (2002)
31. P.R. Durrell, J.C. Mihos, J.J. Feldmeier, G.H. Jacoby, R. Ciardullo: Ap. J. in press (2003)
32. J.J. Feldmeier, R. Ciardullo, G.H. Jacoby: Ap. J. **503**, 109 (1998)
33. P.R. Durrell, R. Ciardullo, J.J. Feldmeier, G.H. Jacoby, S. Sigurdsson: Ap. J. **570**, 119 (2002)
34. K. Krelove, J. Feldmeier, R. Ciardullo, P.R. Durrell: Bull. A.A.S. **32**, 1580 (2000)
35. R. McMillan, R. Ciardullo, G.H. Jacoby: Ap. J. **416**, 62 (1993)
36. J.L. Tonry, A. Dressler, J.P. Blakeslee, E.A. Ajhar, A.B. Fletcher, G.A. Luppino, M.R. Metzger, C.B. Moore: Ap. J. **546**, 681 (2001)
37. G.H. Jacoby, R. Ciardullo, H.C. Ford: Ap. J. **356**, 332 (1990)

38. N. Yasuda, M. Fukugita, S. Okamura: Ap. J. Suppl. **108**, 417 (1997)
39. M.J. West, J.P. Blakeslee: Ap. J. **543**, L27 (2000)
40. M. Arnaboldi, J.A.L. Aguerri, N.R. Napolitano, O. Gerhard, K.C. Freeman, J. Feldmeier, M. Capaccioli, R.P. Kudritzki, R.H. Méndez: A. J. **123**, 760 (2002)
41. R. Ciardullo, G.H. Jacoby, J.J. Feldmeier, R.E. Bartlett: Ap. J. **492**, 62 (1998)
42. G.H. Jacoby, R.J. Quigley, J.L. Africano: Pub. A.S.P. **99**, 672 (1987)
43. R. Ciardullo, H.C. Ford, J.D. Neill, G.H. Jacoby, A.W. Shafter: Ap. J. **318**, 520 (1987)
44. X. Hui, H.C. Ford, R. Ciardullo, G.H. Jacoby: Ap. J. **414**, 463 (1993)
45. J.J. Feldmeier, R. Ciardullo, G.H. Jacoby: Ap. J. **479**, 231 (1997)
46. R.H. Méndez, R.P. Kudritzki, R. Ciardullo, G.H. Jacoby: Astr. Ap. **275**, 534 (1993)
47. S.R. Pottasch: Astr. Ap. **236**, 231 (1990)
48. D.L. Welch, C.W. McAlary, R.A. McLaren, B.F. Madore: Ap. J. **305**, 583 (1986)
49. R.D. McClure, R. Racine: A. J. **74**, 1000 (1969)
50. W.L. Freedman, B.F. Madore, B.K. Gibson, L. Ferrarese, D.D. Kelson, S. Sakai, J.R. Mould, R.C. Kennicutt, Jr., H.C. Ford, J.A. Graham, J.P. Huchra, S.M.G. Hughes, G.D. Illingworth, L.M. Macri, P.B. Stetson: Ap. J. **553**, 47 (2001)
51. D.J. Schlegel, D.P. Finkbeiner, M. Davis: Ap. J. **500**, 525 (1998)
52. R. Ciardullo, J.J. Feldmeier, G.H. Jacoby, R.K. de Naray, M.B. Laychak, P.R. Durrell: Ap. J. **577**, 31 (2002)
53. X. Hui, H. Ford, G. Jacoby: Bull.A.A.S. **26,** 938 (1994)
54. G.H. Jacoby, O. De Marco: A. J. **123**, 269 (2002)
55. J.A. Cardelli, G.C. Clayton, J.S. Mathis: Ap. J. **345**, 245 (1989)
56. D. Burstein, C. Heiles: Ap. J. Suppl. **54**, 33 (1984)
57. D. Mihalas, J. Binney: *Galactic Astronomy.* (W.H. Freeman, New York 1981)
58. V. Weidemann: Astr. Ap. **363**, 647 (2000)
59. J.C. Lattanzio: Ap. J. **311**, 708 (1986)
60. E. Brocato, F. Matteucci, I. Mazzitelli, A. Tornabé: Ap. J. **349**, 458 (1990)
61. M.A. Dopita, G.H. Jacoby, E. Vassiliadis: Ap. J. **389**, 27 (1992)
62. N. Grevesse, A. Noels, A.J. Sauval: 'Standard Abundances'. In: *Cosmic Abundances, ASP Conference 99*, ed. by S.S. Holt, G. Sonneborn (Astronomical Society of the Pacific, San Francisco 1996) pp. 117-126
63. E. Vassiliadis, P.R. Wood: Ap. J. Suppl. **92**, 125 (1994)
64. T. Blöcker: Astr. Ap. **299**, 755 (1995)
65. G.H. Jacoby, R. Ciardullo: Ap. J. **515**, 169 (1999)
66. G.H. Jacoby, J.A. Morse, L.K. Fullton, K.B. Kwitter, R.B.C. Henry: A. J. **114**, 2611 (1997)
67. I. Iben, Jr., G. Laughlin: Ap. J. **341**, 312 (1989)
68. R. Ciardullo, G.H. Jacoby: Ap. J. **515**, 191 (1999)
69. D. Zaritsky, R.C. Kennicutt, Jr., J.P. Huchra: Ap. J. **420**, 87 (1994)
70. R.F. Peletier, R.L. Davies, G.D. Illingworth, L.E. Davis, M. Cawson: A. J. **100**, 1091 (1990)
71. L. Magrini, M. Perinotto, R.L.M. Corradi, A. Mampaso: Astr. Ap. **379**, 90 (2001)
72. G.H. Jacoby, R. Ciardullo, W.E. Harris: Ap. J. **462**, 1 (1996)
73. R. Ciardullo, G.H. Jacoby, W.E. Harris: Ap. J. **383**, 487 (1991)
74. R. McMillan, R. Ciardullo, G.H. Jacoby: A. J. **108**, 1610 (1994)
75. M.M. Phillips, G.H. Jacoby, A.R. Walker, J.L. Tonry, R. Ciardullo: Bull. A.A.S. **24**, 749 (1992)
76. H. Böhringer, U.G. Briel, R.A. Schwarz, W. Voges, G. Hartner, J. Trümper: Nature **368**, 828 (1994)

77. L. Ferrarese, H.C. Ford, J. Huchra, R.C. Kennicutt, J.R. Mould, S. Sakai, W.L. Freedman, P.B. Stetson, B.F. Madore, B.K. Gibson, J.A. Graham, S.M. Hughes, G.D. Illingworth, D.D. Kelson, L. Macri, K. Sebo, N.A. Silbermann: Ap. J. Suppl. **128**, 431 (2000)
78. J.R. Herrnstein, J.M. Moran, L.J. Greenhill, P.J. Diamond, M. Inoue, N. Nakai, M. Miyoshi, C. Henkel, A. Riess: Nature **400**, 539 (1999)
79. A. Gould, O. Uza: Ap. J. **494**, 118 (1998)
80. B. Binggeli, G.A. Tammann, A. Sandage: A.J. **94**, 251 (1987)

14 Distances to Local Group Galaxies

Alistair R. Walker

Cerro Tololo Inter-American Observatory, NOAO, Casilla 603, La Serena, Chile

Abstract. Distances to galaxies in the Local Group are reviewed. In particular, the distance to the Large Magellanic Cloud is found to be $(m - M) = 18.52 \pm 0.10$, corresponding to $50,600 \pm 2,400$ pc. The importance of M31 as an analog of the galaxies observed at greater distances is stressed, while the variety of star formation and chemical enrichment histories displayed by Local Group galaxies allows critical evaluation of the calibrations of the various distance indicators in a variety of environments.

14.1 Introduction

The Local Group (hereafter LG) of galaxies has been comprehensively described in the monograph by Sidney van den Bergh [1], with update in [2]. The zero-velocity surface has radius of a little more than 1 Mpc, therefore the small sub-group of galaxies consisting of NGC 3109, Antlia, Sextans A and Sextans B lie outside the the LG by this definition, as do galaxies in the direction of the nearby Sculptor and IC342/Maffei groups. Thus the LG consists of two large spirals (the Galaxy and M31) each with their entourage of 11 and 10 smaller galaxies respectively, the dwarf spiral M33, and 13 other galaxies classified as either irregular or spherical. We have here included NGC 147 and NGC 185 as members of the M31 sub-group [60], whether they are actually bound to M31 is not proven. Similarly, Leo I and Leo II are classified as satellites of our Galaxy, however [1] has pointed out that the mass of our Galaxy becomes uncomfortably large if they are indeed bound. Of these 36 galaxies, 23 are classified [1], [2] as being dwarf galaxies with $M_V < -14.0$. There are no giant ellipticals, the nearest being some 7 Mpc distant in the Leo I group, nor is there anything so exotic as NGC 5128 (Cen A) at 4 Mpc distance in the Centaurus group. However there are some interesting 'one-off's'; M32 is a dwarf elliptical, and IC 10 is an irregular galaxy presently undergoing very active star formation (starburst galaxy). The LG as defined above is listed in Tables 14.1–14.4. Columns 1-3 give the galaxy name, type and approximate absolute magnitude [1], [2], while column 4 gives an indication of the population mix, which is a guide to the types of distance indicator present. The star formation history of local group dwarf galaxies is remarkably diverse, and the true situation is much more complex than this simple guide, which has divisions of young (less than ~ 1 Gyr), intermediate (1-7 Gyr), and old (7-12 Gyr). Throughout, old populations appear to be ubiquitous, even though their fractional contribution to the total light can be very small, and it is not clear whether the formation times are coincidental, or spread over a few Gyr [3].

A.R. Walker, Distances to Local Group Galaxies, Lect. Notes Phys. **635**, 265–279 (2003)
http://www.springerlink.com/

Table 14.1. Our Galaxy and its companions

Name	Type[a]	M_V^a	Populations[b]
Galaxy	SbcI-II	-20.9	all
LMC	Ir III-IV	-18.5	all
SMC	Ir IV-V	-17.1	all
Sagittarius	dSph	-14:	intermediate, old
Fornax	dSph	-13.1	(young), intermediate, old
Leo I	dSph	-11.9	(young), intermediate, (old?)
Leo II	dSph	-10.1	(intermediate), old
Sculptor	dSph	-9.8	(young, with gas), intermediate, old
Sextans	dSph	-9.5	intermediate, old
Carina	dSph	-9.4	(young), intermediate, old
U. Minor	dSph	-8.9	(intermediate?), old
Draco	dSph	-8.6	old

[a] From [1], [2]
[b] Minority populations are bracketed.

Table 14.2. M31 and its companions

Name	Type[a]	M_V^a	Populations[b]
M31	SbI-II	-21.2	all
M32	E2	-16.5	(intermediate), mostly old
NGC 205	Sph	-16.4	(young), mostly intermediate, (old)
And I	dSph	-11.8	mostly old
And II	dSph	-11.8	intermediate, old
And III	dSph	-10.2	intermediate, (old)
And V	dSph	-9.1	old
And VI	dSph	-11.3	mostly old
And VII	dSph	-12.0	mostly old?
NGC 147	Sph	-15.1	(young & intermediate), mostly old
NGC 185	Sph	-15.6	(young), intermediate, old

[a] From [1], [2]
[b] Minority populations are bracketed.

Table 14.3. Brighter isolated LG galaxies

Name	Type[a]	M_V^a	Populations[b]
M33	Sc II-III	-18.9	all
IC 10	Ir IV	-16.3	all, no globular clusters
NGC 6822	Ir IV-V	-16.0	all
IC 1613	Ir V	-15.3	all, no globular clusters
WLM	Ir IV-V	-14.4	all

[a] From [1], [2]
[b] Minority populations are bracketed.

Table 14.4. Fainter isolated LG galaxies

Name	Type[a]	M_V^a	Populations[b]
Pegasus	Ir V	-12.3	(young), intermediate, old
Sag DIG	Ir V	-12.0	young, intermediate, (old?)
Leo A	Ir V	-11.5	(young), intermediate, old
Aquarius	Ir V	-10.9	young, intermediate, (old?)
Pisces	Ir/Sph	-10.4	young, intermediate, (old?)
Cetus	dSph	-10.1	intermediate, old?
Phoenix	Ir/Sph	-9.8	all
Tucana	dSph	-9.6	old

[a] From [1], [2]
[b] Minority populations are bracketed.

The LG is contained in what is termed the ‘Local Volume’, a sphere with radius approximately 10 Mpc, thus a factor 1000 times the volume of the LG. A systematic census of galaxies likely to lie in this volume [5], those with $V_{LG} < 500$ km/s, listed 179 members, this number has been doubled by more recent work [6]. These galaxies are clustered in rather ill-defined groups, with substantial volumes (e.g. the ‘Local Void’) free or almost free of galaxies. The closest groups have zero-velocity surfaces that are close to that for the LG, for instance the Sculptor group appears to be very elongated and viewed almost end-on, the nearest members such as NGC 55 are less than 2 Mpc from the LG barycenter. The Centaurus group, which is estimated to be about seven times as massive as the LG [7] has zero-velocity surface only ~ 2 Mpc from the LG barycenter. The large numbers of dwarf galaxies recently found in both groups [8] appear more spatially dispersed than do the more massive galaxies, this is also true for the LG.

As far as we know, LG galaxies are typical of the 'mean' population of galaxies, thus a detailed study should allow deductions to be made concerning the general properties of galaxies, in particular their formation and subsequent evolution, throughout the Universe. The common dwarf spheroidal (dSph) galaxies are the best places to test the small scale predictions of hierarchical galaxy formation models, and the nature and distribution of dark matter [9]. Indeed, the favored cold dark matter (CDM) formation theory predicts a factor 10 more dSph galaxies in the LG than are known, however it is estimated [10] that we have found more than half of them. Recent successful [11] and on-going [12] searches are helping to refine the total numbers of LG dSph's, but we have found all the higher surface-brightness members unless they are hidden directly behind the galactic plane.

The latest generation of large telescopes and instrumentation have meant that detailed studies of stellar formation, stellar evolution and chemical evolution have moved from the confines of our Galaxy and the Large and Small Magellanic Clouds (LMC, SMC) to all the LG galaxies. Imaging to faint limits in crowded fields has been made possible with HST, and this has allowed us, with some difficulty, to reach the old main sequence turnoff in M31 and to measure RR Lyraes throughout the LG. For distance scale work this has granted us the extra perspective resulting from the study of distance indicators in a variety of different environments. However interpreting the observations is not an easy task, as almost all galaxies contain multiple populations with complex histories, and we now realize that interactions between many LG dwarf galaxies and the two giant LG spirals are likely to have been a feature throughout their lifetimes, as the present-time assimilation of the Sagittarius dSph by our own Galaxy dramatically illustrates.

Distances to galaxies in the LG are obviously needed as part of the study of the galaxies themselves. Given the large dynamic range of astronomical distances, which means that the distance scale is built up from overlapping indicators starting with those we can calibrate directly nearby, the LG galaxies play an essential role in the verification and extension of the distance scale. In this short review we will cover a selection of the recent work in the field; given the huge amount of recent and on-going work on LG galaxies no attempt is made to be complete and only work relating to the topic in hand will be addressed. For many of the lower luminosity galaxies our knowledge is still quite rudimentary, albeit rapidly increasing due to the efforts by several groups. In Sect. 14.2 we comment briefly on distance indicators relevant to the present topic, and then in Sects. 14.3 through 14.6 discuss companions to our own Galaxy, M31 and its companions, luminous isolated galaxies, and finally faint isolated galaxies. We conclude with a short summary. Note that a previous discussion of this topic is [14], and a convenient table listing LG galaxies and their distances from our Galaxy and the LG barycenter is found in [2]. An extensive database of distances and other useful information is contained in [4], as part of the Distance Scale Key Project. The below discussion relies heavily on [1], [2] for details and evaluation of work prior to 2000.

Two other comments are in order. Firstly, the nomenclature for LG galaxies is clearly a mess, with the tradition of naming newly discovered dSph's after the constellation in which they are found, and only that, is nonsensical and a hinder to computer searches at the very least. This is clearly a matter that the International Astronomical Union should take up. The second comment refers to errors. Unless stated specifically to the contrary, here and elsewhere errors refer to the error associated with the measurement of a distance, and do not include an estimate of the error of the accuracy of the calibration of the distance indicator used. For the latter, systematic errors dominate; these are difficult to evaluate, and are almost always underestimated.

14.2 Relevant Distance Scale Calibrators

Most of the distance indicators discussed elsewhere in this volume (q.v.) are relevant for use within the LG, and only a few general comments will be made here. The more massive LG systems, with the exception of M32 have had continuing, if in some cases spasmodic, star formation over their whole lifetimes and thus all 'population I' and 'population II' indicators can in principle be observed. The lower mass galaxies are mostly dominated by a mixture of intermediate and older populations, and thus indicators such as the brightness of the Tip of the Red Giant Branch (TRGB) and RR Lyraes are very useful, although for the more distant LG galaxies the latter are difficult to measure, even with HST. The metal-poor, low-mass irregulars with recent star formation contain ultra-short period Cepheids, and these have been advocated [15] as a useful indicator for these systems. Perhaps most importantly, the diversity of galaxies allows inter-comparison between distance indicators in a wide variety of environments.

In summary, primary indicators used to find distances to LG galaxies include: Cepheids, Mira variables, RR Lyraes, RGB clump, Eclipsing Binaries and TRGB. Secondary distance indicators whose zeropoint relies wholly or partially on distances to LG galaxies provided by the primary indicators includes Planetary Nebulae Luminosity Function (PNLF), Supernovae, Surface Brightness Fluctuations (SBF), Globular Cluster Luminosity Function (GCLF), Novae, and Blue Supergiants. The distinction is not always absolute, for instance TRGB when calibrated by distances to Globular Clusters which themselves are tied to Hipparcos parallaxes of subdwarfs is primary, but if it is calibrated from the brightness of the Horizontal Branch (HB) and thus dependent on the adopted luminosities of RR Lyraes, then it is secondary. Depending on the degree of the reader's belief in the underlying theory, all the secondary indicators could be considered primary, in principle.

14.3 Companions of Our Galaxy

There are 11 known companions to our Galaxy, although the status of Leo I and Leo II is uncertain. Of these the Sagittarius dSph is in collision with our Galaxy, and thus plays little part in distance scale studies. Its mean distance is

$(m-M)_0 = 17.36 \pm 0.2$ from Mira variables [13] and $(m-M)_0 = 17.18 \pm 0.2$ from RR Lyraes. Given the extended structure of the Sagittarius dSph, such numbers are not particularly meaningful.

The LMC by contrast is pivotal in distance scale work, and will be discussed in some detail here, and elsewhere in this volume [74]. The major use of the LMC is as a sanity check - it includes most of the popular distance indicators and is close enough so that they can be studied in great detail, yet is far enough away so that to a first approximation its contents can all be considered to be at the same distance from us. Recent reviews [16], see also [17], discuss the topic in great detail, however progress has been rapid with improvements to the primary calibrators that have resulted in improved consistency. The comprehensive figure in [18] showing results ranging from $(m-M)_0 = 18.1$ to 18.8, although a good historical summary, is more pessimistic than need be. The smaller moduli mostly come from early results based on using Hipparcos parallaxes for the locally common RGB clump stars, without realization that both age and abundance each have a dramatic effect on the absolute magnitude of the clump. Modeling of these effects [19], [20] has provided quantitative understanding of the evolution of clump stars, and has shown the advantage of observing in the infrared K-band which additionally greatly reduces the significance of reddening corrections compared to observing in the visible. New results for both LMC cluster [21] and field [22], [23] all give LMC moduli near 18.5.

The LMC distance gap between the traditional indicators, Cepheids and RR Lyraes, has also narrowed [27], with the mean RR Lyrae modulus now 18.44 ± 0.05, even with the traditionally short value given by statistical parallaxes of galactic field RR Lyraes included. The realization in recent years that the galactic halo contains star streams, possibly remnants of accreted dwarf galaxies, makes less certain the assumption of velocity homogeneity assumed in the statistical parallax method. We will adopt, see [27]

$$< M_V(RR) >= 0.21([Fe/H] + 1.5) + 0.62 \tag{14.1}$$

For Cepheids, the remaining questions are well summarized elsewhere in this volume [73], [74]; the characterization of the effect of metallicity on the PL relation zeropoint still defies solution, and is the most important unknown. Cepheids are well-understood both observationally and theoretically, and with fundamental astrometric [18] and interferometric [24], [25] observations to add to the Hipparcos parallax measurements [26], the likelihood of there being a significant systematic error in the (metal-normal) PL zeropoint seems remote.

Eclipsing binaries are a promising technique, with the issues very clearly set out by [29], who gives distances for ten SMC binaries found by OGLE [28], solving the technical difficulty of getting enough large telescope time to measure the radial velocities by observing all the stars at once using the wide-field fiber spectrograph 2DF on the Anglo-Australian telescope. The three LMC systems have been recently (re)discussed, see [30], [31], [32].

There are still some disquieting problems [33], and there are still some systematic differences between calibrators that we would like to understand better.

Table 14.5. Distance Modulus Measurements for the LMC

Indicator	Value	Reference
Cepheids	18.55 ± 0.06	[73], [74]
RR Lyraes	18.44 ± 0.05	[27]
RG Clump	18.49 ± 0.06	[21], [22], [23]
TRGB	18.59 ± 0.09	[75], [76]
Eclipsing Bin.	18.46 ± 0.1	[30], [31], [32]
Miras	18.59 ± 0.2	[13]
SN 1987A	18.55 ± 0.17	[16]
Mean	18.52 ± 0.10	

However, the evidence seems strong for an 'intermediate' LMC modulus, and here (Table 14.5) we adopt $(m - M)_0 = 18.52$. It is noteworthy that for the recent determinations by a variety of methods the error bars overlap, this gives confidence that there are not undiscovered systematic errors, and so it seems not too unrealistic to evaluate the overall accuracy of the above mean modulus as ± 0.1 mag, corresponding to $\pm 5\%$ in the distance. Many of the estimates for other LG galaxies below are tied to the LMC at a modulus of 18.50; we have made no adjustments for the slight difference with the Table 14.5 value.

Turning now to the SMC, this galaxy has received far less prominence in comparison to the LMC, mostly due to the considerable extent of the SMC along the line of sight. The degree of this extent is controversial, see [34] for a 3-D model. The SMC Cepheids show considerable dispersion in the period-luminosity (PL) relation, but there is little room from the small dispersion in the period-color relation to allow for a significant range in reddening or possibly metallicity, thus it is difficult to explain the PL dispersion as anything other than a depth effect. Even a 'mean' distance to the SMC derived from different distance indicators may not be comparable if there are differences in the spatial distribution of SMC stars as a function of age. Despite this cautionary note, the SMC has mean metallicity substantially lower than the LMC [35] and thus it is of use for investigating the effects of metallicity on distance indicators [74]. Earlier work, as summarized by [16] gives 0.42 ± 0.05 for the difference between the LMC and SMC moduli, a result largely based on the Cepheids, thus $(m - M)_0 = 18.94$ for the LMC at 18.52.

The remaining galaxies in this group are all of type dSph, and with the exception of Fornax and Sagittarius are amongst the lower luminosity examples of this type, which is likely a selection effect [10]. With their significant old populations, these galaxies all contain many RR Lyraes. We give some updates to the distance estimates tabulated in [1], [2]. For Sculptor, using OGLE photometry [36] and assuming mean $[Fe/H] = -1.9$ for the RR Lyraes, $(m-M)_0 = 19.59$, while restricting the sample to just the double-mode RRd stars, [37] finds $(m-M)_0 = 19.71$.

Photometry for 515 RR Lyraes in Fornax has recently been published [38] who find $< V_0 >= 21.27 \pm 0.10$, with $[Fe/H] = -1.6 \pm 0.2$, $(m-M)_0 = 20.67$. This is in good agreement with their earlier work [39] which gives a TRGB distance of 20.68 mag.

The most recent RR Lyrae photometry for the Carina dSph is by [40]. With $< V_0 >= 20.68$ and assuming a mean $[Fe/H] = -1.7$, $(m-M)_0 = 20.06 \pm 0.12$. This value is in excellent agreement with earlier work [1].

The distance to the Sextans dSph is given [41] as $(m-M)_0 = 19.67 \pm 0.15$, however there are uncertainties in the metallicity which could change this value. These authors also discovered an intermediate age population as evinced by six anomalous Cepheids, and [42] further discuss the multiple populations and their metallicities.

The Draco and Ursa Minor dSphs have recently been compared [43], with respective distances from the horizontal branch magnitude of $(m-M)_0 = 19.84 \pm 0.14$ and 19.41 ± 0.12 being derived. These distances are in good agreement with those found by the TRGB method.

Leo I and Leo II are considerably more distant than the above, and despite morphological similarities have strikingly different star formation histories [78]. The best distances to Leo I appear to be those measured using the TRGB method [77], $(m-M)_0 = 22.16 \pm 0.08$, and from RR Lyraes by [72], $(m-M)_0 = 22.04 \pm 0.14$. Similar data are available for Leo II, where [1] evaluates the distance as $(m-M)_0 = 21.60 \pm 0.15$. For Leo II, the discovery of copious numbers of RR Lyrae variables [90] will likely yield an improved distance.

14.4 M31 and Its Companions

M31 contains all the distance indicators mentioned above and, as well stated by [44] *An SbI-II giant spiral galaxy provides a much more appropriate local counterpart to the Distance Scale Key Project galaxies than does the LMC... M31 is also an important calibrator for the PNLF zeropoint, and also for the Globular Cluster Luminosity Function (GCLF) method, applicable to massive galaxies with large GC populations. Therefore, in any respect except for ease of observations, M31 is a much more important cornerstone for the distance scale than the LMC.* To which might be added the difficulties include both the variable (internal) reddening, and the large angular extent on the sky, the latter now being addressed by the latest generation of wide-field imagers and multi-object spectrometers.

The distance to M31 has long been established using Cepheids, with a much-quoted result [45], referenced to the LMC at an assumed distance modulus of 18.50 and reddening E(B-V) = 0.10, of $(m-M)_0 = 24.44 \pm 0.10$. From HST photometry of M31 clusters, [46] found $V_0(HB) = 25.06$ at $[Fe/H] = -1.5$, then with $M_V(RR) = 0.62$, $(m-M)_0 = 24.44$, while from isochrone fits to the

RGB, [48] found $(m-M)_0 = 24.47 \pm 0.07$. All these results are in remarkably good agreement. A major effort that will improve the amount of data available for M31 Cepheids and Eclipsing Binaries is the DIRECT Project [47] which has the aim of measuring the distance to M31 in one-step via the Baade-Wesselink method for Cepheids and by discovering and measuring a significant number of eclipsing binaries.

Using HST, [44] have shown that it is possible to measure M31 cluster RR Lyraes, but the observational task is less formidable for field RR Lyraes in the companion galaxies to M31. For instance [49] give HST lightcurves for 111 RR Lyraes in And VI, and derive intensity-mean $< V >_0 = 25.10 \pm 0.05$, with $[Fe/H] = -1.58 \pm 0.20$ [50], and the RR Lyrae magnitude-metallicity relation above, $(m-M)_0 = 24.50 \pm 0.06$. The And VI distance from the TRGB method, is $(m-M) = 24.45 \pm 0.10$[50]. Systematic HST photometry of other dSph companions to M31 are yielding distances via the magnitude of the horizontal branch or mean magnitudes of the RR Lyraes. For And II, [51] measure $(m-M)_0 = 24.17 \pm 0.06$, while for And III they find [52] $(m-M)_0 = 24.38 \pm 0.06$. Clearly, with accurate distances relative to M31 the true spatial distribution of the M31 dSph companions can be mapped; this requires accurate photometry and a knowledge of the metallicity.

M32 is the closest companion to M31, it is a dwarf elliptical, with clear indications of interactions and likely tidal stripping by M31 [1]. It is an important site for stellar population studies, until the recent discovery [53] of luminous AGB stars it was argued that M32 contained only an old population. The distance to M32 is usually assumed to be the same as for M31 [1].

NGC 205 is also a close companion of M31, distance estimates are well summarized by [1], with for example a TRGB distance of 24.54 [33]. HST CMDs for NGC 205 clusters are discussed in a preliminary report by [55].

NGC 147 and 185 lie close together on the sky and the evidence is strong that they are bound to each other [1], less certain is whether they are bound to M31 [60]. Early distance measurements, including those via RR Lyraes, are summarized by [1]. The TRGB estimate for NGC 147 by [54] is 24.27, they also give 24.12 for NGC 185, with an independent TRGB estimate [61] of 23.95±0.10. Both galaxies therefore are slightly closer to us than M31, and as pointed out by [1], lie close to the LG barycenter.

14.5 Luminous Isolated LG Galaxies

The spiral galaxy M33 is the third most luminous galaxy in the LG, although it is only slightly brighter than the LMC [1]. Recent distance measurements have shown considerable dispersion, although it has been suggested [59] that they may all be reconciled by reasonable adjustments of the reddening, and it will be interesting to see whether or not that is indeed the case. They also suggest that to circumvent the reddening problem for Cepheids, a technique of determining the periods using optical photometry, followed by a single-epoch infrared K-band observation, should be used. As the phasing is known, the K-band observation need not be taken at random phase but can instead be chosen to correspond to phases near mean light, since although the K band amplitudes of Cepheids are small, they are not negligible. Using periods from the DIRECT Project [47] together with single-epoch HST I-band observations, [56] find for 21 Cepheids $(m-M)_0 = 24.52 \pm 0.14(stat) \pm 0.13(sys)$ assuming $E(B-V) = 0.20$ for M33 and based on an LMC distance of 18.50 mag. and $E(B-V)_0 = 0.10$. The Key Project Cepheid distance, for 11 stars, is very similar at 24.56 ± 0.10. Using the same HST data set, [57] found a rather larger distance from RGB stars in multiple fields, $24.81 \pm 0.04(stat) \pm 0.13(sys)$ from the TRGB and $24.90 \pm 0.04(stat) \pm 0.05(sys)$ from the RGB clump. Photometry of M33 halo clusters [58] gives very similar values, from the horizontal branch magnitude in two clusters $(m-M)_0 = 24.84 \pm 0.16$, while from the position of the RGB clump in 7 clusters $(m-M)_0 = 24.81 \pm 0.24$.

There are four other relatively luminous isolated galaxies, all are Irregulars of type IV or V. Due to its very low galactic latitude and consequent high foreground reddening, IC 10 is difficult to study. Reddening estimates in the literature range over a very wide value, and to complicate matters the internal reddening seems highly variable, perhaps not surprising given the high star formation rate. From V and I observations of Cepheids [64] derive $(m-M)_0 = 24.1 \pm 0.2$, and $E(B-V) = 1.16 \pm 0.08$. With this reddening, their TRGB distance is $(m-M)_0 = 23.5 \pm 0.2$, but they regard this as a lower limit since there is no reason to expect the halo of IC 10 to have reddening as high as the inner regions where the Cepheids are located. To force the TRGB distance to be the same as given by the Cepheids implies that the IC 10 halo has reddening of $E(B-V) = 0.85$, which would then be primarily the amount of galactic foreground reddening. A new estimate of $(m-M)_0 = 24.4$, with $E(B-V) = 0.77$, is given by [65], but with no details. Clearly, infrared measurements for the IC 10 Cepheids would be of value in reducing the distance error for this very interesting galaxy.

There do not appear to be any distance estimates for NGC 6822 more recent than those evaluated by [1], who derives $(m-M)_0 = 23.48 \pm 0.06$ from a weighted mean. Recently, [66] have found many more Cepheid variables in a survey, the reference describes those in a single 3.77 x 3.77 arcmin field.

For IC 1613, [1] derives $(m-M)_0 = 24.3 \pm 0.1$. From the TRGB method, [67] find $(m-M)_0 = 24.53 \pm 0.10$, and also determine $[Fe/H] = -1.75$. As a by-product of the OGLE project [68] measured 138 Cepheids in a central field, and compared to distances from the RR Lyraes and the TRGB, and concluded that the distance is $(m-M)_0 = 24.20 \pm 0.02(stat) \pm 0.07(sys)$. A similar study is that by [69], who compare Cepheids, RR Lyraes, RGB clump stars. and TRGB using deep HST V and I photometry, to find $(m-M)_0 = 24.31 \pm 0.06$. In later work, [62], [63], they examine the question of whether ultra-short period Cepheids (USPC's, Population I Cepheids with periods less than two days) are useful distance indicators, comparing the properties of such stars in the SMC, LMC, IC 1613, Leo A, and Sextans A. It has been long known that metal-poor systems with young populations contain more USPC's than do more metal rich systems. They find that USPC's do indeed appear to be good distance indicators, with excellent agreement between the USPC's and TRGB, RGB clump, longer period Cepheids, and RR Lyraes for Sextans A, Leo A, IC 1613 and the SMC, but not for the LMC where such stars appear to be 0.2 mag. too luminous. In the LMC USPC's are uncommon, and thus it is postulated that these stars are fundamentally different from those in the more metal-poor systems. It is well-known that the light curve amplitudes are much smaller for the LMC USPC's compared to those in the SMC, for example.

The WLM galaxy has a distance [1] of $(m-M)_0 = 24.83 \pm 0.1$ from several Cepheid and TRGB estimates. There are two recent measurements, [70] observed a field with STIS on HST, reaching the level of the horizontal branch. Assuming $[Fe/H] = -1.5$ and $M_V = 0.7$, they find $(m-M)_0 = 24.95 \pm 0.13$. Reddening to WLM is low, they adopt $E(V-I) = 0.03$. A rather similar result is found by [71], who give $(m-M)_0 = 24.88 \pm 0.09$ from HST WFC2 photometry.

In conclusion, the luminous, isolated galaxies in the LG provide a wealth of information relevant to the distance scale. They are relatively rich, so that they contain good-sized samples allowing statistically significant comparisons to be made, and environs sufficiently different one to the other that metallicity and age effects can be investigated in depth. Such work is on-going. Distances are in relatively good agreement for the galaxies with low reddening, objects like IC 10 are clearly much easier to study in the infrared.

14.6 Faint Isolated LG Galaxies

This category consists of the faint dwarf irregulars: Pegasus, Aquarius, Sag DIG and Leo A, together with the fainter 'transition' objects Pisces and Phoenix, plus two dwarf spheroidals: Tucana and Cetus. For the dwarf irregulars, by definition, star formation has occurred at some level up to the present time, however the occurrence of rare stages of star formation depends critically on the star formation rate at any given time. Even for more luminous galaxies this effect is well-seen, an example is the lack of long-period Cepheids in WLM compared to the situation in the rather similar galaxy Sextans A.

The Pegasus dwarf irregular galaxy (DDO 216) appears to have had little attention since the summary by [1], who points out that differences in the reddening adopted between the several studies he quotes means that the distance is not well determined, and he adopts $(m-M)_0 = 24.4 \pm 0.25$. Depending on the true distance, Pegasus may possibly be a distant member of the M31 sub-group.

The most recent distance to the Aquarius dwarf irregular galaxy (DDO 210) is that of [89], who from the TRGB method finds $(m-M)_0 = 24.9 \pm 0.1$

The Sagittarius Dwarf Irregular galaxy (Sag DIG) has a distance from the TRGB method by [79] of $(m-M)_0 = 25.36 \pm 0.10$, and as such it is the outermost galaxy in the LG according to [2].

Leo A has been studied recently by [80], who found a distance by the TRGB method of $(m-M)_0 = 24.5 \pm 0.2$, and by [81], who from HST observations measured the brightness of the RR Lyraes, to find $(m-M)_0 = 24.51 \pm 0.07$.

Pisces, also widely referred to as LGS 3, has been observed by [82], who find from the TRGB, the brightness of the clump RGB stars, and the level of the horizontal branch, that $(m-M)_0 = 23.96 \pm 0.07$. Classified as a transition object, there is still active star formation in a small area approximately 60 pc in diameter near the center of the galaxy.

The central regions of Phoenix were studied using HST by [83], who measured the level of the horizontal branch at $V(HB) = 23.9 \pm 0.1$ which using the calibration of (14.1) corresponds to $(m-M)_0 = 23.3 \pm 0.1$. Their TRGB distance is somewhat shorter, $(m-M)_0 = 23.11$, very similar to earlier results [84], [85].

The Tucana dSph is one of the most isolated galaxies in the LG, TRGB distances [87,86] average to $(m-M)_0 = 24.76 \pm 0.15$. HST imaging of this galaxy [88] has never been published in detail, the CMD appears to show a single, old population.

Finally, the Cetus dSph galaxy was recently discovered [11] and the first stellar populations study, from HST observations, has just appeared [58]. From the TRGB method, $(m-M)_0 = 24.46 \pm 0.14$, for $E(B-V) = 0.03$, identical to the ground-based distance found by [11] using the same method.

14.7 Summary

The LG is a very important place, where we can study galaxies in detail and thus extrapolate our findings to the Universe at large, and it is where we set up and verify the distance scale ladder. With the development of large format imaging mosaics, and the advent of very large telescopes with powerful spectrographs, together with the unique capabilities of HST, there has been an explosion in the amount of high quality data available for LG galaxies, while in parallel there has been substantial progress on the theoretical understanding for most of the popular standard candles, and substantial improvements in their calibrations. Specifically, it appears that the 'long-short' problem for the distance to the LMC has largely vanished. Distances from the reliable indicators are now within one sigma of each other, and although it is clear there are still systematic differences, they have shrunk, and the LMC modulus of $(m-M)_0 = 18.52 \pm 0.10$ seems reasonably secure. Reduction in the size of the error, and improvement in the agreement between distance indicators, will be aided by comparisons made in a variety of environments, and here the LG galaxies are of key value. The wealth of new work reported above will be invaluable in this respect.

References

1. S. van den Bergh: *The Local Group*, (Cambridge Univ. Press, Cambridge 2000)
2. S. van den Bergh: PASP, **112**, 529 (2000)
3. E. Grebel: 'Evolutionary Histories of Dwarf Galaxies in the Local Group'. In: *The Stellar Content of Local Group Galaxies, IAU Symposium 192*, ed. by P. Whitelock, R. Cannon (Astronomical Society of the Pacific, San Francisco 1998) pp. 17-38

4. L. Ferrarese et al.: ApJS, **128**, 431 (2000)
5. R. Krann-Korteweg, G. Tammann: Astr. Nacht., **300**, 181 (1979)
6. W. Huchtmeier, I. Karachentsev, V. Karachenseva: A&A, **377**, 801 (2001)
7. S. van den Bergh: AJ, **119**, 609 (2000)
8. H. Jerjen, B. Binggeli, K. Freeman: AJ, **119**, 593 (2000)
9. G. Gilmore: RevMexAA, in press, (astro-ph/0211023)
10. M. Mateo: ARAA, **36**, 435 (1998)
11. A. Whiting, G. Hau, M. Irwin: AJ, **118**, 2767 (1999)
12. B. Willman et al.: AJ, **123**, 848 (2002)
13. P. Whitelock: 'Luminosities of AGB Variables'. In: *Mass-Losing Pulsating Stars and their Circumstellar Matter*, ed. by Y. Nakada, M. Honina (Kluwer, Dordrecht in press), (astro-ph/0207168)
14. M. Feast: 'Distance Scales and the Local Group'. In: *The Stellar Content of Local Group Galaxies, IAU Symposium 192*, ed. by P. Whitelock, R. Cannon (Astronomical Society of the Pacific, San Francisco 1998) pp. 51-62
15. A. Dolphin et al.: AJ, in press, (astro-ph/0211486)
16. A. Walker: 'The Distances of the Magellanic Clouds'. In: *Post-Hipparcos Cosmic Candles*, ed. by A. Heck, F. Caputo (Kluwer, Dordrecht 1999) pp. 125-144
17. M. Feast: 'The Distance to the Large Magellanic Cloud: A Critical Review'. In *New Views of the Magellanic Clouds, IAU Symposium 190*, ed. by Y-H. Chu, N. Suntzeff, J. Hesser, D. Bohlender (Astronomical Society of the Pacific, San Francisco 1999) pp. 542-548
18. G. Benedict et al.: AJ, **123**, 473 (2002)
19. L. Girardi, M. Salaris: MNRAS, **323**, 109 (2001)
20. M. Salaris, L. Girardi: MNRAS, **337**, 332 (2002)
21. A. Sarajedini et al.: AJ, **124**, 2625 (2002)
22. G. Pietrzynski, W. Gieren: AJ, **124**, 2633 (2002)
23. D. Alves et al.: ApJ, **573**, 51 (2002)
24. T. Nordgren, B. Lane, R. Hindsley, P. Kervella: AJ, **123**, 3380 (2002)
25. B. Lane et al.: ApJ, **573**, 330 (2002)
26. M. Feast, R. Catchpole: MNRAS, **286**, L1 (1997)
27. G. Clementini et al.: AJ, in press
28. G. Pietrzynski, A. Udalski: Acta Astr., **49**, 149 (1999)
29. T. Harries et al.: MNRAS, in press (astro-ph/0210295)
30. M. Groenwegen, M. Salaris: A&A, **366**, 578 (2001)
31. E. Fitzpatrick et al.: ApJ, **564**, 260 (2002)
32. I. Ribas et al.: ApJ, **574**, 271 (2002)
33. M. Salaris et al.: ApJ, in press
34. J. Caldwell, D. Maeder: '3-D Visualization of the Intrinsic Shape of the SMC'. In *Variable Stars and Galaxies, ASP Conf. Ser. 30*, ed. B. Warner (Astronomical Society of the Pacific, San Francisco 1992) pp. 173-178
35. R. Luck et al.: AJ, **115**, 605 (1998)
36. J. Kaluzny et al.: A&A, **112**, 407 (1995)
37. G. Kovacs: A&A, **375**, 469 (2001)
38. D. Bersier, R. Wood: AJ, **123**, 840 (2002)
39. D. Bersier: ApJ, **543**, L23 (2000)
40. M. Dall'Ora et al.: AJ, in press
41. M. Mateo, P. Fischer, W. Kremenski: AJ, **110**, 2166 (1995)
42. M. Bellazzini, F. Ferraro, E. Pancino: MNRAS, **327**, L15 (2001)
43. M. Bellazzini et al.: AJ, **124**, 3222 (2002)

44. G. Clementini et al.: ApJ, **559**, L109 (2001)
45. W. Freedman, B. Madore: ApJ, **365**, 186 (1990)
46. R. Rich et al.:'A Survey of M31 Globular Clusters using WFPC2 on board HST'. In *Extragalactic Star Clusters, IAU Symposium 207*, ed. D. Geisler, E. Grebel, D. Minniti (Astronomical Society of the Pacific, San Francisco 2002) pp. 140-142
47. L. Macri et al.: AJ, **121**, 861 (2001)
48. S. Holland: PASP, **110**, 759 (1998)
49. B. Pritzl et al.:AJ, **124**, 1464 (2002)
50. T. Armandroff, G. Jacoby, L. Davies: AJ, **118**, 1220 (1998)
51. G. Da Costa, T. Armandroff, N. Caldwell, P. Seitzer: AJ, **119**, 705 (2000)
52. G. Da Costa, T. Armandroff, N. Caldwell: AJ, **124**, 332 (2002)
53. T. Davidge: PASP, **112**, 1177 (2000)
54. M. Salaris, S. Cassisi: MNRAS, **289**, 166 (1998)
55. D. Geisler et al.:'HST Color-Magnitude Diagrams of Globular Clusters in NGC 185 and NGC205', *The Stellar Content of Local Group Galaxies, IAU Symposium 192*, ed. by P. Whitelock, R. Cannon (Astronomical Society of the Pacific, San Francisco 1998) pp. 231-236
56. M. Lee et al.: ApJ, **565**, 959 (2002)
57. M. Kim et al.: AJ, **123**, 244 (2002)
58. A. Sarajedini et al.: AJ, **120**, 2437 (2000)
59. G. Jacoby: in preparation
60. S. van den Bergh: AJ, **116**, 1688 (1998)
61. D. Martinez-Delgado, A. Aparicio, C. Gallart: AJ, **118**, 2229 (1999)
62. A. Dolphin et al.: AJ, **123**, 3154 (2002)
63. A. Dolphin et al.: AJ in press (astro-ph/0211486)
64. S. Sakai, B. Madore, W. Freedman: ApJ, **511**, 671 (1999)
65. D. Zucker: AAS, **201**, 26.05 (2002)
66. E. Antonella et al.: A&A, **386**, 660 (2002)
67. N. Tikhonov, O. Galazutdinova: A&A, **394**, 33 (2002)
68. A. Udalski, et al.: Acta Astr., **51**, 221 (2001)
69. A. Dolphin et al.: ApJ., **550**, 554 (2001)
70. M. Rejkuba et al.: ApJ, **120**, 801 (2000)
71. A. Dolphin: ApJ, **531**, 804 (2000)
72. E. Held et al.: ApJ, **562**, L39 (2001)
73. P. Fouqué, J. Storm, W. Gieren: this volume (2003)
74. M. Feast: this volume (2003)
75. M.-R. Cioni et al.: A&A, **359**, 601 (2000)
76. M. Romaniello et al.: ApJ, **530**, 738 (2000)
77. M. Lee et al.: AJ, **106**, 1420 (1993)
78. C. Gallart et al.: AJ, **118**, 2245 (1999)
79. M. Lee, S. Kim: AJ, **119**, 777 (2000)
80. R. Schulte-Ladbeck et al.: AJ, **124**, 896 (2002)
81. A. Dolphin et al.: AJ, **123**, 3154 (2002)
82. B. Millar et al.: ApJ, **562**, 713 (2001)
83. J. Holtzman, G. Smith, C. Grillmair: AJ, **120**, 3060 (2000)
84. E. Held, I. Saviane, Y. Momany: A&A, **345**, 747 (1999)
85. D. Martin-Delgado, C. Gallart, A. Aparicio: AJ, **118**, 862 (1999)
86. I. Saviane, E. Held, G. Piotto: A&A, **315**, 40 (1996)
87. M. Castellani, G. Marconi, R. Buonanno: A&A, **310**, 715 (1996)

88. R. Lavery et al.: ‘HST/WFPC2 Imaging of the Tucana Dwarf Galaxy’. *From Stars to Galaxies: The Impact of Stellar Physics on Galaxy Evolution*, ed. by C. Leitherer, U. Fritze-von-Alvensleben, J. Huchra (Astronomical Society of the Pacific, San Francisco 1996) pp. 333-
89. M. Lee et al.: AJ, **118**, 853 (1999)
90. M. Siegel, S. Majewski: AJ, **120**, 284 (2000)

15 The Globular Cluster Luminosity Function: New Progress in Understanding an Old Distance Indicator

Tom Richtler

Astronomy Group, Departamento de Física, Universidad de Concepción, Casilla 160-C, Concepción, Chile

Abstract. I review the Globular Cluster Luminosity Function (GCLF) with emphasis on recent observational data and theoretical progress. As is well known, the turn-over magnitude (TOM) is a good distance indicator for early-type galaxies within the limits set by data quality and sufficient number of objects. A comparison with distances derived from surface brightness fluctuations with the available TOMs in the V-band reveals, however, many discrepant cases. These cases often violate the condition that the TOM should only be used as a distance indicator in old globular cluster systems. The existence of intermediate age-populations in early-type galaxies likely is the cause of many of these discrepancies. The connection between the luminosity functions of young and old cluster systems is discussed on the basis of modelling the dynamical evolution of cluster systems. Finally, I briefly present the current ideas of why such a universal structure as the GCLF exists.

15.1 Introduction: What Is the Globular Cluster Luminosity Function?

Since the era of Shapley, who first explored the size of the Galaxy, the distances to globular clusters often set landmarks in establishing first the galactic, then the extragalactic distance scale. Among the methods which have been developed to determine the distances of early-type galaxies, the usage of globular clusters is one of the oldest, if not *the* oldest. Baum [5] first compared the brightness of the brightest globular clusters in M87 to those of M31. With the observational technology improving it became possible to reach fainter globular clusters and soon the conjecture was raised that the distribution of absolute magnitudes of globular clusters in a globular cluster system exhibits a universal shape, which can be well approximated by a Gaussian:

$$\frac{dN}{dm} \sim exp\frac{-(m-m_0)^2}{2\sigma^2},$$

where dN is the number of globular clusters in an apparent magnitude bin dm, m_0 is the "Turn-Over Magnitude" and σ the width of the Gaussian distribution. Also a representation by a "t5-function"

T. Richtler, The Globular Cluster Luminosity Function: New Progress in Understanding an Old Distance Indicator, Lect. Notes Phys. **635**, 281–305 (2003)
http://www.springerlink.com/

$$\frac{dN}{dm} \sim \frac{1}{\sigma}(1 + \frac{(m - m_0)^2}{5\sigma^2})^{-3}$$

introduced by Secker [82] found a wide-spread application.

This distribution is called the "Globular Cluster Luminosity Function". In the following "Globular Cluster Luminosity Function" is abbreviated by GCLF, "Turn-Over Magnitude" by TOM, and "Globular Cluster System" by GCS.

The conjecture that the GCLF is very similar in different galaxies, in particular that the absolute magnitude of the TOM has an almost universal value, has been first suggested by Hanes [37] (but also see the references in this paper). The reviews of Harris & Racine [39] , Hanes [38], Harris [40], Jacoby et al. [46], Ashman & Zepf [2], Whitmore [100], Tammann & Sandage [88], and Harris [43] demonstrated both the solidity and the limitations of this conjecture. They also show the progress which has been achieved during the past 20 years both in terms of the number of investigated GCSs and the accuracy of an absolute calibration.

The GCLF as a distance indicator has seen little application to spiral galaxies for several reasons: their GCSs are distinctly poorer than those of giant ellipticals, the identifications of clusters is rendered more difficult by the projection onto the disk, and the presence of dust causes inhomogeneous extinction. The investigation of GCSs of ellipticals or S0-galaxies is much easier due to the homogeneous light background, the richness, and the absence of internal extinction.

The application of GCLFs as distance indicators for early-type galaxies has a simple recipe: Given appropriately deep photometry of the host galaxy, identify GC candidates, as many as you can. In most cases this has to be done statistically by considering only objects with GC-like colors and by subtracting a hopefully well determined background of sources. Then measure their apparent magnitudes, draw a histogram and fit a suitable function, for instance a Gaussian, to determine the apparent TOM. Under the assumption that every GCS has the same absolute TOM, one can use the galactic system and/or the M31 system to calibrate it in terms of absolute magnitudes. Real data, however, make the derivation of the TOM somewhat more difficult, which will be discussed below. The most important restriction is probably that we can follow the GCLF down to faint clusters only in two galaxies, the Milky Way and Andromeda.

There is no physical reason why the GCLF should be a Gaussian or a t5-function. On the contrary, we shall later on learn about physical reasons why it is *not* a Gaussian. Closer scrutiny of the galactic cluster system indeed shows that its GCLF is not symmetric in that it exhibits an extended wing beyond the TOM for smaller masses (for example see Fig. 2 of Fall & Zhang [19]). But Gaussians empirically are fair descriptions for the bright side and most observations of GCLFs of distant galaxies seldom reach more than 1 mag beyond their TOMs, so this asymmetry is not relevant for measuring the TOM.

Figure 15.1 shows the GCLF for the galactic system (upper panel). It has been constructed on the basis of the "McMaster-catalog" (Harris [42]) using the horizontal branch (HB) brightness as the distance indicator and adopting the

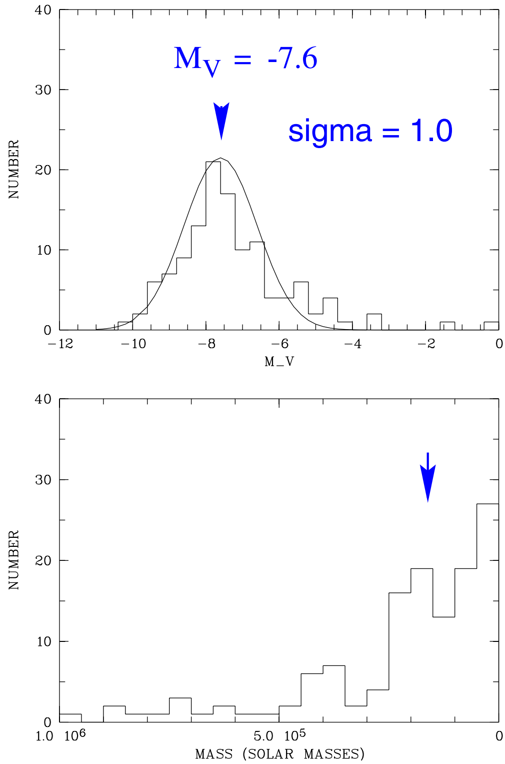

Fig. 15.1. The upper panel shows the globular cluster luminosity function for the galactic system together with a fitted Gaussian to the distribution. Only clusters with reddening E(B-V) less than 0.8 mag, and absolute magnitudes brighter than −4 have been considered in the fit. The lower panel shows the mass distribution in linear mass bins. The mass corresponding to the TOM is indicated

relation $M_V(HB) = 0.2 \cdot [Fe/H] + 0.89$ (Demarque et al. [10]). The Gaussian fit results in $M_V = -7.56 \pm 0.12$ for the TOM and 1.2 ± 0.1 for the dispersion of the Gaussian. The lower panel shows a histogram of the masses, assuming M/L = 2, where the mass which corresponds to the TOM is indicated. In this linearly binned histogram, there is no striking feature at this mass. *Indeed, the existence of a TOM is a consequence of the logarithmic magnitude scale in combination with a change of the power-law slope of the mass function.* We come back to this in a later section.

Throughout this review, we shall consider only TOMs in the V-band, because most modern published data, particularly those from the Hubble Space Telescope, have been obtained in V. Other photometric systems, most notably the Washington photometric system (Geisler et al. [28], Ostrov et al. [72], Dirsch et al. [13]) have been used for the investigations of GCSs as well.

Given the previous excellent reviews on GCLFs as distance indicators, what can be the scope of this contribution? A lot of new data has been published during the last years and it is now possible to compare GCLFs of early-type galaxies with other distance indicators on the basis of a much larger sample than has been possible before. The outstanding publication here is the catalog of distances based on surface brightness fluctuations (SBFs) (Tonry [92]). We shall see that the absolute calibration of GCLFs indeed agrees very well with that of SBFs, demonstrating that *most* GCSs of elliptical or S0-galaxies show absolute TOMs which are not distinguishable within the uncertainties of the measurements. Nevertheless, many discrepancies between GCLF distances and SBF distances exist. These galaxies are of particular interest and we shall discuss them as well.

Beyond the usefulness of the GCLF as a distance indicator is the question why there exists such a remarkably universal structure. Is there a universal formation law for globular clusters, which operates in the same way in such different galaxies as the Milky Way and giant ellipticals? This problem has to do with the initial mass function of globular clusters and the evolution of GCSs. Much progress has been achieved during the last years, on which we will also report.

15.2 Sources of Uncertainty

To begin with difficulties: Even if we trust the universal TOM, the actual measurement may appear straightforward according to the above recipe, but nevertheless one encounters many sources of uncertainty. The identification of GCs as resolved objects from the ground is only possible for the nearest early-type galaxies, for example NGC 5128 (Rejkuba [77]). Unfortunately, no modern investigation of the GCLF of NGC 5128 exists until now. Observations with the Hubble Space Telescope can resolve the largest clusters in galaxies as distant as about 20 Mpc (e.g. Kundu & Whitmore [50,51], Larsen et al. [56]). Therefore, the identification by ground-based observations normally has to use color criteria and the statistical discrimination against a “background”, which actually may consist of foreground stars and of unresolved background galaxies. That the latter contamination is a strong function of the color system used, is nicely shown in Fig. 15.2, taken from Dirsch et al. [13], which compares the color magnitude diagrams V-I and Washington C-T1 for the GCS of NGC 1399, the central galaxy in the Fornax cluster. The C-T1 color recognizes many background galaxies, which have an excess flux in the blue band C, while they are not noticeable in V-I, a color which has been widely used in HST investigations.

The nearest large galaxy clusters (Virgo and Fornax) have distance moduli of about 31. Thus, TOMs for GCSs at this distance and beyond will generally be fainter than V=23.5, where the photometric incompleteness (depending on the data quality) plays an increasingly dominant role. Then there are the factors of the numbers of found GCs and the distance itself: If the photometry does not reach the TOM and/or the GCS is not very rich, the resulting TOM is naturally

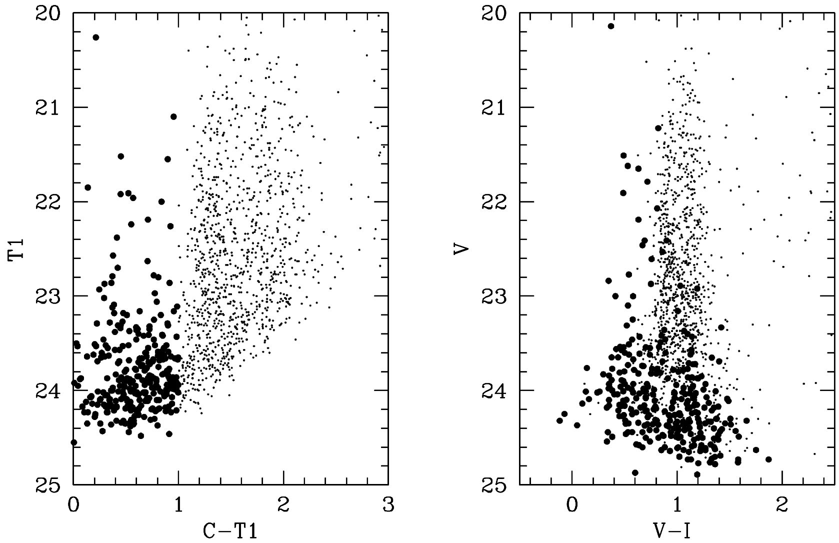

Fig. 15.2. This plot has been taken from Dirsch et al. [13]. It shows a comparison of the colour-magnitude diagrams of the GCS of NGC 1399 in the Washington system and in V-I. The many unresolved background galaxies (a few stars are mixed in as well) with an excess in the blue filter C fall outside the colour-range of the globular clusters in C-T1, whereas they populate that range in V-I and so add significantly to the background at faint magnitudes

less well defined than in the case of a nearby, rich GCS. Then it may depend on the adopted shape of the luminosity function. However, empirically the derived TOM is not very sensitive to whether a t5-function or a Gaussian is used, at least not in the case of well observed GCLFs (e.g. see Della Valle et al. [14] for the GCLF of NGC 1380).

Moreover, the width of the adopted fitting function can be left free or can be fixed. Larsen et al. [56] performed t5-function fits to their sample of 14 early-type galaxies both with the width as a fit parameter and with a fixed with of $\sigma_t = 1.1$ mag. To gain an impression of the effect on the TOM, we show Fig. 15.3, where the TOM corresponding to a free width is plotted versus the difference TOM(var)-TOM(nonvar). Leaving the two outliers NGC 1023 and NGC 3384 aside, the standard deviation of the differences is 0.13 mag. Then there are different ways to fit, for example maximum likelihood methods or direct fits.

One must also not forget the uncertainty of the foreground absorption and another factor which is difficult to nail down: the photometric calibration of the respective data set and the actual realization of the used photometric standard system.

The above error sources are always there, even if the TOM would be strictly universal, which one would not expect: For a given mass the luminosity of a GC depends on its metallicity in the sense that metal-poor clusters are brighter in the optical (e.g. Girardi [30]), but the metallicity distribution within a cluster

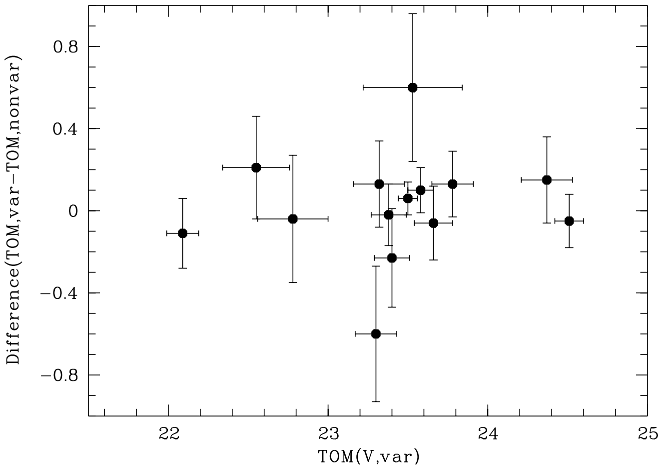

Fig. 15.3. This plot is based on HST observations of a sample of 14 early-type galaxies by Larsen et al. [56]. It shows the differences of the TOMs derived from the t5-function fits leaving the width either variable or non-variable versus the TOM derived by fits with a variable width. The two most deviating galaxies are NGC 1023 and NGC 3384

system is not expected to be the same for all early-type galaxies. So one should principally correct for this as well (Ashman et al. [3]). There is also empirical evidence for a metallicity dependence of the TOM: Larsen et al. [56] find by HST observations in V and I of a sample of 15 early-type galaxies the TOMs for red clusters to be fainter than those for blue clusters by $\Delta m_V \approx 0.4$ mag, which is somewhat larger than predicted by theory. However, as we shall see, it is possible that part of this difference is due to an intrinsically fainter TOM of the red cluster population, so it is difficult to quantify the metallicity effect.

Also if the initial cluster mass distribution would be the same in all galaxies, destruction processes like disk shocking or evaporation are expected to act differently in different environments and may create intrinsically varying TOMs (see Sect. 15.10 for this topic). Last, but not least, one has to assume that the members of a GCS all have the same old age, while we shall see that the number of examples where this is not the case is growing.

Given all these possible error sources, it may come as a surprise that GCLFs seem to work so well as distance indicators, and it is plausible that an accuracy of, say, 0.2 mag or less can only be achieved in the case of rich GCSs and a high quality dataset.

15.3 The Galaxy and M31

The two massive galaxies where the GCLF can be best observed down to faint clusters are the Milky Way and M31. A calibration of the absolute TOM therefore via these galaxies always has to face the caveat that both are spiral galaxies and the application to early-type galaxies may not be justified. However, as we will see, the zero-point gained from using the Galaxy and M31 as fundamental calibrators is in very good agreement with the one obtained from the comparison with the method of surface brightness fluctuations (Tonry et al. [92]), which at present offers the largest and most homogeneous catalog of distances to early-type galaxies.

The history of the investigations of the galactic GCS and that of M31 involves the work of many people. To be short, we refer the reader to Harris [43] and Barmby et al. [4] (and references therein) for the Galaxy and M31, respectively. Harris [43] quotes $M_V = -7.40 \pm 0.11$ for the galactic TOM and $\sigma = 1.15 \pm 0.11$. Barmby et al. [4] quote for the apparent TOM of the M31 system $m_V = 16.84 \pm 0.11$ and $\sigma = 1.20 \pm 0.14$. The distance modulus of M31 is $m - M_{M31} = 24.44 \pm 0.2$ (Freedman & Madore [23]), which translates into an absolute TOM of $M_V = -7.60 \pm 0.23$. The weighted average of these two TOMs is -7.46 ± 0.18, which we will compare with the distance moduli derived from surface brightness fluctuations.

15.4 The Data

During the last few years, many new TOMs of early-type galaxies in the V-band have been published. The majority of them are based on HST observations and stem from the papers by Kundu & Whitmore [50], Kundu & Whitmore [51], and Larsen et al. [56]. Other new papers on individual galaxies are from Okon & Harris [71], Kavelaars et al. [47], Woodworth & Harris [104], Drenkhahn & Richtler [15]. For TOMs published earlier we refer the reader to the compilation of Ferrarese et al. [20] and references therein. As mentioned above, the main problem with such a data set is its inhomogeneity for a variety of reasons. For example, Kundu & Whitmore [50] and Kundu & Whitmore [51] fitted Gaussians with both variable and fixed dispersions (1.3 mag) to their GCLFs. We adopt their TOMs resulting from the fixed dispersions because of the larger number of galaxies included, leaving out a few TOMs with very large uncertainties. Larsen et al. [56] fitted t5-functions with both non-variable and variable widths, from which we adopt the latter because the scatter of the dispersions points to real differences. However, the TOMs are not strongly influenced by whether the dispersions are fitted or keep fixed. Since we are interested rather in the bulk properties of the available data than in hand-selected data according to certain quality criteria, we included also work which was mentioned but rejected by Ferrarese et al.

We end up with 102 TOMs (corrected for foreground extinction and including a few double and triple measurements) in the V-band for 74 galaxies, which should be almost complete from the present day back to 1994.

15.5 The Hubble Diagram

Can we say something about the Hubble constant from our data set, assuming that the TOM indeed has the universal value of $M_V = -7.46 \pm 18$, adopted from

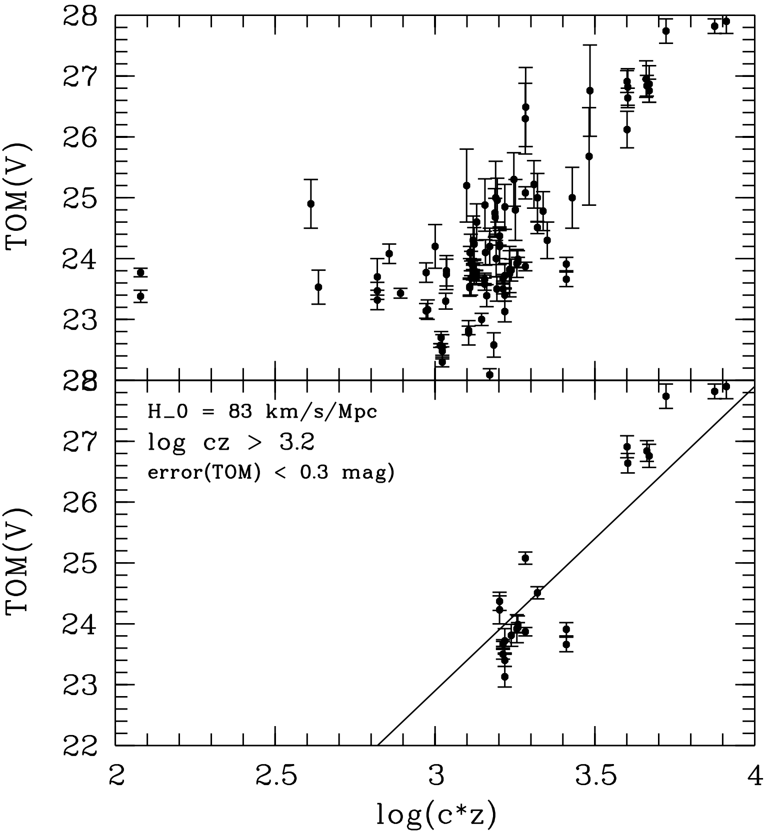

Fig. 15.4. The upper panel shows all of our collected TOMs versus their recession velocities, defined here as the radial velocities related to the microwave background. Many of these galaxies obviously have peculiar velocities of the same order as their recession velocities, in which case this definition is not adequate. The lower panel selects those galaxies with TOM uncertainties less than 0.3 mag and log(cz) larger than 3.2 to reveal a Hubble constant of 83 km/s/Mpc. Also here, the TOMs do not define very well a slope of 5 in the Hubble diagram. Note that the group at V=27 are not directly measured TOMs, but deduced from surface brightness fluctuations, see Lauer et al. [60] and Kavelaars et al. [47]

the Milky Way and M31? A set of standard candles whose redshifts are only due to their recession velocities give a straight line in the Hubble diagram when their apparent magnitudes (their TOMs in our case) are plotted versus their redshifts according to

$$m = 5 \cdot log(c \cdot z) - 5 \cdot log(H_0) + M - 25,$$

where H_0 is the Hubble constant in units of km/s/Mpc and M the constant absolute magnitude of the standard candles.

The upper panel of Fig. 15.4 shows the Hubble diagram for our entire database. The velocities of the host galaxies have been *individually* related to the microwave background (which of course is not a good approach). It is obvious that such a diagram is not suitable for deriving the Hubble constant. Many objects show radial velocities which are simply not in the Hubble flow, most strikingly for NGC 4406 (which is represented by the double measurement with the lowest velocity). If we select galaxies with $\log c{\cdot}z > 3.2$ and furthermore only those with uncertainties less than 0.3 mag, we end up with about 20 galaxies. If these galaxies are used to calculate the zero point in the Hubble relation, it gives a Hubble constant of 83 km/s/Mpc, adopting a TOM of $M_V = -7.5$ mag. It is clear that one cannot be content with this. Standard candles in a Hubble diagram should define a straight line with a slope of 5, whereas the slope in this diagram is clearly steeper. To resolve this discrepancy, one has to carefully look into each individual GCS, select those TOMs with the highest degree of trustworthiness, and then investigate the recession velocities of individual galaxies. The measured radial velocities of galaxies within the space volume under consideration may not be good indicators for their recession velocities due to the existence of large scale peculiar motions, which are under debate (e.g. Tonry et al. [91]).

Following Kavelaars et al. [47], a better way might be to consider only groups of galaxies, average the TOMs and assign a recession velocity to each group. Kavelaars et al. use the Virgo, the Fornax and the Coma cluster and arrive at 69 ± 9 km/s/Mpc for the Hubble constant. But to fix the recession velocities even for these three galaxy clusters is far from trivial.

To avoid very lengthy discussions, a better way of deriving the Hubble constant is perhaps the use of standard candles which are so distant that peculiar velocities act only as minor perturbations of the Hubble flow, i.e. the Hubble diagram of Supernovae Ia (Freedman et al. [24]).

15.6 The Comparison with Surface Brightness Fluctuations

To evaluate the accuracy and reliability of the method of the GCLF, we must compare it with other distance indicators of early-type galaxies. This results in a complicated task, if one's objective is to select the most reliable measurements, to quantify possible biases inherent to different methods, and to discuss the uncertainties claimed by the authors. See for example Ferrarese et al. [20], who conclude that GCLFs do not provide reliable distances, mainly based on a deviating distance to the Fornax cluster, and Kundu & Whitmore [50], who contrarily find GCLF distances as least as accurate as distances from surface brightness fluctuations. We do not want to follow these lines but rather investigate what can be seen from the entirety of TOMs if they are compared with a distance indicator which provides distances to most of our GCSs.

Today, the most homogeneous and largest sample of distances to early-type galaxies is the catalog resulting from the survey of surface brightness fluctuations (SBFs) (Tonry et al. [92]; see also the preceding papers by Tonry et al. [90], Blakeslee et al. [6], and Tonry et al. [91]) which contains distances to about 300

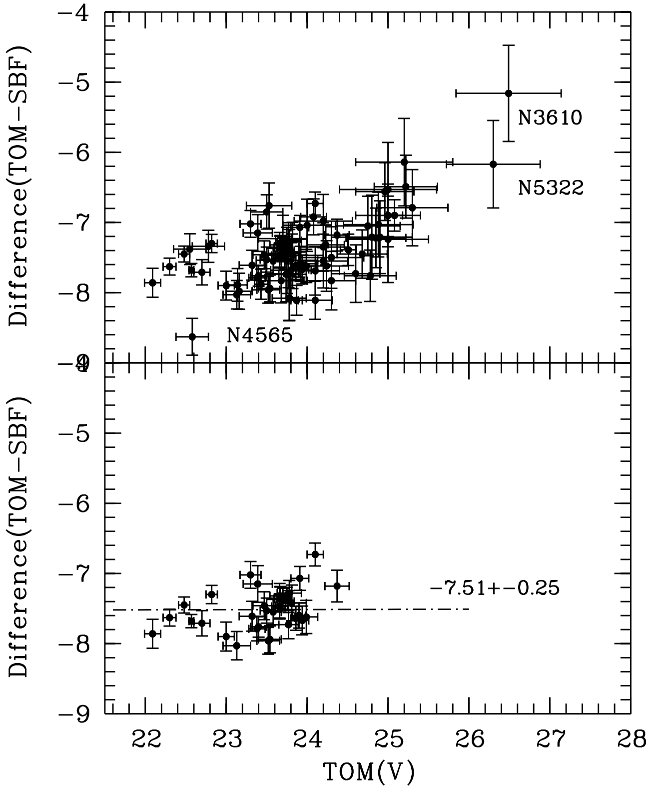

Fig. 15.5. The *upper panel* shows the difference between the TOMs and the SBF distance moduli. For faint TOMs exists a trend to overestimate the distance with respect to the SBF distance. The *lower panel* selects those galaxies with uncertainties of both the TOM and the SBF distance less than 0.2 mag. The mean difference agrees very well with the absolute TOMs from the Milky Way and M31

galaxies. Therefore we restrict ourselves to a comparison with this important distance indicator. Basically, it analyzes that part of the pixel-to-pixel scatter of a CCD image of an early-type galaxy which is caused by the finite number of bright unresolved stars covered by each CCD pixel. These fluctuations of the surface brightness are large for nearby galaxies and small for more distant galaxies.

Figure 15.5 plots for all galaxies in our database (irrespective of whether there are double or triple measurements) the TOM versus its difference to the distance moduli from Tonry et al. [92]. The error bars of the differences simply are the square roots of the quadratic sums of the uncertainties in the GCLF and SBF distance moduli. The first impression seems to be somewhat discouraging. Where we would have expected to see a horizontal line at an ordinate value of −7.5 with some scatter, we see a large spread with often dramatic deviations, particular for the fainter TOMs. What is striking is that the deviating galaxies do not scatter symmetrically around a mean value, but that the faint TOMs give systematically larger distance moduli than do the SBFs. A direct and naive conclusion could be that perhaps the very faint TOMs are observationally not reached and that an extrapolation from the bright end of the luminosity function to the TOM gives a TOM which is systematically too faint. In fact this is not the case and the strongly deviating TOMs belong to interesting galaxies (we come back to this point).

But also at the bright end there are irritations. The deviating galaxy at -8.6 is NGC 4565, and even the one with the brightest TOM, the Sombrero galaxy NGC 4594, does not fit very well to our assumed universal value. Both are the only spiral galaxies in our sample. We note that the GCS of NGC 4565 is very poorly populated (Fleming et al. [22]), so this deviation might not bear much significance.

15.7 Absolute TOMs and the Distances to Virgo and Fornax

However, if we select according to the quoted uncertainties, the situation starts to look better. The lower panel of Fig. 15.5 plots all galaxies where the uncertainties of both the SBF distance and the TOM according to the various authors are lower than 0.2 mag. The dispersion of the scatter is 0.25 mag and thus is compatible with the claimed selection. Thus we can confirm the statement by Kundu & Whitmore [51] that the GCLF distances, at least for the sample under consideration, are not less accurate than the SBF distances. The mean difference is -7.51 mag with a dispersion of 0.24 mag and thus in excellent agreement with the zero-points coming from the Milky Way and from M31. These three zero-points give a weighted mean of -7.48 ± 0.11.

The average TOM of 8 galaxies in the Fornax cluster is 23.79 mag with a dispersion of 0.17 mag, the one for the Virgo cluster (16 galaxies) is 23.62 with a dispersion of 0.16 mag, which translate into distance moduli for Fornax and Virgo of 31.27 ± 0.2 and 31.10 ± 0.2, respectively. The corresponding distance moduli from the SBFs are 31.02 ± 0.15 and 31.49 ± 0.12. A discussion of the absolute calibration is not our objective. However, we can conclude that indeed many GCLFs can provide good distances but one is reluctant to label the GCLF "universal" at this point because there are too many deviations with the SBF distances. We shall see that these deviations are apparently related to the existence of intermediate-age populations in early-type galaxies.

15.8 Deviations and Intermediate Age Populations

Like in human society, deviations from the norm may be sometimes more interesting and illustrative than reconciliation with it. Let's look at Fig. 15.6. Plotted are those TOMs which deviate from the "universal" TOM by more than what is suggested by their uncertainties. Since we see from Fig. 15.5 that the scatter

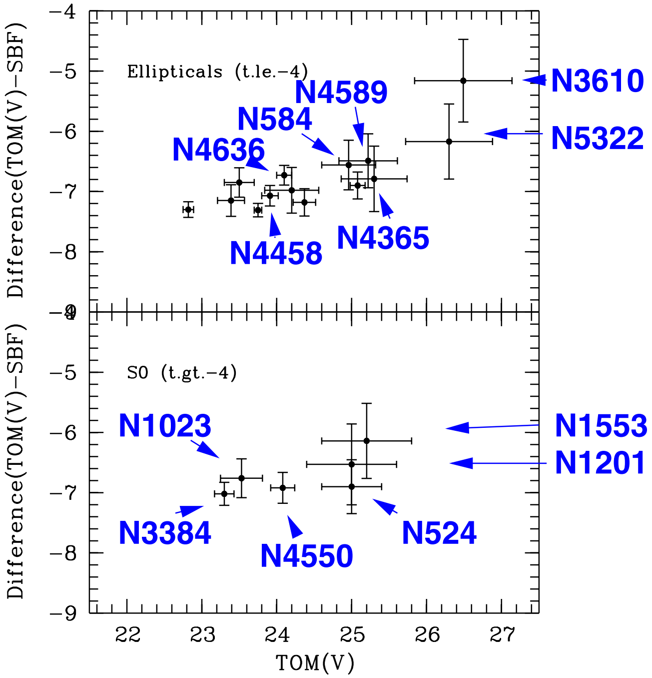

Fig. 15.6. This graph shows those galaxies, whose GCLF distances deviate more than suggested by the measurement uncertainties from SBF distances. The upper panel shows the elliptical galaxies (t-parameter less than −4), the lower panel the S0-galaxies (t-parameter higher than −4). In the majority of these objects, one finds evidence that the stellar populations are not exclusively old. A certain fraction of intermediate-age clusters would make the deviation from the SBF distance understandable, as explained in the text

is by no means symmetric but that the most striking deviations prefer a TOM, which is systematically fainter than expected from the SBF distances, only these fainter TOMs are shown.

Among the elliptical galaxies, the largest deviation is shown by NGC 3610, admittedly with a large error. But more interesting is the fact that this galaxy violates one important condition for the TOM to be a viable distance indicator, namely that its GC population is old. NGC 3610 is known to host GCs of intermediate-age. Whitmore et al. [99] and Whitmore et al. [102] estimate an age of about 4–6 Gyr for the red (and presumably metal-rich) GCs which plausibly have their origin in a merger event (Schweizer & Seitzer [80]). However, many of the metal-rich clusters probably had been brought in by the progenitor galaxies. Strader et al. [85] find among their sample of 6 metal-rich clusters only one with an age of 1–5 Gyr. But since the other clusters are located in the outer halo, this cannot strongly constrain the fraction of intermediate-age metal-rich clusters.

As we later shall discuss, the GCLF is expected to change its TOM, resulting in fainter TOMs for younger cluster populations. Indeed, Whitmore et al. [102]

find a TOM of 25.44 ± 0.1 for the blue clusters alone, while no TOM is visible at all for the red cluster population. This decreases the difference to the SBF distance, however, it still remains large. On the other hand, the existence of an intermediate-age population also influences the SBF distance by enhancing the fluctuation signal (mainly through the enhanced number of asymptotic giant branch stars) and thus would lead to a spuriously smaller distance without any correction term. Normally, the color V-I is used to correct for differences in the population (see Liu et al. [62] and Blakeslee et al. [7] for a deeper discussion). Whether this correction is always sufficient or fails in some cases, cannot be discussed here.

So the suspicion arises that a difference between the GCLF distance and the SBF distance may in general be produced by intermediate-age GCs. This conjecture indeed gets support by looking at other galaxies in Fig. 15.6. Besides NGC 3610, younger clusters have been detected in NGC 4365 (Larsen et al. [59], Puzia et al. [75], also conjectured to be a merger remnant (Surma & Bender [87]). Note, however, that Davis et al. [11] did not find evidence for intermediate-age populations from their integral-field spectroscopy in the galaxy itself.

Other ellipticals show strong H_β-lines, indicating as well a younger population, and NGC 4636 hosted a supernova Ia, whose progenitors should also be of intermediate age (e.g. Leibundgut [61]).

However, there are also examples where the existence of an intermediate-age population is not supported by the present literature. For NGC 3379 and NGC 4472, the difference to the SBF distance is anyway marginal, perhaps still so for NGC 4660. The case of NGC 4291 is hard to assess because of the large uncertainties, but NGC 4473 and NGC 5846 pose a problem. The spectroscopic evidence for intermediate-age populations normally come from the central regions and it may be that the outer parts, from which the globular clusters are sampled, still host younger populations. The other possibility is that either the SBF distance or the TOMs are erroneous. In any case one has to wait for further observations.

Turning to the S0's, NGC 1023 and NGC 3384 are perhaps candidates for hosting intermediate-age populations. Both galaxies show indications of star formation activity in their inner regions (Kuntschner et al. [52], Sil'chenko [83]). However, the faint TOM of NGC 1023 does not seem to be related to intermediate-age clusters. Larsen & Brodie [55] identified beside the "normal" compact GCs (both red and blue) a population of faint extended red GCs. The inclusion of these latter objects in the luminosity function is mainly responsible for the deviating position of NGC 1023. Leaving them aside results in a distance modulus well agreeing with the SBF distance. A similar finding is reported for NGC 3384 by Larsen et al. [56]. Brodie & Larsen [8] found that these faint extended clusters belong to the disk populations of their host galaxies and quote an age of at least 7 Gyr.

NGC 4550 contains two counterrotating stellar disks (Rix et al. [79]) and molecular gas has been detected by Wiklind & Henkel [103] which is supposed to have its origin in a recent accretion event. Similarly striking findings are not reported for NGC 1553 or NGC 1201. However, both are shell galaxies (e.g. Longhetti et al. [64]), which hints at earlier interactions or mergers.

NGC 524 again is a supernova Ia host galaxy. The question whether the appearance of a supernova of type Ia in an early-type galaxy always indicates an intermediate-age stellar population is beyond the scope of this article, but a few remarks on GCSs of Ia host galaxies are appropriate. NGC 1316 in the Fornax cluster, a merger remnant and host to two SN Ia's, has a GCS where 2–3 Gyr old clusters have been found, probably formed during the merger event (Goudfrooij et al. [34,35]). Deep VLT and HST photometry does not reveal a TOM; the GCLF increases steadily down to beyond the observation limit (Grillmair et al. [36], Gilmozzi, this volume). In the work of Gómez & Richtler [33] who quote a TOM which is in good agreement with the SBF distance, the TOM was not actually reached, but extrapolated, and the agreement with the SBF distance perhaps stems from the fact that in the outer region, where this data has been sampled, the fraction of intermediate-age clusters is low.

Other early-type Ia host galaxies with investigated GCSs, where intermediate-age cluster populations have been identified, are NGC 5018 (SN 2002 dj) (Hilker & Kissler-Patig [44]) and NGC 6702 (SN 2002cs) (Georgakakis et al. [29]). Unfortunately, NGC 6702 is too far for an analysis of its GCLF and the TOM of the NGC 5018 system must be largely extrapolated, so it remains uncertain.

But we also have examples of Ia hosts, where the GCLF distance agrees quite well or is even smaller than the SBF distance, e.g. NGC 4621 (2001A), NGC 1380 (1992 A), NGC 4526 (1994D) and NGC 3115 (1935B). If there are intermediate-age populations in these galaxies, they do not seem to contaminate the GCLF.

An interesting note regarding Ia host galaxies and GCSs can be made from the paper of Gebhardt & Kissler-Patig [27]. These authors analyze the V-I colour distribution of the GCs of a sample of early-type galaxies. Their "skewness" parameter measures the asymmetry of the colour distribution with respect to the mean colour. The two GCSs which are skewed strongest towards red (e.g. metal-rich) clusters both belong to Ia host galaxies (NGC 4536, NGC 4374) as well as does the fourth in this sequence (NGC 3115).

All this, of course, does not mean that in those cases where GCLF and SBF distances agree within the uncertainties, the stellar populations are necessarily old. However, a comparison with the compilation of galaxy ages by Terlevich & Forbes [89] reveals that among the ellipticals, only NGC 720 (3.4 Gy) is quoted with an age lower than 5 Gyr. Among the S0's we have only NGC 3607 (3.6 Gyr) and NGC 6703 (4.1 Gyr), i.e. strikingly less candidates for hosting younger populations than among the deviating ones.

Summarizing, it seems that many of the cases where the SBF distance does not agree with the GCLF distance, can be related to the presence of intermediate-age populations, particularly among the ellipticals.

Table 15.1 lists all galaxies in Fig. 15.6 with their TOM, its difference with the SBF distance, references for the TOM and a reference for other properties of the host galaxy.

Table 15.1. A list of galaxies whose TOMs indicated larger distances than the SBF distances beyond the uncertainty limits. For many of these galaxies one finds evidence for the existence of intermediate-age (IM) populations

Name	TOM	diff(TOM-SBF)	Ref.	Remarks
	Ellipticals			
N3610	26.49 ± 0.65	-5.16 ± 0.69	[50],[102]	IM clusters
N5322	26.30 ± 0.58	-6.17 ± 0.62	[50],[73]	IM age
N4589	25.22 ± 0.39	-6.49 ± 0.45	[50],[93]	$H\beta$ strong
N0584	24.96 ± 0.36	-6.56 ± 0.41	[50],[49],[93]	$H\beta$ strong
N4636	24.10 ± 0.10	-6.73 ± 0.16	[48]	Ia host
N4291	25.30 ± 0.44	-6.79 ± 0.54	[50]	old?
N4697	23.50 ± 0.20	-6.85 ± 0.24	[47],[73]	IM age
N5846	25.08 ± 0.10	-6.90 ± 0.22	[26],[52]	old?
N4458	24.20 ± 0.36	-6.98 ± 0.38	[50],[52]	$H\beta$ strong
N4473	23.91 ± 0.11	-7.07 ± 0.17	[50],[52]	old?
N4660	23.39 ± 0.18	-7.15 ± 0.26	[50],[52]	old?
N4365	24.37 ± 0.15	-7.18 ± 0.23	[56],[75],[87]	IM clusters
N3379	22.82 ± 0.07	-7.30 ± 0.13	[50],[52]	old?
N4472	23.75 ± 0.05	-7.31 ± 0.11	[50],[52]	old?
	S0			
N3384	23.30 ± 0.13	-7.02 ± 0.19	[56],[52]	extended GCs, $H\beta$ strong
N4550	24.08 ± 0.16	-6.92 ± 0.26	[50],[103]	molecular gas, merger
N0524	25.00 ± 0.40	-6.90 ± 0.45	[51]	Ia host
N1023	23.53 ± 0.28	-6.76 ± 0.32	[55],[8],[83]	extended GCs, IM nucleus
N1201	25.00 ± 0.60	-6.53 ± 0.67	[64]	shell galaxy
N1553	25.20 ± 0.60	-6.14 ± 0.62	[64]	shell galaxy

15.9 Why Does It Work?

What could be the reason for an universal TOM of old GCSs? A globular cluster with $M_V = -7.5$ mag has a mass of about 150000 $M_\odot$, adopting an average M/L_V of 2.5 (Pryor & Meylan [74]). Is this particular mass somehow distinguished? One has to realize that the magnitude scale is logarithmic. Binning in linear luminosity units instead of magnitudes, we would not see any striking feature at the luminosity corresponding to the TOM. After remarks by Surdin [86], Racine [76], and Richtler [78], regarding the power-law nature of the linear luminosity function of galactic GCs, McLaughlin [65] put this concept on a formal basis. If the luminosity function can be described as $NdL \sim L^{\alpha(L)}$, where N is the number of clusters found in the luminosity interval L+dL and $\alpha(L)$ a function of L, then one has in magnitudes $NdM_V \sim 10^{0.4M_V(1-\alpha)}$, i.e. the TOM is found where $\alpha(L)$ just changes from smaller than -1 to larger than -1. So the location of the TOM does not express a specific physical property at this particular mass. However, the underlying universal property must be a universal mass function. Harris & Pudritz [41] first investigated the mass function of GCSs of different galaxies, assuming a constant M/L. They found that such diverse systems as that of the Milky Way and of M87 can be described by a common power-law exponent of $\alpha \approx -1.8$ for masses higher than about 10^5 solar masses. Larsen et al. [56] found in their larger sample on the average $\alpha = -1.74 \pm 0.04$ between

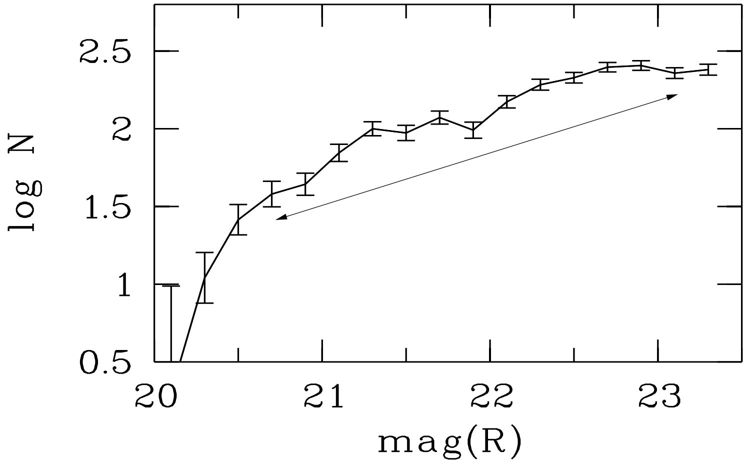

Fig. 15.7. This plot shows the luminosity function in the R-band for the GCS of NGC 1399, the central galaxy in the Fornax cluster (Dirsch et al. [13]). This luminosity function comprises about 2600 clusters brighter than R=23 and thus is one of the best available. For magnitudes fainter than R=20.5, the linear luminosity function is well represented by a power-law with an exponent of about −2 (the slope s in the present diagram is related to the power-law exponent α by α = s/0.4 - 1). It steepens considerably for brighter magnitudes. However, a representation by a log-normal function for the entire magnitude range is as good

10^5 and 10^6 solar masses. However, in very rich GCSs, such as that of M87 or NGC 1399, the slope becomes distinctly steeper for cluster masses larger than about 10^6 solar masses (see Fig. 15.7).

Ten years ago, GCSs had been almost exclusively associated with old stellar populations. Meanwhile, systems of young globular clusters have been detected in many merging galaxies, the most prominent ones being the Antennae NGC 4038/4039 (Whitmore & Schweizer [98]) and NGC 7252 (Whitmore et al. 1993) (see Whitmore [101] for a complete listing until 2000), but also in normal spiral galaxies (Larsen & Richtler [53], Larsen & Richtler [54]).

Determinations of the luminosity functions resulted so far consistently in power-laws with an exponent of about −2, without compelling indications that this exponent changes over the observed luminosity range as in the case of the GCSs of giant ellipticals (Whitmore [101]), given the uncertainties caused by internal extinction and by the age spread among a cluster system. There was some debate regarding the mass function of GCs in the the Antennae as derived from the luminosity function. The Antennae may show a bend at about $M_V = -11$, becoming steeper towards the bright end (Whitmore [101], Zhang & Fall [105]). Fritze-v. Alvensleben [25]) found a log-normal mass distribution like for old systems, which was contradicted by Zhang and Fall ([105]), who attributed this difference to the effect of varying extinction and ages, and found a uniform power-law. If we assume that young GCs are born obeying a universal luminosity function like $dN/dL \sim L^{-2}$, and accordingly with a mass function of the same shape, then we must ask, what processes can transform such a luminosity function into the approximately log-normal luminosity functions of old GCSs. If these processes work in a universal manner, then the universality of the TOM could be explained.

15.10 How Does an Initial Cluster Mass Function Change with Time?

A young star cluster is exposed to different destruction mechanisms. If it is still young, mass loss from massive star evolution plays an important role. At later times, two-body relaxation, dynamical friction, and tidal shocks, when the cluster enters the bulge region of its host galaxy or moves through a disk, can be efficient in decreasing the cluster's mass, depending on its mass, its density and its orbit in the host galaxy. The most general statement is that low-mass clusters are more affected by disruption processes than high-mass clusters, so an initial power-law of the mass distribution is more strongly destroyed on the low mass end and may develop a shape which finally resembles a log-normal distribution.

Many people have worked on this problem, among them Aguilar et al. [1], Okazaki & Tosa [70], Elmegreen & Efremov [17], Gnedin & Ostriker [31], Murali & Weinberg [67–69], Vesperini [94,95], Fall & Zhang [19]. We cannot present all work in detail, instead we choose the analytical model by Fall & Zhang in order to illustrate the most important results. Figure 15.8 (Fig. 1 of Fall & Zhang 2001) shows the time evolution for three different masses for a cluster which is on a slightly elongated orbit. The dotted lines indicate the effect of two-body relaxation alone. The dashed lines additionally include gravitational shocks, and the solid lines add the effect of mass loss by stellar evolution.

Under a wide variety of conditions, the mass function of a GCS develops a peak which is progressively shifted to higher masses, as the evolution of the cluster system proceeds. After, say, 12 Gyr, Fall & Zhang get from their model a peak mass (in logarithmic bins) which may well represent the mass corresponding to the TOM observed in the Milky Way or in elliptical galaxies (Fig. 15.9).

However, it seems that the assumption of a power-law with an exponent around -2, as suggested by the young cluster systems in merging galaxies, cannot reproduce well the log-normal shape in the mass-rich domain observed in many galaxies. This is because the shape of the mass function above a few times $10^6 M_\odot$ practically does not change by evolutionary processes. Instead, an initial log-normal mass function works much better in resembling the bright end of the luminosity function of ellipticals (Vesperini [95,96]) (but see the section on the brightest clusters).

The dynamical evolution of a GCS may raise doubts on the general quality of the GCLF as a distance indicator, if the evolutionary history of a GCS is not negligible. The GCLF might also depend on whether the TOM is measured at small or large galactocentric radii. In the inner parts of a galaxy, the TOM is expected to be brighter. Gnedin [31] finds significant differences in this sense for the Milky Way, M31, M87, which for M31 has been confirmed by the improved sample of

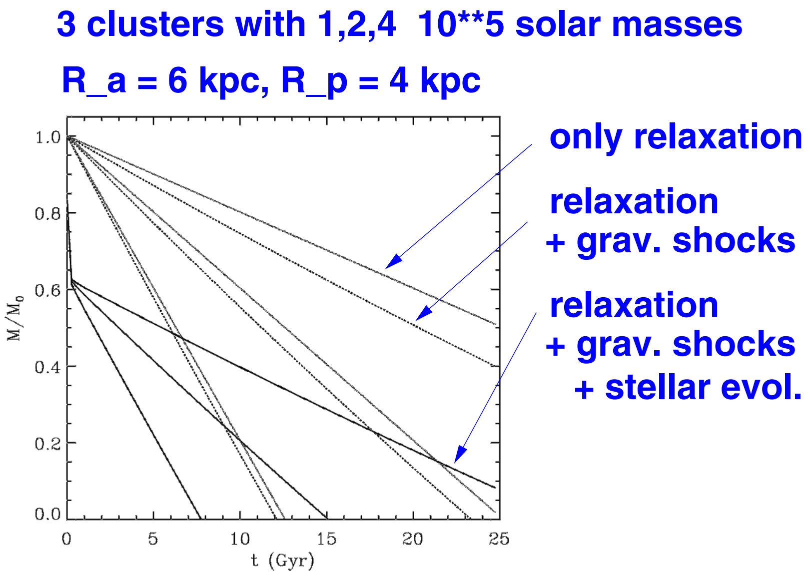

Fig. 15.8. This plot is taken from Fall & Zhang [19]. It shows for three different clusters ($10^5, 2 \cdot 10^5, 4 \cdot 10^5$ solar masses) the cumulative growth of the relative mass loss by two-body relaxation (*upper line*), two-body relaxation plus tidal shocks (middle line), and added to that the mass loss from stellar evolution (*lower line*)

Barmby et al. [4]. Also the brighter TOM (with respect to the SBF distance) of the Sombrero may have its explanation in the dynamical history of this GCS. The Sombrero possesses an extraordinary large bulge, where dynamical shocks might work more efficient than in other galaxies (naively assuming, of course, that the SBF distance is correct). Note, however, that the HST-observations by Larsen et al. [55] reveal a GCLF for the Sombrero whose TOM is not very well defined.

One of the best investigated galaxies among those which shows a marked difference between the GCLF and the SBF distance is the elliptical galaxy NGC 3610. Scorza & Bender [81] found a disk and other morphological signatures indicating previous interaction or a merger event. Its location in Fig. 15.5 corresponds to the TOM quoted by Kundu & Whitmore [50]. In a subsequent paper, Whitmore et al. [102] performed a more detailed investigation of the GCS of NGC 3610, based on new HST data. Figure 15.10 shows the LFs separately for the blue and the red clusters. While for the blue clusters the TOM is measured to be at $V = 25.44 \pm 0.1$, the red clusters show a LF rising until the photometry limit. Whitmore et al. combined the destruction model of Fall & Zhang with evolutionary models of stellar populations. The resulting model LFs are indicated in the lower panel. The data are not yet deep enough to show a turn-over for the red clusters, which by the models is predicted to be at around $V \sim 26$. Whitmore et al. state that in the context of the Fall & Zhang models, the brightening of the

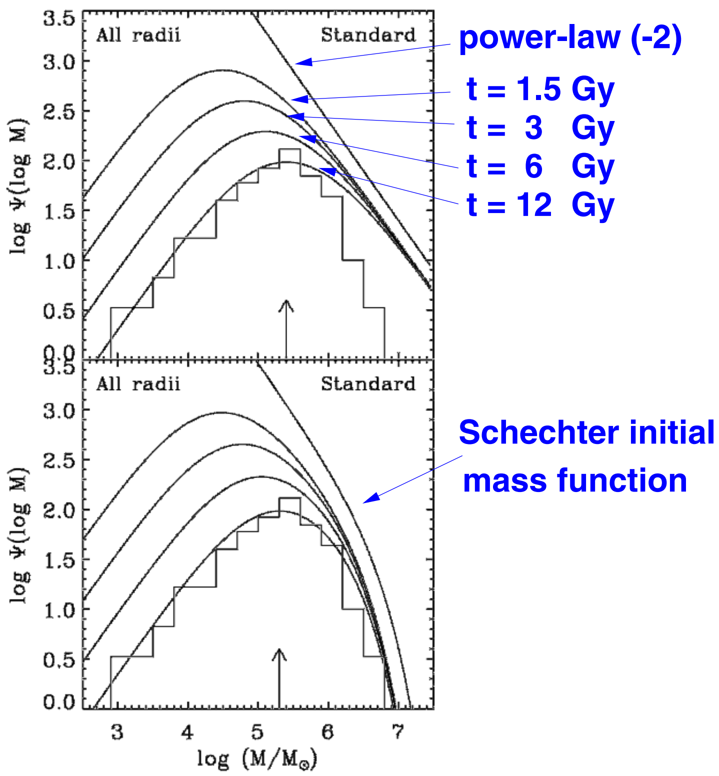

Fig. 15.9. This plot is taken from Fall & Zhang [19]. It shows the evolution of a cluster system for two different initial mass functions: a power-law with an exponent of -2 (*upper panel*) and a Schechter function (*lower panel*)

TOM during the dynamical evolution of the cluster system is almost completely balanced by the fading of the stellar population during this time. This may well be an explanation for the universality of the TOM. However, given the approximate nature of the analytic models of Fall & Zhang and the the dependence of the destruction processes on the actual environment, this probably does not apply to every galaxy.

We therefore can conclude that in the case of NGC 3610, a large part of the deviation of the GCLF distance from the SBF distance comes from the fact that the contribution of the presumably younger red clusters causes a fainter TOM than from the blue, metal-poor and presumably older clusters alone. But also when we use only the TOM of the blue clusters to determine the distance modulus, which then would be 32.94, a significant difference remains to the SBF modulus, which is 31.65. This cannot be resolved here. The modelling of SBF's accounts for the population structure (Liu et al. [63], Blakeslee et al. [7]) but may fail in extreme cases.

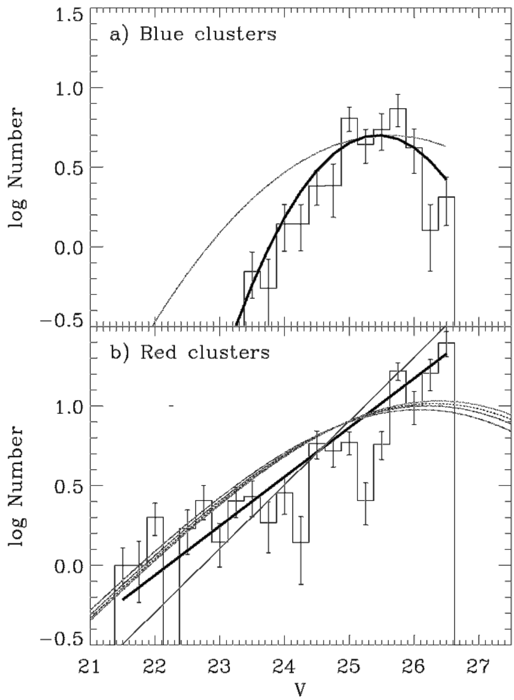

Fig. 15.10. This plot is taken from Whitmore et al. [102]. It shows the luminosity functions (LFs) of blue (upper panel) and red (lower panel) globular clusters in NGC 3610. The blue clusters exhibit a TOM at V = 24.55. The solid line marks a Gaussian fit with $\sigma = 0.66$, the dotted line with $\sigma = 1.1$, which obviously do not fit. The LF of the red clusters increases with no sign of a flattening. The thick solid line is a power-law fit with $\alpha = -1.78$. The other curves are model LFs based on Fall & Zhang [19] in combination with population synthesis models of Bruzual & Charlot (unpublished). The thin solid line is the zero-age LF (power-law with $\alpha = -2$), the others correspond to ages of 1.5 Gyr, 3 Gyr, 6 Gyr, and 12 Gyr (from top to bottom). The TOMs are hardly distinguishable because in these models the brightening of the TOM by dynamical evolution is balanced by the fading due to stellar evolution

15.11 The Brightest Clusters

Regarding the significance of the GCLF as a distance indicator, its shape in the domain of the brightest clusters is less important. But since dynamical models indicate that the GCLF for clusters more massive than about $10^6 M_\odot$ is not modified by destruction processes, they bear potential information about the formation of a GCS. Two different views on a GCLF like that of Fig. 15.7 exist: It can be seen as a power-law with an exponent around -2 with a cut-off at higher masses or it can be seen as a log-normal function.

Adopting the first view, the GCLF would resemble in large parts the LF found in young cluster systems. The cut-off at high masses may have different reasons.

Possibly these very massive clusters (the brightest clusters in NGC 1399 have about $10^7 M_\odot$) are not globular clusters in the normal sense, but the dynamically stripped nuclei of dwarf galaxies. In the Milky Way, we have ω Centauri as a possible example (e.g. Hilker & Richtler [45]). In this case, the LF at the bright end would depend on the accretion rate of dwarf galaxies, which plausibly is highest in massive galaxies in dense environments like NGC 1399 or M87. Or the formation history of the most massive clusters is principally different from the less massive ones. The peculiar cluster in NGC 6946 (Larsen et al. [57,58]) with a mass of about $10^6 M_\odot$ and an age of 15 Myr is surrounded by a round, star forming complex of about 600 pc diameter, which gives the impression of a disk-like structure with the massive cluster near its center. Such a configuration suggests that the cluster mass is determined or partly determined by accretion from a larger region, resulting in a steeper mass function for massive clusters.

Taking the second view of a log-normal function, one has the possibility to relate such a shape to coagulation processes by which GCs might have been formed through the merging of smaller subunits. Based on ideas by Harris & Pudritz [41], McLaughlin & Pudritz [66] developed a model, in which GCs form inside the cores of supergiant molecular clouds. These cores are built up by internal collisions and subsequent coagulation of smaller clouds. Star formation tends to partly disrupt these cores and in an equilibrium between coagulation and disruption, a mass spectrum of cores results, which directly resembles the GC mass spectrum. This is because the formation of GCs in these cores must occur with a high star formation efficiency in order for the GC to stay bound, i.e. the mass of the core is closely related to the mass of the final cluster.

See also Burkert & Smith [9] who argue that the mass spectra of GCSs can be fitted with a form $dN/dm \sim m^{-3/2} \cdot exp(-m/m_c)$, where m_c is a "truncation mass". Such a shape resembles the long-time solution of the coagulation model of Silk & Takahashi [84], initially starting with small progenitor clouds of equal mass.

Although the relation between the GC mass spectrum and the mass spectrum of the progenitor clouds is open to speculation, the power-law interpretation of the GCLF has some attractive features over the log-normal law interpretation.It relates the GCLF of old clusters system with young ones, and it offers a simple explanation by a direct link to the mass spectrum of molecular clouds.

It is amazing that molecular clouds in the Galaxy exhibit a mass spectrum resembling so closely that of GCs. See the introductory part of Elmegreen [18] for a compilation of references. This power-law behaviour may be the result of a fractal structure of the interstellar gas caused by turbulence and selfgravitation (Fleck [21], Elmegreen & Falgarone [17], Elmegreen [18]). Therefore the universality of the GCLF probably has its ultimate explanation in the universality of the interstellar gas structure.

15.12 Conclusions

We have seen that the method of globular cluster luminosity functions (GCLFs) allows one to determine distances to early-type galaxies, which are as accurate as those derived from surface brightness fluctuations (SBFs), once the conditions of high data quality and sufficiently rich cluster systems are fulfilled. The achievable accuracy of distance moduli is of the order 0.2 mag. The absolute turn-over magnitudes (TOMs), if calibrated by SBF distances, agree very well with those of the globular cluster systems of the Milky Way and the Andromeda nebula. Therefore the TOM is indeed a universal property of old globular cluster systems.

The comparison of SBF distances with GCLF distances reveals however many discrepant cases, in which the GCLF distances are systematically larger than the SBF distances beyond the limits given by the uncertainties. In some elliptical galaxies, direct evidence for the existence of intermediate-age globular clusters is available. In others, intermediate-age stellar populations are indicated by a variety of findings, which again may suggest a certain fraction of intermediate-age globular clusters as well. The S0-galaxies NGC 1023 and NGC 3384 exhibit a population of faint extended red clusters, which cause a fainter TOM, if they are included in the luminosity function.

That a globular cluster system, consisting mainly of old clusters, in which intermediate-age clusters are mixed in, exhibits a fainter TOM, can be understood by the dynamical evolution of cluster systems. Young globular clusters, which are found in large numbers in merging galaxies, are formed according to a power-law mass function with an exponent around -2. The cluster system then undergoes a dynamical evolution where the mass loss of individual clusters is caused by two-body relaxation, tidal shocks and mass loss by stellar evolution. This results in a preferential destruction of low-mass clusters, modifying the initial power-law mass function in such a way that the corresponding luminosity function on the magnitude scale shows a TOM which becomes brighter as the system evolves. The fading of clusters by stellar evolution counteracts this brightening to some degree.

The universality of the GCLF probably has its origin in the fractal structure of the interstellar medium, which results in a power-law mass spectrum for molecular clouds with an exponent of -2, similar to that found for young globular cluster systems.

Acknowledgements

Thanks go to Doug Geisler for a careful reading of the manuscript and helpful criticism. I am indebted to Søren Larsen for indicating unclear points and calling attention to NGC 1023 and NGC 3384. Many discussions with Boris Dirsch are gratefully acknowledged as well as support by the FONDAP Center for Astrophysics, Conicyt 15010003.

References

1. Aguilar L., Hut P., Ostriker J.P. 1988, ApJ 335, 720
2. Ashman K. M., Zepf S. E. 1998, Globular Cluster Systems, Cambridge University Press, Cambridge
3. Ashman K.M., Conti A., Zepf S.E. 1995, AJ 110, 1164
4. Barmby P., Huchra J.P., Brodie J.P. 2001, AJ 121, 1482
5. Baum W. 1955, PASP 67, 328
6. Blakeslee J.P., Davis M., Tonry J.L. et al. 1999 ApJ 527, L73
7. Blakeslee J.P., Vazdekis A., Ajhar E. 2001, MNRAS 320, 193
8. Brodie J.P., Larsen S.S. 2002, AJ 124, 1410
9. Burkert A., Smith G.H. 2000, ApJ 542, L95
10. Demarque P., Zinn R., Lee Y.-W., Yi S. 2000, AJ 119, 1398
11. Davies R.L., Kuntschner H., Emsellem E. et al. 2001, ApJ 548, L33
12. de Vaucouleurs G., de Vaucouleurs A., Corwin Jr. H.G. et al. 1991, Third Reference Catalogue of Bright Galaxies, Springer-Verlag Berlin Heidelberg New York
13. Dirsch B., Richtler T., Geisler D., Forte J.-C., Gieren W. 2003, AJ 125, 1908
14. Della Valle M., Kissler-Patig M., Danziger J., Storm J. 1998, MNRAS 299, 267
15. Drenkhahn G., Richtler T. 1999, A&A 349, 877
16. Elmegreen B.G., Falgarone E. 1996, ApJ 471, 816
17. Elmegreen B.G., Efremov Y.N. 1997, ApJ 480, 235
18. Elmegreen B.G. 2002, ApJ 564, 773
19. Fall S.M., Zhang Q. 2001, ApJ 561, 751
20. Ferrarese L., Ford H.C., Huchra J. et al. 2000, ApJS 128, 431
21. Fleck R.C., Jr. 1996, ApJ 458, 739
22. Fleming D.E.B., Harris W.E., Pritchet C.J., Hanes D.A. 1995, AJ 109, 1044
23. Freedman W., Madore B. 1991, PASP 103, 933
24. Freedman W., Madore B., Gibson B.K. et al. 2001, ApJ 553, 47
25. Fritze-v.Alvensleben U. 1999, A&A 342, L25
26. Forbes D.A., Brodie J.P., Huchra J.P. 1996, AJ 112, 2448
27. Gebhardt K., Kissler-Patig M. 1999, AJ 118, 1526
28. Geisler D., Lee M.G., Kim E. 1996, AJ 111, 1529
29. Georgakakis A.E., Forbes D.A., Brodie J.P. 2001, MNRAS 324, 785
30. Girardi L., Bertelli G., Bressan A. et al. 2002, A&A 391, 195
31. Gnedin O.Y. 1997, ApJ 487, 663
32. Gnedin O.Y., Ostriker J.P. 1997, ApJ 474, 223
33. Gómez M., Richtler T., Infante L., Drenkhahn G. 2001, A&A 371, 875
34. Goudfrooij P., Alonso M.V., Maraston C., Minniti D. 2001, 328, 237
35. Goudfrooij P., Mack J., Kissler-Patig M., Meylan G., Minniti D. 2001, 322, 643
36. Grillmair C.J, Forbes D.A., Brodie J.P., Elson R.A.W. 1999, AJ 117, 167
37. Hanes D.A. 1977, MNRAS 180, 309
38. Hanes D.A. 1979, MNRAS 188, 901
39. Harris W.E., Racine R. 1979, ARAA 17, 241
40. Harris W.E. 1991, ARAA 29, 543
41. Harris W.E., Pudritz R. 1994, ApJ 492, 177
42. Harris W.E. 1996, AJ 112, 1487
43. Harris W.E. 2001, "Globular Cluster Systems", in Star Clusters, Saas-Fee Advanced Course 28. Lecture Notes 1998, Swiss Society for Astrophysics and Astronomy. Edited by L. Labhardt and B. Binggeli, Springer-Verlag, Berlin, 2001, p.223
44. Hilker M., Kissler-Patig M. 1996, A&A 314, 357

45. Hilker M. Richtler T. 2001, A&A 362, 895
46. Jacoby G.H., Branch D., Ciardullo R. et al. 1992, PASP 104, 599
47. Kavelaars J.J., Harris W.E., Hanes D.A. et al. 2000, ApJ 533, 125
48. Kissler M., Richtler T., Held E.V. et al. 1994 A&A 287, 463
49. Kodama T., Arimoto N. 1998, MNRAS 300, 193
50. Kundu A., Whitmore B.C. 2001, AJ 121, 2950
51. Kundu A., Whitmore B.C. 2001, AJ 122, 1251
52. Kuntschner H., Lucey J.R., Smith R.J. et al. 2001, MNRAS 323, 615
53. Larsen S.S., Richtler T. 1999, A&A 345, 59
54. Larsen S.S., Richtler T. 2000, A&A 354, 836
55. Larsen S.S., Brodie J.P. 2000, AJ 120, 2938
56. Larsen S.S., Brodie J.P., Huchra J.P. et al. 2001, AJ 121, 2974
57. Larsen S.S., Brodie J.P., Elmegreen B. G. et al. 2001, ApJ 556, 801
58. Larsen S.S., Efremov Y.N., Elmgreen B. G. et al. 2002, ApJ 567, 896
59. Larsen S.S., Brodie J.P., Beasley et al. 2002, ApJ in press (astro-ph/0211434)
60. Lauer T.R., Tonry J.R., Postman M. et al. 1998, ApJ 499, 577
61. Leibundgut B. 2000, A&ARv 10, 179
62. Liu M.C., Charlot S., Graham J.R. 2000, ApJ 543, 644
63. Liu M.C., Graham J.R., Charlot S. 2002, ApJ 564, 216
64. Longhetti M. Bressan A., Chiosi C., Rampazzo R. 2000, A&A 353, 917
65. McLaughlin D.E. 1994, PASP 106, 47
66. McLaughlin D.E., Pudritz R.E. 1996, ApJ 457, 578
67. Murali C., Weinberg M.D. 1997, MNRAS 291, 717
68. Murali C., Weinberg M.D. 1997, MNRAS 288, 740
69. Murali C., Weinberg M.D. 1997, MNRAS 288, 767
70. Okazaki T., Tosa M. 1995, MNRAS 274, 48
71. Okon W.M.M., Harris W.E. 2002, ApJ 567, 294
72. Ostrov P.G., Forte J. C., Geisler D. 1998, AJ 116, 2854
73. Proctor R.N., Sansom A.E. 2002, MNRAS 333, 517
74. Pryor C., Meylan G. 1993, in "Structure and Dynamics of Globular Clusters", ASP Conf. Ser. 50, eds. S.G. Djorgovski and G. Meylan, p. 357
75. Puzia T.H., Zepf S.E., Kissler-Patig M. et al. 2002, A&A 391, 453
76. Racine R. 1980, in IAU Symp. 85, Star Clusters, ed. J.E. Hesser, Dordrecht, Reidel, p.369
77. Rejkuba M. 2001, A&A 369, 812
78. Richtler T. 1993, in The Globular Cluster-Galaxy Connection, ASP Conf.Ser. 48, eds. G.H.Smith and J.P. Brodie, p.375
79. Rix H.-W., Franx M., Fisher D., Illingworth G. 1992, ApJ 400, L5
80. Schweizer F., Seitzer P. 1992, AJ 104, 1039
81. Scorza C., Bender R. 1990, A&A 235, 49
82. Secker J. 1992, AJ 104 1472
83. Sil'chenko O.K. 1999, AJ 117, 2725
84. Silk J., Takahashi T. 1979, ApJ 229, 243
85. Strader J., Brodie J.P., Schweizer F. et al. 2002, AJ in press (astro-ph/0211156)
86. Surdin V.G. 1979, Sov. Astron. 23, 648
87. Surma P., Bender R. 1995, A&A 298, 405
88. Tammann G.A., Sandage A. 1999, in "Harmonizing Cosmic Distance Scales in a Post-Hipparcos Era", ASP Conference Series, vol. 167, eds. D. Egret and A. Heck. p. 204
89. Terlevich A.I., Forbes D.A. 2001, MNRAS 330, 547

90. Tonry J.L., Blakeslee J.P. Ajhar E.A. et al. 1997, ApJ 475, 399
91. Tonry J.L., Blakeslee J.P. Ajhar E.A. et al. 2000, ApJ 530, 625
92. Tonry J.L., Dressler A., Blakeslee J.P. et al. 2001, ApJ 546, 681
93. Trager S.C., Faber S.M., Worthey G., Gonzalez J.J. 1999, AJ 119, 1645
94. Vesperini E. 1998, MNRAS 299, 1019
95. Vesperini E. 2000, MNRAS 318, 841
96. Vesperini E. 2001, MNRAS 322, 247
97. Whitmore B.C., Schweizer F., Leitherer C. et al. 1993, AJ 106, 1354
98. Whitmore B.C., Schweizer F. 1995, AJ 109, 960
99. Whitmore B.C., Miller B.W., Schweizer F., Fall S.M. 1997, AJ 114, 1797
100. Whitmore B.C. 1997, in The Extragalactic Distance Scale, eds. M. Livio, M. Donahue, and N. Panagia, StScI Conf., Baltimore, p.254
101. Whitmore B.C. 2000, in STScI Symp. Ser. 14, ed. M. Livio (astro-ph/0012546)
102. Whitmore B.C., Schweizer F., Kundu A., Miller B.W. 2002, AJ 124, 147
103. Wiklind T., Henkel C. 2001, A&A 375, 797
104. Woodworth S.C., Harris W.E. 2000, AJ 119, 2699
105. Zhang Q., Fall S.M. 1999, ApJ 527, L81

Index